An investigation into the use of low aspect ratio spherical wells to reduce flow separation on an inverted wing in ground effect

Author:

Beves, Christopher Charles

Publication Date:

2009

DOI:

License:

UNSW

THE UNIVERSITY OF NEW SOUTH WALES

"AN INVESTIGATION INTO THE USE OF LOW ASPECT RATIO SPHERICAL WELLS TO REDUCE THE FLOW SEPARATION ON AN INVERTED WING IN GROUND EFFECT"

Christopher Charles Beves

A thesis submitted for the degree of Doctor of Philosophy

The University of New South Wales
School of Mechanical and Manufacturing Engineering

2009

Abstract

Flow separation is a source of aerodynamic inefficiency; however by using vortex generators the issue of flow separation can be controlled. This is of particular benefit to flows around bluff bodies which are susceptible to large scale separated flows, such as bodies in ground effect. Previous studies concerning heat transfer applications focused on the ability of low aspect ratio spherical wells (dimples) to produce vortices for flow mixing. Dimpled surfacing on an inverted Tyrrell026 airfoil in ground effect (indicative of high performance automotive aerodynamic applications e.g. Formula One) has been investigated for similar vortex enhanced wake reductions.

Experimental measurements using Laser Doppler Anemometry (LDA) and Particle Image Velocimetry (PIV) were taken inside a dimple to provide validation and verification of numerical analyses of dimple flows. The k-ω SST turbulence model showed good agreement to the experimental measurements. Additionally experiments were conducted using LDA and PIV with various configurations of dimple arrays placed from a fixed separation point of a 16° rearward facing ramp to determine how the array configuration influenced the large scale separation.

The airfoil wake with numerous dimple configurations and placements were measured using LDA. Results showed that an array of dimples with close dimple to dimple spacing there was flow recovery in the airfoil wake from the velocity deficit of $u/U_{o,min}$=-0.1 with no dimples, to $u/U_{o,min}$=0.4 with a dimple array, (at α=10°, ground clearance h/c=0.313). At α=10° reductions in the wake size of 30%, 33%, 58% and 68% were found for the ground clearances of h/c=0.112, 0.134, 0.224 and 0.313 respectively.

For numerous dimple array configurations, closely spaced dimple arrays were more effective in reducing the wake size, turbulence intensity and Reynolds stresses than those where dimple spacing was further apart. The chord wise location of the array on the wing affected the angle of incidence of the wing for which the wake was able to be reduced. Arrays placed towards the trailing edge improved wake losses at lower angles of incidence. Dimples placed further forward yielded the most improvement at higher angles of incidence, in part due to the increased venturi effect under the wing.

Acknowledgements

I would like to thank my supervisors Dr Tracie Barber and Professor Eddie Leonardi for their support and guidance throughout the project. They were always available when needed and no problem with the experimental results or wind tunnel design was ever too great to sit down, discuss and solve. Although it was an individual project, at times it seemed more like a team effort and I would like to express my sincere thanks to Ian Cassapi, Radha Kottieth and Vince Carnevale in the workshop for turning my drawings into reality, making me a better engineer as a result and having a good laugh along the way. Also thanks to Sammy Diasinos and Graham Doig in the office for making uni more enjoyable that it was probably meant to be in between LDA alignments, they were always there to bounce ideas off and turned late night hallway Frisbee into an extreme sport. To my friends Yonah, Bec, Samantha, Chris, Jordan, Michael, Michella and Dejan for making life outside of Room 505 and L110 more amazing than I could hope for. Finally I wouldn't be here without my family, so the biggest thank you of all is saved for Elizabeth, Allan, Geoffrey, my brother David and my grandparents Dorothy and Charles, Jocelyn and Richard. I quite possibly would have not survived this whole ordeal without them, and this who this thesis is dedicated to.

Table of Contents

List of Figures

List of Tables

Nomenclature

α	Angle of Incidence
α_{stall}	Stall Angle
α_{1D}	Angle of Incidence of 1D LDA probe head to horizontal plane
α_{2D}	Angle of Incidence of 2D LDA probe head to horizontal plane
c	Airfoil chord length
c_{flap}	Airfoil flap chord length
C_D	Coefficient of drag
C_L	Coefficient of lift
C_p	Coefficient of pressure
Δ	Difference
Δt_p	PIV twin laser pulse separation time
δ	Dimple depth
δ_{BL}	Boundary Layer thickness or height
δ_f	Fringe spacing
d_p	Particle diameter
D	Dimple Print Diameter
D_{Ball}	Ball Diameter
f_D	Doppler Frequency
H	Height of channel or test section
h_{VG}	Height of Boundary Layer protruding vortex generator
l_{VG}	Length of vortex generator
$h_{VG,Dimple}$	Height of Flow Effect from Submerged Dimple above Surface
h/c	Airfoil ground clearance gap height to chord ratio
k	Turbulent Kinetic Energy
λ	Wavelength of light
max,min	Maximum or minimum value
ρ	Air density (kg/m^3)
Re_{chord}	Reynolds number based on airfoil chord
Re_D	Reynolds number based on dimple diameter
Re_H	Reynolds number based on test section or channel height
Tu	Turbulence Intensity

U_o	Freestream Velocity
u, v, w	Velocity components
u', v', w'	Velocity component fluctuations of u, v, w
u-RMS	u component Root Mean Square (RMS) Velocity
uu	Reynolds stress component of: turbulent normal stress
uv	Reynolds stress component of: primary shear stress
u/U_o	Normalized u velocity component to freestream velocity
$u/U_{o,min}$	Minimum value of normalized u velocity component
$u/U_{o,max}$	Maximum value of normalized u velocity component
v/U_o	Normalized v velocity component to freestream velocity
w/U_o	Normalized w velocity component to freestream velocity
Ω	Vorticity
Ω_x	Vorticity in X axis or Streamwise Vorticity
$\Omega_{x,max}$	Maximum value of Streamwise Vorticity
x/D	Distance x direction relative to dimple print diameter 'D'
y/D	Distance y direction relative to dimple print diameter 'D'
y/c	'y' or vertical position in the airfoil wake
$(y/c)^T$	Vertical position in the wake translated to trailing edge at h/c=0.313
x_{sep}	Distance to Flow Separation Point
x/c	'x' or dowsntream position in the airfoil wake
y_{norm}	Distance normal to airfoil surface
z/D	Distance z direction relative to dimple print diameter 'D'

Introduction and Literature Review

1

This section introduces the main topic and the literature that underpins the relevant work in the areas covered. Several different previously researched areas are merged to outline the aim of the thesis, these include: numerical and experimental studies involving low-aspect ratio spherical wells, golf ball aerodynamics, passive vortex generators and ground effect aerodynamics of airfoils. The scope of the project is outlined into how the two areas of the low-aspect ratio spherical well investigations and the inverted airfoil in ground effect analysis fuse to study the benefits of modifying the airfoil surface.

1.1 Introduction to Topic

Surfaces employing a series or array of low aspect-ratio spherical wells (dimples), have the ability to efficiently produce discrete vortices and turbulent mixing in a flow near a surface due to their positioning beneath the boundary layer, with little pressure loss (i.e. in heat exchangers) or drag penalty (i.e. golf balls). Wider ranging aerodynamic applications of using dimples as vortex generators are lacking. Therefore an investigation of whether dimples can reduce flow separation on a body in ground effect is timely; particularly as the transport industry seeks to increase aerodynamic efficiency.

Ground effect aerodynamics, as the name suggests, refers to the aerodynamic study of a body that is in close proximity to the ground. This can take various forms; lifting airfoils with the suction surface away from the ground, downforce generating or inverted airfoils with the suction surface facing the ground, specific shapes (aircraft, vehicles etc.) or a generic shape such as the Ahmed body. The aerodynamic characteristics of ground effect bodies have larger wakes; more pronounced flow separation (even for low angles of incidence), higher drag and earlier flow separation points compared to more conventional freestream aerodynamic bodies, i.e. aircraft in flight. The need to control the size of the wake can be related to drag reduction and has led to the use of vortex generators in order to suppress the size and extent of flow separation. The use of traditional boundary layer protruding vortex generators have been used to reduce flow separation, but efficiency is limited due to additional form drag of the individual generators. Thereby utilizing the sub-boundary layer vortex

generation by using dimpled surfacing should result in reductions of certain wake characteristics.

The flow in a single dimple and the flow separation of a rearward facing ramp as well as an inverted Tyrrell026 airfoil in ground effect, are measured experimentally. The Laser Doppler Anemometry and Particle Image Velocimetry measurement techniques are used to focus on the wake structure changes in velocity, turbulence intensity and Reynolds stresses. These properties are measured with respect to a base-line flow separation structure with no dimple array, and then compared to the change in the flow separation structure with the use of various different dimple configurations and locations. This is in order to develop an understanding of which dimple array configuration will be most effective in reducing a separated flow structure of a ground effect body that can have a migrating separation point.

1.2 Motivation and Applicability of Research

Previous studies of using dimpled surfaces to improve near wall flow mixing involved heat transfer applications and as vortex generators on turbine blades and golf balls. Most of the benchmark numerical work on dimples was conducted by Isaev and Leont'ev, where as Ligrani's work focused on experimental investigations. The use of dimpled surface treatment may allow for greater range of angle of incidence and potentially greater airfoil camber design than would otherwise be possible. The applications are broad ranging and not limited solely to ground effect aerodynamic bodies such as automotive vehicles or aircraft. Turbine blades used in power generation such as wind and hydrodynamic (conventional as well as wave and tidal) may also benefit from generating higher airfoil sectional lift (due to more camber or higher angle of incidence) for similar drag.

1.3 Literature Review Introduction

An extensive range of literature (both experimental and numerical) exists for each of the main segments of the literature review; dimple related flow measurements, standard vortex generator studies on separated flows and wings in ground effect. Figure 1.1 outlines how the synthesis of these individual topics forms the literature review as a whole.

Literature Review

Dimples

- Single Dimple
- Array of Dimples

  (channel, duct or pipe)

Previous Applications:
- Golf Balls
- Turbine Blades

FOCUS

Vortex Generators

Standard Vortex
Generators on
Separated Flows

Airfoils

Wings in Ground Effect

(inverted & non-inverted)

Vortex Generators applied
to Wings in Ground Effect
(inverted & non-inverted)
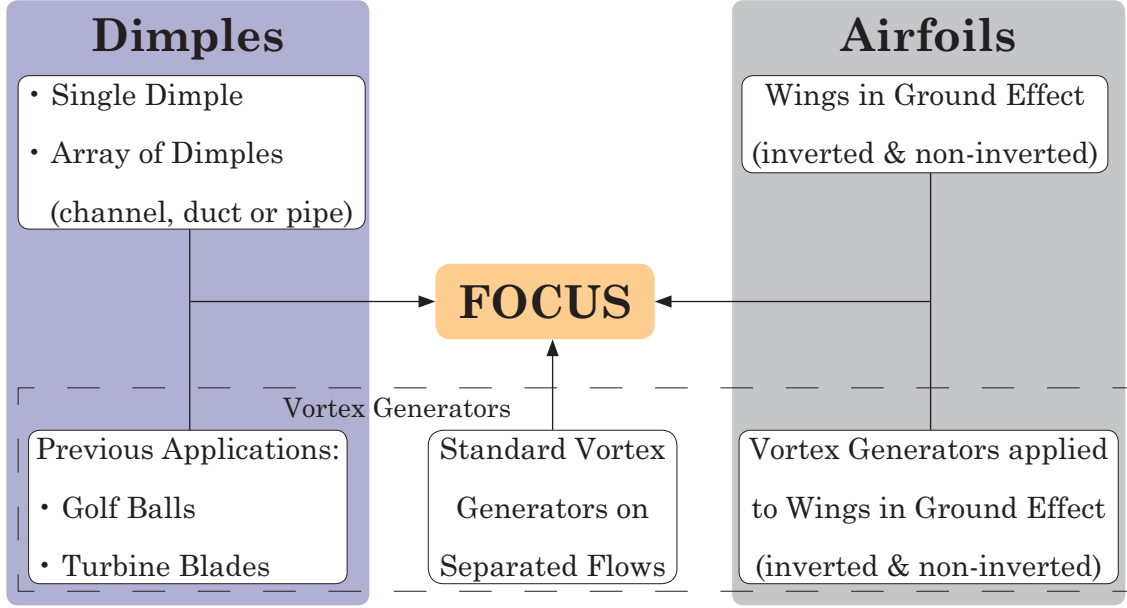
Figure 1.1 Flow Chart Outlining Literature Review

1.3.1 Single Dimple Flow Dynamics

1.3.1.1 Experimental Results

Khalatov & Byerley et al. (2004) studied the flow structure in a single spherical dimple with dimple depth to dimple print diameter (δ/D) of 0.1. Dimple print diameter refers to the diameter of the dimple rim on the surface which it is recessed into. The channel height to dimple print diameter (H/D) ratio was 12, so upper wall effects were minimal. They showed that as the dimple print diameter based Reynolds number (Re_D) increases beyond 5125 the recirculation covers most of the dimple's volume. The pathlines injected upstream that are in-line with the dimple's edge are drawn in towards the dimple slightly, which they attributed to a slight suction or a 'vacuum effect'. Their laminar numerical simulation proved good agreement with the flow visualization experimental images captured downstream of the dimple.

Chew & Khoo (2005) completed a similar flow visualization study for a single dimple with a range of δ/D=0.05-0.50, and H/D=10. Their observations showed for δ/D=0.2 at Re_D=2277, the flow is laminar and two stable, symmetric vortices are present in the dimple linked by a transverse-axis vortex. As Re_D increased one vortex increased in strength, becoming dominant with an inclined axis for 5420<Re_D<5792 and the flow structures became unstable. At Re_D>6183, the flow became symmetric again and tornado-like vortices at each side of the dimple were ejected.

Ezerskii & Shekov (1989) showed the tornado-like vortices leaving the dimple have a disturbing action on the flow 3D-5D downstream. The vortices join together approximately 0.5D-2.5D downstream from the dimple.

The study by Chew & Khoo (2005) also investigated the effect of dimple rim rounding, which indicated the separation line is located further inside the rounded off dimple, they suggested this will lead to lower form drag, whereas sharp edged dimples stabilised the vortices in the dimple. They remarked that complex vortex structures are generated inside a dimple with $\delta/D > 0.2$ irrespective of edge rounding. Additionally, strong vortices are ejected out of the dimple and high turbulence intensity exists downstream. They concluded that it is likely to be difficult to employ deeper depth dimples to realize drag reduction on a flat plate under turbulent flow conditions as a result of this. Kesarev & Kozlov (1993) showed for a vortex leaving a dimple with $\delta/D = 0.5$, the ejected vortices actually pushed oncoming external flow away and likely to increase drag.

1.3.1.2 Numerical Analysis

Reynolds Averaged Navier-Stokes numerical simulations into single dimple flow dynamics have been conducted by various researchers to determine the influence that the δ/D and Reynolds number influences play. The main parameters of the numerical analyses are listed in table 1.1.

Table 1.1 Single Dimple Numerical Analysis Parameters

Reference	Grid Step	δ/D	Re_D	Turbulence model
Isaev & Kharchenko (1994)	0.027D	0.067	4.138×10^4	$k\text{-}\varepsilon$
Isaev & Leont'ev (1999)	-	0.06-0.22	$700\text{-}2.52 \times 10^4$	$k\text{-}\varepsilon$
Isaev & Leont'ev (2000)	0.005D	0.175	2.34×10^4	Low Re-Menter
Isaev & Leont'ev (2001)	0.005D	0.22	$102\text{-}2.5 \times 10^3$	Low Re-Menter
Isaev & Leont'ev (2002)	0.0008D	0.14	$2.6 \times 10^4\text{-}6.4 \times 10^4$	Low Re-Menter
Isaev & Leont'ev (2003)	0.0005D	0.04-0.24	1.0×10^4	$k\text{-}\omega$ SST
Isaev, Leont'ev et al. (2003)	0.0008D	0.03-0.2	2.34×10^4	$k\text{-}\omega$ SST
Wang et al. (2003)	-	0.2	2.5×10^3	$k\text{-}\omega$ SST
Lee & Ferguson (2004)	-	0.13, 0.26, 0.5	5.9×10^4	$k\text{-}\varepsilon$

1.3.1.2.1 Flow Structure

Due to local flow acceleration, regions of low pressure occur in front of and behind the dimple near the surface (Isaev & Kharchenko 1994). Isaev & Kharchenko (1994) concluded that a likely triggering mechanism for generating three-dimensional vortex structures is the flow accelerating and turning toward the symmetry plane in the zone of the dimple facing the flow. This was an initial study with very shallow dimple depth and low grid density and no flow separation in the dimple resulted; as for similar depth in experimental results (Chew & Khoo 2005).

Isaev & Leont'ev (1999) showed the flow into the dimple folded over on itself toward the incoming external flow, thus forming the detached zone occupying most of the cavity (observed in Khalatov & Byerley et al. 2004 and Chew & Khoo 2005). Deeper cavities exhibit liquid circulation that is drawn from the peripheral wall layers, the 'vacuum effect' (Khalatov & Byerley et al. 2004), and then recirculates in the dimple. This 'vacuum effect' draws fluid from the wall layers into the dimple and forms a jet flow from the dimple in the symmetry plane zone. Pathlines show fluid both in the cavity and outside it, are involved in vortex motion, interacting on the symmetry plane. The wall layer velocity vectors also demonstrated the initiation of flow circulation in the horizontal plane.
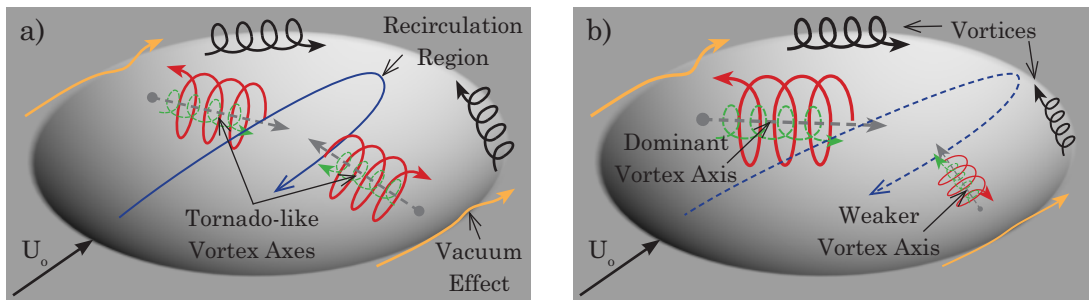
Figure 1.2 Flow Structure Characteristics of a Dimple a) Symmetric (Low Re_D) b) Asymmetric (High Re_D)

The open side 'windows' (Isaev & Leont'ev 2000), are shown to form at $Re_D \approx 10^3$ (Isaev & Leont'ev 2001). Isaev & Leont'ev (2001) suggested that if the fluid is trapped in these structures, which form on the side slopes of the dimple, it can leave the cavity. Pathlines reveal the rearrangement of the vortex structure from low to moderate Reynolds numbers is associated with the formation of tornado-like flows emerging from the region of the foci on the surface of the dimple (figure 1.2a). As $Re_D > 10^3$, fluid

from the side region moves to the centre and subsequently is swept out of the symmetry plane. The axes of the tornado structures at higher Reynolds numbers are straight lines that connect the foci on the walls of the dimple with the plane of symmetry. As Reynolds number increased the minimum value of the transverse velocity that characterizes the degree of the 'vacuum effect' also increases. The separation region becomes larger with increasing Reynolds number and the separation point moves towards the upstream dimple edge. At $Re_D=2.5\times10^3$, two vortical cells are formed that are symmetric to the plane of the flow.

1.3.1.2.2 Reynolds Number Effects

In a study by Isaev & Leont'ev (2002) a finer grid than previous studies made it possible to use the low-Reynolds zonal model of Menter, which they remark is more suitable for calculating near-wall turbulent flows. The development of the separated flow region changed with increasing Reynolds number, becoming slightly asymmetric (see figure 1.2b). The separated flow is intensified, with the maximum velocity of the reverse flow in the dimple increasing by 20% over the Reynolds number range. In the zones adjacent to the symmetry plane there are two vortex rings. Isaev & Leont'ev (2002) observed that each of these vortex rings is built into a curvilinear vortex tube or 'cocoon', see green and red lines around the tornado axes in figure 1.2 with an inner channel (green) transporting fluid from the side of the dimple to the centre. The fluid flows back to the sides (red) over the outer surface of the vortex tube, and a tornado-like structure transfers fluid through the dimple. Particles enter this zone from the incoming flow after several revolutions in the separation region.

1.3.1.2.3 Dimple Depth (δ/D) Effects

Varying depth for the same Reynolds number was studied by Isaev & Leont'ev (2003). The normal velocities increased by 30% for δ/D=0.22 and by 18% for δ/D=0.24, indicating an optimal vorticity production for δ/D=0.22. The maximum value of turbulent energy (*k*) decreased upon approaching δ/D=0.22, in this case *k* was ten times that of the boundary layer. Results obtained in an earlier study by Isaev & Leont'ev (2002), where δ/D=0.14, results showed *k* reaches a value five times higher than the boundary layer for $Re_D=6.4\times10^4$, the peak magnitude differing little from $Re_D=2.35\times10^4$. However at the higher Reynolds number they indicated that the zone of increased turbulence had a larger length.

As depth increases the generation of turbulence by the dimple becomes greater showing agreement with the view of dimples acting as elements of artificial roughness (Isaev & Leont'ev et al. 2003). Isaev & Leont'ev et al. (2003) showed that with increased depth the separation zone occupied more of the dimple, and the peak reverse flow velocity reached 20% of the freestream for δ/D=0.2 (a similar value suggested in Isaev & Leont'ev 2002). Using comparable grid, boundary conditions and turbulence model the peak reverse flow velocity is 25% of the freestream for δ/D=0.24 at a lower Reynolds number (Isaev & Leont'ev 2003).

The results from the investigation by Isaev & Leont'ev et al. (2003) showed the vortex motion became asymmetric for δ/D=0.18-0.2. The 'side windows' remained open on one side only relative to the incoming flow, closing the window on the other side, in this case one vortex cell actually disappears. Results from Isaev & Leont'ev (2001), Isaev & Leont'ev (2003) indicated a symmetrical vortex structure maintained up to δ/D=0.22, for a lower Reynolds number.

1.3.1.2.4 Unsteady Flow Characteristics

A time dependant analysis conducted by Wang et al. (2003), used a time step of 0.02sec, and tracked the movement of particles released in the dimple. Particles released near the dimple edge vortex cores were sucked into the centre of the vortices and ejected onto the centre plane of the dimple. Particles released near the centre of the dimple circulated around the transverse vortex axis with little transverse movement. Particles released in between these two points spiralled into the centre of the dimple, which they suggested was a symmetric 'horse-shoe' vortex in the dimple. This demonstrated the the presence of a vortex tube transporting fluid from the side of the dimple to the centre (Isaev & Leont'ev 2002); shown in figure 1.2a & figure 1.2b.

Investigating higher Reynolds number effects with increasing δ/D, Lee & Ferguson (2004) looked into unsteady flow phenomena. Despite the coarse grid that was used (211,000), they were able to show two vortex centers form and grow until one vortex leaves the dimple. They suggest this confirms oscillation of the vortex centre's, and comment although two vortex centres exist in the dimple; there is little mass transfer between them.

1.3.1.2.5 Dimple Geometry

Flow for both symmetric and asymmetric dimple geometries was investigated by Isaev & Leont'ev. (2000). The high ejection ability of the symmetric vortex structure in the symmetric dimple is evident, which they remarked is due to the open side 'windows' at the dimple edge intensifying the vortex. The change of the flow structure for the asymmetric dimple is marked by a single-vortex tornado, with a snail-like flow structure. This is a result of the transverse velocity in the asymmetric vortex structure doubling. Another study showed that for an upstream induced flow perturbation, the symmetric dimple can behave like an asymmetric dimple of equivalent Reynolds number (Isaev & Leont'ev. 2000).

Flow visualisation in both Khalatov & Byerley et al. (2004) and Chew & Khoo (2005) used the technique of injecting dye into the flow inside and around the dimple. The Reynolds number of the dye being injected from the ports was not given for either study to be able to ascertain the level of turbulence input into the flow by the dye injection. Clearly low speed, sensitive flow exists within the dimple and actively injecting dye may impact on the stability of the dimple, and the range of Reynolds numbers at which it exhibits different flow features as predominately studied in Chew & Khoo (2005). Comparison with numerical studies showed similarities only with flow recirculation size in the dimple, the 'vacuum effect', the presence of tornado-like vortices and some shedding phenomena. The numerical studies showed no direct comparison of turbulence model for the same δ/D and Re_D to determine which model is more appropriate, nor did they attempt to match conditions to previous flow visualisation experiments. The dependency of the solution with respect to the grid size as outlined in AIAA Guide for Validation and Verification of CFD (1998) was only conducted in Isaev & Leont'ev (2001). So whilst numerical work exists on the flow in the dimple, the nature of its accuracy with numerical validation and verification to experimental measurements remains undetermined.

1.3.2 Dimple Array

Shchukin & Kozlov (1998) conducted a literature survey into the use of dimple arrays. They conclude that for flow passing over a system of dimples, the hydrodynamics in any of them are roughly equivalent to the flow over a single dimple.

1.3.2.1 Flow Visualization

Flow visualization experiments by Ligrani (2000) looked at various types of vortices produced by components in turbine engines. For dimples of D=50.8mm, δ/D=0.2, and Reynolds number based on channel height (H) of Re_H=1250, and H/D=0.5, smoke wires were used to track the flow. Images taken in a spanwise normal plane to the flow indicated the dimples produced a mushroom shaped cloud from the central portion. Ligrani (2000) commented this region corresponded to the strongest upwash down the centre-line of each dimple (also noted in Mahmood & Ligrani 2002). The upwash region and vortex pair are approximately symmetric, as seen in figure 1.3. Images taken at 45° diagonals to the flow indicated that secondary flows in each vortex pair possibly impact on the flat surface adjacent to each dimple. Ligrani (2000) noted that as a result of this, the smaller vortex pairs that are formed near the rim of the dimple periodically impact on the downstream edge of the next dimple and the downstream flat surface.
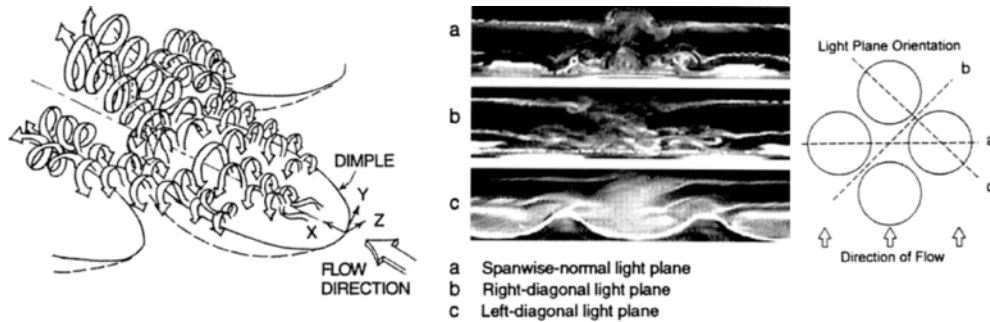
Figure 1.3 Instantaneous flow visualization images from dimple array; δ/D=0.2 and Re_H=1250 Ligrani (2000)

Mahmood & Ligrani (2002) presented flow structures in an array of dimples D=50.8mm and δ/D=0.2, Re_H=600, 900 and 2560, for H/D=0.25, 0.5 and 1 respectively. The technique and experimental set up was identical to Ligrani (2000). The images taken suggest that regardless of H/D, each dimple in the array periodically shed vortical fluid and vortex pairs from the dimples, which became stronger and less periodic as H/D decreased. This phenomenon is reflected in experiments measuring the vortex strength with changing H/D (Ligrani & Harrison 2001).

Ligrani et al. (2001) commented that the periodicity and organization associated with the shedding of vortical fluid from individual dimples, is one of the most important features of dimpled surfaces. In a dimpled surface the behaviour of the flow in each of the dimples appears to be linked; evidenced by the flow visualization conducted.

Vortices were shed simultaneously with those from dimples in the same streamwise row, but out of phase with those from adjacent upstream or downstream dimple rows. They believed the pressure variations in one dimple affected the variations in other adjacent dimples. It is suggested the fluctuation in pressure in an individual dimple is a result of the outward flow from each dimple, as vortical fluid is expelled it is then followed by an inflow into the dimple.

The flow visualization experiments mentioned above did not state the wire diameter and its Reynolds number in order to determine the impact of the wire presence producing turbulence, especially as they were located very close to the dimple surface. Only video footage was used to capture the images and no information relating to the lens aperture or exposure time was mentioned to be able to account for the level of blurring or streaking as the video frames were captured.

1.3.2.2 Friction Experiments

Numerous experiments investigating the heat transfer capabilities of dimpled surfaces also include friction performance tests for a range of Reynolds numbers. These dimpled surfaces comprise array patterns of a specific dimple-to-dimple spacing (referenced to the dimple print diameter D), and the angle at which the following row of dimples is translated from the first. In some studies, the friction factor from the moody diagram or the measured smooth surface equivalent test (f_o) is used to normalize the result, in others the smooth Fanning friction factor (C_{fo}) is used. A full list of friction test experimental variables is listed in table 1.2.

Ekhad & Nasir (2001) measured the friction factor with dimples on one wall. The normalized friction factor decreased from 3.0 at Re_H=10K to remain constant at 2.7 for Re_H>30K. They concluded it is evident that dimples did not enhance the pressure drop that typical vortex generators or ribs do. In a similar single walled experiment, with a greater δ/D value, Burgess & Olivera (2003) showed f/f_o increasing from 1.5 to 3 as Re_H increased. The conclusion was that generally f/f_o increases as the number of dimpled surfaces or δ/D increased. Curiously their δ/D is twice that of Ekhad & Nasir (2001), yet for low Re_H their f/f_o is half.

Friction factors were measured and compared to a smooth pipe with and without dimples by Bunker & Donnellan (2003). Normalized C_f for δ/D=0.23 results in a C_f/C_{fo} increase of 2.2-3.0 over the Reynolds number range, less than the increase of 4.2-6.8

for deeper dimples of $\delta/D=0.27$. It was shown that the larger spaced array pattern for a given δ/D marginally resulted in the lowest friction. They concluded the effect of concavity depth clearly dominated the friction factor enhancement. Shchukin & Kozlov (1998) referenced a study in Russian by Belen'kii (1992), in which it was noted an un-staggered (in-line) array of dimples reduced friction by 25% and a checkerboard (staggered/offset) array pattern by 35%. By using a staggered row offset the friction may show higher spacing dependency, as there is less interference with the dimple rim vortices being formed by those in the next downstream row.

Table 1.2 Friction Experimental Parameters

Reference	Re_H	D(mm)	H/D	δ/D	Spacing (D)	Friction
Ekkad & Nasir (2001)	10×10^3-65×10^3	19	1.33	0.167	1.33	f/f_o 3-2.7
Mahmood & Sabbagh (2001)	5×10^3-35×10^3	50.8	0.5	0.2	1.14	f/f_o 4-3
Bunker & Donnellan (2003)	20×10^3 90×10^3	8.738 10.312	4.36 3.69	0.229 0.271	1.24-1.5 1.05-1.28	Cf/Cf_o 2.2-3.0 Cf/Cf_o 4.2-6.8
Bunker & Gotovskii (2003)	5×10^3-20×10^3	3.3	1	0.227	1.21	ΔP (mmH20)
Burgess & Olivera (2003)	12×10^3-70×10^3	50.8	1	0.3	1.61	f/f_o 1.5-3

Bunker & Gotovskii (2003) analysed the effect of different dimple geometry cavities including; cone shaped, straight cylindrical and standard dimples on one surface. These were tested in three channels; straight, converging and diverging. The dimples showed 5% increase in friction coefficient over smooth surfaced straight channel (with experimental uncertainty at $\pm5\%$), this was not repeated for the cone geometry. The converging and diverging tests looked directly at the static pressure loss, as they point out that the friction coefficient for variable area channels is not clear. It was evident that hemispherical and cone cavities resulted in lower pressure drops compared to the other cavities tested. The cone cavity outperformed the dimple for the diverging channel test.

For the friction factors stated, dimpled surfaces show an advantage over other boundary layer vortex generating methods. The study of Mahmood & Sabbagh (2001), looked at protruding the equivalent dimple volume into the flow. For the channel with protruding dimples f/f_o=4-3 (decreasing), for the smooth channel it was roughly constant at f/f_o=1.5 for Re_H range. They concluded this was a direct result

of the protrusion form drag. Bunker & Donnellan (2003) provided the explanation that the dimple vortex penetrates and interacts with the mainstream flow, bringing fresh core fluid to the surface. As the motion is organized rather than the more dissipative effect of shearing layers, the pressure loss is less. This is an important explanation as to why dimples pose a benefit in the application to airfoils in order to improve their aerodynamic efficiency, than traditional boundary layer protruding vortex generators.

1.3.2.3 Pressure Probe and Hot Wire Measurements

Flow measurements relating to dimpled surface performance in heat transfer augmentation were performed by; Ligrani & Harrison (2001), Ligrani & Burgess (2005) and Ligrani et al. (2005). Flow measurements were taken close to the dimpled surface using a five hole pressure probe and hot wire techniques. The physical constraints of the probes meant that measurements were not taken closer than 2.5mm to the surface. Table 1.3 references the key experimental parameters.

Table 1.3 Pressure Probe and Hot-Wire Experimental Parameters

Reference	Re_H	D(mm)	H/D	δ/D	Spacing (D)
Ligrani & Burgess (2005)	3.7×10^3 - 20×10^3	50.8	1	0.1	1.62
Ligrani & Harrison (2001)	0.6×10^3 - 11×10^3	50.5	0.25	0.2	1.62
Ligrani et al. (2005)	2.1×10^3 - 20×10^3	50.8	1	0.1, 0.2, 0.3	1.62

The studies listed in table 1.3 consistently showed large positive magnitudes of normal velocity near the central portion of the dimple; indicating fluid moving away from the surface in the upwash region. The normal velocity increased as δ/D increased, due to differing rates of flow ejection. Streamwise velocity, total pressure and static pressure all showed deficits near the dimpled surface at locations where upwash regions were present. Spanwise velocity measurements showed positive and negative directions either side of the upwash region, which was a similar trend for vorticity.

Reynolds normal stresses showed increases in this region too, all corresponding to the primary central vortex pair. Ligrani & Burgess (2005) and Ligrani et al. (2005) noted

that the deeper dimples produced higher magnitudes of; time averaged streamwise vorticity, vortex circulation, longitudinal Reynolds normal stress as well as greater shear, mixing and strain rates. In both studies the assumption was that this was due to increased production of turbulent kinetic energy and increased three-dimensional turbulent transport. Ligrani et al. (2005) noted the effect of dimples in altering time-averaged flow behaviour occur mostly within one-half of one dimple print diameter from the dimple.

1.3.2.4 Numerical Analysis

Numerical investigations by Park & Desam (2004), Won & Ligrani (2004) and Ligrani & Park (2005), analyzed the flow structure of a dimpled surface in a channel. All numerical models used the k-ε Realizable turbulence model with grid y^+=0.5, not utilizing any wall functions. Key experimental parameters for the three studies are listed in table 1.4.

Table 1.4 Numerical Array Reference Parameters

Reference	Re_D	D(mm)	H/D	δ/D	Spacing (D)	Array angle
Park & Desam (2004)	12×10^3	50.8	1	0.3	0.81	45°
Won & Ligrani (2004)	10×10^3	50.8	1	0.1, 0.2, 0.3	0.81	45°
Ligrani & Park (2005)	12×10^3	50.8	1	0.3	0.81	45°

The normalized streamwise, normal and spanwise velocity augmentations all corresponding to the central vortex pair for the numerical results of Park & Desam (2004), showed similarity in shape and location as the experimental results of Ligrani & Harrison (2001), Ligrani & Burgess (2005) and Ligrani et al. (2005). The velocity vectors are dominated by streamwise flow and are greatest near the downstream and upstream rim of the dimple, indicating regions of local flow acceleration, also noted in Isaev & Kharchenko (1994). The largest value of spanwise velocity is at the dimple's spanwise edge, which were unable to be measured experimentally. This increased spanwise velocity is attributed to the edge vortex pairs zig-zagging through the array (Park & Desam 2004), and may also be a result of an increased 'vacuum effect' due to lower pressure in the dimple as depth increases.

Park & Desam (2004), showed the counter-rotating flow recirculation zones in the

upstream half of each dimple form the central vortex pair, which is periodically shed. During each period the outflow of fluid from the dimple is followed by an inflow, occurring concurrently or sequentially with the outflow event. The central vortex pair and outflow region interact with the bulk flow as it advects downstream, enhancing fluid mixing. Stronger vortex pairs form near the edges of each dimple, which they indicate is enhanced by a staggered surface array. The multiple pairs of vortices that are ejected in an array interact with each other as they move downstream. Park & Desam concluded this ordered interaction increases local three-dimensional turbulence.

Won & Ligrani (2004) investigated the influence of dimple depth on flow structure and vorticity. Their results showed good agreement with results obtained experimentally for increasing δ/D (Ligrani et al. 2005). The normalized streamwise velocities generally are lowest in the bottom of the dimples as δ/D increased. The normalized normal velocity is generally higher outside of the dimple above the flat surface just downstream of it due to flow ejection. Normalized spanwise components generally became larger within the dimple on the slope near its edge as the depth increased.

The results of Won & Ligrani (2004) consistently showed the vorticity is higher at the spanwise edges than the vortices produced by the central vortex pair providing agreement with experimental data (Park & Desam 2004). These vortices then advect onto the flat surface downstream of the dimple (measured in Ligrani & Harrison 2001, Ligrani & Burgess 2005 and Ligrani et al. 2005). Won & Ligrani (2004) made comparisons with experimental data at a much higher Reynolds number $Re_D=2.0 \times 10^4$, the nature and measurement of which was not explained. The comparison shows qualitative agreement for regions of high and low velocity and vorticity in the spanwise normal planes investigated and were only measured above the dimple.

Ligrani & Park (2005) studied depressions of similar relative cavity depth to diameter ratio as a spherical dimple of $\delta/D=0.3$ for various geometries. These cavity geometries included arrays of cylindrical dimples with the base tilted to face downstream, cylindrical dimples with an un-tilted base and several combinations of similarly tilted-base triangular cutouts. The steady-state results show spherical dimples and the tilted-base cylindrical dimples are superior to other forms of depressions in generating repeating, coherent vortex structures. The peak vorticity is consistently

higher in the spherical dimple case, and around half the value for the tilted-based cylindrical dimple.

The numerical studies investigated both grid size and iterative convergence tests to be able to account for the degree of numerical error in the solutions. No check of using a different turbulence model for the same numerical model was conducted. The experimental comparison was for a Reynolds number twice that of the numerical model, which could have been easily matched. Essentially the comparison showed the central vortex pair from the dimple producing the large scale vortices and flow structures above the dimple, missing the stronger vortices inside the dimple. This was a limit of the experimental measurements as the hot wire and pressure probes could not measure within 2.5mm of the wall.

1.3.3 Golf Ball Aerodynamics

Dimples have been used on golf balls for drag reduction for most of the 20th century since it was noticed in the mid 19th century that rougher/older balls tended to fly further than the smooth surfaced new ones. A study into golf ball lift and drag with varying spin by Davies (1949) used a standard British golf ball, of diameter (D_{Ball})=1.68inch and effective roughness parameter δ/D_{Ball}=0.77x10^{-2}. The ball was spun at different speeds and dropped into a wind tunnel section for Re_{DBall}=9.29x10^4. The lift and drag forces were derived by crudely measuring the translational drift of the ball from the drop point and averaged over 5 drops. Large variation in the drag results existed for spin speeds greater than 4000rpm, where the smooth sphere actually had lower drag than the dimpled ball (potentially due to being in the critical Reynolds number regime for smooth spheres with higher surface roughness). No indication was given of any surface roughness or additional surface treatment of the smooth sphere.

Bearman & Harvey (1976) conducted an investigation into the lift and drag forces of a golf ball in a wind tunnel; a support system via wires locating the ball in a fixed position in the wind tunnel. The wires enabled a motor in the ball to spin it to the required speed; the ball was scaled to a diameter of 102.75mm and subsequently a Reynolds number of Re_{DBall}=6.47x10^5 resulted (higher than Davies 1949), with roughness δ/D_{Ball}=0.9x10^{-2}. Lower C_D values are achieved with dimples for all spin speeds compared to a smooth sphere, but retain some of the C_D instability seen in

Davies investigation. The amount of harmonic instability and noise of the motor in the ball is not indicated, which if quite high may have the potential to impact on the force values. They did not repeat a smooth ball experiment which would have been a good base line C_D comparison using their experimental technique.

The results of Bearman & Harvey (1976) indicated that dimpled balls showed a critical Reynolds number behaviour (i.e. the point of rapid C_D reduction), at lower Reynolds numbers than a smooth sphere, which they suggested showed that dimples are effective in tripping the boundary layer. Their investigation into using hexagonally shaped dimples indicated they produce marginally lower drag values, the most extreme C_D improvement being only 3-4%. No uncertainty analysis of the force values were provided; however they remarked that the hexagonal dimples may shed more discrete vortices due to their straight edges into the boundary layer.

Choi et al. (2006) used a load cell to measure lift and drag on a golf ball with no spin and conducted hot wire velocity measurements inside the dimples. The ball diameter was 150mm, $\delta/D_{Ball}=0.4 \times 10^{-2}$ and $Re_{DBall}=0.51 \times 10^5$-$2.86 \times 10^5$. The C_D values compared to a smooth sphere were approximately 50% lower by using dimples. Although δ/D_{Ball} was less, this increased the critical Reynolds number and led to a marginally lower constant value of C_D compared to a smooth sphere. They failed to note that for the lower δ/D_{Ball} the C_D started to show the same C_D rise as a smooth sphere, which is understandable as their dimples were quite shallow.

The fact that shallow dimples are less likely to generate shedding vortices was observed by Isaev & Kharchenko (1994) and Chew & Khoo (2005). Flow visualization (Choi et al. 2006) confirms this as there were no tornado-like vortices ejected from the dimples, yet the drag reduction due to the presence of the dimples is for the most part still present. The hot wire measurements show the dimples initiating instability along the separating shear layer, generating large turbulence intensity. It is claimed that with this increased turbulence, the flow reattaches to the sphere surface with a high momentum near the wall and overcomes the adverse pressure gradient in the rear sphere surface (Choi et al. 2006). The conclusion made by Choi et al. (2006) is that unless the disturbances are introduced the flow keeps the laminar flow characteristics of their experiment before separation. However as seen by Choi's data, the deeper dimples in Bearman & Harvey (1976) result in more consistent C_D

values over a larger Reynolds number range. Whilst the shear layer instability they refer to is likely at work to reduce the drag, the tornado-like vortices produced at the edges of deeper dimples for the same Reynolds number have the biggest effect on the drag reduction.

Numerical analysis of a golf ball by Kato et al. (2001), showed even for a model compromised by low grid density that flow separation upstream of 90° is not present. This was for Re_{DBall}=2.05x10^5 and ball surface spin speed to freestream velocity ratio of 0.5. As the bottom surface velocity opposes the freestream, flow separation occurs well ahead of 90°. For a finer grid, where y$^+$=0.5, Kim et al. (2006) observed that when spin was induced on a golf ball, the vortices moved out of the dimples and onto the ridges between them. Their investigation of lift and drag showed that for dimples with a steeper edge (but same depth as the spherical dimples), the drag was higher (noted by Bunker & Gotovskii 2003 and Ligrani & Park 2005), which showed a drag to Reynolds number relationship of a sphere with higher surface roughness than that of the spherical dimpled ball.

There is inconsistency across both the numerical and experimental results on the dimple geometry, Reynolds number and the spin speeds used for the golf ball. For the results in Choi et al. (2006) they do not state their δ/D_{Ball} value, or why it was not equivalent to that in Bearman and Harvey (1976), which is an important parameter when comparing the different dimple effects. This makes direct comparison between the two difficult, particularly when the smooth sphere data was not obtained for direct comparison within the individual studies. The overall trend of drag reduction with dimpled balls compared to smooth ones is all that can really be concluded from the data.

1.3.4 Dimpled Turbine Blades

Lake & King (2000) presented experimental results for dimples on a Pratt and Whitney PAK-B airfoil section with airfoil chord based Reynolds numbers (Re_{chord})=4.3x10^4-17.2x10^4, for a 177.8mm chord. The dimple array pattern consisted of one single row δ/D=0.1, spaced 1.26D apart centre to centre. Three array locations were tested at 50%, 55% and 65% chord to determine the effectiveness with a variable separation point. For all Reynolds numbers the presence of the dimples on the suction surface reduced separation losses. Locating the dimples closest to the airfoil separation

point yielded the greatest reduction in the loss coefficient, even though only one row of dimples was tested.

Passive and active control of separated flows has been proven, using longitudinal and streamwise vortices (Rivir & Sondergaard 2004). The role of these vortices being to re-energize the wall boundary layer by entraining and redistributing momentum from the primary flow, enhancing early transition. Rivir & Sondergaard (2004) repeated the experiment in Lake & King (2000), however placed the dimple rows at 50%, 55%, 65% and 76%. Two rows of dimples were tested in an un-staggered (in-line) pattern with the second row placed at 76%. Rivir & Sondergaard's numerical analysis used a laminar turbulence model to determine separation locations on the non-dimpled blade, as the k-ε, k-ω or Spalart-Allmaras turbulence models yielded no separation. No information relating to the grid or y^+ value was given.

Rivir & Sondergaard's results indicated blade separation occurring at 62%-75% chord for freestream turbulence (Tu) of 1%, and 75%-77% chord for Tu=4%, confirming that turbulent boundary layers are able to follow surfaces better; delaying separation (Davies 1949 and Choi et al. 2006). The largest reduction in pressure loss coefficient (45%-50%) was consistently achieved with 65% chord dimple location. The addition of a second row of dimples at 76% chord did not impact on the loss coefficient. Increasing the spacing by a factor of two on the 65% chord dimple blade did not adversely affect the loss coefficient reduction; in fact the results were nearly identical within the experimental uncertainty (±8%). They concluded the dimple location does not have to be located precisely at the separation location to be effective. The dimples have the potential to be effective when placed after the natural flow separation location, but are more effective before separation. So even if the precise flow separation location is not known, dimples can have a positive effect on the suction surface of an airfoil.

When the five tested Re_{chord} for the turbine blades are scaled to Re_D this yields 1148, 2127, 3659, 7318 and 14,636 respectively. Comparing this with flow visualization for the same δ/D (Chew & Khoo 2005) for most of the tested Reynolds numbers the dimples are likely to not be producing vortices. It is possible that the shear layer instability is yielding the benefit as in Choi et al. (2006), which is why the dimple spacing and second row (inside the separated zone) are not affecting the results greatly. The advantages of a checkerboard array of dimples, as opposed to an

un-staggered (offset) dimple pattern (Belen'kii 1992) seem to have been over looked by Lake & King (2000) and Rivir & Sondergaard (2004). Multiple rows may allow a greater tolerance of operation with regard to a migrating separation point. Additionally multiple rows may produce higher vorticity as the dimple array produces multiple sets of vortices, yielding increased turbulent transport and greater mixing (Park & Desam 2004, Ligrani & Burgess 2005 and Won & Ligrani 2004).

Robarge & Stark et al. (2004) used the profile of a single dimple as a channel spanning a NACA0015 airfoil. For the angle of incidence (α) of 3° at Re_{chord}=2.38x10^5, δ/D=0.15, Re_D=2.2x10^3, the presence of the cavity reduced local flow separation present on the untreated airfoil from occurring at 40% chord. Subsequent force measurement experiments showed an increase of drag and a decrease of lift, as predicted by their two-dimensional numerical analysis. Discrepancies in the separation points, particularly for when α=0°, are indicative of not matching the turbulence intensity in the numerical model to the experimental levels in the test section.

As noted in Davies (1949), Rivir & Sondergaard (2004) and Choi et al. (2006) higher turbulence tends to alter the separation points. The drag coefficient (C_D) increase corresponding to the pressure coefficient (C_p) spikes at the upstream and downstream rim of the channel cavity seem understandable. This is because the cavity is a channel across the airfoil, distributing the augmented C_p across the entire airfoil span. The dimpled surface array will not have the same effect, as they are localized in discrete points and are not likely to have as high a maximum value. As is already shown in golf ball applications the dimple array reduces drag, even for no spin.

1.3.5 Ground Effect Aerodynamics of Inverted Airfoils

The aerodynamics of bodies close to the ground have numerous real world engineering applications; aircraft in take-off, aircraft that operate at very low altitudes (Ekranoplan) but more widely the effect of the ground influences automotive aerodynamics. Several generic automotive shapes have been studied as in: Ailor & Eberle (1976), Bearman et al. (1988), Carr (1988), Steinbach & Jacob (1991), Kim & Geropp (1998), Garcia & Katz (2003) and Zhang & Senior (2004). Inverted wings in ground effect have the suction surface towards the ground, as opposed to a more conventional lifting wing; where the suction side is the upper surface. With the

suction side towards the ground the airfoil generates substantial negative lift, or downforce. This is an important feature that is utilised (to some degree) in order to improve the dynamic handling and stability of automotive vehicles (Katz 1985, Daniel Metz 1987, Katz & Largman 1989 and Katz & Dykstra 1992), such as high performance road cars and racecars.

Research of lifting NACA profiles in ground effect indicate increased lift and lift to drag ratio when approaching the ground (Chawla & Edwards 1990, Steinbach & Jacob 1991, Steinbach 1997, Maddah & Bruun 2002 and Ahmed et al. 2006). Some data exists for inverted NACA airfoil sections in ground effect (Ranzenbach 1994, 1996 and 1997) but the single element camber for these sections is usually lower than specially designed airfoil sections for ground effect, such as the Tyrrell026 airfoil. In recent years this profile has been studied (Zhang & Zerihan 2003, Moryossef & Levy 2004 and Mahon & Zhang 2005), both numerical and experimental data exists for both lift, drag and some limited information on the wake flow field. For inverted airfoils in ground effect, most experience higher downforce with reducing ground clearance (h/c) until a point where these gains in downforce rapidly diminish. A significant feature of inverted wings in ground effect is the trailing edge separation at low (and zero) angle of incidence (α), which is otherwise not present when the airfoil is modeled out of ground effect (Zhang & Zerihan 2003). The upstream migration of this separation point is highly dependent on reducing h/c (Zerihan (2001).

Ranzenbach & Barlow (1997), investigated an inverted multi-element wing in ground effect of a NACA 63_2-215 Mod B airfoil. They stated that when the airfoil operates at height roughly equal to the airfoil thickness, significant downforce is generated (i.e. it is in ground effect). They deem using a two-dimensional airfoil as a reasonable simplification to the three-dimensional flow case of a low aspect ratio airfoil with endplates, as it is likely large regions of two-dimensional flow exist in the centre of the wing. From their wind tunnel results it is concluded that downforce of the wing increases as h/c is reduced. This is until a critical height is reached, at which decreasing the height further causes the airfoil to generate substantially reduced downforce or possibly positive lift. When no force reduction phenomenon is present, the boundary layers along the ground and the airfoil do not merge. It can be seen that the boundary layers along the ground and airfoil remain distinct and

far apart throughout the flow field from their results. The phenomenon of downforce reduction occurs in their experiments at the non-dimensional height of h/c=0.222, as the ground plane boundary layer thickens beneath the airfoil. From the comparison of experimental data to the computational results they achieved, lift as a function of ground clearance is qualitatively similar to the wind tunnel case but more downforce is generated at any given height. They conclude that the force reduction phenomenon occurs at a much higher h/c for high-lift devices, and have not considered three-dimensional effects which require investigation.

Zhang & Zerihan (2003) provided a near wake study of velocity, vorticity, normal turbulent stresses and primary shear stresses for an inverted Tyrrell026 airfoil (noted by Mahon & Zhang 2005 as a derivative of the LS(1)-0413 MOD profile) at $\alpha=0°$ $Re_{c\,hord}=4.6\times10^5$ for a range of h/c<1. They showed that as the wing is brought closer to the ground the accelerated flow causes increased peak suction and a higher pressure recovery demand. At a critical ground clearance the pressure recovery is high and boundary-layer separation occurs at the trailing edge of the suction surface, even for a low angle of incidence $\alpha=0°$. Valarezo & Dominik (1991), showed that even for a lifting configuration (non-inverted) wing out of ground effect, separation can also occur on the suction side of a multi-element airfoil at 90% chord of the main element (for $\alpha=0°$ of the main element and the flap at 35° deflection).

The wake of a wing in ground effect becomes thicker or more spread out as it advects downstream, which is attributed the velocity deficit in the wake reducing as a result of turbulent mixing (Zhang & Zerihan 2003). As the ground is approached, the path (and angle) of the wake changes with reducing ground clearance, coupled with this is the thickening of the boundary layer on the suction surface at the trailing edge. They suggested it was this phenomenon that caused the wake to grow as the ground is approached, because of the observed change in the velocity profile of the bottom part of the wake. Zhang & Zerihan note that this boundary layer thickening results from the increased peak suction and associated adverse pressure gradient near the trailing edge.

Zhang & Zerihan's results indicated that the normal stress distribution in the airfoil wake is characterized by a twin peak profile, as a result of separated shear layers from both surfaces and the primary shear-stress distribution shows two peaks of

opposite signs. Two stress peaks are at each ground clearance, for the larger heights they are approximately the same magnitude. The wake becomes larger as the ground clearance reduces, and as a result the normal and primary shear stresses become larger. The increased stresses result in strong turbulent mixing, and ensures the spread of the wake (Zhang & Zerihan 2003).

Moryossef & Levy (2004) conducted numerical modelling using RANS and a one equation turbulence model on an inverted Tyrrell026 airfoil in ground effect. When the boundary layer on the ground merges with the airfoil (in some circumstances, h/c<<1) the turbulence model they utilised (developed by Goldberg 2001), provides an advantage. Their study focused on the airfoil for $\alpha=3.2°$, $Re_{chord}=4.6x10^5$ with a sharp trailing edge. The results for C_L showed the force reduction ground clearance as h/c<0.15. At h/c=0.671 there is very good numerical and experimental agreement of the surface pressures. As h/c reduced the numerical model over-predicted the surface pressure on the suction side; this over-prediction actually increased with reducing h/c. However as opposed to the numerical turbulence model comparison in Mahon & Zhang (2005) they did not investigate C_L and C_D with reference to the experimentally obtained force coefficients to further compare the turbulence model used.

A steady-state two-dimensional numerical validation by Mahon & Zhang (2005) focused on the inverted Tyrrell026 airfoil in ground effect centered on the condition of $\alpha=+3.6°$, $Re_{chord}=4.6x10^5$ and a 0.7% chord blunt trailing edge. The grid consisted of 350,000 cells with the initial spacing normal to the wall set to $y^+\approx1$. The ground clearance, was only set at two heights, h/c=0.224 and 0.09. At h/c=0.224, most turbulence models resulted in the same surface pressures, apart from k-ω SST, which was nearly identical to an earlier experimental investigation (Zerihan 2001). At h/c=0.09, k-ω SST again almost replicated the experimental surface pressures, standard k-ω and k-ε were similar and were approximately in between the experimental results and the Spalart-Allmaras model which was the least accurate. Overall for the compared turbulence models they concluded that the k-ω SST model gives a better prediction at all heights, particularly on the suction surface (although slightly over predicted). This over prediction can be a result of the root-mean-square value of the fluctuating lift is over predicted in two-dimensional simulations (Tombazis 1997).

For the airfoil section forces in Mahon & Zhang's study, the experimentally measured lift force was $C_{L,max}$=-1.55, lift prediction using *k-w* SST is $C_{L,max}$=-1.65 (+6.5% of experimental C_L), both indicate that the force reduction ground clearance occurs at h/c=0.1. The *k-ε* Realizable turbulence model has $C_{L,max}$=-1.9 (+22.6% of experimental C_L) and only just starts to indicate the onset of the force reduction phenomenon occurring at h/c=0.09, no lower h/c values were investigated.

Mahon & Zhang's results for the separation location at various ground clearances show a 10% chord earlier separation point prediction for *k-ω* SST and a 5% chord earlier separation point for *k-ε* Realizable. The results were compared with experimental results of a wing with no forced transition, and the turbulence intensity was the same as the experimental facility. Independent of the various turbulence model discrepancies, it clearly shows the trend of the separation point (position 'x_{sep}') at the trailing edge advancing towards the suction peak was h/c reduced, experimentally it occurs in the order of x_{sep}/c=0.8 at h/c=0.1.

A lifting NACA4412 in ground effect for α=0˚-10˚, Re_{chord}=3x10⁵, h/c=0.05-1 was studied experimentally by Ahmed et al. (2006) and focused on different drag components. Drag increased with reduced h/c mainly because of the modification to the pressure distribution on the lower surface. Ahmed et al. comments that the wake turbulence had a significant effect on drag coefficient, and that for small angles of attack the mean velocity profile of the wake showed little deficit and the turbulence was low, indicating a small momentum loss. Ahmed et al. remarked that the shifting of the transition point downstream with reduced h/c minimized the region of turbulent flow and thus skin friction for all angles of attack.

For most of the detailed inverted airfoil wake studies conducted, the airfoil has been at a relatively low angle of incidence. The flow behind the airfoil for a higher angle of incidence is expected to be more complicated and become more analogous to real world aerodynamic applications. Zerihan (2001) did investigate higher angles of incidence but only to substantiate the lift versus angle of incidence curve in order to determine stall. This was also to plot lift coefficient versus ground clearance with respect to α to determine the force reduction phenomenon for various low to mid range angles (-3˚ to +9˚). His results showed that from the freestream airfoil (where h/c>>1) that stalls very gradually at 10˚ for C_L=1.4, when h/c=0.313 stall angle advanced to 8˚ and

C_L=-1.7 and started to stall abruptly. For h/c=0.212 stall angle is 12° for $C_{L,max}$=-2.2. As h/c reduced to 0.045, stall occurred at 5° and lift reduced to C_L=-1.7. Results for the lift reduction effect of reducing h/c showed that as the angle of incidence increased, so does the height at which this occurred, from h/c=0.08 for α=-1°, to h/c=0.13 for α=+9°.

With the above studies, no wake flow field properties are investigated at higher angles of attack that approach stall. The only high lift conditions investigated are: the use of flap to increase C_L (Ranzenbach 1997, Valarezo 1991 and Zerihan 2003) and a gurney flap on the single element Tyrrell026 airfoil (Zerihan 2001). This produces a gap in the understanding of the separated flow mechanics at higher angles approaching stall. An understanding of this flow field may achieve insight into using various boundary layer control mechanisms in order to reduce the wake, thereby improving the aerodynamic efficiency of automotive shapes in general.

1.3.6 Passive Vortex Generators

Passive flow control devices rely purely on the aerodynamic effects of disturbances to the flow by mechanical means; active flow control relies on momentum being added to the flow by use of jets or moving surfaces. Numerous studies have investigated the benefits of passive vortex generators in; improving the aerodynamic efficiency of airfoils (Nickerson 1986, Lin 1992, Storms 1994, Storms & Ross 1995, Klausmeyer 1996, Isaev & Sudakov 2001, Rae et al. 2002, Lee & Kroo 2004 and van der Berg et al. 2004), regaining the lost momentum in adverse pressure gradient boundary layers (Wetzel 1998, Cullen et al. 2002 and Lim 2004) and reducing the separated flows from a forced separation point (Lin 1990).

Studies concerning separation point delay and reattachment position migration (Lin 1990 and Lim 2004), surface pressure coefficient changes (Nickerson 1986, Lin 1990, Storms 1994, Storms & Ross 1995, Klausmeyer 1996, Wetzel 1998, Isaev & Sudakov 2001, and van der Berg et al. 2004) and skin friction measurements on a zero pressure gradient boundary layer (Watterson et al. 2005) and to improvements in the lift and drag values of airfoils (Nickerson 1986, Lin 1990, Bearman & Harvey 1993, Storms 1994, Storms & Ross 1995, Klausmeyer 1996, Schoppa 1997, Isaev & Sudakov 2001, Rae et al. 2002, Lee & Kroo 2004 and van der Berg et al. 2004). All of these studies confirm that boundary layer protruding vortex generators provide

near wall augmentations of shear stress and turbulence transport that are a result of vortex production. These vortices overcome the adverse pressure gradient on the surface with no vortex generators such that separation point will be delayed and the separation zone will be reduced. A majority of these studies look at the overall benefits to the lift and drag coefficients or the separation zone reduction with various vortex generator geometries. Fewer studies investigate the vortex production of the individual vortex generator such as in Klausmeyer (1996) and Lin (1992).

Lin et al. (1994) studied the effect of passive separation control on a high lift three-element Douglas airfoil using trapezoidal (height (h_{VG}) of 0.0045c) and delta shaped vortex generators (h_{VG}=0.0018c) for both counter-rotating and co-rotating configurations. Flow separation on the flap caused a wake resulting in y≈0.5c in the vertical direction, whilst with vortex generators this reduced to the wake thickness to y<0.25c, taken in the wake at x≈2c. A later study using the same three-element Douglas airfoil by Klausmeyer (1996), took three-dimensional LDA spanwise plane measurements of the flow behind the vortex generators. The generators were counter-rotating, trapezoidal-wing type with h_{VG}=0.0023c at x=0.2c. The presence of the vortex generators caused complete flow reattachment of the flap when placed at x=0.92c, 20% of flap chord. Separation was indicated by flattening of the pressure distribution aft of x=0.97c, at 40% of flap chord. They noted their calculated streamlines show a 'de-cambering' effect due to the recirculation/separation bubble leading to lift loss.

Lin (2002) conducted a literature survey focusing on boundary layer control with low profile vortex generators. He noted that low profile vortex generators with height h_{VG}, in boundary layer thickness (δ_{BL}) of 0.1<h_{VG}/δ_{BL}<0.5 were best applied to applications where flow separation locations are relatively fixed and the generators can be placed reasonably close to the base-line separation. As a result their placement is more critical than that of conventional vortex generators. Lin noted that low profile vortex generators use the approach of 'minimal near-wall protuberances' to produce vortices just strong enough to overcome baseline separation. In summarizing results on micro vortex generators he indicated that vane type vortex generators of h_{VG}/δ_{BL}=0.2 produce a 35% improvement in separation delay, a 90% reduction in reattachment distance and for the larger generators, h_{VG}/δ_{BL}=0.8, a 32% improvement in separation delay, 88% reduction in reattachment distance.

Table 1.5 outlines the changes in the aerodynamic performance of various airfoils with different vortex generator methods. Some studies used a gurney flap on the trailing edge in combination with vortex generators. The improvements to the lift and stall angle are indicated, most of these result in drag increases where $h_{VG}/\delta_{BL}>3$ (Storms 1994). Lee & Kroo (2004) use small delta wings as vortex generators, offset from the surface of the airfoil where $h_{VG}/\delta_{BL}<1$ resulting in a drag reduction and lift increase. Rae et al. (2002) investigated vortex generators where $h_{VG}/\delta_{BL} <<1$, he noted that drag is virtually unaffected, apart from a small decrease above $C_L=2$ (for $\alpha>5°$), thus the sub-boundary layer vortex generators appear not to carry a drag penalty as the vortex generators used in Storms (1994). Circulation strength is important (Klausmeyer 1996 & Angele 2005), it is not derived in Storms (1994) but would be high; however the C_D is.

1.4 Literature Review Concluding Remarks

1.4.1 Single Dimple

Issues exist relating to consistent numerical modelling of the flow within the dimple and the comparison to flow visualization. These include the flow mechanics described from the numerical models listed in table 1.1 have not been validated against quantifiable experimental measurements inside a dimple. The numerical models were largely validated against flow visualization experimental observations, which involved injecting dye into the presumably delicate flow inside and upstream of the dimple. The expected low pressure region within the dimple due to upstream surface flow separation (regardless of turbulence modelling or grid density will almost surely always induce the vacuum effect). Most cite this as being an important flow phenomenon to check the numerical model exhibits, as the flow visualization exhibits this. Thus non-intrusive experimental measurements inside the dimple are required, as is a numerical model that exhibits the same flow structures as the experiment that are not related to the edge vacuum effect. The numerical model validation and verification will contribute to developing an understanding of the vorticity production and to what extent it acts downstream of the single dimple.

1.4.2 Dimple Array

It was shown experimentally that friction measurements resulted in low pressure losses for tightly spaced dimple arrays. One of the few studies to investigate larger

Table 1.5 Literature Survey Results of Vortex Generator Aerodynamic Performance

Reference	Airfoil	Generator type	VG Position	Result
Wickerson (1986)	NACA0024	Co-rotating trapezoidal h_{VG}=0.04c l_{VG}=0.015c, α=25˚	x=0.07c	$α_{Stall}$=19˚, C_l 15.2% increase over baseline C_l=0.632 at $α_{Stall}$=8˚.
Storms & Jang (1994)	NACA4412	Counter-rotating 'wheeler' wishbone h_{VG}=0.005c $hV_G/δ_{BL}$=3-4. 0.00125c gurney flap at x=1.0c	x=0.12c	Baseline: $α_{Stall}$=12˚, C_l≈1.4, C_d=0.025 VG: C_l=1.8 $α_{Stall}$=19˚, C_d=0.035 VG+0.00125c gurney: C_l=2, α=16˚, C_d=0.05
Storms & Ross (1995)	NACA 632-215 Mod-B single slotted flap 30%c	Counter-rotating 'wheeler' wishbone h_{VG}=3/16in gurney flap in main element cove	x=0.1c_{flap}	Flap deflection 42˚ cove gurney flap increased C_l 10.3%, the addition of vortex generators to the flap eliminated lift-cure hysteresis and reduced flow separation at high flap deflections.
Rae et al. (2002)	M477 (flap deflection 40˚)	'Counter-rotating wedge vanes' $h_{VG}/δ_{BL}$=0.3	x=0.25c_{flap}	flap gap=1%: C_L=2.875(base) C_L=3(VG) flap gap=2%: C_L=2.75(base) C_L=3.125(VG) flap gap=3%: C_L=2.61(base) C_L=3.125(VG)
Lee & Kroo (2004)	HQ17 Laminar airfoil	'slotted' gurney flap h=0.001c gap=0.0005c, 0.001c,0.002c	x=1.0c	C_D=0.015 did not vary greatly C_L increased by 30%
van der Burg et al. (2004)	KH3Y Multi Element	'Free Flying Delta' l_{VG}=0.02c, h_{VG}=0.007c, 65˚delta wing α=10˚	x=0.01c_{flap}	$C_{L,max}$ increased +0.0338 C_D reduced by -0.0089

spaces between the dimples utilized the non-staggered pattern as opposed to the checkerboard pattern (Bunker & Donnellan 2003). The checkerboard pattern is seen as being more efficient (Belen'kii 1992). A question remains regarding increasing the dimple to dimple spacing; how this will affect the flow 'zig-gagging' (Park & Desam 2004) between the dimple edges in the array. This may potentially affect the vortex production at the edge of the dimple and within the dimple itself. Although

the previous studies may have shown benefits of utilizing dimples, the dimples may have been too close and interfering with the flow of adjacent dimples in the array. Therefore there is perhaps a more efficient configuration of dimple spacing.

In relation to the dimple depth parameter δ/D, the results of the friction tests in table 1.2, comments made by Ligrani et al. (2005) (see table 1.3) and the numerical investigation of Won & Ligrani (2004) (see table 1.4), show that δ/D≈0.2 is a good compromise of vortex production and low pressure losses. Thus the depth of δ/D=0.22 will be carried into the experimental component of this study, as lower Reynolds numbers are being studied than in previous studies of heat exchange experiments (see tables 1.2 & 1.3), or golf ball and turbine blade applications. The golf ball and turbine applications did however show the positive influence on drag that the dimpled surfacing produced, again albeit it for a lower δ/D value. The placement of only one row of dimples to the turbine blade yielded improved pressure loss compared to standard vortex generators; however more rows with a checkerboard array pattern may yield further gains. Detailed wake measurements investigating the presence of the dimples was lacking, which would assist in determining the best location of the dimple array for the flow separation size and minimal turbulence.

1.4.3 Standard Passive Vortex Generators

The influence of boundary layer protruding vortex generators has been well observed and noted in table 1.5, notably the improvement in stall angle increases and lower drag for vortex generators that do not protrude too far into the flow. The studies listed in table 1.5 all indicate that placement is crucial to how the stalling behaviour changes or wake separation characteristics reduce. Therefore the ability to generate streamwise vortices without adversely increasing drag requires highly efficient vortex production and minimal boundary layer protrusion. It is noted that as dimpled surface vortex production is organized rather than the more dissipative effect of shearing layers (in standard boundary layer protruding vortex generators), the pressure loss is less (Bunker & Donellan 2003). This is an important explanation as to why dimples pose a benefit in their application to airfoils in order to improve their aerodynamic efficiency, than traditional boundary layer protruding vortex generators. It is expected that the vortex generation of dimples is less than boundary layer protruding vortex generators, thus the dimple array placement is critical.

1.4.4 Inverted Airfoils in Ground Effect

Data relating to lift, drag, stall angle changes, force reduction phenomenon with lower ground clearance and pressure coefficient exist for a wide variety of inverted and non-inverted airfoils in ground effect. However more detailed investigation of the airfoil wake sensitivity to the ground presence is limited to measurements taken for low angles of incidence. A greater understanding of the flow separation behaviour is sought, particularly near stall angle and how these change with increased ground effect to better understand the nature of the wake. Therefore influences of surface modifications due to the presence of dimpled surfacing can be resolved in terms of wake structure differences.

These four areas all combine into how using a dimpled surface will improve the flow and what configuration the array needs to have in order to reduce separation. The application of dimples in such a manner on an inverted airfoil's suction surface to suppress separation and improve aerodynamic efficiency is the focus of the project.

1.5 Research Program Methodology

Primarily experimentally based, the investigation of the dimple array acting on the airfoil to reduce flow separation will have two parts that will be combined in order to locate the dimple array on the airfoil. The first relates to developing an understanding of the flow in the single dimple, and then progressing toward measuring the impact of various configurations of an array on a simplified flow separation. The second part relates to measuring the airfoil wake with no dimples, in order to then finally measure the impact of the dimple arrays in various positions on the wing to compare which works the most effectively to reduce the flow separation. Figure 1.4 outlines this process.

In order to conduct the experiments it is a requirement that a moving ground wind tunnel facility must be built for the ground effect study. Using the non-obtrusive experimental techniques of Laser Doppler Anemometry and Particle Image Velocimetry, velocity measurements will be conducted in the centre plane of the dimple, the recirculation region of the rearward facing ramp and the wake of the wing. Reynolds Averaged Navier-Stokes solutions will supplement the experimental velocity measurements of the single dimple to assist developing an understanding of the fluid flow mechanics within it, and the vorticity production from it.

The airfoil section used is based on the work conducted by Zerihan (2001) on the Tyrrell026 airfoil. This was originally based around the NASA GA(W) profile, type LS(1)-0413 MOD; which was modified by having suction surface camber slightly reduced, pressure surface flattened slightly and the lowest point on the suction surface moved forward to reduce pressure recovery demands, (Zerihan 2001). The data existing for the Tyrrell026 airfoil section measured by Zerihan's study was useful for stall behaviour characteristics and how these change with ground clearance. The airfoil models used have no fixed transition point to trip the boundary layer; as it was deemed any potential flow augmentations of vorticity or turbulence as a result of the dimple array may be overwhelmed by producing more with a transition wire or strip. However the surface finish on all wings was left to a consistent surface with 800 grit sand paper, and not polished any further. One measurement of the boundary layer and the flow underneath the airfoil was conducted with a transition wire to determine the difference between the dimpled array wing, the clean wing and the fixed transition cases.

The method of applying the dimples to reduce the flow separation and wake characteristics effectively with respect to the array position is of primary interest in this investigation. In this case it is important to understand the mechanics of how the wake is altered due to the dimple vortex generators and their placement (i.e. where and how they are working) with changing angle of incidence and ground clearance, as opposed to simply measuring the overall lift and drag. It is possible the lift and drag forces may not change due to the dimple array as the form drag reduction may be equalized by a viscous drag increase (although it is likely the viscous drag increase will be outweighed by the form drag reduction). The force improvement may be marginal and within experimentation error levels (especially at the low Reynolds number of this facility) and not indicative of an improvement, as the wake is more sensitive to changes and an improvement to its structure will be more immediate and noticeable. An improvement in the wake size, velocity deficit and fluctuation of the flow (from the separating shear layer) is of particular benefit to additional bodies that may be in the wake. Flows deflecting onto other bodies from the wake of the wing, for example on the front wing of a race car, may net a larger overall drag reduction of a whole vehicle, not just the incremental reduction of drag (if any) of the
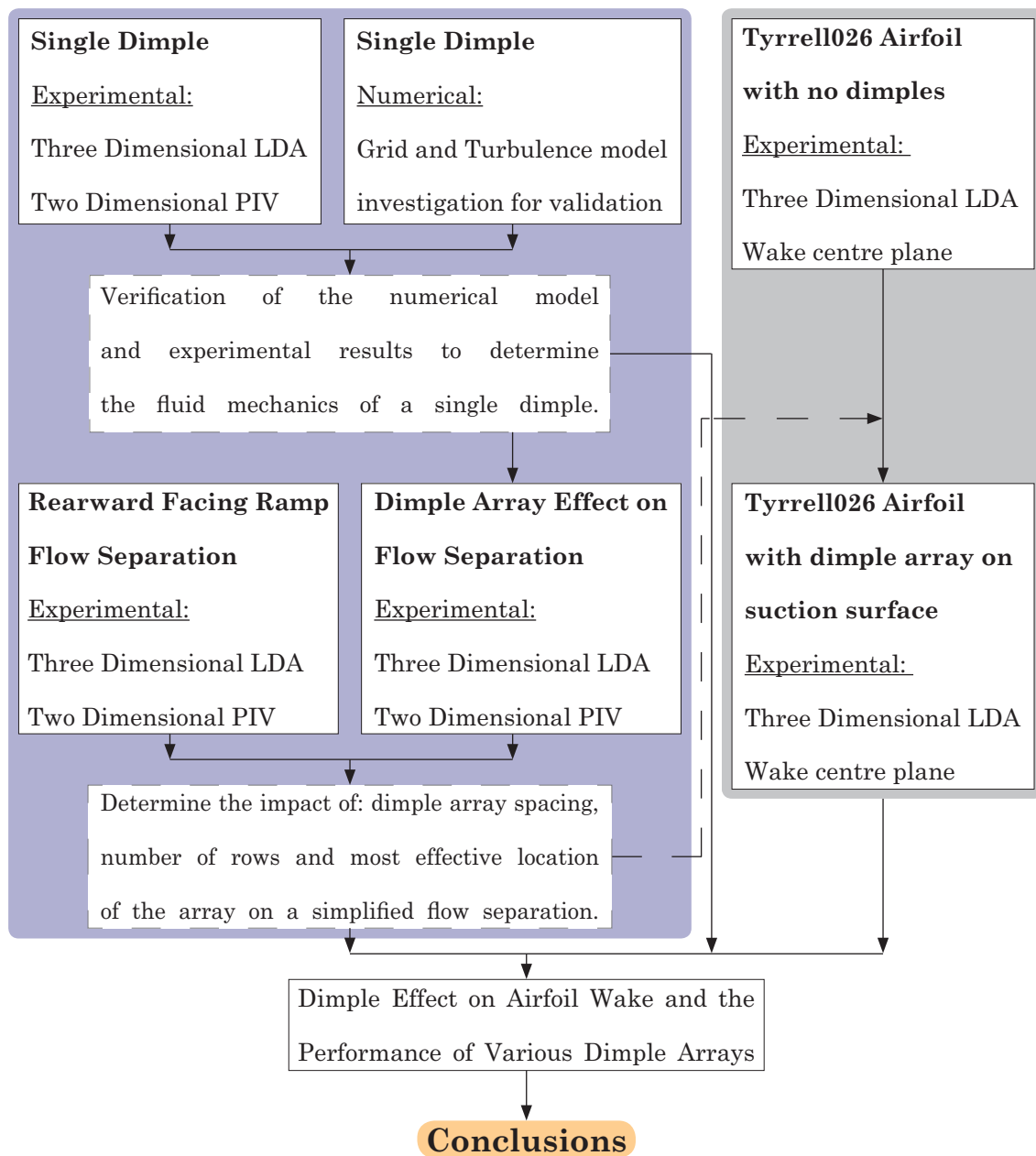
Figure 1.4 Flow Chart of Research Program Methodology

wing alone. A detailed flow mechanics survey of the concept is required to determine the feasibility of numerous potential configurations outlined in this study before C_L and C_D can be measured.

1.6 Thesis Chapter Outline

The following list outlines the content of each chapter:

Chapter 1: Introduction and Literature Review

Chapter 2: Theory explaining experimental measurement techniques.

Chapter 3: Outlines experimental facility design, experimental models and errors.

Chapter 4: Theory relating to computational fluid dynamics utilized for numerical modelling.

Chapter 5: Single dimple numerical and experimental validation and verification.

Chapter 6: Dimple array configuration and location effectiveness on a simple separated flow.

Chapter 7: Wake characteristics of Tyrrell026 airfoil with no dimples.

Chapter 8: Wake alterations of Tyrrell026 airfoil with the 1.5-3-23 series dimple array airfoil.

Chapter 9: Analysis of the changes to the wake due to various other dimple array geometries.

Chapter 10: Conclusions and Future work.

Experimental Measurement Techniques

2

The theory of the experimental methods used to measure the flow velocities are presented in this chapter. Also included are all the relevant settings, hardware and parameters used to record the data in order to outline the information specific to the equipment used in the study. A thorough understanding of the measurement techniques are required so that sources of error in both the measurement itself and those inherent in the system in regards to the setup and its operation are minimized. A more complete examination of the actual experimental errors are addressed in chapter 3.7.

2.1 Laser Doppler Anemometry

Laser Doppler Anemometry (LDA) is a non-obtrusive measurement technique of flow velocities and turbulence statistics at a discrete point in a flow field that is seeded by particles. The LDA method uses a laser that is combined with a Bragg cell, colour splitter, focussing lens, photodetector and a photomultiplier, as outlined by figure 2.1. It allows high spatial resolution measurements of fluid flows, and higher order statistical terms such as turbulence and Reynolds stresses can be determined.
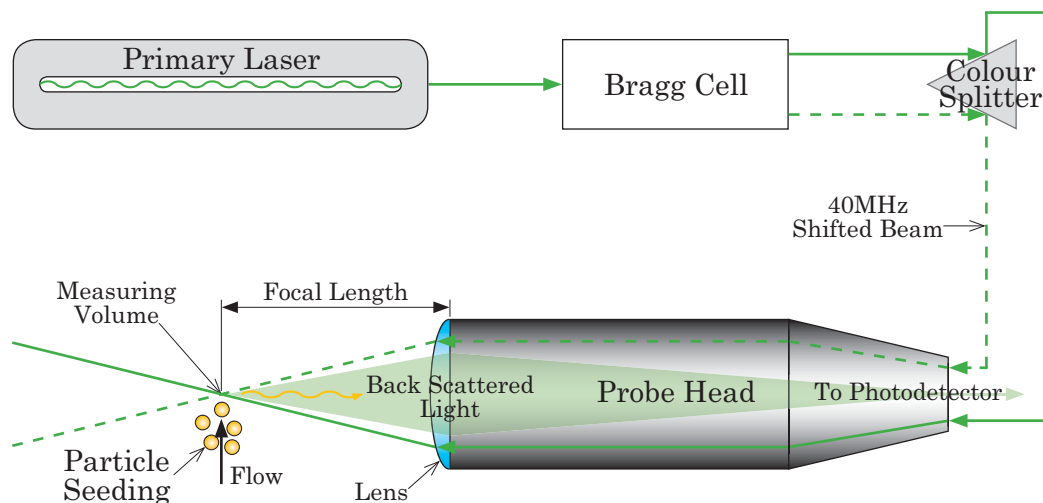
Figure 2.1 One Dimensional LDA System Diagram

The Bragg cell acts to split the primary laser beam into a 40MHz shifted beam and a non-shifted beam. This is then split by the colour splitter into green (514.5nm), blue (488nm) and violet (476.5nm) wavelengths for a three velocity component measuring system. The 6 beams; shifted and non-shifted each of; green, blue and violet, pass

through a lens attached to each of the two probes. There is one probe for both the green and blue beams (the two-dimensional probe) and a separate probe for the violet only (the one-dimensional probe). The lens converges the beams to a point (the measuring volume) at a set focal length, and records the frequency at which the light is scattered from particles moving through the measuring volume via the photodetector. This is achieved by receiving optics in the probes, which send the frequency of the scattered light information to a photomultiplier and a filter, and back to the photodetector.

2.1.1 Three component, Back Scattered, Coincident LDA Measurement Technique

The properties of the gas laser such as wavelength, power, spatial coherence and temporal coherence, make it indispensable as a measurement tool (Albrecht 2003). At all cross sections of the laser beam, the intensity has a Gaussian distribution, and the width is usually defined by the edge intensity being $e^{-2}=0.13$ of the core intensity (DANTEC 2006). At one point the cross section narrows significantly; this is known as the beam waist. It is in this region that LDA measurements should take place, as the wave fronts that propagate in the beam become planar instead of curved.

The back scatter mode of receiving a signal from a particle refers to the reflected light being captured by the receiving optics on the same side as the incident laser beams, as can be seen in figure 2.1, with the reflected light going back into the probe head through the front lens. According to the Lorenz-Mie light scattering theory (DANTEC 2006), in section 3.4 (figure 3.9), for a 1µm vegetable oil particle in air light will be scattered through all angles at different light intensities. The highest light scattering intensity occurs at 180° and considerably weaker intensity at the incident angle; this results in less light being scattered back in the direction of the receiving optics. Signal detection techniques have advanced enough for this method to not be seen as a compromise, and indeed is an advantage as there is less equipment to align at the measurement volume; minimising set up time. Figure 2.2 shows the incident beams (e_1 and e_2), reflected or scattered light (e_s) and particle velocity direction, **U**.

The Doppler Effect is crucial to LDA, since the technique is based on the Doppler shift of the light reflected from the seeding particle. The incident laser beams have a
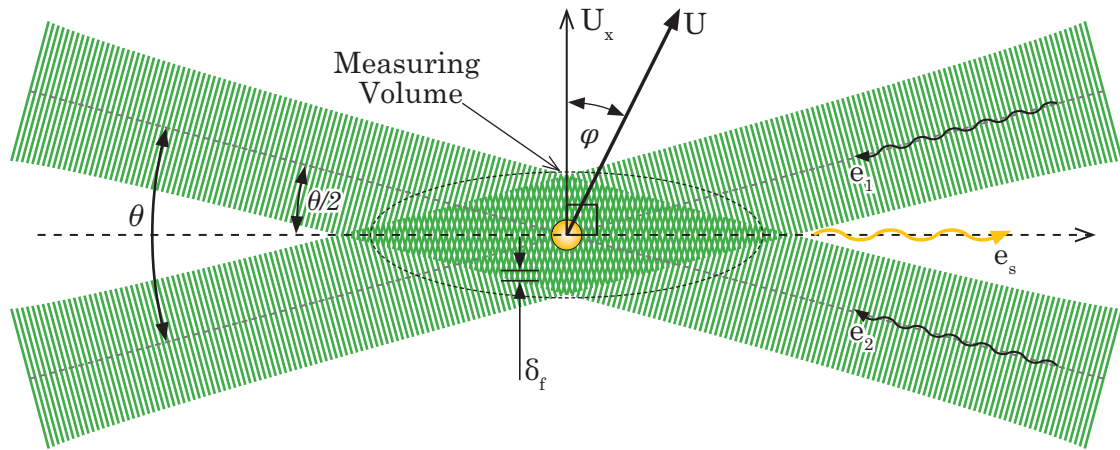
Figure 2.2 Fringe Pattern in the Measuring Volume of Two Interfering Beams

velocity c and a frequency f_i but the particle due to its movement **U** sees a different frequency f_D which is subsequently scattered back to the receiver. Taking into account that there are two intersecting beams in the measurement volume, two coherent laser beams will interfere, as the wave fronts develop a planar profile at the beam waist.

This interference results in producing parallel planes of high and low intensity light in the measurement volume. The distance between these regions, δ_f depends on the wavelength of the incident beam, λ, and their separation angle, θ, see equation 2.1. The fringes develop such that they are parallel to the bisector of the two beams (i.e. $\theta/2$), and the resultant measured velocity component will be normal to this, when orientated correctly to coincide with the x axis this will result in U_x. So given that the Doppler frequency f_D (equation 2.2) depends on the particle travelling through the fringes of a set distance the velocity of that component can be determined from equation 2.3.

$$\delta_f = \frac{\lambda}{2\sin(\theta/2)} \quad \text{...} \quad [2.1]$$

$$f_D = \frac{u_x}{\delta_f} \quad \text{...} \quad [2.2]$$

$$u_x = \frac{f_D \cdot \lambda}{2\sin(\theta/2)} \quad \text{...} \quad [2.3]$$

The issue of directional ambiguity arises, which for an un-shifted beam $f_D=\pm u$ (figure 2.3a), hence a frequency shifted beam is introduced by the Bragg cell to counter this. The Bragg Cell acoustically excites the incoming beam, frequency f_I,

and splits it in two components, the first beam having the input beam frequency f_I and the second diffracted beam being $f_I + f_0$. Some distortion of the incident beam can occur, but will be minimised if the beam width is significantly smaller with respect to the Bragg Cell's excitation transducer (Albrecht 2003). A stationary particle in the measuring volume will have the shifted frequency $f_D = f_0$, and for $u_x > 0$; $f_D > f_0$ and $u_x < 0$; $f_D < f_0$. Thus f_D will now become equation 2.4:

$$f_D = \left| f_0 + \frac{2\sin(\theta/2)}{\lambda} u_x \right| \quad \text{.......................... [2.4]}$$
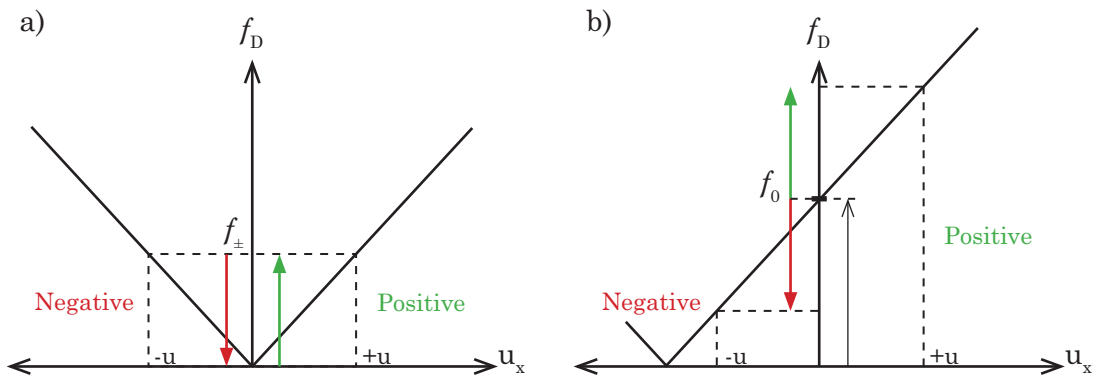
Figure 2.3 a) Non-Shifted and b) Shifted frequencies resolving directional ambiguity

A three component LDA system will allow for u_x (u) , u_y (v) and u_z (w) to be measured, thus all six beams must converge in the one measuring volume. To process higher order terms such as turbulence, Reynolds stresses and statistical information, coincident measurements must be taken. By using coincident measurements, the measuring volumes are essentially coupled into one 'net' measuring volume and all data relating to an individual particle is processed simultaneously and its three velocity components will be recorded. This ensures that velocity measurements are of the particle in the instantaneous flow, allowing higher order moments to be calculated. With non-coincident measurements the measuring volumes are essentially de-coupled into separate measuring volumes per beam pair. A velocity reading on one channel, may not simultaneously generate a signal on the others, and is not ensured to measure at the same point in space. As velocity data is processed for all particles travelling through each independent measuring volume, and is more a mean flow measurement. Thus coincident LDA measurements are used in the experimental measurements in this study.

2.1.2 Laser Doppler Anemometry System
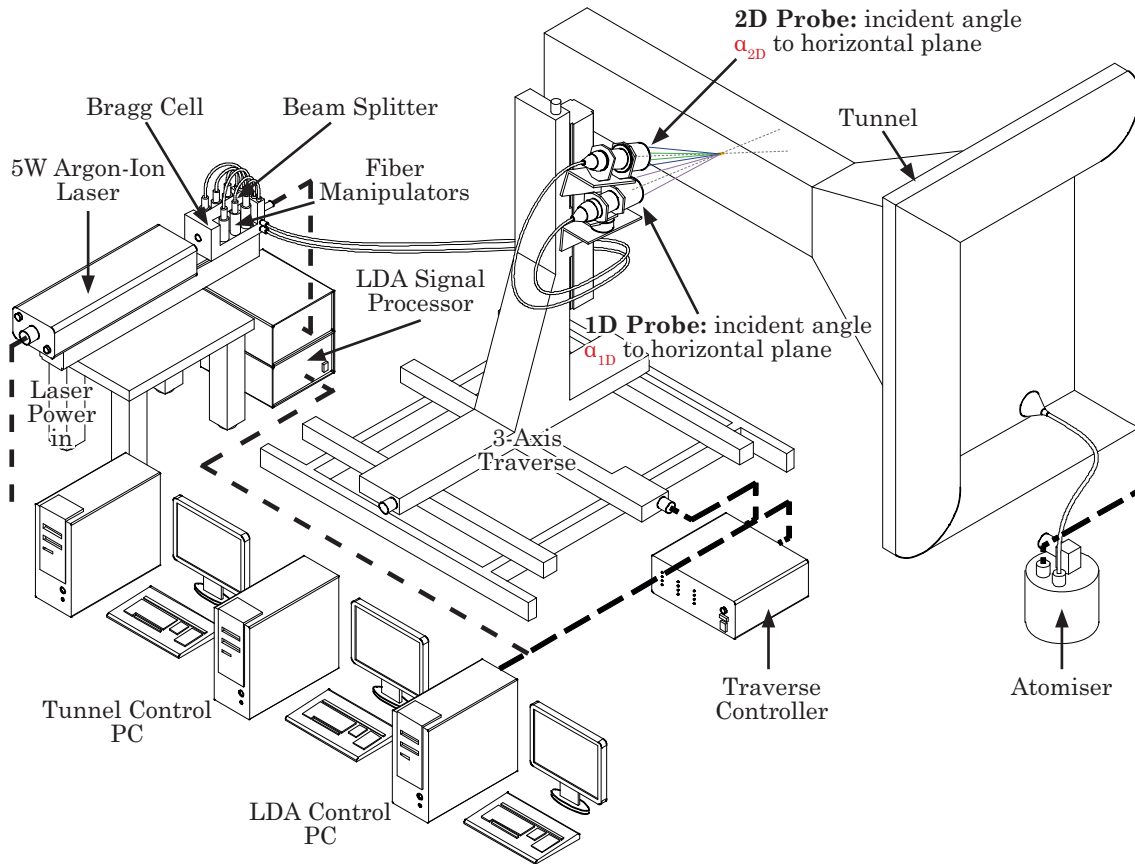
Figure 2.4 LDA system Setup

<u>Coherent INNOVA 70C 5W Argon Ion (Arg-Ion) Laser:</u> The main laser unit supplies the primary beam to the transmitter box, then to the LDA probe heads. It is supplied by a chilled constant temperature water circuit to ensure thermal stability of laser tube, and maintain consistent beam output.

<u>DANTEC 60x41 Transmitter and 60x24 Fibre Manipulators</u>: Is an integrated colour separator and frequency shifter (Bragg Cell), it also provides a base for the manipulators which couple the light into the fibre plugs in the probes. The manipulators position the beam from the transmitter with respect to the optical axis of the fibre; adjustments are made by four screws controlling beam angle and beam displacement. Individual beam powers are measured with a power meter to ensure peak optimum beam power performance.

<u>60x83 (two dimensional) 60x82 (one dimensional) 85mm Probe Heads:</u> These are connected to transducer heads which couple to the fibre optic cable. These deliver the 6 beams and operate in the backscatter configuration with, two receiving beams to collect the scattered light from the measuring volume. The probes can operate with

240mm & 500mm front lenses depending on required focal length, beam expanders reduce the measuring volume size at high focal lengths.

Processors: DANTEC 62N series BSA based system, with an integrated photomultiplier and detector unit. All data is received and modulated by this unit and is transferred to BSA Flow Software on a local computer for post processing.

Traverse and Seeding Systems: The probes are mounted to a DANTEC 41T333 lightweight 3 axis traverse system controlled by an ISEL C142-4 Motor controller. Atomised vegetable oil, at 1bar gauge pressure supplied by a PivTec atomiser, see section 3.4 for more details.

Setup plus transformation matrix: This is required in order to resolve the 3 Cartesian components of velocity (u,v,w) by transforming the velocity recorded from the probes (u_1, u_2, u_3) with any given in-plane orientation. For the 2D and 1D probe configuration in figure 2.4, applying $\alpha_{2D}=22°$ and $\alpha_{1D}=-5°$ (negative, as original derivation DANTEC (2006) requires probes face in toward each other), the transformation matrix for probes at unequal angles is:

$$\begin{Bmatrix} u \\ v \\ w \end{Bmatrix} = \begin{Bmatrix} 1 & 0 & 0 \\ 0 & \dfrac{-\sin\alpha_{1D}}{\sin(\alpha_{2D}-\alpha_{1D})} & \dfrac{\sin\alpha_{2D}}{\sin(\alpha_{2D}-\alpha_{1D})} \\ 0 & \dfrac{\cos\alpha_{1D}}{\sin(\alpha_{2D}-\alpha_{1D})} & \dfrac{\cos\alpha_{2D}}{\sin(\alpha_{2D}-\alpha_{1D})} \end{Bmatrix} \cdot \begin{Bmatrix} u_1 \\ u_2 \\ u_3 \end{Bmatrix} \quad \text{.................} \quad [2.5]$$

2.2 Particle Image Velocimetry

Particle Image Velocimetry (PIV) is a well established experimental technique that uses a laser sheet to illuminate seeded particles in a fluid flow. When coupled with a camera to record the images, a velocity vector map of the particles can be calculated. PIV is classed as a non-invasive experimental technique, due to the fact that seeding particles should be small enough that they track with the flow, the camera is more than likely situated outside the test volume and the external laser sheet (of high excitation light energy) should not affect the fluid flow, demonstrated in figure 2.5.

The nature of the light sheet illumination producing a discrete thickness, the camera lens and CCD located parallel to minimise image distortion errors result in the calculation of two velocity components from a thin light sheet. Therefore the spanwise velocity component cannot be resolved, so the basic form of PIV presented
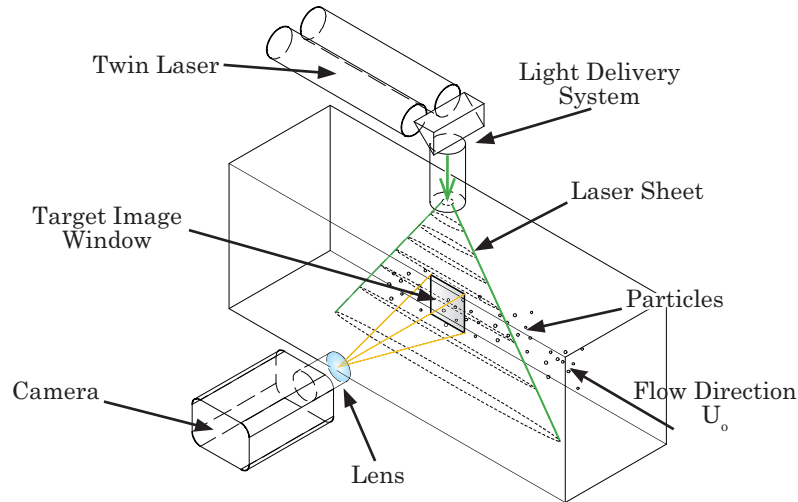
Figure 2.5 Typical PIV Setup

here is two dimensional. The light sheet illumination and image capturing allows a whole flow field region to be instantaneously recorded in the interrogation area. Other techniques such as Hot Wire Anemometry, Laser Doppler Anemometry and Pitot Static Probes are more time averaged point measurements.

2.2.1 High Density, Double Pulsed, Cross correlated PIV technique

The system used in the study is categorised as producing high density PIV images (Adrian 1991). Essentially this is when many seeding particles in the interrogation area are illuminated for very short periods of time, resulting in increased accuracy (Raffel et al. 1998). The nature of high density PIV images requires a double pulsed laser to provide a light sheet several μ-seconds apart. Cross-correlation analysis is optimum for double-pulsed laser, high density images to resolve the particle displacements for a single frame, single exposure camera (Keane & Adrian 1992).

In order for the two images to be taken at time t_1 and t_2, a double pulse of the laser sheet is required, at a constant Δt_p (μsec). Figure 2.6 illustrates the laser sheet timing with the camera, which is achieved using a function signal generator. Energy is supplied to excite the Nd:YAG (Neodymium-doped Yttrium Aluminium Garnet) rod intermittently by high voltage flashlamps operating at 20Hz. When used in conjunction with a Q-switch located between the two internal mirrors, a very short duration (5ns) high powered light sheet is supplied. A Q-switch comprises of a high voltage supplied Pockels cell and a polarizer plate letting light pass at a defined polarization angle. The two rapid, successive, high intensity laser sheets are due to the use of two Nd:YAG lasers at the same repetition rate, albeit phase shifted.
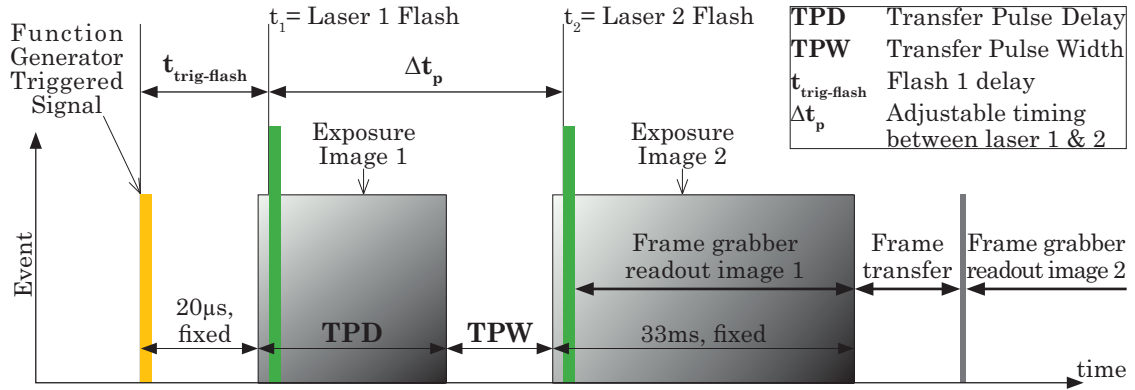
Figure 2.6 Double Pulsed PIV Image Capture Event Sequencing for Camera

The cross-correlation method maps two images of the seeding particles at two instances in time as seen in figure 2.7. The image data is stored as a matrix form $[I_1]$ and $[I_2]$ of the image intensity of the scattered light from the seeding particles at time t_1 and t_2 respectively. Mathematically these two matrices are overlapped by a pixel amount Δi, Δj. A good overlap (Δi, Δj) will result in that pixels of high intensity when multiplied will yield a higher value than those with a poor overlap, explained graphically in figure 2.7. This relates to the cross-correlation function as defined by equation 2.6. Auto-correlation exists for single frame multiple exposures (outlined in Raffel et al. 1998), but leads to a directional ambiguity resulting in pixel peak overlaps for $\pm\Delta i$, $\pm\Delta j$, and is not ideal for reversing flows (Hall 2001).

$$R(\Delta i, \Delta j) = \sum_{\Delta i=-N}^{N} \sum_{\Delta j=-N}^{N} I_1(i,j) \cdot I_2(i + \Delta i, j + \Delta j) \quad \text{.................} \quad [2.6]$$

The most likely particle displacement takes place between the values of the largest peak intensity, between I_1 and I_2 this can lead to an error associated with the loss of data due to digitization of the real image of ± 0.5 pixels (Raffel et al. 1998, Huang et al. 1997). To overcome this issue sub-pixel interpolation is utilised, particularly as a seeding particle will ideally span more than one pixel, and allows the displacement to be resolved to an accuracy of 0.05-0.1 pixels for particles of 2-3 pixels in an 8-bit image with good contrast (Raffel et al. 1998).

This process is fundamental to PIV as once the distance between the pixel peaks is calculated, the particle displacement D in the measurement plane (see figure 2.7) can be resolved once the imaging geometry is known from a calibration image. This relates pixel size to distance, which is specific to experimental set up (i.e. camera and
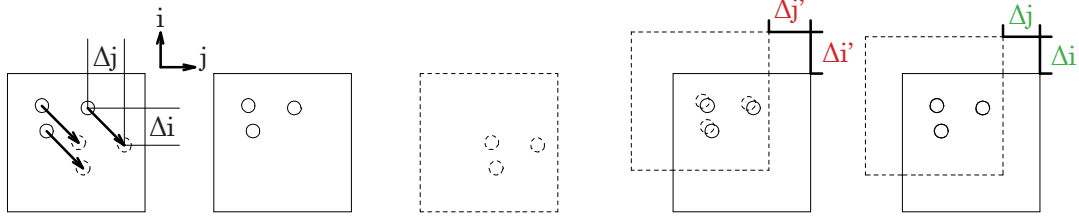
Figure 2.7 Optimum Cross-correlation Displacement Overlap

image resolution, focal length of camera). As the pulse separation time Δt_p is known and assuming negligible slip between flow and the seeding particle (see section 3.4), then the fluid velocity can be determined from the particle velocity, satisfied by equation 2.7:

$$V = \frac{D}{\Delta t_p}$$ .... [2.7]

2.2.2 Particle Image Velocimetry System

The PIV system setup used is shown in figure 2.8, and utilises a 3-axis traverse system onto which the camera is mounted. A specially designed light delivery system was developed and incorporated into the EKSPLA laser to generate the laser sheet. Full wind tunnel, camera, traverse, moving ground and laser control is achieved by three desktop computers.

<u>EKSPLA NL301-2G Nd:YAG Laser:</u> comprises two lasers (each containing an Nd:YAD rod, flashlamp and Pockells Cell), a unit distributing the high voltage, beam combining optics, a frequency doubling crystal, and a dichroic mirror to separate the green wavelength (532nm) from the infrared (1064nm). The maximum allowable flashlamp voltage is 1600V which delivers output energy of approximately 100mJ. It is all internally cooled by a separate cooling circuit, and controlled by software developed and outlined in Coray (2005) to individually control Laser 1 and Laser 2 output power and timing.

<u>Light Delivery Head:</u> this was developed to have a back focal length of 450mm-810mm and a width of 120mm-180mm, equating to a beam thickness of approximately 2-5mm. A series of converging 150mm, diverging 50mm lens 30mm apart, were separated by a variable length focussing tube to the final converging 125mm and a final diverging 25mm cylindrical lens.
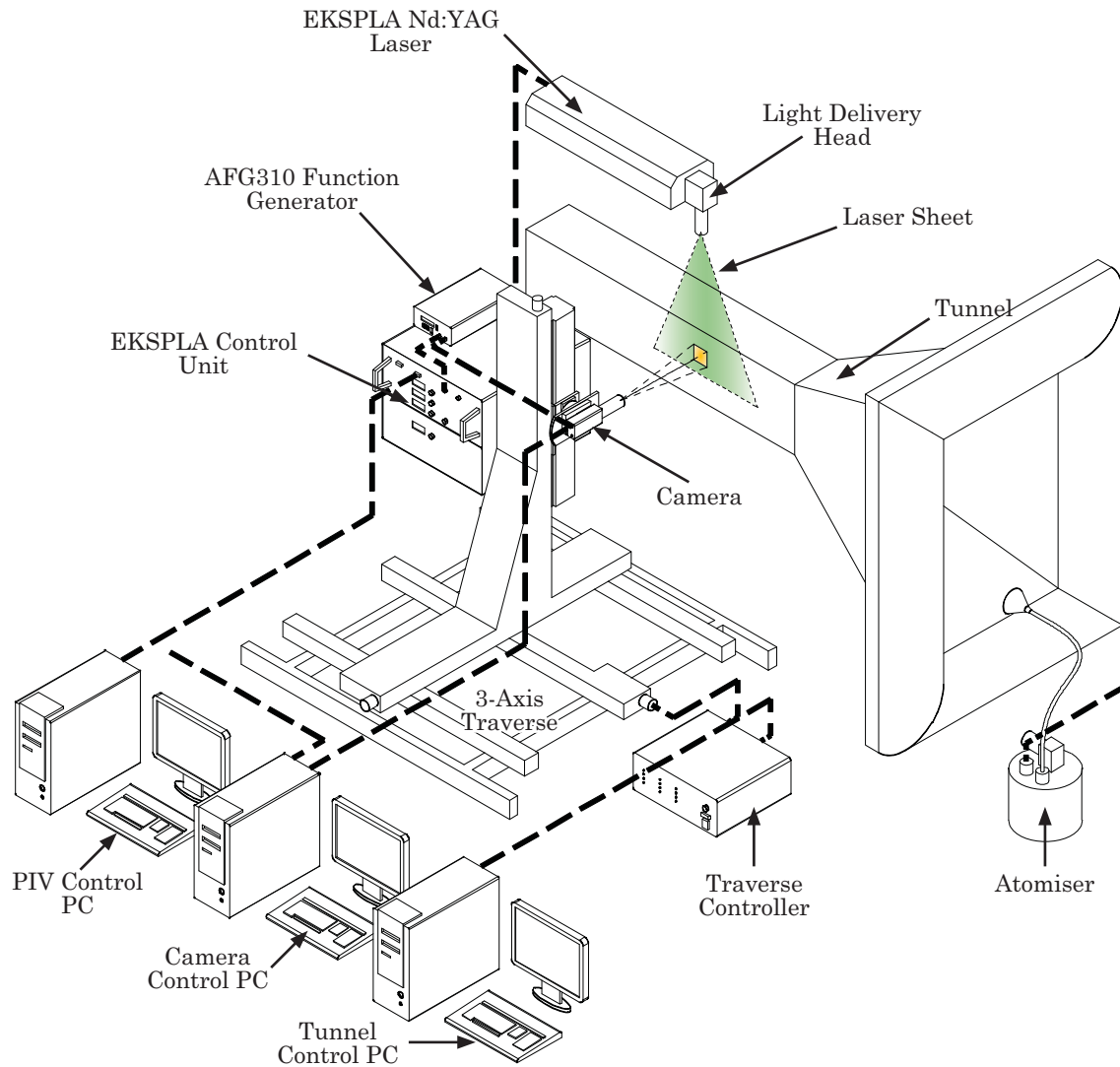
Figure 2.8 PIV System Setup

<u>Redlake Megaplus ES1.0 Camera:</u> operates with a double frame exposure of at least 0.2µs, and captures 10-bit images at 1 megapixel resolution. A frame grabber card is operated using EPIX software from Redlake to capture images from the camera. A 55mm F2.4 Nikkor lens utilising a 532nm bandpass filter with 10nm bandwidth is used to limit ambient light interference on the CCD.

<u>SONY Tektronix AFG310 Function Generator:</u> When terminated to 50Ω to produce a square form trigger signal, the function generator produces a trigger signal 144µs before the first double flash, in order to produce the double exposure timing of the camera and the double pulsed laser events as outlined in figure 2.6.

<u>Traverse System:</u> The camera was mounted to a DANTEC 41T333 lightweight 3 axis traverse system controlled by an ISEL C142-4 Motor controller. This allowed repeatable positioning of the camera for combining multiple PIV images.

2.2.3 Image Processing

Using the commercially available image analysis software VidPIV v4.6 from ILA GmbH, processing of the captured images is possible to allow for further post processing.

Cross correlation: The interrogation image is split up into discrete grids which are mapped to produce the vector field of the flow. Typically 32x32, 64x64 or 128x128 pixels for the entire image depending on resolution required and how far the particles are travelling, if particles leave the correlation region this will produce spurious vectors. Generally a 64x64 with 12 pixel spacing cross correlation box was used with Gaussian spectral filtering.

Filtering: Window velocity filtering allows spurious vectors across all interrogation areas to be disregarded and clipped to a 95% confidence limit. Local velocity filtering based on the median statistics of neighbouring vectors can then be conducted, typically for standard deviation of ±0.1 for 0.25 pixels. This is reasonable to ensure filtering of spurious vectors at such low Reynolds numbers. Once sufficient filtering is applied, interpolated vectors are required for the missing vector data, typically using a 3x3 kernel.

Once applied, averaged velocity vectors are taken across the number of image pairs. This was set at 600 image pairs for the large scale flow separation on the rear-ward ramp and 300 image pairs for the wings in ground effect. Vorticity and Turbulence Intensity were also calculated in VidPIV based off the u-RMS and v-RMS velocity components.

Experimental Facility

3

This chapter outlines the design of the wind tunnel configurations that were required for each of the three separate experiment modules required to satisfy the topic areas outlined in figure 1.4. Other components are addressed that are critical to the velocity measurements such as the particle seeding. Experimental errors are discussed in detail that affect the LDA and PIV systems as well as the mechanical errors from the 3-axis traverse system, model manufacture and secondary velocity measurements such as the Pitot tube and digital manometer that were used to operate the tunnel.

3.1 Introduction

There exist a number of ways to experimentally reproduce a ground effect flow; using a moving ground to simulate the equalized relative velocity of the ground and fluid with respect to the model (Beauvis et al. 1968, Sardou 1986, Carr 1988, Bearman et al. 1988, Kim & Geropp 1988 and Hucho & Sovran 1993), using a stationary plane that is either a wind tunnel wall or suspended into the test section (Beauvis 1968, Sardou 1986, Bearman et al. 1988, Kim & Geropp 1998 and Hucho & Sovran 1993), sucking the boundary layer off the floor underneath the model (Carr 1988, Hucho & Sovran 1993 and Wickern & Dietz 2003), tangential blowing of fluid from jets located in the wall under the model (Hucho & Sovran 1993, Wickern & Dietz 2003), the symmetry model technique (Sardou 1986) and if possible full scale on road testing in the case of a vehicle (Beauvis et al. 1968 and Hucho & Sovran 1993). The suitability of each type of representation mainly depends on the shape of the model tested and how close it is located to the ground. Barber & Leonardi (2002) provide a detailed summary of ground effect modelling (both experimental and numerical).

An early experimental study compares; moving ground, stationary wall and full scale on road testing of the aerodynamic performance of a 1965 Ford Galaxie (Beauvis (1968). It was shown that the ground plane boundary layer has significant adverse effects. Flow visualization showed the differences in the flow field of various ground plane models for; ground on and off, and symmetry (Sardou 1986). Symmetry yielded a close flow structure in the wake when compared to the moving ground. The stationary wall yielded a region of flow separation on the ground upstream of a

body that is pitched upwards, which is shifted downstream of a body that is pitched downwards; substantially minimizing the wake of the body. Sowdon & Hori (1996) stated the image method does not adequately represent the turbulence and flow separation.

The investigation of suction and moving ground techniques on various generic automotive shapes showed little variation in pressure coefficients existing for flat bodied objects in ground effect, apart from the flow in the immediate throat of the model at the lowest ground clearance (Carr 1988). For a venturi shaped object in ground effect, pressure coefficients in the diffuser section are similar for all ground representations. At smaller ground clearance however the differences become more pronounced. The moving ground simulation technique yielded consistently lower C_P compared to the plain floor. C_P plots indicated the stagnation point shifted at the front of the vehicle relative to all other methods when using a moving floor. Lift and drag coefficients obtained in Carr (1988), showed a high dependency on C_L for a flat bottom bluff body with the method of ground simulation used. Near wake velocity field measurements of a bluff body and a wheel in ground effect showed the recirculation region is longer above the moving ground (Bearman et al. 1988 and Kim & Geropp 1998). Bearman et al. (1988) stated that the turbulence measurements indicated the shear layer separating from the lower edge of the body spreads more rapidly in the stationary case. The flow in the immediate wake of the body appears to be insensitive to floor movement; suggesting that configurations with more underbody upsweep may show a greater sensitivity.

In a later study by Hucho & Sovran (1993), they commented that the moving ground technique represents, in principle, an almost perfect way to simulate the road and it is not uncommon for a test section/model blockage ratio of 20%. If the model is located too close to the exit nozzle in the test section this can affect the upstream flow in the nozzle, even in an open circuit wind tunnel. The struts used to support the model and measure the forces can produce significant aerodynamic interference. They compared moving ground with tangential blowing and suction methods. Tangential blowing results in a flow field somewhere in between the moving and fixed ground simulations. Suction on the plane under the model can lead to an induced angle of attack, angling the free stream flow towards the ground upstream of the body.

Transient flow effects in the wake of a model with respect to the ground were investigated by Kim & Geropp (1998). They indicated that for a half ellipse, the moving ground provided flow damping. With Strouhal number reducing 12% at the lowest clearance (h/c=0.2) compared to the stationary ground case. For a 50% increase in Reynolds number at h/c=0.2, Strouhal number reduced by only 8%.

3.2 Wind Tunnel and Moving Ground

Figure 3.1 Wind Tunnel in Primary 'Moving Ground' Configuration

A fundamental requirement was to design and build a wind tunnel and moving ground system for the experimental component of the research program. Budget, time and space constraints necessitated a smaller than full scale test facility, coupled with it being designed and manufactured in-house concurrently with the research program. The nature of experimentation involving laser flow measurement via Laser Doppler Anemometry and Particle Image Velocimetry required transparent surfaces of reasonable optical quality throughout the test section, thus a predominately acrylic sheet construction was preferred. Scale effects on moving to a larger, full scale moving ground posed various engineering challenges that were out of the time scope of the project after a preliminary design investigation proved it to be too costly and technically intensive.

Initial design for optimum flow profile consistency over the moving ground was

conducted using Computational Fluid Dynamics on the non-moving ground test section in figure 3.3. This focused on wind tunnel test section expansion taper to limit boundary layer growth, contraction inlet geometry and moving ground duct size. The other requirement was that due to the narrow test section cross section aspect ratio of approximately 1:1.51 the central portion had to largely have two-dimensional flow, as the side wall effects on the cross flow velocity would be appreciable. With such considerations the commissioning process of the tunnel took 12 months and a high quality moving ground aerodynamic testing facility resulted; shown in figure 3.1, for technical data see table 3.1.

Table 3.1 Technical Data for Wind Tunnel in Moving Ground Configuration

Type	Open Circuit, Closed Test Section
Test Section Cross section	280mm x 225mm
Inlet Contraction	7.8:1
Fan power	3.7 kW
Maximum speed air speed	17 m/s
Design speed air speed	10 m/s
Moving Ground Motor Power	1.1 kW
Reynolds Number (Test Section Height)	$Re_H = 2.8x10^5$
Flow Angularity	<0.6˚
Turbulence Intensity	0.01%
Belt Boundary Layer thickness δ	5 mm

3.2.1 Wind Tunnel and Moving Ground Control System

A LABview program was devised to allow various sensors regarding belt speed and flow velocity to be read and fed back to the fan and moving ground controller in order to set and maintain the correct velocities respectively.

Wind Tunnel Fan: A TORIT VS1500 industrial vacuum chamber with a 5Hp fan is used to draw the flow through the tunnel. Flow straighteners were used in the box to reduce the effects of the fan being off axis with the tunnel centre line. As the box is located downstream of the test section and simply applies negative pressure behind the tunnel test section outlet the fan effects on the flow to the test section is negated, aside from the off axis orientation.

Pitot tube and Digital manometer: A KIMO TPL-3-100-T 3mm diameter pitot tube incorporating 6 static pressure holes and a thermocouple in the tip, measuring the differential pressure and temperature in the test section above the belt. It is

located 30mm into the flow above the boundary layer of the roof of the test section. A Furness FCO510 Digital Micromanometer measures the differential pressure and temperature from the Pitot tube, and this information is read directly into the control software and used to adjust the frequency to the vacuum box fan motor.

Moving Ground Motor/Controller: CMG Electric, 3 phase, 415V, 1.1kW, 2800 rpm motor and Danfoss VLT6000 HVAC frequency converter.

Moving Ground Hall Effect speed sensor and belt slip: A US Digital 800.736.0194 encoder disc reads the drive roller angular velocity using US Digital HEDS-9000 optical encoder which has an LED source and a monolithic detector Integrated Circuit. The belt speed is fed back to the motor controller which adjusts the moving ground motor frequency. Belt slip has been measured to be negligible when the correct amount of belt tension is applied.

Belt Tracking System: A purely mechanical system controls the belt tracking. The front (non-drive) roller sits in self-aligning roller bearings and the whole front roller is hinged, so that by using an adjustable slider the angle of the roller can be set so the belt tracks in the centre as dependent on the applied belt tension. As belt operational speeds are low, no complex automated tracking systems are required.
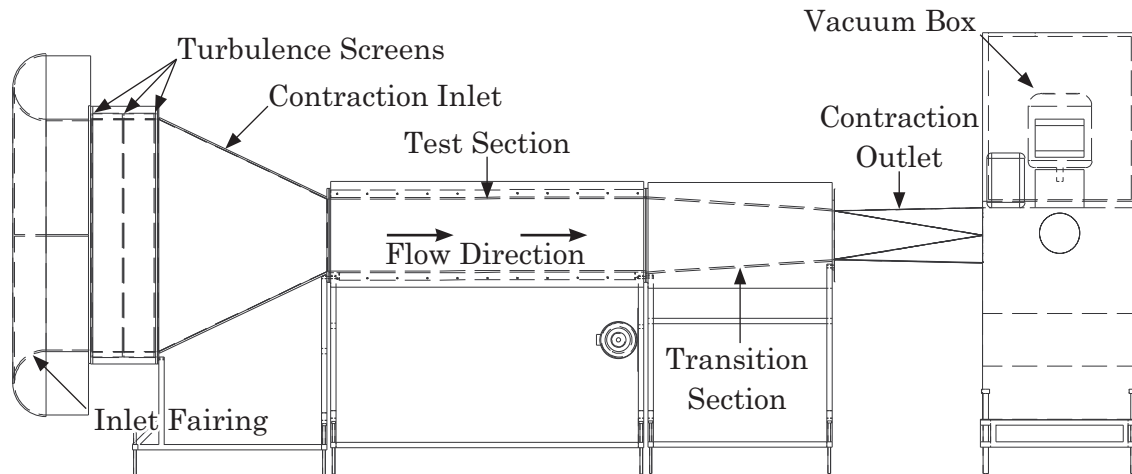
Figure 3.2 225mmx340mm UNSW Wind Tunnel

3.2.2 Wind Tunnel and Moving Ground Design

The contraction inlet and test section expansion were designed based on numerical analysis results and similar facilities in the literature; Barlow et al. (1999), Motson & Archer (1969). This was considered necessary to eliminate the need for scaled prototypes to be built and tested first (Motson & Archer 1969). The driving parameters

of the contraction inlet were its length, the degree to which rounded corners inside the inlet helped the flow and whether any bell mouth inlet fairing was needed. This was to ensure velocity profile consistency throughout the test section. A two dimensional, finite volume RANS analysis was conducted using k-ε RNG turbulence modelling with 350,000 grid points and wall y^+=2; allowing enhanced wall treatment with pressure gradient effects. Boundary condition information can be found in Appendix A figure A.1. A verification and validation analysis outlined by the AIAA Guide (1998) was conducted.

The width of the tunnel was to be based around the UNSW 225mmx115mm open circuit tunnel as used previously (Hall 2001 and Barber 2000), so components could be shared to reduce cost and manufacture time. Thus the height was the only parameter that could be used to control the blockage ratio of the test section, and maintain an appropriate free stream Reynolds number. The maximum velocity was 40m/s in the 225mmx115mm test section using the same vacuum box, so the target operational free stream velocity was 10m/s in the new 340mmx225mm test section, see figure 3.2. Based on the 75mm chord wing in its lowest ground clearances at highest angle of attack and taking the height of the trailing edge to the ground this is approximately 15% blockage, the inlet contraction ratio of 7.8:1 was specified by Motson & Archer (1969).

The length of the test section was designed around preferred inlet and outlet length specifications of numerical models of approximately a minimum of 6 chord lengths from the inlet and 12 chord lengths from the outlet. This decision was to simplify later numerical models of experiments in order to merely model the test section, and not have to conduct a validation of the proximity of the inlet and outlet boundary conditions to the test object. The total length of the test section is 20 chord lengths or 1500mm, with the wing ¼ chord placed at around 7.5 chord lengths from the test section inlet. The boundary layer growth over such a length was calculated to have considerable adverse effect on the consistency of the velocity profile throughout the test section length. By tapering the walls by 4mm, or 0.15˚, the static pressure along the length of the test section would remain relatively constant. Subsequent numerical models (see figure 3.4 and 3.6) confirmed this, thereby allowing the test section area Reynolds number to remain constant along its length.
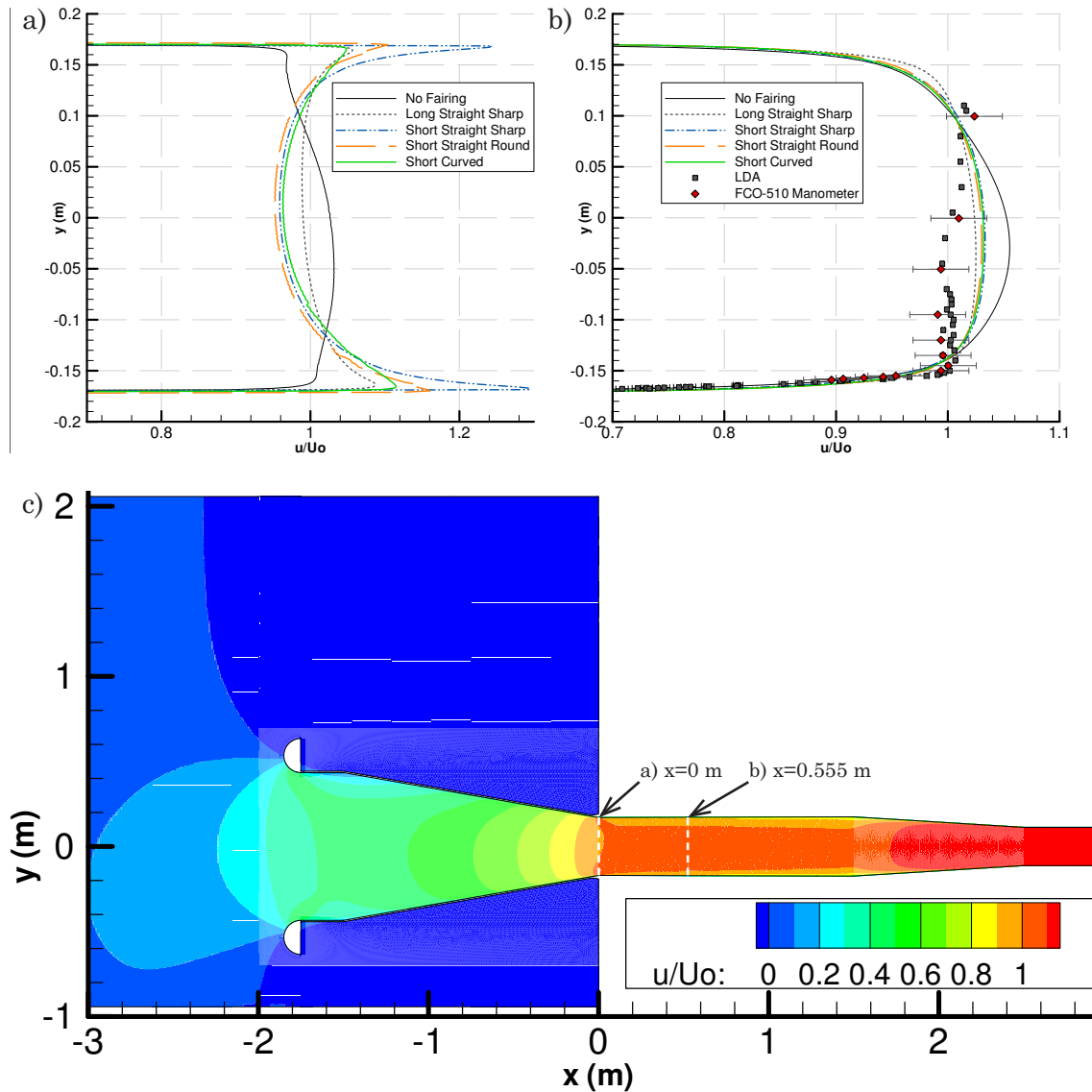
Figure 3.3 Baseline Test Section Velocity Profiles a) at x=0 m b) at x=0.555 m c) Full Tunnel

The moving ground is deployed in the test section, offset from the floor. A duct under the moving ground negates the effect of the increased velocity in the test section by reducing the test section area above the belt. The fluid in the duct returns further downstream from the belt, as opposed to other highly complex suction techniques prior to the belt. The ducting method also allows the boundary layer on the test section floor to be separate from the belt, and small leading edge fairing develops a thinner boundary layer ahead of the belt. A NACA 6-series airfoil profile establishes a laminar boundary layer to its thickest point (Abbot & Von Doenhoff 1959), in this case the junction between the fairing and the belt. This produced the most uniform velocity profile, with the thinnest boundary layer thickness on the belt and a minimal increase in turbulence intensity.

Figure 3.3a relates to the immediate transition from inlet to test section. The apparent spikes in the x-velocity are due to the local acceleration of the flow caused by the contraction. This is lower for the long straight section of 1150mm, as the turning angle for the flow and the rate of acceleration is less. The inlet with no fairing results in an inconsistent and asymmetric velocity profile, as the lack of a faired inlet produces large scale separation upstream of the test section. Moving to a shorter length inlet of 500mm causes no velocity profile difference other than slightly less uniformity, however the turbulence intensity (figure A.6) increases approximately 30% of the peak turbulence intensity at the throat. The curved inlet geometry only reduced the peak velocity at the corner of the transition from the inlet to the test section. This is due to the acceleration occurring gradually over the radius of the curvature instead of the sharp corner, and does not benefit the test section flow uniformity (figure 3.3b).

A higher rate of stress has been put on the flow in the shorter contraction inlet as the flow has been accelerated over a shorter distance. This results in higher turbulence intensity in the test section (figure A.7), compared to the longer contraction inlet where the acceleration is more gradual. For the low Reynolds number of the test section (Re_H=2.8x10^5), moving to the radiused internal geometry for the contraction inlet would not necessarily show any benefit as the comparison of sharp to radius edges of figures 3.3a and 3.3b show. The construction cost and technical skill required to fabricate it will increase appreciably, so the longer length inlet with non-radius internal corners (but a smaller angle) was used.

A further computational model of the moving ground in the 225mmx340mm test section was produced to focus on the shape of the leading edge fairing, the height of the duct and the size of the duct outlet at the trailing edge of the belt. The larger duct size was expected as the lower free stream tunnel velocity would produce a thicker boundary layer. A duct height of 60mm was decided upon based on the results for the boundary layer profiles at the wing ¼ chord position (see figure 3.4b)

Initial testing of the system with smoke visualization showed a rotation of the flow down the central axis of the tunnel, so honeycomb section was placed throughout the length of the contraction outlet to negate any adverse turning the flow experiences as it enters the vacuum box. Turbulence screens were designed and built in order
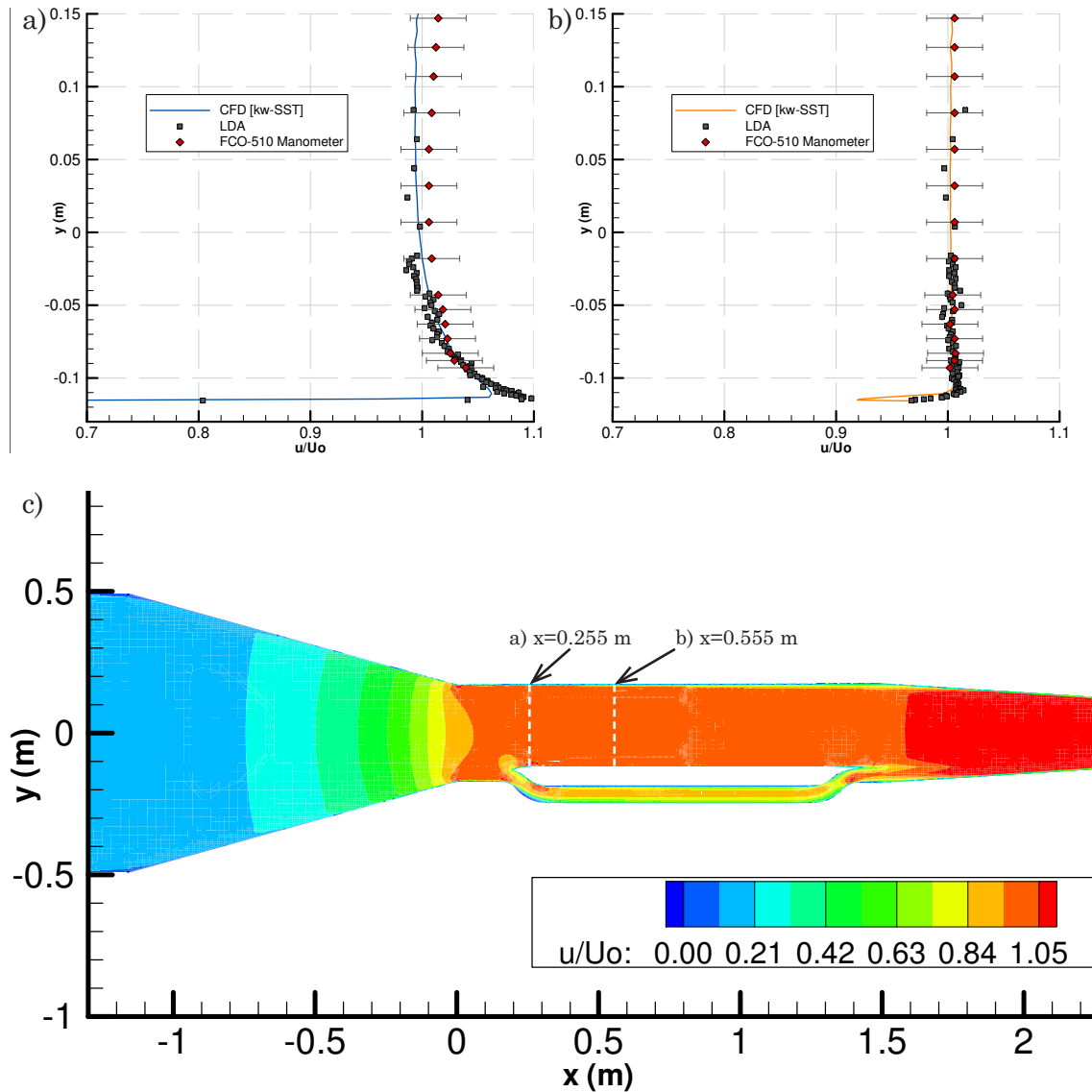
Figure 3.4 Moving Ground Test Section Velocity Profiles a) x=0.255 m b) x=0.555 m c) Full Tunnel

to settle the flow in the room before it enters the tunnel and assists in reducing turbulence in the test section (Motson & Archer, 1969). A screen with Reynolds number range of 30<Re<60 (based on the individual wire diameter) was selected in order to generate minimal turbulence, (Schubauer et al. 1950). The inlet velocity based on the test section area and speed was calculated at 1.3m/s, therefore a wire diameter of 0.3mm was used. Three brass gauze screens of 0.3mm were placed in series 150mm apart from one another between the inlet fairing and the contraction inlet; this eliminated the rotation which later LDA measurements confirmed.

3.3 Wind Tunnel Array Configuration

The interchangeable design of the test section allows multiple configurations to be used. In order for the experimental analysis into the more basic dimple array affects
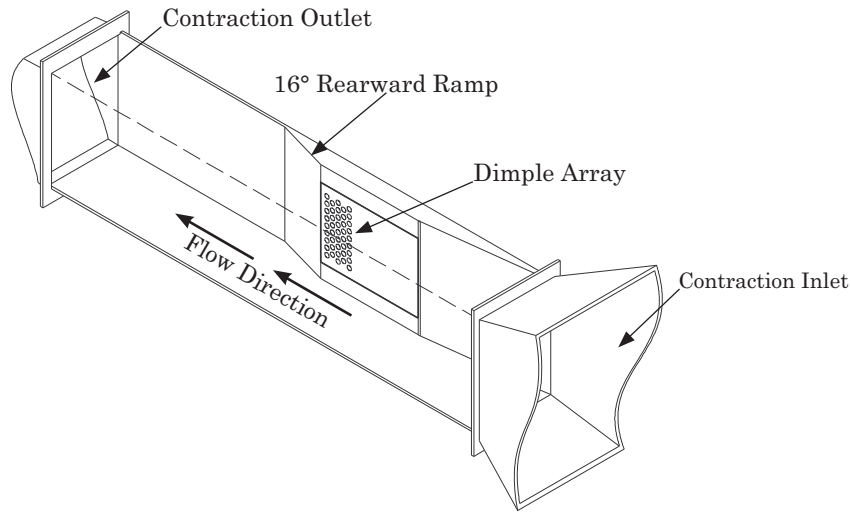
Figure 3.5 Wind Tunnel in Secondary 'Rearward Ramp' Configuration

to be investigated on a rearward facing ramp, the experiments were conducted on the side wall of the test section. This was primarily due to the original test section aspect ratio being narrow but tall, so to minimize corner effects the larger span was used. Secondly this configuration resulted in better optical access for the LDA probes, so the moving ground was replaced with a normal floor and all existing equipment remained in place. Technical information is listed in table 3.2, figure 3.5 shows the test section in this configuration.

Table 3.2 Technical Data for Wind Tunnel in Array Configuration

Test Section Cross section	340mm x 175mm
Maximum speed air speed	30 m/s
Design speed air speed	4.5 m/s
Test Section Reynolds number	$Re_H = 5.3 \times 10^4$
Flow Angularity	$<0.9°$
Turbulence Intensity	0.01%

3.3.1 Wind Tunnel Array Configuration Design

The test section for the rearward facing ramp configuration was limited to the 340mm x 225mm dimensions of the primary test section configuration. The study by Hall (2001) included the flow over a rearward 90° step and used a test section of 225mm x 115mm, so a similar aspect ratio of 1.95:1 and expansion ratio of 1.3:1 was used. This meant that the side structure had 50mm in which to locate the dimple experiments and the 16° ramp. An added benefit of side wall mounting was the improved flow by limiting the effect the side walls had in a narrower aspect ratio duct; the wall taper remaining the same as before. The mounting of the ramp and dimple structure in
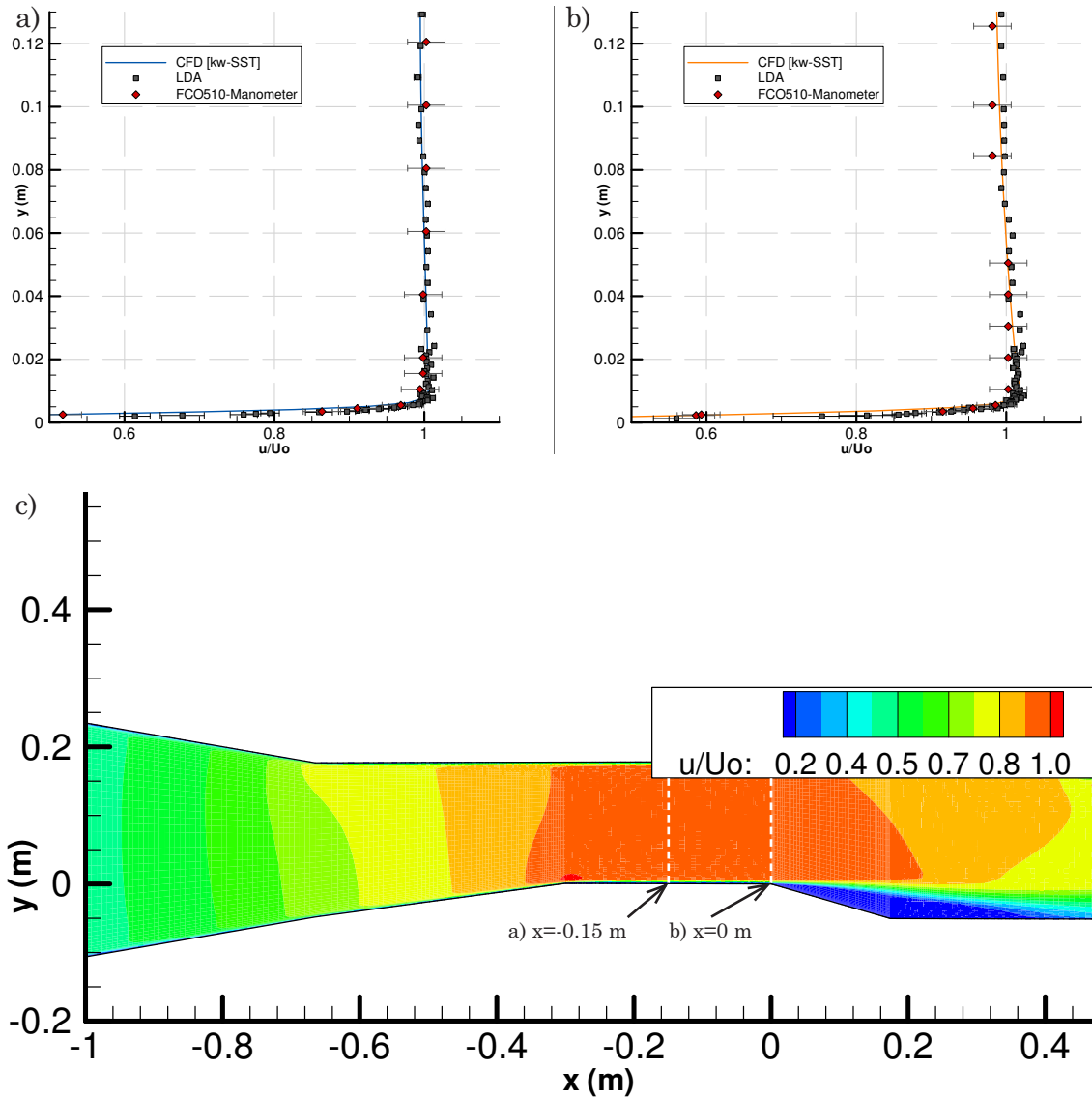
Figure 3.6 Rearward Ramp Test Section Velocity Profiles a) x=-0.15 m b) x=0 m c) Full Tunnel

the side wall allowed the LDA probes to take the measurements and the horizontally positioned PIV system to measure immediately after the LDA.

A known flow separation point and separated flow structure was required to determine the effectiveness of various dimple array geometries in reducing the size of the separation zone, and the location they are required to be from the point of separation. The addition of the 50mm side wall structure including the ramp and the dimple array produced the obvious issue of not having symmetric test section geometry, and initial numerical analysis was conducted to determine how severe this would be. Figure 3.6 shows the numerical results on the central horizontal plane for the test section in the ramp configuration with no dimples. The results were obtained from a three dimensional 1.7×10^6 grid point mesh using $k\text{-}\omega$ SST with $y^+=2.18$.

The normalized velocity profiles of figure 3.6a and figure 3.6b show a consistent velocity profile along the length of the 300mm section ahead of the rearward ramp. In figure 3.6 c); u/U_o=1 throughout most of the test section, the separation zone is clearly present behind the ramp at x=+0.15m; where u/U_o<0.2. The existing taper of the 340mmx240mm cross section is fairly negligible and boundary layer growth does not affect the test section Reynolds number along the length. This is demonstrated by upper and lower boundary layers being 6mm thick in figure 3.6a and figure 3.6b, as the core flow velocity is fairly consistent despite some acceleration from x=-0.15m to x=0m. So the effect of the modifying the existing tunnel into the configuration required for the investigation of the effect of the dimple array on a separated flow from the rear ward ramp is minimal.

3.4 Particle Seeding
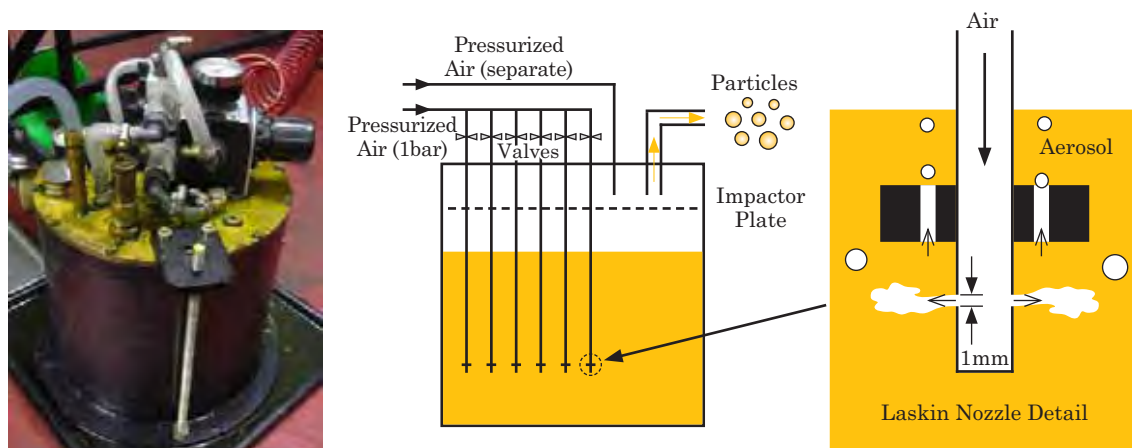
Figure 3.7 Atomizer and Laskin Nozzle mechanism

The ability to conduct PIV and LDA measurements relies heavily on seeding the flow appropriately. This requires that the seeding particle follows the flow exactly, such that the particle should be indistinguishable from the fluid. This would require the particle density to be equivalent to the surrounding flow's density, which is rare, so particle sizing becomes essential in ensuring minimal particle slip. The seeding system used comprises an atomizer using Laskin Nozzles and vegetable oil in order to generate the particles. Figure 3.7 shows the atomizer used, and a diagram of the Laskin nozzles. These nozzles function by pressurized air being forced out of 1mm holes which cause bubbles to form. For 1 bar gauge air pressure, specific to this type of atomizer, 1μm droplets of vegetable oil will form inside the air bubbles due to the

high shear stresses induced by the tiny jets. These bubbles and larger particles are then retained by an impactor plate, allowing the smaller vegetable oil particles to exit. The mean particle diameter is more dependent on the liquid being atomized, and only slightly on the operating pressure of the nozzles (Raffel et al. 1998).

Once the particles are generated, they must have characteristics that are suitable to measuring the flow phenomena. There are two main criteria, the first being to have sufficient light scattering capability, as both PIV and LDA rely heavily on the scattered light to take the velocity measurement. The second criterion is minimal particle slip between the fluid velocity and the particle velocity, such that the particle immersed in the flow follows the flow with minimal deviation. Both of these are dependent on the particle size.

Table 3.3 Particle Slip Velocity Formulae; Albrecht (2003) & Raffel et al. (1998)

$$\tau_o = \frac{\rho_P d_P^2}{18\mu_f} \quad \text{............ [3.1]} \quad 1 - s = \frac{v_P}{u_f} = \frac{1}{\sqrt{1 + \omega_c^2 \tau_o^2}}, \quad \omega_c = 2\pi f_c \quad \text{.......... [3.3]}$$

$$s = \frac{u_f - v_p}{u_f} \quad \text{.......... [3.2]} \qquad d_P < \sqrt{\frac{18\mu_f}{\rho_P f_c} \frac{1}{2\pi} \sqrt{\frac{1}{(1-s)^2} - 1}} \quad \text{................. [3.4]}$$

Light scattering behaviour is important as the PIV camera and LDA receiver optics are located with respect to their respective light sources and the particle. The Mie scatter theory for vegetable oil particle diameter (d_p) of 1μm (Kahler 2004), is shown in figure 3.8, relates the light incidence angle, to the ratio of the refractive index of the particle and the medium it is in. The intensity is in the logarithmic scale, and it can be seen that for particles (1μm) the intensity can be magnified by: 10^5 at 0°, 10^3 at 90°, and 10^8 at 180°. Particles of larger diameter provide greater intensity, however this may lead to increased noise due to the frequency and amplitude of the maxima and minima of the light intensity are more severe as the light is scattered through 360° of the particle. So although 1μm may not have the highest intensity of light scattering, it gives a consistent light scattering behaviour.

The ability of the particle to accurately follow the flow is critical to ensure as accurate a measurement of the real velocity flow field as possible. This is true for both LDA and PIV measurement methods. Figure 3.9 shows the forces and velocities driving the particle's motion in the flow field, and we see that there is the flow velocity V, the particle velocity V_P, and the relative velocity between the two resulting in the slip velocity (V_{slip}), also present are the drag and lift forces F_D and F_L respectively. Taking the vegetable oil used into consideration, the slip velocity of the seeding used can be calculated.

The characteristic time or relaxation time (τ_o) is a measure of the responsiveness of the particle to achieve equilibrium to the accelerations placed on it by the flow field (see equation 3.1), where d_P and ρ_P are the particle diameter and density respectively and μ_f is the fluid viscosity. In this case $d_P=1.0\text{x}10^{-6}$m, $\rho_P=894$kg/m^3 for vegetable oil, thus $\tau_o=2.759\text{x}10^{-6}$ sec. Another important parameter is the velocity slip ratio, s, (equation 3.2), where u_f and v_P are the fluid and particle velocities respectively, and is a measure of a seeding particles lag to the fluid flow.
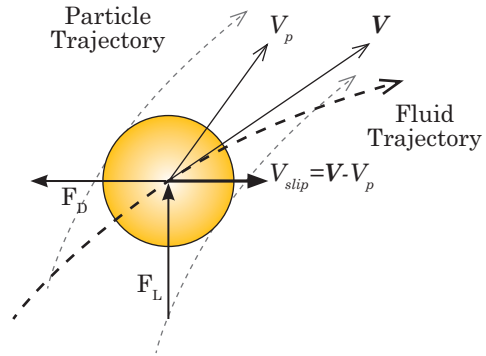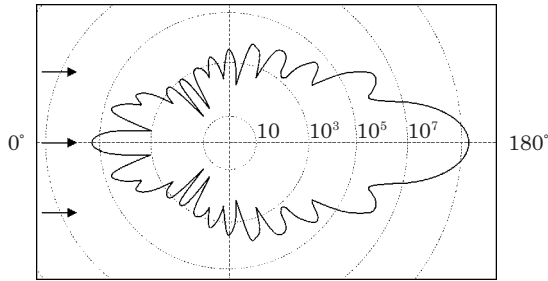
Figure 3.8 Mie Scatter Diagram for d_p= 1μm, Vegetable Oil in air, λ = 532nm   Figure 3.9 Forces on a particle following a fluid

For large particle density to fluid ratios $\rho_P/\rho_f \gg 1$, upon solving for the equation of motion of a particle in a fluid as described by the Basset-Boussinesq-Oseen equation, Albrecht (2003) gave a closed solution by neglecting the body force terms and the Basset term and is a reasonable assumption for a high density ratio (ρ_P/ρ_f). Then for a one dimensional flow field, applying a sinusoidal velocity fluctuation we have equation 3.3; where ω_c is a critical frequency for which a given slip value (of (1-s)=v_P/u_f) can be tolerated. Equation 3.3 also equates ω_c to be a function of the cut off frequency, f_c, where by the particles still follow the oscillations in the velocity, (Albrecht 2003); thus for 1% slip $f_c = 0.0227\tau_o$.

To be able to measure turbulence, the particles must follow the fluctuations in the flow, so particle size and density can limit the fluctuating velocity component of the flow which can be measured (e.g. u-RMS, u' etc). The particle diameter, d_p, for a given cut off frequency must satisfy equation 3.4, Albrecht (2003), so for a vegetable oil particle to have 1% slip velocity, (1-s)=99%, this gives d_p=2.5µm, as the particles used are 1µm, (1-s) approaches 100%. So the atomized vegetable oil particles have good optical and physical characteristics for seeding the flow.

3.5 Three-Axis Traverse System
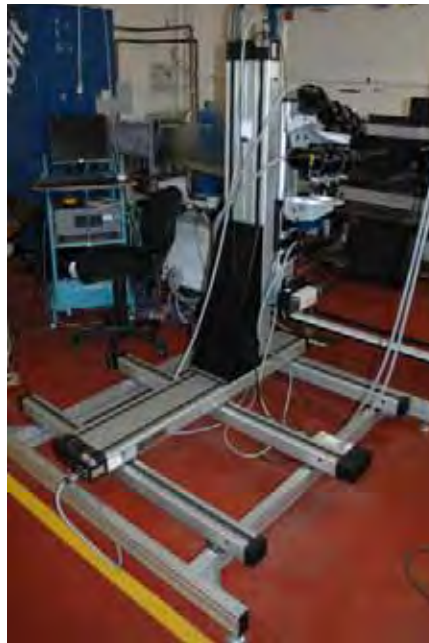
Figure 3.10 Three-Axis Traverse

Integral to the LDA and PIV measurements is the fact that the LDA probes and PIV camera are mounted to a three axis (x,y,z) traverse system, allowing rigid mounting of each system located consistently with respect to the wind tunnel test section. The traverse allows accurate, repeatable positioning of the LDA probes and PIV camera relative to the test object, and removes the need for the PIV camera to be mounted to a tripod so that for composite PIV images, the degree of overlap for a multi-image result will minimize spatial positioning error. For repeating LDA and PIV results of the same grid and orientation, this allows direct comparison between flow fields. The DANTEC 41T333 traverse (shown in figure 3.10) allows 1010mm range in all three axes, with a tolerance of 0.01mm. The traverse system is controlled by using an Isel model C142-4 motor controller.

3.6 Model Dimensions and Reynolds Numbers

Tables 3.4 to 3.7 outline the main reference dimensions and Reynolds numbers for the four main experimental investigations. The single dimple experiments of table 3.4 are outlined in chapter 5. The data related to the rearward facing ramp measurements with and without dimple arrays listed in table 3.5 and 3.6 are covered in chapter 6. The Tyrrell026 clean and dimpled wake measurements are in chapters 7 and 8 respectively, and the key information relating to wing chord and Reynolds number are listed in table 3.7.

Table 3.4 Single Dimple Experiment

δ/D	'D'	Re_D	Freestream U_o	Test Section (Height x Width)	Re_H
0.22	90 mm	9.0×10^3	1.5 m/s	320mm x 225mm	3.2×10^4

Table 3.5 Rearward Facing Ramp Experiment

Ramp Angle	Freestream U_o	Test Section (Height x Width)	Re_H
16°	4.5 m/s	175mm x 340mm	5.3×10^4

Table 3.6 16° Rearward Facing Dimple Array Experiments

δ/D	'D'	Re_D	Freestream U_o	Test Section (Height x Width)	Re_H
0.22	14.75 mm	4.43×10^3	4.5 m/s	175mm x 340mm	5.3×10^4

Table 3.7 Wing Experiments

δ/D	'D'	Re_D	Freestream U_o	Test Section (Height x Width)	Re_H	Wing Chord	Re_C
0.22	4.425mm	4.5×10^3 to 10×10^3	10 m/s	280mm x 225mm	2.8×105	75mm	5.0×104

3.7 Experimental Error

Every measurement has an error associated with it, without a quantitative statement of the error a measurement lacks worth (Cook 2002). Uncertainty is a value related to the result of a measurement that characterizes the distribution of values that can be realistically attributed to the quantity being measured. The ISO Guide (1998) assumes combined uncertainty has a distribution approximate to a normal distribution, i.e. of two standard deviations (σ). A 95% confidence limit approximates to such a range; beyond this the approximation is less reliable (Cook 2002). When dealing with a

value for uncertainty which is linked to another variable, the cumulative sum of an uncertainty 'R' of variable 'Z' is defined by Kline and McClintock (1953) in equation 3.5.

$$\delta R = \sqrt{\sum_{i=1}^{M} \left(\frac{\partial R}{\partial Z_i} \delta Z_1 \right)^2} \quad \text{................................ [3.5]}$$

Table 3.8 Geometric and Measurement Uncertainties

Model Geometrical Errors	Measurement Errors
Single Dimple D±0.01%, δ±0.05%	Atmospheric Pressure error: ±2mmHg
Dimple Array D±0.07%, δ±0.31%	Temperature = ±0.2°C
Wing ground clearance h/c=±0.013%	Pitot Tube Error: ±1%
Wing chord length c=±0.13%, Array D±0.25%	Manometer: 0.25% of reading between 10% and FSD, in calibration throughout testing
Wing angle α=±0.08°	Traverse error: ±0.01mm

Table 3.9 Velocity Setting Uncertainties

Experiment	Velocity	Re$_D$
Single Dimple	1.5m/s ±1.1%	1.11%
16° Rearward Ramp	4.5m/s ±1.1%	1.17%
Wing in Ground Effect	10m/s ±1.1%	1.35%
Moving Ground Speed	10m/s ±0.5%	-

Table 3.8 lists the model geometrical error based on manufacturing tolerances of the models produced, as well as equipment measurement errors given in product data sheets. The Pitot static probe was used to set the tunnel speed, and table 3.9 outlines the free stream velocity measurement error of the three main experimental configurations, the moving ground velocity error is also given.

3.7.1 PIV Error

Various steps were taken in order to minimize the error associated with the PIV measurements. Primarily the camera for recording images was fitted to the traverse, such that repeatable camera positioning was allowed to 0.01mm. Different grid correlation schemes were used in order to determine the free-stream velocity with reference to the digital micro-manometer and Pitot tube. Masking was used to eliminate backscattered light from the test section entering the camera CCD array so high laser sheet intensities were able to be used. This technique was also applied at fringes of the laser sheet entering the tunnel to ensure no excess scattered light would enter the test section and artificially 'thicken' the laser sheet.

$$\varepsilon_{TOT} = \varepsilon_{sys} + \varepsilon_{resid} = \varepsilon_{bias} + \varepsilon_{rms} \quad \text{..} \quad [3.6]$$

Measurement uncertainty in PIV is a combination of various aspects, relating from the digital image recording process and to the methods of evaluation. The absolute measurement error, ε_{TOT}, is defined by a group of systematic errors, ε_{sys}, and another group of residual errors, ε_{resid} (Raffel et al. 1998). The systematic errors relate to potential short falls of the chosen parameters in the statistical cross correlation evaluation, which are prevalent in regions of high velocity gradients (those pertaining to the post image capture analysis). Residual errors comprise those which are due to measurement uncertainty, and remain even when all systematic errors are removed. It is quite difficult to separate some residual error from the systematic error. So it becomes beneficial to split up the total error into being the sum of a bias error (ε_{bias}) due to over or under estimation, and a random error or measurement uncertainty
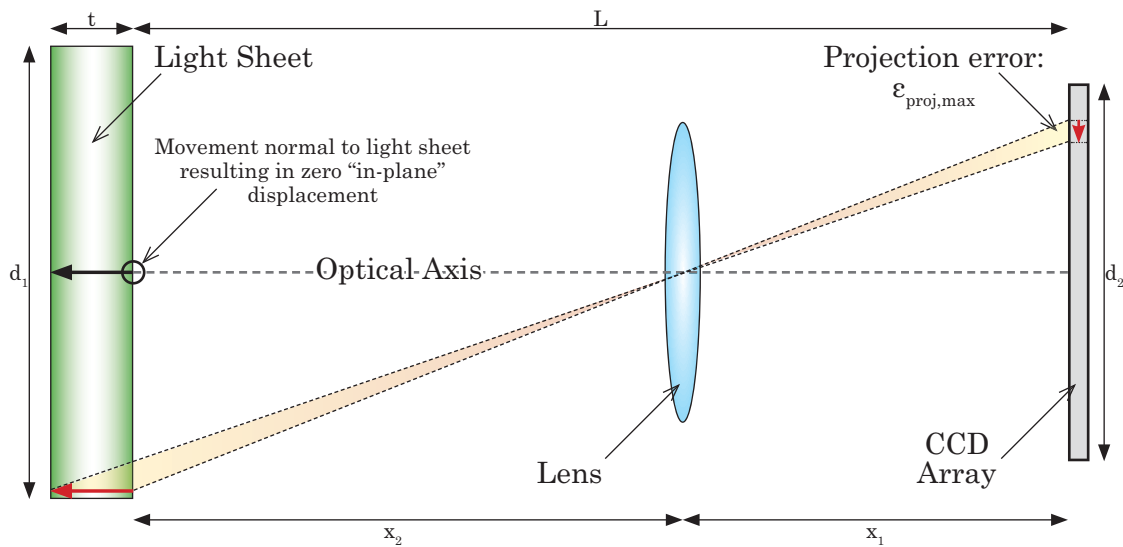
Figure 3.11 Image Perspective Error due to Particle Displacement in Laser Sheet

Perspective error arises when a three dimensional displacement is being projected onto a two component plane, see figure 3.11. This is not such an issue when the particle is travelling on or close to the optical axis. When the movement is further away from the optical axis, a transverse particle displacement in the laser sheet plane will be projected as an in plane displacement on the camera CCD chip. The resulting error $\varepsilon_{proj,max}$ can be calculated using the geometrical relation of equation 3.7. For the given dimensions the typical set up is t=0.2mm, L=400mm, d=1018 pixels equates to $\varepsilon_{proj,max}$=0.25px.

Image distortion arises separate to perspective error, and relates to the image distortion that the focused two dimensional in plane particles are captured onto the CCD through a lens which has some curvature. This gives rise to distortion ΔD mostly around the image periphery, based on the calibration image for the NIKKOR F1.4/55mm lens there is no measurable distortion for the short focal length used. Another image based error arises from image quantization levels. Essentially this is due to the loss of information from recording an analogue input into a digital output relating to the level of compression the image undergoes, i.e. saving from 16 bits/pixel to 8 bits/pixel. Figure G.1, (Raffel et al. 1998), for 8 bits/pixel and particle image shift >1.2px $\varepsilon_{RMS} \approx 0.011$pixels.

$$\varepsilon_{proj,max} = \frac{d_1}{2}\left(1 - \frac{1}{1 + \frac{t}{L}\left(\frac{d_1}{d_2} + 1\right)}\right) \approx \frac{d_1}{2} \cdot \frac{t}{t + L} \quad \dots\dots\dots\dots\dots\dots \text{[3.7]}$$

The laser pulse duration and separation also has an effect on the overall uncertainty of the measurement. If the laser pulse duration is too long the particle can blur or appear streaked. For the system the pulse duration is of the order of 5ns which is short enough to lock particles in a defined position even at very high velocities. The pulse separation was measured with a photo resistor to Δt_p = 1ns.

Due to the nature of the displacement measurement (D) being essentially statistical between the two interrogation windows, a flow with varying velocity gradients will tend to cause slower particles to occur more frequently than the faster particles. This is due to the faster particles leaving the interrogation region more frequently when the slower ones generally stay bounded within it. This means that the calculated velocity can be biased towards the lower values (Raffel et al. 1998). The ε_{RMS} from figure G.2 shows for the approximate displacement gradient of 0.06 (displacement average 4 pixels, window 64px), for N_1=20, 64x64pixel, $\varepsilon_{RMS} \approx 0.5$ pixels.

Background noise will produce an effect on the resultant vectors due to reflections in the tunnel, from models or just back ground interference of the camera. Using a band pass filter on the lens to limit all but the specified wavelength of light from the scattered particles ensures background noise effects to be negligible. The tunnel walls and models are painted black to absorb reflected light, so a minimal noise assumption is valid. When considering random noise generation in figure G.3 for particle shift >1.2 $\varepsilon_{RMS} \approx 0.115$ pixels.

Particle image diameter is of importance to the Gaussian pixel peak approximation (to determine the particle centre) for the correlation as it must be wide enough to ensure there is more than one component exceeding the background noise level. Figure G.4 shows that optimally for a seeded particle to occupy 2 to 3 pixels in the interrogation region, $\varepsilon_{RMS} \approx 0.01$px (Raffel et al. 1998), which is the case for the images taken. Particle image shift is dependent on the flow velocity and Δt_p, based on figure G.5 given an average displacement of 5 pixels, of 64x64 pixels gives $\varepsilon_{RMS} \approx 0.0175$pixel, and also an $\varepsilon_{bias} \approx -0.01$pixel (figure G.5) which is an underestimation due to the correlation estimates being biased due to the in-plane loss of pairs Raffel et al. The parameter Δt_p was generally derived so that for a given pixel/mm ratio based on the calibration image, and for a velocity 75% of free stream to account for low speed particles in the wake a particle would travel on average 5 pixels.

Particle image density will affect the PIV evaluation, as displacement detection increases as more particles enter in the interrogation area and subsequently the correlation calculation. Particle density (or occurrence) in the interrogation region also has a direct impact on the measurement uncertainty. Based on figure G.6, the probability of valid vector detection would be in the order of >90% for $N_I = 7.8$, 64x64px. Given the small cross flow velocity (w) in the experiment, the assumption would be that F_o (out of plane loss of pairs) is small, particularly as the absolute value of w is low given the low freestream velocity of the tunnel. Thus the cross flow velocity, w, will not adversely affect the in-plane two-dimensional PIV measurement of u and v. The band pass filter and laser power setting tends to make N_I (image intensity) more than satisfactory and Δt_p adequate enough that F_i (in-plane loss of pairs) is low, such that an $N_I F_i F_O$ range of 5 to 10 is reasonable, ensuring a valid vector.

In summary, the PIV error analysis outlined above dictates that the perspective error is; $\varepsilon_{proj,max} = 0.25$pixel at edge of the image and $\varepsilon_{proj,max} = 0$ at the centre. The bias errors (ε_{bias}) from the pulse separation (of $\Delta t_p = 1$ns) are negligible, therefore $\varepsilon_{bias} \approx 0$pixel, and for the particle image shift $\varepsilon_{bias} \approx -0.01$pixel, so from equation 3.6, $\varepsilon_{bias,TOT} \approx 0$ pixel. The random error (ε_{RMS}), is comprised of the following; image quantization $\varepsilon_{RMS} \approx 0.011$pixel, displacement measurement $\varepsilon_{RMS} \approx 0.5$ pixel, background noise $\varepsilon_{RMS} \approx 0.115$pixel, particle image density $\varepsilon_{RMS} \approx 0.025$pixel, particle image diameter $\varepsilon_{RMS} \approx 0.01$pixel and particle image shift $\varepsilon_{RMS} \approx 0.0175$pixel. Therefore from equation 3.6

the combined random error $\varepsilon_{RMS,TOT} \approx 0.52$pixel, and 0.77pixels at edges. Thus at the image centre; $\varepsilon_{TOT} = 0.52 + 0 = 0.52$pixels and at the edge $\varepsilon_{TOT} = 0.52 + 0.25 = 0.77$pixels

Therefore the total pixel distance travelled by the particle has an error of 11±**0.52pixels** and 11±**0.77pixels at the edges; based on setting** Δt_p accordingly to the particle displacement of 11 pixels at the respective maximum velocity of the experiments. Thus the error in the PIV due to the image processing for the Single dimple PIV experiment is 6% and for the 16° Rearward Ramp experiments 4%. In reality however it is expected these to be lower, as assumptions were made based on how closely the data in figures G.1-G.7 matched the settings used in the VidPIV analysis software. The good agreement between the LDA and PIV results shown in section 5.3 & 5.4 shows the high ε_{TOT} calculated may be conservative. This is only an estimate to the error induced as a result of the image processing, as information regarding this is limited outside that based on the numerical simulations (Raffel et al. 1998).

3.7.2 LDA Error

Benedict and Gould (1996) outlined uncertainty values for turbulence measurements using LDA on a fluid flow with a normal distribution assumption, listed in table 3.10. The same quantities are listed in table 3.11 as given by the DANTEC LDA software. For a property being measured 'φ', with variable 'x', the uncertainty is determined over a number 'N' of samples by equation 3.8, where h=1.96 for a 95% confidence level. The other velocity components can be found by replacing u with v or w.

$$\Phi = \bar{X} \pm h \left(\frac{\zeta}{N} \right)^{0.5} \quad \text{.................} \quad [3.8]$$

Table 3.10 Statistical variance Benedict & Gould (1996)

Variable: $\bar{X}$	Value for ζ
$\bar{U}$	$\overline{u'^2}$
$(\overline{u'^2})^{1/2}$	$\overline{u'^2}/2$
$\overline{u'^2}$	$2(\overline{u'^2})^2$
$\overline{u'v'}$	$(1 + R_{uv}^2)(\overline{u'^2})(\overline{v'^2})$
R_{uv}	$(1 - R_{uv}^2)^2$

Where:

$$R_{uv} = \frac{\overline{u'v'}}{(\overline{u'^2})^{1/2}(\overline{v'^2})^{1/2}}$$

Table 3.11 Statistical variance, DANTEC (2006)

Mean: $\bar{U}$	$\sum_{i=0}^{N-1} \eta_i u_i$
95% confidence limit, $\bar{U}$	$1.96 \times \sqrt{\dfrac{\overline{u'^2}}{N}}$
Variance: $\sigma^2 = \overline{u'^2} = \overline{u'u'}$	$\sum_{i=0}^{N-1} \eta_i (u_i - \bar{u})$
RMS: $(\overline{u'^2})^{1/2}$	$\sqrt{\sigma^2}$
95% confidence limit, RMS	$1.96 \times \sqrt{\dfrac{\overline{u'^2}}{2N}}$
Cross-Moments: $\overline{uv} - \bar{u}\bar{v} = \overline{u'v'}$	$\sum_{i=0}^{N-1} \eta_i (u_i - \bar{u})(v_i - \bar{v})$
Transit Time Weighting: η_i	$\dfrac{t_i}{\sum_{j=0}^{N-1} t_j}$

The error associated with incorrect angular setting of the one dimensional and two dimensional probes in the transformation matrix equations (equation 2.5) was minimized by direct measurement of the probe angles in the test section. This was achieved by measuring the vertical translation of the beams by putting the focal point (once aligned) on 0.5mm graph paper and moving the probed a set distance backwards. The probes were leveled to ensure the probes were co-planar. High data rates were achieved by a special technique of alignment using a CCD camera allowing beam alignment to a resolution of 5 pixels $\approx 50\mu m$, by placing the beam centre's and receivers all at a coincident point on the CCD display software.

One of the difficulties arising during LDA measurements is the velocity bias associated with recording particle velocity data at a given point (Albrecht 2003 and DANTEC 2006). This is due to the rate of particle movement being attributed to the volume flux of fluid through the measuring volume, Albrecht. The sampling rate of the velocity will increase with the velocity, thus for a given measurement point in the flow, higher velocities will be sampled more frequently than the lower velocities. The arithmetic mean will be positively biased towards the higher velocity over the true mean velocity, thus affecting the results particularly in turbulent flow measurements. The mean velocity is calculated from equation 3.9:

$$\bar{u} = \sum_{i=0}^{N-1} \eta_i u_i \ , \ \ \eta_i = t_i \left(\sum_{j=0}^{N-1} t_j \right)^{-1} \quad \quad \text{............................ [3.9]}$$

where η_i is a weighting factor (for arithmetic weighting is $\eta_i = N^{-1}$) to ensure statistically independent, non-biased velocity results transit time weighting is applied, for which η_i is given in equation 3.9. Transit time weighting (also known as residence time weighting) is consistently reliable for a range of data densities, (Albrecht 2003); alternatively the integral time scale can be calculated and the dead-time can be set accordingly. If it is calculated incorrectly it will affect the results in much the same way as the arithmetic weighting, thus transit time weighting will be used to ensure bias free results.

A fundamental source of error arises from the variation of the fringe spatial frequency, Albrecht. This is due to non-planar wave fronts in the measurement volume and also the beam intersection (hence measurement volume) not coinciding at the beam

waists. This will arise in an error in the Doppler frequency of the particle due to the fringe spacing not being consistent. This is of importance to highly focused beams, where the beam has strong divergence in the beam waist, and strong wave front curvature, (Albrecht 2003). The error due to the fringe separation from the plane wave case results in an error of the Doppler frequency (f_{Err}) described as:

$$f_{Err} \approx \frac{1}{2 \tan \Theta/2} \left(\frac{x_1 z_1}{z_1^2 + l_{R1}^2} - \frac{x_2 z_2}{z_2^2 + l_{R2}^2} \right)$$ ....[3.10]

This error increases with highly focused beams, where there is a strong divergence in the beam waist (Albrecht 2003), as well as if the beams do not intersect exactly at their beam waist (misalignment). So for equation 3.10 and the given optical LDA setup where x is the beam waist, z is the length to the measuring volume along the beam axis; which is directly a result of misalignment, I_R is the ratio between the aperture of a Gaussian beam at the beam waist to the wavelength of the beam and θ is the beam separation angle. Given an ideal alignment; where the beam waist coincides at the measuring volume for both beams, equation 3.10 yields $f_{Err} \approx 0$, which for the accuracy of the CCD alignment method to approximately 50μm is valid to count the frequency error due to large misalignment as negligible.

The mesh used accounted for maximum stiffness in the traverse being vertical, as the moment arm of the probes from the traverse mounting point was the least in this direction. Structural damping was highest in the z-axis (vertical) and worst in the x axis (transverse) as there was little structural stiffness in this direction. The dwell time from traverse stop to measurement start was not programmable and preset to approximately 0.5 seconds, x y z times to dampen sufficiently were measured on the CCD and found to be 4 seconds, 2 seconds and 1 second respectively. Thus to ensure measuring volume 'oscillation' affecting the velocity measurements the traverse direction was predominately in the vertical direction, with a non-measuring x-axis step over at the free stream.

3.7.3 Repeatability

Tests were conducted to show Reynolds number variation in all baseline wing and dimple experiments and best performing cases of the dimpled wing or dimpled ramp to be minimal outside the specified uncertainty of the freestream velocity measurement, for LDA and PIV data sets. The high level of LDA data rate (>1500Hz

3D coincident, transit time weighted samples) and the large number of PIV image pairs taken (1000 i.e. 2000 images over 5 minutes) ensured that repeatability was consistent. Attention was taken to design experimental models that had consistent manufacture tolerances and installation, as well as no disturbances between runs such that geometrical displacement error of the model was negated.
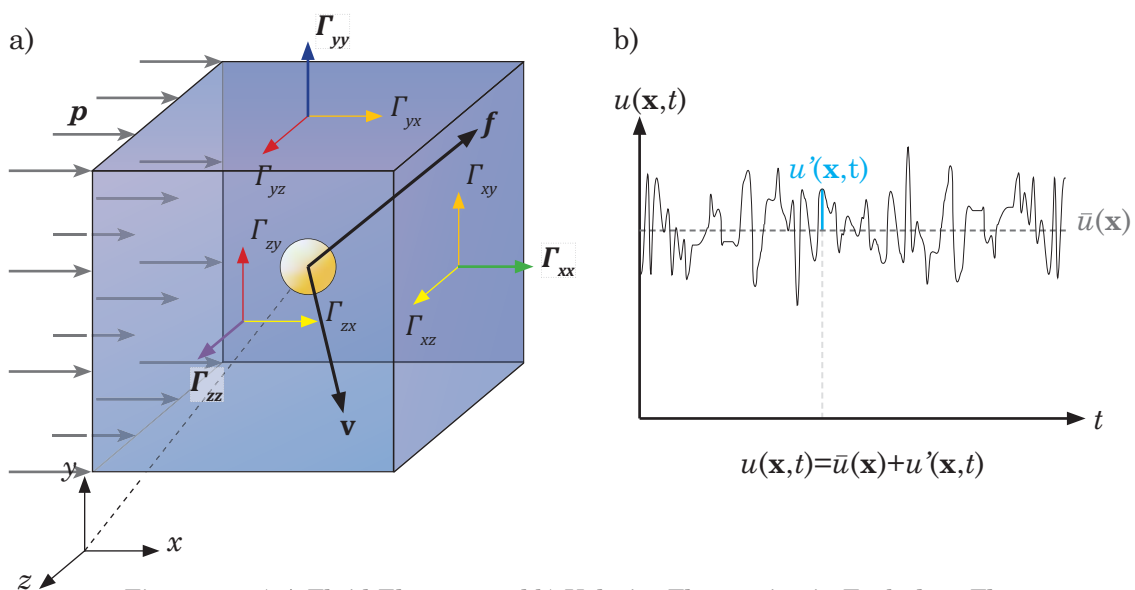
Computational Fluid Dynamics

4

Whilst experimental methods are the primary focus of this study, the theory behind solving the Reynolds Averaged Navier-Stokes equations is addressed in this section. These equations were used on numerical models of the wind tunnel design outlined in chapter 4 and the single dimple flow analysis in chapter 5. Various turbulence modeling methods are outlined, as well as the discretization scheme used and the boundary conditions utilized to numerically model the physical problem. Sources of numerical error are also addressed by discussing the importance of validation and verification

4.1 Introduction

Computational Fluid Dynamics is the application of algorithms and numerical methods to solve fluid flows. In order to numerically model a fluid flow, solving the Navier-Stokes equations of each element of fluid in the control volume is required. The Navier-Stokes equations take into account the forces acting on a fluid element (figure 4.1a), and the physical constraints that are placed on it: conservation of mass, energy (not considered in this study) and momentum. The Navier-Stokes equation is written in general form in equation 4.1 where; **v** is velocity, $\boldsymbol{\rho}$ is the fluid density, p is the pressure, $\boldsymbol{\Gamma}$ is the stress tensor, and $\boldsymbol{f}$ is a body force acting on the fluid.

$$\rho \left(\frac{\partial \mathbf{v}}{\partial t} + \mathbf{v}.\nabla \mathbf{v} \right) = -\nabla p + \nabla.\Gamma + \boldsymbol{f} \qquad \text{............................} \quad [4.1]$$

Figure 4.1 a) A Fluid Element and b) Velocity Fluctuation in Turbulent Flow

4.2 Reynolds Averaged Navier-Stokes Solutions

The Navier-Stokes equations can be solved taking into account incompressible, constant-property flow (i.e. velocity, pressure etc), which gives rise to the Reynolds Averaged Navier-Stokes (RANS) equations. Wilcox (1989) states that time averaging is appropriate for turbulent flow that on average does not vary with time; such as flow in a pipe driven by a constant speed blower, which is the flow condition imposed in the wind tunnel itself. The RANS method replaces the instantaneous values of velocity with time averaged values; refer to solution in Appendix B. One difference between the time-averaged and instantaneous momentum equations is the term $\overline{u'_i u'_j}$, which is a time averaged rate of momentum transfer due to turbulence. Computing $\overline{u'_i u'_j}$ is required if the mean flow properties are to be calculated numerically.

$$\rho\left(\frac{\partial \bar{u}}{\partial t} + \bar{u}\frac{\partial \bar{u}}{\partial x} + \bar{v}\frac{\partial \bar{u}}{\partial y} + \bar{w}\frac{\partial \bar{u}}{\partial z}\right) = -\frac{\partial \bar{P}}{\partial x} + \mu\nabla^2\bar{u} - \frac{\partial\rho\,\overline{u'u'}}{\partial x} - \frac{\partial\rho\,\overline{u'v'}}{\partial y} - \frac{\partial\rho\,\overline{u'w'}}{\partial z} \quad \text{..............} \quad [4.2]$$

$$\rho\left(\frac{\partial \bar{v}}{\partial t} + \bar{u}\frac{\partial \bar{v}}{\partial x} + \bar{v}\frac{\partial \bar{v}}{\partial y} + \bar{w}\frac{\partial \bar{v}}{\partial z}\right) = -\frac{\partial \bar{P}}{\partial y} + \mu\nabla^2\bar{v} \quad \frac{\partial\rho\,\overline{v'u'}}{\partial x} - \frac{\partial\rho\,\overline{v'v'}}{\partial y} - \frac{\partial\rho\,\overline{v'w'}}{\partial z} \quad \text{..............} \quad [4.3]$$

$$\rho\left(\frac{\partial \bar{w}}{\partial t} + \bar{u}\frac{\partial \bar{w}}{\partial x} + \bar{v}\frac{\partial \bar{w}}{\partial y} + \bar{w}\frac{\partial \bar{w}}{\partial z}\right) = -\frac{\partial \bar{P}}{\partial z} + \mu\nabla^2\bar{w} - \frac{\partial\rho\,\overline{w'u'}}{\partial x} - \frac{\partial\rho\,\overline{w'v'}}{\partial y} - \frac{\partial\rho\,\overline{w'w'}}{\partial z} \quad \text{..........} \quad [4.4]$$

The Reynolds stresses are components of stress developed in a fluid by turbulent motions and reveal the principle effects of turbulence on a flow (Hall 2002). Terms on the diagonal; $\overline{u'u'}$, $\overline{v'v'}$, $\overline{w'w'}$ are normal stresses, while the remaining six are shear stresses. Due to the complementary nature of shear stress: $\overline{u'v'} = \overline{v'u'}$, $\overline{u'w'} = \overline{w'u'}$ and $\overline{v'w'} = \overline{w'v'}$, see figure 4.1a, thus six independent Reynolds stresses exist.

4.3 Discretization and the Finite Volume Method

In order to solve the RANS equations for a fluid flow, the control volume defining the region being analyzed must be discretized or broken up into smaller control volumes with no overlap, (Versteeg & Malalasekera 1995). The finite volume method can be applied to these sub-mapped control volumes; this step is required to account for the diffusion throughout the fluid domain. The finite volume method interpolates pressure and velocity terms from discrete grid points of the sub-mapped control volumes, to derive the terms at the cell face between the volumes. Several finite volume differencing schemes exist; central, upwind, hybrid, power-law and Quadratic Upwind (QUICK), however upwind differencing (second order) is the discretization

method used in this study. The hybrid, power and QUICK schemes all utilize the upwind scheme in some form; as the upwind scheme is able to identify the direction of the flow when determining the value at a cell face, (Versteeg & Malalasekera 1995). Figure 4.2 outlines the upwind differencing scheme centering on the central node 'P'. Taking into account diffusion and conduction in the direction East (E) to West (W) as an example; the discretized form of the governing equations for node 'P' in general form is; $a_P = a_W + a_E + (F_e\text{-}F_w)$, where 'a' is the diffusive flux term and 'F' is a convection term across the respective cell face. Therefore now the neighboring nodes can account for the direction, i.e. positive $(F_W{>}0,\ F_E{>}0)\ a_W{=}D_w + max(F_w,\ 0)$ or negative $(F_W{>}0,\ F_E{>}0)\ a_E{=}D_e + max(0,\ \text{-}F_e)$, where 'D' is is a diffusion term, see equations B1-B6 in appendix B for further details.
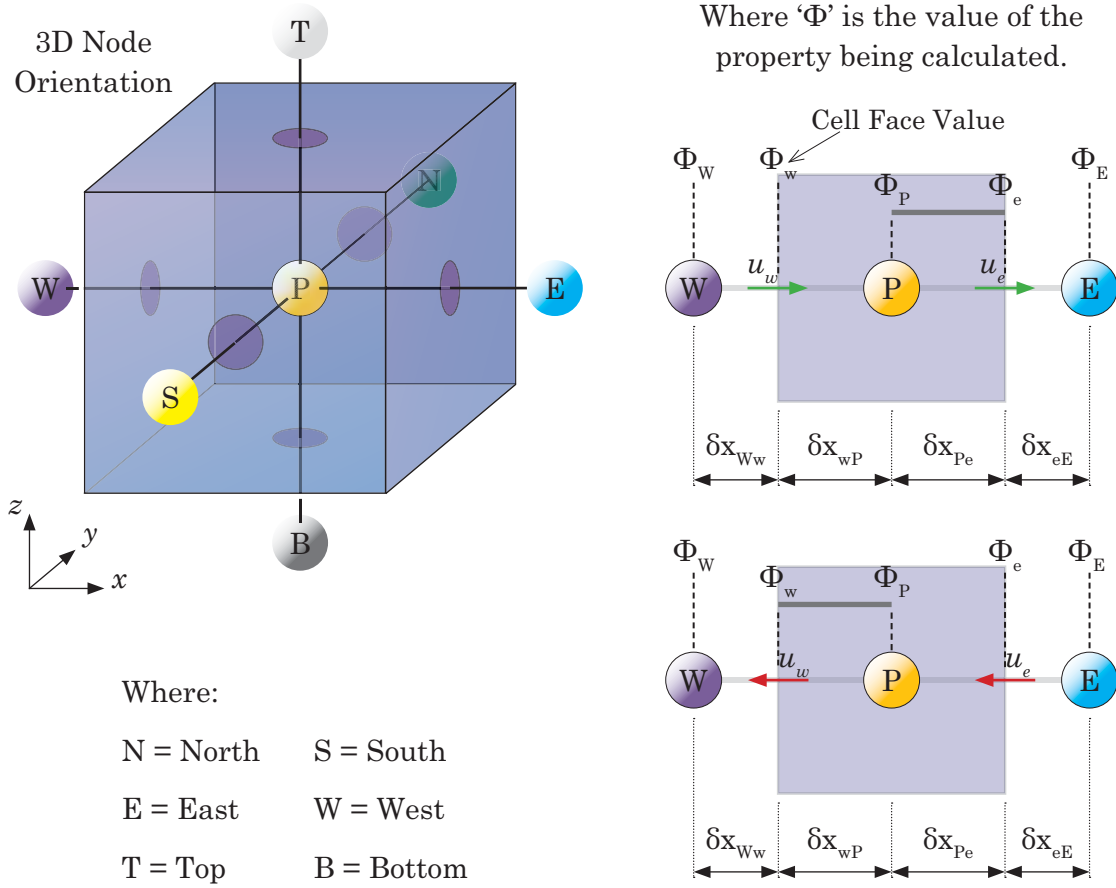
Figure 4.2 Upwind Differencing Scheme

For the Navier-Stokes equations, velocity is coupled to the momentum and continuity equations, but pressure is only expressed in the momentum equation. The SIMPLE velocity-pressure coupling (Patankar & Spalding 1972) is an iterative estimation procedure, whereby a pressure field is guessed and the velocity components are solved

as a result of this estimation. The SIMPLEC (SIMPLE-Consistent) pressure-velocity coupling algorithm (Van Doormal & Raithby 1984) is used to solve the Navier-Stokes equations in this study. This is due to SIMPLEC including terms that are omitted by the SIMPLE algorithm, (Versteeg & Malalasekera 1995).

4.4 Turbulence Modelling and y⁺

The ability to solve the Reynolds Averaged Navier-Stokes equations requires a method of modeling the turbulence in order to close the set of equations by determining the values of $\overline{u'_i u'_j}$. Turbulence models that have been widely used are the two-equation models: k-ε and k-ω, as well as the Reynolds Stress Model. The two-equation turbulence models provide computation of k but also the turbulence length scale, thus are complete and no prior knowledge of the turbulence structure is required, Wilcox (1989). The realizable k-ε model differs from the standard model of Jones & Launder (1972), in that it uses a new formulation for the turbulent viscosity and utilizes a new transport equation for the dissipation rate, ε. This new equation for ε was derived from an exact equation for the transport of the mean-square vorticity fluctuation, (Wilcox 1989). One of the characteristics of this turbulence model is that it satisfies certain mathematical constraints of the Reynolds stresses, which is consistent with the physics of turbulent flows (FLUENT 2006), which standard k-ε and RNG k-ε do not.

The k-ω turbulence model is also used to close the Navier-Stokes equations. The standard k-ω model in FLUENT is based on the Wilcox k-ω model which incorporates modifications for low Reynolds number effects, compressibility and shear flow spreading, FLUENT. The specific dissipation rate (ω), can be thought of as a ratio of ε to k. The Shear Stress Transport model, (developed by Menter), is an addition to the standard k-ω theory. It differs from the standard k-ω model in that there is a gradual change from the standard k-ω model in the inner region of the boundary layer to a high Reynolds number version of the k-ε model in the outer part of the boundary layer. Additionally, the k-ω SST model modifies the turbulent viscosity formulation to account for the transport effects of the principal turbulent shear stress, FLUENT.

A grid related factor that influences solution accuracy is y⁺; where y⁺ is a dimensionless sublayer-scaled distance of velocity. When turbulence-model equations are

integrated through the viscous sublayer, Wilcox (1989) states that it has been shown that it is imperative to require $y_2^+ < 1$, where y_2^+ is the value of y^+ at the first grid point above the surface. If these limits are not adhered to, solution errors throughout the boundary layer are generally large. Wilcox found that grid insensitive computations using wall functions that account for pressure gradients can be obtained with block-implicit methods provided $10 < y_2^+ < 100$. This range appears to hold for boundary layer computations as well, provided that the pressure gradient is accounted for (Chambers & Wilcox 1977).

4.5 Boundary Conditions

Boundary conditions can be introduced by cutting links with the appropriate faces and modifying the source term (Versteeg & Malalasekera 1995). The physical geometry comprising the numerical model needs to be represented in the case of a stationary boundary as a wall with no slip, or with the moving ground plane as a wall with the matched free-stream velocity (i.e. 10m/s). Inlet and outlet conditions need to be set such that fluid can enter and leave the numerical control volume. The inlet boundary condition describes velocity direction and magnitude as well as the turbulence intensity (Tu) and length scale (L) of the flow. Unless experimentally measured turbulence values can be used as the reference, this is prescribed in equation 4.5 where H is the Hydraulic diameter or height of the inlet (Versteeg & Malalasekera 1995). The outlet boundary condition means that the conditions on that boundary cell face are extrapolated from the domain and have no impact on the upstream flow, or zero diffusion flux (FLUENT). It is essential there is no time varying flow over this boundary, thus sufficient downstream placement is required from the model.

$$Tu = 0.1\text{-}5\%, \quad L = 0.07 \times H \quad \text{.....................................} \quad [4.5]$$

Figure 4.3 outlines the method used to input inlet boundary conditions, whereby a larger control volume of the whole wind tunnel was analyzed with a constant velocity inlet and outflow boundary conditions. This ensures that a developed velocity and turbulence profile exists at the contraction inlet to test section interface and is input into the smaller control volume of the test section only. This allows a finer grid in the subsequent 'refined' model, rather than uniform velocity and turbulence set at the faces of the cells across the entire velocity inlet. The outflow distance to the
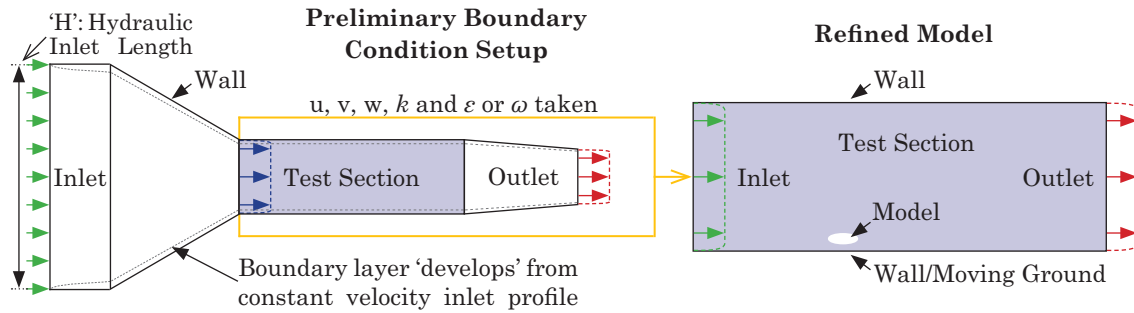
Figure 4.3 Numerical Model Boundary Conditions

smaller numerical model was extended in order to minimize its influence on the model. For the three dimensional boundary conditions used for the moving ground, single dimple and rearward facing ramp see Appendix B: figures B.1, B.2 & B.3.

4.6 Numerical Uncertainty

Uncertainty and error are associated with loss in accuracy of modeling and simulation. In Computational Fluid Dynamics solutions there are four predominant sources of error; insufficient spatial discretization convergence, insufficient temporal convergence, insufficient iterative convergence and programming related issues, (AIAA Guide 1998). Essentially these relate to grid size and quality, time step selection, convergence criteria and programming issues such as: boundary condition location and selection, turbulence modeling, discretization scheme and pressure-velocity coupling method.

Verification and validation is used to determine the accuracy of the numerically predicted result, (AIAA Guide 1998). Verification determines if the numerical model accurately represents the theoretical description of the model and its solution, pertaining to programming. Validation determines whether a numerical model represents the physical process being analyzed, and requires a benchmark experimental result for comparison. A quantifiable level of numerical error in relation to a particular quantity is attainable if a specific property is being solved for i.e. lift force, temperature etc. Whereas for flow structure the process is not as straight forward, velocity profile information (x, y and z velocity components) have to be compared and require an experimental result as a base-line comparison to determine the level of accuracy in the simulation.

4.7 Summary

The steady-state RANS numerical simulations outlined in 5.1 are solved using FLUENT 6.3.17 (solver) and GAMBIT 2.3.16 (meshing) and utilize the following methods:

- Second Order Upwind Differencing Scheme
- SIMPLEC pressure-velocity coupling
- Turbulence Intensity 0.01% relating to experimental measurements in 3.1

Verification and validation focused on grid sizing and turbulence modeling methods, and boundary condition location were able to be assessed with comparable experimental analyses.

Validation and Verification of Dimple Flow Dynamics

5

Measurements inside a single dimple were taken using three-dimensional LDA and two-dimensional PIV. These results are the focus of chapter 5 and comparing them to RANS numerical simulations to not only conduct a verification and validation analysis, but to investigate the flow within a single dimple in greater detail. The vorticity inside the dimple as well as the surrounding volume and downstream surface is investigated to determine how much of the surrounding flow is affected as a result of the dimple and how effective it is in producing vorticity in the boundary layer.

5.1 Introduction

In order to establish the legitimacy of a numerical analysis, it is effective to compare the results to those obtained experimentally where possible. Previous numerical studies directly compare against measurable quantities such as; surface pressure (Moryossef & Levy 2004), wake profiles and force coefficients (Mahon & Zhang 2005), while other studies compared the numerical error specific to the grid density (Park & Desam 2004, Won & Ligrani 2004 and Ligrani & Park 2005). To obtain an efficient, robust numerical model of physical flow phenomena, a combination of comparing the model to an experimentally obtained data set and to the numerical model itself is required, as outlined in AIAA Guide (1998).
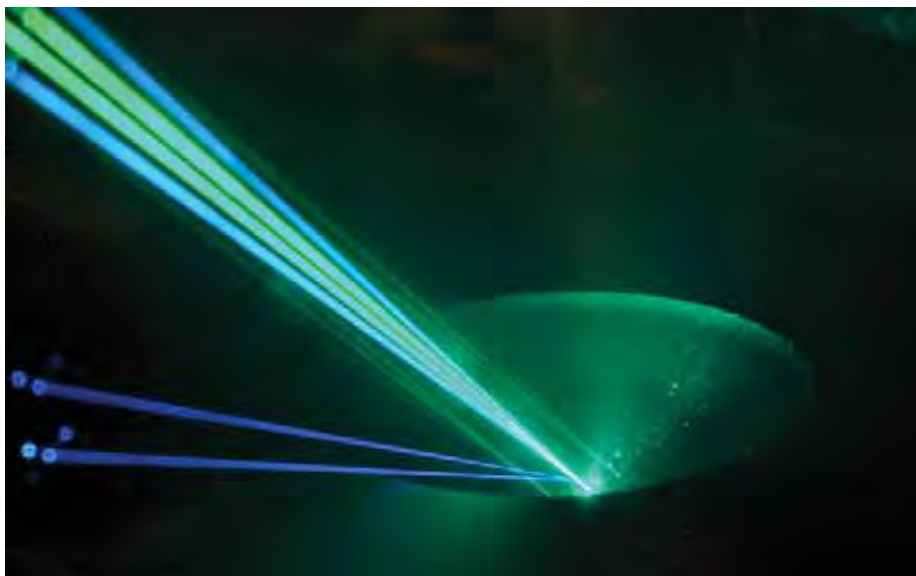
Figure 5.1 LDA Measurements Inside Dimple; 90mm Diameter, δ/D=0.2

For the analysis of the flow within an array of dimples, it would be prudent to begin with understanding of the basic flow in the dimple at the operational Reynolds numbers particular to the study. This will also minimize the amount of variables and flow interaction encountered in such a potentially complicated flow field by starting with the base line case of a single dimple recessed into a flat plane. As stated earlier (Chapter 1.4.2) δ/D is set to 0.22, to maximize the vortex producing effect for minimal drag, as well as a sharp edge radius in order to have a definite separation point in the dimple. The Reynolds Number range based on the dimple print diameter (Re_D) is set according to the expected flow speeds of the experiment. For a dimple with print diameter D=4.425mm placed on an inverted wing in ground effect, the flow over the surface can vary from the freestream speed of $U_o \approx 10$m/sec, to u>20m/sec for lower ground clearances where C_P can be greater than 2, (Zerihan 2001). Thus in its operational range Re_D can be expected to vary from 4.5×10^3 to 10×10^3. Taking this into consideration the upper and lower Reynolds number limits will be considered in a Reynolds Averaged Navier-Stokes analysis of the three dimensional geometry.

5.2 Experimental Equipment and Setup
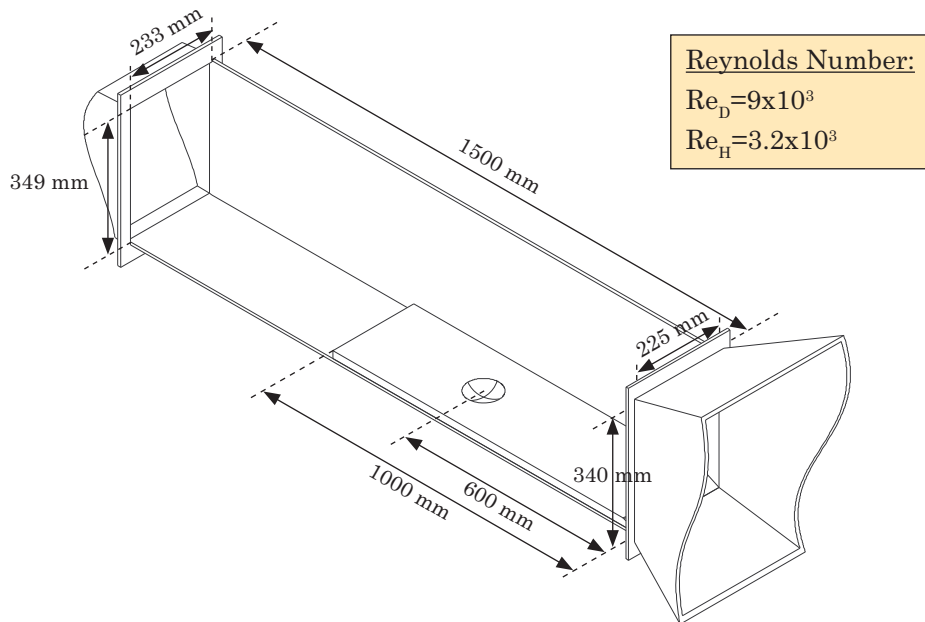
Figure 5.2 Test Section Dimensions and Single Dimple Model Position

An experimental requirement of the LDA measurements dictated a large single dimple was needed for validation and verification purpose, figures 5.1 to 5.4 show the model used, how it is positioned in the tunnel and the dimple geometry. A dimple

with 90mm print diameter (D) and 19.8mm depth (δ) was used, this maintained the depth to diameter ratio of $\delta/D=0.22$, see figure 5.4. The size allowed more precise grid discretization inside the dimple for the LDA as the traverse mechanism is limited to 0.05mm increments; resulting in 1300 mesh points in the cavity centre plane, see figure 5.5a.

Figure 5.3 Single Dimple Test Model

Dimple Print Diameter '**D**'

90 mm

Dimple depth '**δ**' 19.8mm
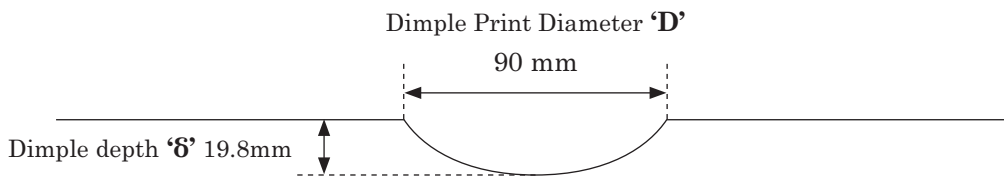
Figure 5.4 Dimple Dimensions: dimple diameter to depth ratio 'δ/D' of 0.22

The LDA probes were positioned so the beams from the two probes could record three velocity components down to the surface of the dimple (see figure 5.1), without being broken by the spanwise rim of the dimple closest to the probes. This required an orientation of 47.5° and 27° for the two-dimensional and one-dimensional probe respectively. The surface of the 90mm dimple was anodized matt black to reduce the amount of reflection of the aluminium surface, however the curvature of the surface still produced back scattered light which affected the readings close to the surface.

In order to position the PIV camera such that it could also capture images to the dimple surface an angle of 12° was required so that the rim of the dimple was not blocking the light sheet. For larger images such an angle can cause distortion in the upper and lower parts of the PIV image. However for the lens used, the actual part of the image used to record the velocity was reasonably small and the seeded particles in the laser sheet were in focus. The agreement with the LDA data set ensures this error was negligible, a full account of which is found in chapter 3.7. The major source of interference comes from backscattered light off the surface of the dimple facing the camera and also the rim of the dimple.

The nature of the PIV analysis being resolved with a grid of 62x62 pixels with a 16x16 offset results in a 'smoother' time averaged flow field than the LDA; which takes individual point measurements only. Data recorded by the LDA was taken over 1.5 seconds with an average data rate of 1500Hz and peak of 3500Hz above the dimple, PIV was processed with 1000 image pairs (over 180 seconds). Due to the two-dimensional nature of the PIV system, only streamwise and normal velocities are measured on the centre plane of the dimple. No other planes were measured in the dimple with the PIV, therefore only positions 1 and 3 (figure 5.6) have PIV measurements for u and v. LDA data exists for u, v and w at all three positions.
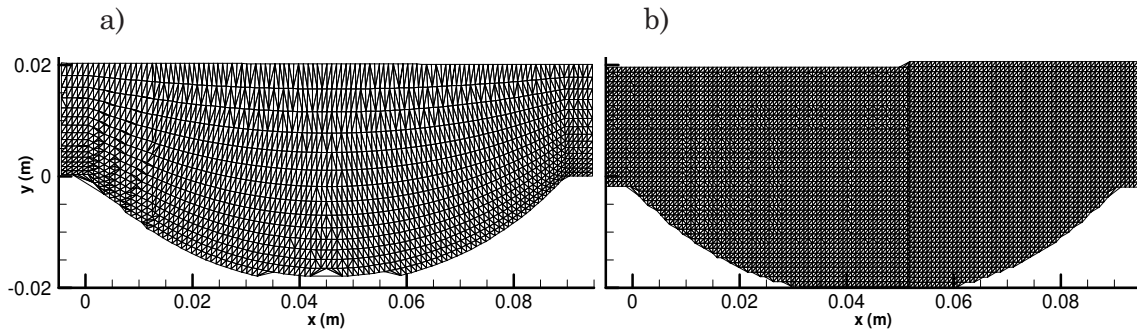
Figure 5.5a) LDA grid and b) PIV grid on z/D=0 plane

Error bars for the PIV experimental uncertainty and the LDA 95% confidence limit for velocity are shown in figures 5.7 to 5.19. LDA uncertainty is low due to alignment and seeding techniques, apart from where wall reflections affect the measurement of seeding particles. Figure 5.22 shows a region of low velocity at x=0.09m y=0m, this relates to laser sheet reflections on the dimple rim. The PIV cross correlation mistakes this as seeding, as it present at the surface in both images, and does not move ('D' in equation 2.7) the velocity is zero.

5.3 Single Dimple Validation and Verification

The numerical analysis for the single spherical dimple is based around a scaled up dimple diameter of D=90mm, and only the higher experimental Re_D is considered. The results concern the numerically predicted three-dimensional flow profiles within the dimple in reference to the experimentally obtained flow profiles for the three-dimensional LDA measured velocities and the two-dimensional PIV velocities. The velocity profile analysis will be largely qualitative as in Mahon & Zhang (2005). For the case of the flow in the dimple, three specific locations are taken to determine the

three-dimensional flow profiles, as seen in figure 5.6. The locations attempt to show; the initial separated flow region in the upstream face of the dimple at x/D=0.27D z=0D, the downstream flow and recirculation centre at x/D=0.61 z=0D and the flow off the centre plane of the dimple at x/D=0.5 z=0.22D.
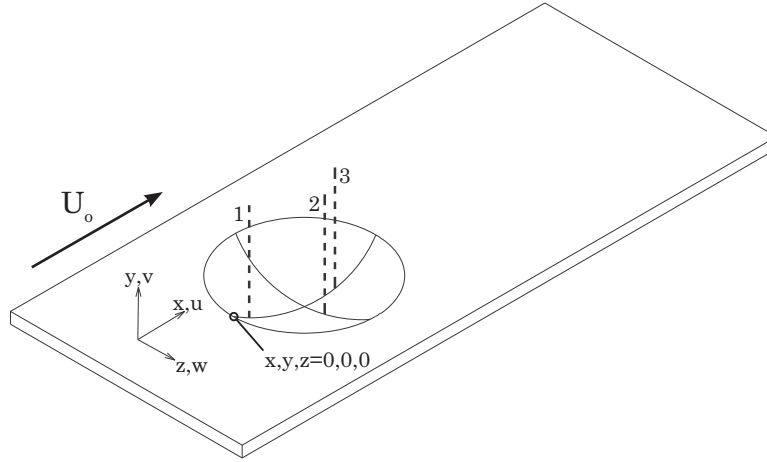
Figure 5.6 Dimple Dimensions: dimple diameter to depth ratio 'δ/D' of 0.22

The Reynolds Averaged Navier-Stokes equations need closure with a turbulence model in order to be solved, as outlined in Chapter 4. There are several commonly used two equation turbulence models; k-ε standard, k-ε RNG (Renormalized Group Theory), k-ε Realizable, k-ω standard and the k-ω SST (Shear Stress Transport), which have been used in numerical modelling of dimple flow, see table 1.1. As part of a complete numerical verification the influence of the turbulence modelling method, the cell size used and the degree to which the level of the error between iterations converges all need to be assessed with respect each other and preferably also to an experimental result. This will determine the validity of the numerical representation of a physical flow. Several studies have investigated k-ε and k-ω turbulence models, but not a direct performance comparison of each other with equal Re_D and δ/D, nor with any reference to a flow field measurement inside a spherical dimple such as Isaev & Kharchenko (1994), Isaev & Leont'ev (1999, 2000, 2001, 2002).

The boundary layer state upstream of the dimple is shown in figure 5.7 for experimental, numerical and theoretically 'ideal' laminar/turbulent boundary layer profiles. The approach boundary layer for the k-ω SST model shows reasonable agreement with the LDA measured profile, whereas the laminar model predicts a boundary layer profile in between the experimental result and the ideal laminar

boundary layer. It is evident from figure 5.7, that the flow upstream of the dimple in the experiment is approaching a turbulent profile. Thus utilizing turbulence modelling for the RANS numerical solution seems appropriate, particularly as the grid is fine enough the boundary layer will be derived from non-equilibrium wall functions (i.e. it is calculated, a standard boundary layer profile is not mapped to the surface) as is the case for k-ω SST in figure 5.7.
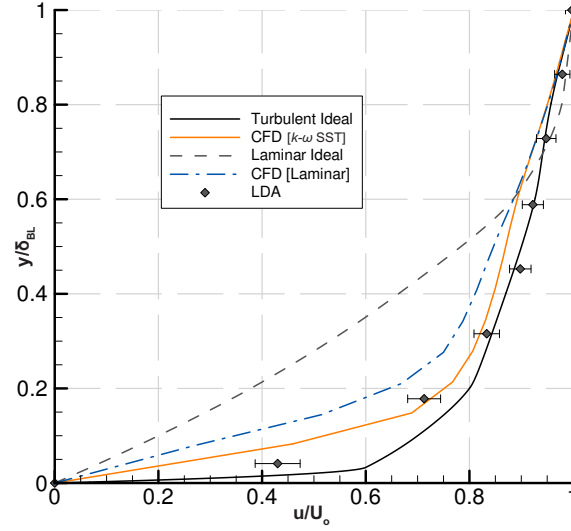
Figure 5.7 Boundary Layer Profile 30mm upstream of Dimple, $\delta_{BL} \approx 24.3$mm
[$Re_D = 9.0 \times 10^3$, $Re_H = 3.2 \times 10^4$]

Previous studies outlined in the literature, either experimental/numerical only outlined Re_H for the test section or Re_D for the dimple, no boundary layer measurement ahead of the dimples was made, thus information relating to the type of boundary layer (i.e. laminar/turbulent) upstream of the dimple largely does not exist. Throughout the literature, the flow physics within the dimple was based off Re_D, which seems to be more critical for the previously described flow mechanics within the dimple.

5.3.1 Streamwise Velocity

At the first ordinate, in figure 5.8 at the upstream region of the dimple, experimental results for the LDA and PIV both indicate a large scale reversed flow region from y/D=-0.05, to the surface of the dimple. This region is beneath a shear layer from y/D=±0.05. The two equation turbulence models using k-ε all exhibit an under prediction of the size of this recirculation zone, k-ε standard shows more of a stalled velocity profile up to y/D=-0.13. The k-ω SST and Reynolds Stress turbulence models both yield bigger recirculation zones, although the shear layer is not as strong as

the k-ω SST model. The result for u/U$_o$ of k-ω standard behaves erratically, showing positive velocity near the wall in this region, this is due to the prediction of two small, counter-rotating vortex cells either side of the profile position and a third, bigger vortex cell in the downstream half of the dimple, (see figure C.6).

Further downstream (figure 5.9) at the off centre position, x/D=0.5 z/D=0.22, the streamwise velocity shows good agreement for the k-ω SST turbulence model. It is clear that k-ω standard is not affected by the presence of the two vortex cells it predicts in the upstream face of the dimple. The Reynolds Stress model over predicts the thickness of the shear layer, and the wall treatment continues to show insufficient grid discretization very close to the wall of the dimple before u/U$_o$=0 at the surface. Results for k-ε standard, Realizable and RNG all show a similar stalled flow regime as at the first position; however u/U$_o$>0.

The final downstream ordinate at x/D=0.61 z/D=0, in figure 5.10, shows the shear layer weakening as it loses energy and breaks down within the dimple. A large recirculation zone exists (as u/U$_o$<0 for y/D<-0.075), which k-ε standard, RNG and Realizable for the most part do not predict, (similar to figure 5.8). The streamwise velocity profile for k-ω standard no longer shows the influence of the double vortex cell on the upstream face of the dimple. Although the Reynolds stress and k-ω SST still perform nearly identically in predicting the size of the recirculation zone, albeit that the Reynolds stress turbulence model over predicts the shear layer thickness more than k-ω SST.

The numerical data outlined in figures 5.7, 5.8, 5.9 and 5.10 show reasonable agreement for the k-ω SST and Reynolds Stress turbulence models with the experimental data set. However, only comparing one velocity component, as in Mahon & Zhang (2005), does not indicate the overall accuracy of a numerical solution, as this does not account for the secondary flows. Analysis of the normal and spanwise velocity components will add to the validity of the numerical model in being able to say if it is an accurate description of the physical three-dimensional flow field.

The difference between the numerical results and the experimental results for u/U$_o$ above the dimple for y/D>0.1 can be seen in figures 5.8, 5.9 and 5.10, and additionally comparing the numerically predicted upstream boundary layer in figure 5.7. The numerical results tend to be slower than the experimental results which can be
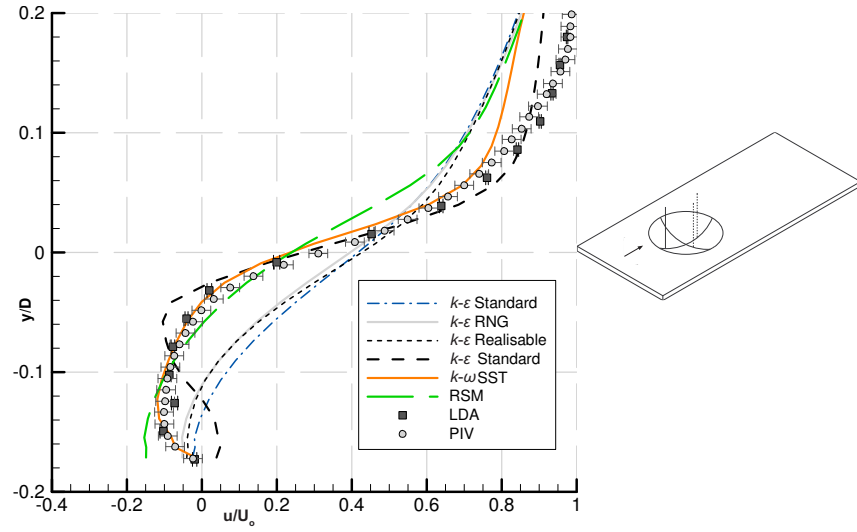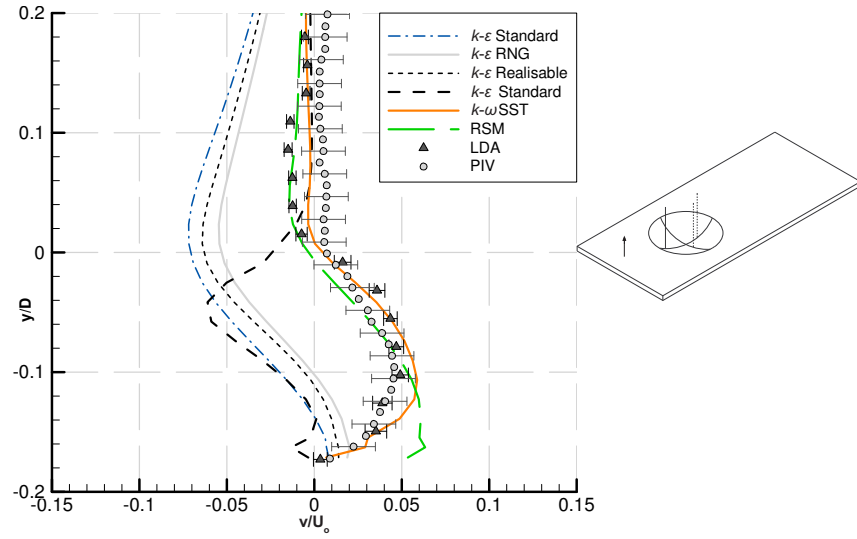
Figure 5.8 Position 1 Normalized Streamwise Velocity Profiles for $Re_D = 9 \times 10^3$
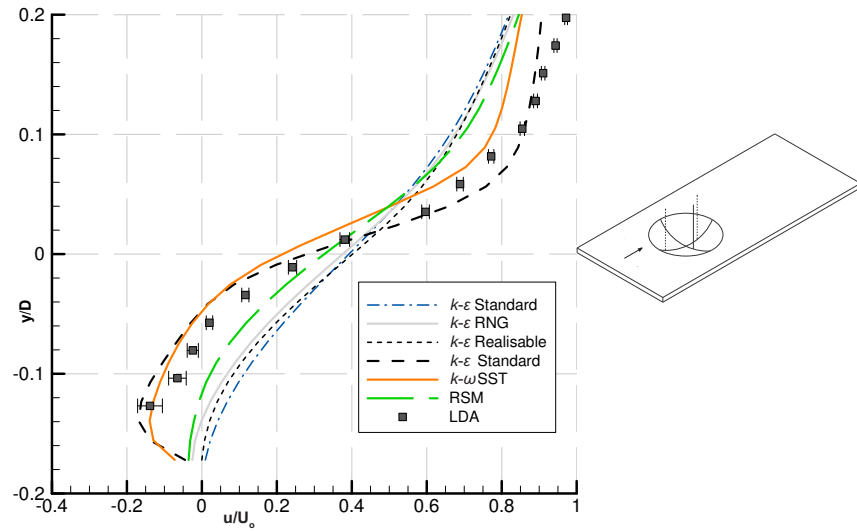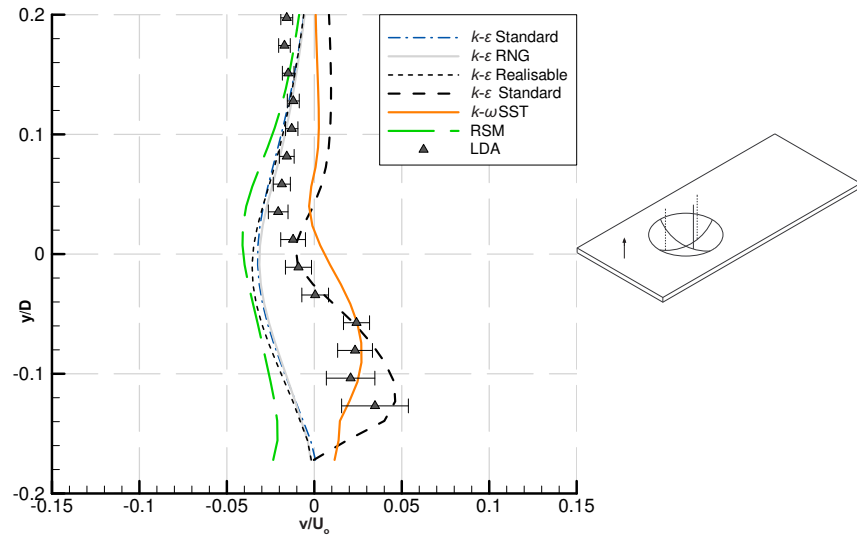

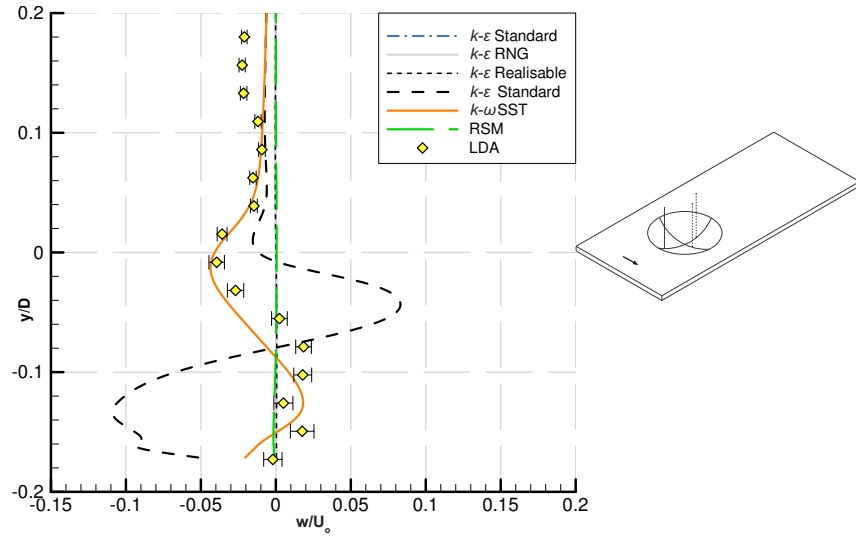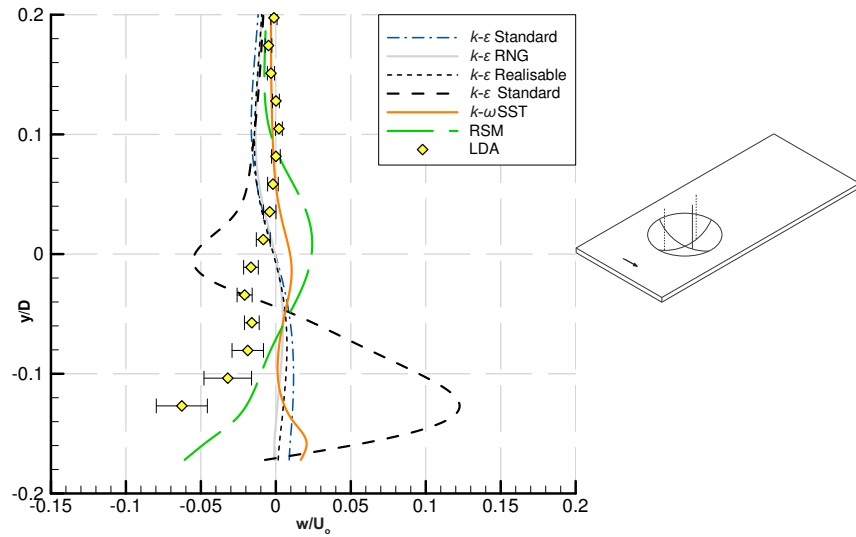Figure 5.9 Position 2 Normalized Streamwise Velocity Profiles for $Re_D = 9 \times 10^3$
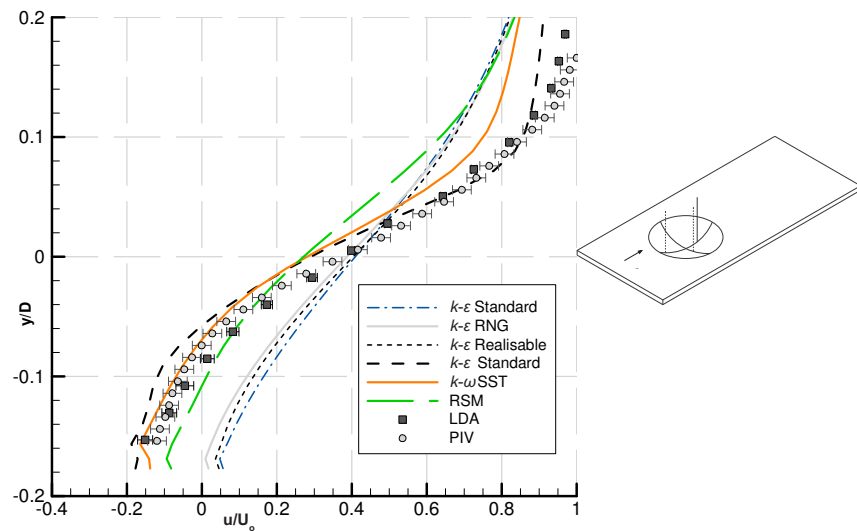
Figure 5.10 Position 3 Normalized Streamwise Velocity Profiles for $Re_D = 9 \times 10^3$

attributed to the velocity inlet boundary condition. A constant velocity was set at the inlet of the tunnel (see figure B.2) to match the 1.5m/sec in the test section. Initial wind tunnel design numerical models showed the affect of the tunnel inlet geometry gap to the floor by slightly speeding up the boundary layer on the lower test section surface as the floor gap is smaller than the distance to the roof (see figure A.1 at x=0m). As the room conditions were not considered along with any initial seeding particle velocity as it left the atomizer, these affects would be greater at the lower Re_H here.

5.3.2 Normal Velocity

A positive velocity component exists on the upstream face of the dimple as seen in figure 5.11 for y/D<0. This is a result of the flow in the recirculation zone returning against the bulk flow along the surface of the dimple. The curvature of the upstream face of the dimple forces the flow up towards the free surface where it is constrained by the shear layer. At the first ordinate the k-ε turbulence models all predict a downward flow velocity, suggesting that the flow spills into the cavity from the upstream rim of the dimple and over a small separation bubble and stalled region (Figure C.3, C.4 & C.5). The Reynolds Stress and k-ω SST turbulence models all calculate a strong positive normal flow, although the Reynolds stress turbulence model shows this region is marginally smaller than the experimental and k-ω SST result. The two vortex cells that are predicted by the k-ω standard turbulence model which are present in upstream face of the dimple result in a negative normal velocity for y/D<0.05. This results in the upstream vortex cell spinning against the flow and down the upstream face of the dimple

The second ordinate downstream at x/D=0.5 z/D=0.22, shows some downward flow of fluid into the dimple from the boundary layer above the dimple for y/D>-0.03, seen in figure 5.12. This can be attributed to this position being closer to the spanwise edge of the dimple and near the side 'windows' that capture the fluid from wall layer outside and above the dimple. From y/D<-0.03 positive flow from the main recirculation zone still exists, although it is weaker. At this position only k-ω standard and k-ω SST predict this positive normal flow velocity component. The Reynolds Stress and all of the k-ε turbulence models all indicate downwards flow that is spilling in from the sides of the dimple and the upstream rim.

Figure 5.11 Position 1 Normalized Normal Velocity Profiles for $Re_D=9x10^3$

Figure 5.12 Position 2 Normalized Normal Velocity Profiles for $Re_D=9x10^3$
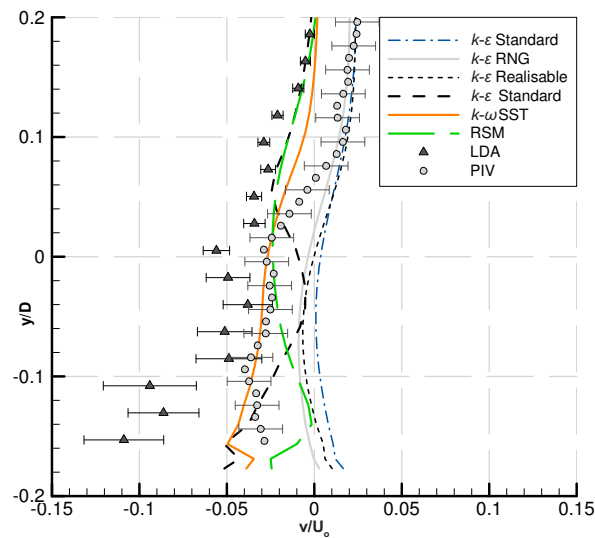
Figure 5.13 Position 3 Normalized Normal Velocity Profiles for $Re_D=9x10^3$

The normal flow velocity profile at x/D=0.61 z/D=0 of figure 5.13, shows low normal velocity for the whole range of y/D, coupled with the transition from positive to negative streamwise flow seen in figure 5.10 at y/D=-0.075. This position corresponds to the main flow recirculation zone centre on the centre plane of the dimple. The increase in the negative normal velocity of the LDA measurements for y/D<-0.1, is a trend reflected by the k-ω SST result. This is due to the fluid following the surface of the cavity of the dimple as it moves to the lowest point of the bottom surface of the dimple, as seen in figures 5.27, 5.28 and 5.29. Both the k-ω SST and PIV results show good agreement with the general trend of the LDA measurements. The LDA and PIV results are strongly affected close to the surface of the dimple at this point, both by lower seeding and surface laser sheet reflections respectively. This causes an in increase both the error and the discrepancy between the two results.

The Reynolds Stress turbulence model yields results similar to the velocity profile distribution of k-ω SST, LDA and PIV in figure 5.13. Although for the Reynolds Stress model the recirculation zone centre is further upstream at x/D=0.52 and appears to be flatter. Thus the Reynolds Stress model calculates a lower stagnation point in the downstream surface of the dimple than k-ω SST, see figure C.7 and C.10.

5.3.3 Spanwise Velocity

The spanwise component of velocity shows the largest discrepancy between the turbulence models. The agreement between the LDA measurements and the k-ω SST turbulence model is quite good for the three different positions in the dimple. At the first position, x/D=0.27D z=0D in figure 5.14, k-ω standard shows significant spanwise velocity components. However the flow in this region is affected by the two vortex cells predicted by k-ω standard, and not indicative of the real flow. The Reynolds stress and k-ε turbulence models all show negligible spanwise velocity, for both position 1 and 3, whereas the LDA measurements are indicating a highly three dimensional spanwise flow in the centre of the dimple.

The flow for the position at x/D=0.5 z=0.22D, as seen in figure 5.15, shows higher negative spanwise velocity for the LDA measurements. This is due to the position near the spanwise edge of the dimple allowing more influence by the side 'windows' noted in Isaev & Leont'ev (2000, 2001). Fluid enters the recirculation zone of the dimple from the side, the negative flow here indicates it moves to the centre plane.

Figure 5.14 Position 1 Normalized Spanwise Velocity Profiles for $Re_D=9x10^3$

Figure 5.15 Position 2 Normalized Spanwise Velocity Profiles for $Re_D=9x10^3$
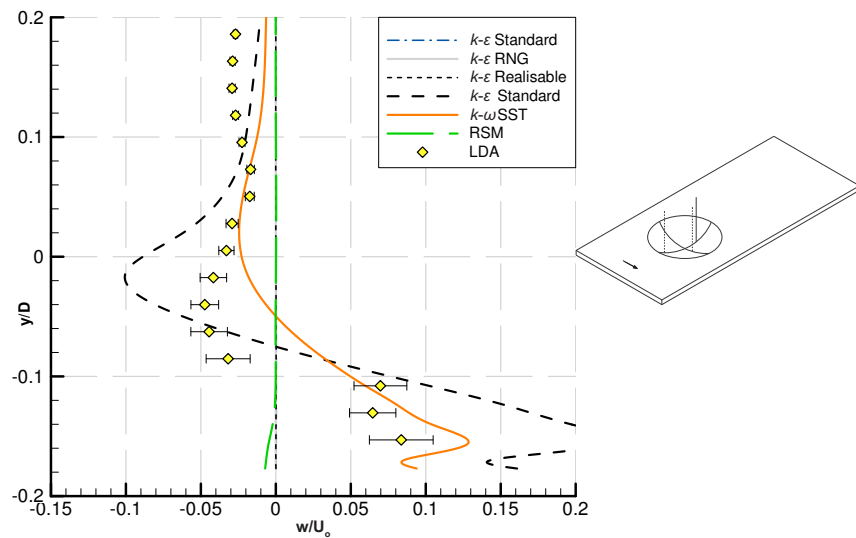
Figure 5.16 Position 3 Normalized Spanwise Velocity Profiles for $Re_D=9x10^3$

The LDA error increases as y/D reduces to the wall, as the curvature of the side face of the dimple causes reflections which affect the data rate, however the agreement holds. The Reynolds stress and k-ε turbulence models all show some deviation in the spanwise velocity. Low pressure is likely to be present in the middle of the dimple which (regardless of the turbulence model) will augment the spanwise velocity.

The spanwise velocity component at the final downstream ordinate corresponding to x/D=0.61 z/D=0, is shown in figure 5.16. At this point the LDA measurement indicates the highest change of spanwise velocity for the three positions, which suggests significant flow asymmetry in the dimple. The biggest discrepancy between the predicted spanwise velocity for the turbulence models exists at position 3 in figure 5.16. At this location, only k-ω SST predicts the large positive and negative velocity variation, all other turbulence models predict minor changes. It is interesting to note that Reynolds Stress closely reflected the experimental results for streamwise and normal flow, but the spanwise velocity component shows poor agreement.

5.3.4 Grid convergence
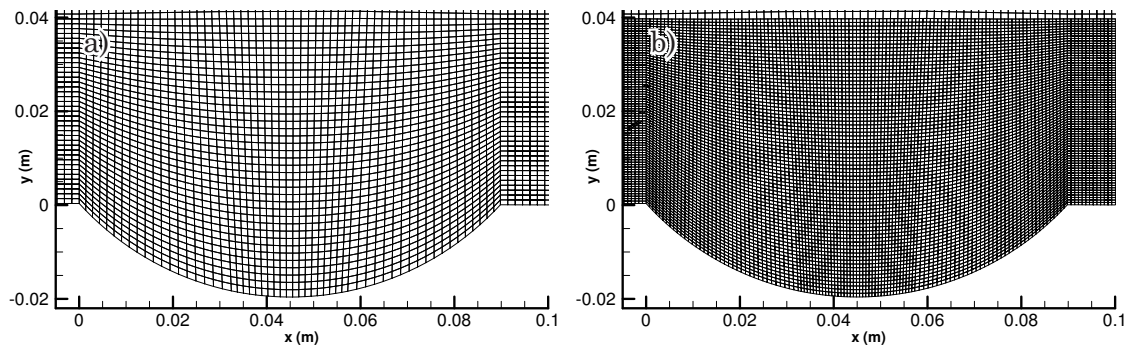
Figure 5.17 Dimple Wall Zone Cells a) Grid1 b) Grid 3 (Grid 1 with hanging node adaption)

From the turbulence model study in 5.3.1-5.3.3, only k-ω SST and Reynolds Stress turbulence models are discussed to determine if a finer grid yielded a more accurate description of the flow in the dimple. This is because these turbulence models showed the best agreement to the velocity components of the experimental measurements. For the three grids used, grid 1 was the base-line case with which a subsequent grid refinement was made. Grid 2 was based on grid 1 with a refinement zone using hanging node adaption in-line with the boundary layer (i.e. for y/D<0.2). Grid 3 had this zone extended to x/D=-0.06 and x/D=+1.24 from the upstream leading edge of the dimple, and the upper bound increased from y/D=0 to y/D=+0.44 (equal to 2δ),
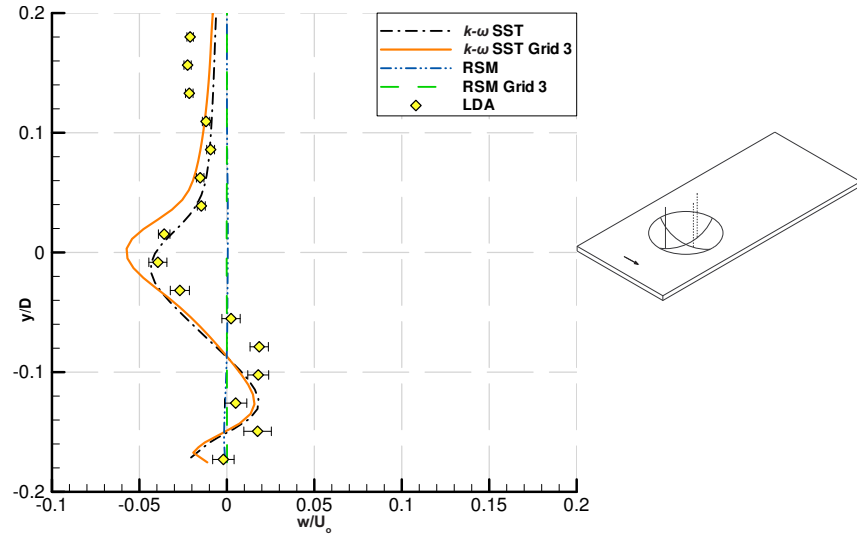
Figure 5.18 Position 1 Grid Refinement on Normalized Spanwise Velocity Profile Re_D=9x10^3
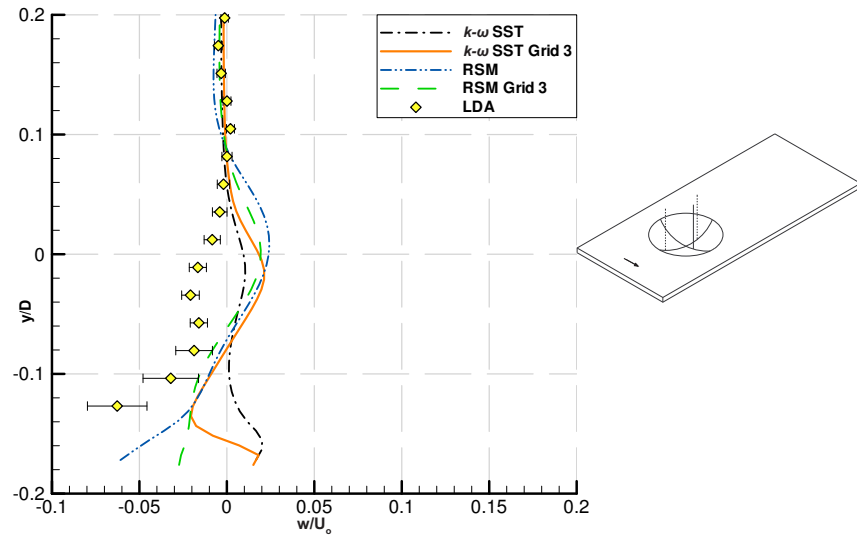
Figure 5.19 Position 2 Grid Refinement on Normalized Spanwise Velocity Profile Re_D=9x10^3
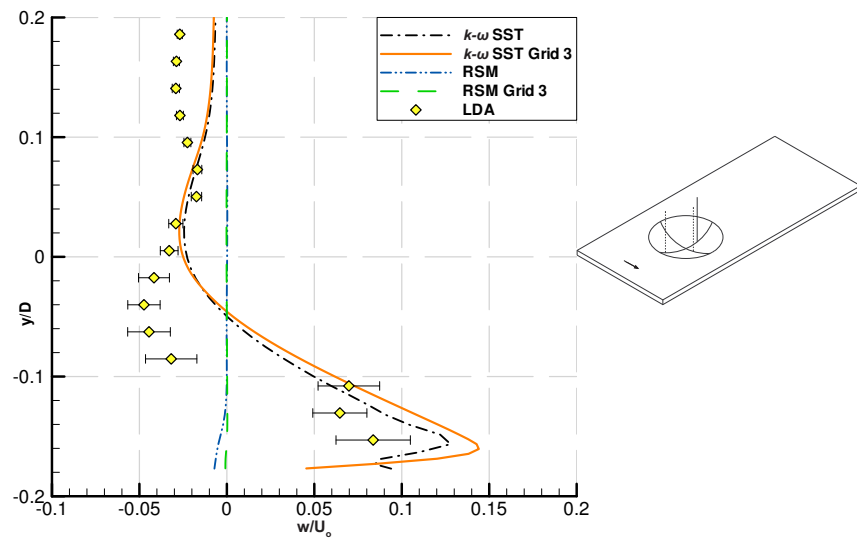
Figure 5.20 Position 3 Grid Refinement on Normalized Spanwise Velocity Profile Re_D=9x10^3

the spanwise width increased to z/D=±0.6. A plane on the geometric centre of the dimple in figure 5.17 shows a section of the three dimensional grid for grid 1 & 3.

All cases employ the use of a fully structured grid of hexahedral elements throughout the numerical domain. Table 5.1 shows the key information of the three grids used, relating to number of cells utilized and the y^+ value for each case. Results for Grid 2 were omitted due to the fact that the hanging node adaption in-line with y/D=0 caused false diffusion in calculating the shear layer from the dimple leading edge, and yielded erratic, unsystematic results for the velocity profiles, particularly in the shear layer (figure C.8). Figures 5.18-5.20 show the normalized spanwise flow velocity for the different grid densities investigated to determine the effect on the flow field. Only these are referenced as u and v component changes were negligible.

Table 5.1 Single Dimple Cell Size

Grid	No. of cells	No. of cells in dimple	y^+	Cell (length/width/height)/D
1	1,589,016	106,985	8.3	0.026 x 0.026 x 0.034
2	1,955,207	213,970	7.6	0.013 x 0.013 x 0.017
3	2,274,764	213,970	7.6	0.013 x 0.013 x 0.017

The normalized streamwise and normal velocity components did not vary greatly by effectively doubling the number of cells within the dimple. The finer grid discretization allowed the Reynolds Stress turbulence model to more accurately model the wall flow at the surface of the dimple, however the recirculation zone size and shear layer thickness did not increase in accuracy towards the either the LDA or the PIV result. Only slight augmentations in peak values of the spanwise velocity component resulted from increasing the grid density in the dimple, and better near wall modelling of the flow resulted.

The effect of the finer grid is seen for the spanwise flow at x/D=0.5 z/D=0.22 (figure 5.19). At this location for k-ω SST, the coarse grid's minimum normalized spanwise velocity component inside the dimple is close to zero. However grid 3 increases the minimum normalized spanwise velocity component to $w/U_o \approx -0.025$ at y/D≈-0.12. The result for grid 3 with k-ω SST, predicts closer agreement for the negative spanwise flow to the LDA measured flow velocity. For y/D<-0.12, the LDA near wall data rate reduced greatly due to surface reflections, therefore no velocity measurements were possible and no comparison can be made. In the region where y/D=0 the numerical

model predicts positive w/U$_o$ and the LDA negative. This is attributed to the numerical model over predicting the extent of the vortex cell magnification, resulting in positive flow towards the centre of the dimple in the vortex core.

Positions 1 and 3, in figures 5.18 and 5.20, show no noticeable improvement in the *k-ω* SST predicted flow is achieved by increasing the numerical grid resolution. For the side position of figure 5.19, the finer grid clearly shows an improvement in modelling the amount of fluid entering the dimple through the 'side windows' (w/U$_o$<0 for y/D<-0.075), as it is evident that fluid is moving in towards the central region of the dimple.

It is of interest to note the increase of the positive spanwise velocity at the first and last positions in figure 5.19 and 5.20. This pronounced skew indicates a highly asymmetric motion of the fluid at the centre plane of the dimple at Re$_D$=9.0x10^3. This asymmetry is indicative of one main vortex cell being present within the dimple and the other vortex cell weakening, which at lower Reynolds numbers are more symmetric and of even strength (Isaev & Leont'ev et al. 2000, Chew & Khoo 2005). This gives rise to asymmetric flow exiting the dimple, and has been noted in previous numerical studies in Isaev & Leont'ev et al. (2000), and the flow visualization by Khalatov & Byerley et al. (2004) and Chew & Khoo(2005).

5.3.5 Iterative convergence

The convergence limit of Grid 1 for continuity was 1x10^{-4} due to the mesh being too coarse, yet 1x10^{-7} for velocity and turbulence still was possible. For the finer grids used, convergence for velocity, turbulence, and continuity of 1x10^{-7} was held for all analyses as the fully structured grid used proved robust and numerically efficient.

5.4 Flow Analysis

The LDA and PIV results shown in section 5.3 were from a larger set of data obtained for the flow within the dimple which is investigated in this section. These are compared to the RANS numerical analysis using the *k-ω* SST turbulence model as specified by the agreement with the LDA and PIV results at the three positions as outlined in 5.3.1 to 5.3.3. The geometric centre plane of the dimple was investigated as it would give the best indication of any flow asymmetry, the size of the expected flow recirculation region and the position of any flow rotation centre.
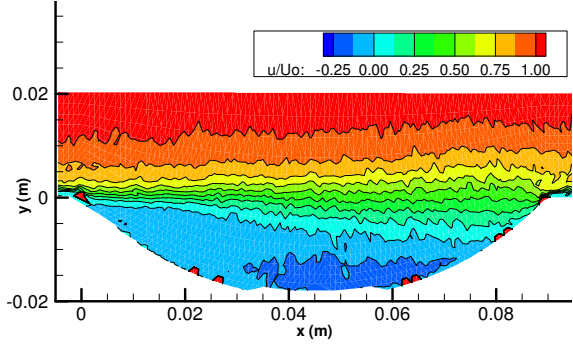
Figure 5.21 Normalized Streamwise Velocity LDA $Re_D=9.0\times10^3$
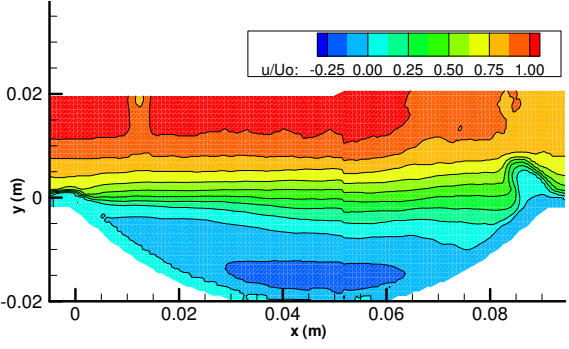
Figure 5.22 Normalized Streamwise Velocity PIV $Re_D=9.0\times10^3$
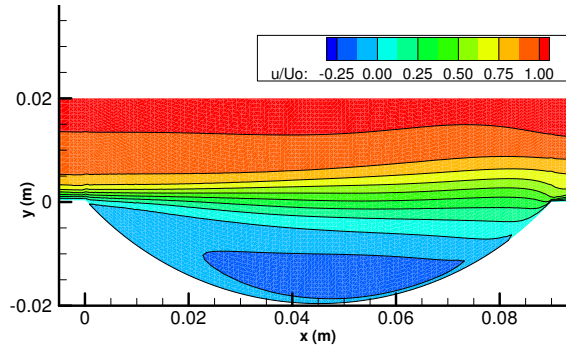
Figure 5.23 Normalized Streamwise Velocity CFD $Re_D=9.0\times10^3$

Figures 5.21, 5.22 and 5.23 show the normalized streamwise flow field for the LDA, PIV and CFD simulation respectively for $Re_D=9.0\times10^3$. Apparent in these figures is the predominately negative streamwise flow that exists beneath the rim of the dimple. This is located beneath the shear layer formed by the flow separation from the sharp upstream edge of the dimple. This shear layer then proceeds to increase in thickness towards the rearward edge of the dimple as it breaks down. All three show a reversed flow of $u/U_o=-0.25$ in the bottom most part of the cavity near the dimple surface. PIV results in figures 5.22 and 5.28 show a region of low velocity at the downstream edge of the dimple, a result of a constant reflection (albeit weak) due to the dimple rim, refer to the images in Appendix figure C.1. The cross correlation treats this as a region of stagnant particles, thus with no 'particle displacement' resolves the velocity in this region to zero.

The normalized normal velocity component is shown in figures 5.24, 5.25 and 5.26 for the LDA, PIV and CFD data sets respectively. The weakest, yet larger, up flow region is located in the upstream half of the dimple and is due to the recirculation of the flow in the dimple and the curvature of the surface turning the flow within
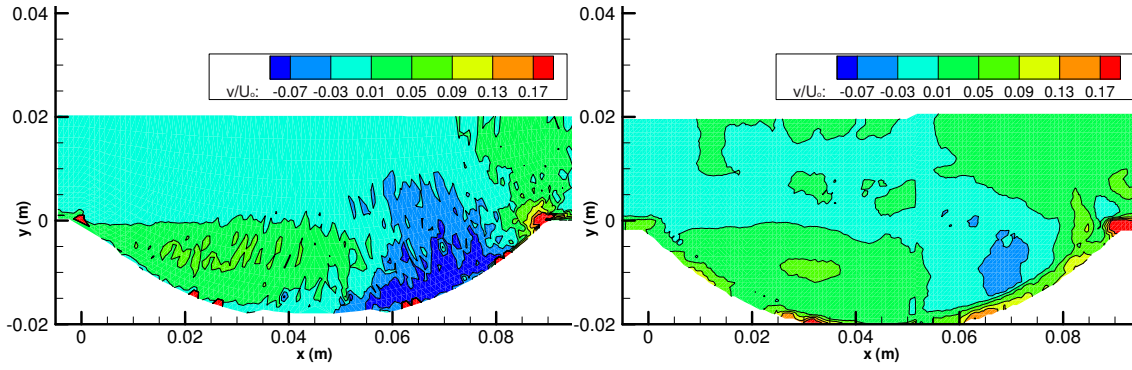
Figure 5.24 Normalized Normal Velocity LDA
Re_D=9.0x10^3

Figure 5.25 Normalized Normal Velocity PIV
Re_D=9.0x10^3
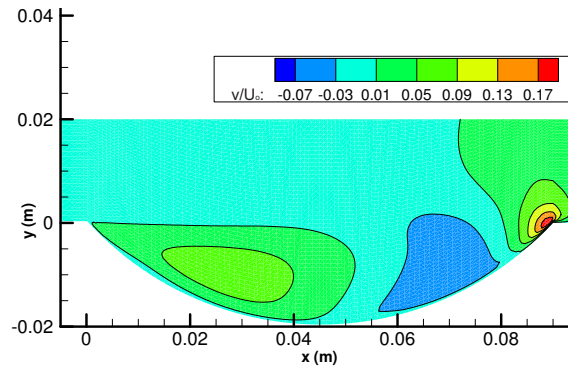
Figure 5.26 Normalized Normal Velocity CFD
Re_D=9.0x10^3

the dimple back towards the upstream edge, which is confined by the strong shear layer. Negative flow into the dimple occupies the downstream third of the centre plane forf v/U_o<-0.03. This is then proceeded by the peak positive normal velocity component of v/U_o=0.175 corresponding to the fluid being both ejected by the dimple and accelerated over the downstream rim.

It is clear from figures 5.27, 5.28 and 5.29 that the recirculation in the flow within the dimple rotates about a common point. On the central plane of the dimple, this rotation centre is located from the upstream rim of the dimple at x≈0.055m, y≈-0.005m, or x/D≈0.61, y/D≈-0.055 respectively for all data sets. Deviation of pathlines above the dimple show the effect of the negative normal flow velocity region above the dimple by causing a slight dip or suction effect. With the strength of the shear layer and the side 'windows' entraining fluid from the spanwise edges of the dimple, it is likely that there is minimal mass transfer in the central plane of the dimple between the bulk flow and the recirculation region. Pathlines indicate the recirculation centre acts as a source, as few cross into the main flow or vice versa.
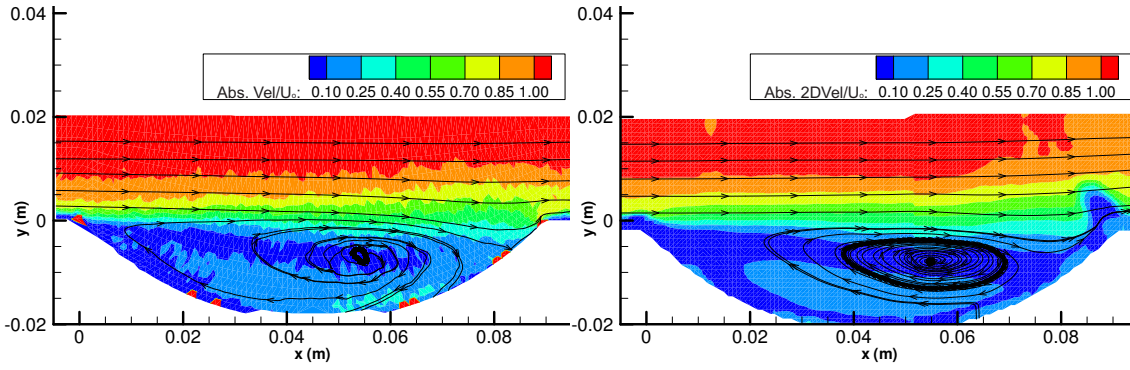
Figure 5.27 Pathlines & Normalized Absolute
3D Velocity LDA Re_D=9.0x10^3
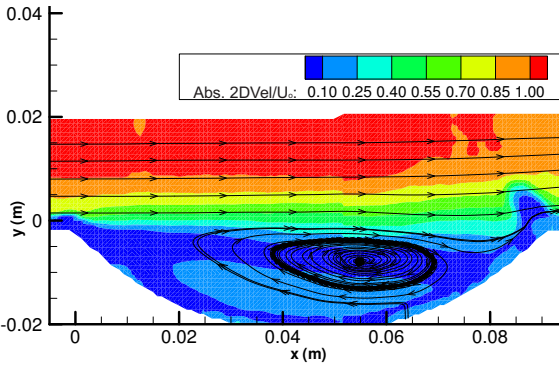
Figure 5.28 Pathlines & Normalized Absolute
3D Velocity PIV Re_D=9.0x10^3
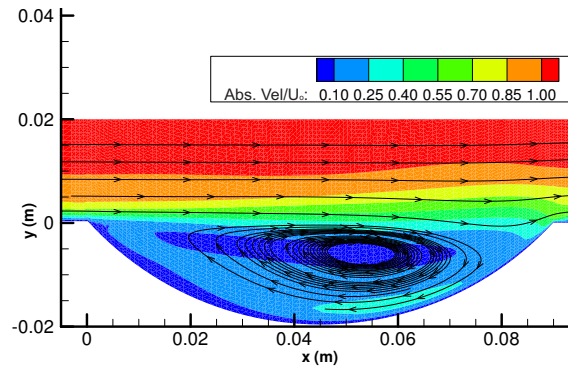
Figure 5.29 Pathlines & Normalized Absolute
3D Velocity CFD Re_D=9.0x10^3

The spanwise flow velocity is only comparable between the LDA results and the numerical analysis as the PIV system is a two-dimensional flow measurement only and omitted from the comparison of the planes shown in figures 5.30 and 5.31. Two distinct regions of positive and negative spanwise velocity exist in the central plane of the dimple and overlap each other. The peak positive value of w/U_o=0.1 is evident over most of the downstream half of the dimple adjacent to the surface. It is clear when comparing the normal and spanwise velocities that the spanwise flow component is dominant, as the peak normal velocity (v/U_o=0.175) is confined to a significantly smaller zone over the downstream rim of the dimple. This indicates a high level of asymmetry in the flow due to one of the vortex cells becoming dominant in the dimple as noted in Isaev & Leont'ev et al. (2000), Chew & Khoo (2005). It is likely this will have the result of capturing more fluid from one side of the wall flow external to the dimple. This will bias the spanwise flow velocity in one direction which can be seen in figures 5.33, and 5.35.
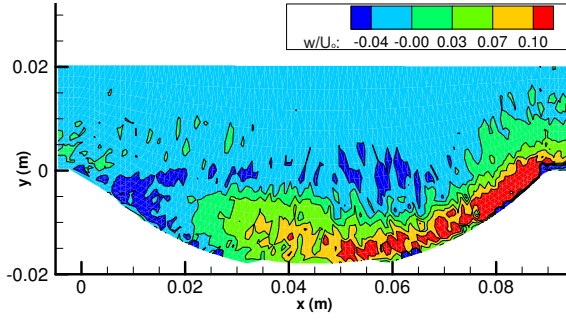
Figure 5.30 Normalized Spanwise Velocity
LDA $Re_D = 9.0 \times 10^3$
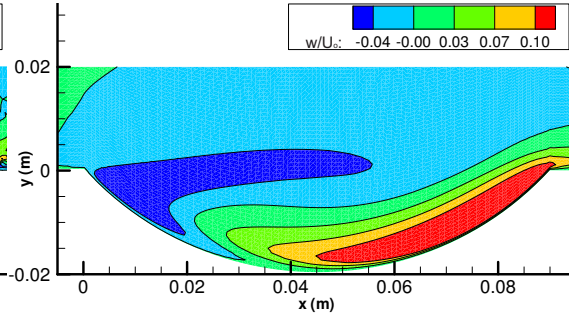
Figure 5.31 Normalized Spanwise Velocity
CFD $Re_D = 9.0 \times 10^3$

Previous investigations into the three dimensional flow within a spherical dimple either relied on flow visualization techniques to verify the numerical model (Park & Desam 2004), or with obtrusive pressure and hot wire probes (refer table 1.3). None of these methods measured velocity components inside the dimple. With the verification of the numerical model of the dimple against LDA and PIV results shown in sections 5.3 and 5.4, using the *k-ω* SST turbulence model with an adequately refined grid will yield a numerically predicted result that shows good agreement to the experimentally obtained data of the flow in the dimple. Therefore as the numerical model used sufficiently represents the experimental flow field, the numerical model can be utilized to develop the understanding of the flow in the dimple.

5.4.1 The Three Dimensional Flow Field in a Single Dimple

The numerically predicted velocity components in the single dimple will be outlined so an understanding is developed, specific to the dimple geometry used. This is in order to quantify the flow field produced by the dimple and to show its effectiveness at producing vortices at the Reynolds number range experienced experimentally by the dimpled wing surface.

Visualization of the flow in figures 5.32 and 5.33 show pathlines inside the dimple. It is evident that two lateral vortex cells exist that lie beneath the rim of the dimple. For the lower Reynolds number in figure 5.32, two symmetric cells are formed, the core fluid of which is from the upstream half each respective side of the dimple. The effect of increasing the Reynolds number results in one vortex cell becoming dominant seen in figure 5.33, noted by Chew & Khoo (2005). The resulting asymmetric flow field is obvious; also evident is the core fluid of the weaker vortex coming from the opposite half of the dimple.
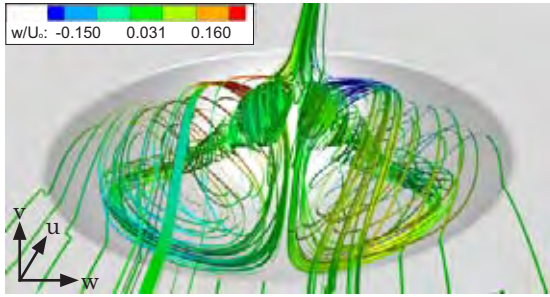
Figure 5.32 Pathlines $Re_D=4.3\times10^3$, coloured by w/Uo
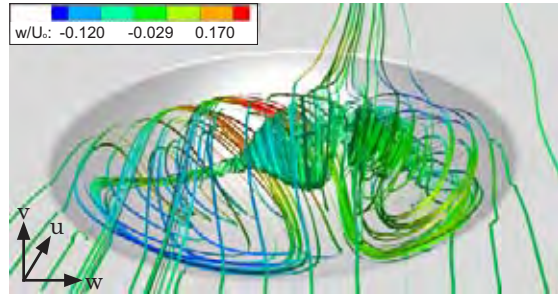
Figure 5.33 Pathlines $Re_D=9.0\times10^3$, coloured by w/Uo

The size of the positive and negative spanwise flow regions and the peak value of the positive and negative regions are clear in figures 5.32 and 5.33, as the pathlines are colored by w/U_o. It is likely that due to the stronger vortex cell at the higher Reynolds number increasing this leads to the increas of spanwise velocity intensity (+w) and region on the downstream face of the dimple; thus fluid is fed into the weaker vortex region. This affects the ability of the vortex in the right hand half (+w) of the dimple to develop with increasing Reynolds number. The +w spanwise velocity component in the dimple limits the volume in which the weaker vortex core can develop and assists the main vortex, allowing it to elongate.

Figure 5.34 Surface Pathlines $Re_D=4.3\times10^3$ Coloured by Particle Position on Surface
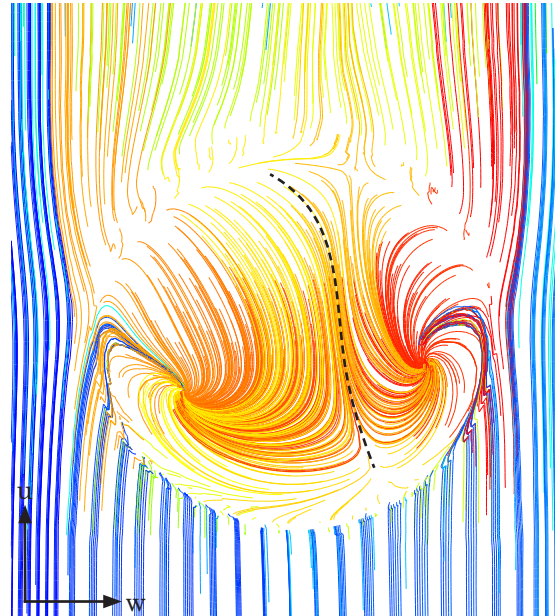
Figure 5.35 Surface Pathlines $Re_D=9.0\times10^3$ Coloured by Particle Position on Surface

Pathlines coloured by the position where they are released on the surface are shown in figures 5.34 and 5.35. The movement of fluid on the dimple surface at lower

Reynolds number is clearly symmetric, and the vortex cores result in two 'sinks' forming near the spanwise edge. As Reynolds number increases the stronger vortex cell sink point advances slightly in the upstream direction, which is indicative of more fluid entering the downstream region of the dimple and elongating the vortex. This is likely to assist the flow asymmetry, resulting in an apparent rotation of the flow field in the dimple at the higher Reynolds number. The surface flow is also clearly being sourced for the weaker vortex from z/D=-0.25 in the opposing half of the dimple (see the dashed line in figure 5.35). Core vortex fluid at the sink is also being fed at the spanwise extreme edge of the dimple. This resulting spanwise movement of fluid and the axial flow velocity in the vortex cores causes the pathline deviation known as the 'vacuum effect' at the wall region (Isaev & Leont'ev 2000 and 2001, Chew &. Khoo 2005 and Khalatov & Byerley et al. 2004), which is greater (more spanwise or lateral deviation) at the higher Reynolds number on the left hand side of the dimple and less on the right. As in figure 5.33, the pathlines exiting the dimple in figure 5.35 are heavily biased towards the positive spanwise direction, again as a result of the higher region of spanwise flow at the larger Reynolds number.

In order to understand the size and extent of the spanwise velocity throughout the dimple, the iso-surface of $w/U_o=\pm0.01$, corresponding to the low scale spanwise velocity of the fluid upstream, downstream and inside the dimple is shown in figures 5.36 and 5.37. The iso-surface corresponding to the normalized velocity of $v/U_o=-0.25$ & +0.1 in figure 5.38 and 5.39, shows the extent of down-flow into and the ejection of fluid out of the dimple.

The symmetric nature of the low Reynolds number flow is evident not only within the dimple but the periphery of the wall in which it is located. Figure 5.36 shows the three dimensional positive and negative spanwise flow field, which shows for the low scale w/U_o range four distinct cells, two of which overlap in each half of the dimple. Within the initial separated shear layer from the upstream rim of the dimple, outwards spreading is combined with an inflow region around the dimple rim; corresponding to two separate vortex cells. The inflow at the spanwise edge is clearly seen here forming the 'side windows' first noted in Isaev & Leont'ev (2000). Increasing the Reynolds number yields the iso-surface distribution in figure 5.37. Instead of four separate cells there are now two regions of positive and negative

spanwise flow that are linked, and a third region of negative spanwise flow remaining on the dimple rim with the 'bridge' connecting these two regions in the low Reynolds number flow being weaker. The amount of fluid entering the dimple from the weaker vortex side is minimal, along with the positive region which envelopes it is now fed from the rear downstream opposing face of the dimple, see figure 5.33 and 5.35. The two negative spanwise flow cells are now linked, in the region corresponding to where the vortex cells axes meet. At the lower Reynolds number these are distinctly separate bodies (figure 5.32 and 5.34).
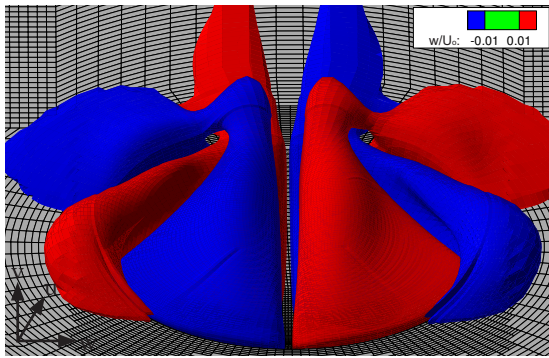
Figure 5.36 Normalized Spanwise Velocity Iso-Surface $Re_D=4.3x10^3$
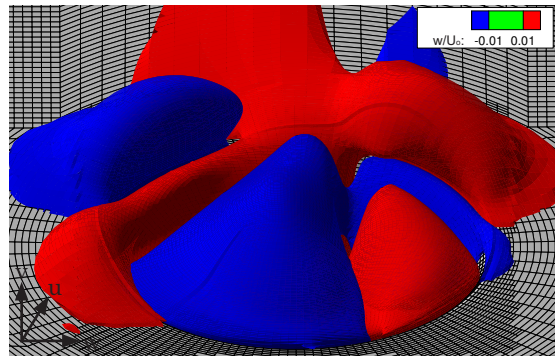
Figure 5.37 Normalized Spanwise Velocity Iso-Surface $Re_D=9.0x10^3$

A large positive region of spanwise flow ejected by the dimple develops as the Reynolds number and flow asymmetry increases. At the higher Reynolds number in figure 5.37, there is one small negative region of spanwise flow on the -w downstream rim and a more dominant positive region of spanwise flow on +w downstream rim. This may be a result of the negative spanwise flow 'bridge' being weakened due to the vortex cell being stronger within that half of the dimple. The vortex cell magnification within the dimple will result in more spanwise fluid ejection from that side, seen by the extended $w/U_o=+0.01$ region downstream in figure 5.37, and the surface pathline skew in figure 5.35 behind the dimple.

The normalized normal velocity is limited to $v/U_o=-0.025$ and 0.1, to show the down-flow into the dimple and the ejection ($+v/U_o$) on the downstream rim in figure 5.38 and 5.39. The low Reynolds number case of figure 5.38 indicates flow exiting the dimple (+v component) is evenly distributed across the downstream rim. A single structure of downwards flow into the dimple occupies the downstream half of the dimple volume near the surface. Two peaks extend just above the dimple rim, the
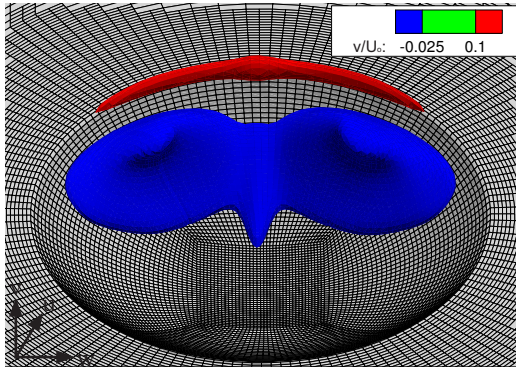
Figure 5.38 Normalized Normal Velocity
Iso-Surface Re_D=4.3x10^3
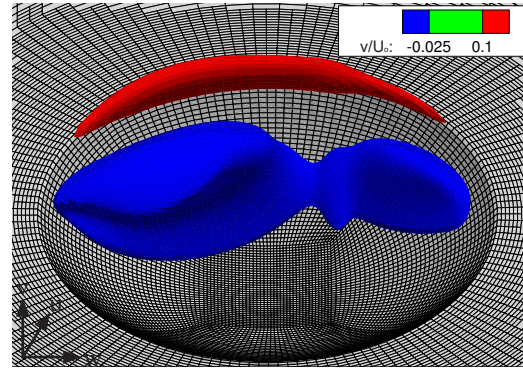
Figure 5.39 Normalized Normal Velocity
Iso-Surface Re_D=9.0x10^3

size and values of which can be seen in figure 5.11-5.13 & 5.24-5.26. This corresponds to down-flow of the fluid in the vortex core, which traps fluid from the wall region upstream of the dimple in figure 5.32 and 5.33.

The increase in Reynolds number of figure 5.39 shows a clear enhancement of the size and degree to which this drawing of fluid upstream occurs for the side of the dimple with the stronger vortex cell. Not only does the size increase but the height at which this region extends from the dimple does too. Again this gives evidence to the higher volume of fluid entering this half of the dimple as the vortex cell grows. The ejection behind the dimple also increases appreciably, and the bias of the v/U_o intensity in this half of the dimple once again follows the side with the vortex cell magnification.

5.4.2 Vorticity

The numerically predicted three-dimensional flow field within the dimple cavity has been addressed and showed good agreement to experimental data from both LDA and PIV. As the dimple acts as a vortex generator, the vorticity development within the dimple and in the immediate region behind the dimple will be considered. This is to gain an understanding of the vortex formation, intensity and decay. Given the normal and spanwise velocities of figures 5.39-5.39, the flow is dominated by the large scale, complex spanwise flow within the dimple, thus streamwise vorticity and vorticity magnitude will be the focus. **Figures 5.40 and 5.41 indicate the level of** streamwise or (x-component) vorticity normalized to the peak absolute vorticity on the surface so a direct comparison of the streamwise vorticity intensity of the two Reynolds numbers can be made.
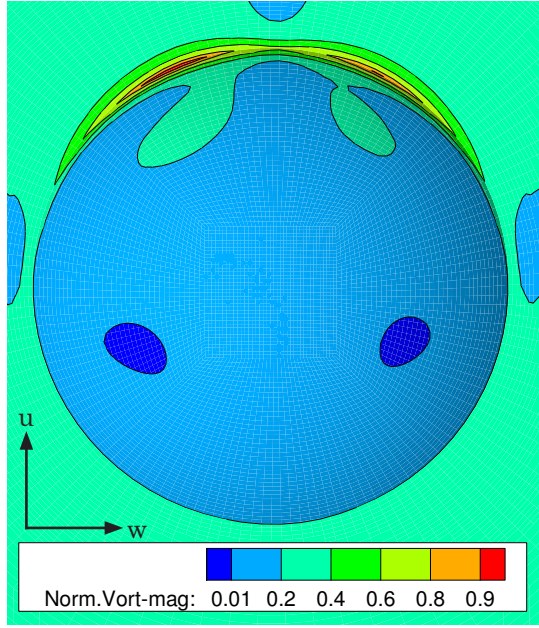
Figure 5.40 Normalized Vorticity
Magnitude Re_D=4.3x10^3 ($\Omega_{x,max}$=690sec-1)
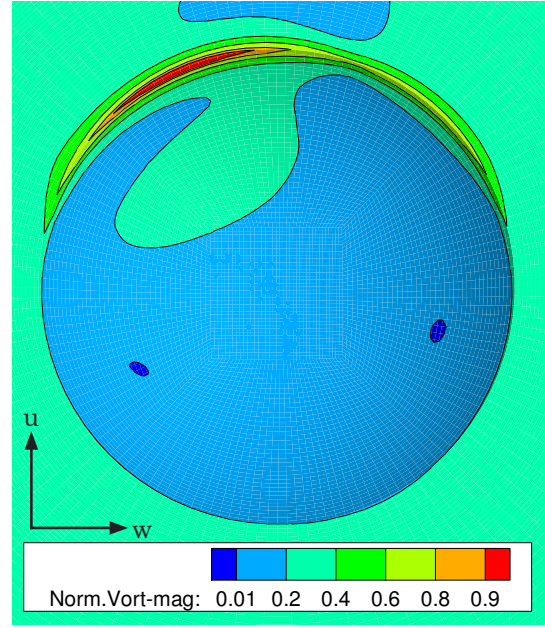
Figure 5.41 Normalized Vorticity
Magnitude Re_D=9.0x10^3 ($\Omega_{x,max}$=1650sec-1)

Vorticity magnitude normalized to the respective peak vorticity magnitudes of 690sec^{-1} and 1650sec^{-1} is shown in figures 5.40 and 5.41. The lower Reynolds number results in two separate regions of peak vorticity magnitude on the downstream rim of the dimple. It can be seen at the higher Reynolds number one of those zones dissipates, corresponding to the side with a reduction in dimple vortex cell strength, whilst the stronger vortex side peak grows. Peak vorticity magnitude throughout the whole dimple is augmented on the dimple downstream rim surface, not at the spanwise 'window' region. The combination of high fluid ejection from the dimple and the fluid being sucked in from the side across the front of the rim result in the high vorticity magnitude at this position. The skewed nature of the higher Reynolds number flow yields the increase of the vorticity magnitude peak by 240%, as less fluid is captured from the half of the dimple with the weaker counter-rotating vortex.

The streamwise vorticity (Ω_x), on the dimple surface in figures 5.42 and 5.43 shows the side window augmentation of Ω_x at the spanwise edge of the dimple, reflected by the positive and negative spanwise flow in figures 5.36 and 5.37. For Re_D=4.3x10^3 in figure 5.42 the streamwise vorticity is +25sec^{-1} (16.5% $\Omega_{x,max}$) & -25sec^{-1} (16.5% $\Omega_{x,max}$) at the spanwise edge, for Re_D=9.0x10^3 in figure 5.43 results in streamwise vorticity change of +125sec^{-1} (26% $\Omega_{x,max}$) & -55sec^{-1}(11% $\Omega_{x,max}$). Maximum streamwise vorticity ($\Omega_{x,max}$) remains at the downstream rim of the dimple as for peak vorticity magnitude.

The largest change in Ω_x is the 470% (from 25 sec^{-1} to 125 sec^{-1}) increase at the left hand spanwise rim of the dimple which experiences the vortex cell magnification. Whereas the increase in the $\Omega_{x,max}$ at the stronger downstream rim edge is only 320% (from -150sec^{-1} to -480sec^{-1}). This highlights a decoupling effect of Ω_x at the downstream rim due to fluid being fed into the weaker half of the dimple from the stronger vortex cell side.
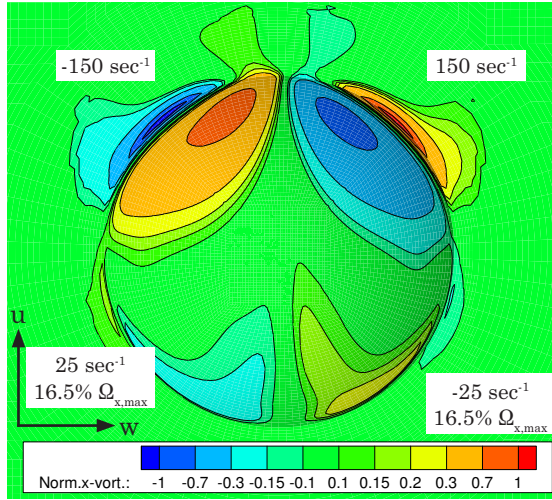
Figure 5.42 Normalized Surface Streamwise Vorticity ($\Omega_{x,max}$=150sec^{-1}) Re$_D$=4.3x10^3
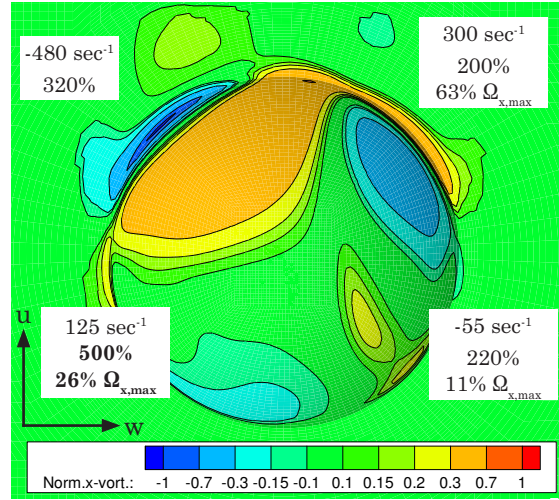
Figure 5.43 Normalized Surface Streamwise Vorticity ($\Omega_{x,max}$=480sec^{-1}) Re$_D$=9.0x10^3

Figure 5.43 shows the increased area of positive Ω_x in the downstream half of the dimple that has the stronger dimple vortex cell. This region is linked to the weaker positive region of Ω_x on the dimple rim of the opposite side, where as in figure 5.42 they are separate. Figure C.2a-C.2r) outline the development of the streamwise vorticity taking spanwise planes from x/D=0, at the upstream dimple rim. The development of Ω_x is consistent not only over the surface of the dimple, but also in the volume of fluid inside the cavity. The spreading of fluid in the separated shear layer in the spanwise direction, seen in figure C.2c, gives rise to the positive and negative regions in Ω_x that exist until x/D≈0.44 for Re$_D$=4.0x10^3. This breaks down as the stronger streamwise vorticity develops due to the 'side windows' and as the downstream dimple rim is approached. The same is true for Re$_D$=9.0x10^3, although the asymmetry in the shape and magnitude of Ω_x in the shear layer is evident and this breaks down earlier at x/D≈0.33. The higher Ω_x region also begins to increase more rapidly and earlier at x/D=0.55 for Re$_D$=9.0x10^3, where as this is delayed until x/D=0.66 for the Re$_D$=4.3x10^3 case.

The rate at which the vorticity magnitude and streamwise vorticity decays is plotted in figure 5.45-5.48. These take into account the values for vorticity magnitude and streamwise vorticity for 'rakes' spanning z/D=±0.06, and positioned vertically y/D≈0, y/D=0.11, y/D=0.22, corresponding to the wall, half the dimple depth height above the surface and the full dimple height above the surface, see figure 5.44. These are then moved downstream from the dimple rim (at x/D=1) by Δx/D=1 to x/D=2 and 3. Figure 5.45 shows the vorticity magnitude close to the wall for the high Reynolds number. Three peaks corresponding to two spanwise peaks of Ω are present at the downstream rim of the dimple and a higher peak of Ω=1400sec^{-1}, (85% of Ω_{max}=1650sec^{-1}) at the downstream dimple rim edge.
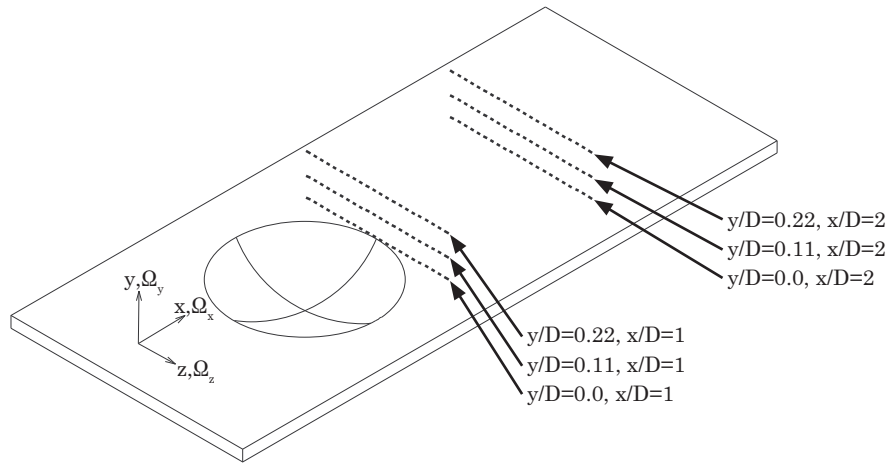
Figure 5.44 Vorticity Magnitude and Streamwise Vorticity (Ω_x) Rake Positions

Given the large normal velocity at the rim at x/D=1, the fact that no centralized peak exists in figure 5.46 at x/D=2-3 indicates the vortex no longer has an affect on the surface, possibly as it has moved away from it. The lower Reynolds number shows two central vorticity peaks but no 'outboard' spanwise peaks as the wall shear would be expected to be lower at the lower Reynolds number. The two peaks at x/D=2 & x/D=3 have less deviation due to flow symmetry. Wall Ω_x in figure 5.46 at x/D=1 shows one negative and two positive regions at Re$_D$=9.0x10^3, where for ±0.5<z/D<±0.2, Ω_x=-70sec^{-1} and Ω_x=+32sec^{-1}. The -70sec^{-1} region decays 85%-93% for x/D=2-3, and +32sec^{-1} region decays 75%-96% for x/D=2-3. At Re$_D$=4.3x10^3 only two peaks for streamwise vorticity exist, +51sec^{-1} & -30sec^{-1}, both decay evenly at 91%-94% for x/D=2-3.

Vorticity magnitude in figures 5.45 and 5.47 shows that as the wall distance increases to y/D=0.11 (i.e. height equals half the dimple depth) the vorticity magnitude reduces considerably but is still has a slight influence for the higher Reynolds number. Figure 5.48 shows peak $-\Omega_x$ at x/D=1 becoming positive at x/D=2-3 for y/D=0.11, due to the stronger $\pm\Omega_x$ at y/D=0 impeding Ω_x in the boundary layer and reducing its intensity. In figure 5.48 for an increase in the downstream position at y/D=0.11 (when Re_D=4.3x10³), the vorticity magnitude increases slightly as the vortex moves away from the wall. At y/D=0.11 the symmetry of the vorticity of the flow surrounding the dimple is still influenced by the skew of the flow exiting the dimple.
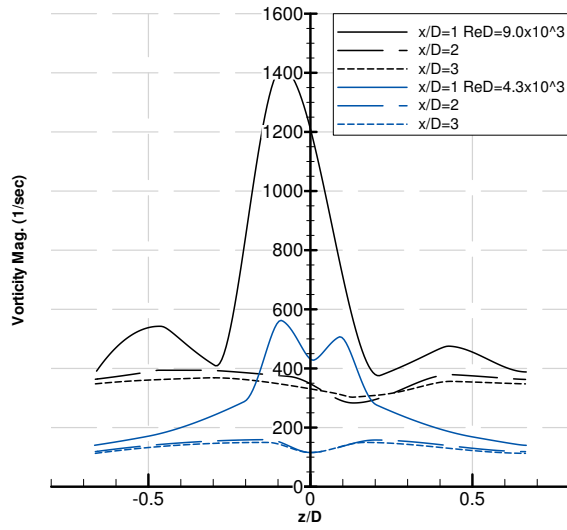
Figure 5.45 Vorticity Magnitude y/D=0
Re_D=4.3x10³, Re_D=9.0x10³
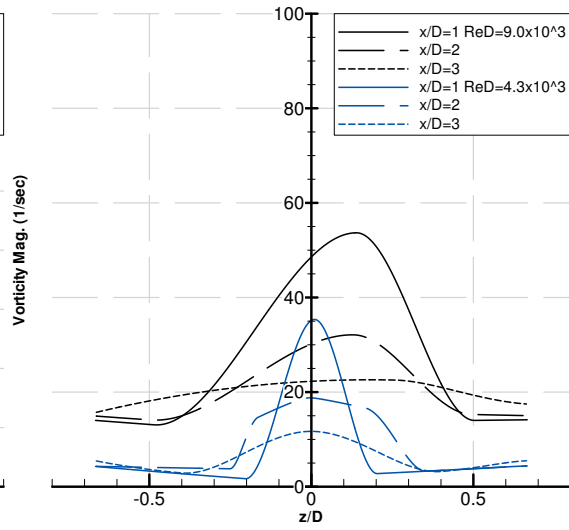
Figure 5.47 Vorticity Magnitude y/D=0.11
Re_D=4.3x10³, Re_D=9.0x10³
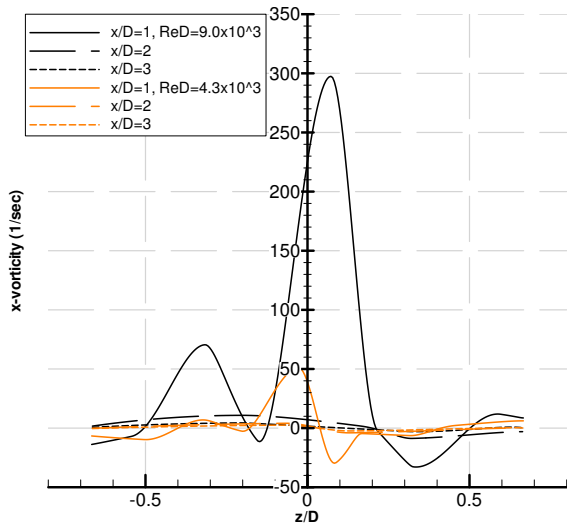
Figure 5.46 Streamwise Vorticity y/D=0
Re_D=4.3x10³, Re_D=9.0x10³
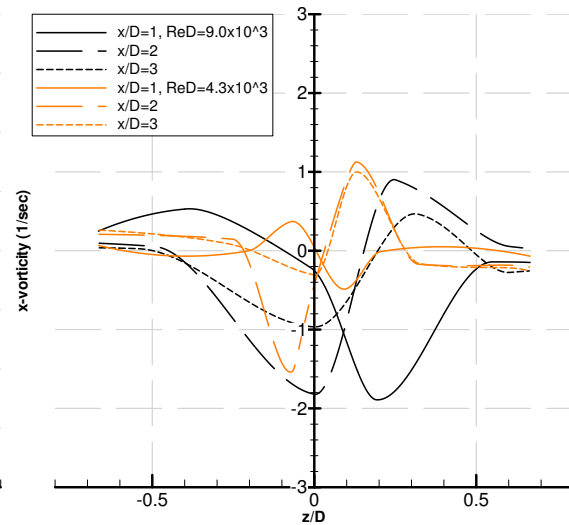
Figure 5.48 Streamwise Vorticity y/D=0.11
Re_D=4.3x10³, Re_D=9.0x10³

Tables 5.2 to 5.5 outline the percentage of the maximum vorticity magnitude to the local vorticity magnitude for; y/D=0, y/D=0.11 in figure 5.45. In table 5.2, the highest vorticity magnitude is 85.8% of the maximum vorticity magnitude (see figure 5.41) at z/D=-0.08 for Re_D=9x10^3, compared to 81.4% in a similar location for Re_D=4.3x10^3 in table 5.4. The figures in bold indicate augmented zones of vorticity magnitude for the data set, such that in table 5.2 the (from z/D=-0.46 to -0.2, and x/D=1-2) indicates the large region of high vorticity magnitude corresponding to the side of the dimple with vortex cell magnification. Whereas figure 5.45 shows this vorticity bias, table 5.2 indicates how these regions of vorticity decay downstream of the dimple.

Table 5.2 Vorticity Magnitude (%Ω_{max}=1650sec^{-1}) Re_D=9.0x10^3 y/D≈0

Position	z/D	z/D	z/D	z/D	z/D	z/D	z/D
x/D	-0.65	-0.46	-0.2	-0.08	0.2	0.42	0.65
1	**23.7**	**32.9**	**24.8**	**85.8**	22.8	**28.8**	**23.5**
2	22.0	**23.9**	**23.9**	22.6	17.2	**23.0**	22.0
3	21.1	21.9	22.3	19.3	18.7	21.6	21.1

Table 5.3 Vorticity Magnitude (%Ω_{max}=1650sec^{-1}) Re_D=9.0x10^3 y/D=0.11

Position	z/D	z/D	z/D	z/D	z/D
x/D	-0.65	-0.5	0.14	0.5	0.65
1	0.8	0.8	**3.3**	0.8	0.9
2	0.9	0.9	**1.9**	0.9	0.9
3	1.0	1.0	**1.5**	1.2	1.1

Table 5.4 Vorticity Magnitude (%Ω_{max}=690sec^{-1}) Re_D=4.3x10^3 y/D≈0

Position	z/D	z/D	z/D	z/D	z/D	z/D	z/D	z/D	z/D
x/D	-0.67	-0.5	-0.2	-0.09	0.01	0.09	0.2	0.5	0.67
1	20.3	**24.7**	**41.7**	**81.4**	**62.0**	**73.3**	**40.1**	**24.3**	20.3
2	17.2	20.1	**23.1**	19.9	16.8	19.8	22.9	20.0	17.2
3	16.3	19.0	21.7	19.2	16.7	19.2	21.7	19.0	16.4

Table 5.5 Vorticity Magnitude (%Ω_{max}=690sec^{-1}) Re_D=4.3x10^3 y/D=0.11

Position	z/D	z/D	z/D	z/D	z/D
x/D	-0.65	-0.2	0	0.2	0.65
1	0.6	0.2	**5.1**	0.4	0.6
2	0.7	0.0	**1.5**	0.1	0.7
3	0.9	1.1	0	1.0	0.9

Tables 5.2 and 5.4 indicate that for y/D≈0; the Re_D=9x10^3 dimple still has sufficient vorticity magnitude to x/D=2-3, where as for Re_D=4.3x10^3 this is more likely between

x/D=0-1. For y/D=0.11, in tables 5.3 and 5.5, some augmented vorticity still exists, z/D=0.14 (asymmetric) for Re_D=9x10^3, and at z/D=0 for Re_D=4.3x10^3, thus vorticity augmentation of the dimple on the flow can be considered to be confined to y/D<0.11 above the dimple surface for both Reynolds numbers. Particularly where 80% of the peak vorticity magnitude is still confined under this height. So even at low Re_D, the vortex production is still effective for some regions albeit that the area and length over which it acts is reduced. This requires placement to be more critical to the separation zone, such that dimple downstream rim will need to be placed at the separation point. Tables 5.2 and 5.4 suggest that x/D=0-1 for Re_D=4.3x10^3, and x/D=2-3 for Re_D=9x10^3.

Having validated and verified the k-ω SST model as showing good agreement to experimental velocity measurements, employing this turbulence model in an analysis of the dimple array will indicate the effectiveness of different dimple array configurations. However, numerically modelling the dimple array interaction for various configurations poses a challenge, particularly with meshing the dimple array using a fully structured hexahedral grid. The vorticity produced from an array of multiple dimples should provide sufficient flow mixing near the surface to reduce a separated flow structure. By measuring the velocity in the separation region, the alteration to the flow due to the dimple array placed upstream of the separation point should result in flow recovery. The effectiveness of a dimple array to generate vortices strong enough to suppress the separation region may depend on: the dimple to dimple spacing, how many rows are in the array and how far the array is placed from the separation point. Therefore it is required that these variables are measured against a fixed separated flow structure to indicate the effectiveness of that dimple array configuration.

Dimple Array Effect on Rearward Facing Ramp Flow Structure

6

This chapter focuses on whether or not an array of dimples can have any impact on a large-scale flow separation. By using different dimple array configurations and looking at the velocity profiles behind the forced separation region from a 16˚ rearward facing ramp, the velocity behind the ramp will either increase (an improvement) or decrease and become larger. The instantaneous flow is also considered for the dimple array providing the most flow recovery to determine if the turbulence produced is higher than the 'clean' ramp. This is so the most optimum dimple array is placed on the airfoil.

6.1 Introduction

Having established the flow and vorticity augmentation to the flow from an individual dimple in chapter 5, a simplified investigation of the dimple array configuration is necessary prior to the more complex interaction of the dimples array on the airfoil. Figure 6.1 shows the analogy between the two flow structures. Whilst not exact there are similarities to both which are utilized in this section to measure the dimple array configuration effectiveness. The flow separated fluid structure was achieved by locating a 16˚ rearward facing ramp (figure 6.2) into the 340mm x 175mm test section. The geometry and placement of the array is outlined in figure 6.2, where the array spacing, the number of rows and the distance in terms of dimple print diameter 'D' from the dimple rim to the flow separation point are varied.
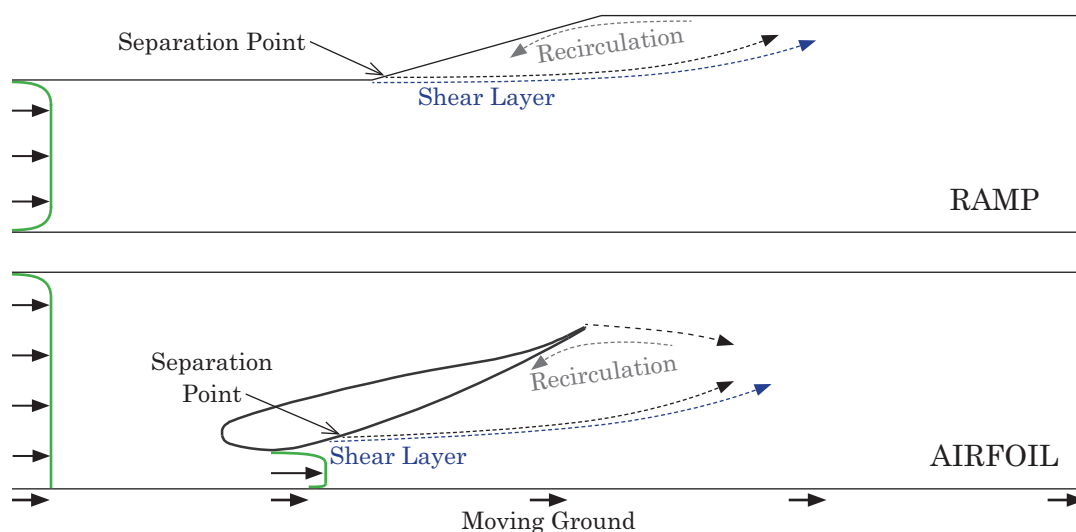
Figure 6.1 Flow Structure Analogy: Rearward Ramp and Inverted Airfoil in Ground Effect

6.2 Experimental Equipment and Setup

LDA was primarily used to measure the flow; 650 data points were taken from 50mm to 230mm downstream of the separation point of the ramp (see figure 6.3a). These points were biased towards the initial shear layer from the ramp separation point and the recirculation zone centre. Due to the beam reflection from the probes measuring at an effective normal incidence to the surface an offset of 10mm was needed, as any closer to the surface resulted in increased noise and no velocity readings within 5mm. Extending the grid further upstream yielded little additional information and just increased the measurement time. A maximum of 2000 samples were recorded at a limit of 4 seconds. PIV was used as a supplementary technique to allow correlation with the LDA results. Four image 'sectors' were taken (see figure 6.3b) and combined by using physical markers in the test section in the region of overlay; 600 image pairs taken were captured in each sector. The PIV camera was mounted to the 3-axis traverse to ensure repeatable and consistent camera positioning. Image discretization was 64x64 pixels with a 12 pixel overlap, equating to a 60mmx60mm sized image.
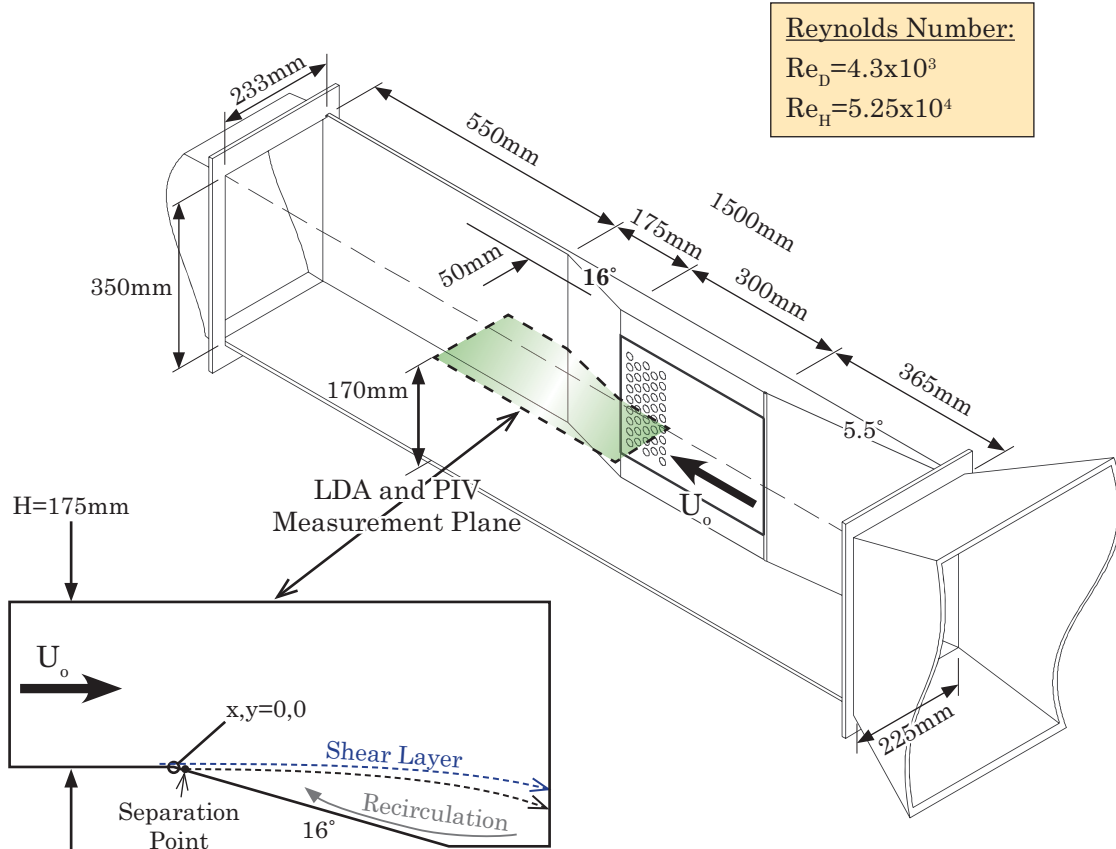
Figure 6.2 Rearward Facing Ramp Dimensions in Test Section
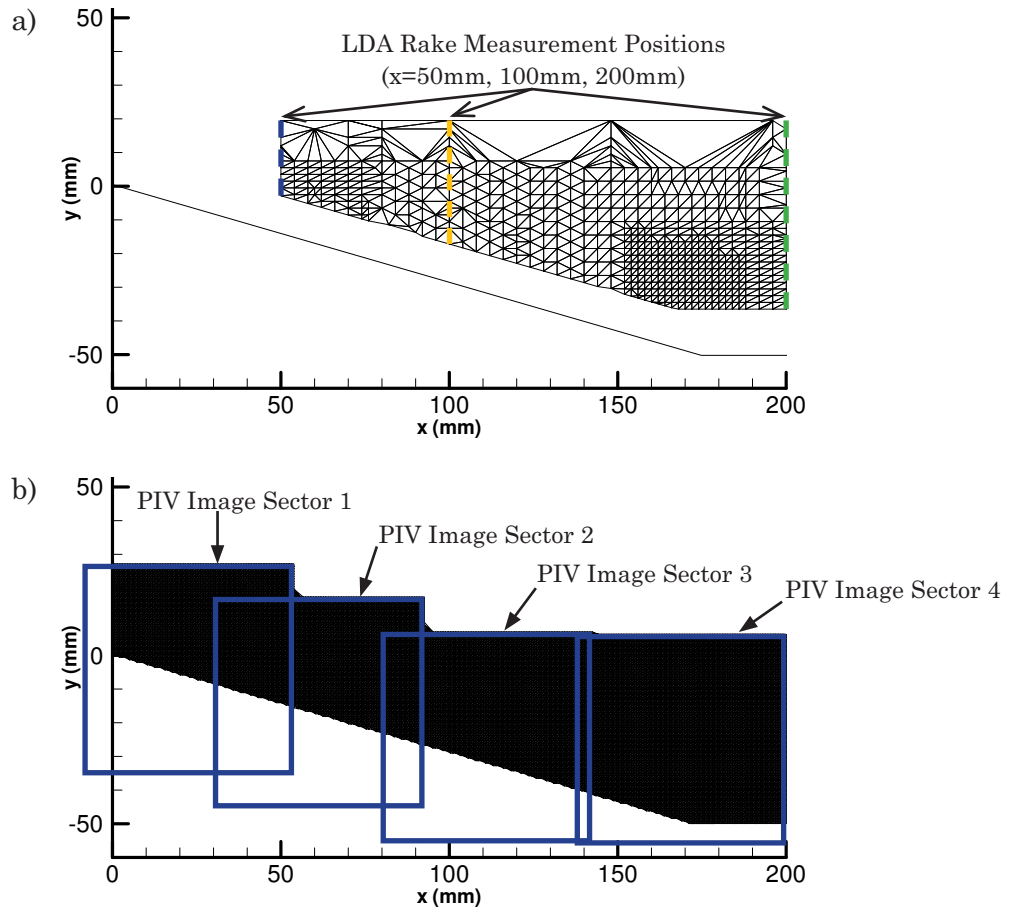
Figure 6.3 a) LDA & b) PIV Measurement Plane

Figure 6.4 indicates the state of the boundary layer ahead of the rearward facing ramp at x=-150mm from the separation point. Both ideal laminar and turbulent boundary layer profiles are plotted against the CFD and both LDA and Pitot tube experimental measurements. It is clear that the flow is laminar ahead of the ramp.
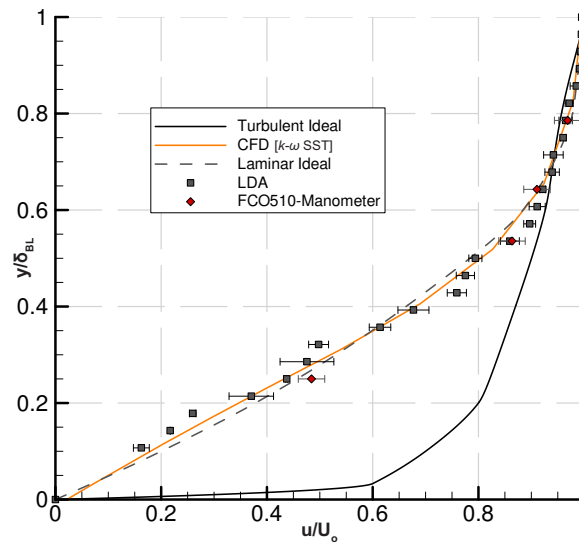
Figure 6.4 Boundary Layer State Ahead of 16° Rearward Facing Ramp

6.3 Rearward Facing Ramp Flow Structure

Previous investigations into rearward facing ramps (Lin & Howard 1990, Cullen et al. 2002, Rae et al. 2002) and backward facing steps (Eaton & Johnston 1981 and Hall 2001) have been used to measure separated flow structure. Eaton & Johnston (1981) noted for a backward facing step, that it is the simplest reattaching flow with a region of separation and reversed flow, see figure 6.1. It is advantageous as it has a fixed separation line, a single separation region and streamlines parallel to the streamwise axis at separation. Thus in terms of measuring vortex generator effectiveness it is an established method (Lin & Howard 1990, Cullen et al. 2002, and Rae et al. 2002).
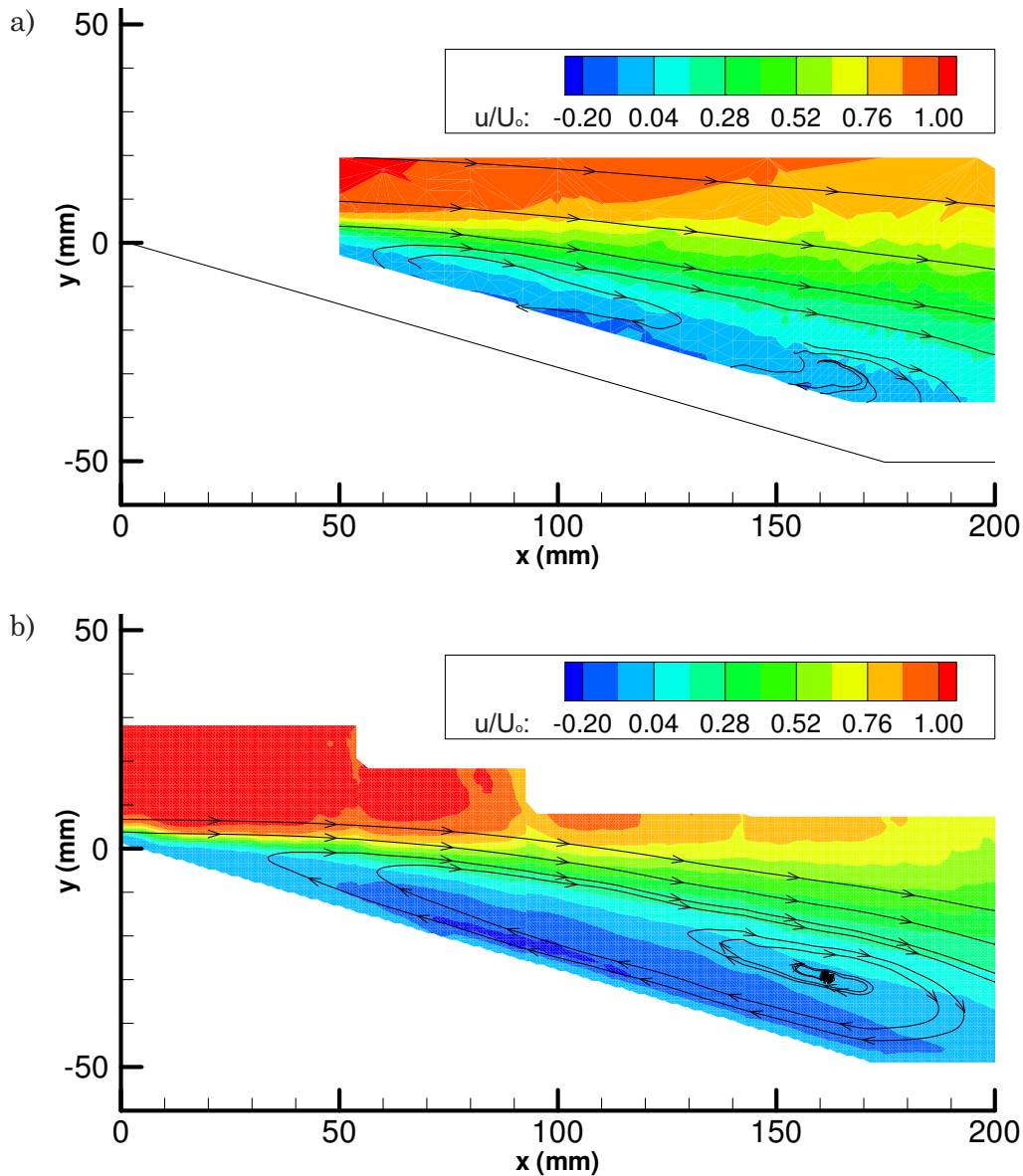
Figure 6.5 16° Rearward Facing Ramp Flow Field, Re_H=5.25x10^4 a) LDA & b) PIV

The recirculating flow structure is clear in figure 6.5a and figure 6.5b for both the LDA and the PIV results. The oncoming flow is tripped by the sharp corner and the rapid expansion of the ramp, combining to generate an adverse pressure gradient as a result of the 16° rearward facing ramp. Pathlines indicate a flow recirculation centre at x=160mm y=-30mm in figure 6.4b. The PIV laser sheet placement and minimal surface reflections allowed velocity measurements very close to the surface. The LDA operates in the backscatter mode and reflections by the beams result in poor LDA data collection below the measured zone (0mm-10mm) from the surface.
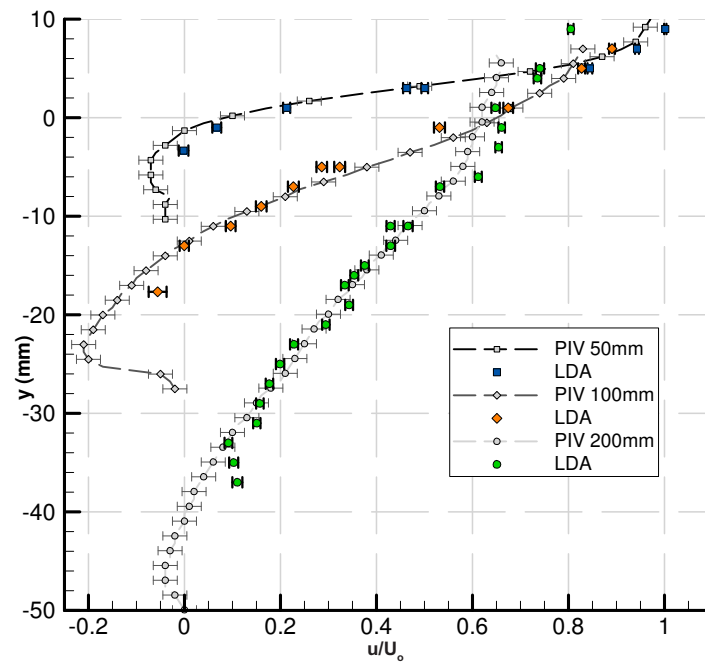
Figure 6.6 16° Rearward Facing Ramp u/U_o Velocity Profiles at x=50mm, 100mm & 200mm

Figure 6.6 outlines the normalized streamwise velocity (u/U_o) at three locations in the separated fluid structure; 50mm, 100mm and 200mm from the start of the ramp. The velocity profile at 50mm indicates a negative streamwise flow (due to the flow recirculation) beneath a shear layer. The size and strength of the recirculation grows at x=100mm; the shear layer also dissipates. At 200mm the reversed flow ($-u/U_o$) is weaker, having recovered somewhat from the adverse pressure gradient of the ramp. Good agreement exists between the LDA and PIV data in figure 6.6. The disparity at x=200mm (for y>-10mm) of the PIV is a result of reduced laser sheet intensity. This is not an issue at 50mm or 100mm, due to sectors 1, 2 and 3 comprising overlapped velocity data from sectors 2, 3 and 4, although it is partially evident in the top right corners of sectors 1 and 2.

6.4 Effect of Array Configuration on Ramp Flow Structure

Establishing the flow for the array with no dimples or the 'clean' ramp is shown by the normalized streamwise velocity profiles in figure 6.5, allows the effect that the dimple array has in reducing the flow separation to be investigated as the change in the u/U_o profile. Essentially if the dimples are to reduce flow separation then the u/U_o profile should increase, indicating the flow has recovered at the measured locations. This section will establish which dimple arrays effectively and consistently minimize the 16° rearward facing ramp flow separation, and where they need to be placed in order to replicate this array configuration on the wing.

Studies utilizing the rearward facing ramp to measure the effectiveness of various types of vortex generators listed in table 1.5. Lin (1989) used a 25° rearward ramp (with 8 inch edge radius), Cullen (2002) employed surface actuators to vary the curvature of the ramp and Rae (2002) employed the use of a concave 'bump' geometry to induce an adverse pressure gradient. These studies investigated fixed configurations of one row of the vortex generators used. In this investigation, location is varied to determine how far from the separation the array needs to be placed to control flow separation on an airfoil.

Results obtained by Lin et al. (1989) showed that vortex generators in a separated flow with a height=$0.1\delta_{BL}$ were effective within $0.2\delta_{BL}$ upstream of the separation line due to reduced vortex strength. In a later study, Lin & Howard (1990) showed that for the comparative flow-separation control studies in low-speed adverse pressure gradient flows, the embedded streamwise vortices produced by low profile vortex generators provided the most efficient means of minimizing both two-dimensional and three-dimensional turbulent boundary layer separation. However they noted that although the downstream effectiveness is reduced to the smaller size, by having placed them in their most effective range, low profile boundary layer protruding vortex generators of height $(H_{VG})=0.1\delta_{BL}$-$0.2\delta_{BL}$ are still effective in separation control. Angele et al. (2005) commented that smaller vortex generators give lower form drag, which is why increased focus has been put on submerged vortex generators (smaller than the boundary layer thickness).

With the three parameters of: dimple spacing, number of rows and the location relative to the rearward facing ramp being altered, equation 6.1 is the notation used

Array Spacing Dimple to Dimple	No. of Rows in Array	Array Spacing Dimple to Ramp

$$\textbf{A\# - R\# - D\#} \quad \dots\dots\dots\dots\dots\dots\dots\dots\dots\dots \quad [6.1]$$
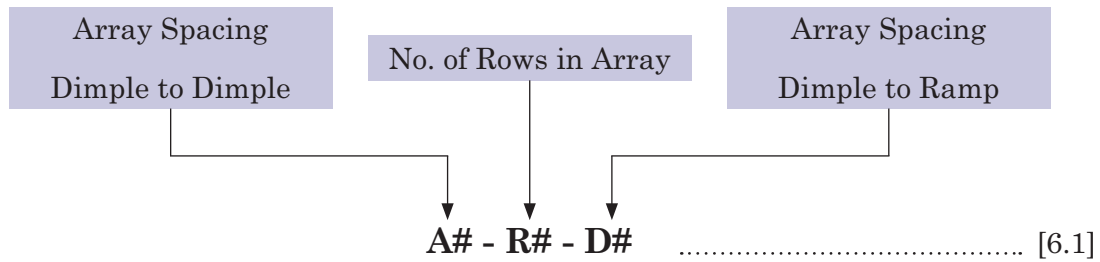
to describe the notation relating the geometrical configuration and placement of the array. For this study there are three types of array corresponding to; overlapping, in-line and offset dimple rims (figure 6.7). This relates to a dimple to dimple spacing of 1.5D, 2D and 2.5D respectively. The degree of dimple to dimple interaction by changing the spacing may enhance or impede the vortex formation at the dimple rim, thus altering how the vortices 'zig-zag' and form throughout the array. Therefore altering the spacing may result in a more effective array.

Table 6.1 Array Configuration Locations Tested From 16° Rearward Facing Ramp

Array Dimple Spacing	1 Row	3 Rows	5 Rows
1.5 D (overlapped)	0D, 1D, 3D, 5D	0D, 1D, 3D, 5D	0D, 1D, 3D, 5D
2 D (in-line)	0D, 1D, 3D, 5D	0D, 1D, 3D, 5D	0D, 1D, 3D, 5D
2.5 D (offset)	0D, 1D, 3D, 5D	0D, 1D, 3D, 5D	0D, 1D, 3D

Given the investigation of the single dimple at $Re_D=4.3 \times 10^3$ - 9×10^3 in section 5.3, particularly the vorticity analysis in 5.3.1, it can be seen that at y/D=0.11 from the surface in figures 5.47 and 5.48 there is vorticity production of the dimple with depth ratio $\delta/D=0.22$. Investigation of the lower dimple Reynolds number on the ramp flow ($Re_D=4.3 \times 10^3$, requiring $Re_H=5.25 \times 10^4$) will establish to what degree the weaker vortex production will act on the separation region if at all. A successful flow separation reduction with $Re_D=4.3 \times 10^3$, it would be reasonable to assume that $Re_D=9.0 \times 10^3$ will also yield a reduction. From figure 6.4 the approach boundary layer thickness is $\delta_{BL} \approx 6$mm, and dimple depth is $\delta=3.245$mm, thus $h_{VG}/\delta_{BL}=-0.541$. However given the vorticity penetration above the surface into the boundary layer from figure 5.48 is y/D=0.11, (with D=14.75mm in this case for equivalent Re_D) gives vorticity at y=1.6225mm from the surface. Therefore an equivalent protruding boundary layer vortex generator for the dimple in this section is $h_{VG(Dimple)} \approx 0.27 \delta_{BL}$.
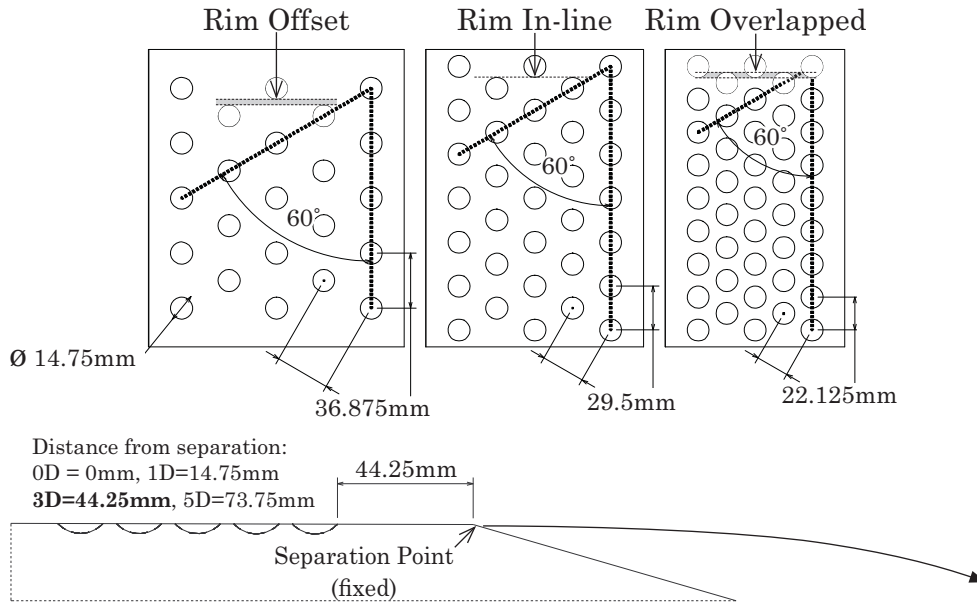
Figure 6.7 Array Parameters for Spacing and Location to Separation Point

Figures 6.8 to 6.17 show results for the measured normalized streamwise velocity profiles at 50mm, 100mm and 200mm from the ramp separation point. The results shown are for the array configurations that result in a favorable u/U_o profile that assits in the flow separation recovery behind the ramp. These results are compared to the non-dimpled ramp or 'clean' configuration, an improvement exists if the normalized streamwise velocity profile increases in u/U_o i.e. shifts to the right, or also reducing in size by the profile reducing in height (decreased y in mm). For the array configurations and locations tested (refer Table 6.1), one row of dimples produced no benefit in relation to the clean ramp velocity profiles, see appendix D.

Figure 6.8 16˚ Rearward Facing ramp flow with A1.5-R3-D3 dimple array configuration [LDA]
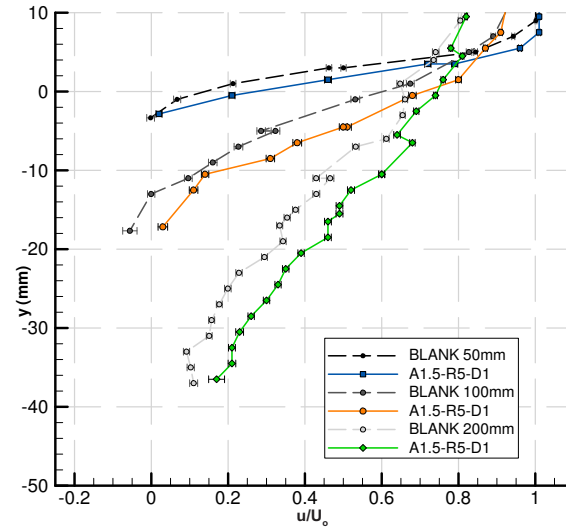
Figure 6.9 16° Rearward Facing ramp flow with A1.5-R5-D1 dimple array configuration [LDA]
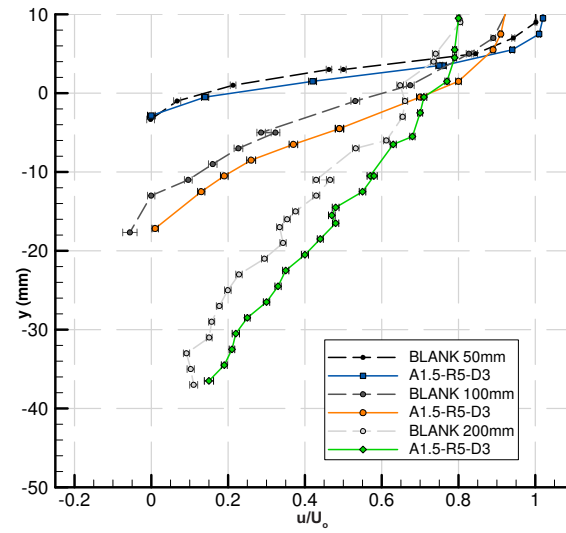
Figure 6.10 16° Rearward Facing ramp flow with A1.5-R5-D3 dimple array configuration [LDA]
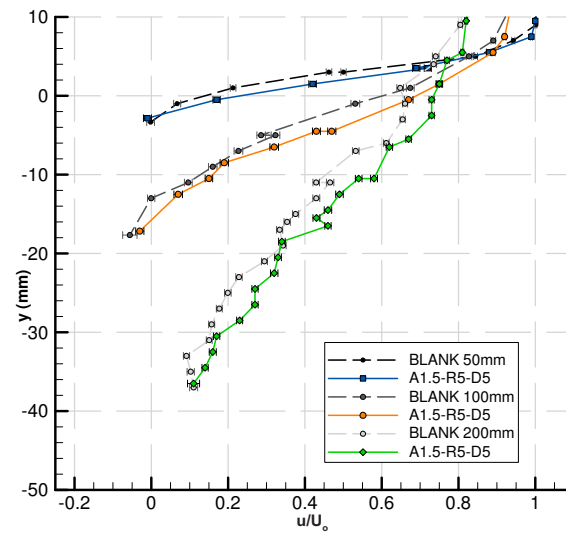
Figure 6.11 16° Rearward Facing ramp flow with A1.5-R5-D5 dimple array configuration [LDA]
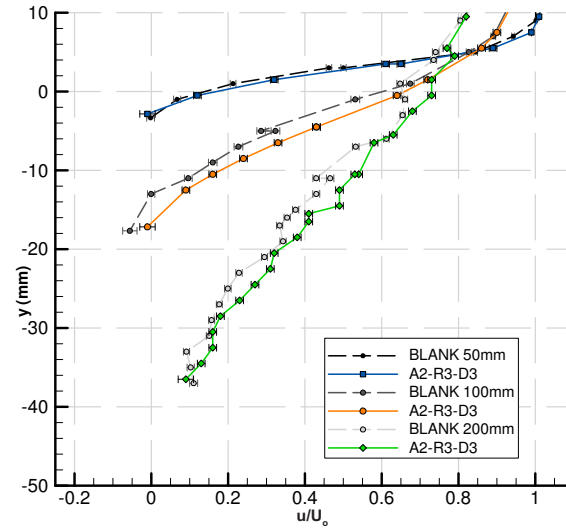
Figure 6.12 16° Rearward Facing ramp flow with A2-R3-D3 dimple array configuration [LDA]
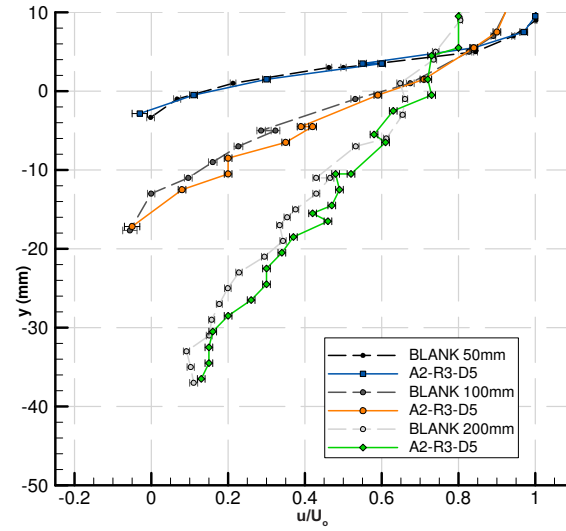
Figure 6.13 16° Rearward Facing ramp flow with A2-R3-D5 dimple array configuration [LDA]
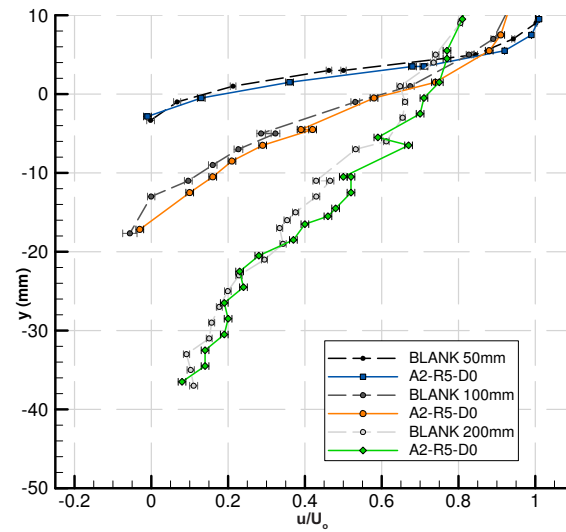
Figure 6.14 16° Rearward Facing ramp flow with A2-R5-D0 dimple array configuration [LDA]
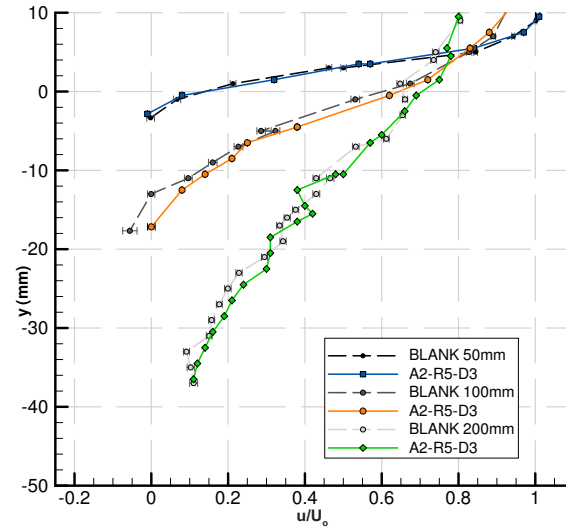
Figure 6.15 16˚ Rearward Facing ramp flow with A2-R5-D3 dimple array configuration [LDA]
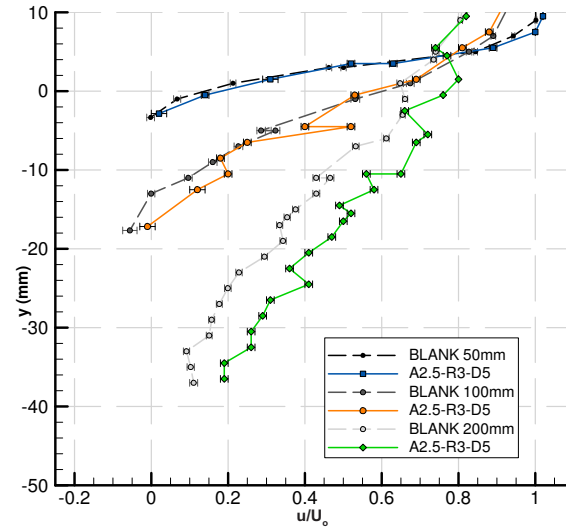
Figure 6.16 16˚ Rearward Facing ramp flow with A2.5-R3-D5 dimple array configuration [LDA]
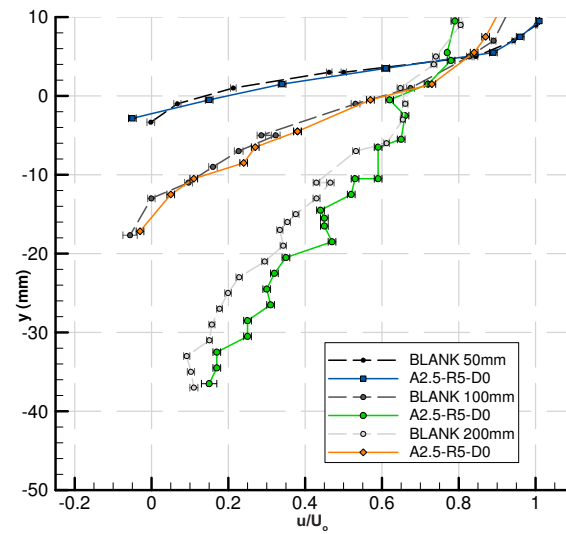
Figure 6.17 16˚ Rearward Facing ramp flow with A2.5-R5-D0 dimple array configuration [LDA]

Figures 6.8 to 6.17 show results for the measured normalized streamwise velocity profiles at 50mm, 100mm and 200mm from the ramp separation point. The results shown are for the array configurations that result in a favorable u/U_o profile that assits in the flow separation recovery behind the ramp. These results are compared to the non-dimpled ramp or 'clean' configuration, an improvement exists if the normalized streamwise velocity profile increases in u/U_o i.e. shifts to the right, or also reducing in size by the profile reducing in height (decreased y in mm). For the array configurations and locations tested (refer Table 6.1), one row of dimples produced no benefit in relation to the clean ramp velocity profiles, see appendix D.

Figures 6.18-6.20 indicate the average change of the u/U_o profile at x=200mm as a result of the dimple array compared to the baseline 'clean' ramp velocity profile. The positions which the average was based on correspond to y=-35mm to 0mm in 5mm increments. A positive $\Delta u/U_o$ indicates flow recovery due to the presence and location of the relevant dimple array, while a negative $\Delta u/U_o$ shows the array has increased the size of the flow separation region. The average $\Delta u/U_o$ change is plotted against the position of the array with respect to the flow separation point (as indicated by figure 6.7 and equation 6.1). This method was used to indicate a quantitative improvement to the flow field at a point where the most flow recovery has occurred, as directly comparing the differences between the dimple array and clean ramp flow (as in figures 6.8 to 6.17) can be misleading. Figures 6.7 to 6.16 are all reflected as $+\Delta u/U_o$ improvements in figures 6.18 to 6.20.

Figures 6.8 to 6.11 relate to the flow recovery due to the 1.5D spaced dimple array, the A1.5-R3-D3 configuration in figure 6.8 and 6.18 is the most effective array configuration and placement to recover the separated flow from the ramp of those tested. Figure 6.18 shows that for 1.5D spaced array's with 1 row all locations resulted in a greater velocity deficit in the separation region. Figures 6.9 to 6.11 and 6.18 show for the 1.5D spaced arrays with 5 rows in the array, the effective location ranges from 1D to 5D from the separation point. It is noticeable from the change relative to the 'clean' ramp that 1D and 3D spaced arrays recover the normalized streamwise velocity profiles to a similar degree, whereas 5D spacing has less (figure 6.11 and 6.18).
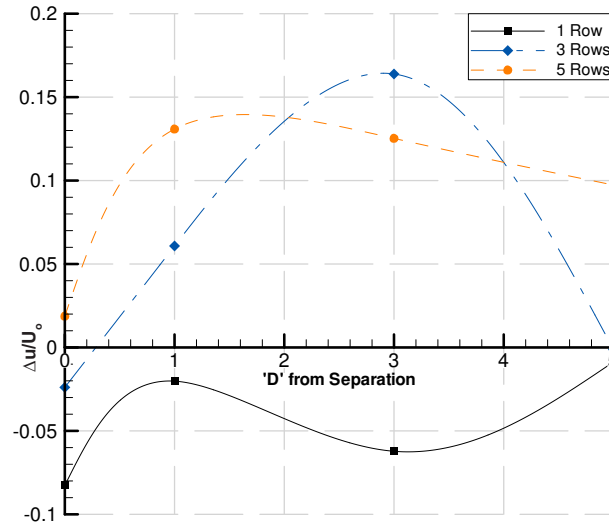
Figure 6.18 Average u/U_o change of 1.5D Spaced Dimple Array to Clean Ramp at x=200mm
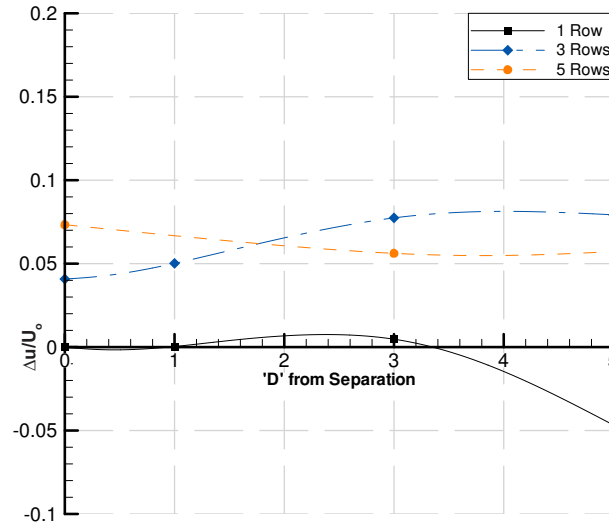
Figure 6.19 Average u/U_o change of 2D Spaced Dimple Array to Clean Ramp at x=200mm
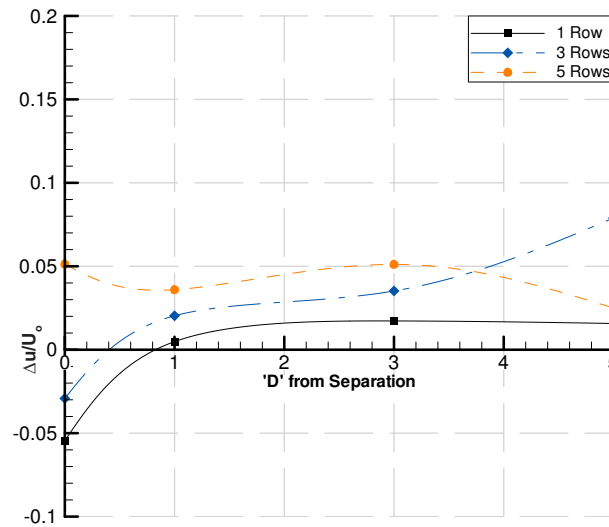
Figure 6.20 Average u/U_o change of 2.5D Spaced Dimple Array to Clean Ramp at x=200mm
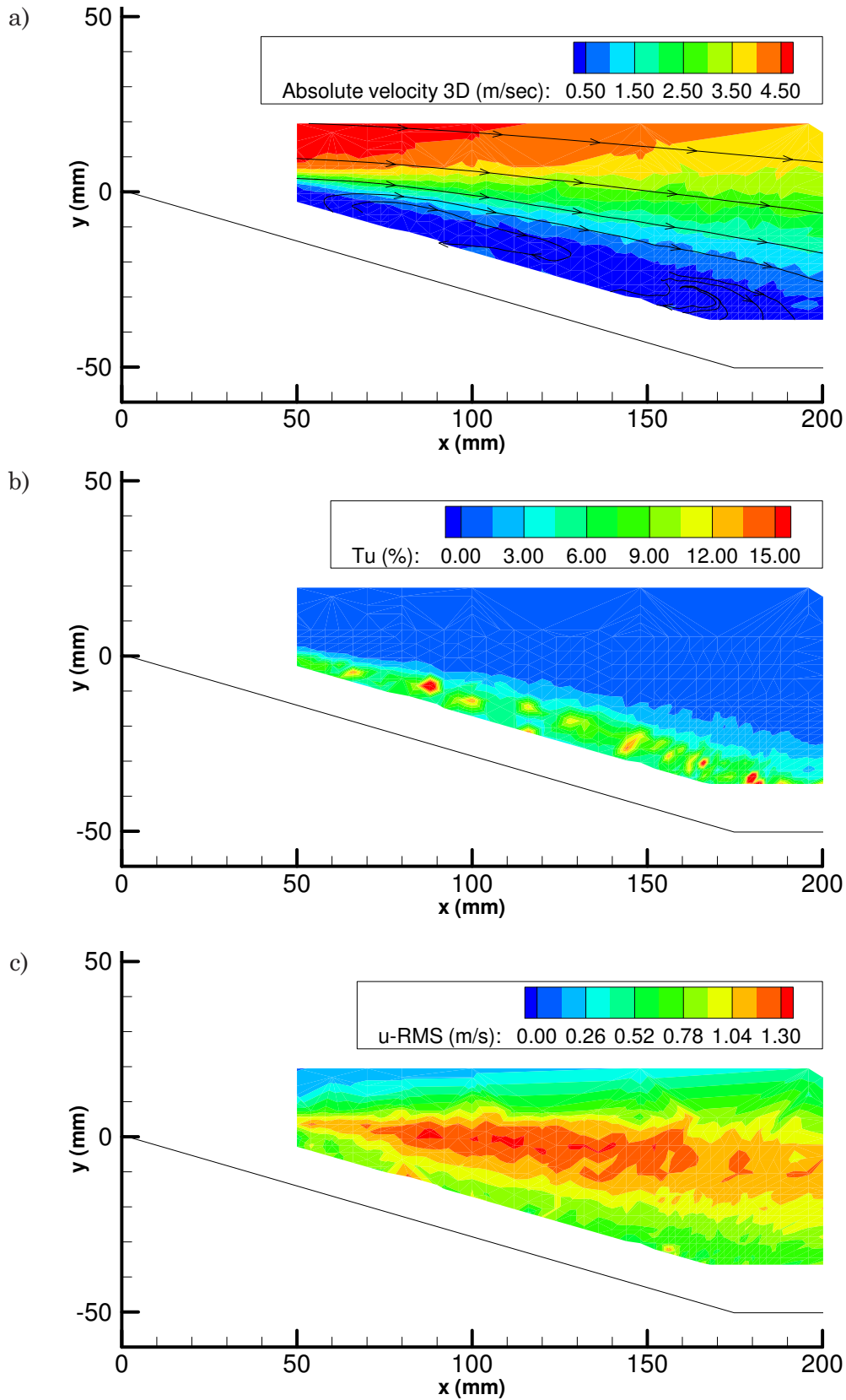
Figure 6.21 'Clean' Ramp, LDA a) 3D Absolute Velocity b) Turbulence Intensity c) u-RMS

The results for the 2D dimple spaced array configuration in figures 6.12 to 6.15 and 6.19 show that whilst there is some flow recovery as a result of this array spacing,
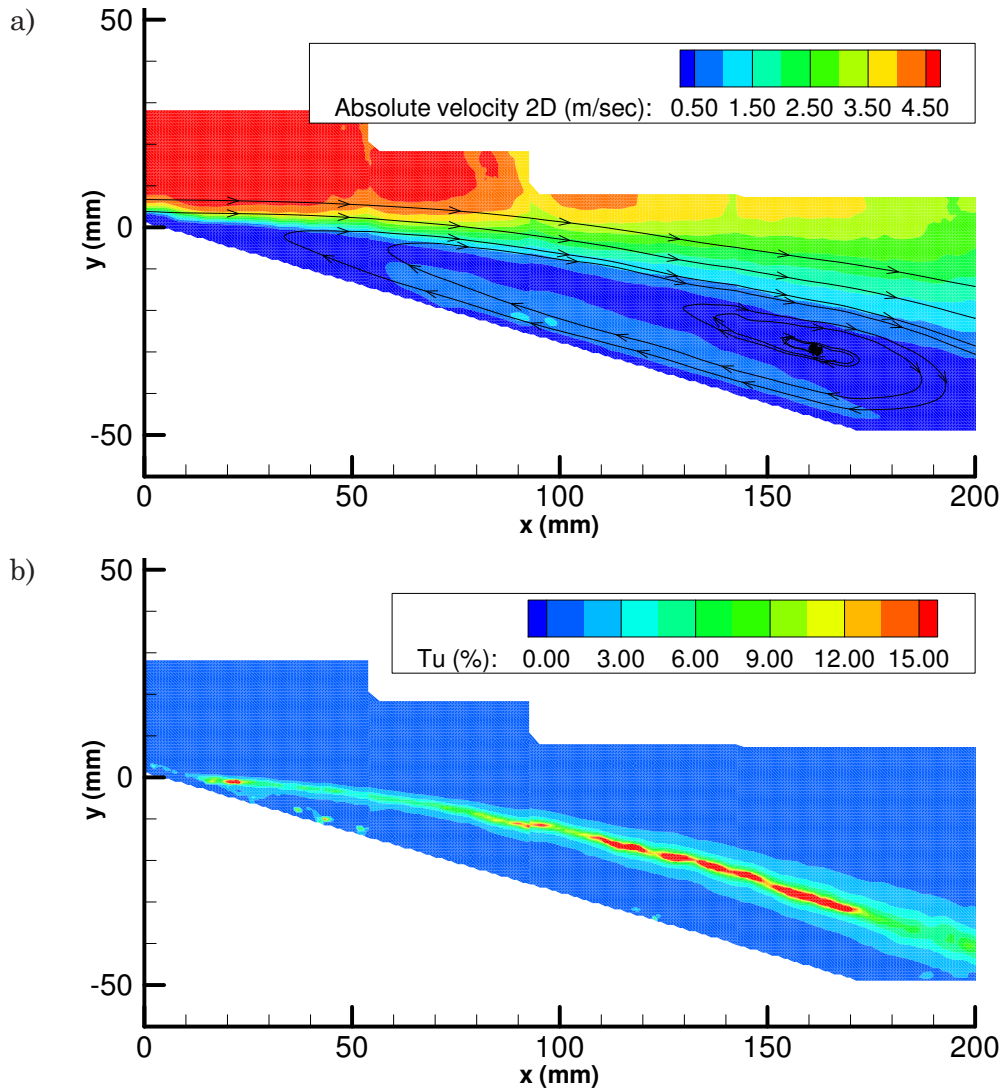
Figure 6.22 'Clean' Ramp, PIV a) 2D Absolute Velocity b) Turbulence Intensity

it is not as great as the 1.5D dimple spaced array. Figure 6.18 indicates a more stable improvement (from $\Delta u/U_o = 0.05\text{-}0.08$) for 3 and 5 rows placed 0D-5D from the separation point. The 2D spaced dimple array with 3 rows in figures 6.12 to 6.13 and 6.19 show similar (albeit slight) recovery of u/U_o at 3D and 5D from the separation point. In figure 6.14 and 6.15 the flow recovery potential of the 2D spaced array with 5 rows reduces as the location increases from 0D to 3D, noted by the trend in figure 6.19. The 2.5D spaced dimple configuration in figure 6.16 , 6.17 and 6.20 shows even lower levels flow recovery compared to the 2D and 1.5D array, thus as the array spacing increases it is clearly approaching the initial 'clean' configuration.

The fluctuating components of the velocity in the separated region must not increase due to any turbulence or vortex shedding from the dimples; on the airfoil these may result in viscous drag increases that outweigh pressure drag reductions.
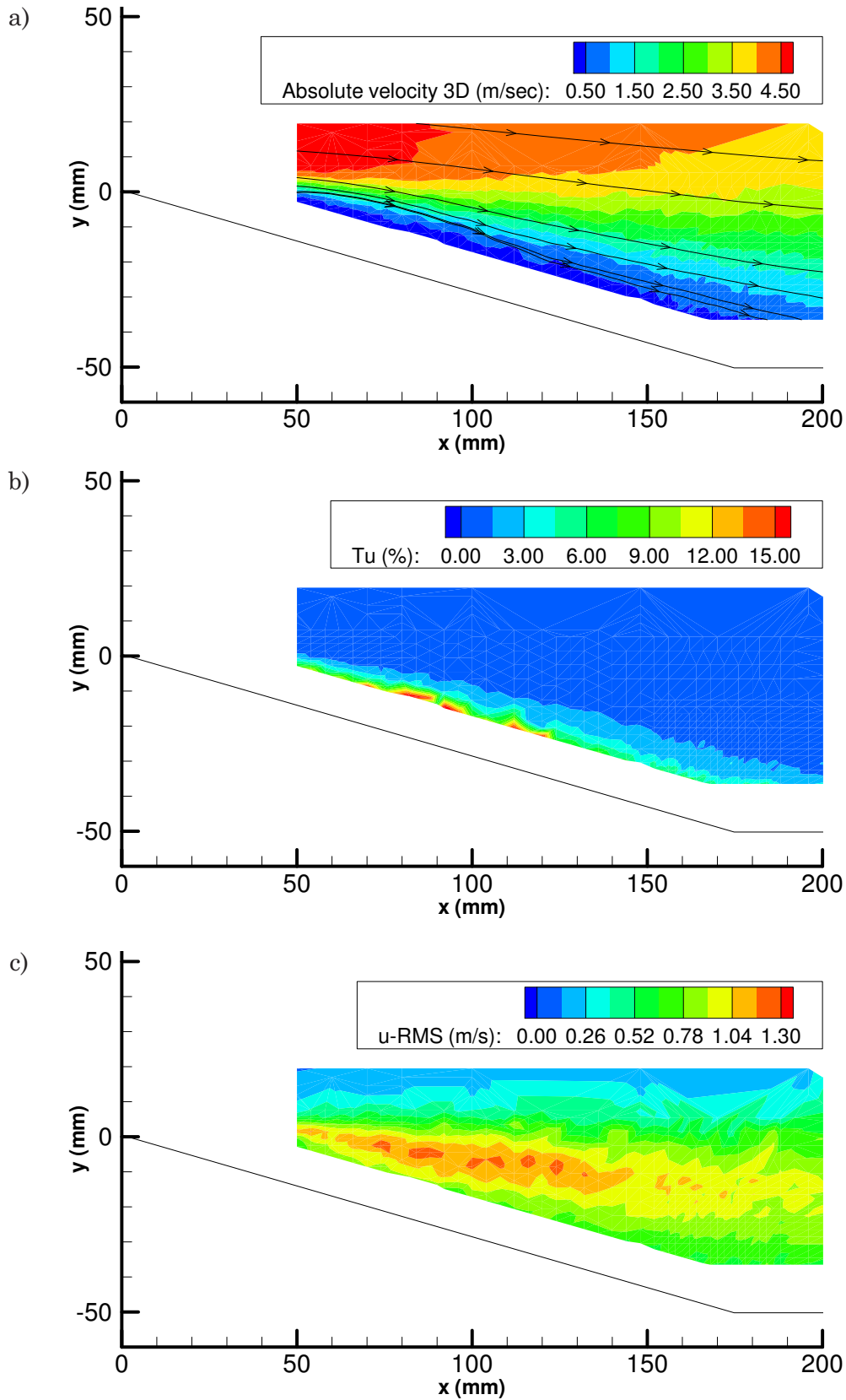
Figure 6.23 A1.5-R3-D3 Array, LDA a) 3D Absolute Velocity b) Turbulence Intensity c) u-RMS

Figures 6.21 and 6.22 outline the flow field of the 16° rearward facing ramp and the turbulence intensity for LDA and PIV results. u-RMS is only plotted for the
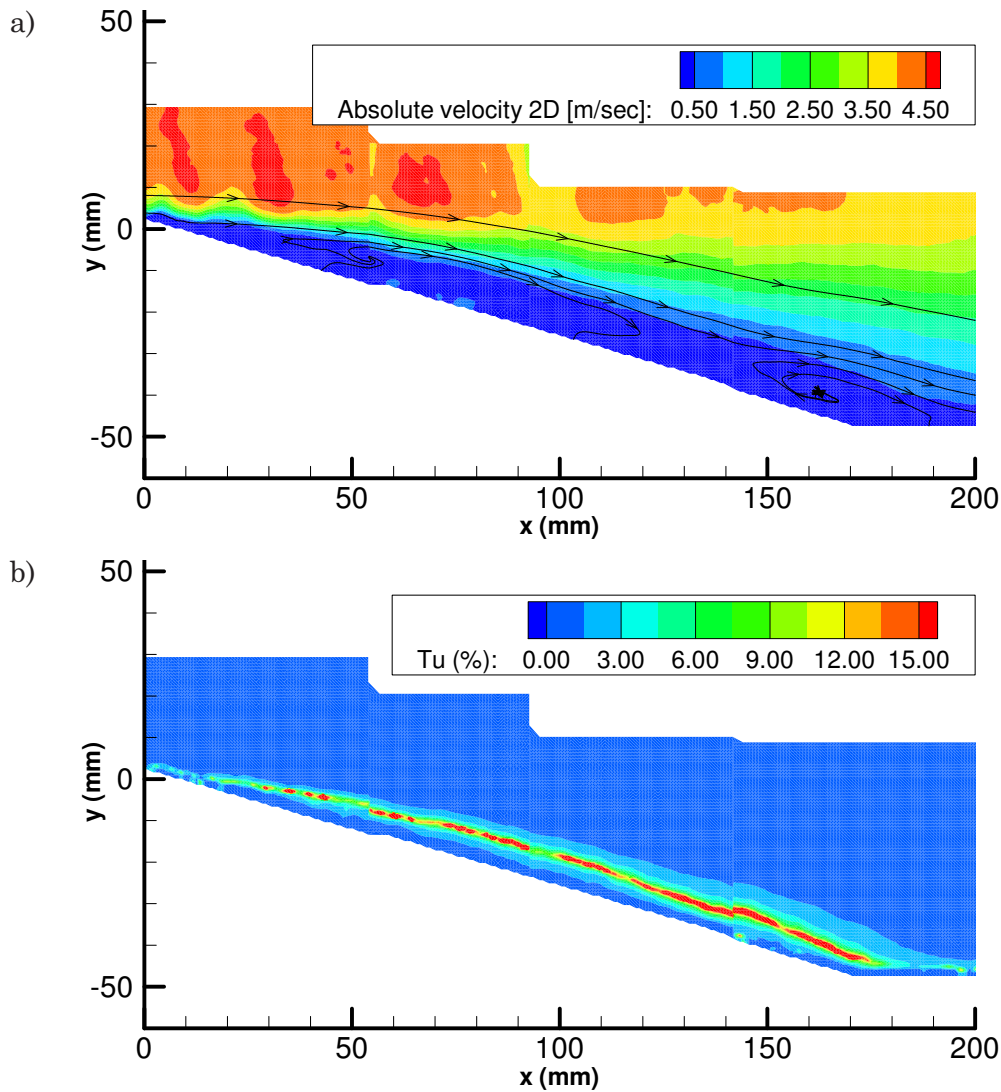
Figure 6.24 A1.5-R3-D3 Array, PIV a) 2D Absolute Velocity b) Turbulence Intensity

LDA in 6.21c, indicating shear layer breakdown from the separation point on the ramp. Good agreement exists between the two techniques; the LDA 3D absolute velocity in 6.21a does not differ greatly from the PIV 2D absolute velocity of 6.22a, reinforcing the 'quasi two-dimensional' nature of the flow. The 3D and 2D turbulence intensity shows a thin arc spanning the ramp recirculation region. The thicker LDA turbulence intensity reflects the 'coarseness' mesh (figure 6.3) as the PIV can resolve higher, more concentrated values of turbulence intensity.

The normalized streamwise velocity profile of figure 6.18 indicated one of the more effective increases in u/U_o with the A1.5-R3-D3 dimple array; the altered flow field is shown in figures 6.23 to 6.24. It is noticeable for both the LDA and PIV absolute velocity contours in figures 6.23a and 6.24a respectively, that the recirculation region is substantially reduced when comparing to the 'clean' ramp flow field in figures

6.21a and 6.22a. The whole recirculation region is shifted into a 'semi-stalled' flow close to the ramp surface. The reversed flow that does exist is below the LDA mesh used thus not able to be accounted for in 6.23a. The turbulence intensity in 6.23b and 6.24b shows the 'arc' of turbulence intensity existing for the 'clean' ramp in 6.21b and 6.22b reducing in size and intensity, and is also shifted very close to the surface. The u-RMS change as a result of the dimple array, figure 6.23c, shows reduced size and intensity, shifting closer to the ramp surface compared to the 'clean' ramp (6.21c).

Dimples spaced 1.5D apart have more effect on the separated flow structure from the rearward facing ramp. The configuration providing the greatest reduction is the A1.5-R3-D3 array of dimples seen in figure 6.10, 6.18 and 6.23. The operational range of this array is limited to placement 1D-3D from the separation point, with 0D and 5D placement providing no 'benefit' to the separation zone. The 1.5D spaced array with five rows consistently reduces the velocity deficit and size of the separated zone for the range 1D-5D (figures 6.18). Thus a five row, 1.5D spaced dimple array is more consistent at reducing flow separation and most suited for an application that is required to be predictable relative to a potentially fluctuating separation point. However in figure 6.18, if 3 rows of the 1.5D spaced array are positioned correctly a large gain for the flow separation suppression can be expected. The 2D and 2.5D spaced dimple arrays for 1D-5D placement from the separation point exhibit consistent flow recovery of $\Delta u/U_o \approx 0.05$-$0.075$ and 0-0.05 respectively (figure 6.18 to 6.19), thus are also suited albeit their flow recovery is less than the 1.5D array.

Given the rearward facing ramp analogy in figure 6.1, flow-field measurements in the wake of a wing are required to determine what extent a dimple array can reduce the flow separation on an inverted airfoil in ground effect. The boundary layer for the test section Reynolds number upstream of the ramp is shown in figure 6.4, and corresponds to a laminar boundary layer profile. The dimple array potential to fully trip the boundary layer to turbulent and thus act to recover the separated flow from the ramp is not compared with other methods such as sand paper or a boundary layer trip wire on the ramp in these experiments. What is important is that the lower Re_D=$4.3x10^3$ used in these experiments is sufficient enough to alter the flow structure of the separated flow from the ramp. More crucial is the comparison of tripping the boundary layer with a trip wire on the airfoil compared with the dimple array in chapter 8.6.

Tyrrell026 Airfoil Wake Investigation

7

This chapter examines the wake of the Tyrrell026 airfoil with no dimples. A detailed survey using the LDA focuses on the wake flow structure, the normalized streamwise velocity as well as the turbulence intensity and the two main Reynolds stress components. This information is vital to understand how the dimple array modification to the suction surface changes these properties in chapter 8. The non-dimpled airfoil measurements also examine the changes of the time averaged velocity and the time varying flow properties with respect to alterations in ground clearance and angle of incidence.

7.1 Introduction

In order to establish the effect of the dimple array on the flow over an airfoil, the flow in the immediate wake behind the airfoil trailing edge to one chord length downstream (i.e. $1 \leq x/c \leq 2$) must be examined in its 'clean' configuration with no dimples. The ground clearance (h/c) and angle of incidence ($\alpha°$) are both varied to gain an understanding of the wake flow field. Angle of incidence ranges from low to quite high, as higher angles of incidence have large scale flow separation (indicative of airfoil stall). Varying the ground clearance from high to low demonstrates the increased ground effect influence on the wake flow structure. The airfoil wake LDA measurements outlined in figure 7.1 focus on; the normalized streamwise velocity, the turbulence intensity and the normal turbulent stress (uu) and the primary shear stress (uv).
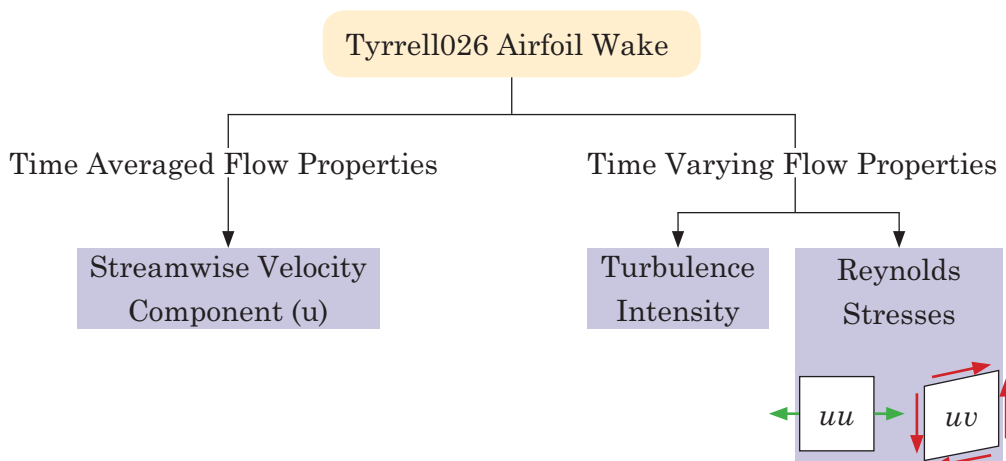
Figure 7.1 Wing Wake Experimental Measurement Study

7.2 Experimental Equipment and Setup

All wings were 3-axis NC-milled from aluminium and finished to an even surface finish with 800 grit sandpaper. A finite trailing edge was used such that it measured 0.8mm (1.06% chord), which limited the full 75mm chord to 70mm (93.3% chord). These wings were mounted into the adjustment mechanism in the side wall, which allows variable height setting from the ground and angle of incidence increments of α=1°. Height gauges were machined for the four ground clearances used, and placed under the wing in order to set the ground clearances consistently. Figure 7.2 shows the model installation in the tunnel in moving ground configuration and outlines the experimental variables and parametric references.
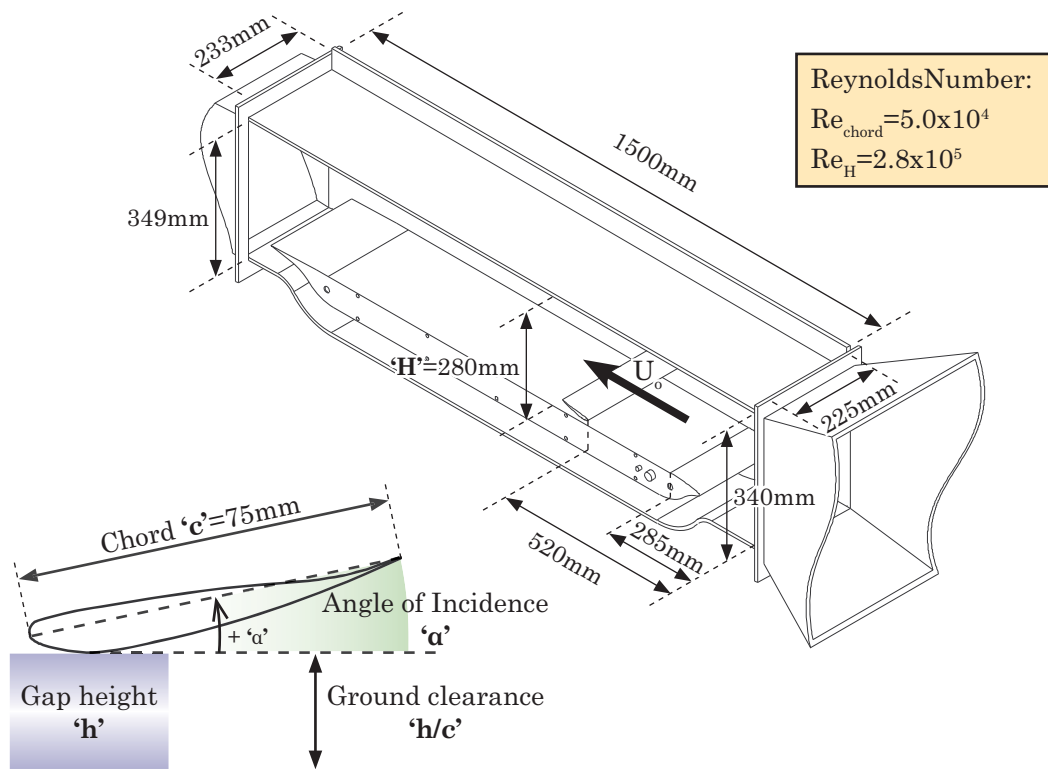
Figure 7.2 Test Section and Wing Variables: α, c & h

Table 7.1 Wing Ground Clearance and Angle of Attack Settings

Angle of incidence (α°)	h/c=0.112	h/c=0.134	h/c=0.224	h/c=0.313
Low Range	-2°	-2°	-2°	-2°
Low Range	0°	0°	0°	0°
Low Range	2°	2°	2°	2°
Mid Range	5°	5°	7°	7°
High Range	10°	10°	10°	10°
High Range	13°	13°	-	-
High Range	15°	15°	15°	15°

a)

b)
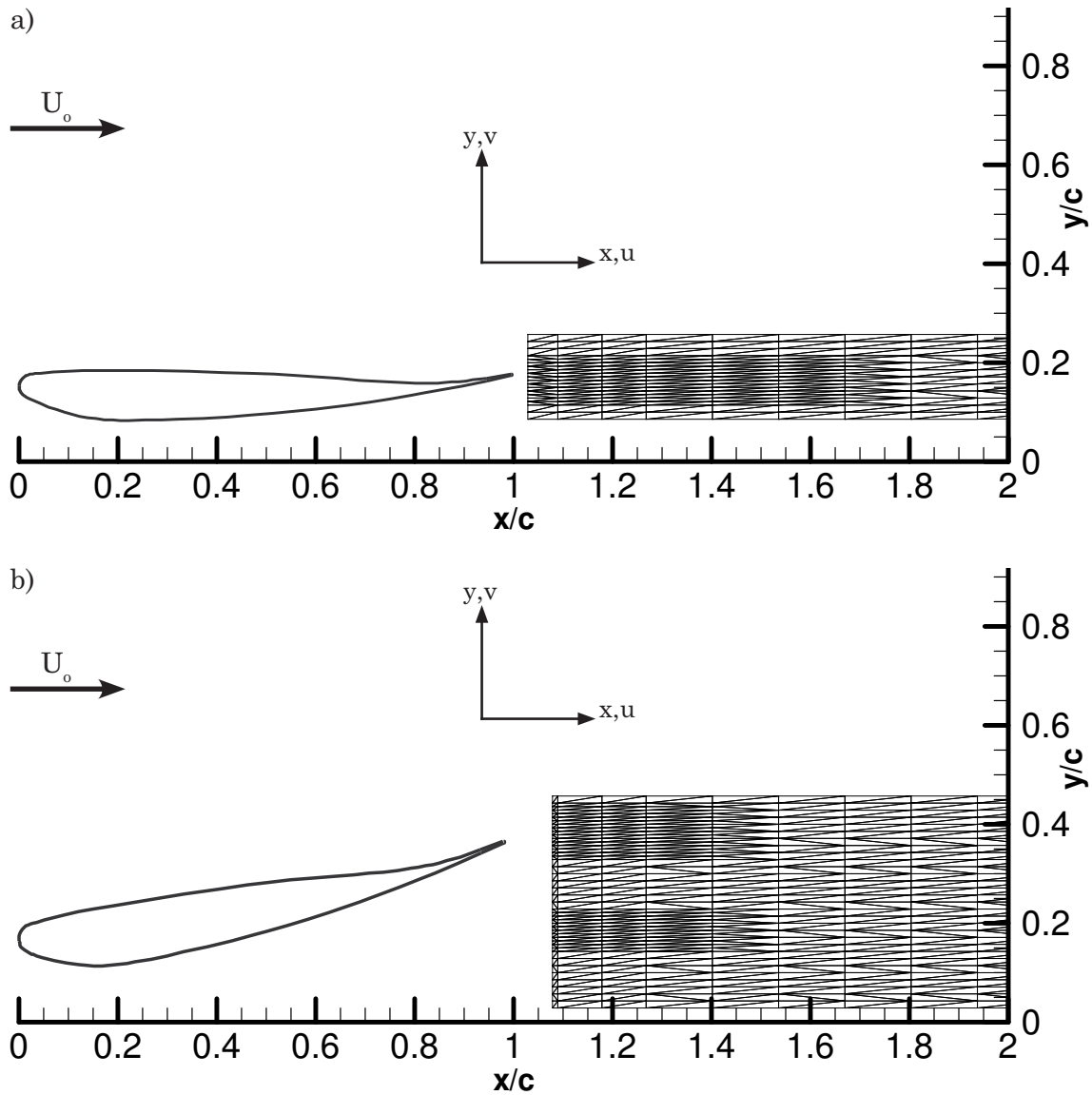
Figure 7.3 Typical LDA grids for a) low and b) high angles of incidence

Figure 7.3 shows two LDA grids used to take the measurements for the low and high angles of incidence, which typically have 200 and 350 points respectively. Points were concentrated near regions of high velocity gradients at the trailing edge and in the case of higher angles of incidence; in the downstream region of the lower surface separated boundary layer. The grids for a given angle of incidence were maintained by translating the height (y/c) to the corresponding h/c of the airfoil. The grids in figure 7.3 are indicative of those used for the case where α=0° and α=13° for figure 7.3a and figure 7.3b respectively at the ground clearance h/c=0.112. Transit time weighting was used to ensure unbiased velocity measurements of the three-dimensional coincident readings. Each point was measured for 3 seconds at an average data rate of 1500-2000Hz.

7.3 Tyrrell026 Airfoil: Wake Streamwise Flow

The base-line 'clean' case (with no dimples present), is a fundamental requirement in order to properly understand the most effective positioning of the dimple array on a 'naturally' migrating separation point, due to changes of the angle of incidence and ground clearance. The 'clean' wing case has no fixed transition point, as forced transition is likely to mask the effects the dimple array is to provide. The variables used to analyze the wake are plotted against a normalized y/c, such that for all ground clearances the trailing edge is translated to the y/c for the given α at h/c=0.313; (y/c)^T. This is done to ensure the vertical deviation of the wake can be accounted for from the 'hard point' of the wing trailing edge. This ensures the influence of the ground on the wake for the range of α and h/c can be observed. The values of α and h/c are based on the lift curve slope outlined by Zerihan (2001) for the same airfoil, such that an indication of stall can be seen in the wake flow structure.
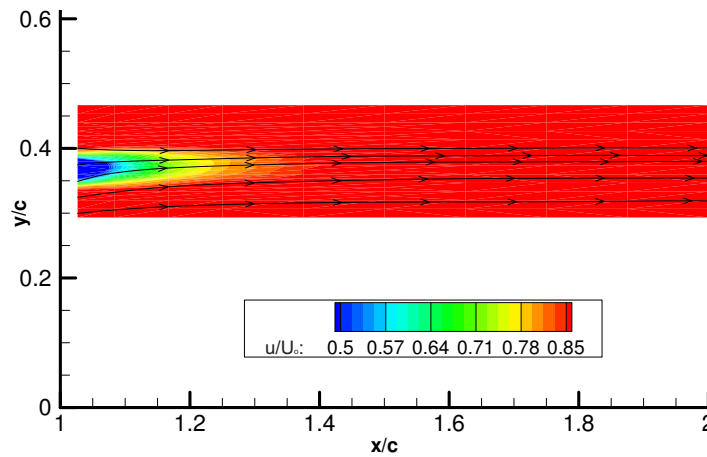
Figure 7.4 Tyrrell026 airfoil wake: α=0˚ h/c=0.313
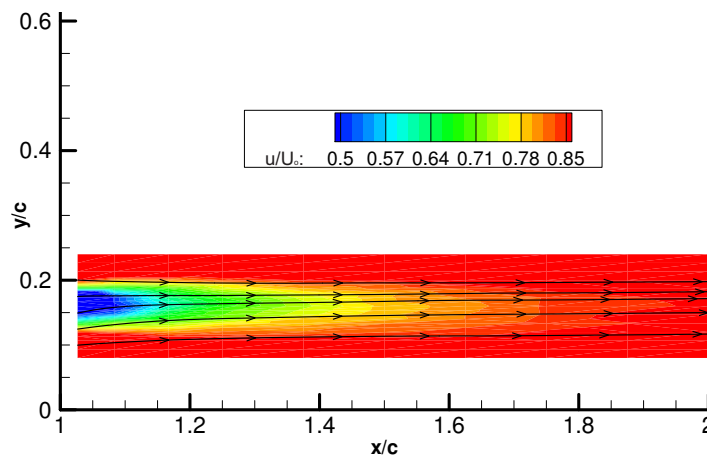
Figure 7.5 Tyrrell026 airfoil wake: α=0˚ h/c=0.112
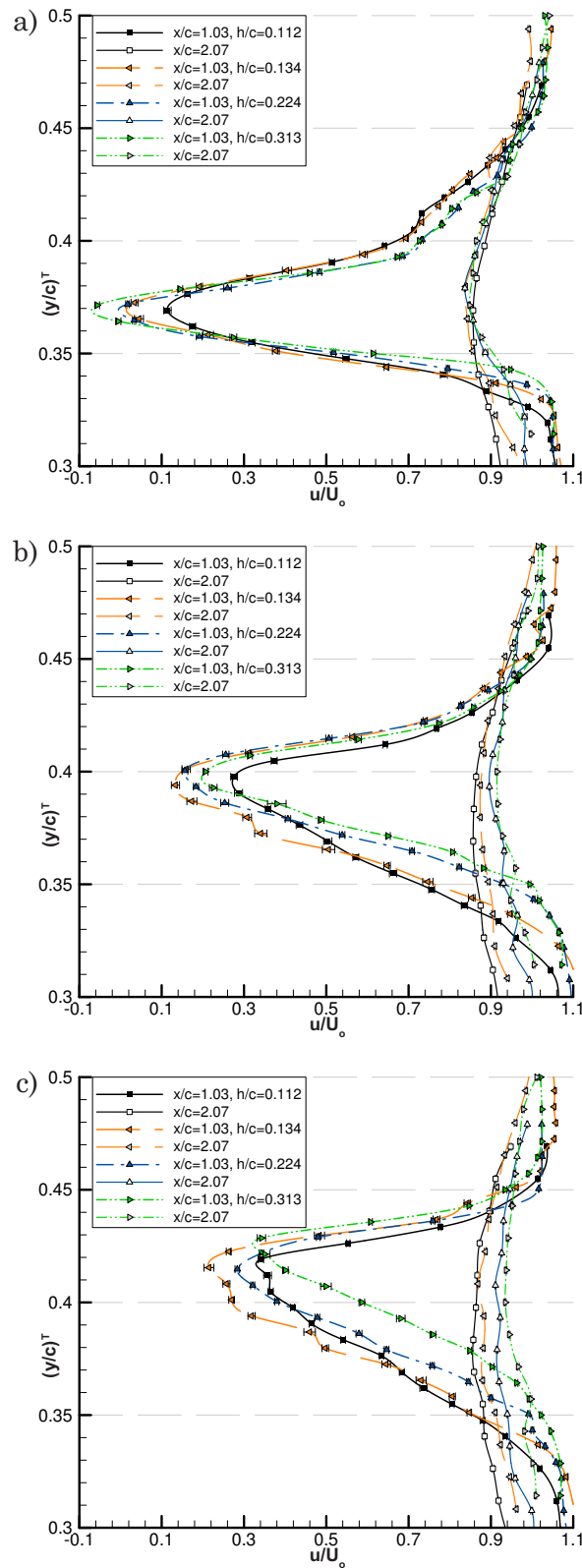
Figure 7.6 Normalized Streamwise Velocity a) α=-2° b) α=0° c) α=2°

Investigation for α=0°, shows the wake velocity profile of u/U_o thickening for h/c=0.122 from h/c=0.313 in figure 7.4-5. The low angle indicates a slight upwash (vertical) component of the flow, which is weaker at h/c=0.112; resulting in a thicker

wake profile. The α=0° u/U_o profile at x/c=1.03 & 2.07 in figure 7.6b shows the wake thickening by Δy/c≈0.02 (at u/U_o=0.9, y/c=0.34-0.36) from the suction surface side of the airfoil for h/c=0.134 & 0.112, over h/c=0.224, 0.313. The lowest velocity in the wake at the trailing edge shows a reducing trend from u/U_o≈0.15 (h/c=0.313) to u/U_o≈0.1 (h/c=0.134). It is noted by Zerihan (2001), that h/c=0.134 is the height at which the onset of the force reduction phenomenon occurs for the Tyrrell026 airfoil. The downstream flow recovery at x/c=2.07 is poor for h/c=0.112 & 0.134 with the profile biased more towards the ground than the higher clearances.

Table 7.2 Wake Flow Recovery for α=-2°, 0°, 2°

h/c	$u/U_{o,min}$ α=-2°	Recovery x/c=2.07	$u/U_{o,min}$ α=0°	Recovery x/c=2.07	$u/U_{o,min}$ α=2°	Recovery x/c=2.07
0.112	0.114	0.743	0.276	0.581	0.341	0.516
0.134	0.034	0.809	0.133	0.741	0.215	0.668
0.224	0.017	0.819	0.157	0.739	0.284	0.631
0.313	-0.057	0.905	0.207	0.710	0.342	0.593

The wake sensitivity for low angle of incidence changes in figure 7.6a and figure 7.6c shows the effect of a ±2°change in angle of incidence from α=0° (in figure 7.6b). The thickness increase of the wake at α=2° is slightly greater than Δy/c=0.02 for the part of the wake closest to the ground at h/c=0.112 & 0.134, and is Δy/c=0.01 for h/c=0.224. For angles lower than 2°, h/c=0.224 reflects the wake profile at h/c=0.313. At α=0°, the difference in the lower portion of the wake is clear between h/c=0.134 and 0.224 of Δy/c=0.02, in effect separating the two upper ground clearances from the two lower ground clearances. The wake thickness at α=-2° for h/c=0.112 to 0.134, increases by Δy/c=0.01 for both upper and lower sides of the airfoil wake. For α=±2° it is clear at x/c=2.07 the wake profiles are biased to the ground more for h/c=0.112. Table 7.2 indicates the degree to which the flow recovers from the peak deficit of the wake at x/c=2.07 from x/c=1.03. In general the recovery of u/U_o increases up to the force reduction ground clearance of h/c=0.134, before decreasing for h/c=0.112. The trend reversal for α=-2° is potentially due to upper surface leading edge separation resulting in negative values for u/U_o at x/c=1.03 in figure 7.6a.

As the angle of incidence increases to 5° and 7° in figures 7.7a and 7.7b, the presence of the ground influences the wake more noticeably than for -2°≤α≤2. It is clear that for all cases when h/c=0.112, the upper part of the shear layer from the trailing

edge is closer to the ground than h/c=0.134, 0.224 and 0.313, as is the lower surface separated zone shear layer. For h/c=0.313 the wake is at a higher y/c position, particularly at α =2°, 7° in figure 7.6c and 7.7b.

The intermediate angles of incidence between the lower values of α in figure 7.6 and higher angles approaching stall of the airfoil are in shown figure 7.7a and 7.7b. The increased angle results in acceleration of the flow over both surfaces and subsequently a thinner boundary layer will result, and increased shear. This is seen by $u/U_{o,min}$ at x/c=1.03 increasing to the freestream constant u/U_o profile; α=0° from y/c=0.39-0.45 (Δy/c=0.06) and α=2° y/c=0.42-0.46 (Δy/c=0.04); in figures 7.6b & 7.6c. Whereas α=5° y/c=0.47-0.5 (Δy/c=0.03) and for α=7° y/c=0.49-0.52 (Δy/c=0.03); figures 7.7a & 7.7b.
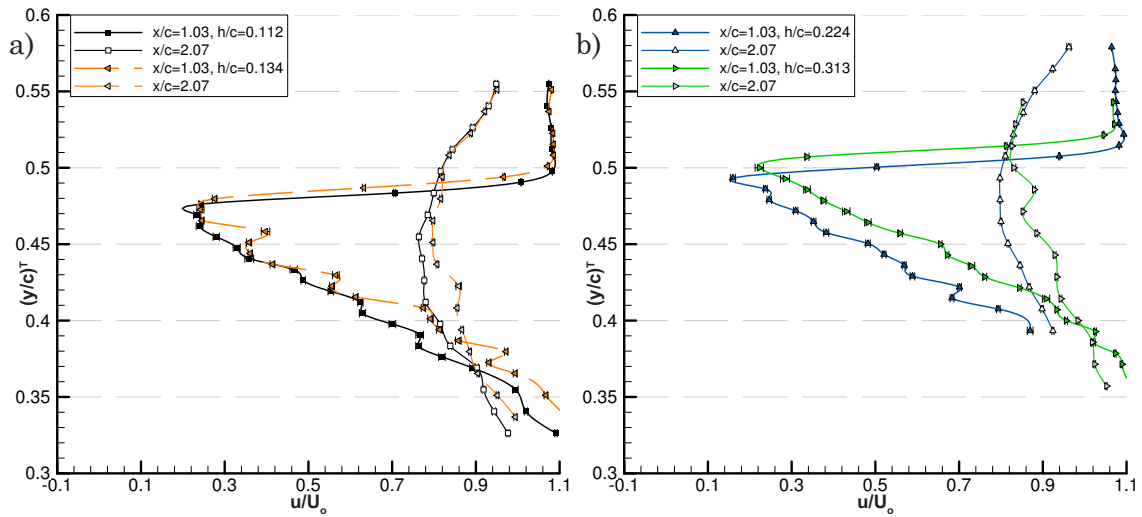
Figure 7.7 Normalized Streamwise Velocity a) α=5° h/c=0.112-0.134 b) α=7° h/c=0.224-0.313

As the ground clearance reduces from h/c=0.313 to h/c=0.112 at α=10° (figures 7.8-7.9), the length of wake increases and the thickness reduces. Streamwise velocity deficits in the wake x/c=1.03-1.4 in figure 7.9 (u/U_o<<0.5) are greater than the in figure 7.8. Reversed flow exists in the region beneath the trailing edge; indicating flow separation on the suction surface of the airfoil. The trailing edge pathline deviation of the airfoil at α=5° & 7° in figures E.3, E.6, E.9 E.12 are positive; indicating upwash. When compared to α=10° in figure 7.8-7.9 the trailing edge pathline deviation is now negative; indicating downwash. This shows that the ground presence limits the ability of the angle of incidence and camber to generate upwash, and can be attributed to the presence of the flow separation in the venturi-like section formed between the ground and the airfoil. The lift curve for h/c=0.112 in Zerihan (2001)
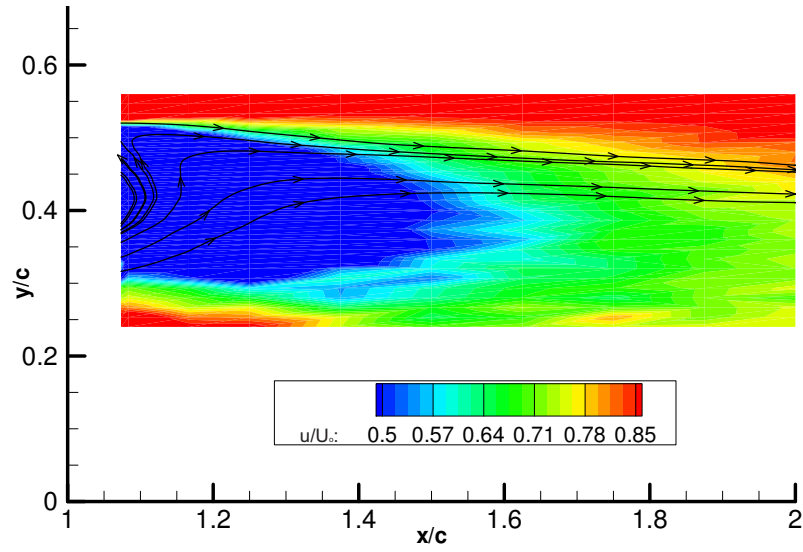
Figure 7.8 Tyrrell026 airfoil wake: α=10˚ h/c=0.313
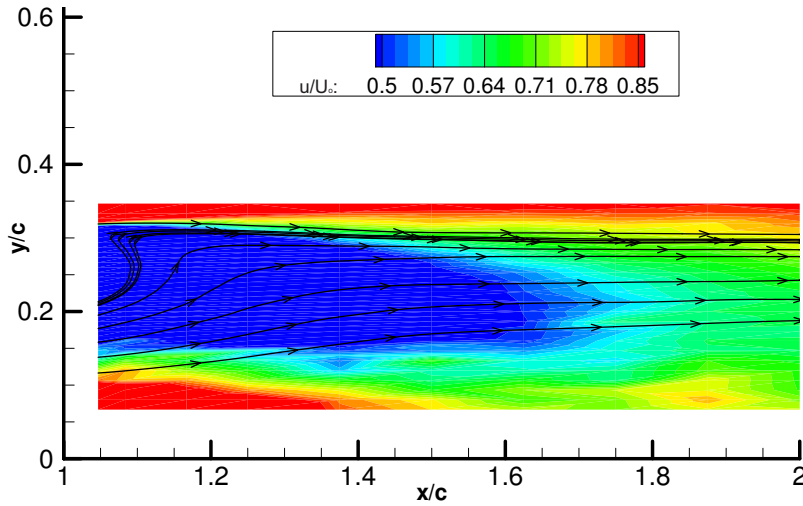
Figure 7.9 Tyrrell026 airfoil wake: α=10˚ h/c=0.112
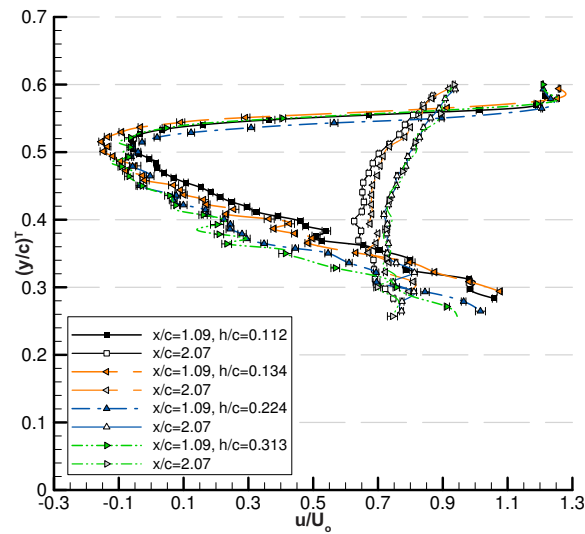
Figure 7.10 Normalized Streamwise Velocity α=10˚

shows that the stall point is not yet achieved, thus the force generation of the airfoil is not impeded by such large scale flow separation.

The u/U_o profile of figure 7.10 for $\alpha=10°$ shows a $\Delta y/c=0.05$ increase in the wake thickness in the lower part of the wake at $x/c=1.03$ for $h/c=0.224$ $h/c=0.134$. It is also clear that reversed flow (where $u/U_o<0$) exists to a greater extent. The wake at $x/c=2.07$ in figure 7.10 shows that while $h/c=0.224$-0.313 does not experience the deficit in the velocity profile as $h/c=0.112$-0.134, the wake at $y/c\approx0.3$-0.4 is showing more bias towards the ground at higher h/c. When comparing the u/U_o profile for $\alpha=13°$ in figure 7.11 at $x/c=2.07$ for $y/c=0.25$-0.4, u/U_o does not increase as much at $h/c=0.112$ than for $h/c=0.134$. The increased interaction of the lower wake near the ground suggests the airfoil has stalled between $\alpha=10°$-$13°$ for $h/c=0.112$ & 0.134, as there is little downstream flow recovery.
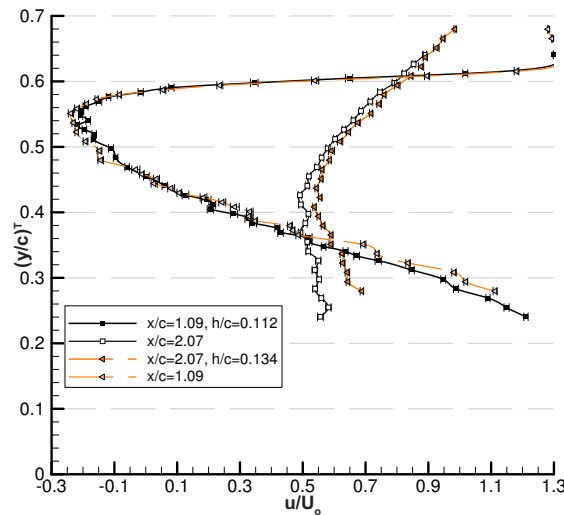
Figure 7.11 Normalized Streamwise Velocity $\alpha=13°$

Figures 7.12, 7.13 and 7.14 show the wake structure for the highest angle of incidence of $\alpha=15°$. Where as a reduction in ground clearance for $\alpha=10°$ in figures 7.9 to 7.11 resulted in a 'thinner' yet longer wake, for $\alpha=15°$ the reduction in ground clearance from $h/c=0.313$ to 0.112 leads to an overall larger wake. This is likely as a result of the 'choked' flow between the wing and ground causing earlier separation and higher velocity gradients. The recirculation zone under the trailing edge is substantially larger than at $\alpha=10°$, which suggests very large scale flow separation existing on the airfoil suction surface. The substantial change in the flow structure for $\alpha=10°$-$15°$ at $h/c=0.112$ as opposed to $h/c=0.313$ (figure 7.9 & 7.13) indicates a higher flow sensitivity
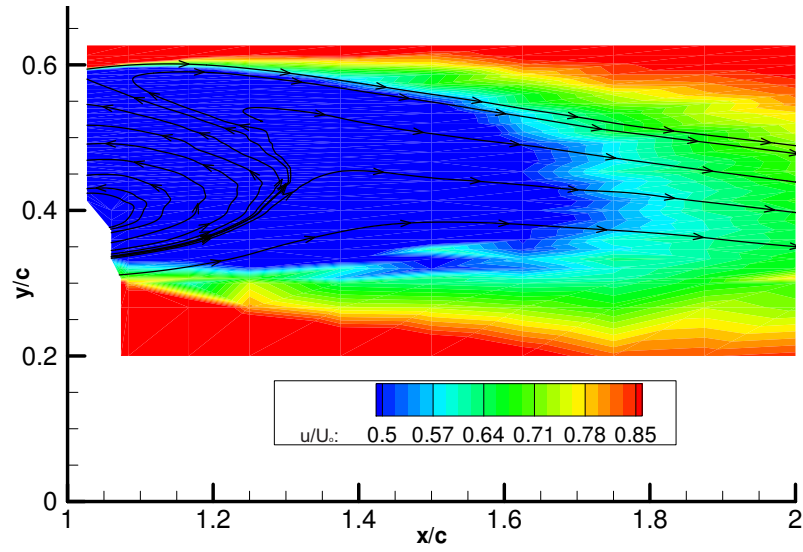
Figure 7.12 Tyrrell026 airfoil wake: α=15˚ h/c=0.313
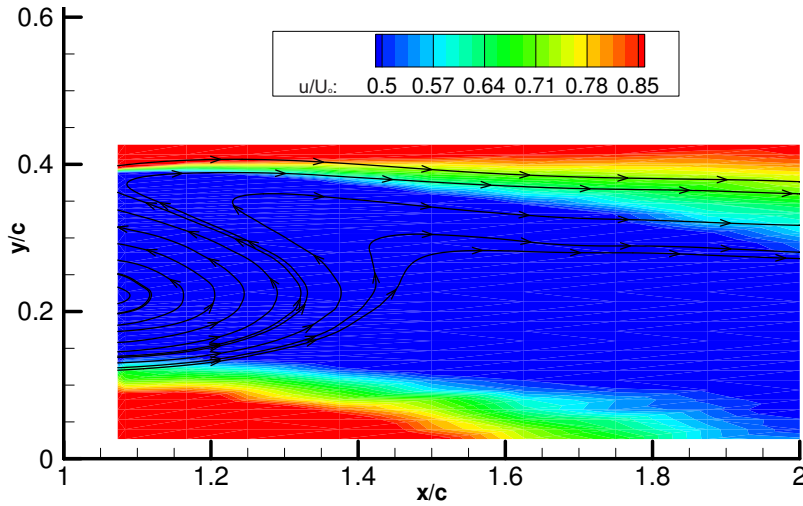
Figure 7.13 Tyrrell026 airfoil wake: α=15˚ h/c=0.112
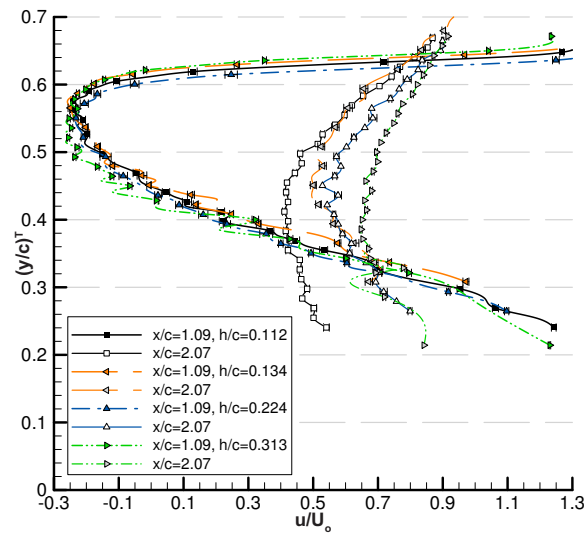
Figure 7.14 Normalized Streamwise Velocity α=15˚

at the lower ground clearance and potentially a sharper stall characteristic.

Table 7.3 Wake Flow Recovery for α=10°, 13°, 15°

h/c	$u/U_{o,min}$ α=10°	Recovery x/c=2.07	$u/U_{o,min}$ α=13°	Recovery x/c=2.07	$u/U_{o,min}$ α=15°	Recovery x/c=2.07
0.112	-0.0614	0.6884	-0.217	0.708	-0.241	0.652
0.134	**-0.154**	**0.829**	**-0.238**	**0.775**	-0.252	0.747
0.224	-0.0619	0.7889	-	-	-0.232	0.761
0.313	-0.1	0.83	-	-	**-0.264**	**0.912**

From figure 7.14 $u/U_{o,min}$ for all ground clearances is similar at $u/U_o \approx$-0.25 (refer to Table 7.3), where it is evident that the flow recovery is lowest for α=15° at h/c=0.112 at x/c=2.07, and is significantly biased towards the ground. This bias is clearly demonstrated by the wake distortion towards the ground in figure 7.13. The flow recovery at x/c=2.07 for h/c=0.134 when α=13°-15° in figure 7.11 and 7.14 is reasonably similar. For α=15° in figure 7.14, the lower bound of the wake at x/c=2.07 for y/c<0.4 is consistent for h/c=0.134, 0.224 and 0.313. It is probable that once the flow has achieved stalled under the wing at h/c=0.112, the downstream wake profile is mostly entrained by the moving ground plane. For a very small height increase of Δh/c=0.022 to h/c=0.134 the degree to which the ground presence affects the downstream flow is significantly reduced, highlighting not only the airfoil angle of incidence sensitivity, but the h/c sensitivity at the force reduction ground clearance on the wake structure as well.

Table 7.4 $u/U_{o,min}$ at x/c=1.08 for the Normalized y/c location; $(y/c)^T$

h/c	α=-2°	α=0°	α=2°	α=5°	α=7°	α=10°	α=13°	α=15°
0.112	0.37	0.38	0.41	0.46	-	0.52	0.53	0.56
0.134	0.37	0.39	0.41	0.46	-	0.52	0.53	0.58
0.224	0.37	0.4	0.415	-	0.49	0.49	-	0.55
0.313	0.38	0.4	0.415	-	0.5	0.49	-	0.53

Table 7.4 outlines the overall position of $u/U_{o,min}$ at x/c=1.08, for the range of angle of incidences and ground clearances tested. It highlights the degree at which the ground presence affects the height of the wake from the trailing edge of the airfoil. For h/c beyond the force reduction ground clearance at h/c=0.134, the normalized y/c position $(y/c)^T$ to the h/c=0.313 trailing edge location is similar for α≤10°. For α<10°, once h/c increases towards h/c=0.224-0.313 for the most part the y/c location of $u/U_{o,min}$ is slightly higher.

7.4 Near Wake Turbulence Intensity

$$Tu = \frac{1}{3}\sqrt{\frac{u'^2 + v'^2 + w'^2}{\overline{U}^2 + \overline{V}^2 + \overline{W}^2}} \quad \text{................................... [7.1]}$$

The turbulence intensity (defined by equation 7.1) comprises all three velocity components measured by the LDA, note that although a 2D plane was measured the three velocity components were considered for the turbulence intensity values given. The values of the turbulence intensity in the wake are outlined in figures 7.15-7.20 for h/c=0.112 and h/c=0.313, additional ground clearances of h/c=0.134 and h/c=0.224 can be found in Figure E.13a to E.13n. A summary of of the peak turbulence intensity for all angles of incidence and ground clearances tested is given in table 7.5. The turbulence intensity for α=-2˚ is higher than for α=0˚, and it is possible that the 'nose up' angle of incidence in this case may be generating leading edge separation on the upper surface, resulting in the higher level of wake turbulence intensity. For α=0˚ and 2˚, the maximum turbulence intensity (Tu_{max}) increases with reducing height from h/c=0.313 to 0.134, at which point for h/c=0.112 Tu_{max} reduces. This is a similar trend as with $u/U_{o,min}$ in table 7.2-7.3. The intermediate angles of incidence of α=5˚ & 7˚ do not exhibit as much dependency on h/c as for -2˚≤α≤˚2. When comparing with u/U_o in figure 7.7 the wake profile deficit at these angles do not differ greatly, particularly for α=5˚ h/c=0.112-0.134.

Table 7.5 Tu_{max} at x/c=1.03 α≤7˚, x/c=1.09 α≥10˚. ()- denotes 2nd peak for α≥10˚

h/c	α=-2˚	α=0˚	α=2˚	α=5˚	α=7˚	α=10˚	α=13˚	α=15˚
0.112	1.06%	0.35%	0.25%	0.35%	-	2.18%	1.83%	1.32%
						(1.40%)	(2.00%)	(2.78%)
0.134	2.82%	**0.96%**	**0.52%**	0.35%	-	1.72%	1.84%	1.53%
						(1.26%)	(2.06%)	(3.00%)
0.224	**4.84%**	0.86%	0.40%	-	0.29%	2.11%	-	1.41%
						(1.30%)		(3.14%)
0.313	1.87%	0.65%	0.30%	-	0.30%	1.86%	-	1.97%
						(1.43%)		(4.26%)

The higher angles of airfoil incidence in figures 7.18, 7.19, & 7.20 (i.e. centering on the stall angle) begin to show turbulence intensity profiles with two clear peaks. The upper peak corresponds to the turbulence in the trailing edge generated shear layer in the upper bound of the wake structure, the lower peak relates to the remnants
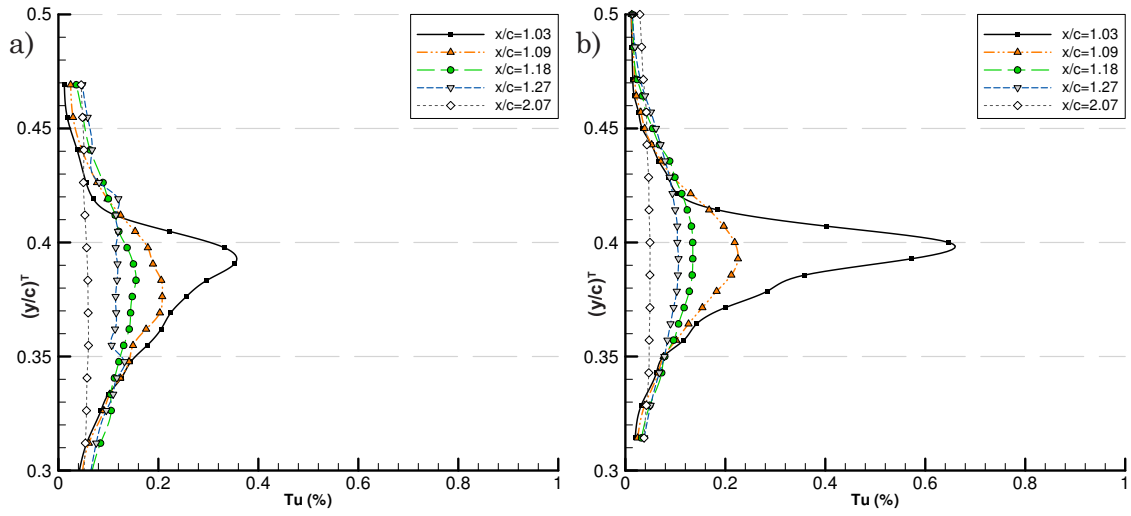
Figure 7.15 Turbulence Intensity α=0° a) h/c=0.112 b) h/c=0.313
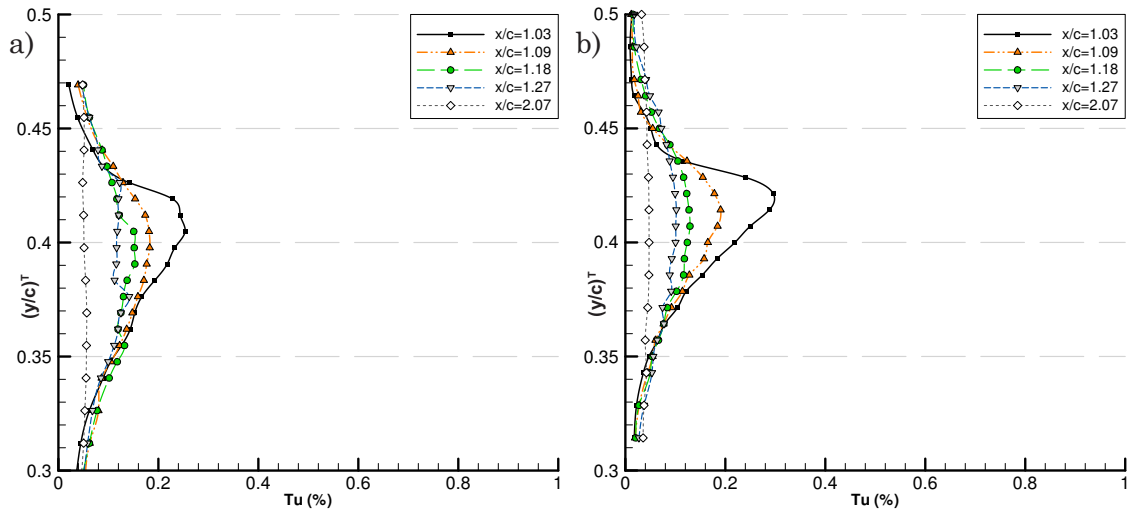
Figure 7.16 Turbulence Intensity α=2° a) h/c=0.112 b) h/c=0.313
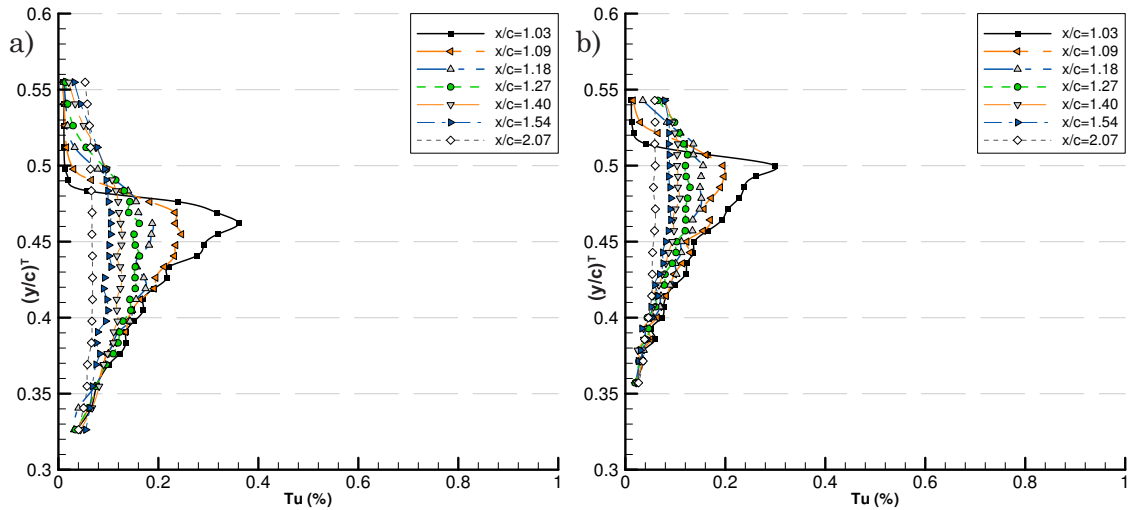
Figure 7.17 Turbulence Intensity a) α=5° h/c=0.112 b) α=7° h/c=0.313

of the separated boundary layer on the suction surface of the wing and the three dimensional turbulence in the wake structure. The structure of this lower peak is constrained by the ground at low h/c and results in a less erratic turbulence intensity distribution.

The change from α=10˚ to 13˚ & 15˚ in figures 7.19 and 7.19 to 7.20 yields two clear peaks with a large deficit in between, the lower peak Tu is referenced in table 7.5 (in brackets). From Table 7.5 and figure 7.18 for α=10˚ it can be seen that as h/c reduces the turbulence intensity from the trailing edge or the lower surface boundary layer breakdown does not greatly differ. However at h/c=0.112, the Tu profile is thinner and there is less definition between the two peaks. There also exists for x/c=1.18 in figure 7.18 a single turbulence intensity peak, which is consistent also for h/c=0.134 & 0.224 (see Appendix E figure E.13i and E.13j). In figure 7.19 for α=13˚ at h/c=0.112, the lower Tu peak increases and and extends to x/c=1.4 when compared to α=10˚ in figure 7.18. This suggests that for the lower ground clearance the suction surface separation has amplified and the increase in the size and intensity of the turbulence intensity profile indicates airfoil stall at α=13˚, h/c=0.112.

For α=15˚ the trailing edge and lower surface separation zones tend to a reduction in Tu as h/c is reduced. However the lower surface separation zone is still substantially greater than for α=10˚ & 13˚, approximately twice that of the wake peak Tu_{max} for α=10˚. The trailing edge Tu strength is also reduced; potentially as a result of the higher flow rate in the venturi section between the airfoil and ground outweighing the component of the flow over the top surface of the wing. Additionally the trailing edge is further from the upper test section wall effects.

It is important to note that the peak value of turbulence intensity increases in the wake as x/c increases downstream to x/c=2.07 for increased angle of incidence, as this accounts for all three u', v' and w' fluctuations in the flow velocity. The peak Tu 'spike' in figures 7.18, 7.19 and 7.20 shows an increase in both turbulence intensity and downstream position for an increase in angle of incidence (x/c=1.18 for α=10˚, x/c=1.4 for α=13˚ and 15˚) and h/c. The low velocity in the separation zone and the additional u', v' and w' velocity fluctuations yield higher turbulence intensity at these downstream positions.
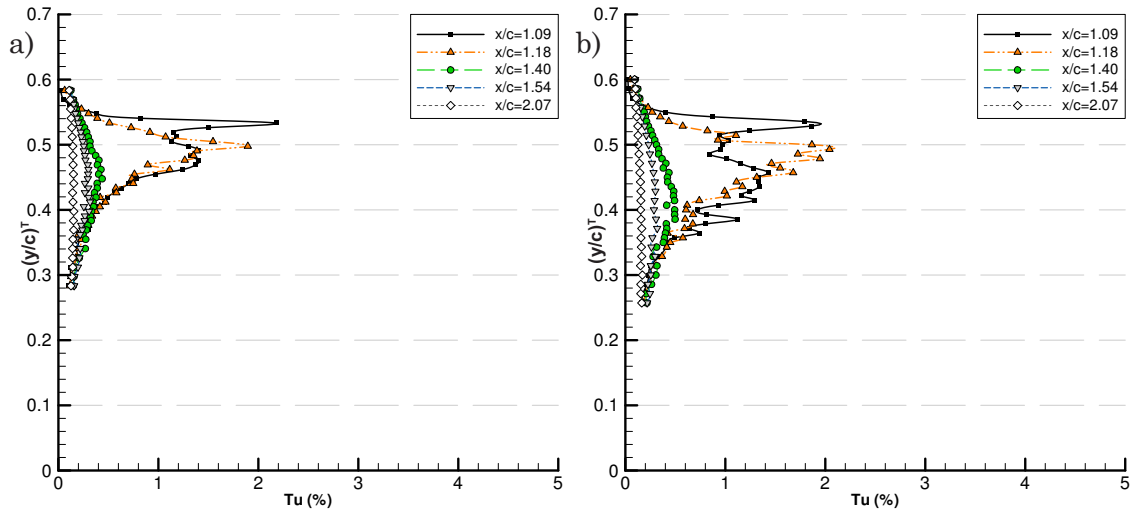
Figure 7.18 Turbulence Intensity α=10° a) h/c=0.112 b) h/c=0.313
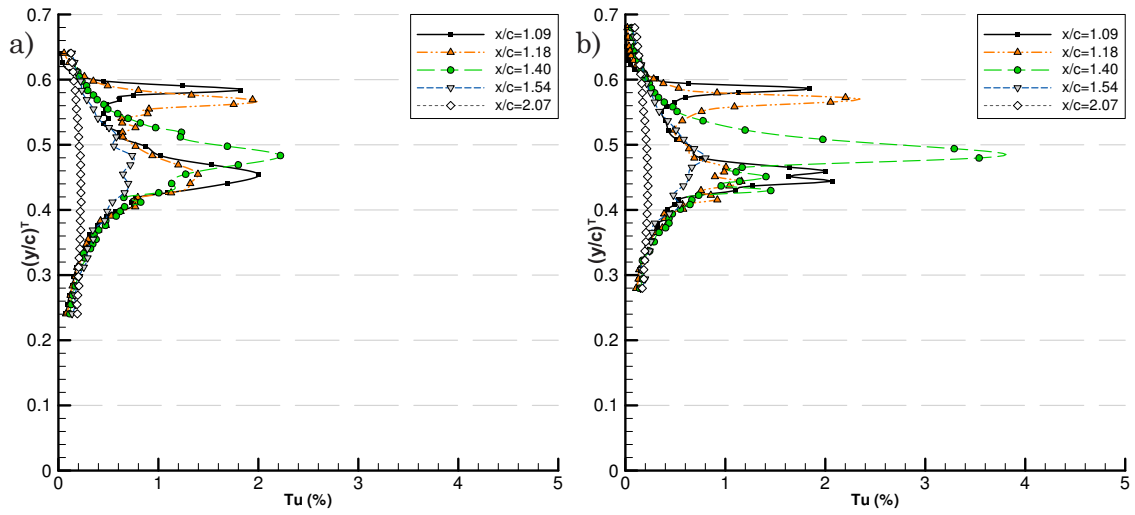
Figure 7.19 Turbulence Intensity α=13° a) h/c=0.112 b) h/c=0.134
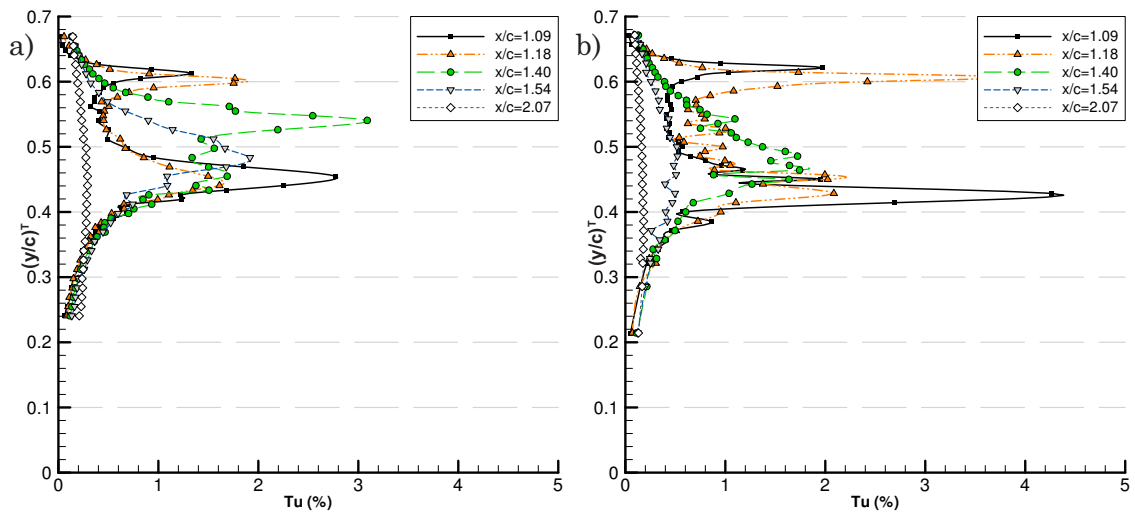
Figure 7.20 Turbulence Intensity α=15° a) h/c=0.112 b) h/c=0.313

7.5 Near Wake Turbulent Normal Stress (*uu*)
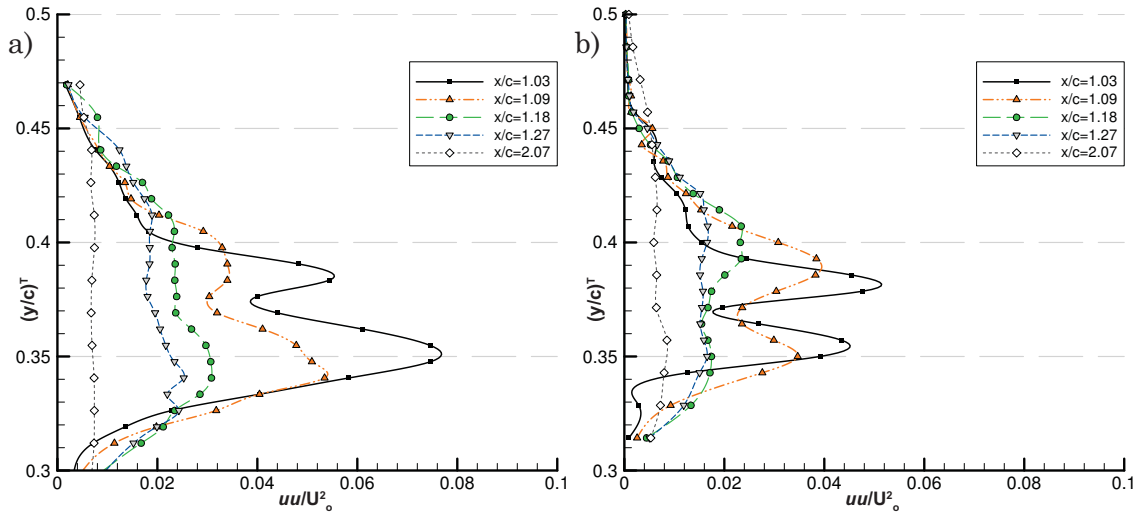
Figure 7.21 Turbulent normal stress α=-2° a) h/c=0.112 b) h/c=0.313

Investigation of the turbulent normal stress (*uu*) in the wake figures 7.21-7.27 and Figures E.14a-l, shows two peaks for all α & h/c tested. The two peaks correspond to the separated shear layer from the trailing edge and the airfoil's suction (lower) surface separated boundary layer; this was also noted by Zhang & Zerihan (2003). However their study only focused on one setting of α=3.45° and did they not investigate higher angles of incidence or stall angle. As α≥5°-7° it can be seen in figure 7.24 that the lower peak of the uu/U^2_o distribution becomes more dispersed. Thus as α increases, the lower wake peak uu/U^2_o distribution is more dispersed ($\Delta(y/c)^T$=0.14 from $\Delta(y/c)^T$=0.1 in figure 7.23) as flow separation becomes dominant towards the stalling angle. Table 7.6 summarizes the peaks of uu/U^2_o for the trailing edge and in the wake (denoted in brackets). For a consistent h/c, as α increases from -2° to 7°, the trailing edge uu/U^2_o intensity decreases whereas the wake has a local maximum peak at α=0°. For α≤7°, the peak wake *uu* value is highest at h/c=0.134, noted as the force

Table 7.6 Turbulent normal stress peak values

h/c	α=-2°	α=0°	α=2°	α=5°	α=7°	α=10°	α=13°	α=15°
0.112	0.055 (0.075)	0.037 (0.078)	0.035 (0.061)	0.011 (0.045)	- -	0.105 (0.111)	0.127 (0.116)	0.126 (0.117)
0.134	0.063 (0.064)	0.048 (0.099)	0.041 (0.078)	0.016 (0.052)	- -	0.103 (0.124)	0.122 (0.102)	0.123 (0.110)
0.224	0.061 (0.062)	0.061 (0.090)	0.030 (0.072)	-	0.027 (0.038)	0.119 (0.177)	-	0.124 (0.110)
0.313	0.048 (0.043)	0.047 (0.079)	0.026 (0.062)	-	0.025 (0.031)	0.113 (0.189)	-	0.119 (0.20)
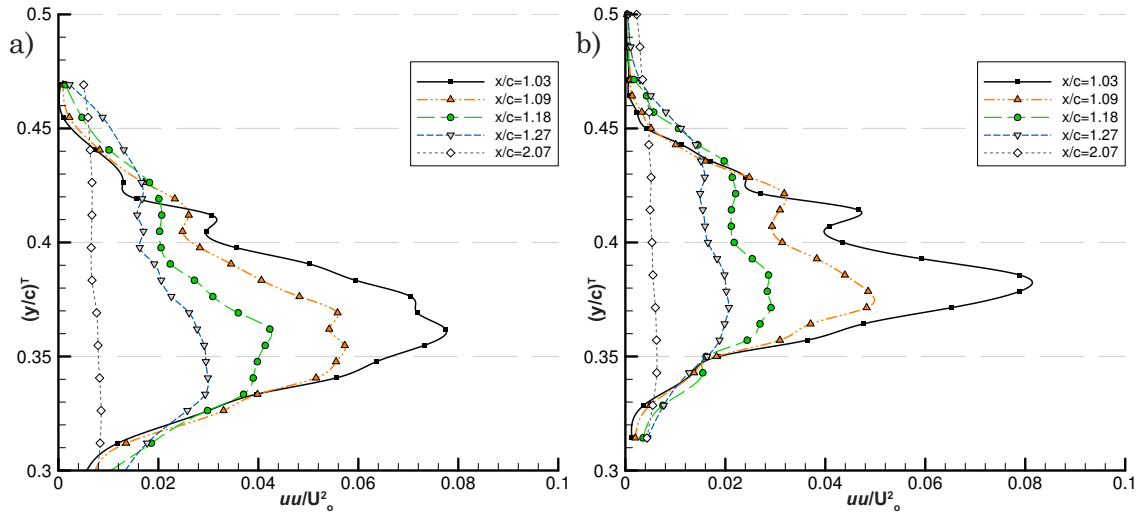
Figure 7.22 Turbulent normal stress α=0° a) h/c=0.112 b) h/c=0.313
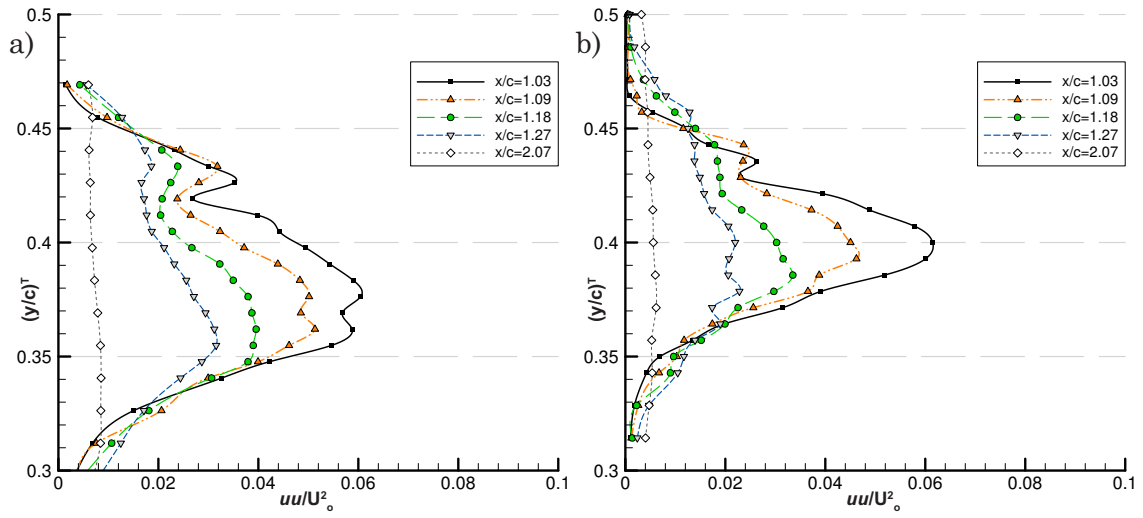
Figure 7.23 Turbulent normal stress α=2° a) h/c=0.112 b) h/c=0.313
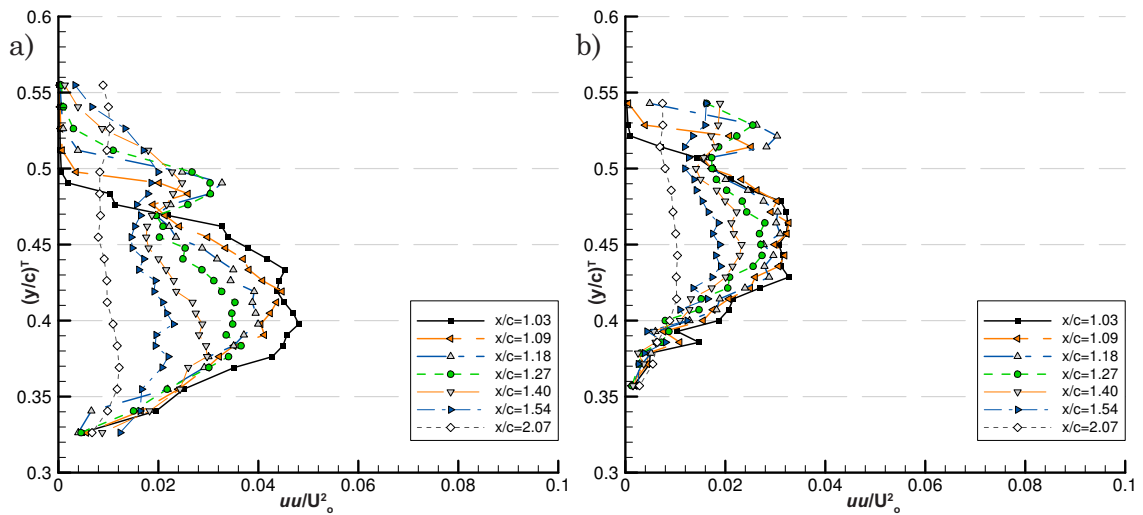
Figure 7.24 Turbulent normal stress a) α=5° h/c=0.112 b) α=7° h/c=0.313
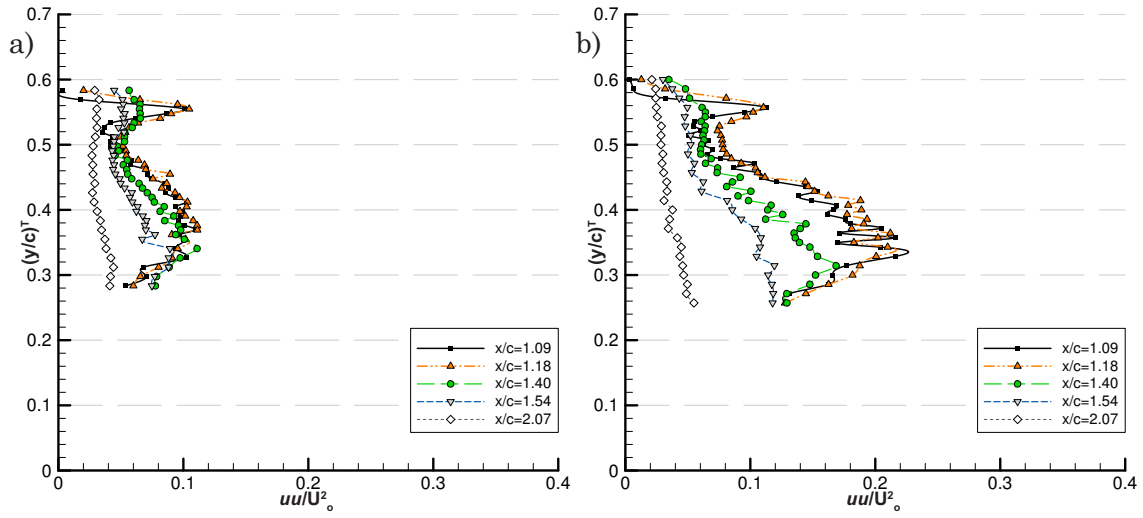
Figure 7.25 Turbulent normal stress α=10˚ a) h/c=0.112 b) h/c=0.313
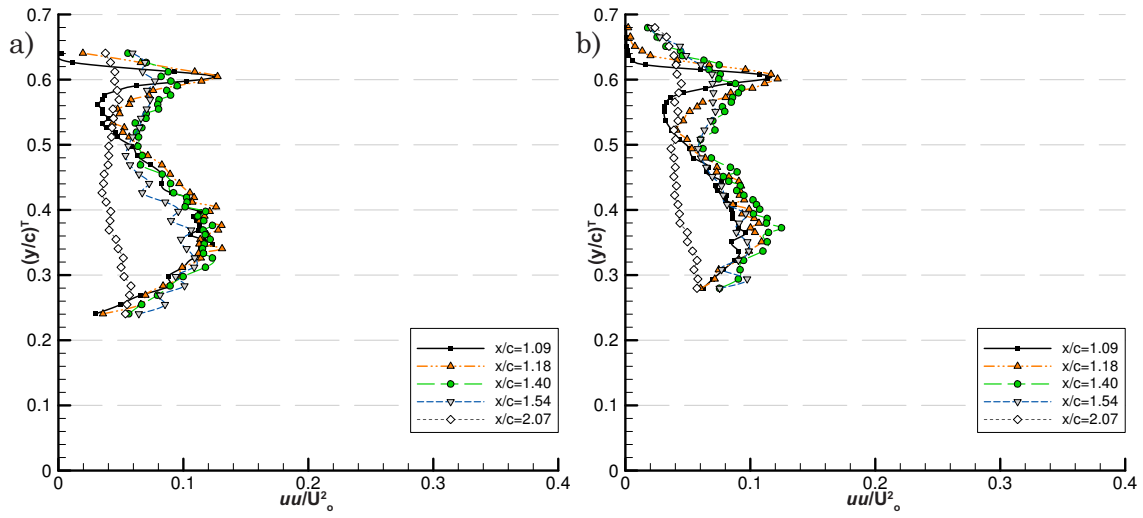
Figure 7.26 Turbulent normal stress α=13˚ a) h/c=0.112 b) h/c=0.134
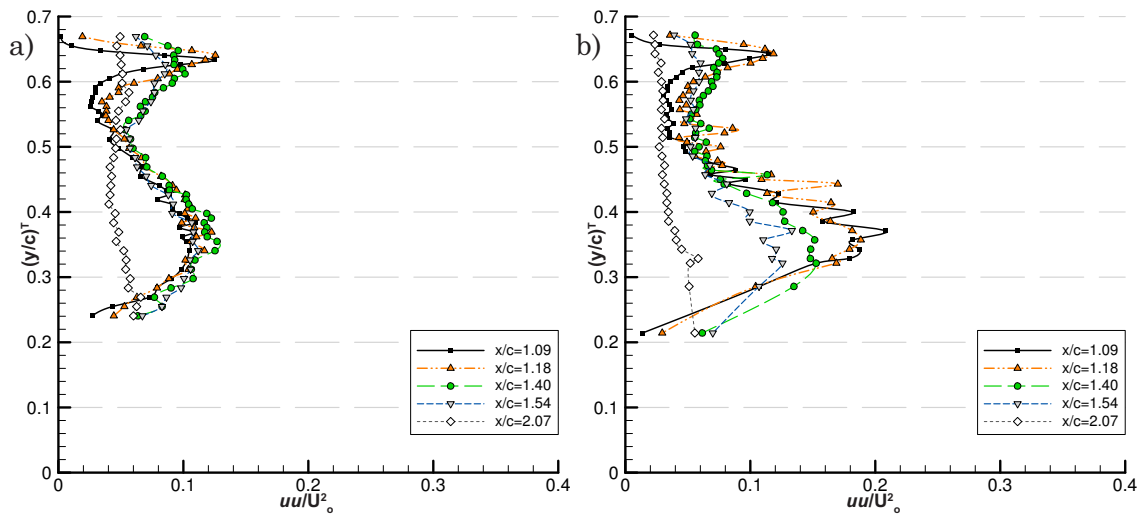
Figure 7.27 Turbulent normal stress α=15˚ a) h/c=0.112 b) h/c=0.313

reduction ground clearance in Zerihan (2001). For a consistent ground clearance (h/c), there is a large uu/U^2_o increase from α=5˚& 7˚ to 10˚. For an increase in h/c, given α=10˚, the lower wake uu/U^2_o peak consistently increases.

7.6 Near Wake Primary Shear Stress (*uv*)
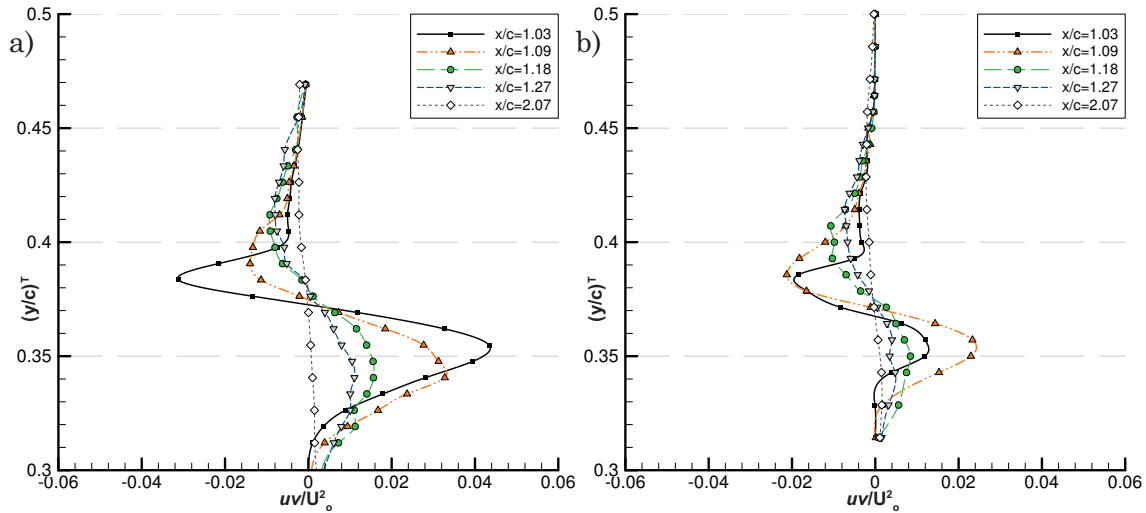
Figure 7.28 Primary shear stress α=-2˚ a) h/c=0.112 b) h/c=0.313

Investigation of the primary shear stress (*uv*) in the wake of figures 7.28-7.34, shows two peaks as for the turbulent shear stress (*uu*) for the α & h/c tested. A negative peak corresponds to the separated shear layer from the trailing edge and a positive peak corresponding to the lower surface boundary layer separation and airfoil wake, again noted by Zhang & Zerihan (2001) for one angle set at α=3.45˚. For a given h/c, as the angle increases from α=-2˚ to α=5˚ & 7˚ (in figure 7.31a and 7.31b) the wake uv/U^2_o peak value reduces, however the distribustion is greater, $\Delta(y/c)^T=0.15$, than the more localized peaks of -2˚≤α≤2˚; where $\Delta(y/c)^T=0.05$ in figure 7.29. As α≥10˚ in figures 7.32, 7.33 & 7.34, the positive component of uv/U^2_o in the wake increases and as the strength of flow separation in the boundary layer increases. Table 7.7

Table 7.7 Primary shear stress peak values

h/c	α=-2˚	α=0˚	α=2˚	α=5˚	α=7˚	α=10˚	α=13˚	α=15˚
0.112	-0.031	-0.011	-0.013	-0.013	-	-0.042	-0.050	-0.049
	+0.043	+0.030	+0.023	+0.016	-	+0.033	+0.038	+0.036
0.134	-0.036	-0.021	-0.016	-0.012	-	-0.047	-0.053	-0.057
	+0.033	+0.038	+0.031	+0.017	-	+0.036	+0.039	+0.039
0.224	-0.019	-0.026	-0.015	-	-0.016	-0.049	-	-0.059
	+0.028	+0.042	+0.030	-	+0.015	+0.047	-	+0.060
0.313	-0.021	-0.014	-0.011	-	-0.013	-0.051	-	-0.048
	+0.023	+0.039	+0.027	-	+0.013	+0.052	-	+0.056
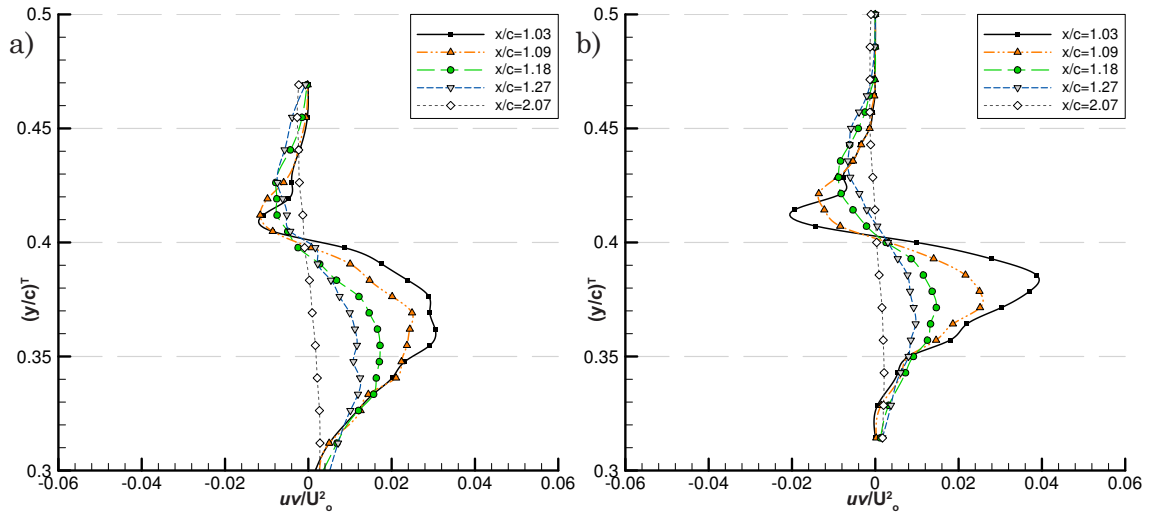
Figure 7.29 Primary shear stress α=0˚ a) h/c=0.112 b) h/c=0.313
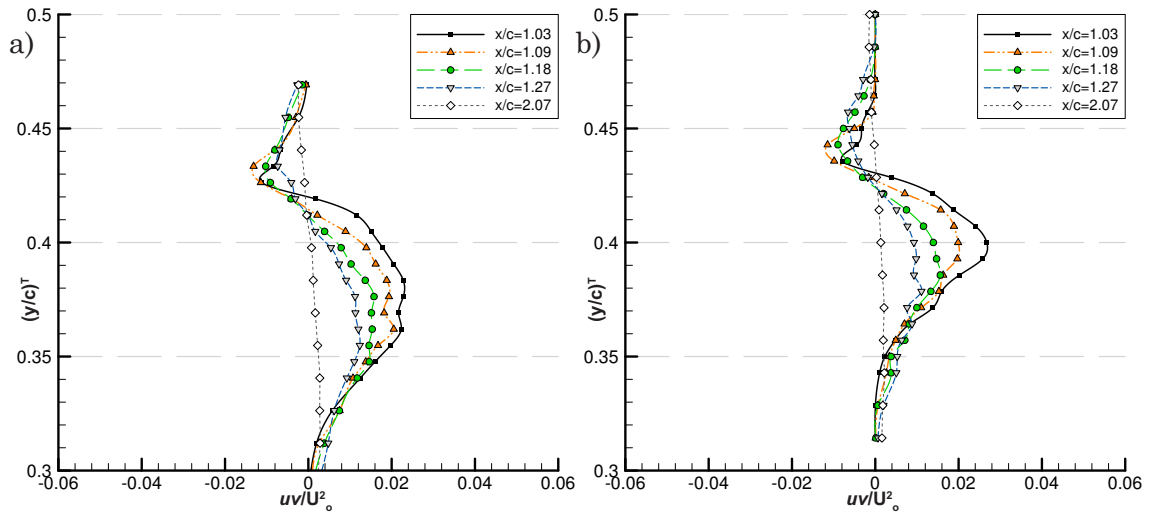
Figure 7.30 Primary shear stress α=2˚ a) h/c=0.112 b) h/c=0.313
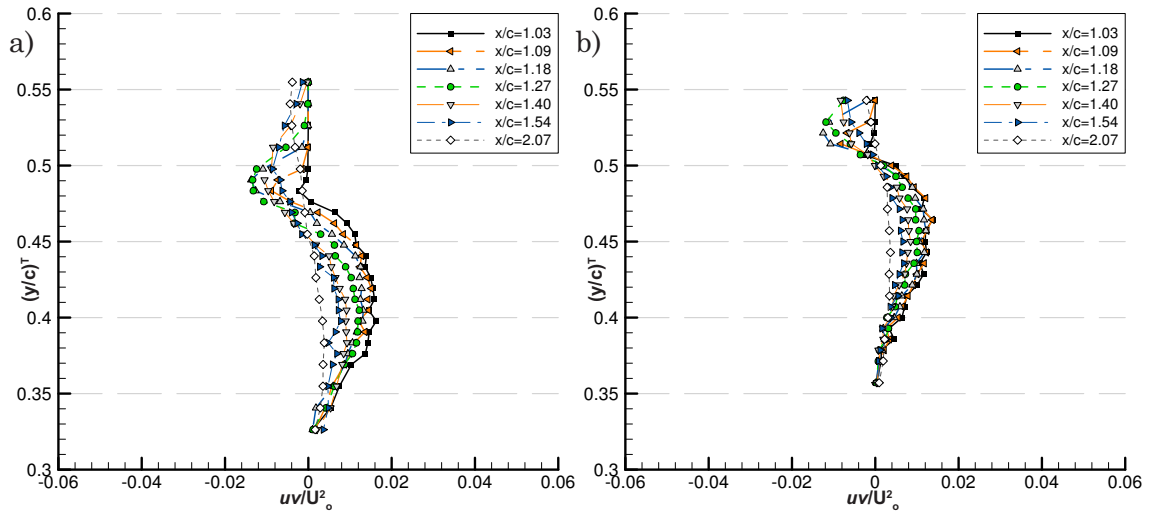
Figure 7.31 Primary shear stress a) α=5˚ h/c=0.112 b) α=7˚ h/c=0.313
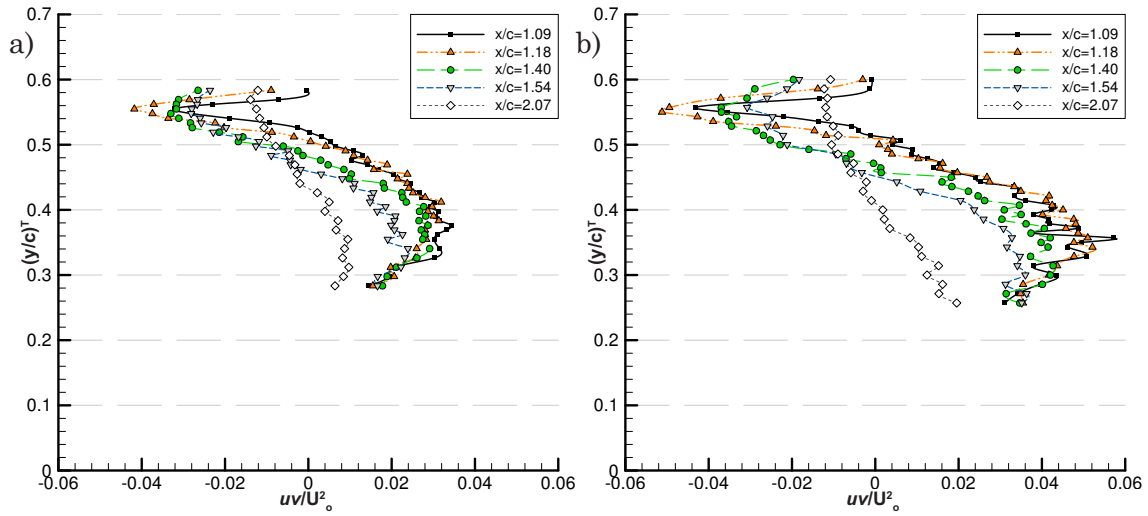
Figure 7.32 Primary shear stress α=10° a) h/c=0.112 b) h/c=0.313
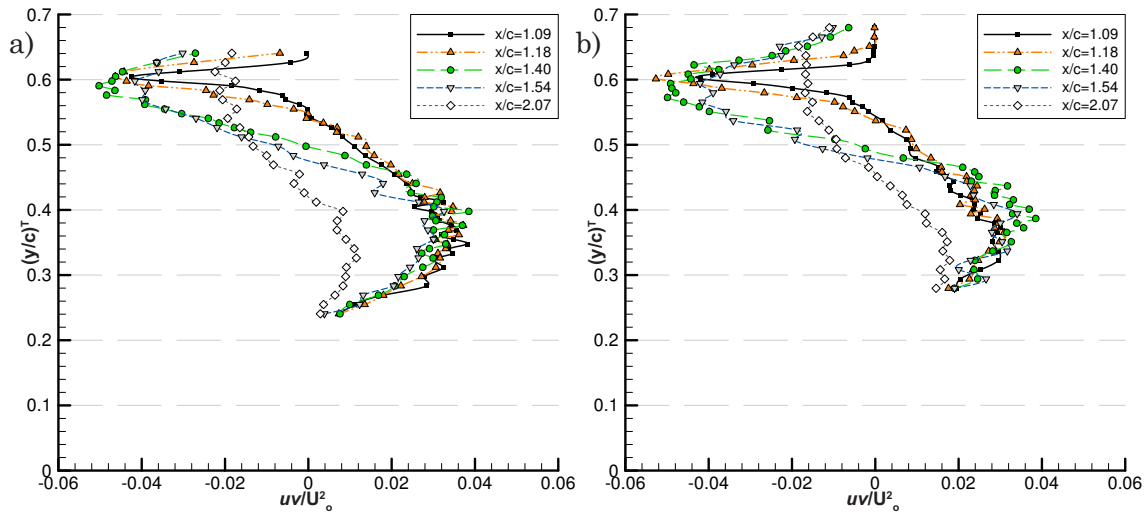
Figure 7.33 Primary shear stress α=13° a) h/c=0.112 b) h/c=0.134
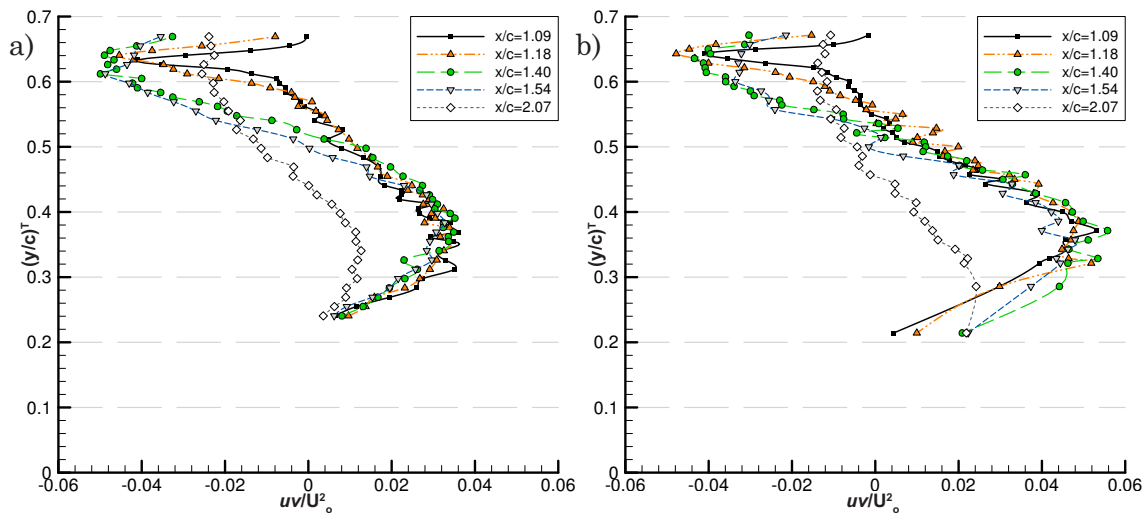
Figure 7.34 Primary shear stress α=15° a) h/c=0.112 b) h/c=0.313

summarizes the peak values of uv/U^2_o, it indicates the trailing edge strength of uv/U^2_o reduces for an increase in α where -2°≤α≤7°, after this it increases towards α=15°. The wake uv/U^2_o increases between α=5°&7° and α=10°, where after uv/U^2_o stabilizes. Both wake and trailing edge uv/U^2_o increase with increasing h/c to 0.313 (for α=10°-15°, the stall angle range), for α≤7° this maximum appears to be h/c≈0.134.

7.7 Discussion

Results by Zerihan (2001) show the lift curve slope for Re_{chord}=4.4x10⁵ at α=10°, h/c=0.313 is just beyond stall angle, and h/c=0.112 is at the onset of stall (delayed to α≈13° at h/c=0.112). Whilst no LDA or PIV data was recorded for angles approaching stall in the wake in Zerihan's study, the measured wake properties of the flow in the present study seem to confirm a similar phenomenon with the wake flow structure (see figure 7.4-7.14 and E.1-E.13). This being that for α=10° at low ground clearances stall angle is delayed, resulting in a thinner wake with less reversed flow (see figures 7.8, 7.9 and 7.10) as opposed to the large flow separation (of a stalled wake on airfoil) in figures 7.12, 7.13, 7.14, E.1, E.4, E.7 and E10.
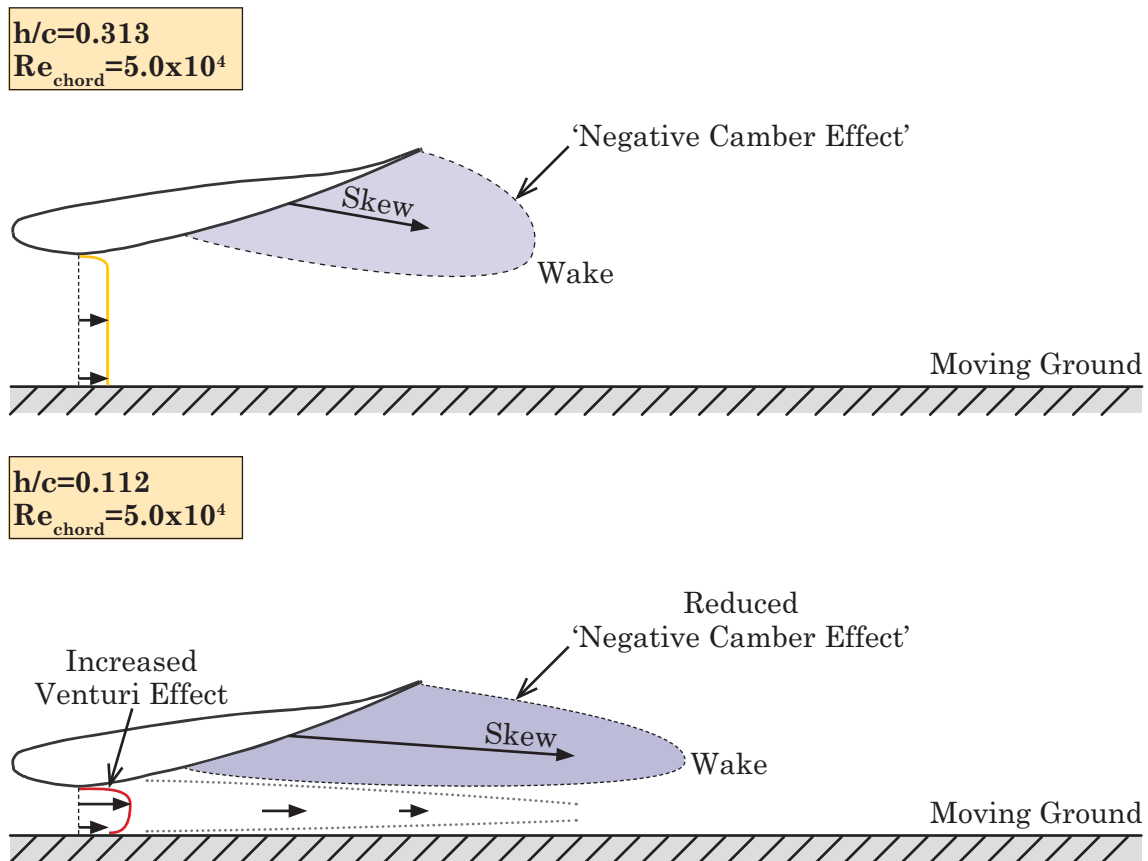
Figure 7.35 Ground influence on wake and Venturi effect with reducing h/c at Re_{chord}=5.0x10⁴

The wake structure, as shown in figure 7.4 to 7.14, indicates that the venturi effect formed by the flow between the airfoil and ground increases as h/c reduces, outlined in figure 7.35. This is a direct result of the gap between the wing and the ground reducing and accelerating the flow to a higher degree than for a larger h/c. The effect this has on the wake structure and the height from the ground for the u/U_o profile at x/c=1.03 & 2.07 is seen in figures 7.6, 7.7, 7.10, 7.11 & 7.14 and in table 7.4, which outlines the upper boundary of the wake height from the ground plane. For α=-2° to 15° there is a consistent downward pull of the wake towards the ground. This is particularly clear at x/c=2.07 for h/c=0.112 for most angles of incidence, as the u/U_o profile is lower towards the ground (y/c=0) than for h/c=0.313.

The increased ground presence at lower h/c clearly influences the pull of the wake towards the ground. At α=10° the lower part of the wake profile (i.e. u/U_o value for y/c<0.5) at h/c=0.313 is lower than h/c=0.112 (figures 7.8, 7.9 & 7.10); a similar phenomenon exists for α=15° in figures 7.12 to 7.14. Figure 7.9 shows the wake thickness remaining constant x/c≈1.2 for h/c=0.112 before starting to thicken (increase), whereas in figure 7.8 the wake thickness starts increasing from x/c=1.03 for h/c=0.313. Table 7.4 indicates that increasing ground clearance from h/c=0.134-0.313 for α≥10°, the y/c position of $u/U_{o,,min}$ lowers. The accelerated flow between the airfoil and ground, forming a venturi section style nozzle, is producing a concentrated region of higher velocity and increased flow rate (for a lower h/c between the wake and ground) which also propagates downstream of the wing. At the higher ground clearance the extent to which the wake structure is pulled (or angled) towards the ground is greater, as the flow velocity beneath the wake is lower, thus less 'constrained' by the region of higher flow velocity beneath the wing at lower h/c; forming a kind of buffer zone. The flow between the wing and ground at lower h/c gives rise to the 'negative camber effect' (downwash opposed to upwash) as outlined in figure 7.35, refer to additional figures E.1-E.12. The 'negative camber effect' is where the wake direction and flow from the wing is less (or opposed) to the camber effect of the flow from the airfoil as it would be out of ground effect. Therefore as the ground clearance reduces, the increased venturi effect flattens out and elongates the wake structure.

For the range of angle of incidence from -2°≤α≤7° the wake profile does not exhibit extensive flow recirculation indicative of larger values of α. The low angle combined

with little flow separation on the suction surface results in a single peak for Tu, which gets larger, moves closer to the ground and increases in magnitude as h/c reduces. The two *uu* peaks, are generated as a result of the trailing edge separation and the breakdown of the boundary layer of the suction surface of the airfoil, which reduces in size and magnitude as h/c reduces, see figure 7.36. Two peaks for *uv* exist where as the upper peak (trailing edge) is negative and the lower (suction surface boundary layer) is positive, see figure 7.36. As the angle of incidence increases to α=10°, two Tu peaks form in the wake corresponding to the flow from the trailing edge and the lower surface boundary layer separation, which forms a single peak downstream at x/c=1.4. As α increases the strength of the lower surface Tu peak also increases.

The trend for *uu*, *uv* and Tu given a set angle of incidence and then varying the ground clearance is outlined in table 7.8 and additionally in Figures E.16, E.17 and E.18. The trends for these wake properties can be split into two groups; the low to mid range angles of incidence (-2°≤α≤7°) and the high range angels of incidence (10°≤α≤15°), as there is a significant increase in the magnitudes of *uu*, *uv* and Tu between α=5° & 7° to α=10° followed by the increases of *uu*, *uv* and Tu for α≥10°.
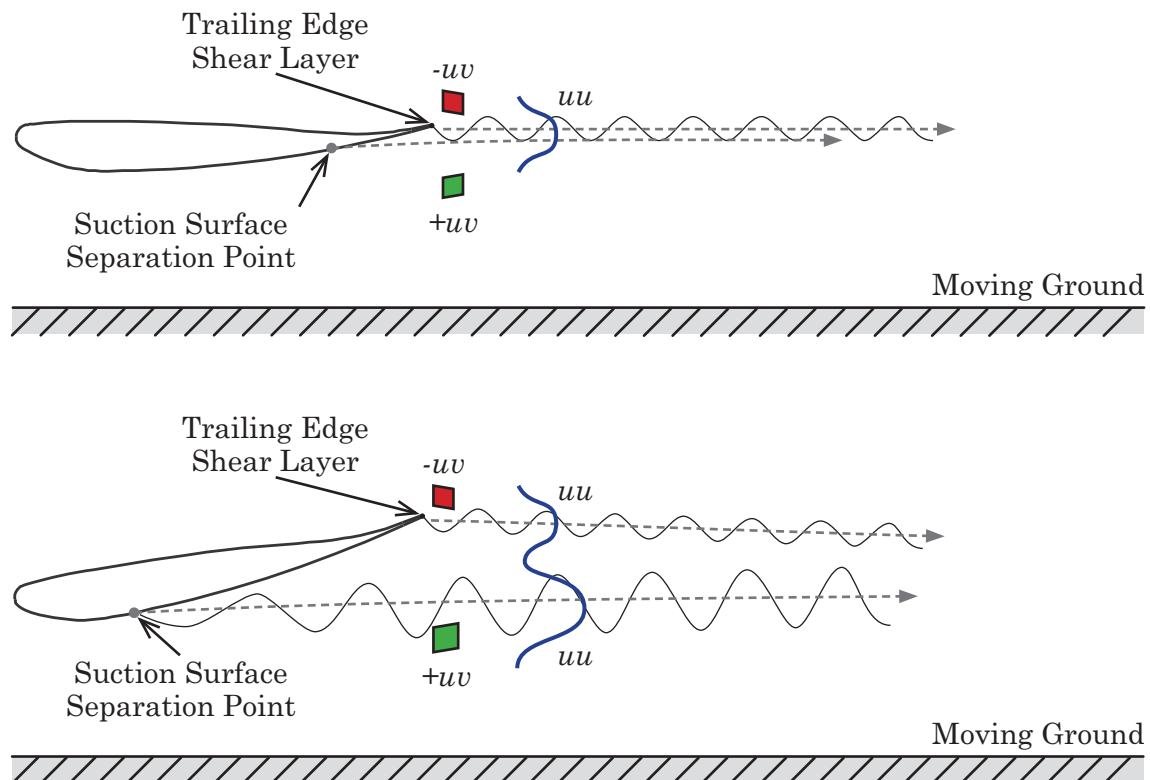
Figure 7.36 Airfoil wake Turbulence and Reynolds stress with increasing α

These trends follow the increased 'negative camber effect' the wake experiences with u/U_o as h/c increases for $\alpha \geq 10°$, as the stresses and turbulence all increase. For h/c=0.112 the trend for *uu*, *uv* and Tu does not hold, as they are generally the lowest magnitudes, with a large increase for a set angle of incidence to h/c=0.134. The discontinuity between h/c=0.112-0.134 in the wake survey of *uu*, *uv* and Tu follows with the force reduction phenomenon outlined in Zerihan (2001); whereby C_L dropped for h/c<0.134. The constraint the ground places on the wake at higher angles of incidence reduces with an increase in h/c due to a weaker venturi effect. Thus it follows that the physical constraint the ground has in 'flattening out' and elongating the wake at lower ground clearances results in the fluctuations in the wake also decreasing (Kim & Geropp 1998), and shows that the ground also has a dampening effect on the turbulence and Reynolds stresses. This contributes to the wake propogating further downstream due to less instability of the flow.

Table 7.8 Summary of Tu, *uu* and *uv* of Tyrrell026 ground effect wake:
varying h/c from 0.134 to 0.313 (for constant α)

Set angle of incidence	*uu*	*uv*	Tu
-2°≤α≤7° (h/c>0.134)	reduces	reduces h/c=0.224-0.313	reduces
10°≤α≤15° (h/c>0.134)	increases	increases	increases

The base-line 'clean' wing wake characteristics have been investigated relating to the parameters of; normalized streamwise velocity, turbulence intensity, primary turbulent stress and normal shear stress. It is clear that the ground clearance and angle of incidence affect the structure, size, skew, fluctuations and stresses of the wake. Given the large scale flow separation on the wing at high angles of incidence, using dimple arrays that generate vortices may reduce flow separation as in the rearward ramp study in chapter 6. Thus a full comparison of the possible implications that dimple arrays have on the wake characteristics: u/U_o, *uu*, *uv* and Tu to determine how they are affected or potentially reduced is needed.

Dimpled Airfoil Wake Investigation

8

Given the 'clean' Tyrrell026 airfoil measurements outlined in chapter 7, this section shows the difference that a dimple array has on the wake parameters of the streamwise velocity, the turbulence intensity and the two main Reynolds stress components: uu/U^2_o and uv/U^2_o. The results concern the 1.5-3-23 dimple array, the performance of other dimple arrays is outlined in chapter 9. Additionally the effect of tripping the boundary layer with a tripwire on the 'clean' airfoil in the same location as the dimple array is investigated, as is the wingtip vortex with an attached endplate.

8.1 Introduction

Changes to the wake as a result of the dimpled surface modification are now presented. The data concerns the 1.5-3-23 dimple array which yielded the most significant alterations to the wake parameters: u/U_o, uu/U^2_o, uv/U^2_o and the turbulence intensity. Measurements taken by the LDA on the dimpled wing (shown in figure 8.1) were in the same manner as chapter 7; with the same Reynolds number. The dimpled surface modification is machined into the suction side of the airfoil only (i.e closest to the ground). The suction surface of the Tyrrell026 airfoil experiences boundary layer separation and large scale flow separation (Zerihan 2001), thus is analogous to the simplified rearward facing ramp of chapter 6. Given different wing angles

Figure 8.1 LDA Measurements in the Wake of a Dimpled Airfoil

of incidence and ground clearances, the behaviour of flow separation strength and cruciall, the flow separation point migration becomes an issue and impacts on the effective placement of any form of vortex generating device. As shown in chapter 5, the dimple's sub-boundary layer influence on the flow, whilst not insignificant, requires exact placement if the vorticity produced from the dimple is to be sufficient to supress flow separation and/or shift the flow separation point on the airfoil towards the trailing edge.

Table 8.1 Dimple Array Configurations on Tyrrell026 Airfoil

Spacing 'D'	**1.5**	1.5	1.5	1.5	2	2	2	2.5	2.5	2.5
No. of Rows	**3**	5	5	5	5	5	5	3	5	5
position 'x/c'	**0.23**	0.53	0.675	0.8	0.53	0.675	0.8	0.53	0.675	0.8

$$\text{Spacing } \textbf{'D'} \quad \text{No. of Rows} \quad \text{Position } \textbf{'x/c'}$$

$$1.5\text{-}3\text{-}23 \quad \text{..} \quad [8.1]$$
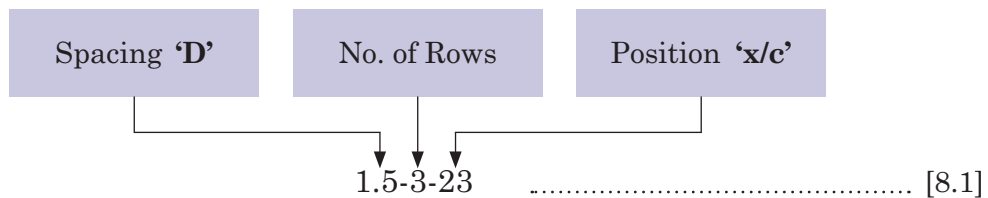
Dimple array size, spacing and location in chapter 6 for the simplified rear ward facing ramp, showed the dimple array configuration placement is crucial if flow separation is to be reduced. Given the effect of a migrating flow separation point on an airfoil changes with the angle of incidence ($\alpha°$) and ground clearance (h/c), several chordwise dimple array positions on the wing and dimple array spacing will be investigated. This will determine how efficient each is by consideration of; where the most effective position on the airfoil is, what spacing provides consistent reduction of the various wake parameters and whether the dimple array can actually cause the wake to adversely increase. Table 8.1 outlines the dimple array configurations used. Some 3 row arrays are used due to physical constraints of placing the array on the wing, as 4th and 5th rows would wrap around the leading edge onto the upper surface. Equation 8.1 explains the notation used to describe the dimpled wing array series taking into account the dimple array configuration of the first column in table 8.1 as the array investigated here. Experimental models are shown in figures F.1-F.10.

The dimpled wing array configuration 'series' comprises the information relating to the dimple spacing in the array in terms of the distance each dimple is spaced in relation to its diameter 'D', the number of rows the array has, and the chordwise
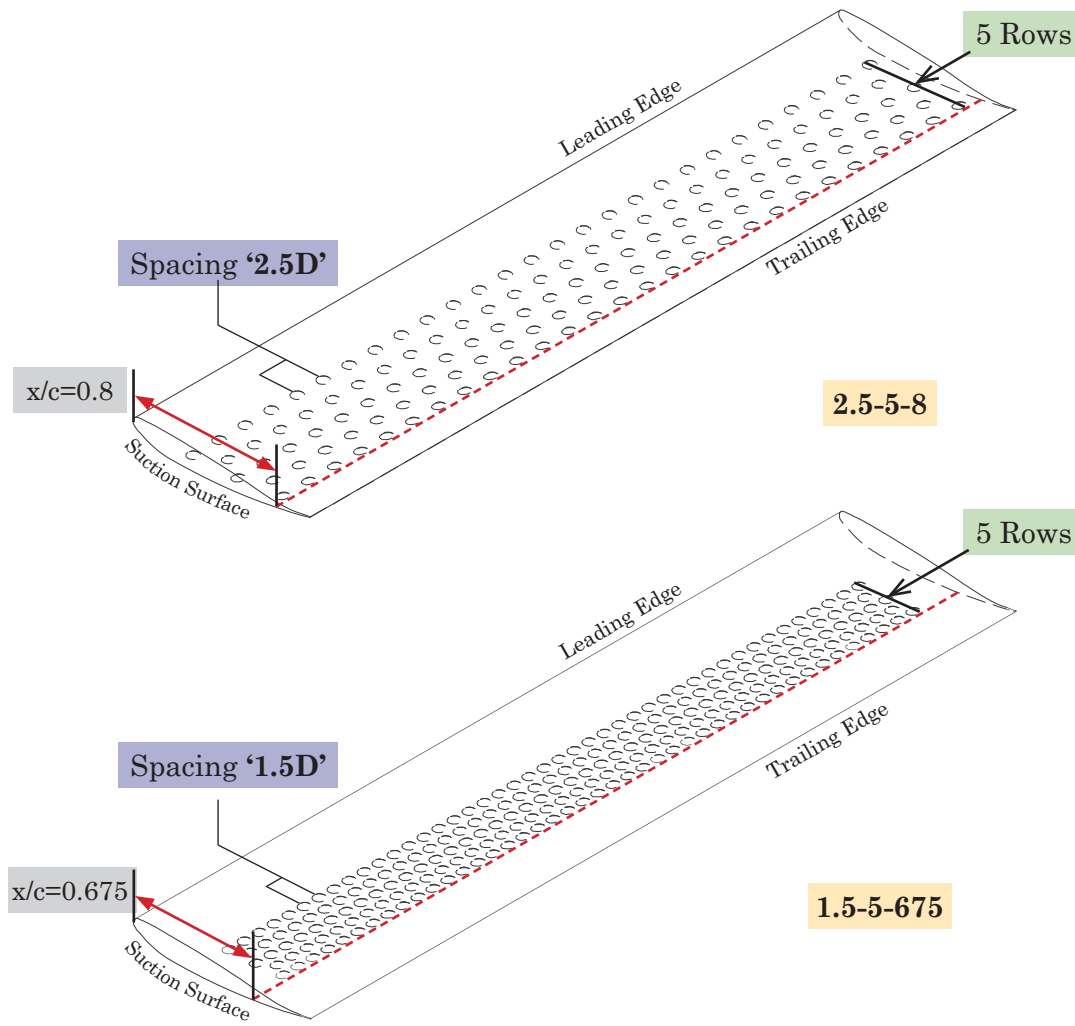
Figure 8.2 Dimple Array Positioning on Wing

position of the array on the wing by x/c. The positioning is determined from the dimple rim radius of the last dimple row in the array (i.e. the array is positioned forward of this point), see figure 8.2.

The wake parameters being investigated are the normalized: streamwise flow (u/U_o), turbulent normal stress (uu/U_o^2), primary shear stress (uv/U_o^2) and the turbulence intensity (as in chapter 7). The influence the dimple array has on the flow is compared to the base-line 'clean' wing such that the dimple array should alleviate the flow separation, reduce Reynold's stresses in the wake and and result in lower turbulence intensity, as seen in the dimple array results in chapter 6. This should result in a higher normalized flow velocity profile and a lower turbulent normal stress, primary shear stress and turbulence intensity profile. All points are taken with the same LDA grid used in the 'clean' wing experiments of chapter 7 for more direct comparison and to minimize spatial error.

8.2 Dimpled Airfoil Wake Normalized Streamwise Flow

Figures 8.3 to 8.13 indicate the normalized streamwise velocity component of the flow in the presence of the 1.5-3-23 series dimpled wing. The **normalized wake** profiles indicate the dimpled wing (in black) for the positions x/c=1.08 and x/c=2.07, which are compared to the clean wing flow (grey). This direct comparison is clear in establishing an improvement in the wake by the reduction in its size, reduced velocity gradients, increasing u/U_o (by moving the profile closer to the right i.e. towards u/U_o=1) and to what degree the minimum streamwise velocity is increased as a result of the dimpled array surface.

The normalized streamwise velocity component is shown for α=-2° for h/c=0.313 (figure 8.3a) and h/c=0.112 (figure 8.3b). For the 3 row dimple array with 1.5D spacing at x/c=0.23c it can be seen that the higher ground clearance of h/c=0.313 yields a significant improvement in $u/U_{o,min}$, for the clean wing at x/c=1.03 $u/U_{o,min}$≈-0.05 and increases to $u/U_{o,min}$=0.3 for the 1.5-3-23 series dimpled wing. In figure 8.3b, there is a marginal performance disadvantage between the dimpled or the clean wing. However for α=-2° at h/c=0.134 and h/c=0.224 in figure F.11-F.12 a consistent increase in the improvement of the $u/U_{o,min}$ with the dimpled wing over the clean wing is exhibited as h/c increases.

Increasing the dimpled wing angle of incidence to α=0° in figure 8.4 exhibits a similar trend as the α=-2° case, where the u/U_o profile increases as h/c increases. In figure 8.4a at h/c=0.313 there is an improvement from clean $u/U_{o,min}$=0.2 to $u/U_{o,min}$=0.4 for the dimpled wing. The flow profile in figure 8.4a of u/U_o for α=0° at h/c=0.313, is generally higher than the clean wing u/U_o profile for more of the wake profile, than for α=-2° at h/c=0.313 in figure 8.3a. This is indicated by the 'cross over' points where the u/U_o profile of the clean wing and the dimpled wing are equal, y/c≈0.34-0.38 at h/c=0.313 (figure 8.3a) and y/c=0.35-0.42 at h/c=0.112 (figure 8.4a). For α=2° at h/c=0.313 in figure 8.5 the advantage due to the presence of the dimples is less, but for h/c=0.134 and h/c=0.224 in figure F.16-F.17 the improvement is greater. However for y/c>0.42, the dimple presence at h/c=0.112 ground clearance showed to be marginal to detrimental to the wake flow profile for y/c<0.32 in figure 8.5. At y/c=0.4-0.33 the dimpled wing u/U_o is higher than the clean wing u/U_o profile.
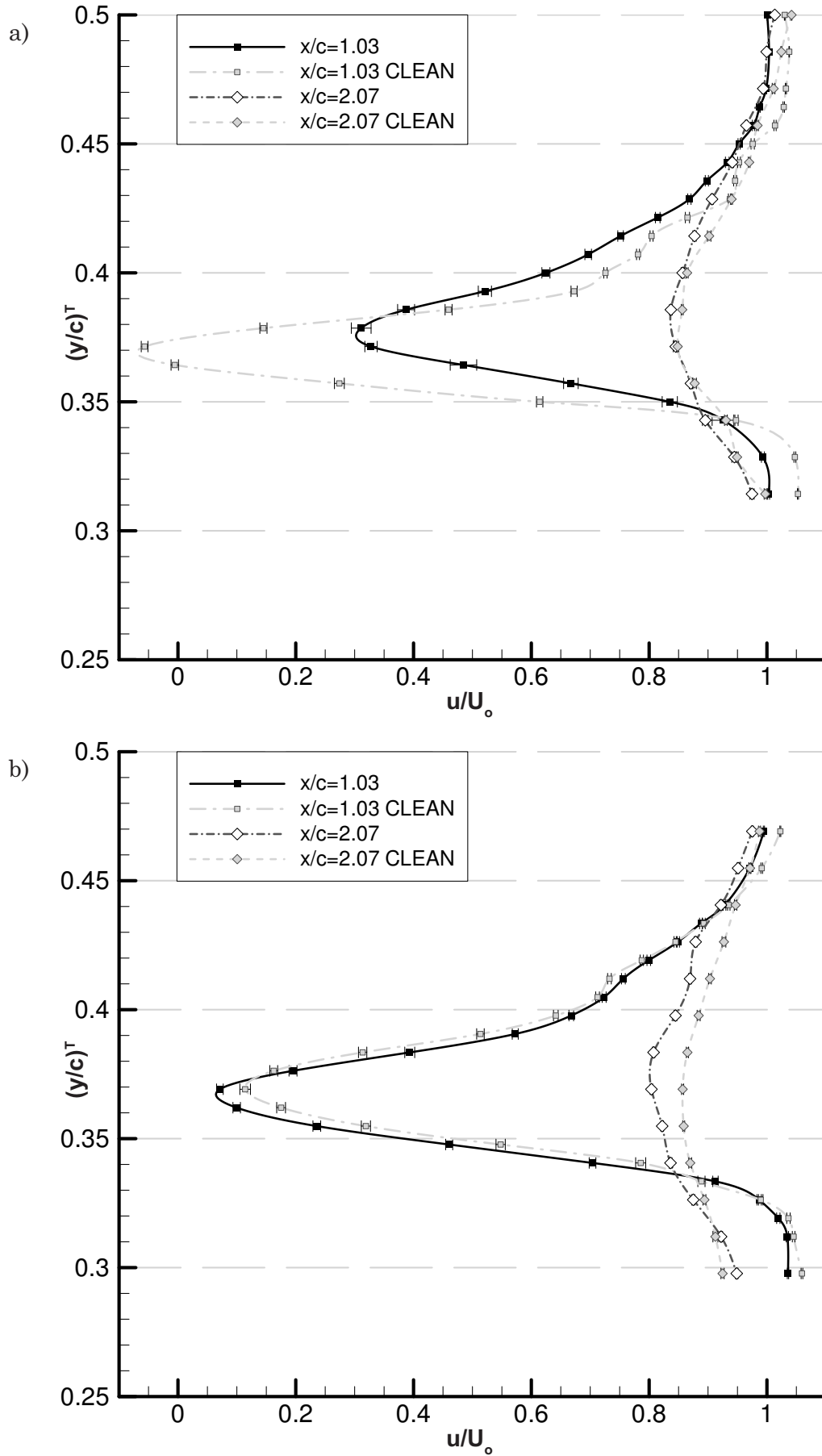
Figure 8.3 Normalized Wake Profiles 1.5-3-23 & Clean Airfoil: α=-2° a) h/c=0.313, b) h/c=0.112
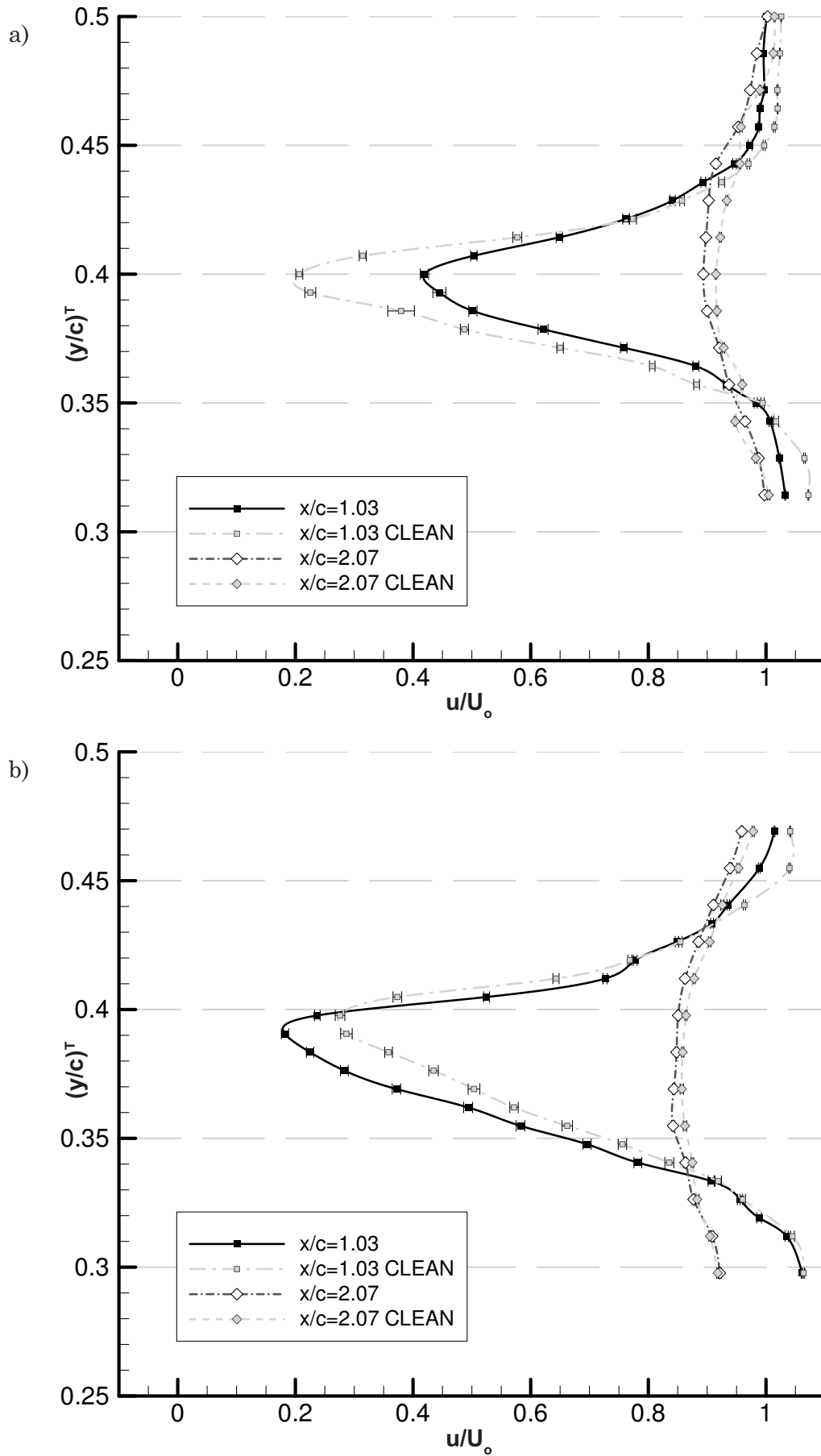
Figure 8.4 Normalized Wake Profiles 1.5-3-23 & Clean Airfoil: α=0˚ a) h/c=0.313, b) h/c=0.112
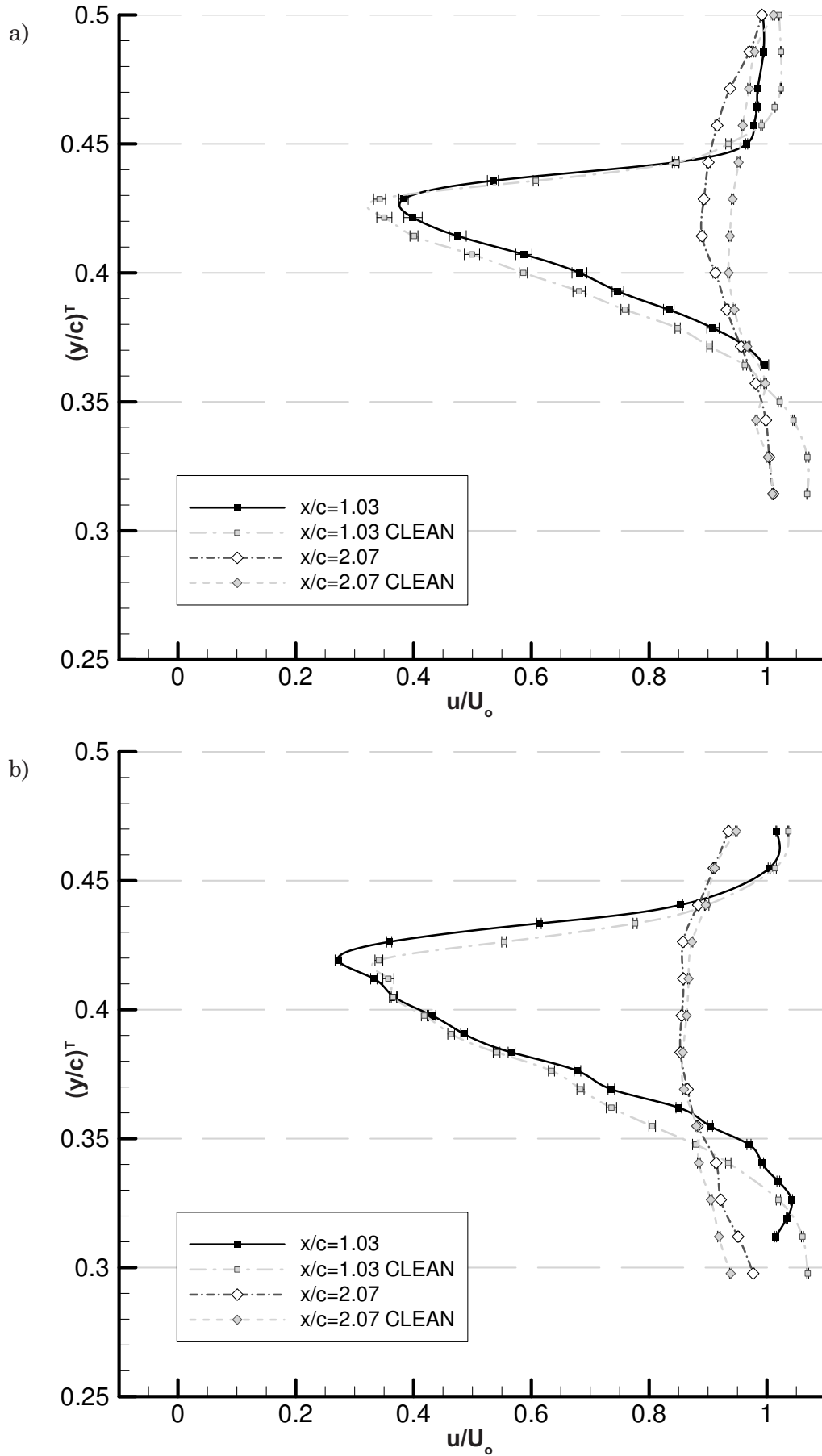
Figure 8.5 Normalized Wake Profiles 1.5-3-23 & Clean Airfoil: α=2° a) h/c=0.313, b) h/c=0.112

Figure 8.6 Normalized Wake Profiles 1.5-3-23 & Clean Airfoil: a) α=7° h/c=0.313, b) α=5° h/c=0.112
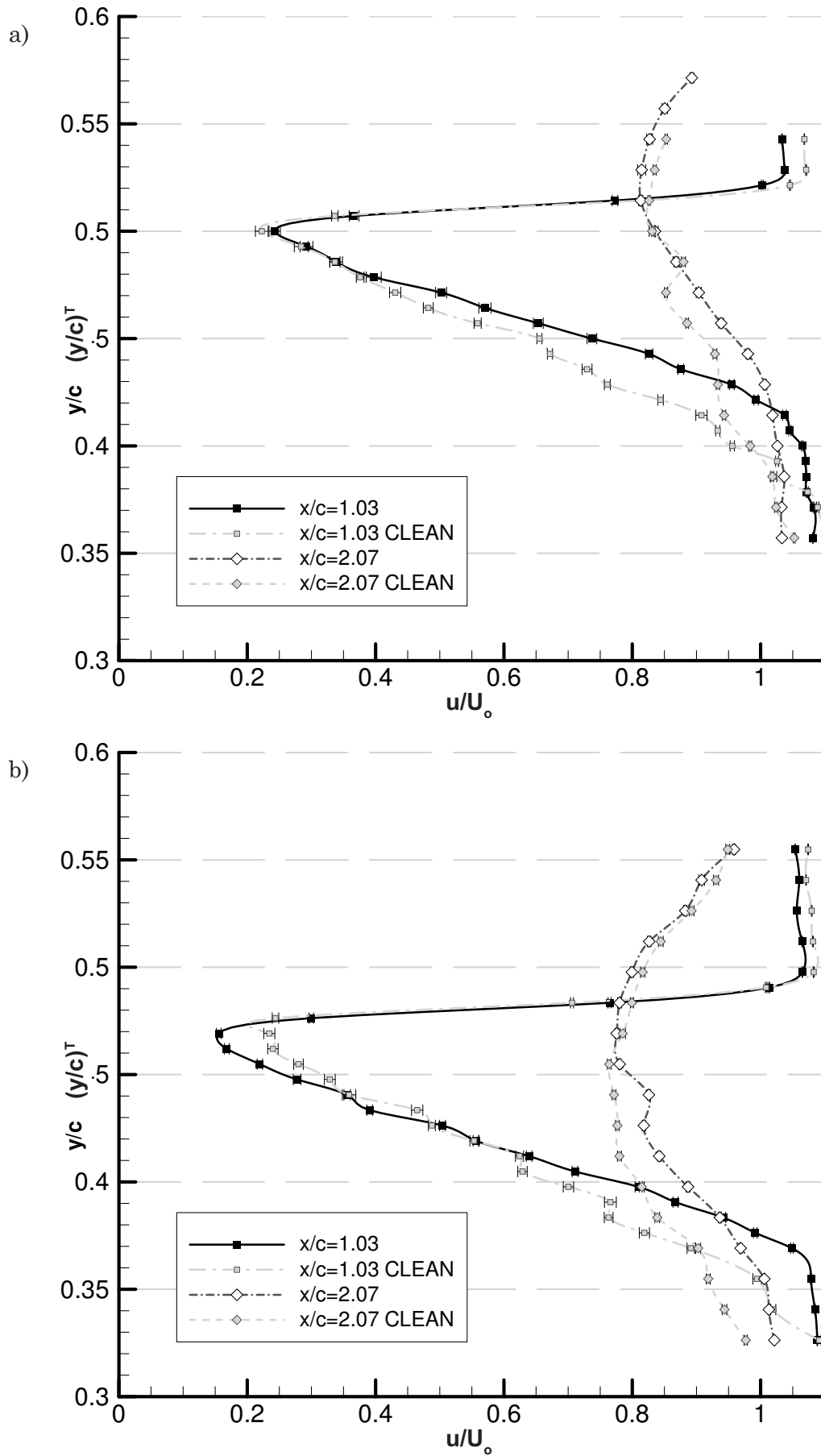
The dimpled airfoil performance at the mid range angle of incidence of $\alpha=5°$ and $\alpha=7°$ in figure 8.6a & 8.6b shows a deficit for $u/U_{o,min}$ with the dimple array at $\alpha=5°$, and no change in $u/U_{o,min}$ at $\alpha=7°$. However for the lower part of the wake for $\alpha=7°$ (y/c=0.35-0.5 in figure 8.6a) and $\alpha=5°$ (y/c=0.325-0.425 in figure 8.6b) the u/U_o profile is greater for the dimpled airfoil, indicating a greater flow recovery towards the ground as the wing angle of incidence increases from the lower angles of incidence. Another difference at $\alpha=5°$ & $7°$ over the lower angles of incidence in figures 8.3 to 8.5, is the downstream increase of the u/U_o profile at x/c=2.07. In figure 8.6a for y/c=0.475-0.35 and in figure 8.6b for y/c=0.45-0.325, u/U_o is greater for the dimpled wing. Out of this range the flow recovery is marginal or detrimental, thus qualitatively comparing the difference is ambiguous and a more quantitative method is outlined in chapter 9.

The change to the 'clean' airfoil wake as a result of the 1-5-3-23 dimpled array airfoil at $\alpha=10°$ is indicated by figures 8.7a & 8.7b. For Figure 8.7a a large positive discrepancy between the dimpled and 'clean' airfoil u/U_o profile exists for both x/c=1.08 and x/c=2.07; for the 'clean' airfoil $u/U_{o,min}$=-0.1 and for the 1.5-3-23 airfoil $u/U_{o,min}$=0.4. As the ground clearance reduces to h/c=0.112 in figure 8.7b the flow recovery provided by the dimple array reduces considerably, but is still present. It is clear at x/c=2.07c the u/U_o wake profile does not exhibit the moving ground plane influence of the wake skewing towards it that the 'clean' airfoil experiences. This is noticeable in figure 8.7b at x/c=2.07, where the 'clean' airfoil u/U_o is consistent for y/c=0.4-0.25.

Investigating the normalized wake contours of u/U_o for the clean and dimpled wing at h/c=0.112 (figure 8.8 to 8.9) and h/c=0.313 (figure 8.10 to 8.11) reinforces the effect the dimples have at this particular array configuration and placement for this angle of incidence. At h/c=0.112 the wake is noticeably thinner, with less downward skew from the ground influence on the wake. As the ground clearance increases to h/c=0.313 in figure 8.9 the biggest difference in the flow structure is observable, being that there is no indication of large scale flow separation or recirculation as in the clean wing case. The flow actually exhibits the upward flow indicative of a medium angle of incidence of a cambered airfoil in free stream. Additionally the pathline upwash with the dimpled wing is lower at low h/c. For the higher angles of incidence $\alpha=13°$ and $\alpha=15°$ in figures 8.12 to 8.13 only a minor improvement is made to the wake u/U_o flow profile.
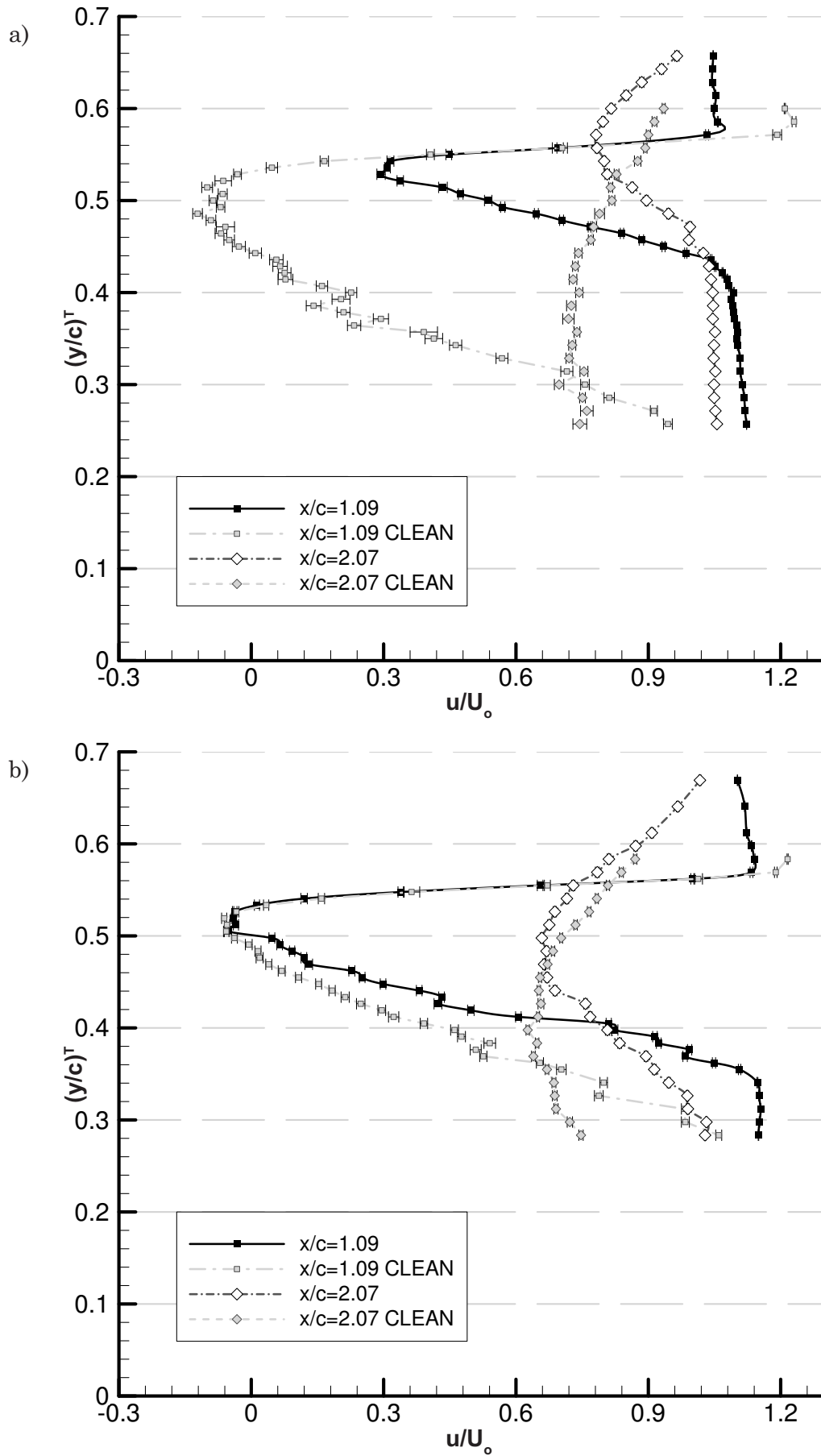
Figure 8.7 Normalized Wake Profiles 1.5-3-23 & Clean Airfoil: α=10˚a) h/c=0.313, b) h/c=0.112
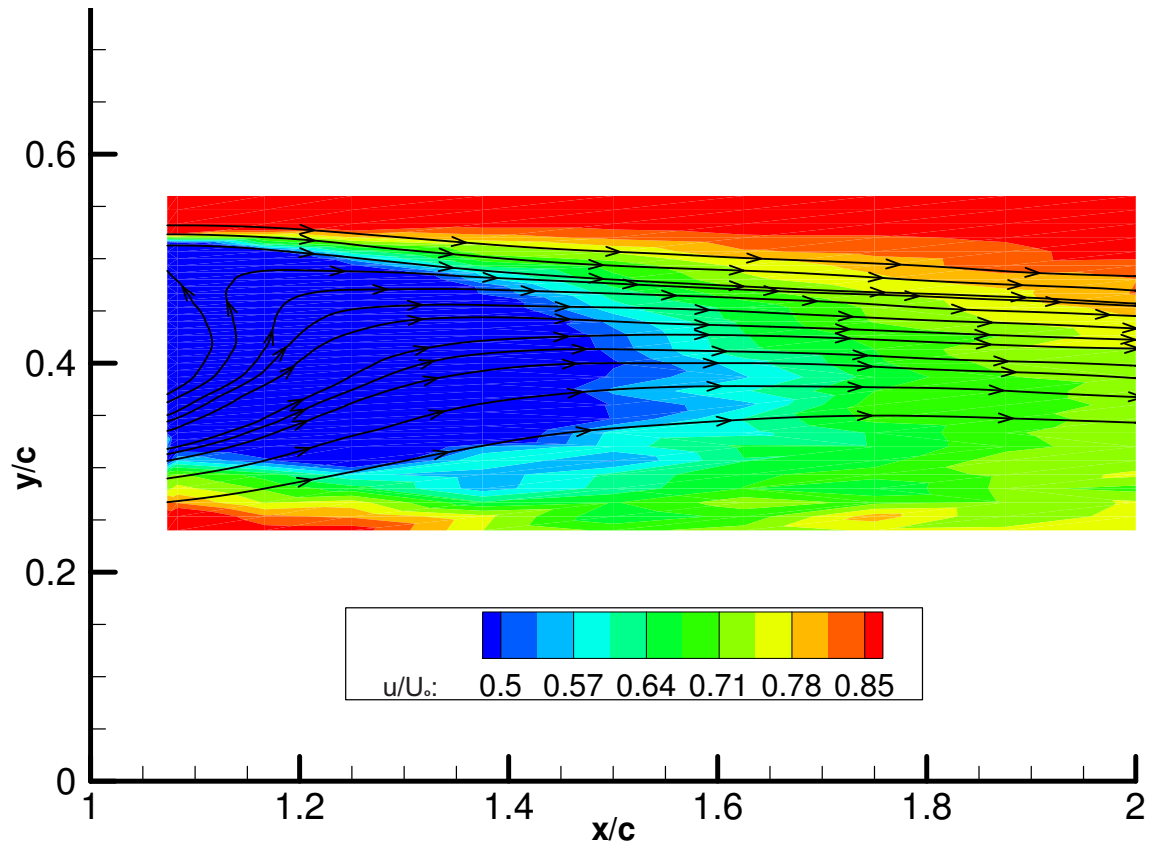
Figure 8.8 Normalized Streamwise Wake Flow Field, **Clean Wing**: α=10˚, h/c=0.313
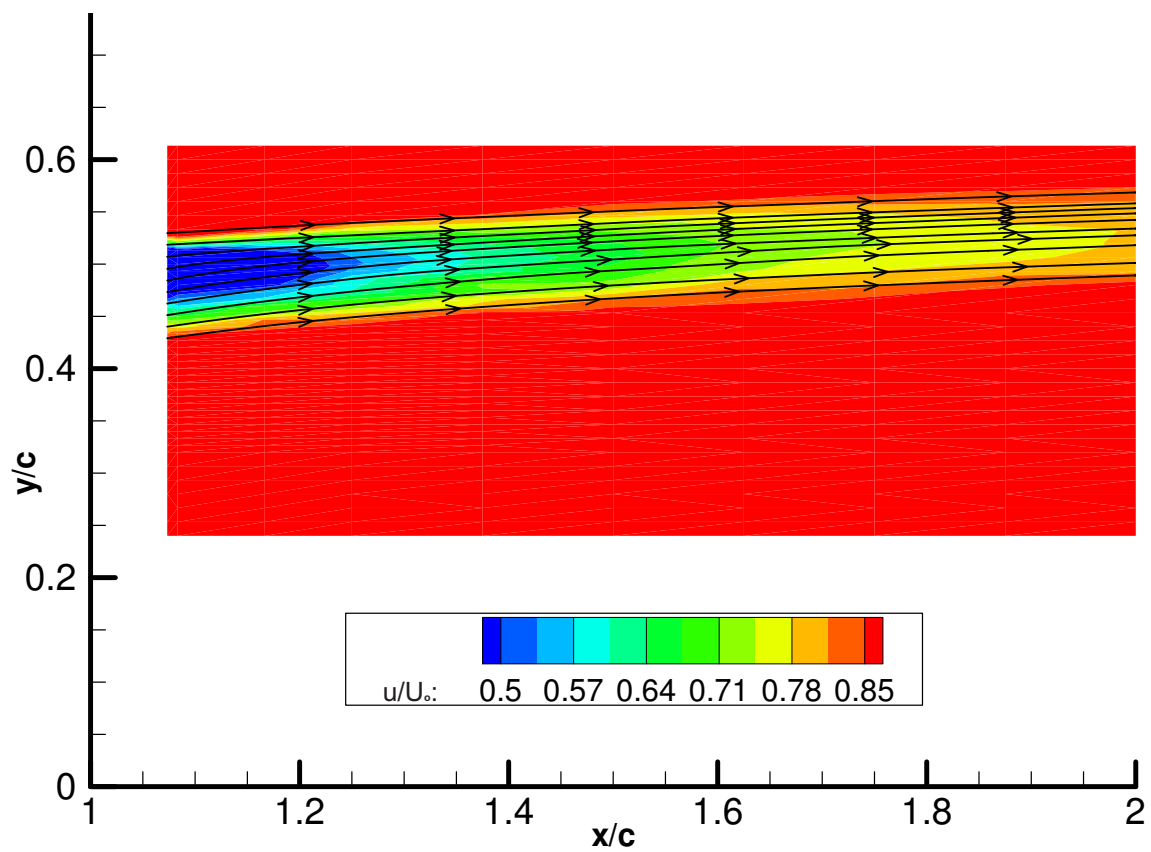
Figure 8.9 Normalized Streamwise Wake Flow Field, **1.5-3-23 Wing**: α=10˚, h/c=0.313
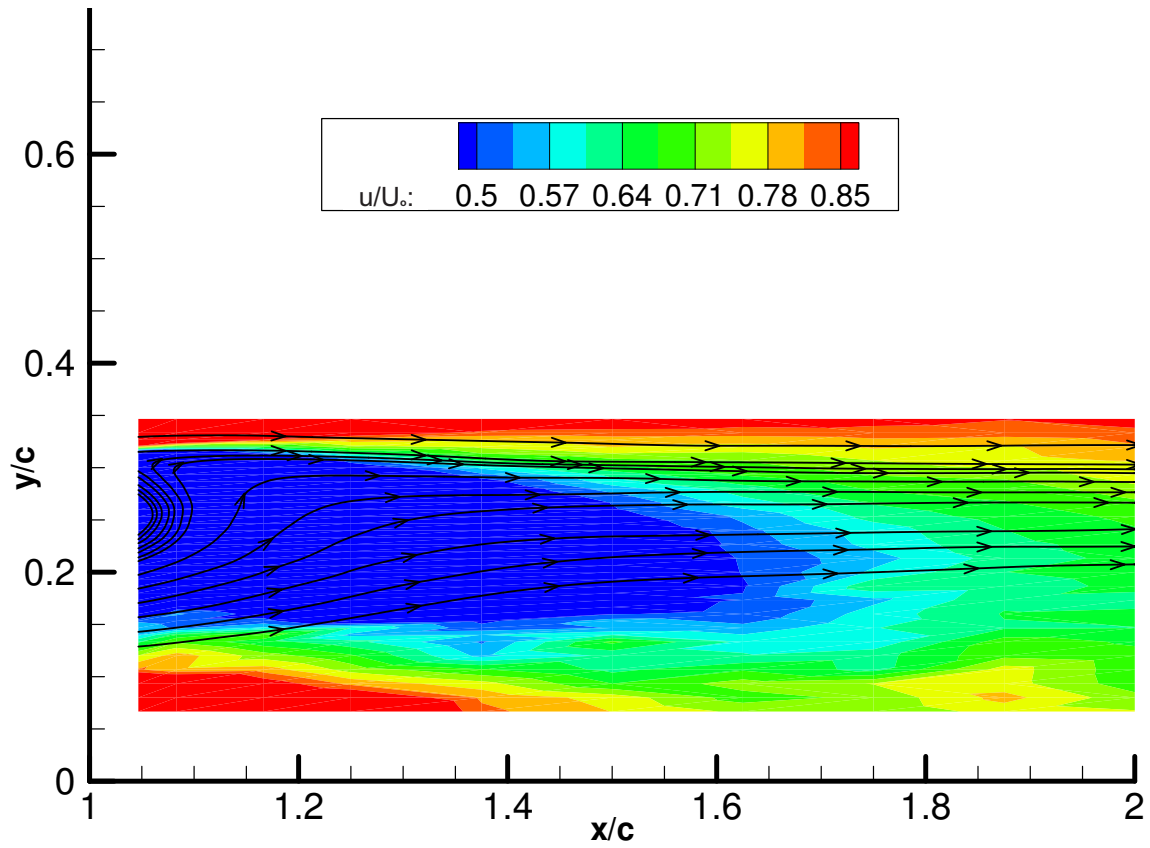
Figure 8.10 Normalized Streamwise Wake Flow Field, **Clean Wing**: α=10˚, h/c=0.112
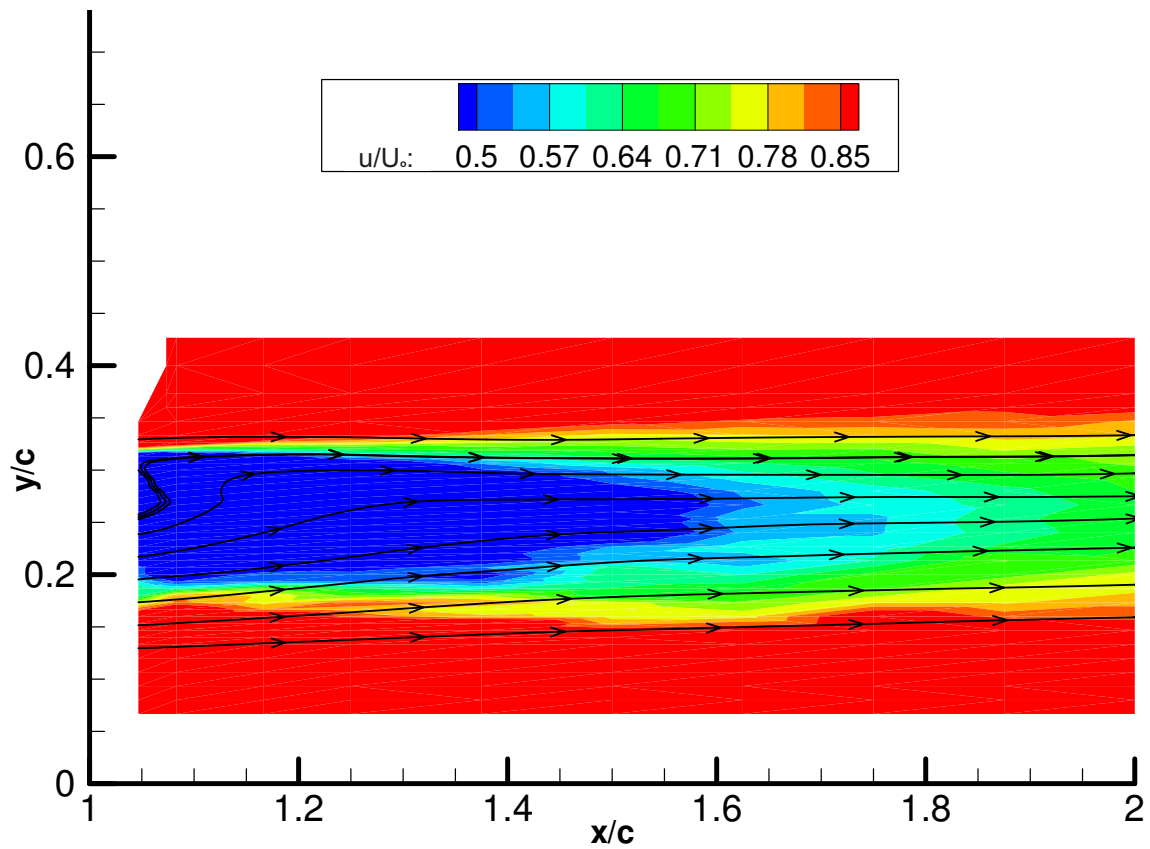
Figure 8.11 Normalized Streamwise Wake Flow Field, **1.5-3-23 Wing**: α=10˚, h/c=0.112
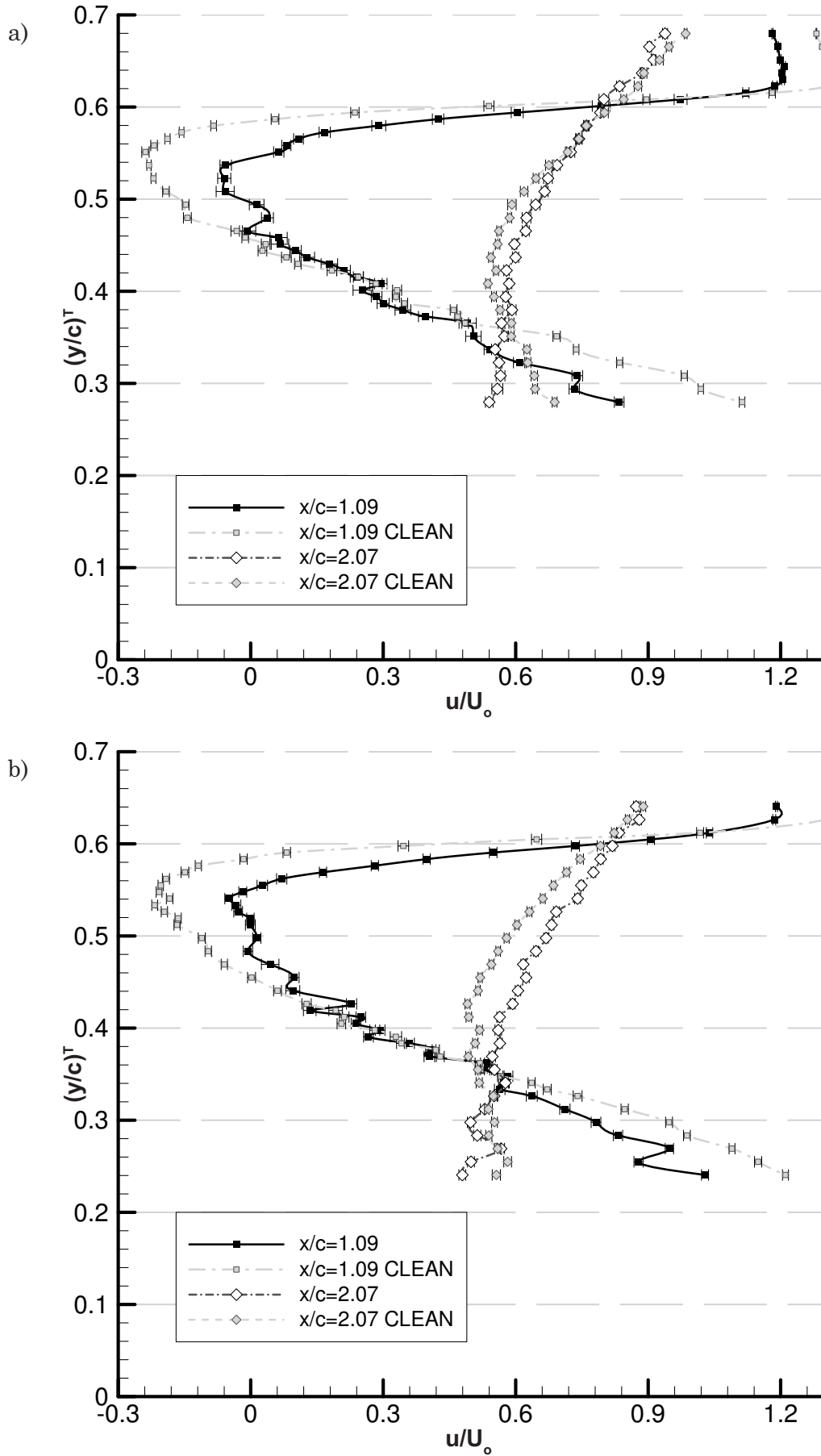
Figure 8.12 Normalized Wake Profiles, 1.5-3-23 & Clean Airfoil: α=13° a) h/c=0.134, b) h/c=0.112
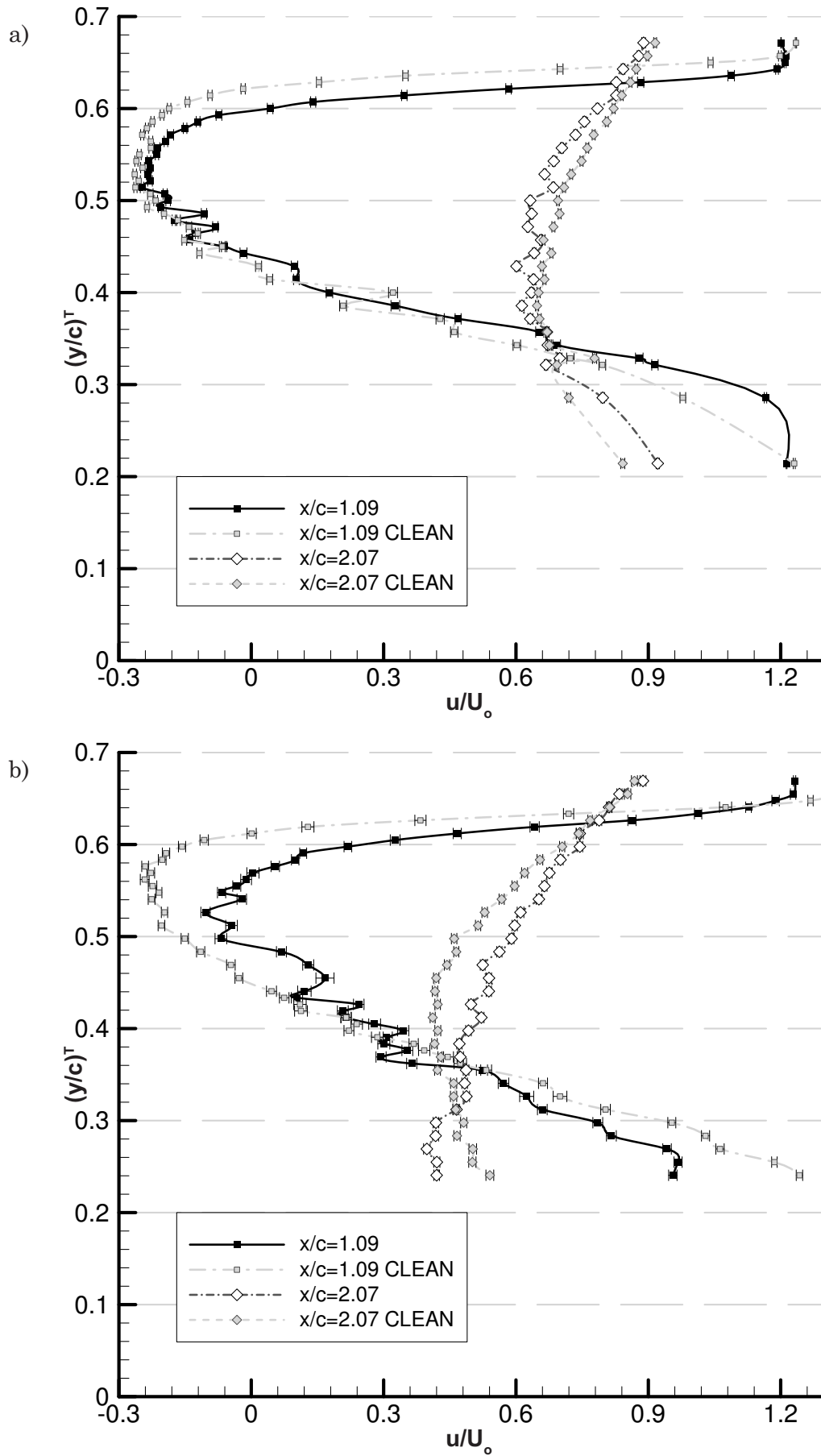
Figure 8.13 Normalized Wake Profiles 1.5-3-23 & Clean Airfoil: α=15˚ a) h/c=0.313, b) h/c=0.112

8.3 Dimpled Airfoil Wake Turbulence Intensity

The turbulence intensity (equation 7.1) is investigated in order to determine how the turbulence of the dimpled airfoil wake (produced by the dimple array on the airfoil) differs to the turbulence intensity of the 'clean' airfoil in chapter 7. Figures 8.14 to 8.16 outline the turbulence intensity profiles at h/c=0.313 and h/c=0.112 for α=-2˚, 0˚ & 2˚. The turbulence intensity corresponding to the ground clearance h/c=0.112 for α=-2˚, 0˚ & 2˚ all indicate the dimpled airfoil produces higher turbulence intensity levels in the wake. Considering figures 8.14, 8.15 and 8.16, as the ground clearance increases the dimpled wing reduces the wake turbulence intensity compared to the clean airfoil.
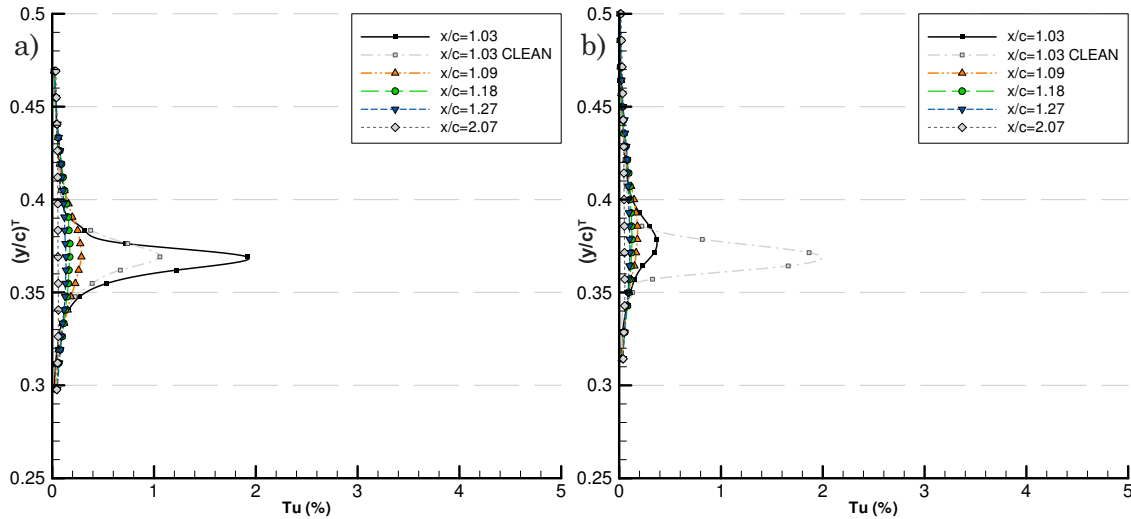
Figure 8.14 Turbulence Intensity 1.5-3-23 & Clean Airfoil: α=-2˚ a) h/c=0.112, b) h/c=0.313
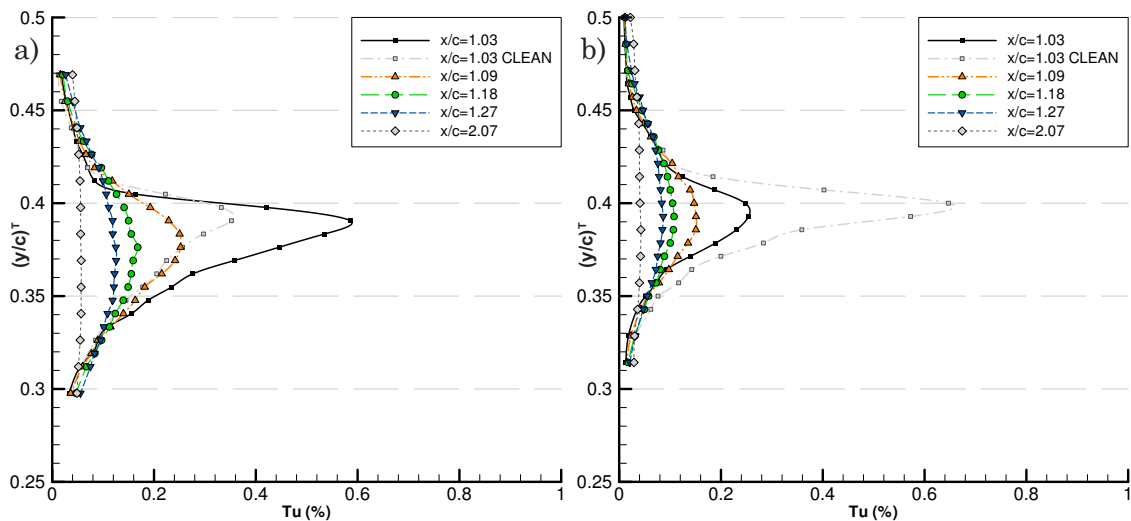
Figure 8.15 Turbulence Intensity 1.5-3-23 & Clean Airfoil: α=0˚ a) h/c=0.112, b) h/c=0.313
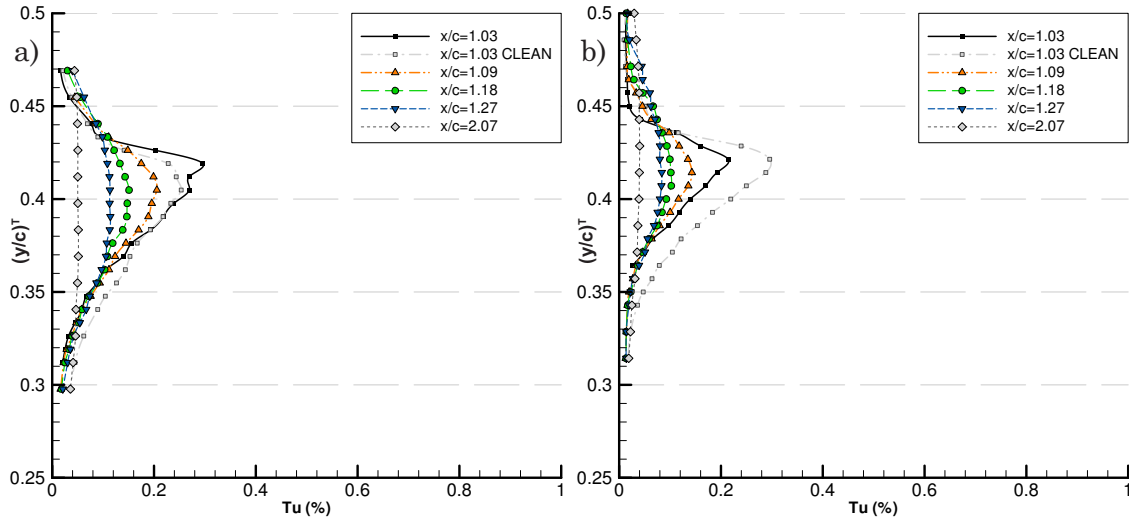
Figure 8.16 Turbulence Intensity 1.5-3-23 & Clean Airfoil: α=2° a) h/c=0.112, b) h/c=0.313
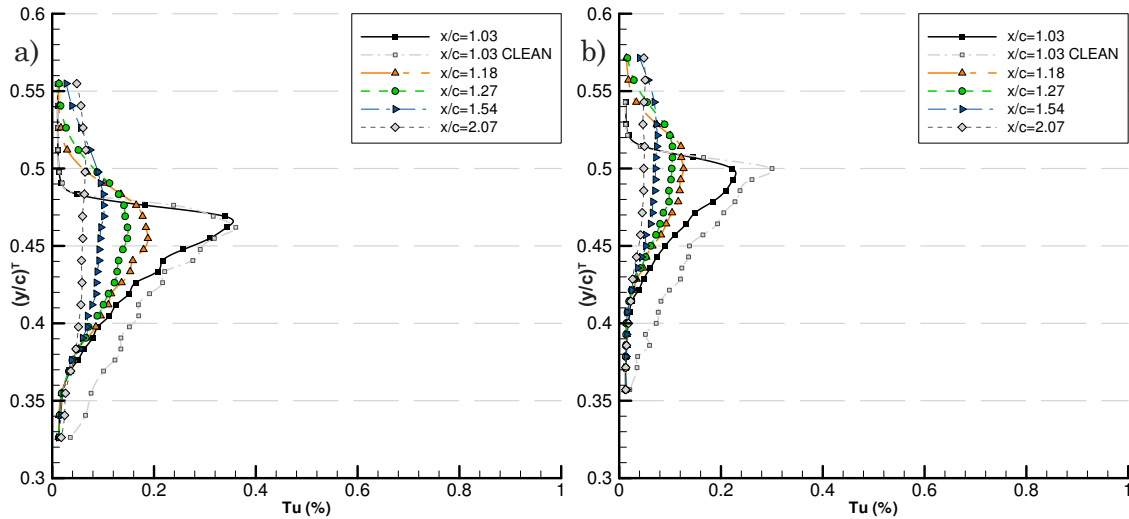
Figure 8.17 Turbulence Intensity 1.5-3-23 & Clean Airfoil a) α=5° h/c=0.112, b) α=7° h/c=0.313

The turbulence intensity maximum, although rather small for α=5°-7° in figure 8.17, shows that whilst the peak value is not altered greatly there is some reduction in the lower part of the wake turbulence intensity that is from the underside of the dimpled wing. This is similar for the wake flow and the two main Reynolds stress components shown in chapter 8.4-8.5. Figure 8.17 indicates that as a result of the dimple array for the mid range angles, increasing the ground clearance reduces the turbulence intensity, see also figure F.23g and F.23h.

The reduction in the streamwise flow profile for α=10° at h/c=0.112 (figure 8.18), the turbulence intensity does not show much reduction. Investigating the turbulence intensity contours in figures 8.18, 8.19a and 8.19b, a decrease is noticeable at x/c=1.09 with the dimpled airfoil. There is some increase in the dimpled wing wake
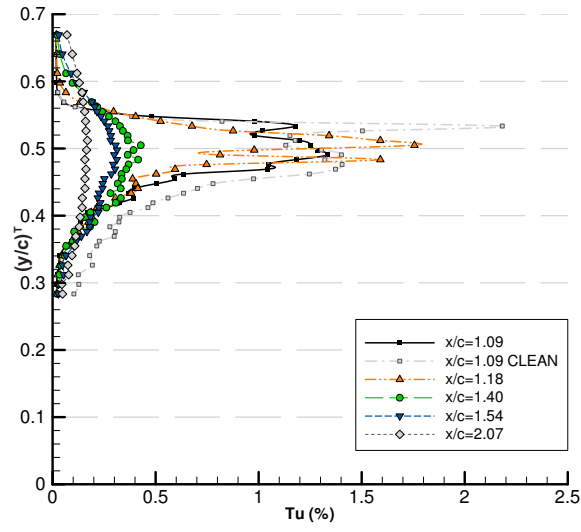
Figure 8.18 Turbulence Intensity 1.5-3-23 & Clean Airfoil: α=10˚, h/c=0.112
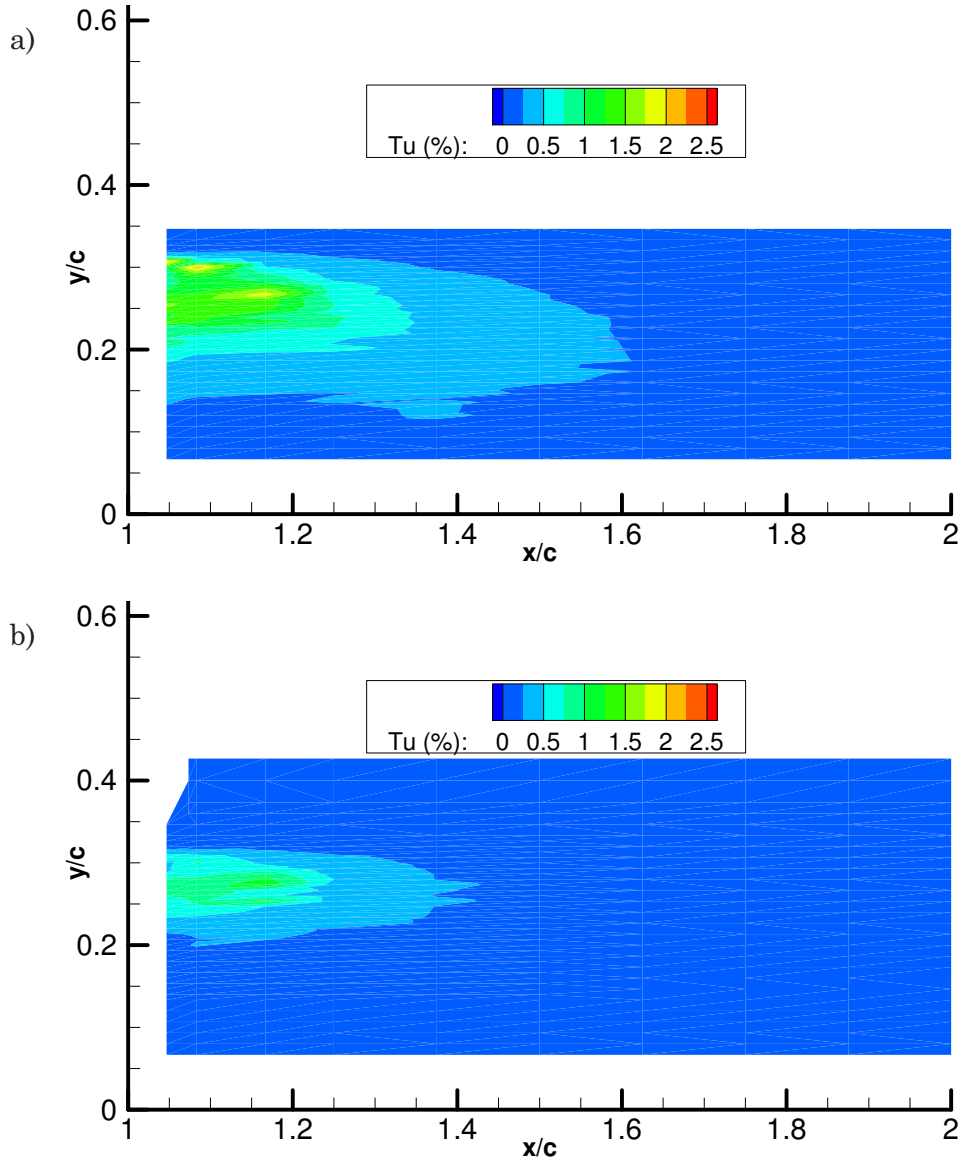
Figure 8.19 Wake Flow Field Turbulence Intensity: α=10˚, h/c=0.112 a) Clean Wing, b) 1.5-3-23
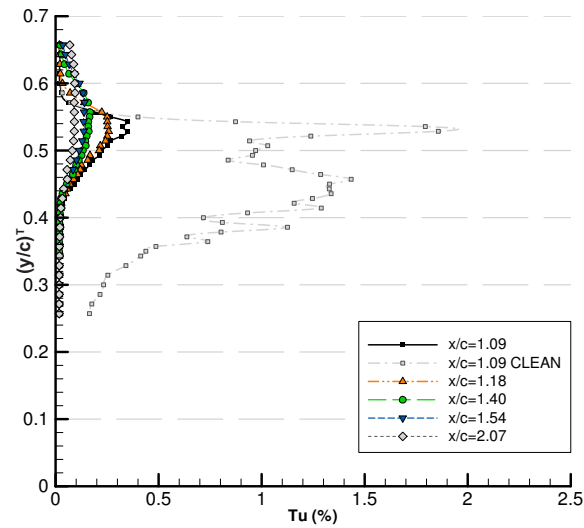
Figure 8.20 Turbulence Intensity 1.5-3-23 & Clean Airfoil: α=10˚, h/c=0.313
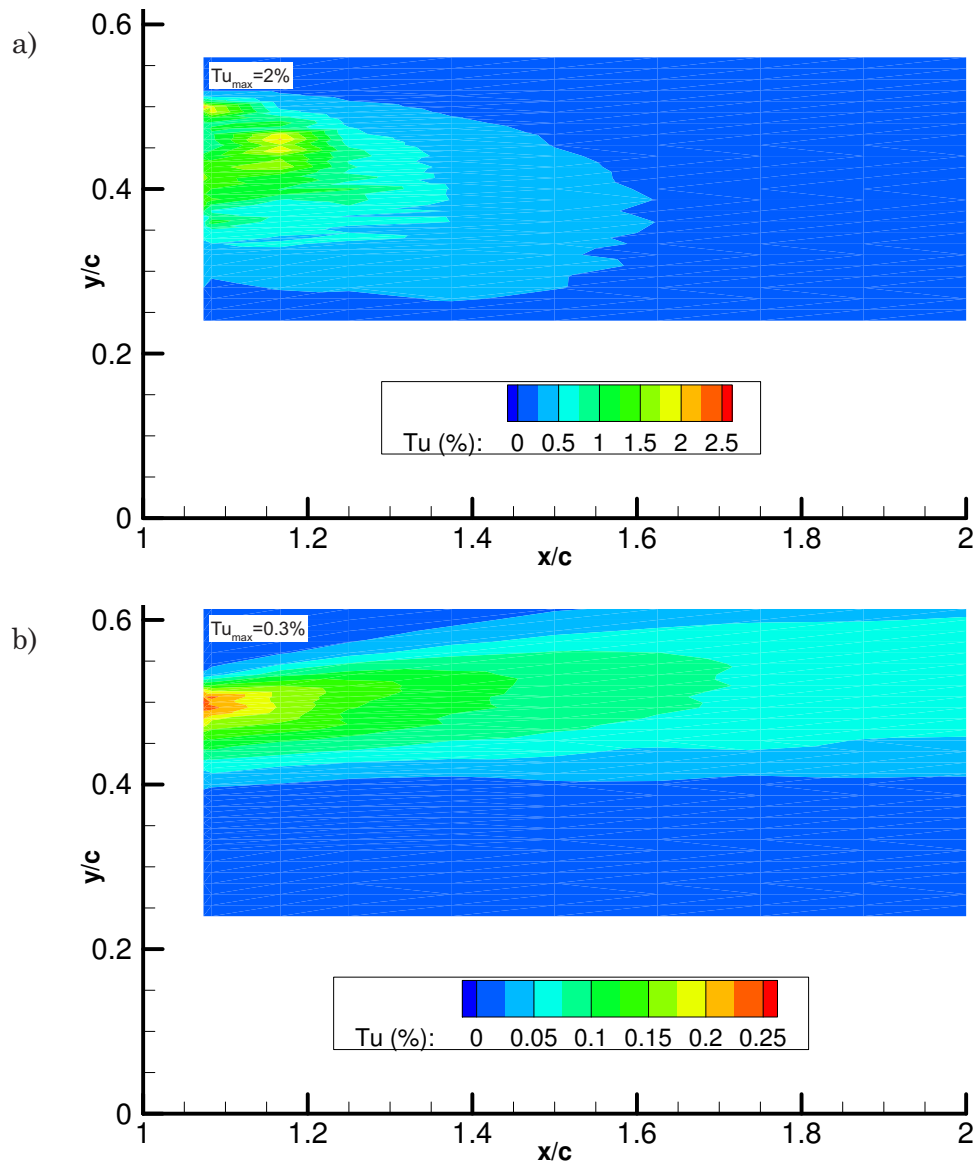
Figure 8.21 Wake Flow Field Turbulence Intensity: α=10˚, h/c=0.313 a) Clean Wing, b) 1.5-3-23
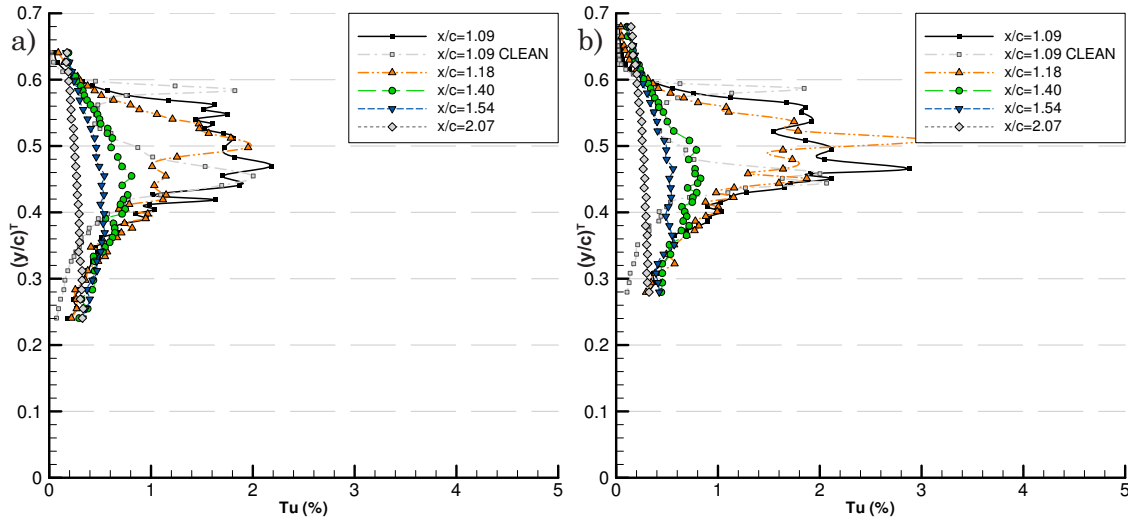
Figure 8.22 Turbulence Intensity 1.5-3-23 & Clean Airfoil: α=13° a) h/c=0.112 b) h/c=0.134
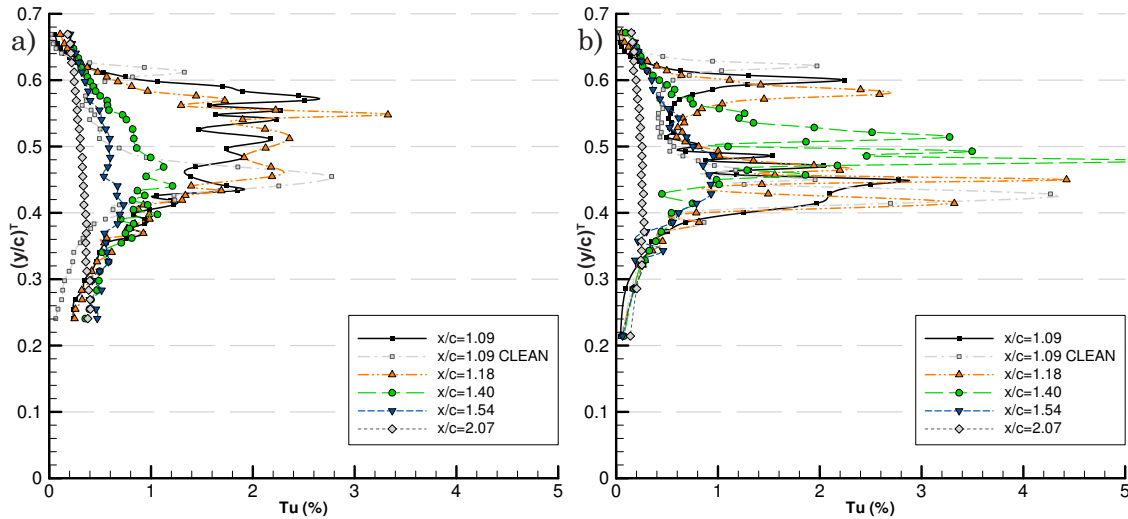
Figure 8.23 Turbulence Intensity 1.5-3-23 & Clean Airfoil: α=15° a) h/c=0.112 b) h/c=0.313

peak turbulence intensity at x/c=1.18, despite being thinner where y/c≈0.48-0.52, as opposed to clean wing thickness from figure 7.18a being y/c≈0.45-53. The two distinct peaks of turbulence intensity in the wake no longer are present for the dimpled wing wake. As already seen for u/U_o at h/c=0.313, the structure and intensity for the wing wake turbulence is substantially reduced by the dimples in figure 8.20 and 8.21b. Figure 8.21b indicates no influence of the moving ground plane on the turbulence intensity structure at the lower turbulence intensity range indicated.

The turbulence intensity for α=13° shows while the magnitude of the peak turbulence intensity is similar, the 'twin peak' profile at x/c=1.08 forms one larger central peak. Whilst the y/c distribution of the Tu peaks remains the same and the central 'spike'

in the Tu peak remains, the overall average has increased at α=13˚. This is similar at x/c=1.09 for α=15˚ (h/c=0.112-0.134), as the decay in turbulence intensity at this angle is abrupt between x=1.09c and x=1.4c. In figure 8.23b at h/c=0.313 the turbulence intensity is marginally thinner and weaker at x=1.09c compared to the clean wing, the downstream increase in turbulence intensity is also reduced, (see figure 7.20b).

8.4 Dimpled Airfoil Wake Normalized Turbulent Normal Stress
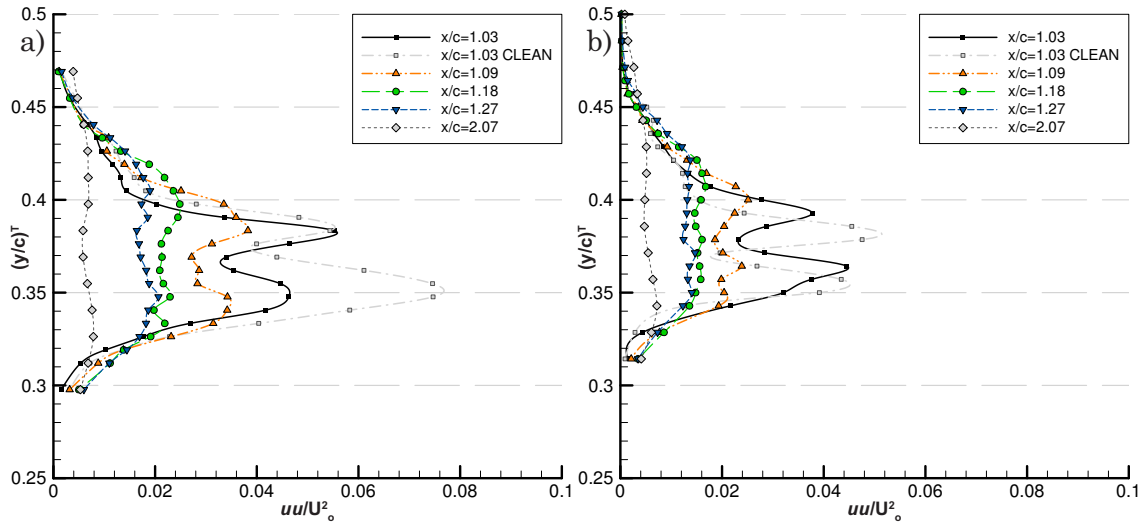
Figure 8.24 Normalized Turbulent Normal Stress: α=-2˚ a) h/c=0.112, b) h/c=0.313

The influence the dimpled wing has on the near wake turbulent normal stress (uu) is compared to the clean airfoil at x=1.03c in figures 8.24 to 8.33. The normalized turbulent stress (uu/U^2_o) profile does not change distribution with the dimples, but the magnitude of the two peaks changes. The reduction in uu/U^2_o shows the dimple array alleviating the stress on the fluid in the wake region. For α=-2˚ in figure 8.24, there is a reduction in the wake uu/U^2_o profile. However the reduction is not as great at h/c=0.313, which interestingly is counter to the improvement in u/U_o at h/c=0.313 in figure 8.3. For α=0˚ and α=2˚, the dimpled wing uu/U^2_o reduction from the 'clean' wing improves with increased h/c; figures 8.25 to 8.26. When α=5˚ and 7˚ in figure 8.27a & 8.27b, the dimpled wing uu/U^2_o profile at the lower peak increases. The lower turbulent normal stress peak is due to the boundary layer on the underside of the wing, its reduction suggests the dimple array improvement to the wake is greater.

Figures 8.28 to 8.31 indicate uu/U^2_o for the wake with α=10˚. As for the u/U_o and Tu wake flow profile reduction at this angle, the dimpled airfoil provides the greatest
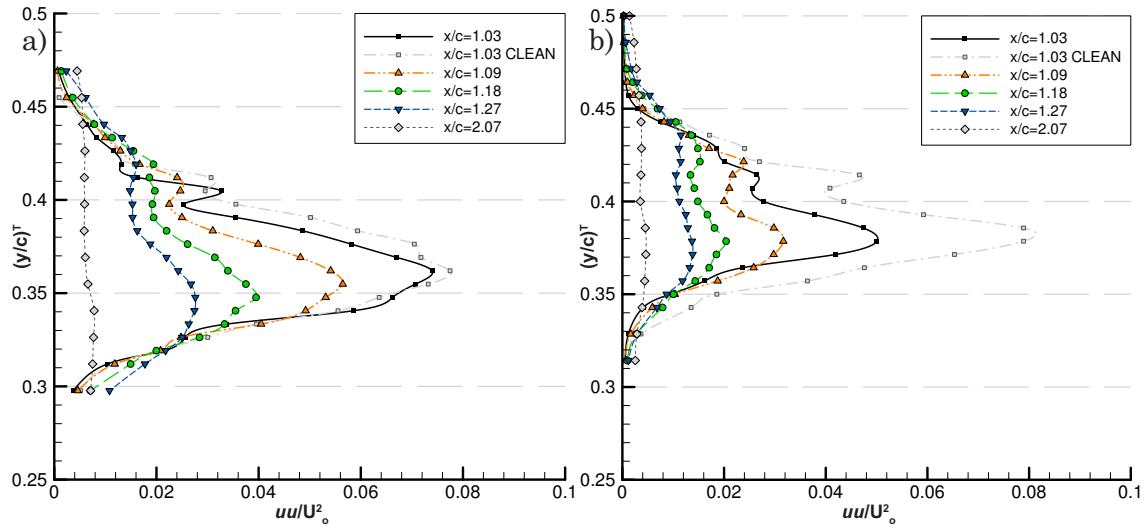
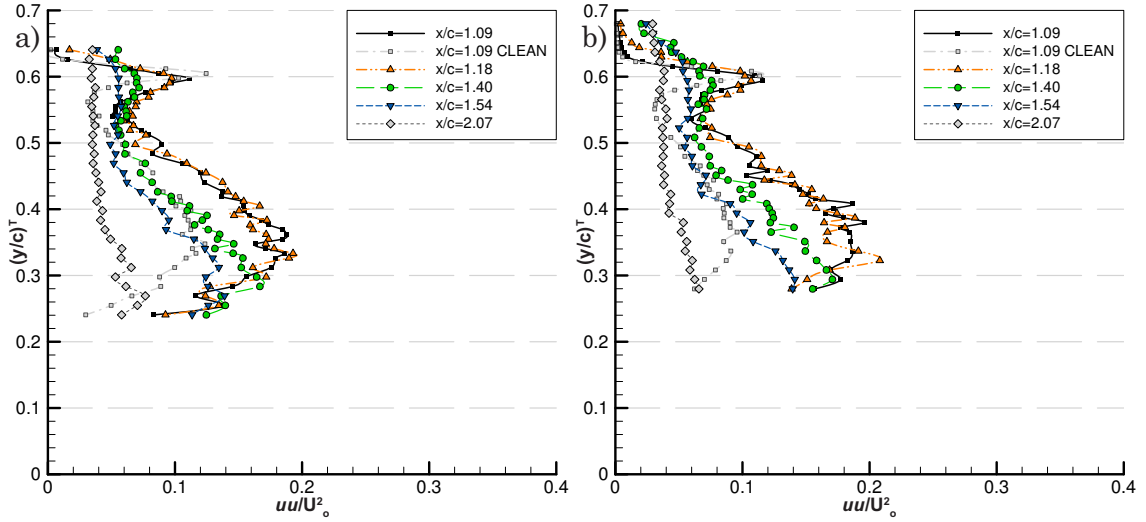Figure 8.25 Normalized Turbulent Normal Stress: α=0˚ a) h/c=0.112, b) h/c=0.313
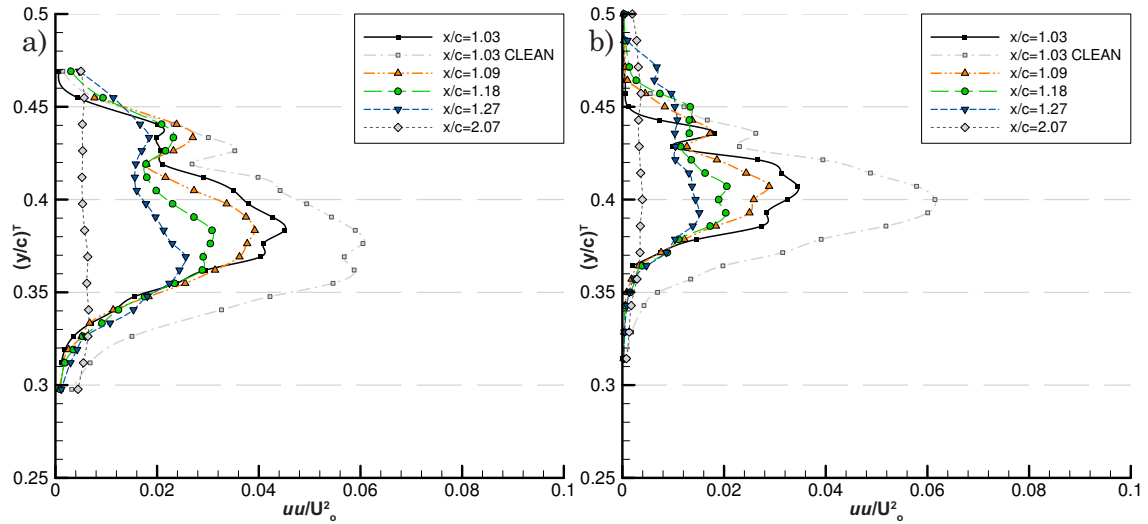
Figure 8.26 Normalized Turbulent Normal Stress: α=2˚ a) h/c=0.112, b) h/c=0.313
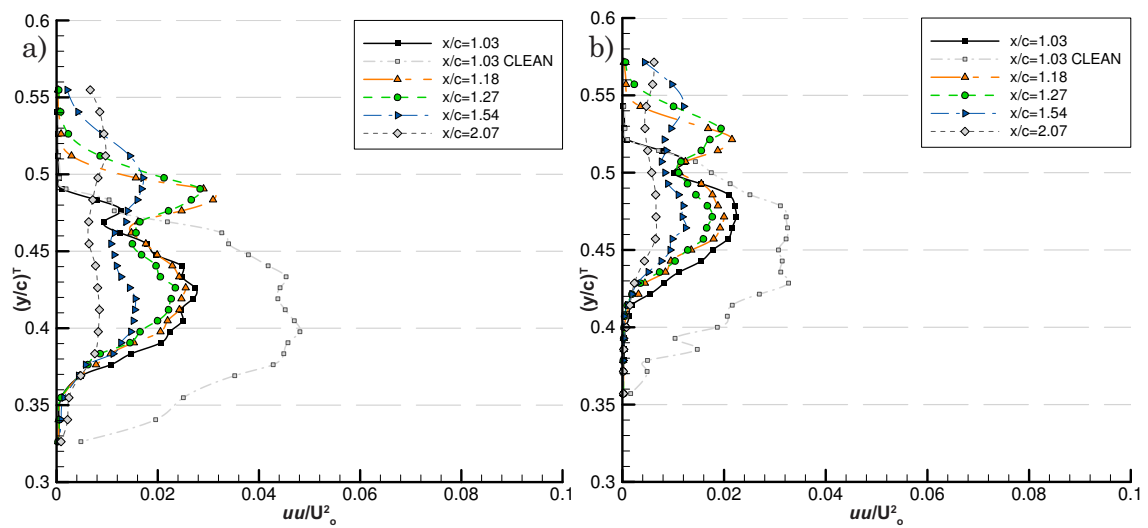
Figure 8.27 Normalized Turbulent Normal Stress: a) α=5˚, h/c=0.112, b) α=7˚, h/c=0.313
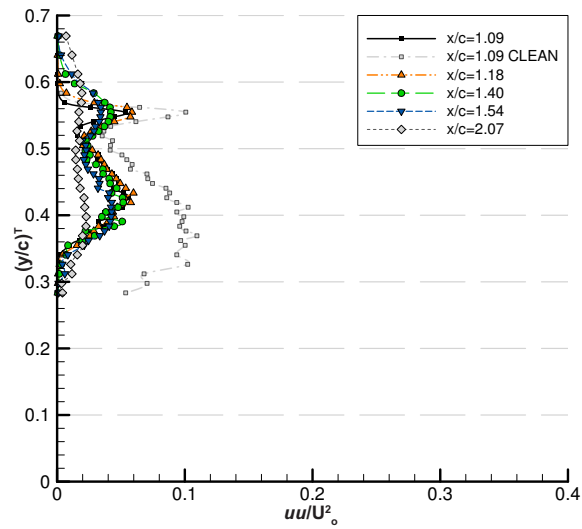
Figure 8.28 Normalized Turbulent Normal Stress: α=10˚, h/c=0.112
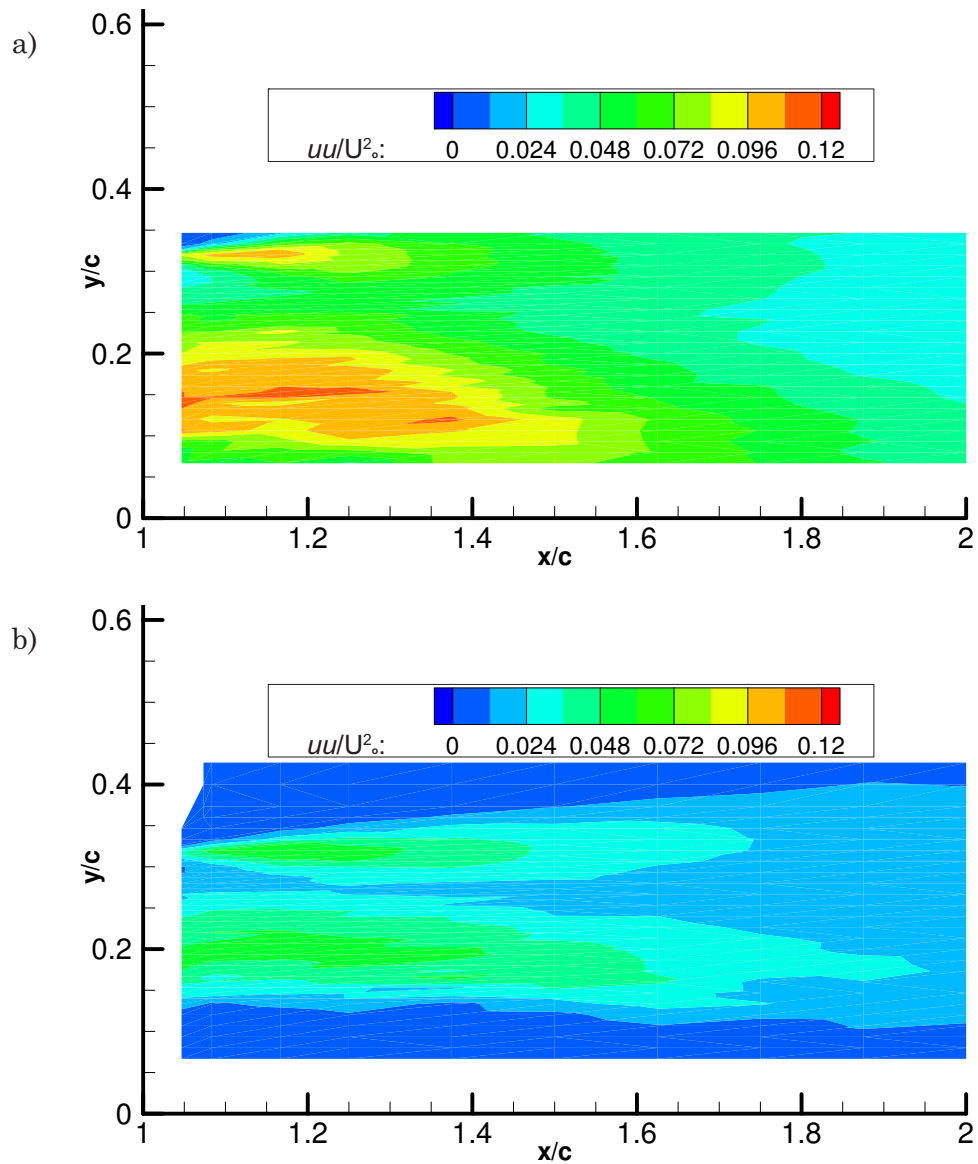
Figure 8.29 Wake Turbulent Normal Stress: α=10˚, h/c=0.112 a) Clean Wing, b) 1.5-3-23
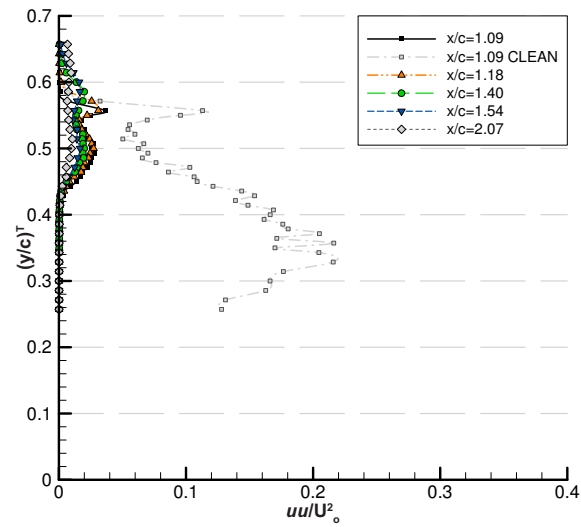
Figure 8.30 Normalized Turbulent Normal Stress: α=10°, h/c=0.313
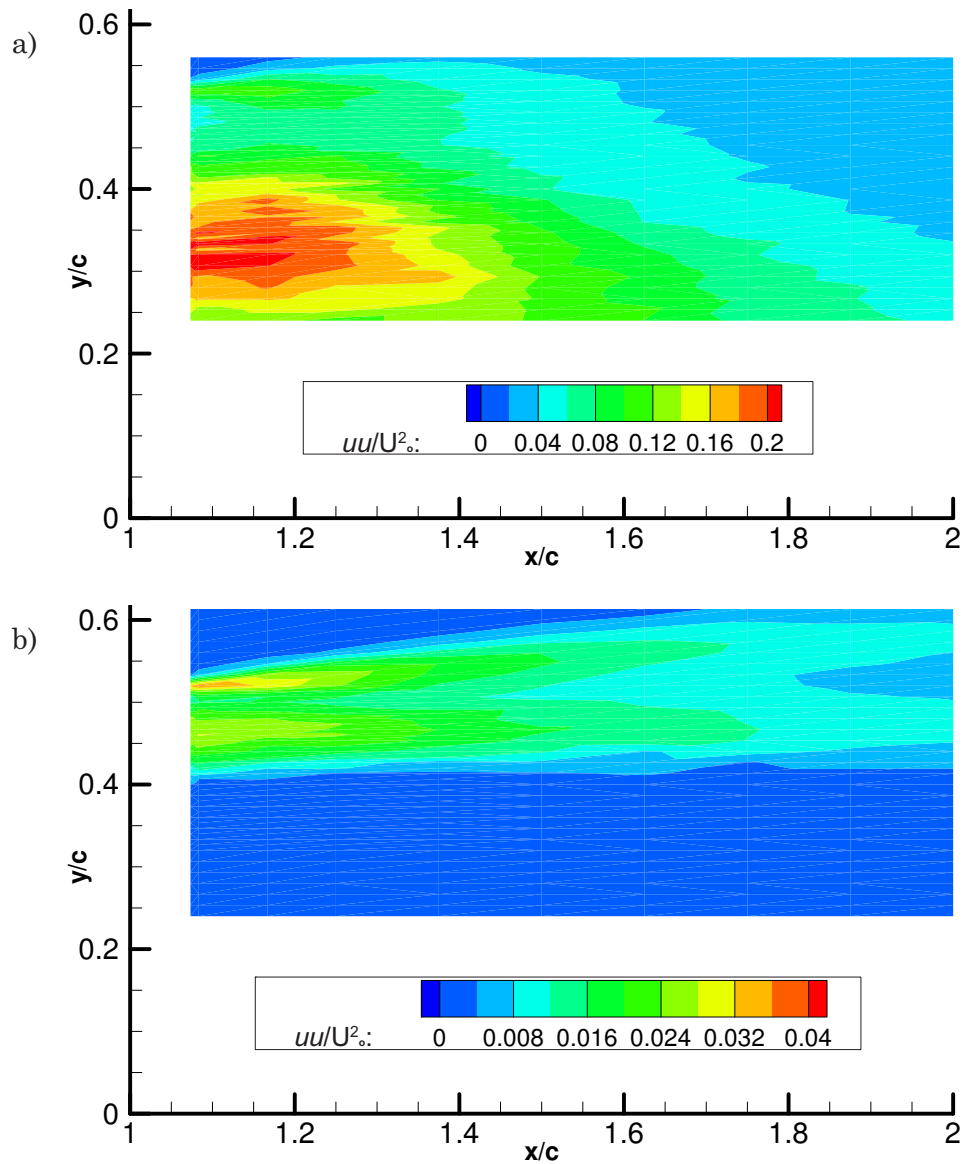
Figure 8.31 Wake Turbulent Normal Stress: α=10°, h/c=0.313 a) Clean Wing, b) 1.5-3-23

reduction in uu/U^2_o. Once again this decrease is more prominent as ground clearance increases to h/c=0.313. Figure 8.29b shows the uu/U^2_o change throughout the wake for α=10˚ & h/c=0.112, where the dimpled airfoil generates significant reductions and dissipates faster over x/c=1.03-2.07 (clean wing uu/U^2_o=0.12-0.07 and uu/U^2_o=0.07-0.02 for the dimpled airfoil) which is less skewed to the moving ground. As the angle increases to α=13˚-15˚ in figures 8.32 to 8.33 the dimpled wing uu/U^2_o profile is worse, as the dimple array may cause the flow to separate earlier. However for α=15˚ at h/c=0.313 in figure 8.33b (and figure 7.27b), the large scale flow fluctuations in the separated boundary layer are reduced with the dimple array as the migrating separation point is positioned where the dimples provide the most flow recovery.

Figure 8.32 Normalized Turbulent Normal Stress: α=13˚ a) h/c=0.112, b) h/c=0.134
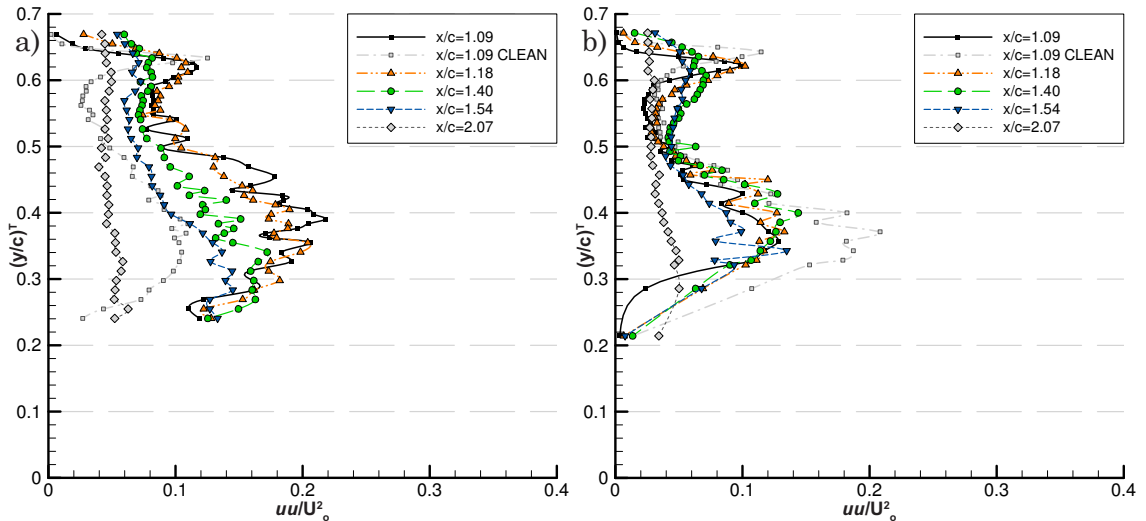
Figure 8.33 Normalized Turbulent Normal Stress: α=15˚ a) h/c=0.112, b) h/c=0.313

8.5 Dimpled Airfoil Wake Normalized Primary Shear Stress

As with the change in the turbulent shear stress, the effect the dimple array has on the change to the primary shear stress will be compared. At α=-2° in figure 8.34a for the dimpled wing there is marginal difference at h/c=0.112; however as h/c increases the dimpled wing uv/U^2_o is higher than the clean wing in figure 8.34b. When α=0° in figure 8.35 the dimpled airfoil shows little difference at h/c=0.112, but the dimpled airfoil starts to reduce the normalized primary shear stress as h/c increases to h/c=0.313. For α=2° in figure 8.36, the dimpled wing reduction is apparent at the positive uv/U^2_o peak closer to the ground plane. For low angle of incidences the uv reduction due to the dimpled airfoil from the clean airfoil reflects the uu trend.
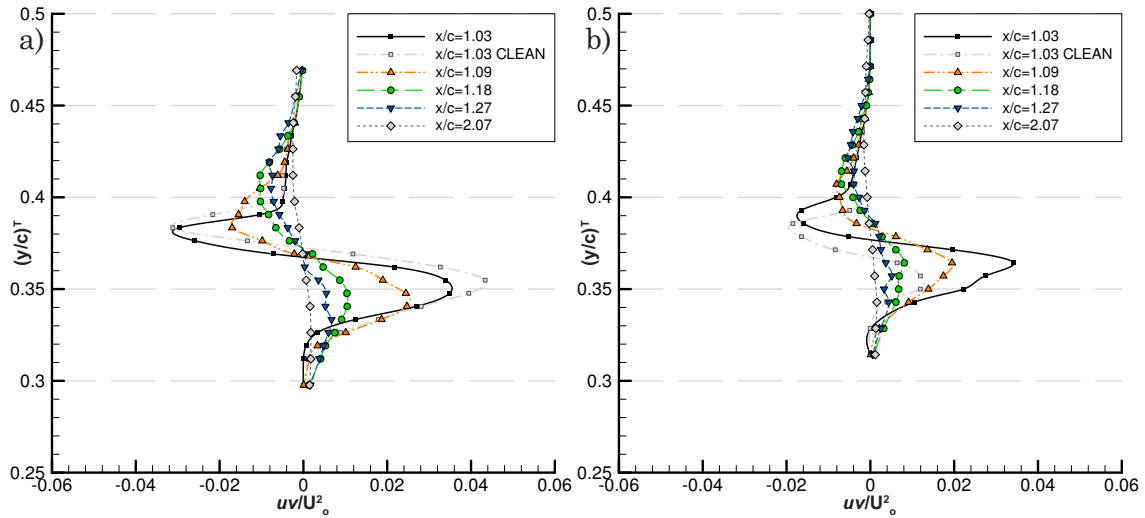
Figure 8.34 Normalized Primary Shear Stress: α=-2° a) h/c=0.112, b) h/c=0.313
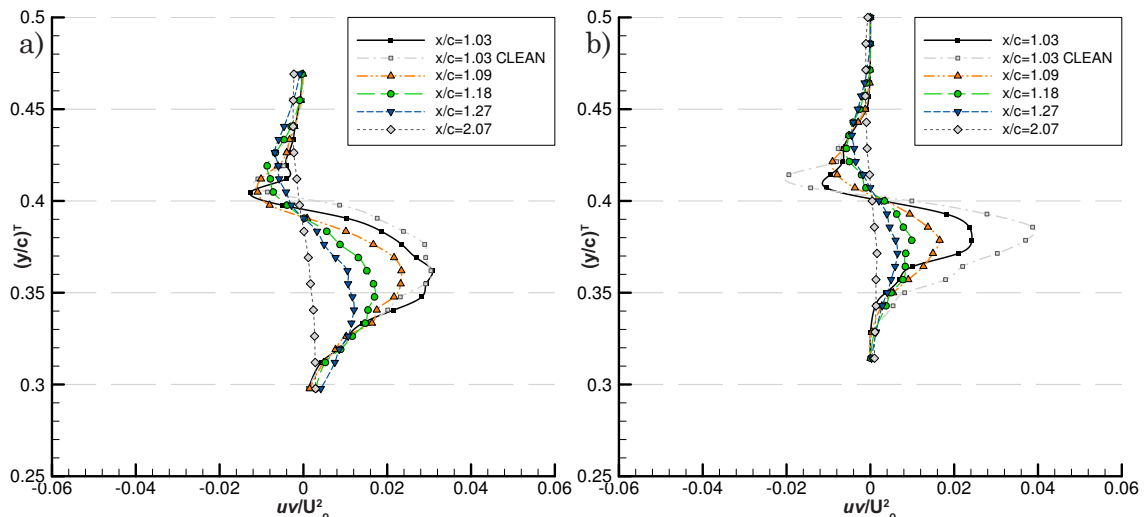
Figure 8.35 Normalized Primary Shear Stress: α=0° a) h/c=0.112, b) h/c=0.313
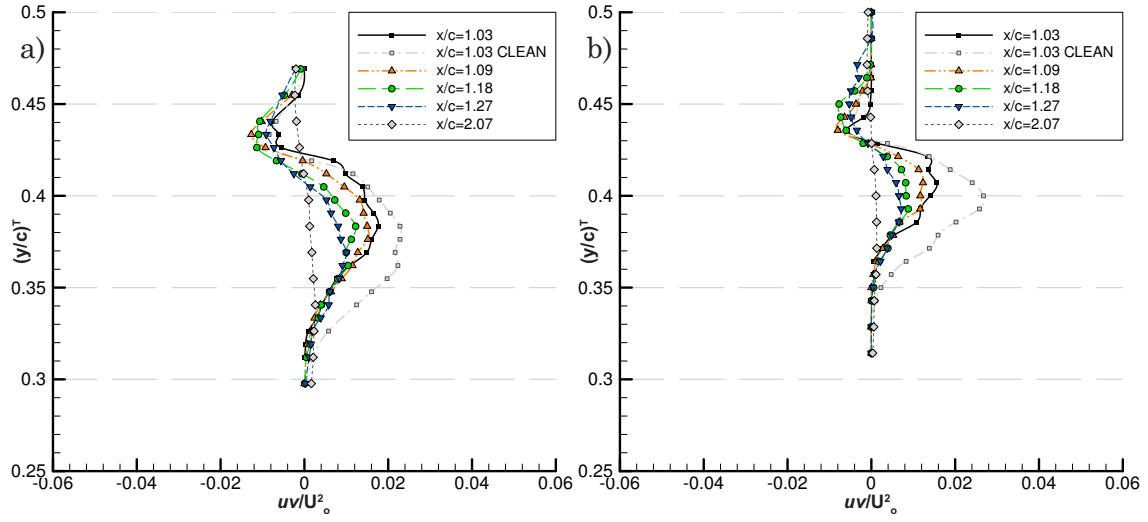
Figure 8.36 Normalized Primary Shear Stress: α=2˚ a) h/c=0.112, b) h/c=0.313
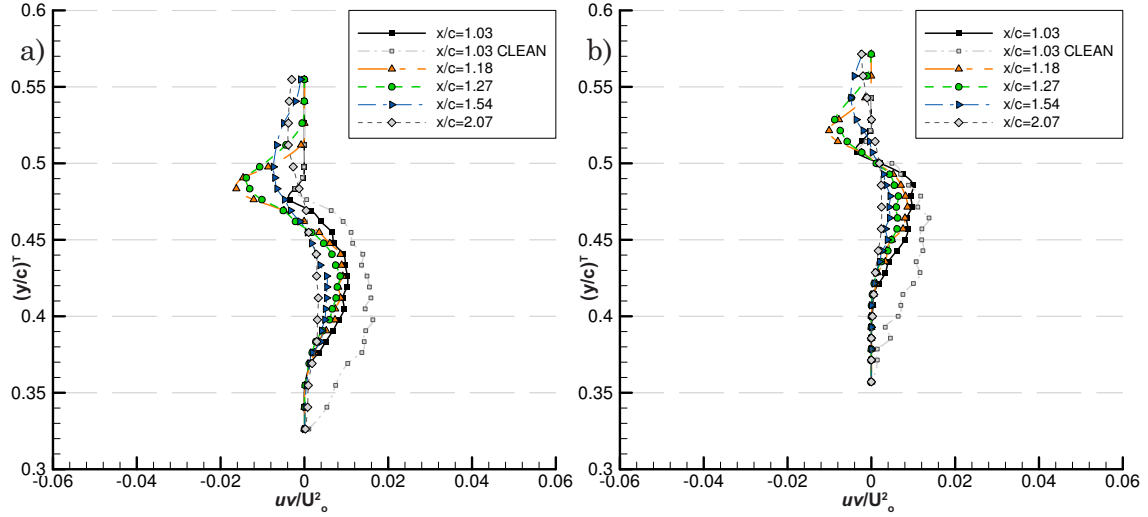
Figure 8.37 Normalized Primary Shear Stress: a) α=5˚, h/c=0.112, b) α=7˚, h/c=0.313

The reduction in uv/U^2_o for the mid range angle of incidence of the dimpled wing is shown in figure 8.37. A consistent reduction in the normalized primary shear stress for all ground clearances is seen, refer to also to figure F.25 for h/c=0.134 and h/c=0.224. This is similar for the consistently lower normalized turbulent shear stress (uu/U^2_o) in figure 8.27 for α=5˚ & 7˚, and for Tu in figure 8.17. As with uu/U^2_o, uv/U^2_o gives a greater overall reduction for the dimpled wing at α=5˚ for h/c=0.112-0.134, and a greater reduction in the bottom of the wake at α=7˚ for h/c=0.224-0.313.

The reduction of the normalized primary shear stress is greatest at α=10˚, in figure 8.38 & 8.39 for h/c=0.112, and at h/c=0.313 in figure 8.40 & 8.41. This is reflected in the significant reductions already demonstrated for the normalized wake profile and the normalized turbulent shear stress. The uv/U^2_o profile of figure 8.38 indicates for
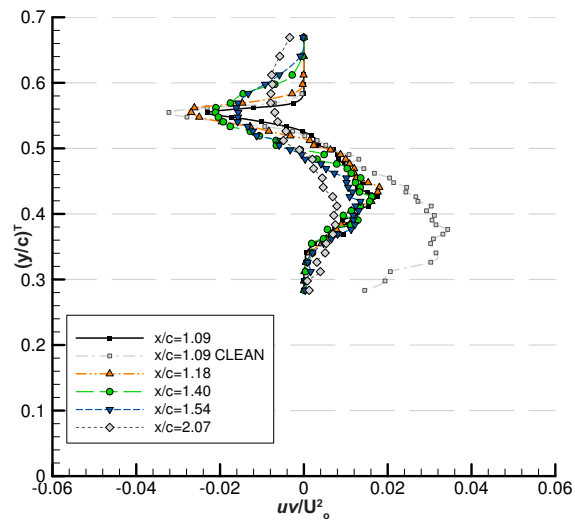
Figure 8.38 Normalized Turbulent Normal Stress: α=10˚, h/c=0.112
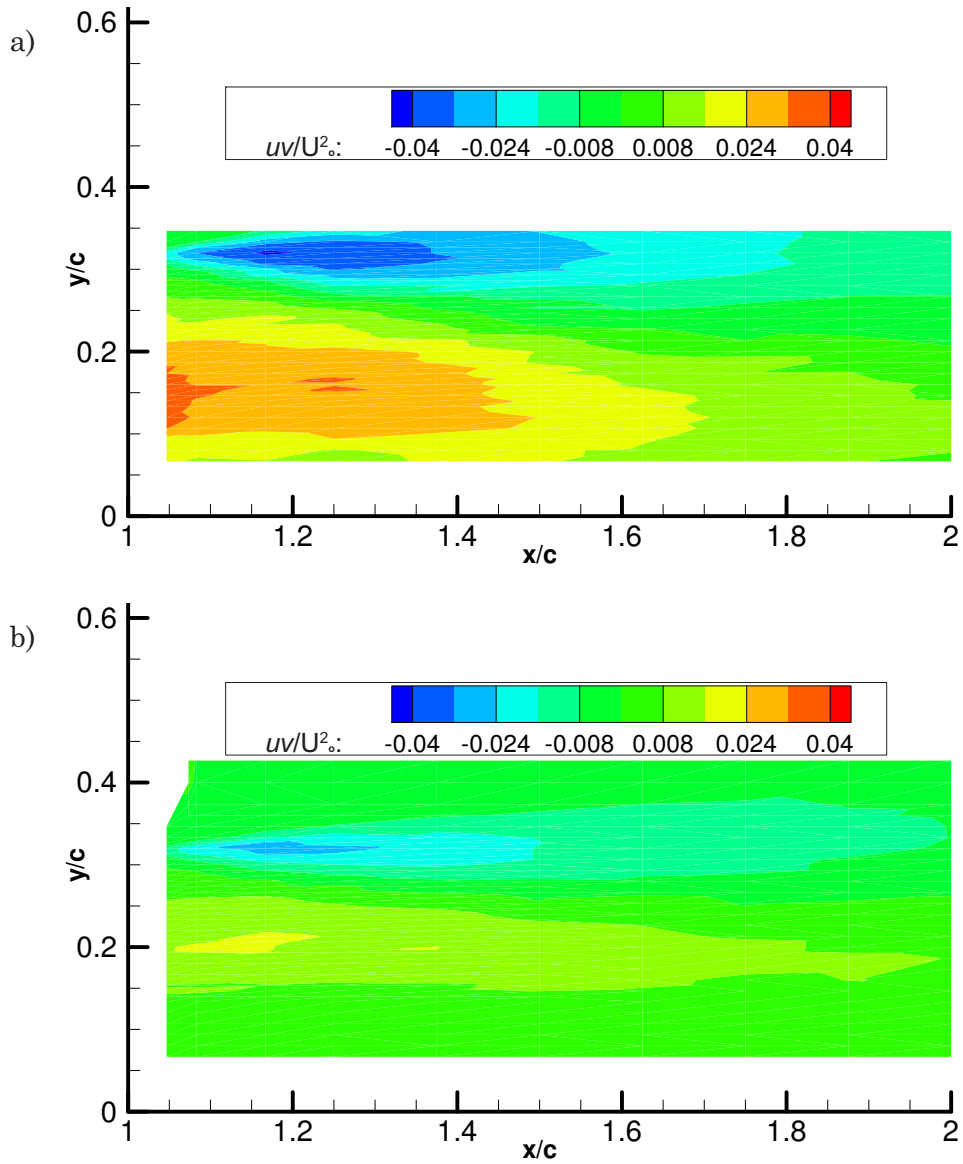
Figure 8.39 Wake Primary Shear Stress: α=10˚, h/c=112 a) Clean Wing, b) 1.5-3-23
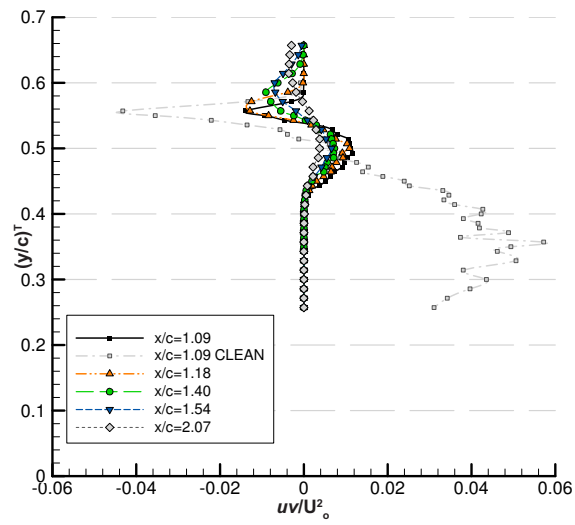
Figure 8.40 Normalized Primary Shear Stress: α=10˚, h/c=0.112
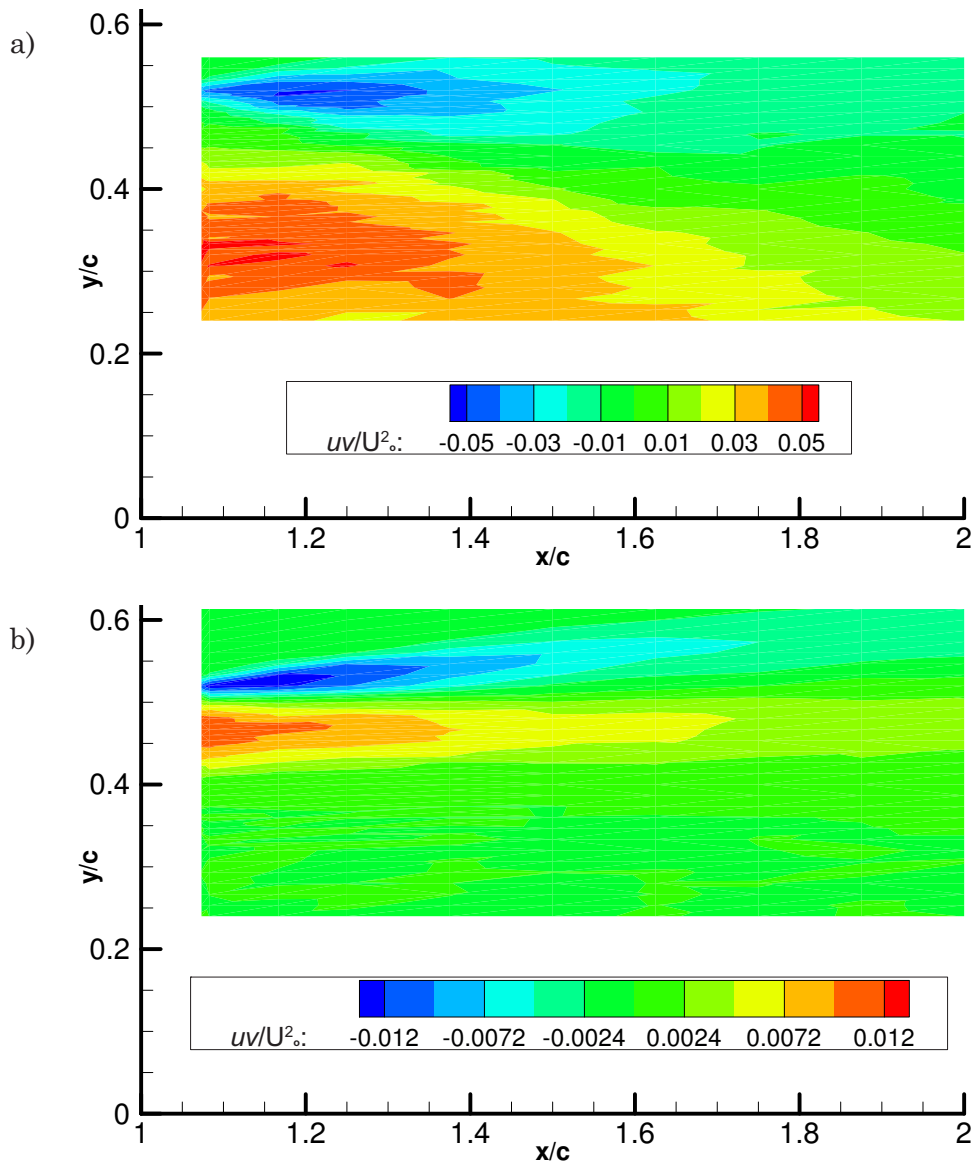
Figure 8.41 Wake Primary Shear Stress: α=10˚, h/c=313 a) Clean Wing, b) 1.5-3-23
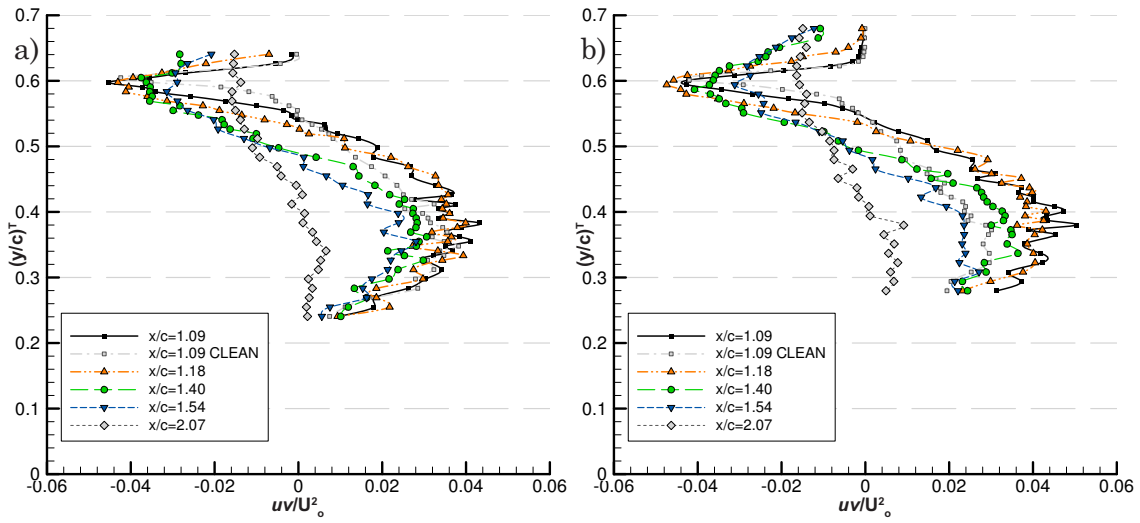
Figure 8.42 Normalized Primary Shear Stress: α=13˚ a) h/c=0.112, b) h/c=0.134
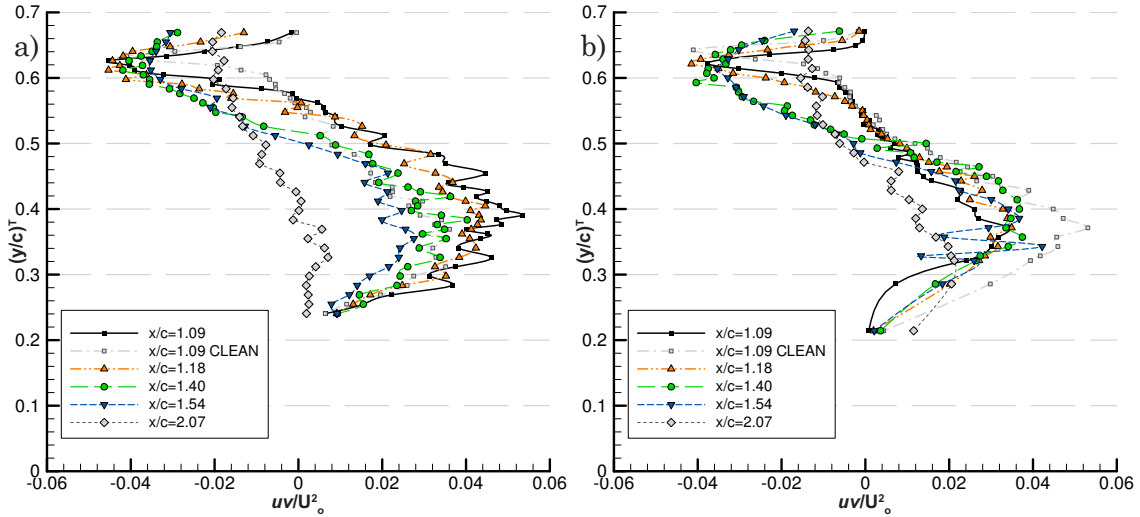
Figure 8.43 Normalized Primary Shear Stress: α=15˚ a) h/c=0.112, b) h/c=0.134

h/c=0.112 that a reduction exists for the large positive region of uv/U^2_o as a result of the dimpled airfoil. Figure 8.39 a & 8.39b shows a comparison of the uv/U^2_o contour throughout the wake. As with u/U_o, Tu and uu/U^2_o the dimpled airfoil uv/U^2_o is weaker, thinner and has less ground effect skew. Increasing the ground clearance shows that whilst the clean airfoil primary shear stress increases, the dimpled wing primary shear stress consistently decreases. Figure 8.40 and 8.41a & 8.41b shows for h/c=0.313, a substantial reduction in the primary shear stress as a result of the dimple array on the airfoil. The contours in figure 8.41a & 8.41b show the dimpled wing reduces uv/U^2_o approximately five times that of the 'clean' airfoil and there is little ground influence on the skew of the primary shear stress. As α increases to 13˚ & 15˚ in figure 8.42a, 8.42b & 8.43a the dimple array no longer reduces uv/U^2_o .

8.6 Tripwire Comparison

The state of the boundary layer on the suction (lower) surface of the airfoil was measured for Re_{chord}= 5.0x10^4, α=10° at h/c=0.112 and 0.313. The largest reductions in wake u/U$_o$, uu/U^2_o, uv/U^2_o and turbulence intensity were at the 10° angle of incidence for all ground clearances with the 1.5-3-23 wing. Figures 8.44 to 8.49 show the boundary layer measurements of u/U$_o$ and u-RMS taken normal to the wing surface (y$_{norm}$) at x/c=0.22, 0.66 and x/c=1 (the trailing edge). Three wing configurations were used: the 'clean', the 1.5-3-23 dimpled wing and the 'clean' wing with a 0.15mm tripwire at x/c=0.23, corresponding to the dimple array location.

The LDA measurements of u/U$_o$ of the boundary layer in figures 8.44a and 8.44b show a laminar boundary layer profile for the flow on the 'clean' suction surface at x/c=0.22 for h/c=0.112 and 0.313. At x/c=0.66-1 for h/c=0.112 in figures 8.45a and 8.46a the u/U$_o$ velocity profile is more stalled under the wing. At h/c=0.112 little difference exists for u/U$_o$ between the 'clean' wing, the wing with the tripwire and the 1.5-3-23 dimple array wing. For h/c=0.313 in figures 8.45b and 8.46b, a significant difference between the dimpled airfoil (u/U$_o$>0, and steadily increases away from the surface), and the 'clean' wing/boundary layer tripwire airfoil exists for h/c=0.313 at x/c=0.66 and 1 (with a large scale flow separation/reversed flow). The increased flow under the wing (i.e. figure 8.44a u/U$_o$=1.6) is not as a result of higher free stream velocity, the flow between the wing and the ground has accelerated. This is due to the flow in the wake downstream is improving due to the dimple array (reduced flow separation and higher u/U$_o$ flow recovery, seen previously in chapter 8.2-8.5). The upstream effect of the dimple array results in more flow being drawn into the gap between the wing and the ground; increasing u/U$_o$ by 0.2 in figure 8.44. The tripwire locally accelerates the flow near the surface, but does not lead to any improved flow in the gap between the wing and the ground as the dimple array flow enhancement.

The u-RMS velocity in the boundary layer of the 1.5-3-23 dimpled wing at h/c=0.112-0.313 (figure 8.47-9.49) is generally lower than either the 'clean' wing or the wing with the trip wire. As h/c increases from 0.112-0.313, the u-RMS under the wing also increases. The increases in u-RMS for the dimpled airfoil is not as large as the 'clean' or tripwire airfoils. Both 'clean' and trip wire wings double their peak u-RMS values (which are also further from the surface) and also increase in size from h/c=0.112-
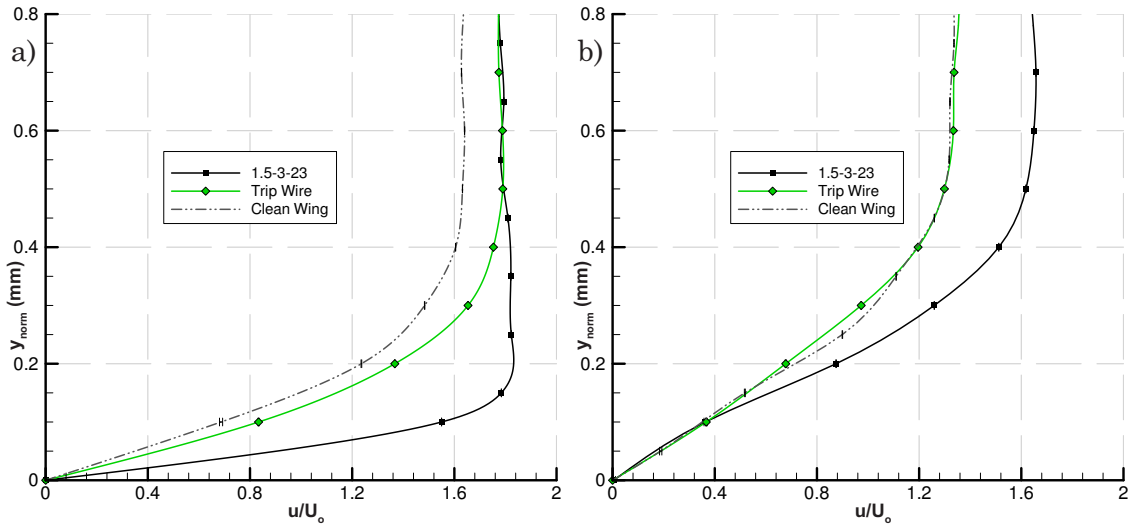
Figure 8.44 Boundary Layer u/U$_o$ for α=10˚, x/c=0.22 (Re$_C$=5x10^4) a) h/c=0.122 b) h/c=0.313
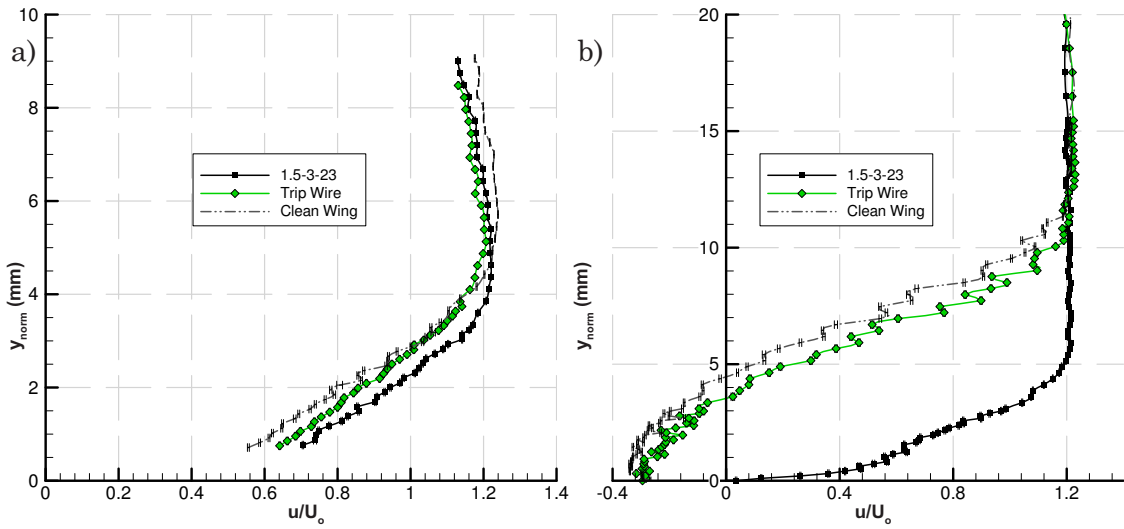
Figure 8.45 Boundary Layer u/U$_o$ for α=10˚, x/c=0.66 (Re$_C$=5x10^4) a) h/c=0.122 b) h/c=0.313
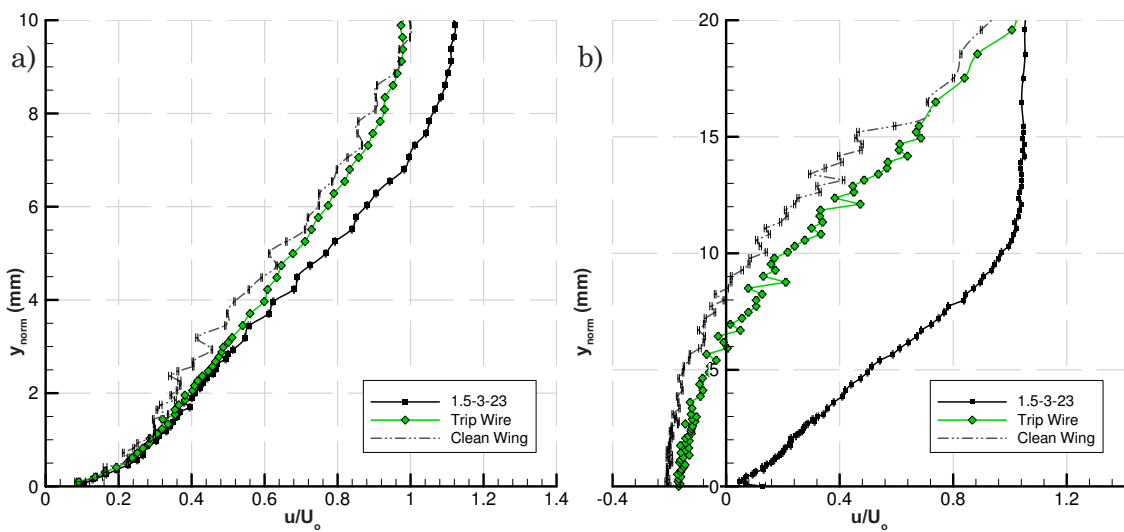

Figure 8.46 Boundary Layer u/U$_o$ for α=10˚, x/c=1 (Re$_C$=5x10^4) a) h/c=0.122 b) h/c=0.313

0.313, compared to the dimple array airfoils u-RMS increases by only 0.5m/sec at x/c=0.66-1 (0.25m/sec at x/c=0.22).

From figure 8.44a, the u/U_o profile at x/c=0.22 for h/c=0.112 shows the dimple array is causing a more turbulent boundary layer profile, yet in figure 8.47a the 1.5-3-23 wing boundary layer maximum u-RMS value is approximately 90% lower than the 'clean' wing value (3.8m/sec 'clean', 0.2m/sec 1.5-3-23). The u/U_o boundary layer profile at x/c=0.22, h/c=0.313 in figure 8.44b for the dimpled wing is similar to the laminar profile of the 'clean' and tripwire wings; yet the improvement in the wake flow field is greater. This is suggests at h/c=0.313 the separation point is now optimally placed after the dimple array where the most gain is to be made (as in chapter 6) and u-RMS on the surface (in figure 8.47b) is significantly lower; 1m/sec at y_{norm}=0.22mm. Whilst there is some improvement at h/c=0.112 the ground influence on the airfoil surface dwarfs the flow recovery ability that the dimples can provide. Indeed u-RMS is higher on the surface at h/c=0.112 in figure 8.47; 3.8m/sec at y_{norm}=0.1mm.

The trip wire diameter (0.15mm) results in a boundary layer protrusion of $0.25\delta_{BL}$ at h/c=0.112, and $0.21\delta_{BL}$ at h/c=0.313 for boundary layer thickness $\delta_{BL}\approx0.6$mm (h/c=0.112) and $\delta_{BL}\approx0.7$mm (h/c=0.313) from figure 8.44a and 8.44b. At h/c=0.112 the boundary layer tripped by the wire tends toward the same effect that the dimple array has on the flow field, as both produce turbulent flow in the (previously) laminar boundary layer; causing it to remain attached to the surface longer. However the difference between u/U_o and u-RMS is more pronounced at h/c=0.313 for the dimple array with respect to the trip wire. In this instance the large scale flow separation is minimized (seen previously in chapter 8) to a significantly greater extent with the dimple array than the trip wire.

The organised, regularly shed vortices from the dimple array mix the boundary layer in a more structured and efficient manner than simply tripping the boundary layer to turbulent with the tripwire. This yields a greater improvement to the flow at x/c=0.66-1. The higher trip wire u-RMS velocity indicates this as there is increased shearing in the boundary layer due to the trip wire protrusion. The ordered shedding of the vortices in the dimple array is seen as the u-RMS augmentation near the surface (y_{norm}<6mm at x/c=0.66 and y_{norm}<10mm at x/c=1) is more consistent than the large scale u-RMS fluctuations that propagate y_{norm}=16mm and y_{norm} >20mm from the surface of the airfoil at x/c=0.66 and x/c=1 respectively for h/c =0.313 (y_{norm}/c=0.21 and y_{norm}/c>0.266 for 75mm airfoil chord at Re_{chord}=5x10^4).
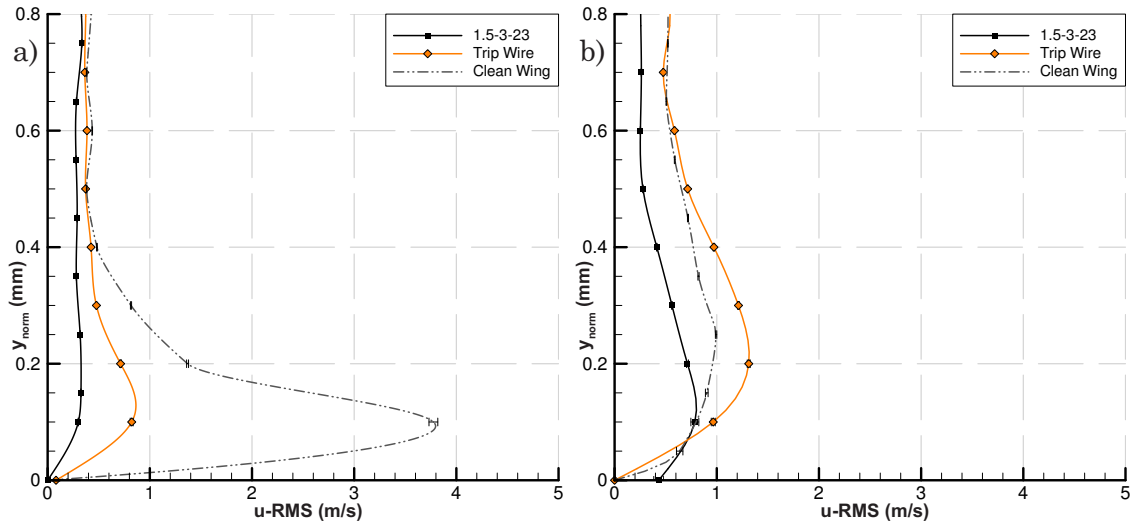
Figure 8.47 Boundary Layer u-RMS for α=10˚, x/c=0.22 (Re$_C$=5x10^4) a) h/c=0.122 b) h/c=0.313
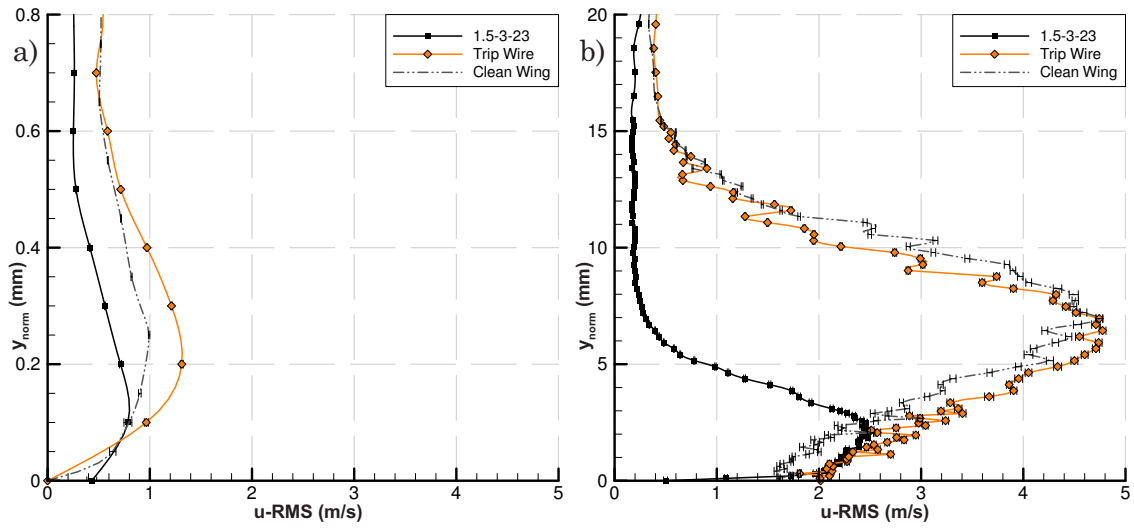
Figure 8.48 Boundary Layer u-RMS for α=10˚, x/c=0.66 (Re$_C$=5x10^4) a) h/c=0.122 b) h/c=0.313
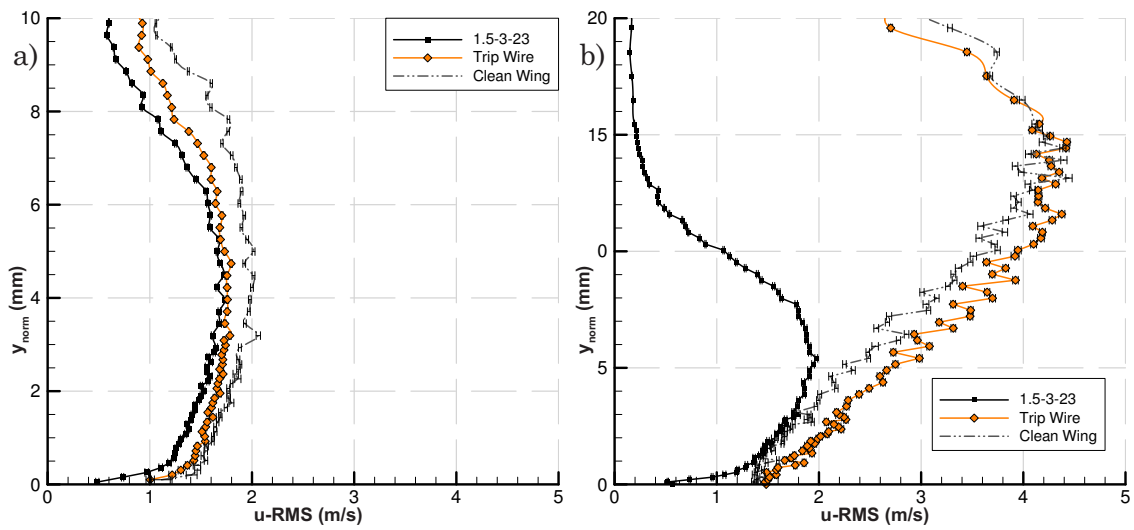
Figure 8.49 Boundary Layer u-RMS for α=10˚, x/c=1 (Re$_C$=5x10^4) a) h/c=0.122 b) h/c=0.313

8.7 Wingtip Vortex

The dimple array influence on the wake and possible effects this has on the vortex shape, size and decay is deemed of interest, particularly in moving towards future more practical automotive applications (Bearman et al. 1988, Carr 1988 and Zhang & Senior 2004). The wingtip vortex for an inverted wing in ground effect with an endplate is shown in figure 8.50, where two counter-rotating vortices form. The large main vortex forms due to the wing suction surface, endplate and ground interaction. The second weaker vortex forms from the wing upper surface and endplate interaction.

8.7.1 Experimental Setup

Reynolds Number:
$Re_{chord}=5.0 \times 10^{4}$
$Re_{H}=2.8 \times 10^{5}$

Endplate thickness = 2mm
Trailing Edge chamfer = 15°
Leading Edge radius = 1mm

95mm

45mm

$\alpha = 10°$

3.5mm

10mm

280mm

Measurement Plane

Secondary Vortex

130mm

Main Vortex

h/c=0.112

225mm

x=0, Leading Edge
y=0, Moving Ground
z=0, Endplate Outer

x/c=2.07

x/c=1.27

U_o

y, v, Ω_y

$\mathbf{x, u, \Omega_x}$

z, w, Ω_z
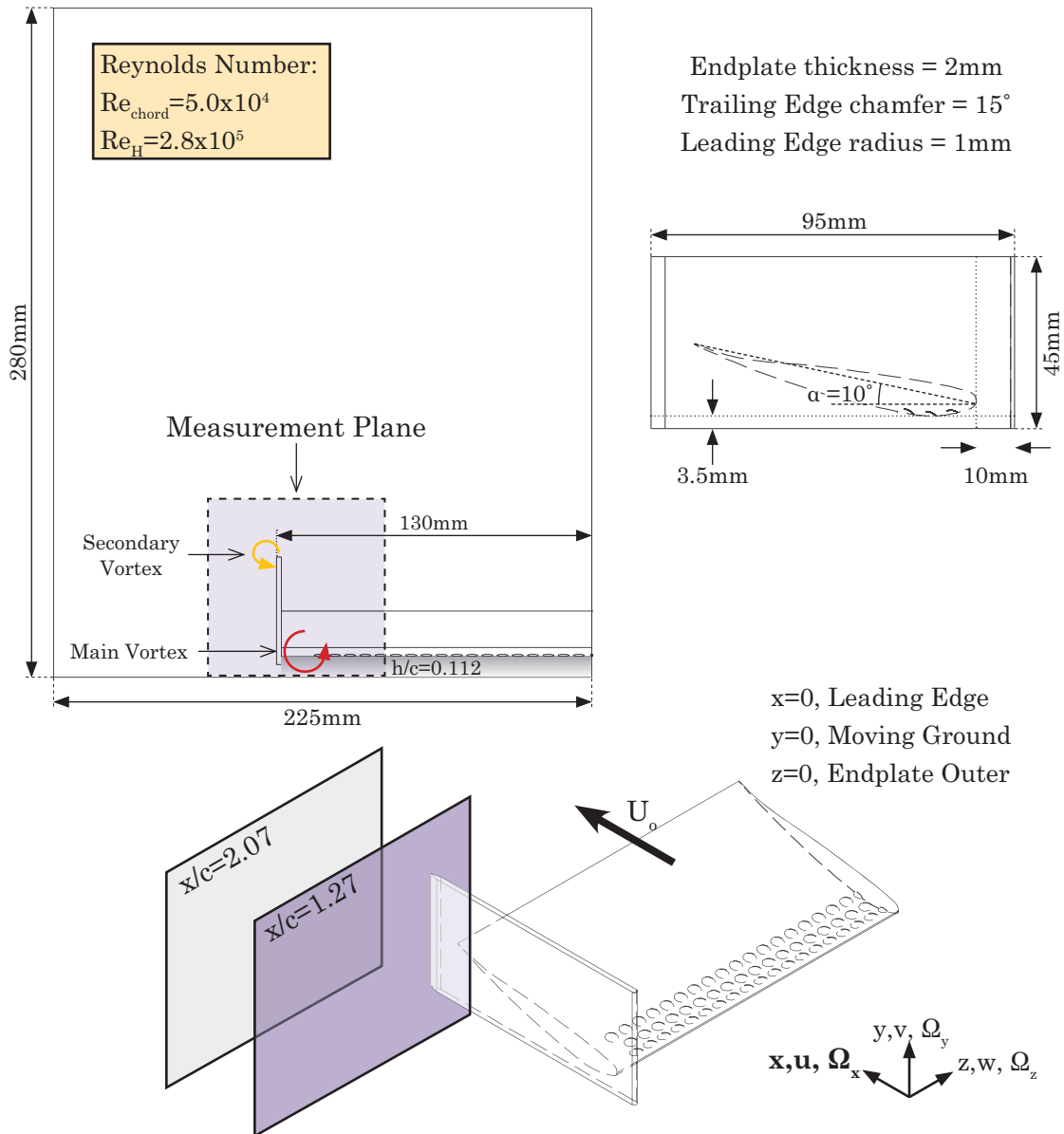
Figure 8.50 Tyrrell026 Airfoil Wingtip Vortex Setup

An acrylic endplate was attached to the Tyrrell026 airfoil (see figure 8.50), for h/c=0.112 for α=10°. Measurements were taken on the 'clean' wing with no dimples and then repeated with the same 1.5-3-23 dimple airfoil used previously. The endplate was offset from the centre of the test section so that the centre of the wingtip vortex would be in the middle of the tunnel (see figure 8.50), and have the least influence from the test section walls. The clean and dimpled wing used for the wingtip vortex experiments used the existing wing sections used previously, and simply retracted through the test section side wall. Three-dimensional LDA measurements were taken on two cross flow planes, with the setup shown in figure 8.50 The wake and wingtip vortex study focused on measuring various parameters; normalized streamwise flow (u/U_o), streamwise vorticity (Ω_x), turbulence intensity and the normalized turbulent normal stress (uu/U^2_o) in two spanwise planes located x/c=1.27 and x/c=2.07.

The normalized streamwise velocity (u/U_o) plotted at x/c=1.27 in figures 8.51 to 8.52 and shows two significant differences with the dimpled wing. These correspond to significant changes in the wake behind the wing (outlined in chapter 8.2-8.6) on the size and shape of the lower wingtip vortex. At x/c=1.27 the 'clean' wing wake profile's thickness, figure 8.51, covers z=0.002m-0.026m for y>0.04m, whereas for the dimpled wing, figure 8.52, (1.5-3-23 array), this reduces to z=0.012-0.026m. This allows the region where u/U_o>0.86 to increase considerably under the dimpled wing. The improvement in the flow under the wing, with the reduction in the wake size as a result of the dimple array, allows the lower wingtip vortex to increase in size and move in toward the remaining wake more, see figure 8.59a and figure 8.60a. The increase in size of the dimpled wing wingtip vortex coincides with reducing the core velocity in the vortex from u/U_o=0.43 (clean) to u/U_o=0.14 (dimpled). Downstream at x/c=2.07 in figure 8.54, the dimpled wing wake is significantly smaller; however the lower wingtip vortex of the dimpled wing is larger than the clean wing, figure 8.53. This is evident in the pathlines shown in figure 8.59b & figure 8.60b. The velocity in the vortex core of the clean wing vortex of u/U_o=0.57, is noticeably higher than u/U_o=0.29 for the dimpled wing.

The streamwise vorticity, Ω_x, in figures 8.55 to 8.58, is not significantly greater for either wing surface. The dimpled airfoil's lower wingtip vortex at x/c=1.27 figure 8.55 is larger than the 'clean' in figure 8.56, but the intensity is similar. The increased
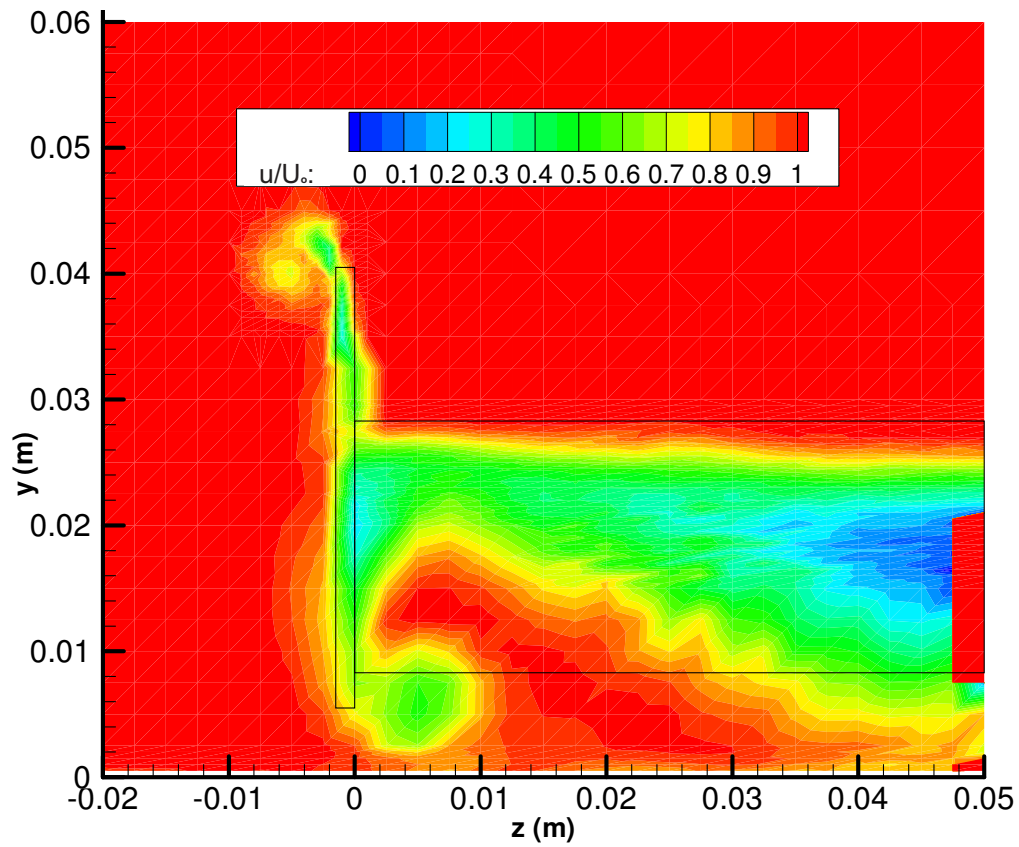
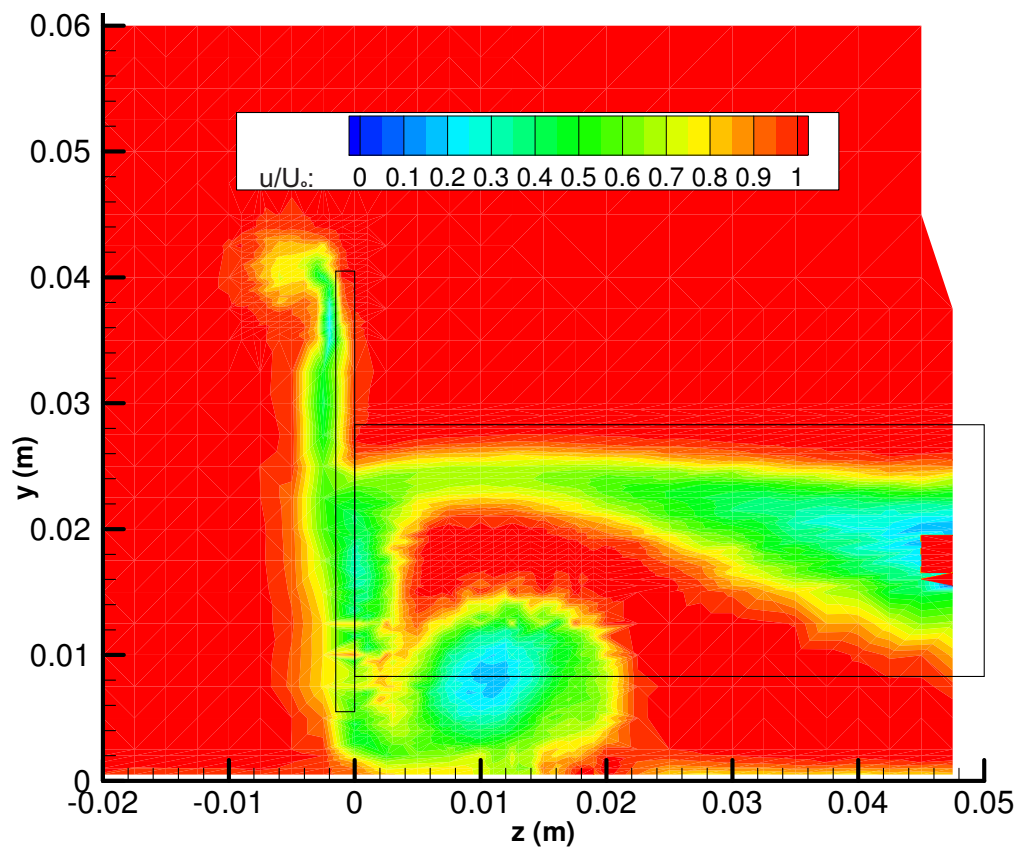Figure 8.51 Wingtip Vortex u/U$_o$ for Clean Wing: α=10˚ at x/c=1.27 plane

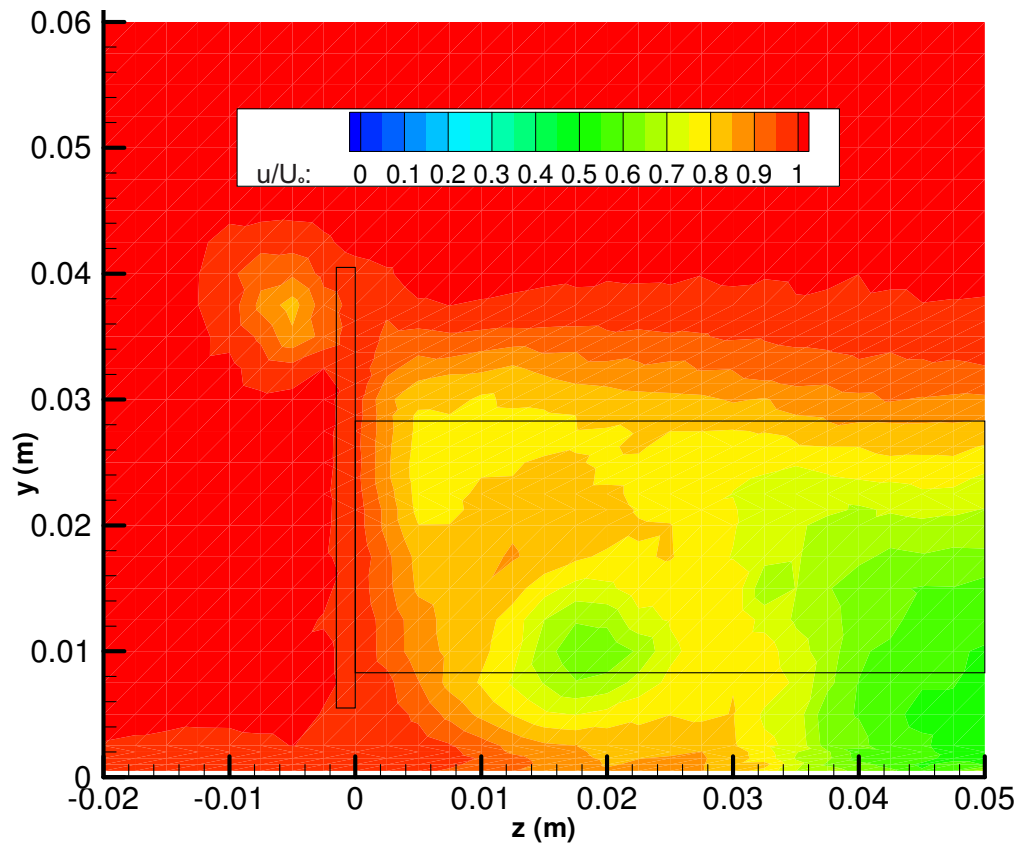Figure 8.52 Wingtip Vortex u/U$_o$ for **1.5-3-23 Wing**: α=10˚ at x/c=1.27 plane

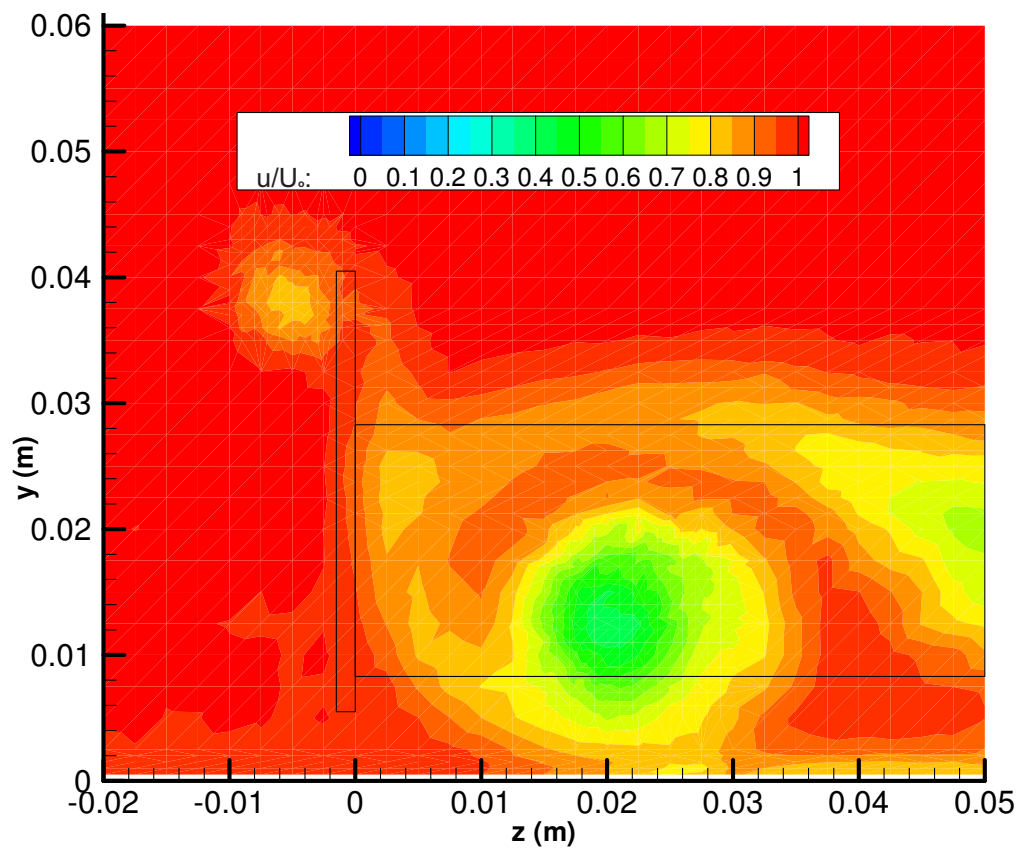Figure 8.53 Wingtip Vortex u/U_o for Clean Wing: $\alpha=10°$ at x/c=2.07 plane

Figure 8.54 Wingtip Vortex u/U_o for **1.5-3-23 Wing**: $\alpha=10°$ at x/c=2.07 plane

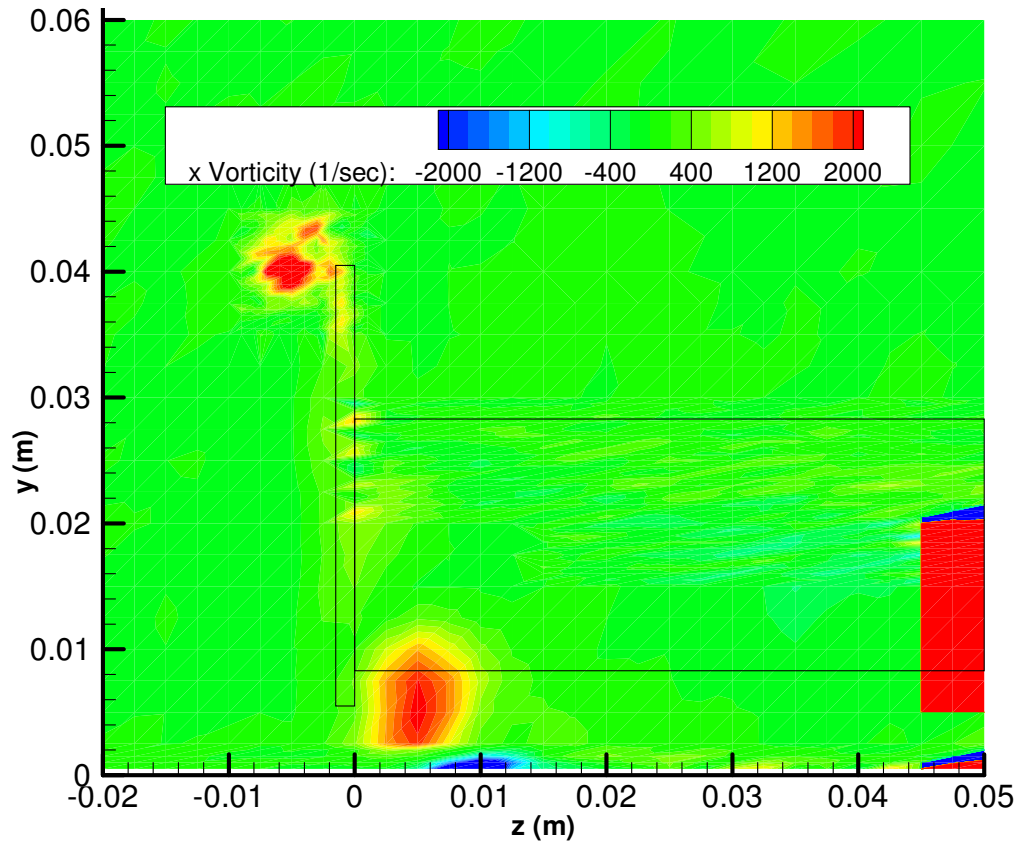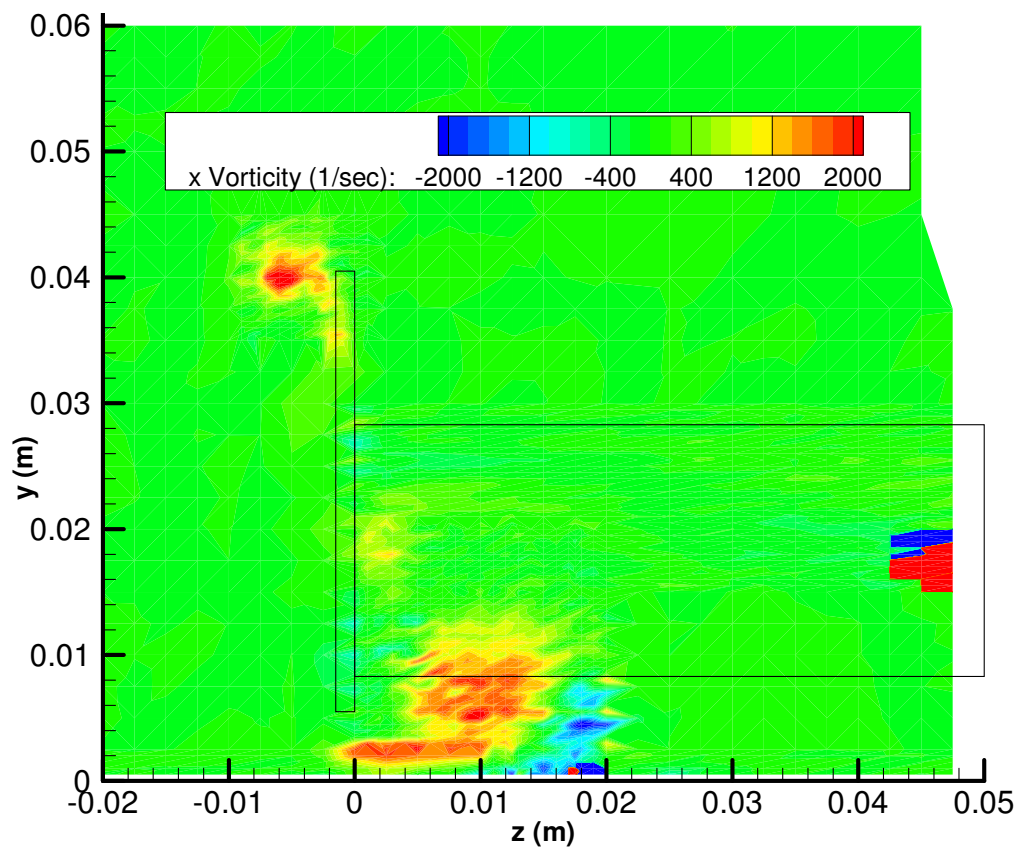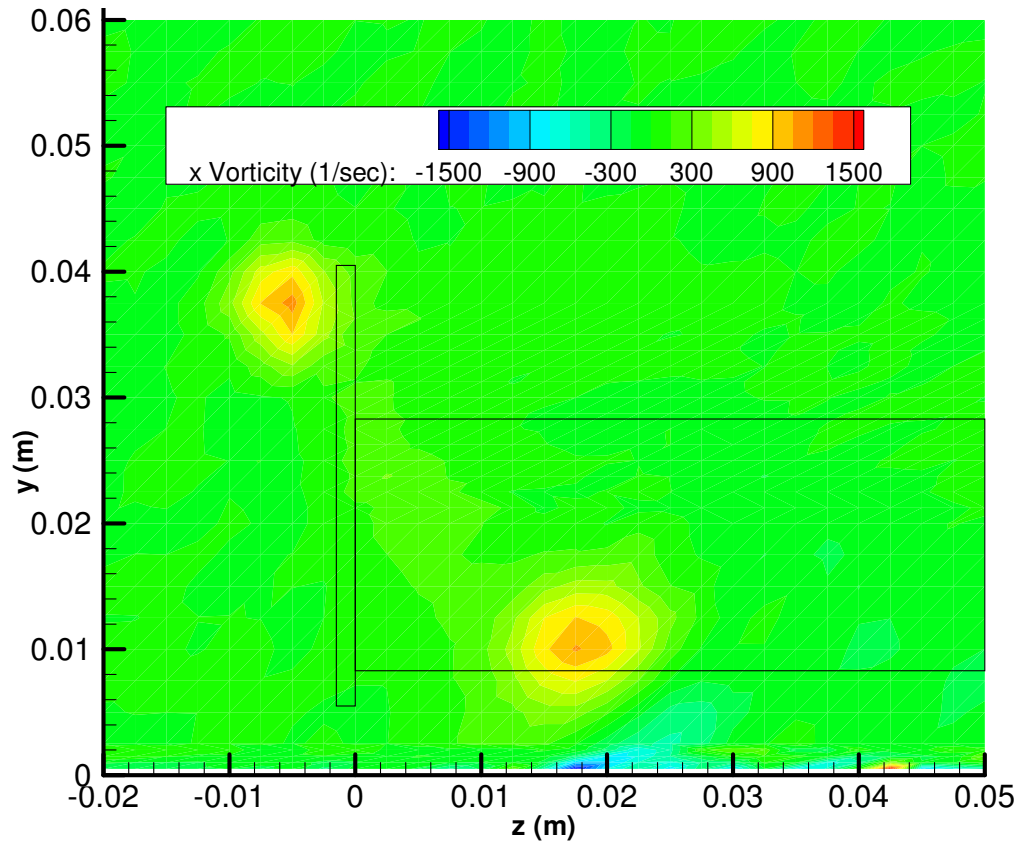Figure 8.55 Wingtip Vortex Ω_x for Clean Wing: α=10˚ at x/c=1.27 plane

Figure 8.56 Wingtip Vortex Ω_x for **1.5-3-23 Wing**: α=10˚ at x/c=1.27 plane

Figure 8.57 Wingtip Vortex Ω_x for Clean Wing: α=10° at x/c=2.01 plane
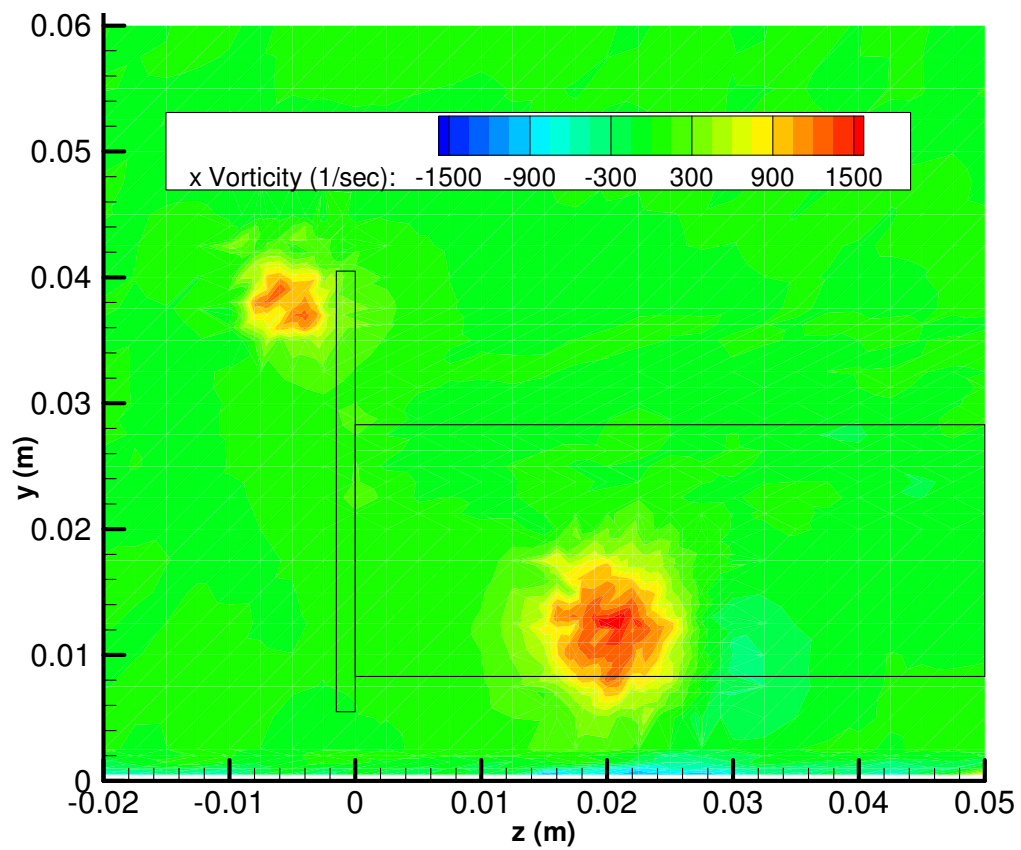
Figure 8.58 Wingtip Vortex Ω_x for **1.5-3-23 Wing**: α=10° at x/c=2.01 plane

size of the dimpled wing's wingtip vortex at x/c=1.27 has more influence on the moving ground plane, with an extended region of $-\Omega_x$ to y=0.008m. At x/c=2.07, the lower wingtip vortex of the dimpled wing, figure 8.58, is slightly stronger (Ω_x=1750sec^{-1} 'dimpled' and Ω_x=1530sec^{-1} 'clean'), thus the size and strength of the dimpled wingtip vortex decays less.
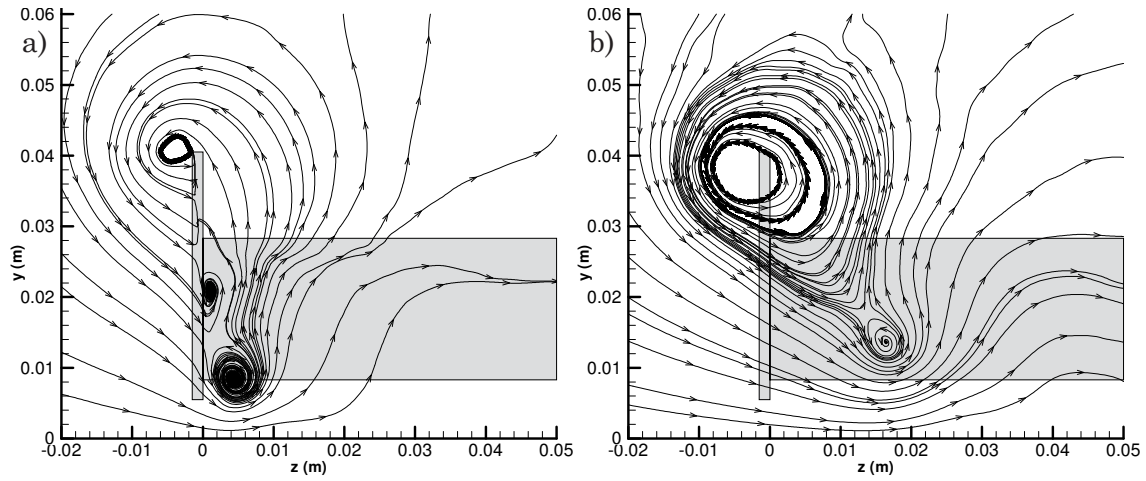
Figure 8.59 Tyrrell026 Clean Wing: Pathlines in spanwise planes at a) x/c=1.27, b) x/c=2.07

Figures 8.61 to 8.64 show the turbulence intensity for the spanwise planes at x/c=1.27 and x/c=2.07, which are not dissimilar in shape to those of u/U$_o$ in figures 8.51 to 8.54. The clean wing wake in figure 8.61 has a turbulence intensity of 5% throughout most of its central structure, which reduces to approximately 2.5-3% in the dimpled wing wake. The lower wingtip vortex increases in size and turbulence intensity (1.5% clean to 4% dimpled) as a result of the dimple array. The presiding flow feature in figure 8.62 as a result of the dimple array is the reduced turbulence intensity (<1%) that separates the wake and the wingtip vortex. At x/c=2.07 in figure 8.63 and 8.64, the clean wing wake's large central structure corresponds to a turbulence intensity of 1.8%, which diminishes in size and intensity to 1% with the dimple array. The downstream dimpled wing vortex core remains quite high at 1.6% and is localized compared to the clean wing core.

The normalized turbulent normal stress (uu/U^2_o) in figures 8.65 to 8.68 shows two quite high regions where uu/U^2_o>0.06, the larger corresponding to the separated flow in the wake, and the small, thinner structure as a result of the trailing edge shear layer. These two regions still remain in the dimpled wing wake at x/c=1.27 in figure 8.61, however are substantially lower intensity, uu/U^2_o<0.05 and a large region of

uu/U^2_o <0.01 separates the wake and the vortex. The main wingtip vortex core in figure 8.66 has uu/U^2_o≈0.045 for the clean wing, whereas uu/U^2_o≈0.015 for the dimpled wing. The dimple wing vortex core also is surrounded by a ring of higher turbulent normal stress. At x/c=2.07 in figure 8.67, the clean wing wake a higher region of turbulent normal stress exists in the region of 0.03<z<0.05 and 0<y<0.01. This corresponds to the downstream skew of the wake as the wing and moving ground boundary layers merge (see figure 8.39) which is less of an issue with the dimple array. However rather than be a consistent band of higher uu/U^2_o it is biased towards the remaining weaker wingtip vortex core. For the dimpled wing turbulent normal stress in figure 8.68, this same region (0.03<z<0.05 and 0<y<0.01) is minimal. Yet uu/U^2_o in the remaining wingtip vortex core is higher, indicating it is no longer damped or impeded by the higher 'clean' airfoil wake turbulent normal stress.
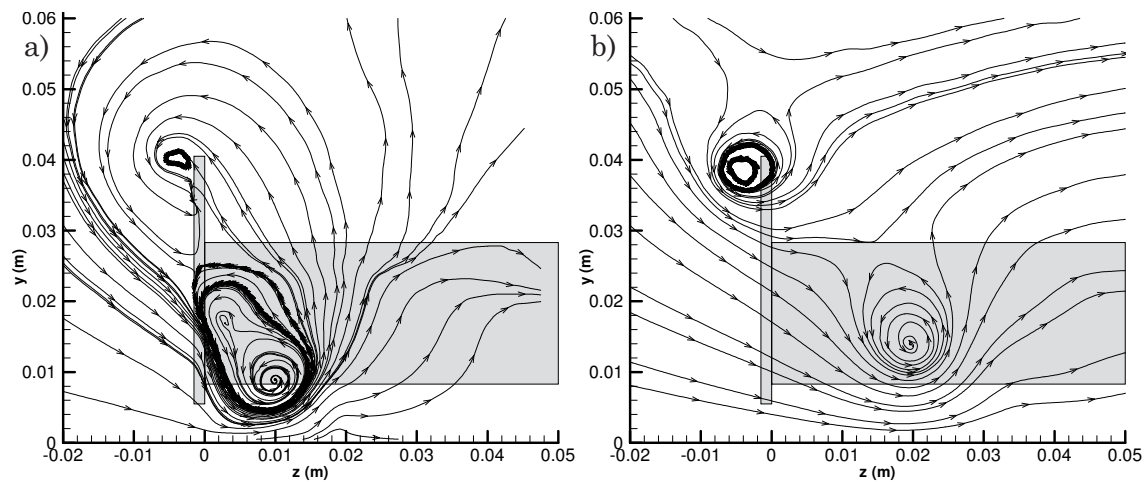
Figure 8.60 Tyrrell026 1.5-3-23 Wing: Pathlines in spanwise planes at a) x/c=1.27, b) x/c=2.07

Therefore the wingtip vortex investigation of the Tyrrell026 wing with an endplate has indicated additional spanwise flow improvements as a result of the dimple array and the implications it may have on the wingtip vortex in a practical application. Most notable in figures 8.51 to 8.54, is the consistently thin wake 'thickness'. Klausmeyer (1996) and Angele (2005) showed that with standard boundary layer protruding vortex generators, the counter-rotating vortex pairs that are formed produce upflow and downflow velocity components which may propagate downstream, see figure 8.69. Therefore by measuring the cross flow plane it has been shown that this effect is negligible.
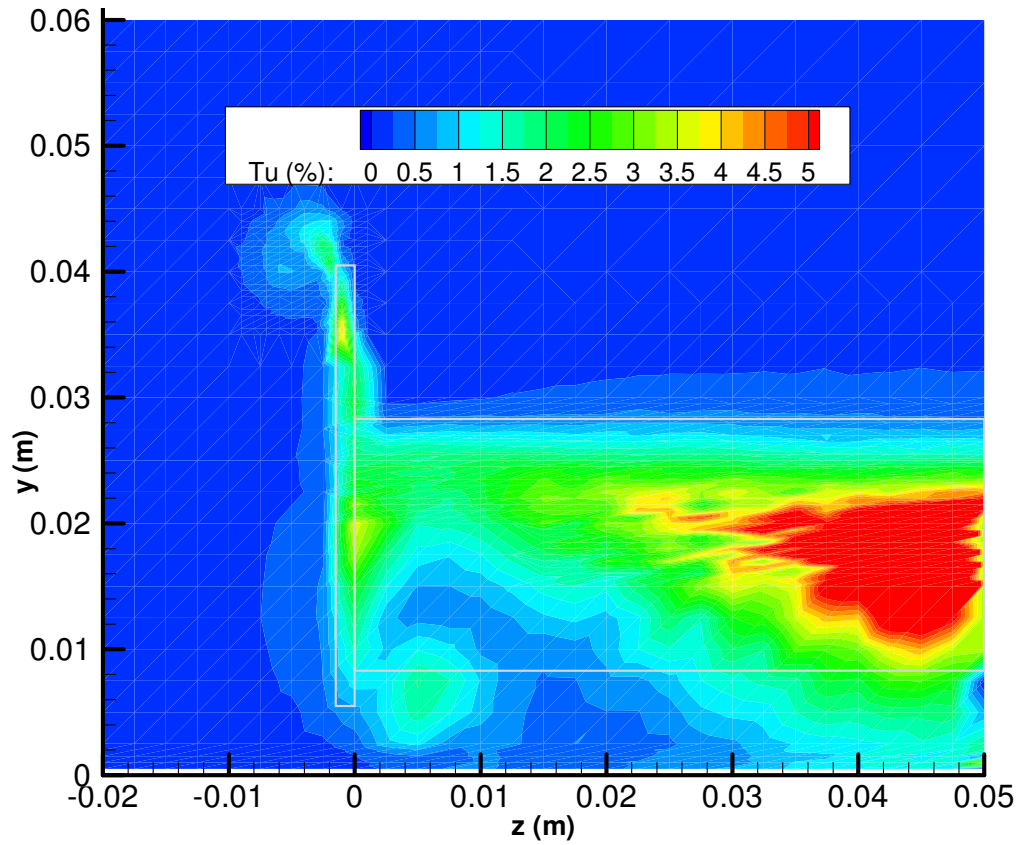
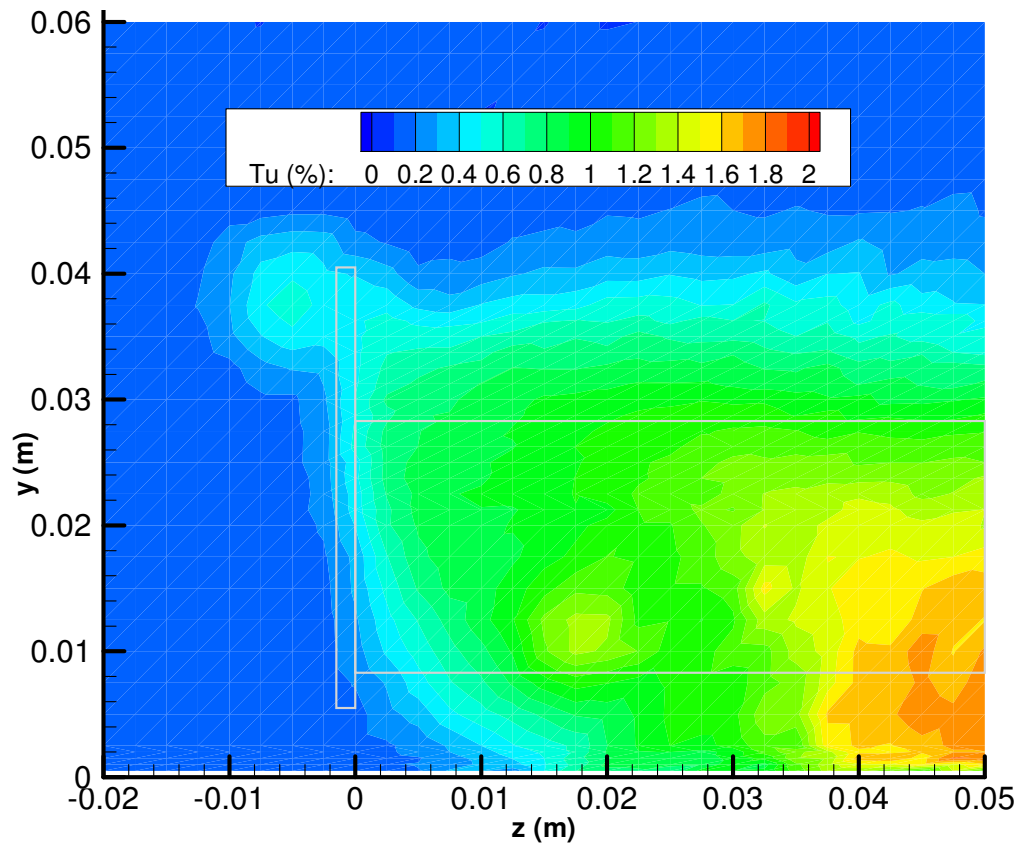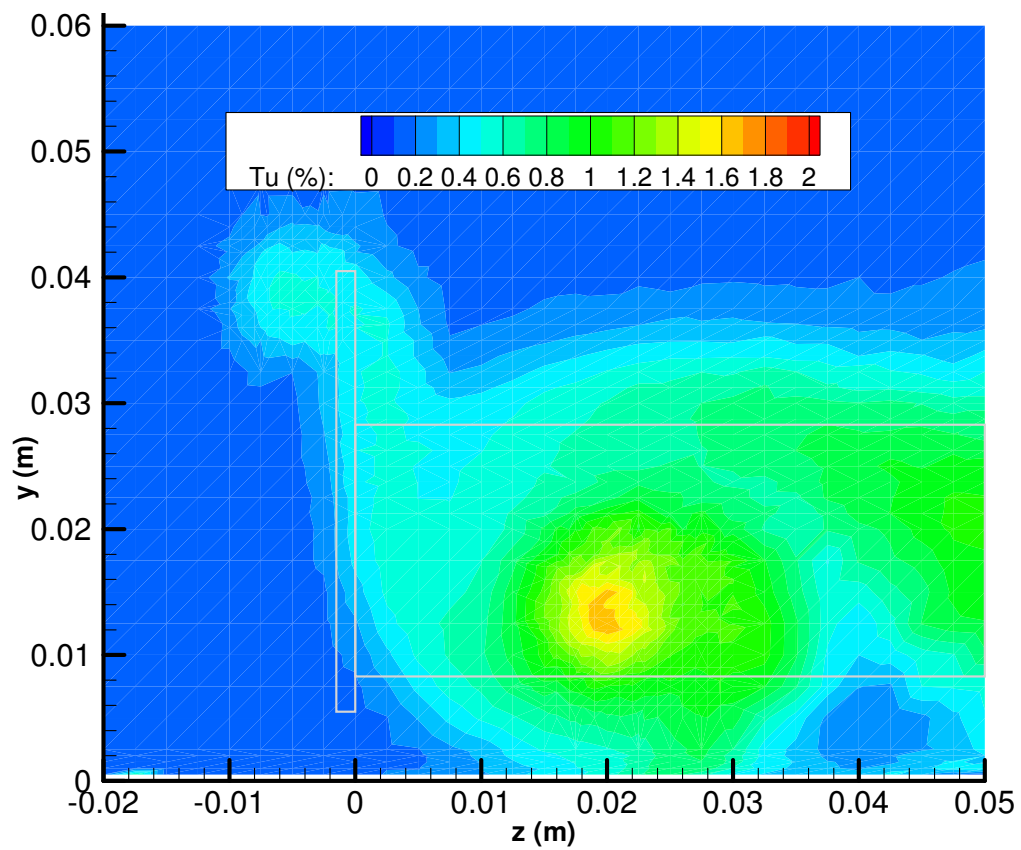Figure 8.61 Wingtip Vortex Turbulence Intensity for Clean Wing: α=10° at x/c=1.27 plane
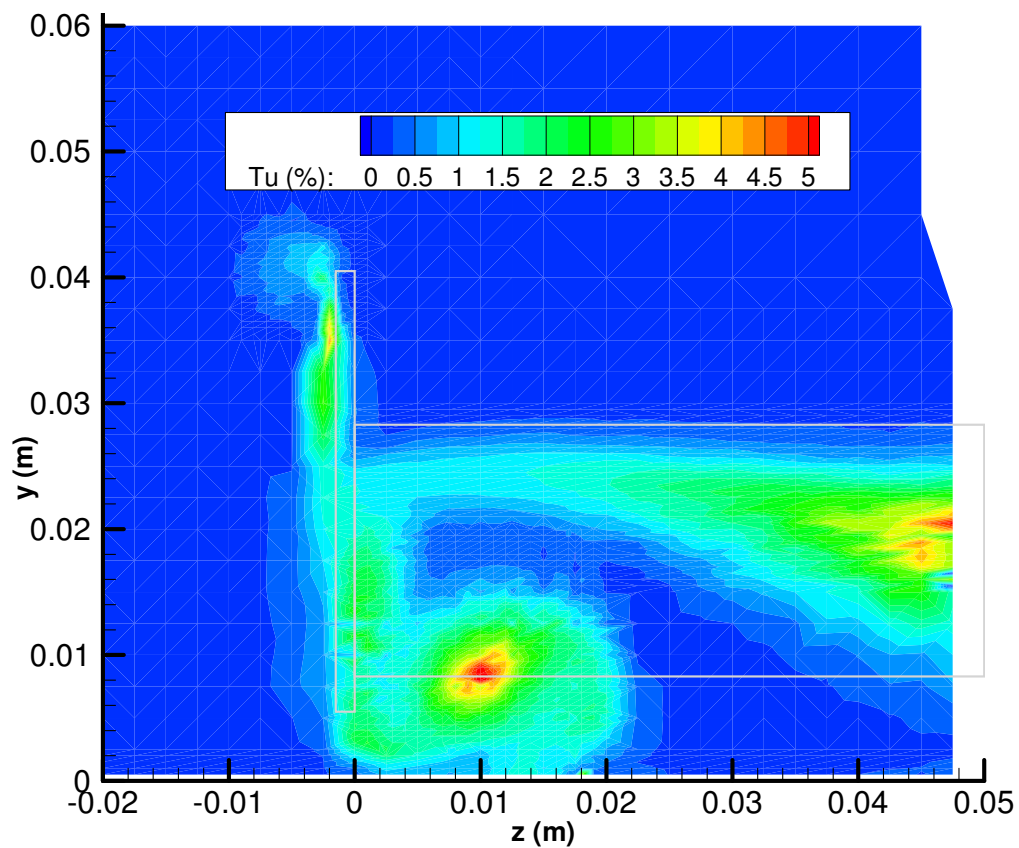
Figure 8.62 Wingtip Vortex Turbulence Intensity for **1.5-3-23 Wing**: α=10° at x/c=1.27 plane

Figure 8.63 Wingtip Vortex Turbulence Intensity for Clean Wing: α=10° at x/c=2.07 plane

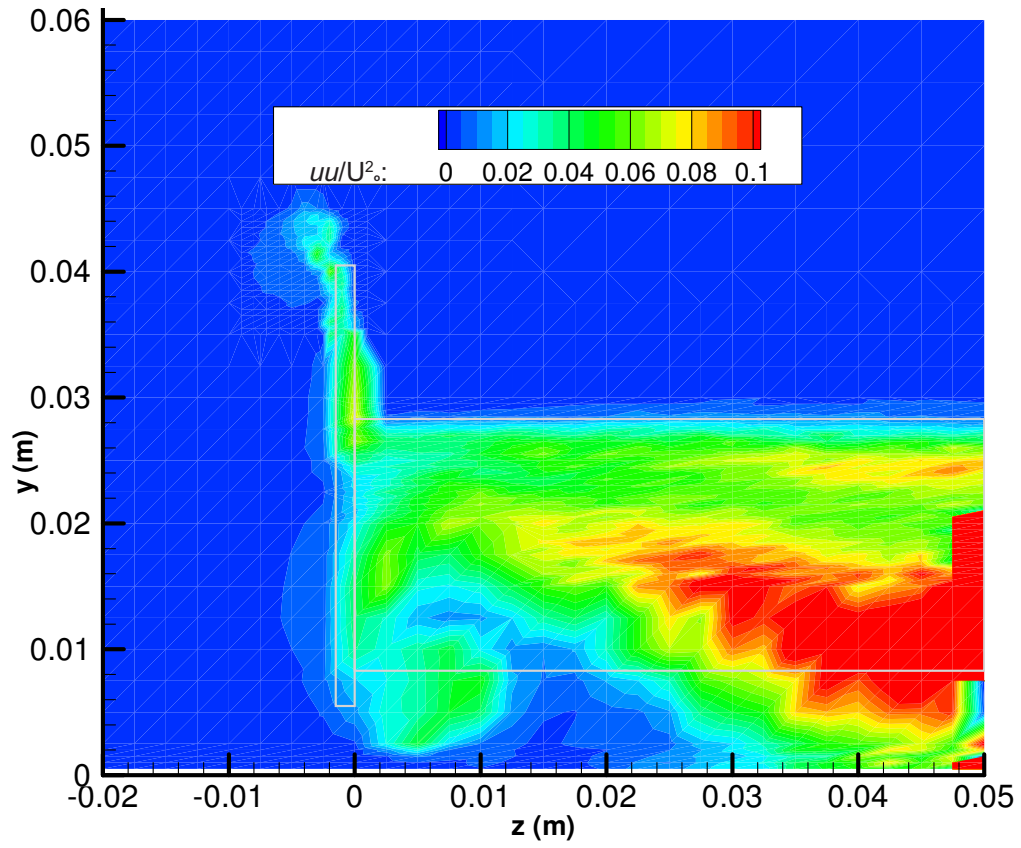Figure 8.64 Wingtip Vortex Turbulence Intensity for **1.5-3-23 Wing**: α=10° at x/c=2.07 plane

Figure 8.65 Wingtip Vortex Normal Stress (uu/U$_o^2$) for Clean Wing: α=10° at x/c=1.27 plane
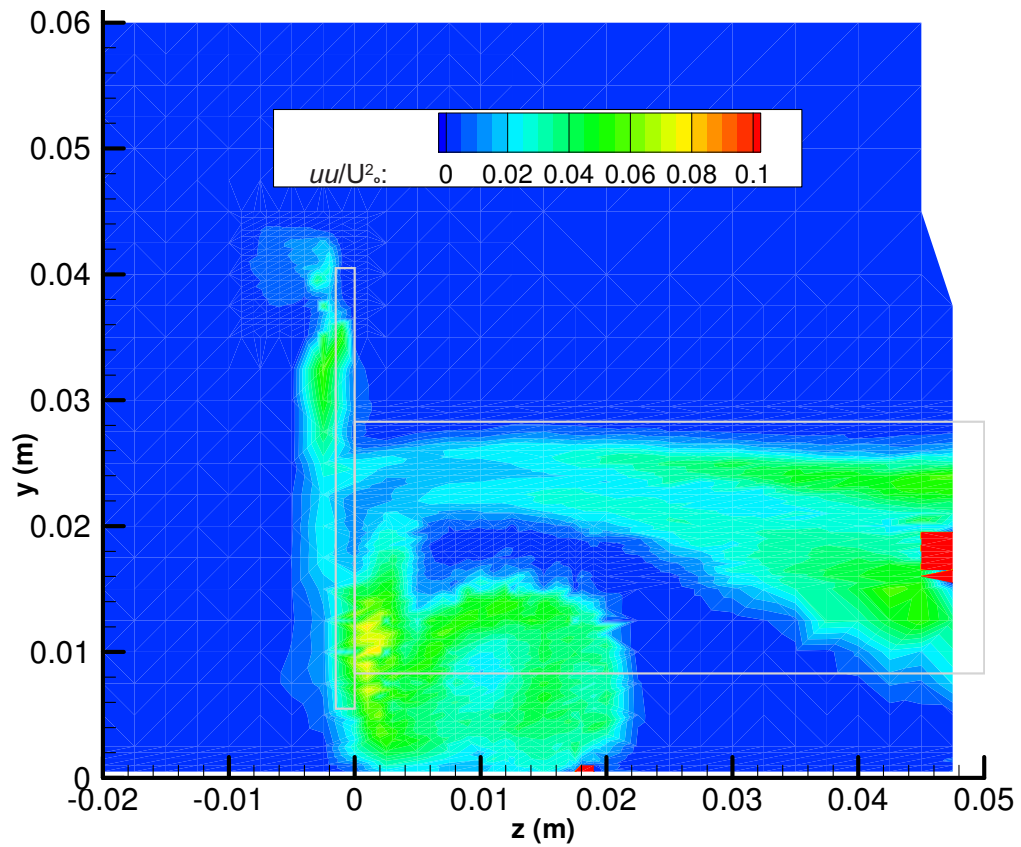
Figure 8.66 Wingtip Vortex Normal Stress (uu/U$_o^2$) for **1.5-3-23 Wing**: α=10° at x/c=1.27 plane
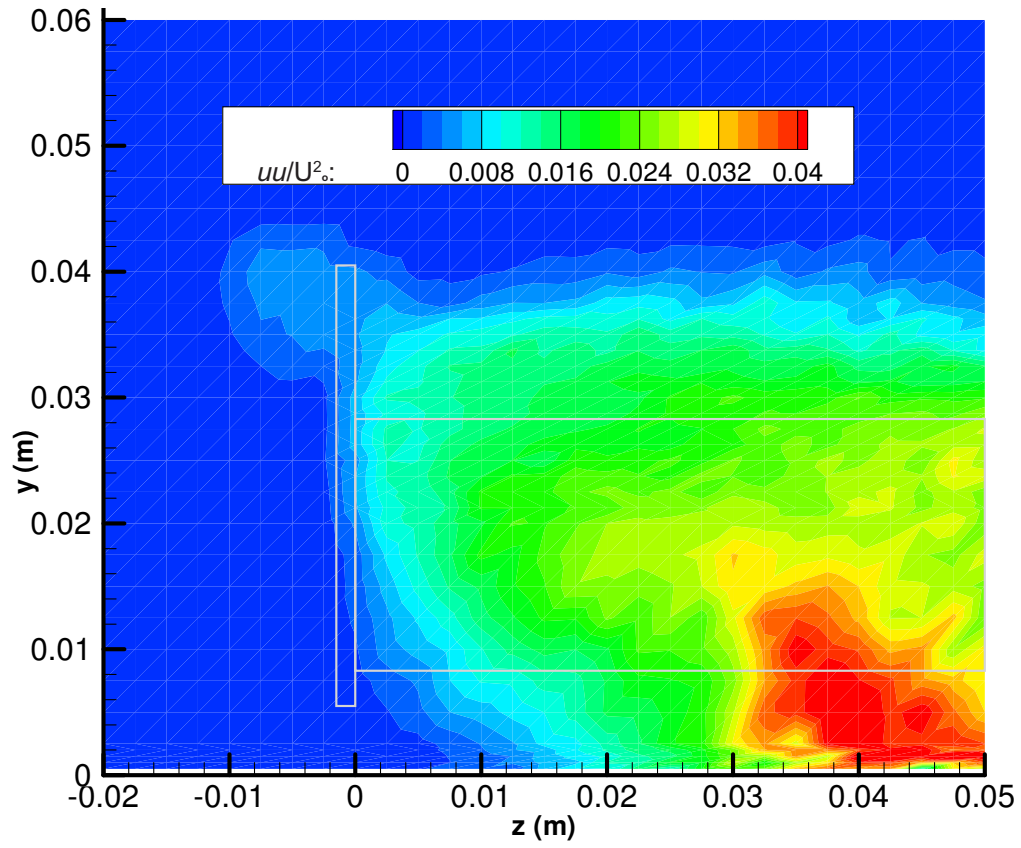
Figure 8.67 Wingtip Vortex Normal Stress (uu/U_o^2) for Clean Wing: α=10° at x/c=1.27 plane
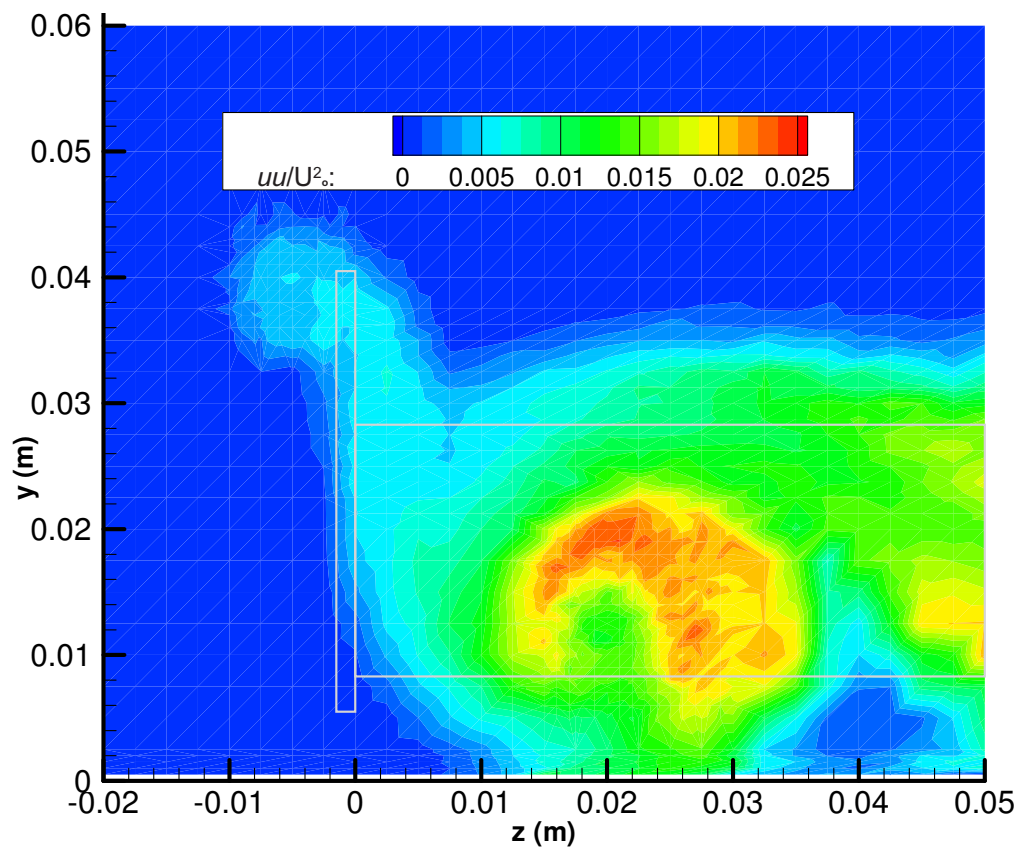
Figure 8.68 Wingtip Vortex Normal Stress (uu/U_o^2) for **1.5-3-23 Wing**: α=10° at x/c=1.27 plane
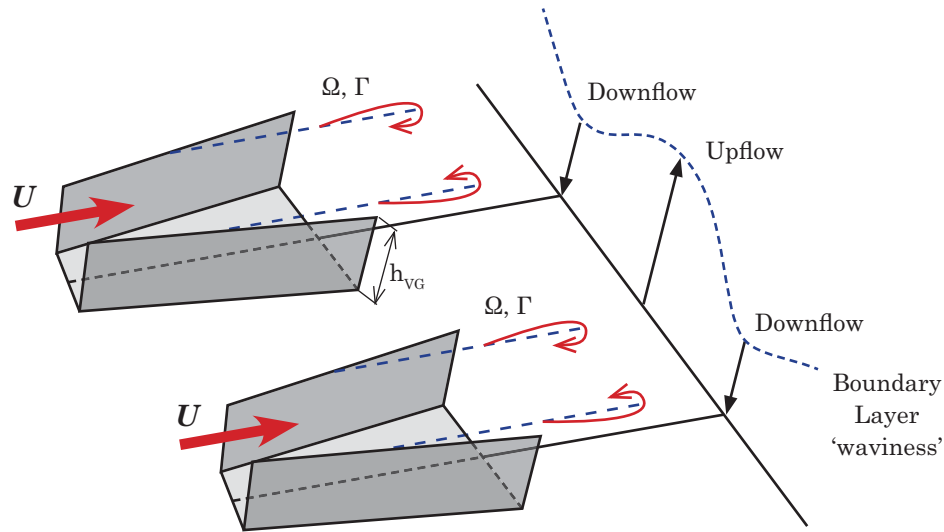
Figure 8.69 Boundary Layer Protruding Vortex Generator Showing Upflow and Downflow
Produced Between Vortex Cores, (Angele 2005)

In relation to the wingtip vortex, figures 8.52 to 8.58 indicate that by the dimpled wing producing a wake with less flow separation, this allows the wingtip vortex to remain intact longer. The flow conditions in the wake downstream of the wing are improved as a result of the dimple array. Thus the main wingtip vortex is able to more freely rotate or spin than the 'clean' wing wake and vortex interaction, which is influenced by the larger 'clean' wing wake with greater u/U_o deficits. Due to this the wingtip vortex of the dimpled wing breaks down or decays less downstream, as seen in figures 8.52 and 8.58. The effect of the less 'constrained' lower wingtip vortex results in more deviation of its position due to the wake improvements of less wing and moving ground boundary layer interaction and merging from h/c=0.134 to h/c=0.112. The upper end plate vortex remains mostly unchanged in size and intensity as its effect is mainly due to the endplate itself.

Dimpled Wing Performance Comparison

9

Given the detailed comparison of the clean Tyrrell026 airfoil and the 1.5-3-23 dimpled airfoil in chapter 8, this chapter summarizes these improvements quantitatively by calculating a percentage increase or decrease in the size of the dimpled airfoil wake. This makes direct comparison between the several dimple array configurations on the airfoils tested possible in a more accurate manner. The trends of the placement, array spacing and number of rows is also easily seen with how the wake alters with varying angle of incidence and ground clearance.

9.1 Introduction

In order to quantify the change in the wake parameters as a result of the dimple array a method of comparing the change to the dimpled wing wake size for the whole measured wake ($1.03 \leq x/c \leq 2.07$) to the clean wing wake is needed. A large data set exists with variables of: α, h/c for the additional dimpled wing array configurations. The technique used allows the wake reduction or increase to be quantified as a percentage for the given wake parameter being investigated, i.e. the profiles of u/U_o, uu/U^2_o, uv/U^2_o and turbulence intensity. This is useful where the wake difference as a result of the dimple array is subjective as in figure 8.3b at one x/c location.
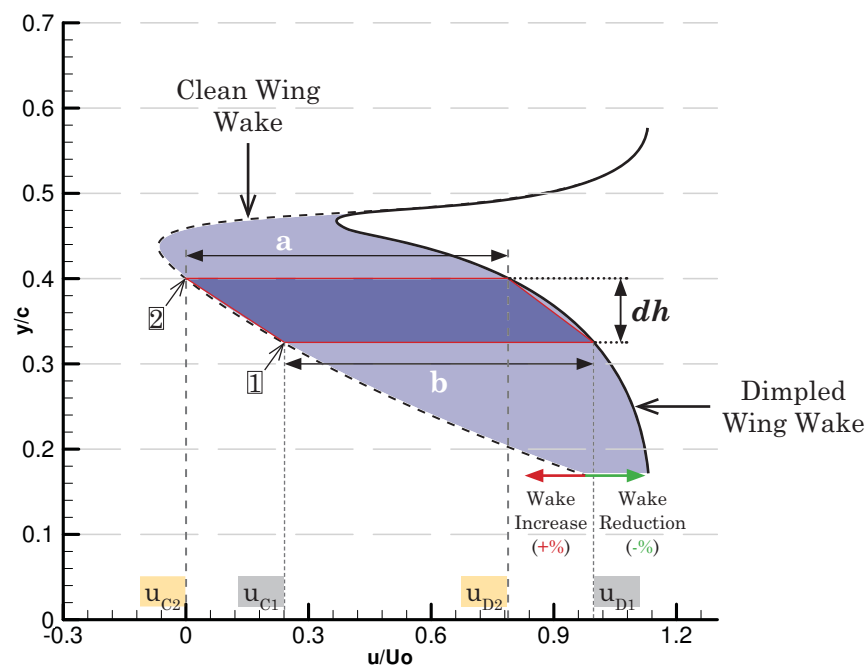

Figure 9.1 Integration Technique Applied at one Wake x/c position for u/U_o

9.2 Wake Profile Integration Technique

$$Area = h\left(\frac{a+b}{2}\right) = \int_{h=1}^{h=2} \left[\frac{(u_{D2} - u_{C2}) + (u_{D1} - u_{C1})}{2}\right] dh \quad \text{.................} [9.1]$$

The difference between the wake profiles of the dimpled wing to the clean wing is taken at one x/c rake position as an area using the trapezoidal rule for integration as defined in equation 9.1. These area differences are summed for all 10 x/c rake positions and then taken as a percentage from the similarly summed clean wing wake areas. The result is an aggregate wake percentage increase (positive i.e. wake is bigger, thus worse), or a decrease (negative i.e. wake is smaller) due to the dimples. Figure 9.1 demonstrates the method applied to the u/U_o profile at one wake x/c location; 'dh' is increased for clarity. In this case the dimpled wake profile (in bold) reduces the size of the wake when applied to the clean base-line case (dashed), the resulting area corresponds to the wake area difference that is of interest.

9.3 Wake Comparative Study: Streamwise Velocity

Results in figures 9.2 to 9.7 show the dimple array configurations impact on the airfoil's wake with respect to the normalized streamwise velocity. The biggest indicated reduction in wake size occurs for the 1.5-3-23 dimpled wings at α=10°, being 30%, 33%, 58% and 68% for h/c=0.112, 0.134, 0.224 and 0.313 respectively. Other array geometries showing reductions at α=10° are: 2-5-53 (h/c=0.313), 2-5-675 (h/c=0.224-0.313), 2-5-8 (h/c=0.313), 2.5-3-53 (h/c=0.313), 2.5-5-675 (h/c=0.212), 2.5-5-8 (h/c=0.313), these dimple array geometries are not as effective as 1.5-3-23, the reductions are less and not as effective; (<7%) for h/c=0.112-0.134.

9.3.1 h/c=0.112

Dimple array geometries that reduce the size of the wake are 1.5-3-23 (α=2°-15°) and 1.5-5-53 (from α=0°-2°), additional 1.5D spaced arrays are not optimally positioned (in terms of x/c to flow separation point) and increase wake size (% difference is positive). Increasing the array spacing to 2D in figure 9.4a shows that apart for 2-5-675 from α=2°-7° and for 2-5-53 α=2°-13°, no reduction is achieved. In figure 9.6a the 2.5D array does not reduce the wake at all.

9.3.2 h/c=0.134

There is little change for the 1.5-3-23 dimple array from h/c=0.112, other than at
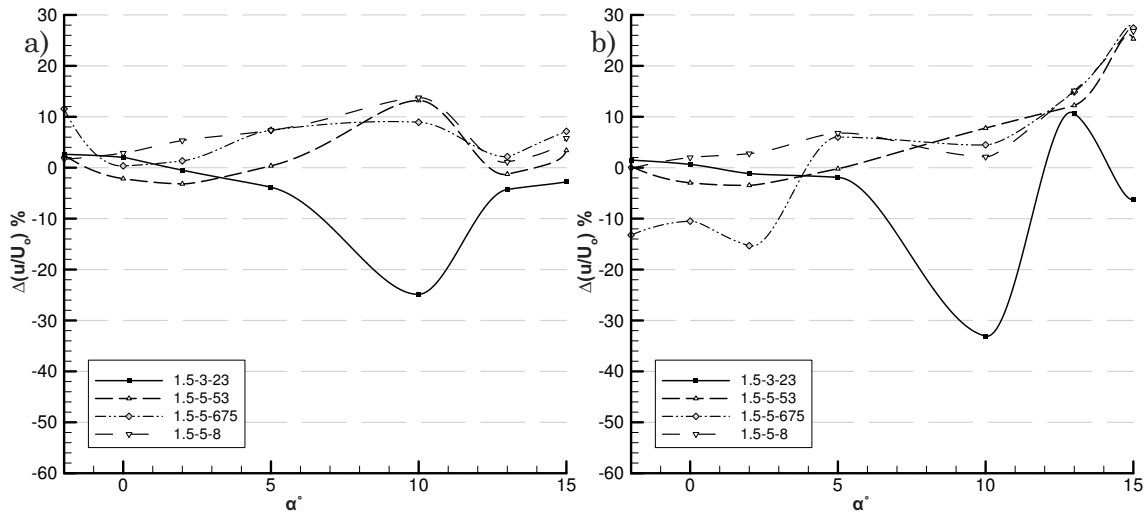
Figure 9.2 Wake Streamwise Velocity Comparison 1.5D Array a) h/c=0.112, b) h/c=0.134
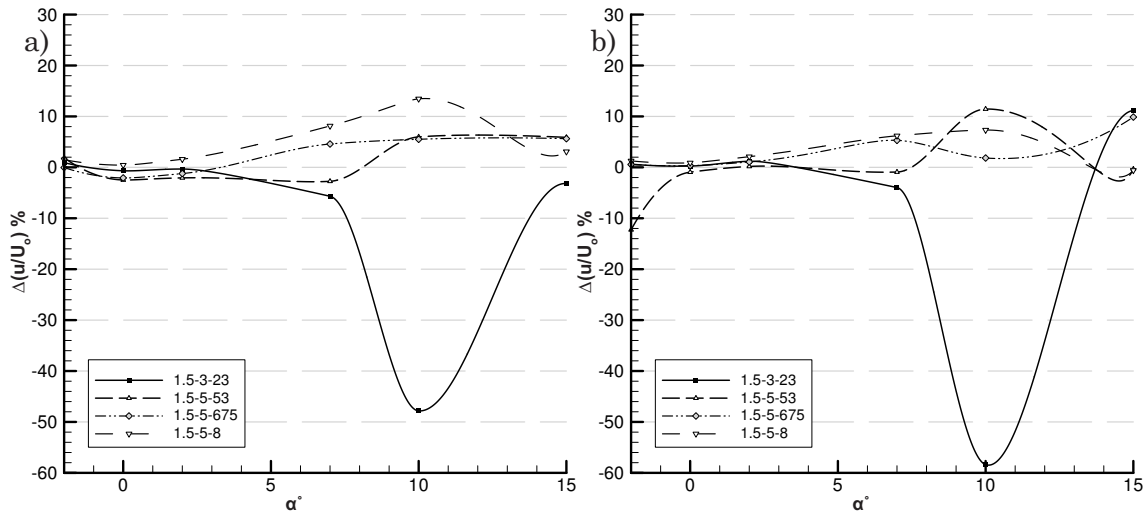
Figure 9.3 Wake Streamwise Velocity Comparison 1.5D Array a) h/c=0.224, b) h/c=0.313

α=10° the wake size reduces a further 10% to -33%, in figure 9.2b. The performance of 1.5-5-53 for α>10° worsens, whereas with the array positioned further towards the trailing edge (1.5-5-675) at lower angles of incidence (-2°≤α≤2°) there is a 12% reduction in the wake. The 1.5-5-675 dimple array then increases the wake size as α increases. Again the 1.5-5-8 dimple array exhibits a consistent increase of the wake size with increasing angle of incidence change. For the 2D spaced dimple array in figure 9.4b at h/c=0.134 apart from the increased wake size at α=13° for all dimple array configurations, no real change in the performance has occurred from h/c=0.112. The 2.5D spaced array at h/c=0.134 figure 9.6b does not differ from the effectiveness at h/c=0.112, and a similar trend at α=13° of wake size increase exists as for the 1.5D and 2D array configurations.
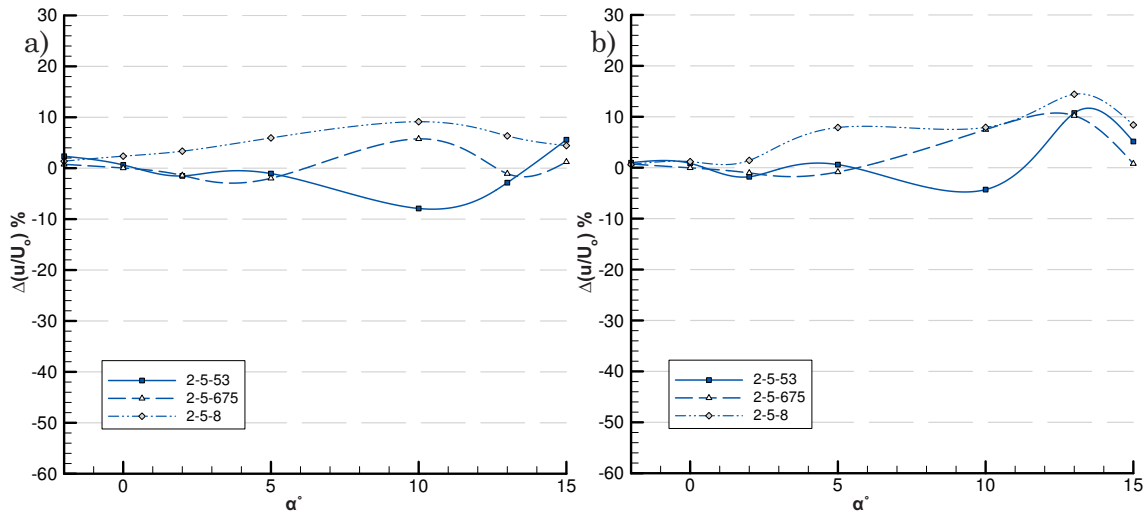
Figure 9.4 Wake Streamwise Velocity Comparison 2D Array a) h/c=0.112, b) h/c=0.134
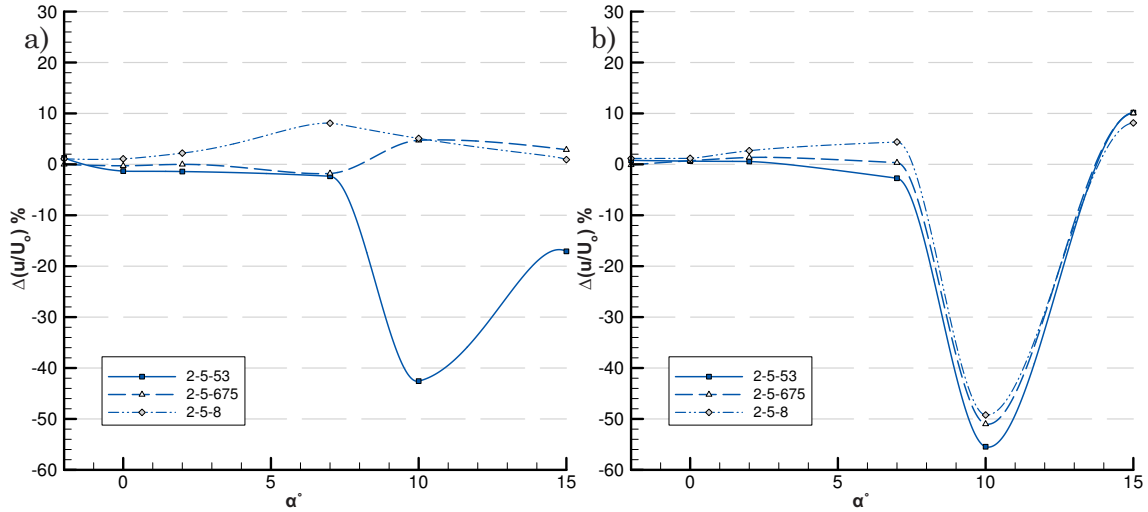
Figure 9.5 Wake Streamwise Velocity Comparison 2D Array a) h/c=0.224, b) h/c=0.313
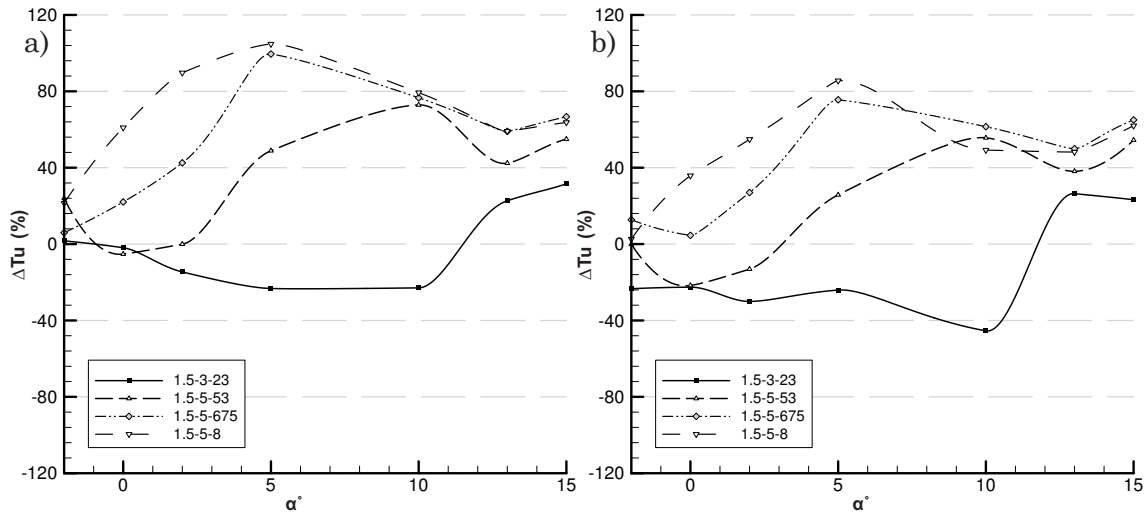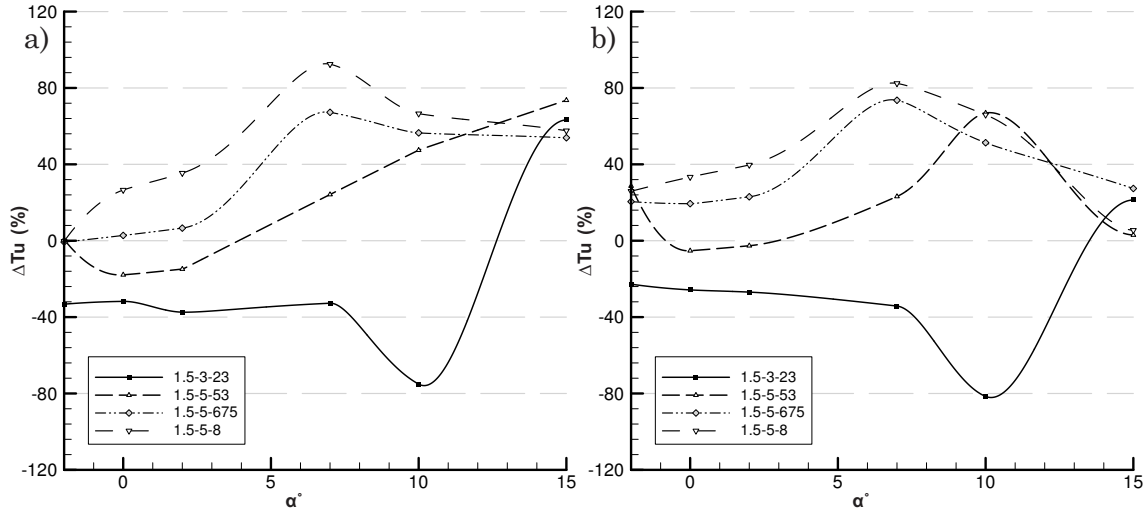
9.3.3 h/c=0.224-0.313

When h/c=0.224 in figures 9.3a, 9.5a & 9.7a, 1.5-3-23 increases its effectiveness at α=10°, 1.5-5-53 no longer increases the wake size with α and slightly reduces the wake to α=7°. The array geometry 1.5-5-675 yields a marginal wake reduction for the low angle of incidence range -2°≤α≤2°, as α increases the wake size increases but to less of an extent as h/c=0.134. The 1.5-5-8 array however shows a consistent increase in wake size for 0°<α<10°, at α=15° the 25% increase at h/c=0.134 reduces to only a 5% increase in wake size. For both the 2D and 2.5D spaced arrays, similar trends develop in that the wake size steadily increases for positioning at x/c=0.675-0.8, however for h/c=0.224 large reductions result at α=10°. The overall trends for h/c=0.224 of the 1.5D dimple arrays are maintained at h/c=0.313 apart from further
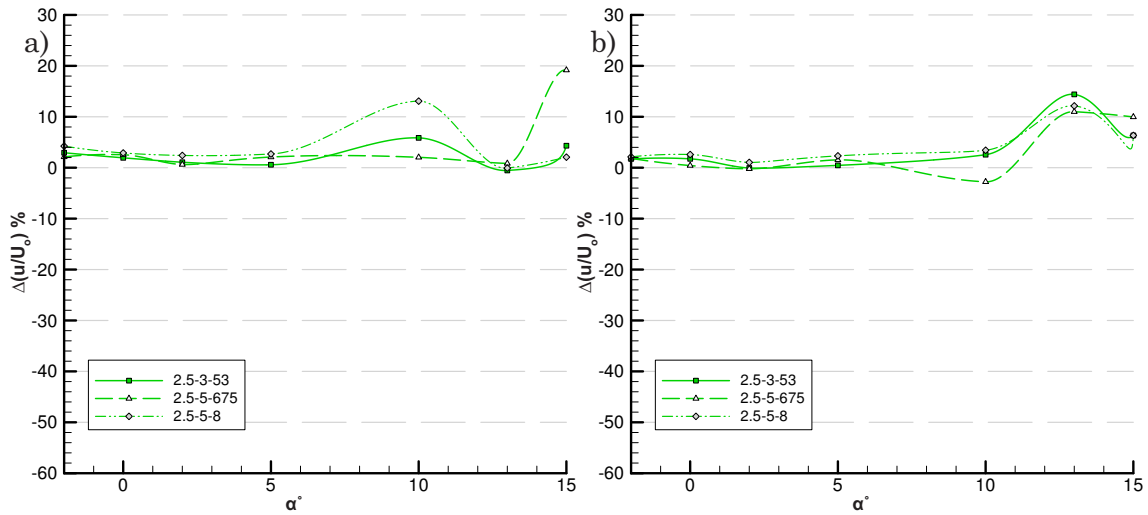
Figure 9.6 Wake Streamwise Velocity Comparison 2.5D Array a) h/c=0.112, b) h/c=0.134
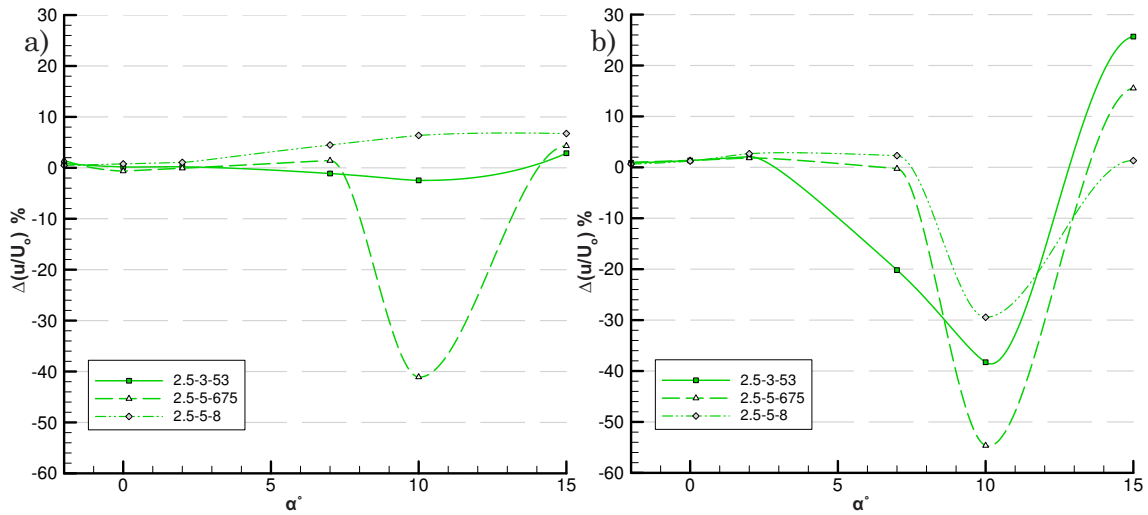
Figure 9.7 Wake Streamwise Velocity Comparison 2.5D Array a) h/c=0.224, b) h/c=0.313

increases for 1.5-3-23 at α=10˚. Additionally there is a wake reduction for all 2D and 2.5D arrays for α=10˚ at h/c=0.313. The amount of wake reduction seems dependent on how close the first row of dimples is to the leading edge, as 1.5-3-23 has the fore most dimple row closer to the wing leading edge than any other array, similarly 2.5-5-675 extends further forward than 2.5-3-53, see figure 9.7b, F.8, F.9 and F.10.

9.4 Wake Comparative Study: Turbulence Intensity

The reduction of the turbulence intensity due to the dimple array throughout the wake is shown in figures 9.8 to 9.13. For the 1.5-3-23 dimple array configuration on the Tyrrell026 airfoil, a reduction in turbulence intensity for angles less than 10˚ exists (which increases further to approximately 30% to h/c=0.313). The largest

Figure 9.8 Wake Turbulence Intensity Comparison 1.5D Array a) h/c=0.112, b) h/c=0.134

Figure 9.9 Wake Turbulence Intensity Comparison 1.5D Array a) h/c=0.224, b) h/c=0.313

reductions in turbulence intensity exist for 1.5-3-23 at α=10° when h/c=0.224-0.313. The 2D and 2.5D spaced arrays yield reductions (mostly at α=10° for h/c=0.224-0.313) but are not as consistent in reducing the wake turbulence intensity as 1.5-3-23.

9.4.1 h/c=0.112

In figures 9.8a 9.10a and 9.12a, it is clear that only the 1.5-3-23 array configuration results in any turbulence intensity reduction, which are consistent (approximately -20%) from -2°≤α≤10°. The trend is that 2D spaced arrays result in more turbulence intensity of the wing wake as a result of the dimple array (on average +40%), and further increases in turbulence intensity result due to 2.5D arrays (above +40%), which increase marginally with increase in α.
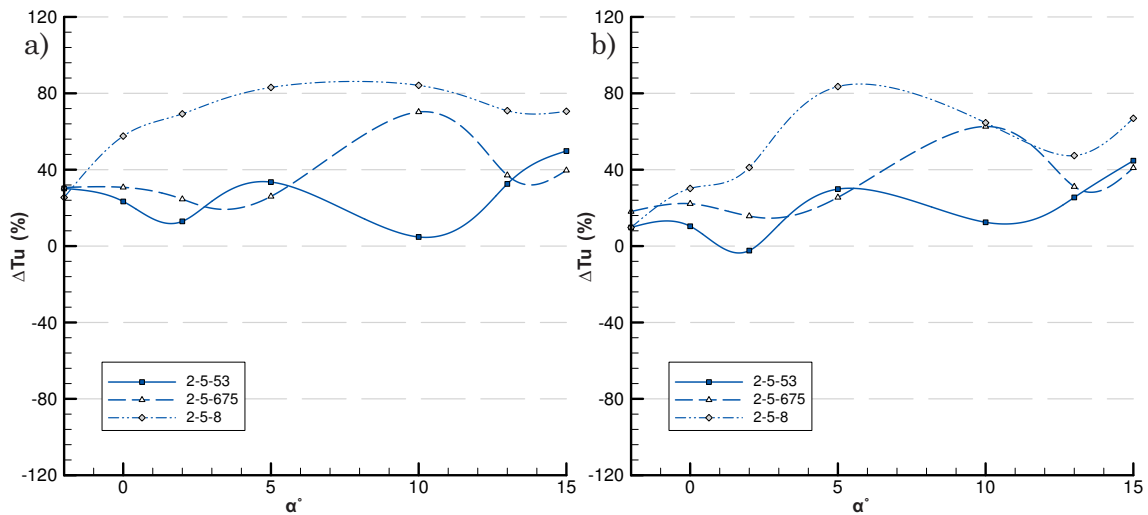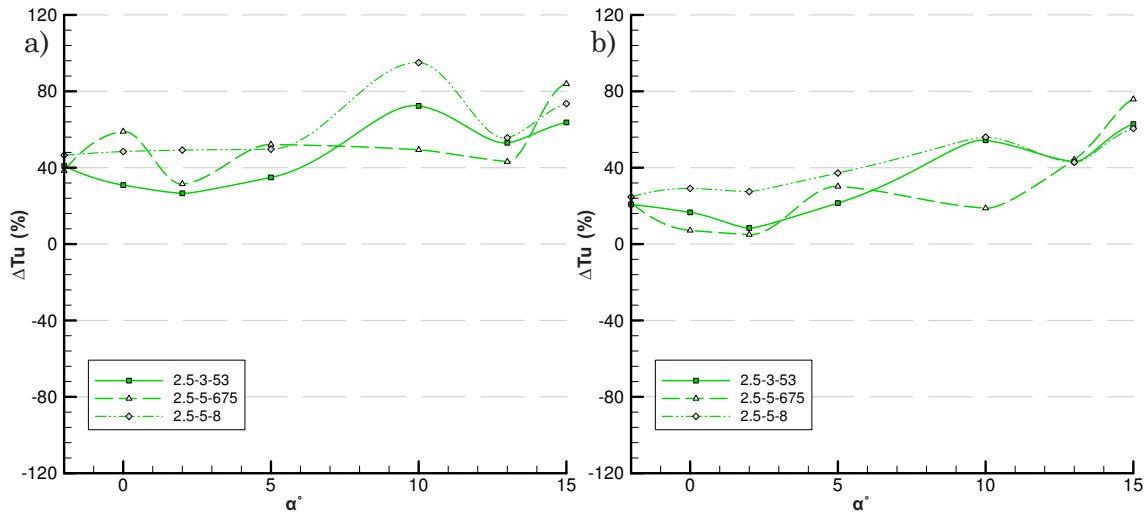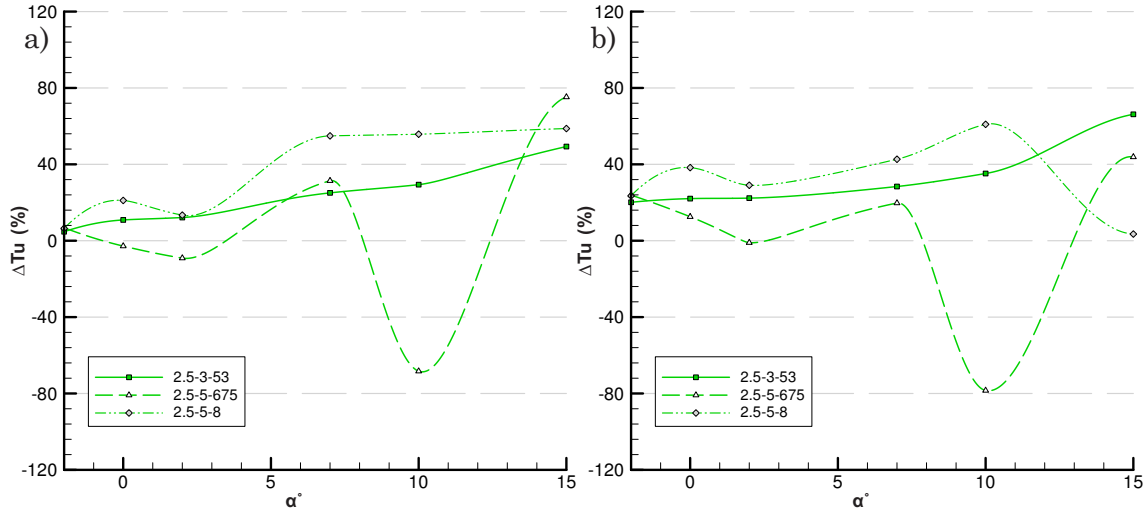
Figure 9.10 Wake Turbulence Intensity Comparison 2D Array a) h/c=0.112, b) h/c=0.134
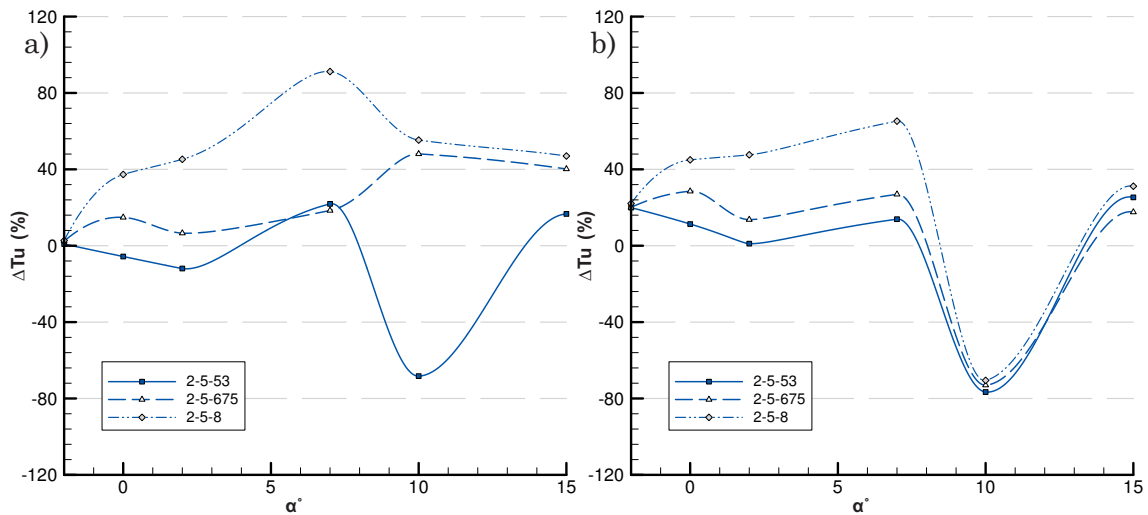
Figure 9.11 Wake Turbulence Intensity Comparison 2D Array a) h/c=0.224, b) h/c=0.313

9.4.2 h/c=0.134

In figures 9.8b, 9.10b and 9.12b the dimple arrays still increase the wake turbulence intensity compared to the 'clean' wing, albeit it to less of a degree than when at h/c=0.112. The peak reduction in turbulence intensity begins to form due to the 1.5-3-23 dimple array α=10° and 1.5-5-53 reduces turbulence intensity for -2°≤α≤2°. For the 2D and 2.5D array configurations only slight augmentation is made in that the turbulence intensity increase of the wake due to the dimples is less than at h/c=0.112, more noticeable in figure 9.12b for the 2.5D array geometries.

9.4.3 h/c=0.224-0.313

In figures 9.9, 9.11 & 9.13, continued reductions in turbulence intensity across 1.5D,

Figure 9.12 Wake Turbulence Intensity Comparison 2.5D Array a) h/c=0.112, b) h/c=0.134

Figure 9.13 Wake Turbulence Intensity Comparison 2.5D Array a) h/c=0.224, b) h/c=0.313

2D and 2.5D dimple array configurations occurs. The peak reduction for the 1.5-3-23 dimple array at α=10˚ for this ground clearance is more distinct. The 2-5-53 and 2.5-5-675 arrays both show large increases of efficiency in reducing the turbulence intensity at α=10˚ at h/c=0.224. The general trend of the 2.5D configuration is an increase in wake turbulence intensity at increased in angle of incidence, whereas the 2D spaced array is most inefficient at 7˚≤α≤10˚ range. The higher ground clearance of h/c=0.313 in figure 9.11b, shows all 2D array configurations yielding reductions in turbulence intensity levels at α=10˚ and improving for α=15˚ at h/c=0.313 from h/c=0.212. In figure 9.13b for 2.5D array geometries at h/c=0.313 little change exists from the h/c=0.212 ground clearance, apart from further reduction in the peak value of α=10˚ for 2.5-5-675. Similar trends as with u/U_o, uu/U^2_o and uv/U^2_o develop,

in that some slight increases are made but there is an overall stabilization in the performance from h/c=0.224 to h/c=0.313.

9.5 Wake Comparative Study: Turbulent Normal Stress

9.5.1 h/c=0.112

For 1.5D spaced dimpled wing configurations in figure 9.14a, it can be seen that for each chordwise array location there is a range of α for which a reduction in uu/U^2_o exists. The strongest reduction occurs for 1.5-3-23 (-60% at α=10˚), and reduces as the array is positioned at x/c=0.53, 0.675 and 0.8. The 1.5-3-23 dimple reduces the wake turbulent normal stress from -2˚≤α≤10˚, whereas for 1.5-5-53, 1.5-5-675 and 1.5-5-8 the uu/U^2_o reduction occurs at a lower angle of incidence range. For 2D

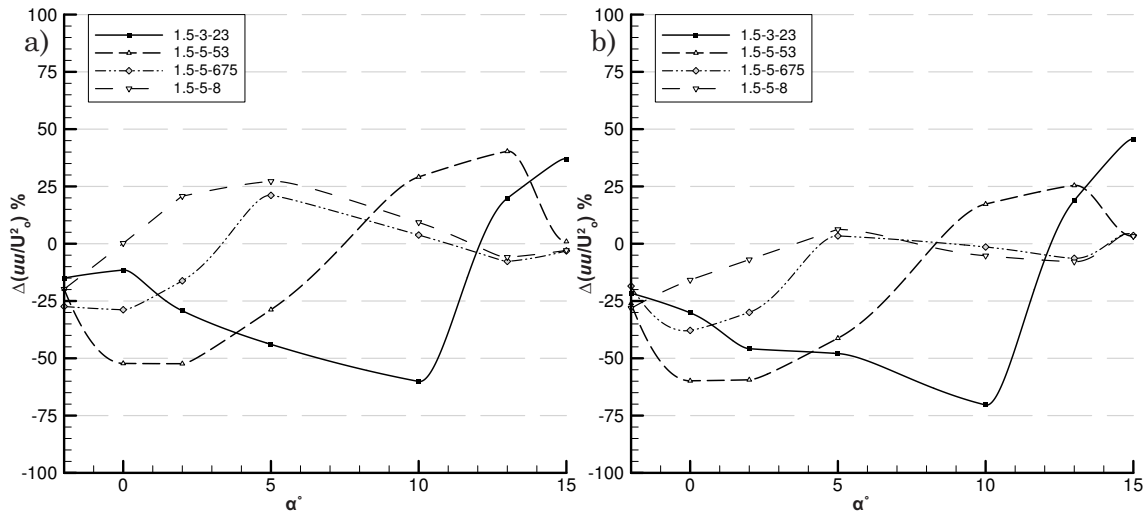
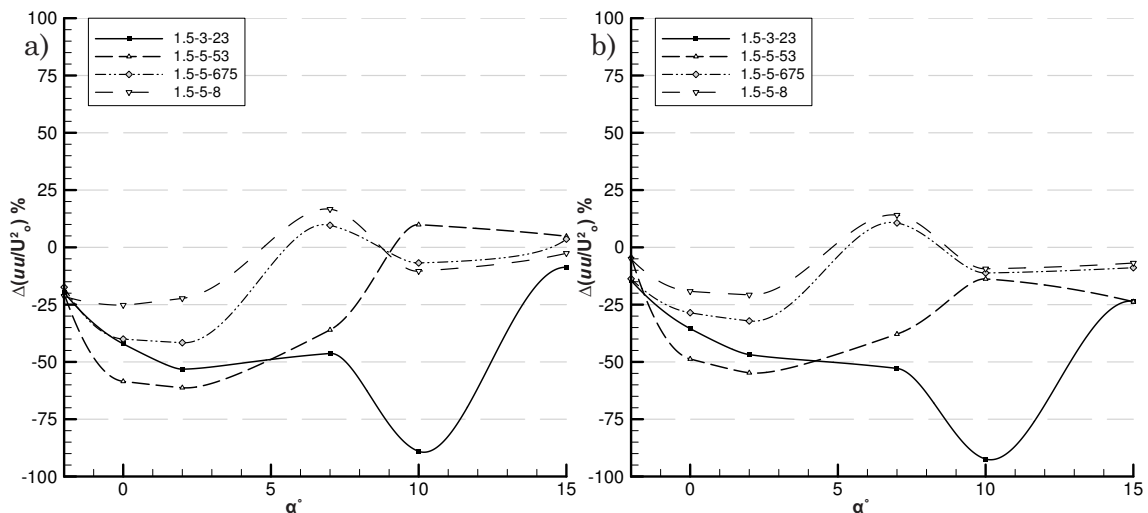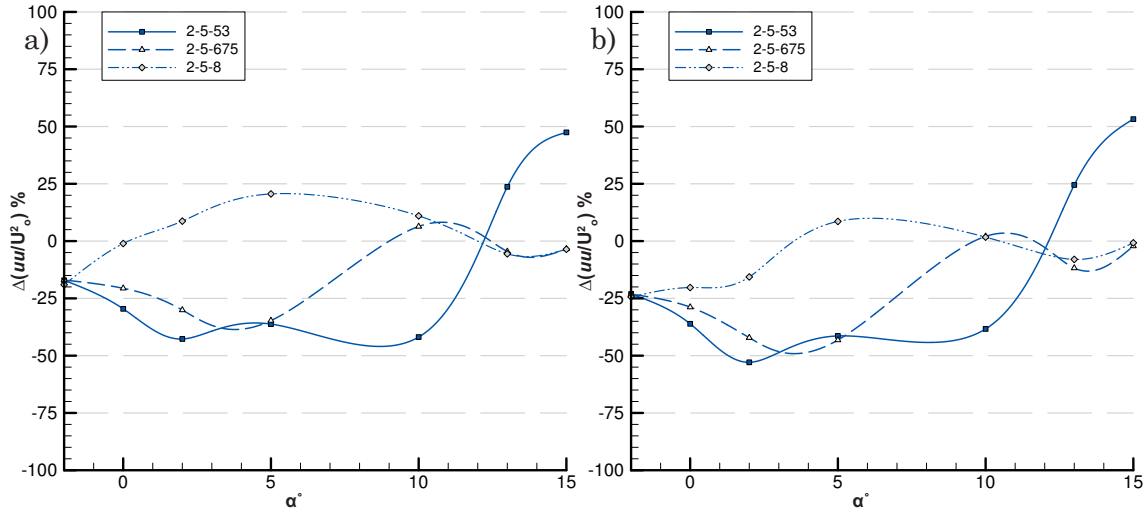Figure 9.14 Wake Turbulent Normal Stress Comparison 1.5D Array a) h/c=0.112, b) h/c=0.134
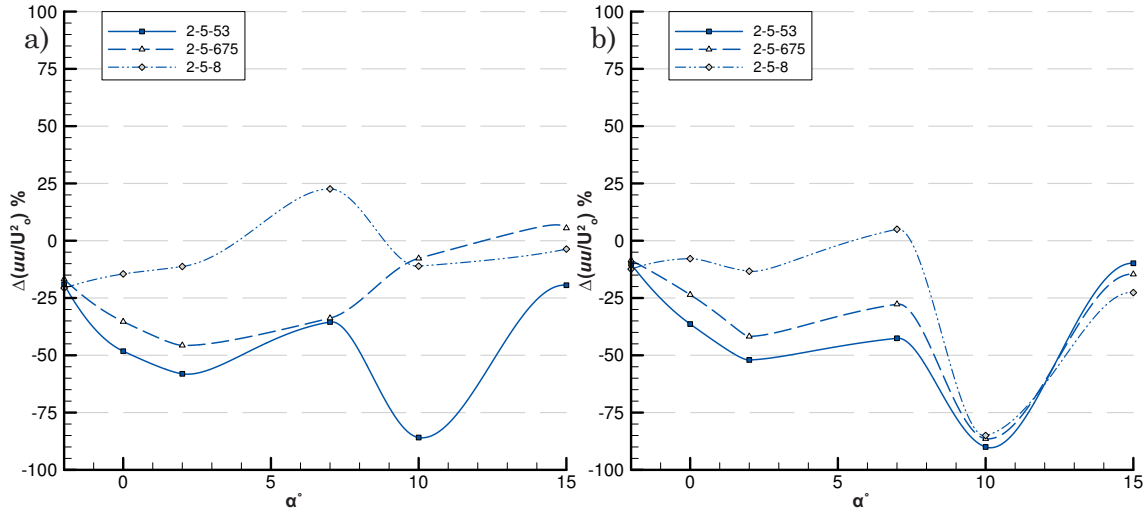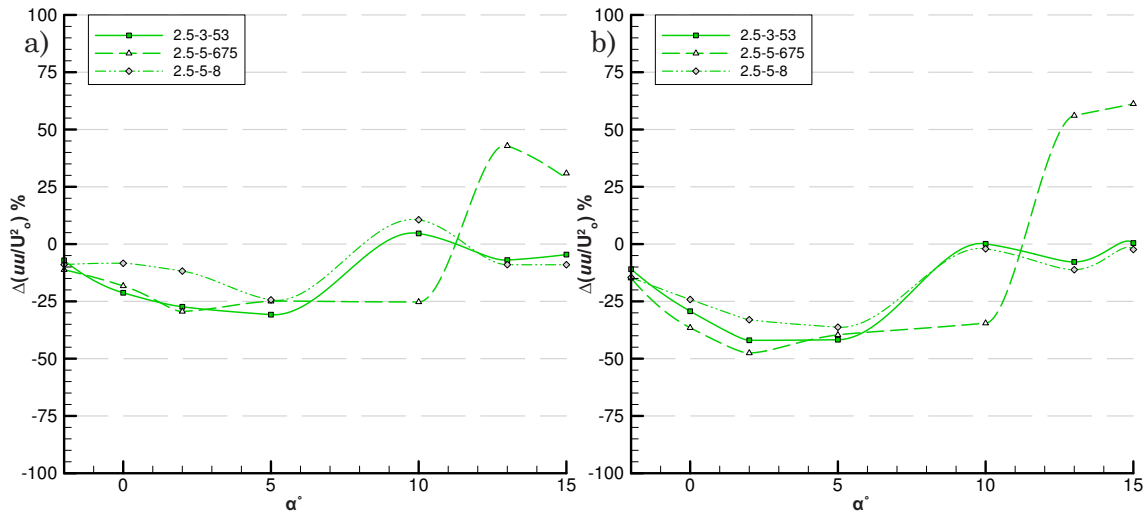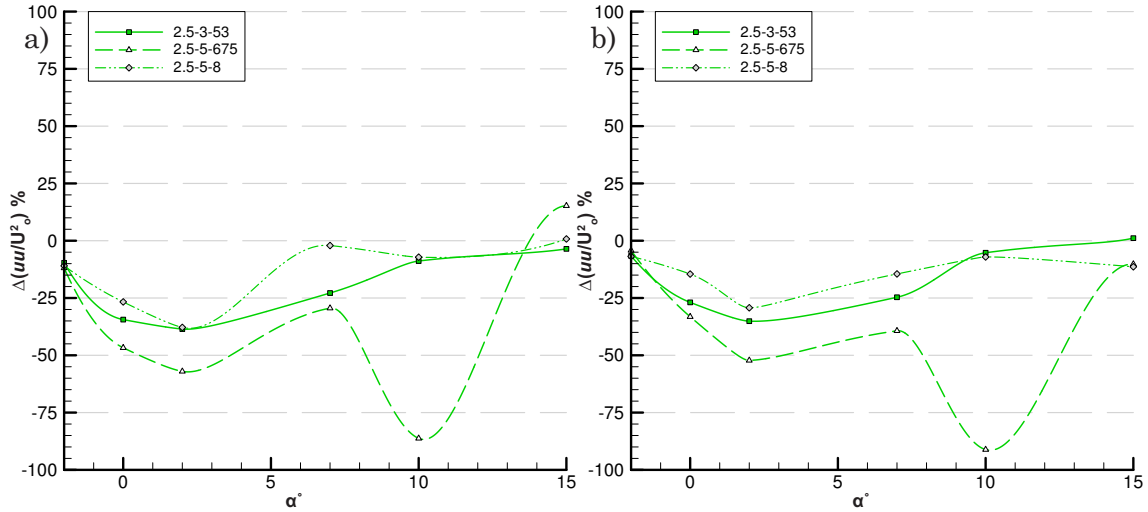

Figure 9.15 Wake Turbulent Normal Stress Comparison 1.5D Array a) h/c=0.224, b) h/c=0.313

Figure 9.16 Wake Turbulent Normal Stress Comparison 2D Array a) h/c=0.112, b) h/c=0.134

Figure 9.17 Wake Turbulent Normal Stress Comparison 2D Array a) h/c=0.224, b) h/c=0.313

spaced dimple arrays in figure 9.18a, 2-5-53 yields greater influence on reducing uu/U^2_o and is consistent from $-2° \leq \alpha \leq 10°$ before becoming ineffective at $\alpha > 10°$. So as the 2D spaced array is positioned further towards the leading edge, the uu reduction is greater at lower angles of incidence. In figure 9.19a for the 2.5D spaced dimpled wings, all configurations provide a similar uu/U^2_o reduction from $-2° \leq \alpha \leq 10°$, with 2.5-5-675 providing the most consistent range of reduction from $-2° \leq \alpha \leq 10°$ but is inefficient for $\alpha \geq 13°-15°$. It is clear at h/c=0.112 that as the dimple to dimple spacing in the array increases the turbulent normal stress reduction is less.

9.5.2 h/c=0.134

Increasing the ground clearance to h/c=0.134 has little effect on the 1.5-3-23 and 1.5-5-53 arrays apart from a further 10% reduction in uu/U^2_o. The 1.5-5-675 and

Figure 9.18 Wake Turbulent Normal Stress Comparison 2.5D Array a) h/c=0.112, b) h/c=0.134

Figure 9.19 Wake Turbulent Normal Stress Comparison 2.5D Array a) h/c=0.224, b) h/c=0.313

1.5-5-8 dimple arrays, improve at $\alpha \geq 2°$ compared to h/c=0.112. Additionally the 1.5-5-8 array has increased its range of effective angle of incidence from α=-2° at h/c=0.112 to $-2° \leq \alpha \leq 2°$ at h/c=0.134. In figure 9.16b the 2D array configuration does not differ greatly from h/c=0.112 to h/c=0.134 apart from further reductions in uu/U^2_o for 2-5-53 and 2-5-675; 2-5-53 is now most effective at α=2°. The most rearward array configuration (the 2-5-8 dimpled wing) changes the most at the lower angles of incidence, and has increased range of effective α to $-2° \leq \alpha \leq 2°$ (from α=-2° at h/c=0.112), and for $\alpha \geq 2°$ does not increase uu/U^2_o as much compared to h/c=0.112. The 2.5D dimple array in figure 9.19b has more consistent uu/U^2_o reduction at $-2° \leq \alpha \leq 10°$, but is largely unchanged from h/c=0.112. The 2.5-5-675 wing is most efficient at reducing uu/U^2_o at α=2° (similar for 2-5-675 wing).

9.5.3 h/c=0.224-0.313

The influence of increasing ground clearance to h/c=0.224 and h/c=0.313 (figure 9.15) for the 1.5D spacing yields only slight changes for $\alpha \leq 10°$; the greatest change is for $\alpha=15°$ at h/c=0.224 from h/c=0.134. The uu/U_o^2 wake increase due to the dimples for ground clearances h/c$\leq$0.134 is mostly recovered, and results in reductions in wake uu/U_o^2 for all 1.5D spaced dimple arrays for $\alpha \geq 10°$ at h/c=0.313 compared to the clean wing. This trend is reflected for the 2D and 2.5D spaced configurations with increasing h/c. The uu/U_o^2 wake reduction for the 2D spaced dimpled wings at h/c=0.313 for $\alpha=10°$ are similar, as for turbulence intensity in figure 9.11.

9.6 Wake Comparative Study: Primary Shear Stress

9.6.1 h/c=0.112

For the 1.5-3-23 configuration in figure 9.20a, uv/U_o^2 reduces for the range $\alpha \leq 13°$ and peaks at $\alpha=10°$. The 1.5-5-53 wing produces a similar reduction in uv/U_o^2 at $\alpha=0°$ and reduces uv/U_o^2 for a lower angle of incidence range of $-2° \leq \alpha \leq 5°$. As the dimple array is positioned towards the trailing edge of the wing, this lowers the angle of incidence range that uv/U_o^2 is reduced. As for the 1.5-5-675 and 1.5-5-8 dimpled wings the reduction range becomes $-2° \leq \alpha \leq 2°$ to $\alpha=-2°$ respectively. Above this α range uv/U_o^2 increases in the wake due to the dimple array, with 1.5-5-8 increasing wake uv/U_o^2 by 35% at $\alpha=5°$. The 2D spaced arrays in figure 9.22a show the 2-5-53 array reduces uv/U_o^2 by 40% at $\alpha=2°$ & 10° (1.5D reduce uv/U_o^2 by a maximum of 60%) and is effective throughout the $-2° \leq \alpha \leq 15°$ range. For 2-5-675 the wake uv/U_o^2 is similar to 2-5-53 for $\alpha \leq 5°$, however uv/U_o^2 increases in the wake for $\alpha=10°$. The 2-5-8 array only provides a reduction of uv/U_o^2 for $\alpha=-2°$, and increases wake uv/U_o^2 at $5° \leq \alpha \leq 13°$. Increasing the dimple array spacing to 2.5D in figure 9.25a shows most configurations reduce the primary shear stress apart from most notably 2.5-3-53 and 2.5-5-8 at $\alpha=10°$. Wake reductions for 2.5D spaced arrays are not that great, but are more consistent than 1.5D and 2D spaced arrays. 2.5D arrays are most effective at $\alpha=2°$, the 5 row 2.5-5-675 array reduces uv/U_o^2 up to $\alpha=10°$, as the dimple array coverage on the wing is further toward the leading edge than the 3 row 2.5-3-53 array.

9.6.2 h/c=0.134

Increasing h/c provides a slight increase in the effectiveness of the arrays but does not alter the trends of the primary shear stresses, seen in figures 9.20b, 9.22b &
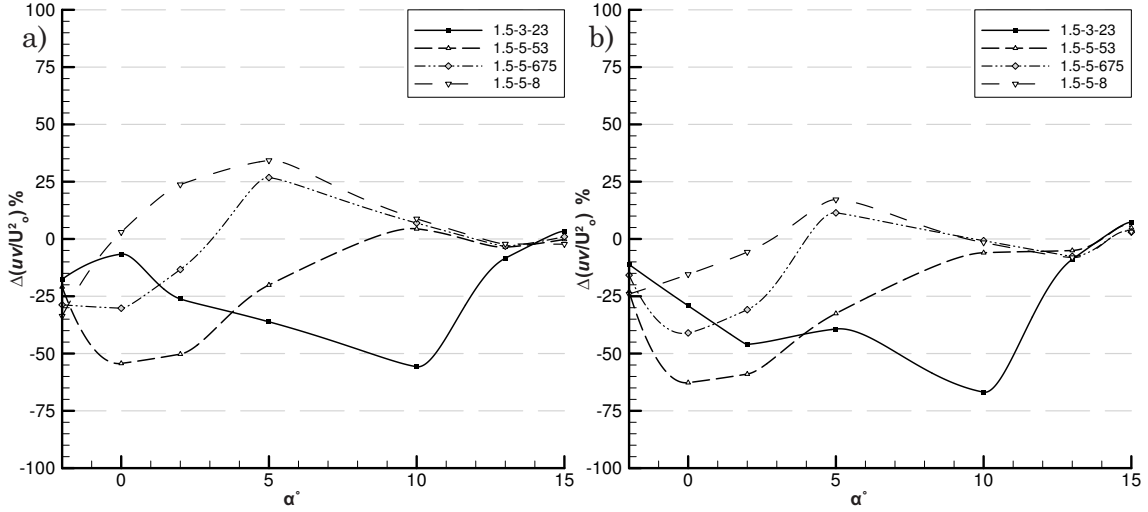
Figure 9.20 Wake Primary Shear Stress Comparison 1.5D Array a) h/c=0.112, b) h/c=0.134
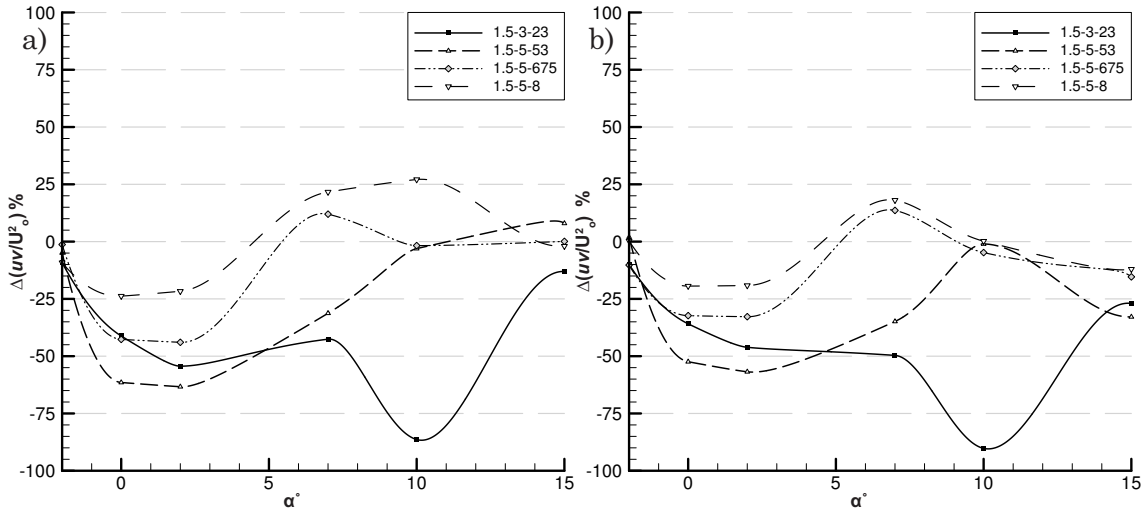
Figure 9.21 Wake Primary Shear Stress Comparison 1.5D Array a) h/c=0.224 b) h/c=0.313

9.24b. The only exceptions being both 1.5-5-8 and 2-5-8 increase the range of angle of incidence for wake uv/U^2_o reduction to $-2° \leq \alpha \leq 2°$ from $\alpha = -2°$ at h/c=0.112. Both the 2D and 2.5D spaced array configurations bias more to peak wake primary shear stress reduction at $\alpha = 2°$.

9.6.3 h/c=0.224-0.313

Greater alterations to how the dimples reduce the primary shear stress occur at h/c=0.224. The 1.5-3-23 increases its highest reduction of uv/U^2_o by 20% at $\alpha = 10°$, further reductions exist at $-2° \leq \alpha \leq 15°$. The 1.5D spaced arrays all increase low range angle of incidence uv/U^2_o wake reduction. As h/c increases from 0.224-0.313, greater reductions occur for the arrays located closer to the leading edge. For the 2D series of array configurations, a significant reduction of uv/U^2_o for 2-5-53 at $\alpha \geq 0°$ are the only
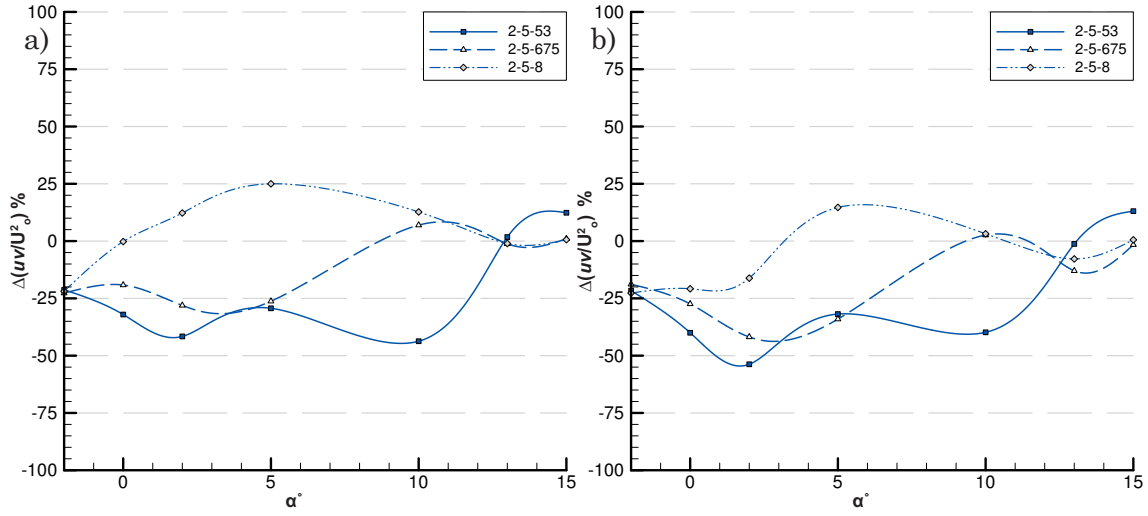
Figure 9.22 Wake Primary Shear Stress Comparison 2D Array a) h/c=0.112, b) h/c=0.134
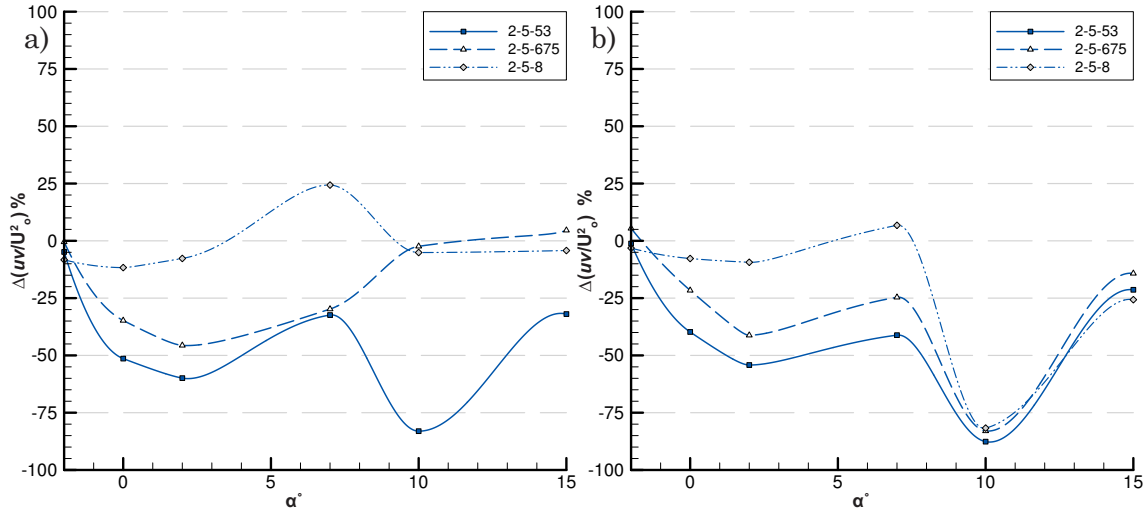
Figure 9.23 Wake Primary Shear Stress Comparison 2D Array a) h/c=0.224 b) h/c=0.313

main performance changes at h/c=0.224, 2-5-675 and 2-5-8 are still comparable with h/c=0.134. In figure 9.25a, 2.5-5-675 reduces uv/U^2_o substantially at $\alpha{\geq}10°$, 2.5-3-53 reduces uv/U^2_o more for $10°{\leq}\alpha{\leq}15°$, and 2.5-5-8 reduces its range to $0°{\leq}\alpha{\leq}7°$ (from $-2°{\leq}\alpha{\leq}10°$ at h/c=0.313). For the clearance of h/c=0.313 in figures 9.21b, 9.23b and 9.25b, the dimple array affect on uv stabilizes, apart from the 1.5D spaced arrays with 5 rows at $\alpha{>}10°$ all reducing uv/U^2_o further, and the 2D dimple arrays reducing uv/U^2_o at $\alpha{=}10°$.

9.7 Discussion

It is apparent that the further forward the array is placed on the wing (i.e. towards the leading edge), the greater the extent the dimples effectively reduce the wake
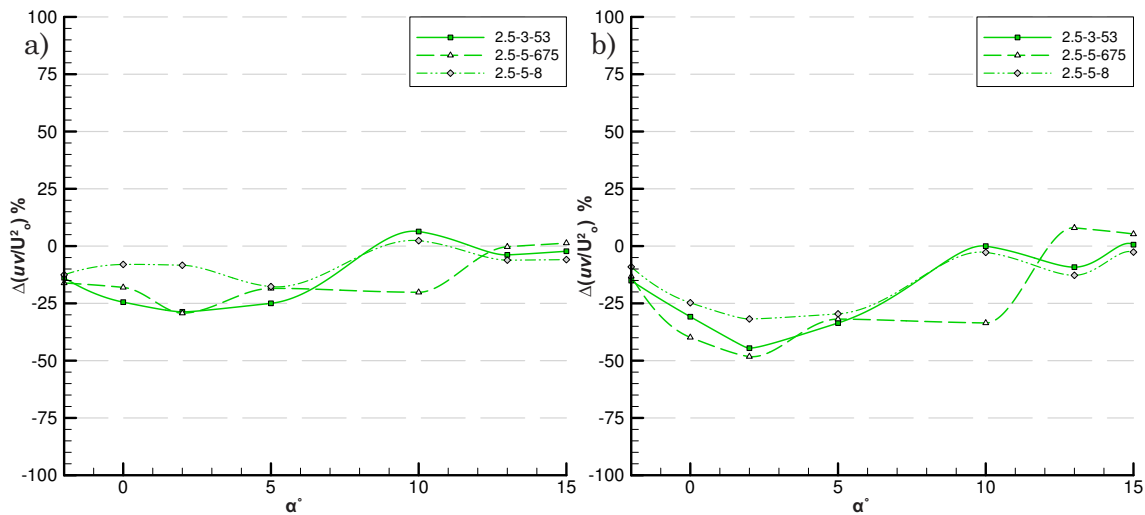
Figure 9.24 Wake Primary Shear Stress Comparison 2.5D Array a) h/c=0.112, b) h/c=0.134
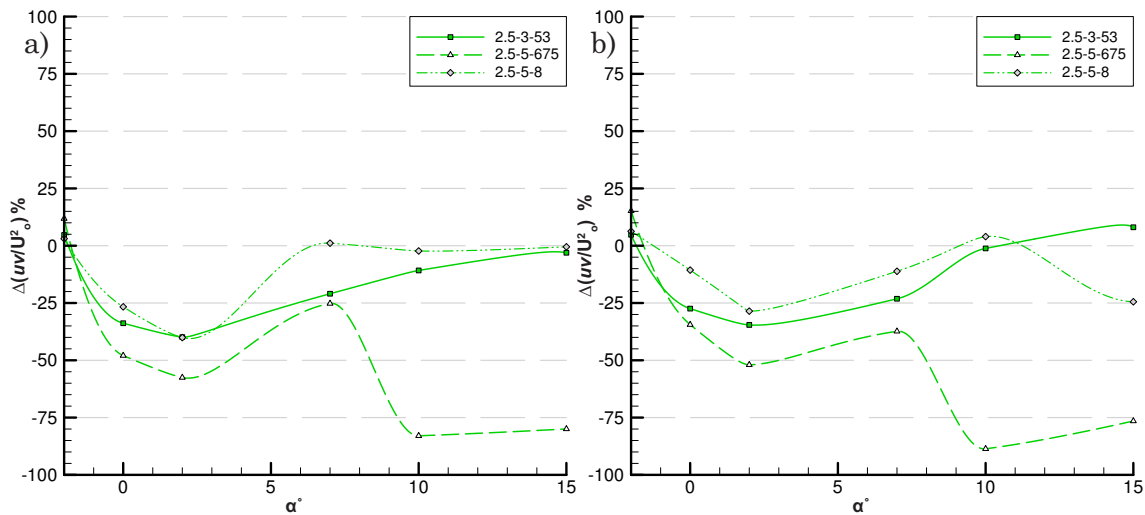
Figure 9.25 Wake Primary Shear Stress Comparison 2.5D Array a) h/c=0.224 b) h/c=0.313

parameters u/U_o, uu/U^2_o, uv/U^2_o and turbulence intensity for all ground clearances (particularly when α=10˚). At lower angles of incidence a more rearward array placing helps to marginally reduce velocity deficits in the wake and wake Reynolds stresses. The array position closest to the leading edge improves dimple performance as the first row is closer to the expected suction peak of the wing (C_P peak in Zerihan 2001). Thus the velocity between the wing and the ground is higher and the dimple operates in a higher Reynolds number regime with better mixing of the boundary layer. The evidence for this is not solely confined to the 1.5-3-23 series wing, as the 2.5-3-53 and the 2.5-5-675 series wings also show this phenomenon. The 2.5-5-675 series wing has its first row further forward than the 2.5-3-53 series dimpled wing due to geometric limitations of requiring the 2 omitted rows of dimples

to wrap around the leading edge and onto the upper surface, see figure F.1 and F.8. Which is the main influence of the greater reductions in u/U_o, uu/U_o^2, uv/U_o^2 and turbulence intensity for the 2.6-5-675 array.

As far as the efficient reduction of the wake as a result of the use of the dimpled surface, the 1.5D series spaced array configurations provide the most reduction in not only the normalized streamwise flow velocity of the wake, but also the primary shear stress, the turbulent shear stress and the turbulence intensity. The 1.5D series wings are of overlapping dimple configuration, which clearly assists strengthening the vorticity and turbulence production in the arrays at lower ground clearances, as the 2D and 2.5D arrays do not provide as much reduction. This was also seen in the rearward ramp experiments in chapter 6.

It is clear from figure 8.3-8.13 and 9.2-9.25 that the influence the ground clearance has on the ability of the dimple array to reduce the wake size, turbulence and Reynolds stresses reduces as h/c reduces. It is worth noting with regard to this phenomenon that the force reduction phenomenon for the same wing occurs for ground clearances lower than h/c=0.134 (Zerihan 2001), and h/c=0.112 is just beyond this. The interaction of the wing and the ground is clearly greatest at h/c=0.112, so there is a link between the reduced C_L from Zerihan's study and the flow damping effect increase with lower ground clearance in Kim & Geropp (1998); i.e. the Strouhal number reduction with reducing h/c. Therefore as the ground clearance increases, the ability the dimple array has to shed vortices (that are not damped out by the ground influence at lower h/c) also increases. Only the increased vorticity and turbulence production of the 1.5D arrays appear to be strong enough to overcome this effect to reduce the wake at h/c=0.112-0.134.

The angle of incidence is coupled to the migrating separation point with a change in angle of incidence for a given ground clearance. For α=10° the largest wake reductions occur, where as for α=13°-15° the wake parameters increase. This can be attributed to the flow separation point advancing towards the leading edge and into the actual array or in front of it, exacerbating the situation causing the wake to grow. Whereas with the flow separation downstream of the dimple array the positive effects of it are in full use, particularly at α=10°, where the angle, flow velocity under the wing and array position all combine to reduce the wake to a significant extent. For the lower angles of incidence it can be seen that the arrays closest to the trailing edge alleviate the wake to a greater extent.

Conclusions & Future Work

10

The main findings of the preceding chapters are now discussed in detail and how they relate as a whole in referring to the research outline of figure 1.4. Further discussion is included in how the individual sections of work: the single dimple, the rearward facing ramp flow separation and the airfoil wake reduction studies link together. Additionally any future work that would be an extension of work presented here is outlined, whether it be due to experimental or time limitations or was outside the initial scope of the topic.

10.1 Conclusions

The use of low aspect ratio spherical wells (dimples) on an inverted airfoil in ground effect has shown to reduce flow separation for particular configurations and locations of dimple arrays, which would lead to increase the wing's aerodynamic efficiency. Located on the suction surface of an inverted wing, an effective dimple array will reduce the wake size, turbulence intensity and Reynolds stresses compared to a non-dimpled, standard wing.

In referring to the research programme methodology flow chart in figure 1.4, the study has required quantifying the vorticity production and flow structure of a single dimple at the Reynolds number range of that expected on the wing. This followed with an investigation of the dimple array configuration and location influence on a simplified separated flow. The array experiments on the 16° rearward facing ramp were crucial in determining the best placement, configuration and number of rows a dimple array needed to be beneficial to a separated flow. Thus confidence was held that measurable changes would result with the manufactured suction surface dimpled wings.

10.1.1 Single Dimple

The validation and verification of CFD results with LDA and PIV measurements in the single dimple yielded an accurate numerical model of the flow within the dimple. With good agreement between the numerical model and experimental results, further analysis of the numerical model yielded information not able to be measured due to experimental limitations; surface reflections and LDA traverse/mesh resolution.

Only relatively few numerical models outlined in table 1.1 were validated against experimental flow visualization observations of the 'vacuum effect'. All turbulence models investigated in this study indicated the 'vacuum effect', such that using this flow phenomenon to validate against is not adequate. Results show:

· The RANS k-ω SST turbulence model with a fully structured grid and y^+ able to resolve non-equilibrium wall functions at the surface showed good agreement with experimental measurements within the dimple of streamwise, spanwise and normal flow velocities.

· The vorticity production is greatest at the downstream sides of the dimple rim, and shows a strong relationship with Reynolds number. For $Re_D=4.3x10^3$ two lateral symmetric vortex cells exist in the dimple which are effectively separate flow structures with little mass transfer between them. The two separate lateral vortex cells within the dimple become asymmetric with the higher Reynolds number ($Re_D=9x10^3$) as a result of one increasing in size and strength, allowing fluid transfer between the now linked lateral vortex cells which are now linked

· The vortex cell magnification in one half of the dimple with increasing Re_D results in more fluid being ejected from that half of the dimple. The bigger volume the larger vortex cell occupies in the dimple limits the size of the second weaker vortex can form. This closes off the 'side window' the weaker vortex has at the spanwise edge, therefore reducing the 'vacuum effect' of that half.

· Vorticity was contained at both Reynolds numbers at a height of y/D<0.11 from the wall, this height can be used to equate a boundary layer protruding vortex generator of equivalent strength to compare against the height of other vortex generators.

· The vorticity production downstream of the dimple indicated augmented levels at; x/D=0-1 for $Re_D=4.3x10^3$ and x/D=2-3 for $Re_D=9x10^3$. This requires, at least for a single dimple, a very accurate placement relative to a separated flow structure.

10.1.2 Dimple Array and Rearward Facing Ramp

The influence of various dimple array configurations and locations on a separated flow structure were measured, aimed at replicating the most effective arrays on the suction surface of the airfoil. The adverse pressure gradient and flow separation from the 16° rearward ramp is not entirely dissimilar to the flow separation of an airfoil at high angles of incidence that approach stall. Chapter 6 indicated:

· The placement of numerous dimple arrays (where D=14.74mm, δ/D=0.22 at Re_D=4.3x10^3) upstream of a fixed flow separation from a 16° rearward facing ramp (at Re_H=5.25x10^4) were able to alter its large scale flow structure. This is as a result of the regular, discrete vortex shedding and low level boundary layer mixing that the dimples produce (y/D<0.11 from chapter 5).

· Dimple arrays that altered the size of the recirculation region the most in the separated flow structure of the 16° rearward facing ramp also led to greater flow recovery downstream of the separation point and reductions in both u-RMS velocity and turbulence intensity.

· An array with 1.5D dimple to dimple spacing and 3 rows placed 3D from the flow separation point reduced the flow separation size, recovered the u/U_o profile greater as well as reduced the turbulence and u-RMS the most of any other array. A 1.5D spaced array with 5 rows most consistently provided flow recovery when placed anywhere between 1D-5D from the flow separation point.

· Some dimple arrays (A1.5-R1 from D0 to D5, A1.5-R3-D0, A2-R1-D5, A2.5-R1-D0 and A2.5-R3-D0) increased the flow separation size and gave greater u/U_o deficits.

· A single row dimple array with 1.5D spacing yielded the greatest increases to flow separation size. Increasing the dimple to dimple spacing to 2D yielded little flow change to the clean configuration, 2.5D spacing of the dimples in the array actually reduced the flow separation zone size to some extent. Highlighting for a single row that the dimple to dimple spacing of the array may limit the vortex production at the dimple rim, and the further the dimples are placed from each other the vortex production is impeded less; resulting in more mixing and flow separation reduction.

· Increasing the number of rows in the array to three and five resulted in reductions to the recirculation zone size and intensity. The most effective location from the flow separation point was x/D≈3, however flow recovery existed from x/D=1-5.

· The dimple to dimple spacing, or degree of 'offset' showed that 1.5D spaced dimples with multiple rows, whose rims or edges 'overlap' had more of an effect on the recirculation zone than the 'inline' 2D and the 'offset' 2.5D spaced arrays. Only minor flow recovery resulted by the increased spacing to 2D and 2.5D.

10.1.3 Tyrrell026 Airfoil, no dimples

Whilst the non-dimpled Tyrrell026 airfoil was not the primary focus of the study,

detailed wake measurements were required to eventually compare how the dimpled suction surface altered the wake characteristics of velocity, turbulence and Reynolds stresses. Previous studies took measurements of the same airfoil but at low angles of incidence (Zerihan 2001, Zerihan & Zhang 2003) and no data existed on the wake flow for stall or large scale flow separation. Therefore the LDA wake measurements for a range of angles of incidence up to and beyond stall (for various ground clearances), provided further insight into the wake characteristics of an inverted wing in ground effect. Namely:

• For a constant h/c, increasing α results in a larger wake and lower values of streamwise velocity. The difference between the flow field of α=13˚ and 15˚ is not substantially different, the increase in velocity deficit (-u/U_o), and wake size is greater from α=10˚-13˚ (beyond stall α).

• As h/c reduces for all angles of incidence the wake elongates, resulting in greater velocity deficits in the wake at x/c=2.07. The skew of the wake towards the ground is also greater at low h/c for α>13˚, as the u/U_o profile is pulled towards the ground. The greater venturi effect between the airfoil and ground at h/c=0.134 for α=10˚ yields less skew of the wake than higher ground clearances; at h/c=0.134 for α=10˚ resulted in $C_{L,max}$ in Zerihan (2001).

• At h/c=0.112, the u/U_o profile at x/c=2.07 for α≥10˚ is skewed greater to the ground (lower u/U_o towards y/c=0) due to the wake interaction with the boundary layer on the moving ground being greater at lower h/c.

• Wake thickness (Δy/c of u/U_o) for angles of incidence α<5˚ is greater at low h/c, whereas for α>7˚ the wake thickness increases with greater h/c as a result of the larger flow separation.

• Two turbulence intensity peaks form for α>10˚ due to turbulence from the trailing edge (upper peak) and the boundary layer flow separation on the suction surface of the airfoil (lower peak); for α<10˚ only one peak exiss. As h/c increases, the two peaks for α>10˚ become more distinct.

• The turbulent normal stress (*uu*) and primary shear stress (*uv*), form two peaks in the wake as a result of the trailing edge and suction surface boundary layer separation. The turbulent normal stress has two peaks which are positive, whereas the primary shear stress has two peaks of opposing signs. A negative *uv* peak in

the upper y/c part of the wake is due to the trailing edge shear layer and downwash interaction with the airfoil wake. The positive uv peak in the lower y/c part of the wake forms due to the suction surface boundary layer separation and subsequent upwash of the wake as a result of the venturi section the wing's suction surface shape forms between the moving ground.

· Turbulence intensity, turbulent normal stress and primary shear stress all increase significantly from midrange angles (α=5° & 7°) to α=10°; for α>10° as h/c increases they increase. For angles of incidence -2°<α<7°, Tu, uu and uv reduce with increasing α and h/c from 0.134-0.313. Therefore for large separated flows or bluff bodies in ground effect (i.e. Tyrrel026 for α>10°), as h/c increases the turbulence intensity, turbulent normal stress and primary shear stress increase for h/c>0.134.

· A discontinuity at h/c=0.112 in the trends of uu, uv and Tu from h/c=0.313-0.134 coincided with the onset of the force (C_L) reduction phenomenon with reducing ground clearance at h/c=0.134 in previous work by Zerihan (2001). The values of turbulent normal stress, primary shear stress, turbulence intensity were generally lower at h/c=0.112 for the majority angles of incidence and ground clearance than for h/c≥0.134. Additionally, the greatest u/U_o deficit existed at x/c=2.07 for h/c=0.112 for all angles of incidence.

10.1.4 Dimpled Tyrrell 026 Airfoil

The wake measurements of the dimpled Tyrrell026 airfoil indicated that the 1.5-3-23 series dimple array (1.5D spacing, 3 rows at x/c=0.23) most effectively reduced the wake size and increased the wake velocity from the clean wing (u/$U_{o,min}$=-0.1) to u/$U_{o,min}$=0.4 for the 1.5-3-23 wing. Chapter 6 indicated that 1.5D, 2D and 2.5D arrays with 3-5 rows located 1D-5D from the separation point can all potentially reduce the flow separation, thus various 5 row dimple array configurations and some 3 row configurations were tested on the wing. In order to evaluate the wake improvements due to multiple dimple array configurations and locations, the difference between the velocity profiles of the clean wing and the dimpled wing wake were taken for x/c=1.03-2.07. Numerically analysing the difference of the dimpled and clean wing wake's (using equation 9.1) allowed a quantitative improvement of the wake to be calculated rather than a qualitative estimate of the graphed differences in the wake profile's size and intensity.

・The 1.5D spaced arrays yielded the biggest reduction of the wake properties studied. The 2D and 2.5D arrays generally had less effect on the wake, and only reduced the wake at α=10°.

・Although the 2D and 2.5D spaced arrays reduced the size and velocity deficit of the wake, turbulence intensity reduction only existed for both arrays at α=10° for h/c=0.224-0.313. Only the 1.5D spaced array resulted in the additional turbulence intensity reduction for all ground clearances for a broader range of angle of incidence.

・The 1.5-3-23 series dimple array wing had the biggest improvement to the wake flow structure at α=10° for all range of h/c tested. In some instances however the 1.5-3-23 series dimple wing did not improve the flow compared to the 'clean' airfoil. The placement of the array in such a forward position (at x/c=0.23) on the wing resulted in u/U_o increasing between -2°≤α≤2° for all h/c. As the lower angle of incidence with the forward dimple array results in earlier separation compared to the 'clean' airfoil. Additionally there are increases of Tu for α≥13° at h/c=0.112-0.313, as well as uu and uv for α≥13° at h/c=0.112-0.134 with the 1.5-3-23 series dimple array wing. The large scale flow separation at the higher angle of incidence with the dimple array is potentially due to the separation point existing within the array, causing greater flow instability, thus u/U_o reductions or increases are less predictable.

・Positioning the dimple array towards the trailing edge had some benefit by reducing uu, uv and minor u/U_o profile recovery in the wake at lower angles of incidence. This being due to separation point being further towards the trailing edge for a lower angle of incidence, thus the dimple array is optimally positioned to recover the flow in the wake. As velocity gradients are low in the wake for low angles of incidence, the dimple array Re_D is lower thus any potential 'benefit' to the flow is reduced.

・The position of the array furthest towards the leading edge of the airfoil, such that the array was closest to the point of the minimum distance between the airfoil and the ground (i.e. at which point on the airfoil h/c is defined) ensured the most gain by the dimple array in reducing the wake. The expected higher velocities between the wing and the ground will increase the vorticity production of the dimples (as Re_D is higher) for a constant h/c.

・The effect the dimple array has on the wake is greater with increasing ground

clearance, the largest wake reductions occur at h/c=0.313. This follows that as the ground clearance reduces the dampening effect the moving ground plane has on the flow around the wing increases. This impacts on the ability of the array to mix the flow within the boundary layer. Only the dimple array with the closest dimple to dimple spacing (1.5D) will produce enough vortex strength/shedding to overcome this trend to yield any benefit in reducing the wake.

· The wing tip vortex study of the dimpled wing indicated that the absence of the large velocity deficit in the wake, as a result of the improved flow allows the vortex to rotate freely. Therefore the wing tip vortex does not break down as much, and the vortex core's path deviates more to occupy the zone where the clean wing's large scale wake existed.

10.2 Concluding Remarks

The research programme methodology outlined in figure 1.4 indicates how the focus of chapters 5, 6, 7, 8 and 9 integrate with each other. Primarily this relates to the interaction of the flow from the dimple array with the wing in ground effect, or the simplified case of the separated flow from the rearward ramp. This ties in with the investigation of the vorticity production of a single dimple (with the expected experimental Reynolds numbers based on the dimple print diameter) indicating: how strong the vorticity is, how far away above the surface and downstream from the dimple the vorticity acts on the surrounding boundary layer.

It was shown for the single dimple for Re_D=4.0x10^3 and 9.0x10^3, that the vorticity magnitude penetrates into the boundary layer y/D≤0.11, and that this propagates downstream of the dimple x/D=0-1 for Re_D=4.0x10^3, and x/D=2-3 for Re_D=9.0x10^3. Additionally the highest vorticity occurs on the rearward or downstream dimple rim, not on the spanwise dimple rim, as the fluid ejection from the rear of the dimple and the inflow from the open side windows combine in this region. The flow in an array of dimples (and subsequent vortex production) may be more complicated as the flow 'zig-zags' between dimples in the array, this may only increase in complexity as the dimple to dimple spacing reduces. However the results from chapter 6 for the dimple array effect on the 16° rearward ramp flow separation show that for Re_D=4.3x10^3, the vorticity produced from an array of multiple rows of dimples is best positioned 3D-5D from a separation point. For a single dimple (Chapter 5) the vorticity is augmented

x/D=0-1 downstream of the dimple, therefore the increased number of rows has increased the vorticity production further downstream. For one row of dimples if they are placed too close to the separation point the flow separation increases and if the dimple to dimple spacing is further apart the better it is.

The different configurations of dimples acting on the 16° rearward ramp indicated that 3 to 5 rows placed 1D-5D from the separation point most effectively reduced flow separation. The closer that the dimples were spaced in an array, the greater the improvements to u/U_o profile recovery were. However 2D and 2.5D spacing also yielded benefits, although these arrays had less u/U_o profile recovery there were more consistent reductions i.e. a flatter $\Delta u/U_o$ curve in figure 6.19 and 6.20. The 1.5D dimple to dimple spaced array with 3 rows placed 3D from the separation point (A1.5-R3-D3) gave the highest flow recovery at x=200mm downstream of the separation point. The 1.5D dimple to dimple spaced array with 5 rows also yielded high u/U_o profile recovery, although less than the A1.5-R3-D3, but was more consistently improved the u/U_o profile when placed 1D-5D from the separation point. Upon selecting mostly 5 row dimple arrays for the dimpled wing experimental investigation (apart from where physical placement on the wing towards the leading edge dictated only 3 rows would fit), the results of the dimple array acting on the 16° rearward ramp were reflected by the dimpled wing results.

When the dimple arrays are applied to the suction surface of the wing in chapter 8, results indicated that the array with 1.5D dimple to dimple spacing and 3 rows placed at x/c=0.23 (1.5-3-23 series wing) most effectively reduced the wake size, and minimized the velocity deficit from $u/U_{o,min}$=-0.1 of the clean wing, to $u/U_{o,min}$=0.4 for (figure 8.7a). This also corresponded to the most effective array in chapter 6 (A1.5-R3-D3) when placed 3D from the separation point. Therefore a closely spaced dimple array with three rows shows the most potential wake improvement, as the vorticity production is clearly the highest and most efficient. Five rows of dimples results in too much vortex interaction as the multiple vortices interweave throughout the bigger array and interweave thus impede or interfere with each other. An array with one row has little influence as the vortex strength is insufficient.

Chapter 6 showed that the greater dimple spacing in the array resulted in less flow separation reduction; additionally this was reflected for the dimple to dimple

spacing on the wing. However, the closest dimple to dimple spaced array (1.5D) did result in wake size increases (and greater velocity deficit) when the dimples were not located properly to the flow separation point. As the dimple spacing within the array increased, the detrimental influence of the array on the wake of the wing (where it occurred) was less. Again this follows that the greater the spacing, the more consistent the changes in wake size are with varying placement of the array, albeit the potential flow recovery of the wake is less. Additionally it was shown that the further forward the array was located towards the leading edge of the wing, the better it acted at reducing the higher angle of incidence flow separation. Whereas the lower angle of incidence dictates the array is placed towards the trailing edge. The change in optimum position of the array is due to the migrating separation point as both ground clearance and angle of incidence vary.

As seen in chapter 6, maintaining a distance of 1D-5D from the separation point is significant, as the further it is placed from the separation point several things can occur depending on the angle of incidence. For a low angle of incidence a forward placed array can: advance the separation point and increase the wake, be located within the separation point and cause little change and/or increase the wake. For higher angles of incidence the turbulent mixing and vortices produced from the dimple array can dampen out before the separation point and yield no little or no change. For rearward placed arrays at higher angles of incidence they can be located entirely behind the separation point and result in only a minor change, or be located within the separation point and cause little change and/or increase the wake. It appears that only for a high angle of incidence a forward placed array consistently reduces the wake, and that for a lower angle of incidence a rearward placed array reduces the wake.

The ability of the array of dimples to produce discrete vortices has resulted in the mixing of the boundary layer on the airfoil and on the simplified rearward ramp experiments to reduce the amount of flow separation of these bodies. Placing the dimples upstream of the flow separation point also results in an interaction of the shedding frequency of the dimples and the frequency of the initial separated boundary layer. The reductions in both u-RMS and turbulent normal stress (uu) are seen in chapters 6 and in chapter 8 respectively. The fact that the separated shear layer has

reduced u-RMS and *uu* indicates that the lower fluctuations in the boundary layer are a result of it being re-energized by the dimple array. Due to the reduction of flow separation size and intensity, the pressure recovery demands of the curvature of the surface are less as a result of the dimples; as with normal vortex generators. The improved overall flow conditions under the wing and in the wake result in reduced turbulence and Reynolds stress. In some cases where little or no flow recovery exists, there are reductions to turbulence and Reynolds stresses in the wake.

The presence of the dimple array does not simply act as a boundary layer trip on the wing. In comparing the dimple array with a boundary layer trip wire it was shown that the boundary layer trip/transition wire resulted in a flow condition somewhere in between the clean wing and the dimple array. This highlights that the dimple array is producing more vortical mixing within the boundary layer than the shearing action of the boundary layer transition wire tripping it from laminar to turbulent. It is also not merely a case of the dimples acting the same was as the trip wire but more effectively, as when the most effective dimple array on the wing (1.5-3-23 at α=10˚) was at a lower angle of incidence (-2˚≤α≤2˚) the wake grew due to earlier separation on the lower surface of the wing.

The ability of the dimpled wing to reduce flow separation at α=10˚ improves as the ground clearance of the wing increases. This is seen in the suction surface boundary layer measurements of both the dimpled wing compared to the clean wing, as large reductions exist for the dimpled wing u-RMS values at h/c=0.313 from h/c=0.112 in figures 8.48 and 8.49 in chapter 8.6. The large reduction of both u-RMS and *uu* of the dimpled wing with increasing height runs counter to the non dimpled wing, as *uu* in the wake increases with increasing h/c; seen in figures 7.21-7.27 in chapter 7.5. Thus the degree to which fluctuations in the boundary layer and the flow over the clean wing increase, the ability of vortex shedding from the dimple array has a larger interaction with the separation point and suppresses the wake to a higher extent upon dimpling the surface of the wing.

The relationship with the ground clearance is critical to many properties of the aerodynamic characteristics of the airfoil. It was shown that downforce enhances for the 'clean' Tyrrell026 airfoil as the ground clearance reduces to h/c=0.134, beyond which the force reduction phenomenon as h/c lowers further reduces the downforce

gains (Zerihan 2001) and the Strouhal number reduces from h/c=1.0 to h/c=0.2 for a half ellipse body (Kim & Geropp 1998). The results for the 'clean' Tyrrell026 wing in chapter 8 showed turbulence intensity (Tu), turbulent normal stress (*uu*) and primary shear stress (*uv*) all increase significantly from α=5˚ & 7˚ to α=10˚. For α≥10˚, as h/c increases Tu, *uu* and *uv* increase further still. Therefore for large separated flows or bluff bodies in ground effect, as h/c increases the turbulence intensity, turbulent normal stress and primary shear stress increase for h/c>0.134. However as these fluctuating flow components and Reynolds stresses increase in the wake with increasing h/c, the flow structure of the wake of the 'clean' wing becomes shorter (the u/U_o deficit is less at x/c=2.07) and the u/U_o profile is biased or 'skewed' towards the ground more at h/c=0.313.

The dominating factor in the flow field of the inverted wing in ground effect is the venturi style duct that is formed between the wing and the ground. For higher angles of incidence (α=10˚) and reducing ground clearance, the moving ground plane's influence on the suction surface of the wing causes earlier separation and reduced u-RMS and *uu* in the boundary layer compared to higher h/c; whilst the flow velocity between the wing and the ground increases. The higher velocity fluid exiting the narrow gap between the wing and the ground propagates downstream, forming a 'barrier' of higher velocity fluid between the wake and the ground. For α=10˚ at h/c=0.134 this limits the amount deviation the wake has towards the ground. At h/c=0.313, the boundary layer separates later as well as having higher values of u-RMS and *uu*. The larger gap results in lower flow velocity under the wing which leaves the wake less constrained due to the faster flowing fluid 'barrier' weakening and subsequently is skewed down to the ground more as the wake interaction is decoupled to the moving ground boundary layer

With the ground clearance h/c=0.112, below the expected force reduction ground clearance of h/c=0.134 (Zerihan 2001), there are several discontinuities in the trends of: u/U_o profile distribution, Tu, *uu* and *uv*, in that the previous reductions from h/c=0.313 to h/c=0.134 now increase to h/c=0.112 (but are still less than h/c=0.313). For h/c<0.134, the venturi section is now in its more critical flow regime, the wake 'skew', velocity deficit and flow interaction is now considerable with the moving ground boundary layer. The increased velocity deficits of u/U_o at x/c=2.07 show the

wake has elongated. This coincides with the reduced Reynolds stresses, and lower *uu* and u-RMS values in the boundary layer which 'dampen' the wake less, allowing it to propagate further downstream. The smaller gap between the wake of wing and the boundary layer on the moving ground cause the two previously separate entities to merge. This gives rise to the flow separation 'blockage' due to the now larger wake behind the wing limiting the upstream flow rate in the gap between the wing and ground, choking the flow. The pressure between the wing and the ground would inturn rise and give lead to the force reduction noted in Zerihan (2001). The boundary layer measurement at h/c=0.313 and 0.112 shows a decrease in u-RMS at the lower ground clearance. However it was not established whether, like Tu, *uu* and *uv*, there is a sudden increase in u-RMS of the wing boundary layer from h/c=0.134 to 0.112 by measuring the boundary layer at h/c=0.134.

The dimpled wing reverses the clean wing trend of Tu, *uu* and *uv* increasing as h/c increases, as the shedding frequency disrupts the boundary layer. As h/c increases and the u-RMS of the boundary layer on the wing alters, the dimpled wing now produces a bigger wake reduction. With the increased height and less ground interference with the wing boundary layer fluctuations, the dimple array is able to shed stronger vortices. As the flow velocity, Reynolds stresses and turbulence are stabilized under the wing as a result of the dimple array, the flow recovers quite effectively such that u/U_o is positive at x/c=1.03 for α=10° at h/c=0.313, (figure 8.9 and 8.46b). The previous downward wake 'skew' is negated, and a thin wake results and follows the camber and angle of incidence of the airfoil, refer figure 8.8-8.11.

The measurements in the wake of the dimpled wing in chapter 8 and 9 indicate substantial flow improvements from the clean wing. Given the multiple dimple array configurations and placements investigated, how much the wake can be influenced and reduced has been shown. The aerodynamic performance will not be complete without proper mapping of lift (downforce) and drag forces for the array configurations that have been shown benefit the flow structure. The improved flow under the wing due to the dimples has a higher velocity (u/U_o increases +0.2 in figure 8.44) therefore due to the higher velocity and thus presumably lower pressure it would be reasonable to assume downforce has increased, particularly at α=10° for the range of ground clearance tested. The wingtip vortex study shows a substantial

improvement to the wake and the resultant wingtip vortex has increased strength downstream, this higher vortex strength downstream indicates potential gains to the downforce to drag ratio.

Downforce and drag measurements may also show improvement to the height at which the downforce reduction occurs, the h/c=0.134 ground clearance for the Tyrrell026 airfoil may be reduced as a result of the dimple array. This is a result of the suction surface boundary layer fluctuation reducing and less wake/ground interaction at x/c=2.07 for the 1.5-3-23 series for α=10˚ at h/c=0.112. The respective u/U$_o$ profile for the 'clean wing' at x/c=2.07 for α=10˚ at h/c=0.112 is clearly skewed more towards the ground plane.

For bluff bodies or those with large flow separation, the pressure drag (or form drag) is usually substantially higher than the viscous drag component, thus small changes in pressure drag usually outweigh small changes to viscous drag. The noticeable changes to the wake flow separation would expect to reduce pressure drag of the airfoil. Most vortex generators result in viscous drag increases due to mixing within the boundary layer. As standard boundary layer protruding vortex generators produce increased shearing action to mix the flow than the submerged dimples, it is expected that the dimple array vortex generators will result in less viscous drag increase. Therefore although there is a potentially slight viscous drag increase due to the dimple array, the improved flow recovery of the wake and the elimination of the large scale separation (in particular for the 1.5-3-23 series wing at h/c=0.313 for α=10˚), it is expected that the pressure drag reduction will be greater.

10.3 Future work

The present study focused on improvements to the wake as a result of the dimpled surface on the suction side of the airfoil. This allowed an understanding of the benefits to the flow of different configurations and positions of various dimple arrays. However further work is needed in order to determine the applicability of such surfaces to benefit the aerodynamic performance and efficiency of an airfoil that dimple array vortex generators are applied to. This includes:

• Large scale aerodynamic testing of the dimpled wing to focus on force measurements for both lift and drag. This will allow a lift curve slope to be determined and compare to the clean wing how stall angle changes, and what stability affects the dimples

have at full scale testing speeds (possible panel vibration etc).

• The dimple array positioned towards the trailing edge providing greater wake relief at lower angles of incidence and arrays positioned towards the leading edge providing wake relief at higher angles of incidence. Therefore if combinations of these are used it may lead to greater wake reductions for a larger angle of incidence range.

• Experimental measurements with LDA and micro PIV focusing on the array geometry changes not covered in the current study, i.e. more rows than 5, different dimple to dimple spacing.

• Measurements relating to the dimple array vortex production and interaction with varying boundary layer u-RMS and uu values to see how the shedding frequency and vortex strength changes.

• Further numerical work on: the flow within a dimple array with various dimple to dimple space increases, the affect that surface curvature (as in the suction surface of the airfoil) has on the vortex formation of the dimple and a full analysis of the wing with dimples. This all allow a finer positioning of the array (and the best configuration) with respect to the flow separation point. As well as varying the Reynolds number along the array as the flow under the wing accelerates and then decelerates to see how this alters the flow structure in the array and the dimple to dimple vortex production and interaction.

• By altering the dimple shape to be asymmetric might result in great efficiency of dimple vortex production by utilizing the tendency of a larger vortex to form at higher Re_D. If the larger vortex is impeded less, and vortex cell magnification is promoted to occur earlier larger vorticity production and improvements to the wake reduction may result.

References

[1]   Abbot I.H., von Doenhoff, A.E., "Theory of wing Sections", Dover Publications, New York, 1959

[2]   Adrian, R.J., "Multi-Point Optical Measurement of Simultaneous Vectors in Unsteady Flow - a Review", *International Journal of Heat & Fluid Flow*, Vol. 7(2): pp. 127-145, 1986

[3]   Adrian, R.J., "Particle-Imaging Techniques for Experimental Fluid Mechanics", *Annual Review of Fluid Mechanics*, Vol. 23: pp. 261-304, 1991

[4]   Afanas'yev, V.N., Yu., V., Leont'ev, A.I., et al., "Thermohydraulics of Flow Over Isolated Depressions (Pits, Grooves) in a Smooth Wall on a Plane", *Heat Transfer Research*, Vol. 25, No. 1, pp 22-56, 1993

[5]   Ahmed, M.R., Takasaki, T., Kohama, Y., "Experiments on the Aerodynamics of a Cambered Airfoil in Ground Effect" *44th AIAA Aerospace Sciences Meeting*, AIAA 2006-258

[6]   AIAA Guide, "Guide for the Verification and Validation of Computational Fluid Dynamics Simulations", AIAA, G-077-1998

[7]   Ailor, W., Eberle, W., "Configuration Effects on the lift of a Body in Close Proximity to the Ground", *Journal of Aircraft*, Vol. 13, No. 8, 1976, p584-589

[8]   Albrecht, H.E., Borys, M., Damanshke, N., Tropea, C, "Laser Doppler and Phase Doppler Measurement Techniques", Springer, New York, 2003

[9]   Angele, K.P., "The Effect of Streamwise Vortices on the Turbulence Structure of a Separating Boundary Layer", *Euro. J. of Mech. and B.Fluids*, Vol. 24, 2005, pp. 539-554

[10]   Barber, T., Leonardi, E., "Causes for Discrepancies in Ground Effect Analyses", *The Aeronautical Journal*, Dec. 2002 pp. 653-667

[11]   Barber, T.J., "A study of a lifting wing in ground effect", PhD, University of New South Wales, 2000

[12]   Barlow, J.B., Rae, W.H., Pope, A., "Low-Speed Wind tunnel Testing", 3rd Edition, John Wiley & Sons, 1999

[13]   Bearman, P. W., Harvey, J.K., "Golf Ball Aerodynamics" *Aeronautical Quarterly*, Vol 27. No. 2, May 1976, pp.112-122

[14]   Bearman, P. W., Harvey, J.K., "Control of Circular Cylinder Flow by the use of Dimples" *AIAA Journal*, Vol. 31, No.10, October 1993

References

[15]   Bearman, P.W., De Beer, D., Hamidy, E., Harvey, J.K. "The Effect of a Moving Floor on Wind Tunnel Simulation of Road Vehicles", SAE 880245, 1988

[16]   Beauvis, F.N., Tignor, S.C., Turner, T.R., "Problems of Ground Simulation in Automotive Aerodynamics", SAE 680121, 2968

[17]   Belen'kii, M. Ya., Gotovinskii, M.A., Lekakh, B.M., et al. "Intensification of heat exchange with the use of surfaces formed by spherical indentations", *Heat and Mass Exchange, MMF-92*, Vol. 1, part 1, pp. 90-92, ITMO ANB, Minsk, 1992

[18]   Benedict, L.H., Gould, R.D. "Towards Better Uncertainty Estimates for Turbulence Statistics", *Exp. in Fluids*, Vol. 22, 1996, pp. 129-136

[19]   Bienz, C., Larsson, T., "In Front of the Grid - CFD at Sauber Petronas F1 Leading the Aerodynamic Development", *EACC 1st European Automotive CFD Conference Germany*, June, 2003, pp.51-60.

[20]   Bunker, R.S., Donnellan, K.F., "Heat Transfer and Friction Factors for Flows Inside Circular Tubes with Concavity Surfaces", *Proc. ASME Turbo Expo*, 2003, June 16-19, Atlanta, Georgia, USA

[21]   Bunker, R.S., M. Gotovskii, M., "Heat Transfer and Pressure Loss for Flows Inside Converging Channels with Surface Concavity Effects", *Proc. Of 4th Int. Conf. Compact Heat Exchangers and Enhancement Technology,* 2003

[22]   Burgess, N.K., Olivera, M.M., "Nusselt Number Behaviour on Deep Dimpled Surface Within a Channel", *J. Heat Transfer*, Vol. 125, p11-18, Feb. 2003

[23]   Carr, G.W. "A Comparison of the Grouind Place Suction and Moving Belt Ground Representation Techniques", SAE 880249

[24]   Chambers T.L., Wilcox, D.C., "Critical Examination of Two-Equation Turbulence Model Closure for Boundary Layers", *AIAA Journal*, Vol 15, No. 6, pp.821-828, 1977

[25]   Chawla, M., Edwards, L., "Wind Tunnel Investigation of Wing in Ground Effects" *Journal of Aircraft*, Vol. 27, No. 4, 1990 p289-293.

[26]   Chew, Y.T., Khoo, B.C., "Flow Visualization Studies on Flow Structures Within Spherical Dimples of Different Depths With/Without Round Edges", *Proceeding of 5th PSFVIP*, PSFVIP-5-280, 27th-29th Sept, 2005, Aust.

[27]   Choi, J. W-P. Jeon, W-P., Choi, H., "Mechanism of Drag Reduction by Dimples on a Sphere", *Physics of Fluids*, Vol. 18, 041702-1, 2006

[28]   Coray, P., "Establishing a Partical Imge Velocimetry System for Studying Heat Transfer Enhancements Using Dimpled Surfaces", MEngSc Thesis, University of New South Wales, School of Mech. and Manuf. Eng., 2005

[29]   Cook, R.R., "Assessment of Uncertainties of Measurement for Calibration and Testing Laboratories" 2nd Edition, Rhodes, Australia (NSW), 2001

[30]   Cullen, L.M., Han, G., Zhou, M.D., Wygnanski, I., "On the role of longitudinal vortices in turbulent flow over a curved surface", *1st Flow Control Conference*, AIAA 2002-2828

[31]   Daniel Metz, L., "Aerodynamic Properties of Indy Cars", SAE 870726, 1987

[32]   DANTEC, "BSA Flow Software Installation & User's Guide v4.10", 10th Edition, DANTEC, 2006, Denmark

[33]   Davies, J.M., "The Aerodynamics of Golf Balls", *J. of Applied Physics*, Vol. 20, No. 9 Sept, 1949

[34]   Eaton, J. K., Johnston, J. P., "A Review of Research on Subsonic Turbulent Flow Reattachment", AIAA Journal, 0001-1452, vol.19 no.9, 1981, pp.1093-1100

[35]   Ekkad, S.V., Nasir, H., "Dimple Enhanced Heat Transfer in High Aspect Ratio Channels" *2001 ASME Conf*, Nov 11-196, 2001, New York, Paper No:. 2-14-1-4

[36]   Ezerskii, A.B., Shekov, V.G., "Visualization of a heat flow with air flow over separate spherical depressions", *Izv .AN SSR. MZhG*, no.6, pp. 161-164, 1989

[37]   Fago, B., Linder, H., "The Effect of Ground Simulation on the Flow around Vehicles in Wind Tunnel Testing", *J Wind Eng. & Industrial Aerodynamics*, Vol. 38, 1991, pp.47-57

[38]   "FLUENT User Guide", FLUENT, 2006

[39]   Garcia, D.L., Katz, J., "Trapped Vortex in Ground Effect", *AIAA Journal*, Vol. 41, No.4, April, 2003 pp. 674-678

[40]   Goldberg, U., "Hypersonic Flow Heat Transfer Prediction using Single Equation Turbulence Models", *Journal of Heat Transfer*, Vol. 123, 2001, pp.65-69.

[41]   Hackett, K.C., "Applications of Flow Control to Sections Designed with Upper Surface Trailing Edge Separation", *2nd AIAA Flow Control Conference*, AIAA 2004-2214

[42]   Hall, S.D., "An Investigation of the Turbulent Backward Facing Step Flow with the Addition of a Charged Particle Phase and Electrostatic Forces", PhD, UNSW, 2001

[43]   Hansen, L., Bons, J., "Time Resolved Flow Measurements of Unsteady Vortex Generator Jets in a Separating Boundary Layer", *2nd AIAA Flow Control Conference*, AIAA 2004-2202

[44]   Hemke, P., "Drag of Wings with End Plates", NACA, TR-267 1928

[45]   Huang, H., Dabiri, D., Gharib., M., "On Errors of Digital Particle Image Velocimetry", *Meas. Sci. Tech*, Vol.8, 1997, pp1427-1440

[46]   Hucho, W.H., Sovran, G., "Aerodynamics of Road Vehicles", *Ann. Fluid Rev. Mech*, 1993, Vol. 25, pp.285-537

[47]   Isaev, S.A., Kharchenko, V.B., "Calculation of a Three-Dimensional Flow of a Viscous Incompressible Liquid in the Neighborhood of a Shallow Well on a Flat Surface", *J. Engineering Physics and Thermophysics*, Vol. 67, pp.5-6, 1994

[48]   Isaev, S.A., Leont'ev, A.I., "Numerical Study of the Eddy Mechanism of Enhancement of Heat and Mass Transfer near a Surface with a Cavity", *J. Engineering Physics and Thermophysics*, Vol. 71, No.3, 1999

[49]   Isaev, S.A., Leont'ev, A.I., "Identification of Self-Organized Vortex like Structures in Numerically Simulated Turbulent Flow of a Viscous Incompressible Liquid Streaming around a Well on a Plane", *Technical Physics Letters*, Vol. 26, No.1, 2000

[50]   Isaev, S.A., Leont'ev, A.I., "Bifurcation of Vortex Turbulent Flow and Intensification of Heat Transfer in a Hollow", *Doklady Physics*, Vol. 45, No. 8, 2000, pp 389-391

[51]   Isaev, S.A., Leont'ev, A.I., "Analysis of the Effect of Viscosity on the Vortex Dynamics at Laminar Separated Flow Past a Dimple on a Plane with Allowance for its Asymmetry", *J. Engineering Physics and Thermophysics*, Vol. 74, No.2, 2001

[52]   Isaev, S.A., Leont'ev, A.I., "Modelling of the Influence of Viscosity on the Tornado Heat Exchange in Turbulent Flow around a Small Hole on the Plane", *J. Engineering Physics and Thermophysics*, Vol. 75, No.4, 2002

[53]   Isaev, S.A., Leont'ev, A.I., "Numerical Simulation of Vortex Enhancement of Heat Transfer under Conditions of Turbulent Flow Past a Spherical Dimple", *High Temperature*, Vol. 41, No. 5, 2003, pp. 665-679

[54]   Isaev, S.A., Leont'ev, A.I., et al., "Numerical Analysis of the Influence of the Depth of a Spherical Hole on a Plane Wall on Turbulent Heat Exchange", J. *Engineering Physics and Thermophysics*, Vol. 76, No. 1, 2003

[55]   Isaev, S.A., Sudakov, A.G., "Effect of Supercirculation in a Flow around a Thick Airfoil with Vortex Cells", *Doklady Physics*, Vol. 46, No. 3, 2001, pp. 199-201

[56]   ISO Guide, "Geometrical Product Specifications Part 1", ISO 14253-1:1998

[57]   Park, J. P.R. Desam, "Numerical Predictions of Flow Structure above a Dimpled Surface in a Channel", *Num. Heat Transfer*, Part A, Vol. 45, pp1-20, 2004

[58]   Jeon, S., Jin Choi, et al., "Active control of flow over a sphere for drag reduction at a subcritical Reynolds number", *J. Fluid Mech*, (2004), vol. 517, pp. 113-129

[59]   Jones, W.P., Launder, B.E., "The Prediction and Laminarization with a Two-Equation model of Turbulence", *International Journal of Heat & Mass Transfer*, Vol. 15, 1972, pp. 301-314

[60]   Kahler, C.J., "The significance of coherent flow structures for the turbulent mixing in wall-bounded flows", Dissertation Georg-August-Universitat, Gottingen, 2004

[61]   Kato, T., Fujita, T., Ito., Y., "Computational Analysis of Separated Flows Around a Golf Ball Using Unstructured Grid CFD", *15th AIAA Computational Fluid Dynamics Conference*, AIAA 2001-2569

[62]   Katz, J., "Investigation of Negative Lifting Surfaces Attached to an Open-Wheel Racing Car Configuration", SAE 850283, 1985

[63]   Katz, J., "Aerodynamic Model for Wing-Generated Downforce on Open-Wheel Racing Car Configuration", SAE 860218, 1986

[64]   Katz, J., Dykstra, L., "Effect of Wing/Body Interaction on the Aerodynmaics of 2 Generic Racing Cars", SAE 920349, 1992

[65]   Katz, J., Largman, R., "Experimental Study of the Aerodynamic Interaction Between an Enclosed-Wheel Racing-Car and its Rear Wing", *J. Fluids Engineering*, Vol. 111, June, 1989, pp. 154-159

[66]   Keane, R.D., & Adrian, R.J., "Theory of Cross-Correlation analysis of PIV images", *Applied Scientific Research*, Vol. 49, pp.191-215, 1992

[67]   Kesarev, V.S., Kozlov, A.P., "Flow Structure and heat exchange with a turbulized air flow over a hemispheric depression", Vestnik MGTU, Ser. Mashinostronie, no. 1, pp. 106-115, 1993

[68]   Khalatov, A.A., Byerley, A., et al., "Flow Characteristics Within and Downstream of Spherical and Cylindrical Dimple Configurations on a Flat Plate under Laminar Flow Conditions", *Proceedings of the ASME Turbo Expo*, Vienna, Austria, June 14-17, 2004, ASME Paper No. GT2004-53656

[69]   Kiknadze, G.I., Gachechildze, I.A., Oleinikov, V.G., "Method and Apparatus for Controlling the Boundary or Wall Layer for a Continuous Medium", US Patent, No.6, 119, 987 2000

[70]   Kim, H-C., Kim, H-J., Nakahashi, K., et al., "Flow Analysis around Golf Balls without and with Spinning", *24th Applied Aerodynamics Conference*, AIAA 2006-2996

[71]   Kim, M.S., Geropp, D., "Experimental investigation of the ground effect on the flow around some two dimensional bluff bodies with ground effect", *J. Wind Engineering and Industrial Aerodynamics,* 74-76, 1998, pp.511-519

[72]   Kimura, T., Tsutahara, M., "Fluid Dynamic effects of grooves on a cylinder surface", *AIAA Journal*, Vol. 29(12), pp. 2062-2068, December 1991

[73]   Klausmeyer, S.M., "A Flow Physics Study of Vortex Generators on a Multi-Element Airfoil", *34th Aerospace Sciences Meeting and Exhibit*, Reno, Jan. 15-18, 1996, AIAA-1996-548

[74]   Kline S.J., McClintock, F.A., "Describing uncertainties in single sample experiments", *Mechanical Engineering*, Vol. 75, No. 1, Jan, 1953, pp. 3-8

[75]   Knowles, R.D., Finnis, M.V., et al., "Planar visualization of vortical flows", Proc. IMechE, Vol. 220 Part G: *J. Aerospace Engineering,* pp. 619-627, 2006

[76]   Kozlov, A.P., Shchukin, A.V., Agachev, R.S., "Hydrodynamic effects from spherical epressions on the surface of a cylinder transverse to the flow", *Izv. Vuzov. Aviats. Technika*, no. 2, pp. 27-34, 1994

[77]   Kroo, I., "Drag due to Lift: Concepts for Prediction and Reduction", *Ann. Fluid Rev. Mech,* 2001, 33 pp. 587-617

[78]   Lake, J.P., King, P.I., "Low Reynolds Number Loss Reduction on Turbine Blades with Dimples and V-Grooves", AIAA-00-0738, 2000

[79]   Lee, G., Ferguson, F., "A Numerical Investigation on Aerodynamic Property and Heat Transfer Enhancement for Surfaces with Concave Cavities", *42nd AIAA Aerospace Sciences Meeting and Exhibit*, AIAA 2004-488, 2004

[80]   Lee, H-T., Kroo, I.M., "Computational Investigation of Wings with Miniature Trailing Edge Control Surfaces", *2nd AIAA Flow Control Conference*, AIAA 2004-2693

[81]   Ligrani, P.M., "Flow Visualization and Flow Tracking as Applied to Turbine Components in Gas Turbine Engines", *Meas. Sci. Tech*, Vol. 11, (2000), pp. 992-1006

[82]   Ligrani, P.M., Burgess, N.K., "Nusselt Numbers and Flow Structure on and Above a Shallow Dimpled Surface Within a Channel Including Effects of Inlet Turbulence Intensity Level", *J Turbomachinery*, Vol. 127. April 2005, pp. 321-330

[83]   Ligrani, P.M., Harrison, J.L., "Flow Structure due to Dimple Depressions on a

Channel Surface", *Physics of Fluids*, Vol. 13, No.11, Nov 2001, pp. 3442-3451

[84]   Ligrani, P.M., Park. J., "Numerical Predictions of Heat Transfer and Fluid Flow Characteristics for Seven Different Dimpled Surfaces in a Channel", *Num. Heat Transfer (Part A)*, Vol. 47, pp. 209-232, 2005

[85]   Ligrani, P.M., Won, S.Y., Zhang, Q., "Comparisons of Flow Structure Above Dimpled Surface with Different Dimple Depths in a Channel", *Phys. of Fluids*, Vol. 17, 2005, pp. 3442-3452

[86]   Lim, H-C., Lee, S-J., "Flow Control of a Circular Cylinder with O-rings", Fluid Dynamics Research, Vol. 35, (2004), pp.107-122

[87]   Lin, J., Howard, F., Selby, J., "Turbulent flow separation control through passive techniques", AIAA Paper 89-0976

[88]   Lin, J.C., "Review of Research on Low Profile Vortex Generators to Control Boundary-Layer Separation", *Progress in Aerospace Sciences*, Vol. 38, 2002, pp. 389-420

[89]   Lin, J.C., Howard, F.G., "Investigation of Several Passive and Active Methods for Turbulent Flow Separation Control", *21st AIAA Fluid Dynamics, Plasma Dynamics and Lasers Conference*, Seattle, WA, June 18-20, 1990, p.21

[90]   Lin, J.C., Robinson, S.K., "Separation Control on High Reynolds Number Multi-Element Airfoils", *10th Applied Aerodynamics Conference*, Palo Alto, CA, June 22-24, 1992, AIAA-1992-2636

[91]   Maddah, S.R., Bruun, H.H., "An Investigation of Flow Fields Over Mulit-Element Aerofoils", *J Fluids Enginering*, Vol. 124, March 2002, pp. 154-165

[92]   Mahmood, G.I., Ligrani, P.M., "Heat Transfer in a Dimpled Channel: Combined Influences of Aspect Ratio, Reynolds Number and Flow Structure", *Int. J. of Heat and Mass Transfer*, Vol. 45, pp2011-2020, 2002

[93]   Mahmood, G.I., Sabbagh, M.Z., "Heat Transfer in a Channel with Dimples and Protrusions on Opposite Walls", *J. Thermophysics and Heat Transfer*, Vol. 15, No.3, 2001

[94]   Mahon, S., Zhang, X., "Computational Analysis of Pressure and Wake Characteristics on an Aerofoil in Ground Effect", ASME, Vol. 127, March 2005, pp. 290-298

[95]   McCabe, G., "Explanation and Discovery in Aerodynamics", Physics, Vol. 1, 512224, 22 Dec, 2005

[96]   Moryossef, Y., Levy, Y., "Effect of Oscillations on Airfoils in Close Proximity to the Ground", *AIAA Journal*, Vol. 42, No. 9, Sept 2004

References

[97]   Motson, B.C., Archer, R.D., "Design Features of the Low Speed 4ftx3ft Return Circuit Wind Tunnel", Report No. 19969/FMT/3, UNSW, 1969

[98]   Nagoga, G.P., "Effective Methods of Cooling of Blades of High Temperature Gas Turbines", Publishing House of Moscow Aerospace Institute, p. 100, 1996

[99]   Nickerson, J.D., "A Study of Vortex Generators at low Reynolds Numbers", AIAA Paper No. 86-0155

[100]   Park, J., Desam, P.R., Ligrani, P.M., "Numerical Predictions of Flow Structure above a Dimpled Surface in a Channel", *Num. Heat Transfer (Part A)*, Vol. 45, pp. 1-20, 2004

[101]   Patankar, S.V. Spalding, D.B., "A Calculation Procedure for Heat, Mass and Momentum Transfer in Three-Dimensional Parabolic Flows", *Int. J. Heat Mass Transfer*, Vol. 15, p. 1787, 1972

[102]   Paulson, J., Kjelgaard, S., "An Experimental and Theoretical Investigation of Thick Wings at Various Sweep Angles in and out of Ground Effect", NASA Tech. Paper 2068, 1982

[103]   R.S. Bunker, Gotovskii, M., "Heat Transfer and Pressure Loss for Flows Inside Converging Channels with Surface Concavity Effects", *Proc. Of 4th Int. Conf. Compact Heat Exchangers and Enhancement Tech*, 2003

[104]   Rae, A.J., Galpin, S.A. , Fulker, J., "Investigation into the scale effect on the performance of sub boundary-layer on civil aircraft high-lift devices", *2nd Flow Control Conference*, AIAA 2002-3274

[105]   Raffel, M., Willert, C., Kompenhans., J., "Particle Image Velocimetry: A Practical Guide", Springer, New York, 1998

[106]   Razenbach, R., Barlow, J.B., "Two-Dimensional Airfoil in Ground Effect, an Experimental and Computational Study", SAE 942509, 1994

[107]   Razenbach, R., Barlow, J.B., "Cambered Airfoil in Ground Effect, an Experimental and Computational Study", SAE 960909, 1996

[108]   Razenbach, R., Barlow, J.B., "Multi-Element Airfoil in Ground Effect- An Experimental and Computational Study", AIAA-97-2238, 1997

[109]   Rivir, R.B., Sondergaard, R., "Control of Separation in Turbine Boundary Layers", *2nd AIAA Flow Control Conference*, AIAA 2004-2201, 2004

[110]   Robarge, T.W., Stark, A.M., et al., "Design Considerations of Using Indented Surface Treatments to Control Boundary Layer Separation", *42nd AIAA Aerospace Sciences Meeting*

and Exhibit, AIAA 2004-425

[111]   Sardou, M., "Reynolds Effect and Moving Ground Effect Tested in a Quarter Scale Wind Tunnel over a High Speed Moving Belt", *J. of Wind Eng. & Industrial Aero.*, Vol. 22, 1986, pp.345-370

[112]   Schoppa, W., Hussain, F., "Effective Drag Reduction by Large Scale Manipulation of Streamwise Vortices in Near-Wall Turbulence", AIAA-97-1794

[113]   Schubauer G.B., Spangenberg W.G., Klebanoff, P.S., "Aerodynamic Characteristics of Damping Screens", NACA Technical Note 2001, Jan 1950

[114]   Scott-Collis, S., et al., "Issues in active flow control: theory, control, simulation and experiment", *Progress in Aerospace Sciences*, Vol. 40, 2004, pp. 237-289

[115]   Snedecker, R.S., Donaldson, C., "Observation of Bi-stable Flow in a Hemispherical Cavity", *AIAA Journal*, Vol. 4, No. 4, April 1966, pp. 735-736

[116]   Sowdon A., Hori T., "An Experimental Technique for Accurate Simulation of the Flow Field for Wing in Surface Effect", *Aeronautical J.*, Vol. 100, No. 38, June/July, 1996, pp47-57

[117]   Standingford, D., Tuck, E., "Optimal Rectangular End Plates", *J. Aircraft*, Vol. 33, No. 3, 1996, pp. 623-625

[118]   Steinbach, D., "Comment on Aerodynamic Characteristics on a Two-Dimensional Airfoil with Ground Effect", *J. Aircraft*, Vol. 34, No. 3, 1997, pp. 455-456

[119]   Steinbach, D., Jacob, K., "Some Aerodynamic Aspects of Wings Near Ground", *Trans. Japan Society of Aero. and Space Sci*, Vol. 34(104), 1991, pp. 56-70

[120]   Storms, B.L., "Lift Enhancement of an Airfoil Using a Gurney Flap and Vortex Generators", *Journal of Aircraft*, Vol. 31, No. 3, 1994, pp. 542-547

[121]   Storms, B.L., Ross, J.C., "Experimental Study of Lift Enhancing Tabs on a Two-Element Airfoil", *Journal of Aircraft*, Vol. 32, No. 5, Sept-Oct, 1995

[122]   Sullerey, R.K., Pradeep, A. M., "Secondary Flow Control Using Vortex Generator Jets", *J. Fluids Engineering*, Vol. 126, July, 2004, pp. 650-657

[123]   Tombazis, N., Bearman, P.W., "A study of three-dimensional aspects of vortex shedding from a bluff body with a mild geometric disturbance", *J. Fluid Mech*, (1997), vol. 330, pp. 85-112

[124]   Valarezo, W.O., Dominik, C.J., "Multi-element Airfoil Optimization for Maximum Lift at High Reynolds numbers", AIAA-91-3332-CP, 1991

[125]   van der Berg, J.W., Maseland, J.E.J., Brandsma, F.J., "Low Speed Maximum Lift and Flow Control", *Aerospace Science and Technology*, Vol. 8, 2004, pp. 389-400

[126]   Van Doormal, J.P. Raithby, G.D., "Enhancements for the SIMPLE Method for Predicting Incompressible Fluid Flows", *Numerical Heat Transfer*, Vol. 7, pp.147-163, 1984

[127]   Versteeg, H.K., Malalasekera, V., "An Introduction to Computational Fluid Dynamics", Prentice Hall, 1995, ISBN 0-582-21884-5

[128]   Wang, Z., Yeo, K.S., Khoo, B.C., "Numerical Simulation of Laminar Channel Flow over a Dimpled Surface", *16th AIAA Computational Fluid Dynamics Conference*, AIAA 2003-3964

[129]   Watterson, J.K. et al., "Influence of Sub-Boundary Layer Vortex Generators on Wall Shear Stress", *35th AIAA Fluid Dynamics Conference and Exhibit*, AIAA 2005-4649

[130]   Wetzel, T.G., Simpson, R.L., "Effects of Fin and Jet Vortex Generators on the Crossflow", *Journal of Aircraft*, Vol. 35, No. 3, May-June, 1998

[131]   Wickern, G., Dietz, S., "Gradient Effects on Drag Due to Boundary-Layer Suction in Automotive Wind Tunnels", 2003-01-0655 (SAE)

[132]   Wilcox, D.C., "Turbulence Modeling for CFD", 2nd Edition, DCW, ISBN 1-928729-10-X

[133]   Won, S.Y., Ligrani, P.M., "Numerical Predictions of Flow Structure and Local Nusselt Number Ratios Along and Above Dimpled Surfaces with Different Dimple Depths in a Channel", *Num. Heat Transfer (Part A)*, pp. 549-570, 2004

[134]   Zerihan, J., "An Investigation into the Aerodynamics of. Wings in Ground Effect", Ph.D. Thesis, University of. Southampton, School of Engineering, 2001

[135]   Zhang, X., Zerihan, J., "Off-Surface Aerodynamics Measurements of a Wing in Ground Effect", *Journal of Aircraft*, Vol. 40, No.4, July-August, 2003

[136]   Zhang, X., Senior, A., "Vortices Behind a Bluff Body with an upswept aft section in ground effect", *Int. J Heat and Fluid Flow*, Vol. 25, 2004

[137]   Zhang, X., "An inclined rectangular jet in a turbulent boundary layer-vortex flow", *Experiments In Fluids*, Vol. 28, 2000, pp. 344-354
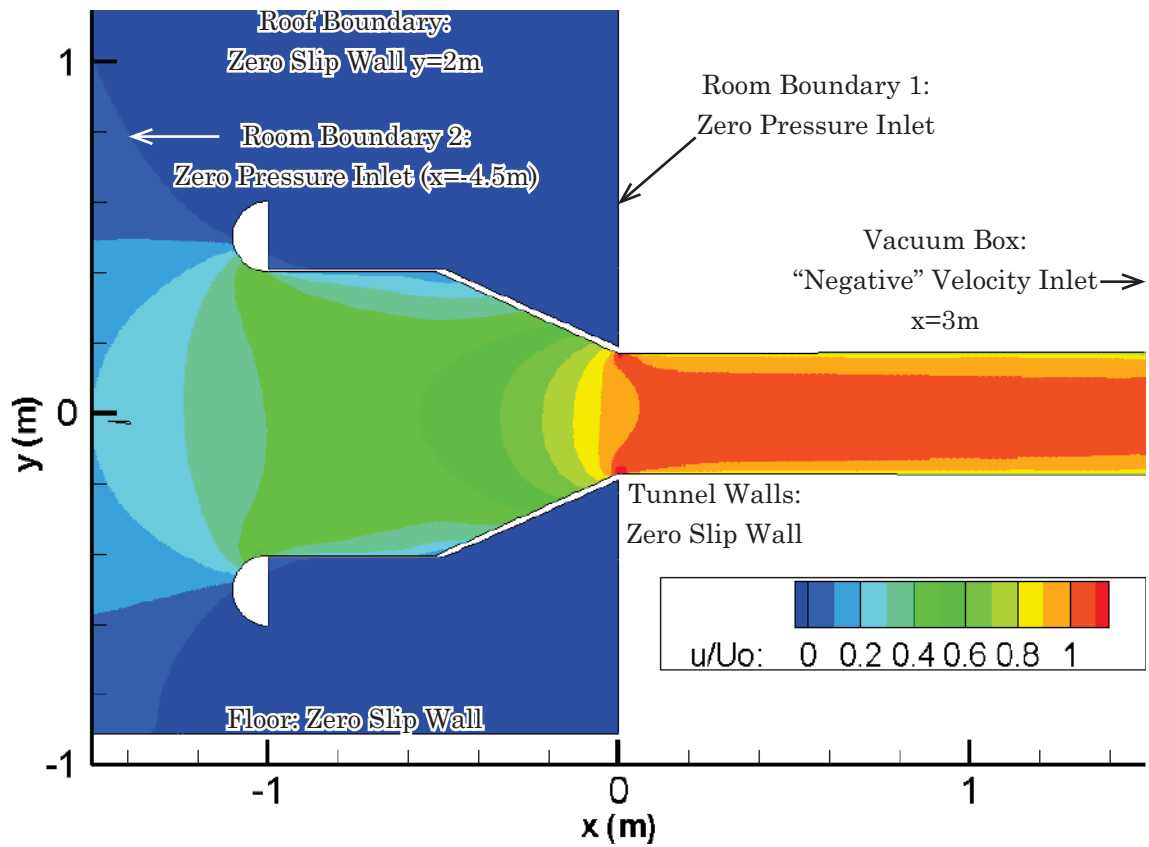
Figure A.1 Short Inlet Geometry (Sharp Corners)
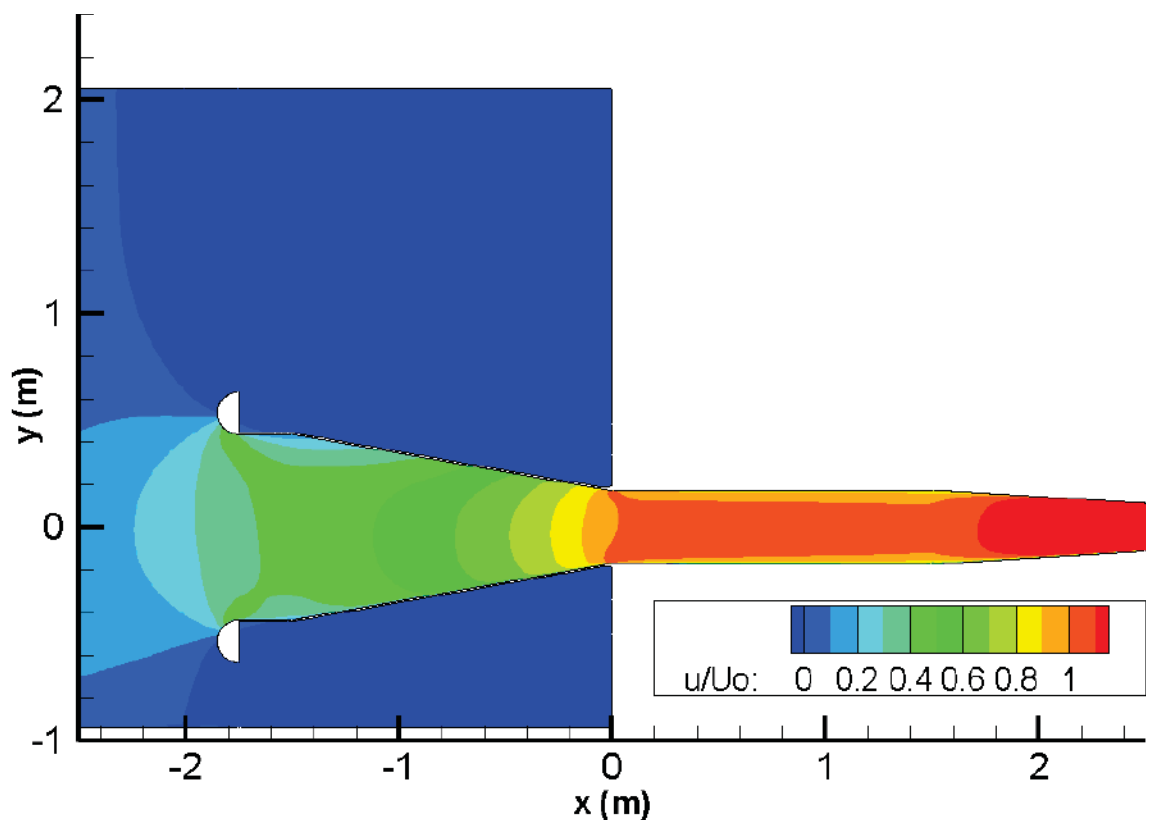
Figure A.2 Long Straight Inlet Geometry (Sharp Corners)
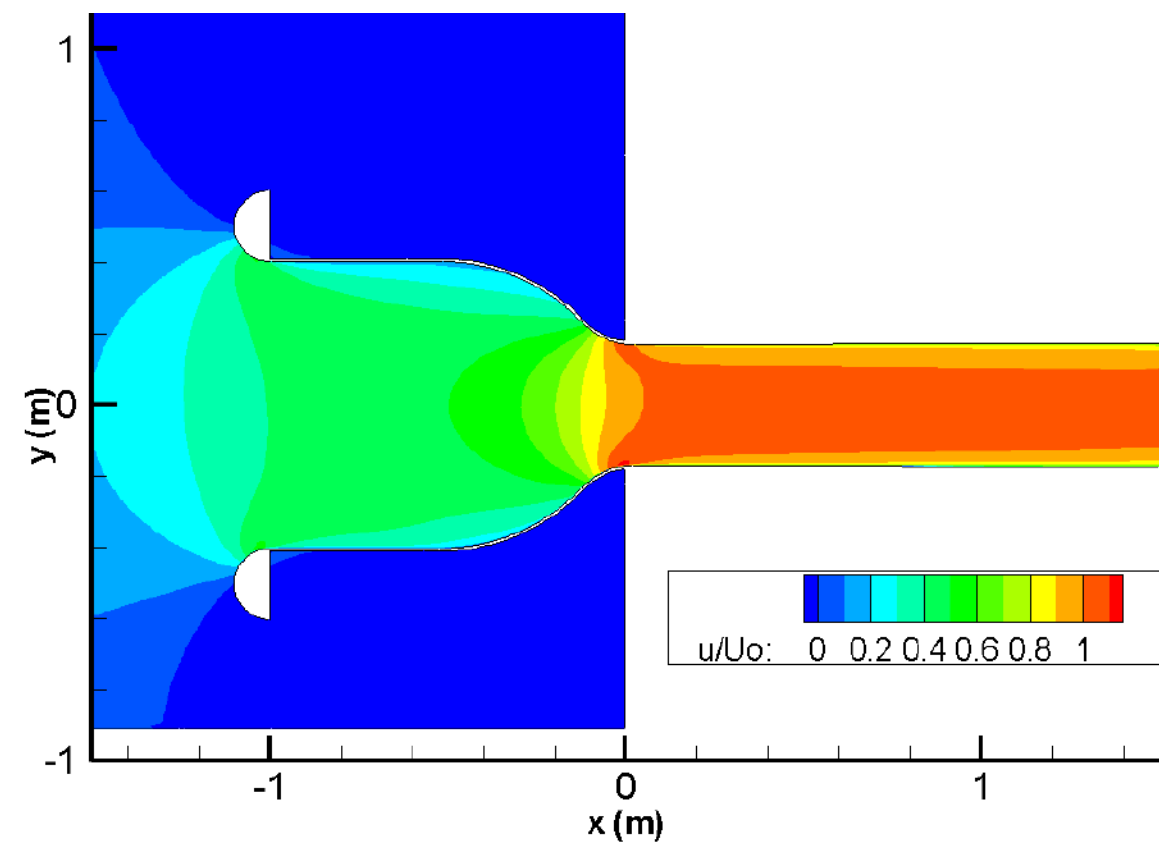
Figure A.3 Short Straight Inlet Geometry (Rounded Corners)
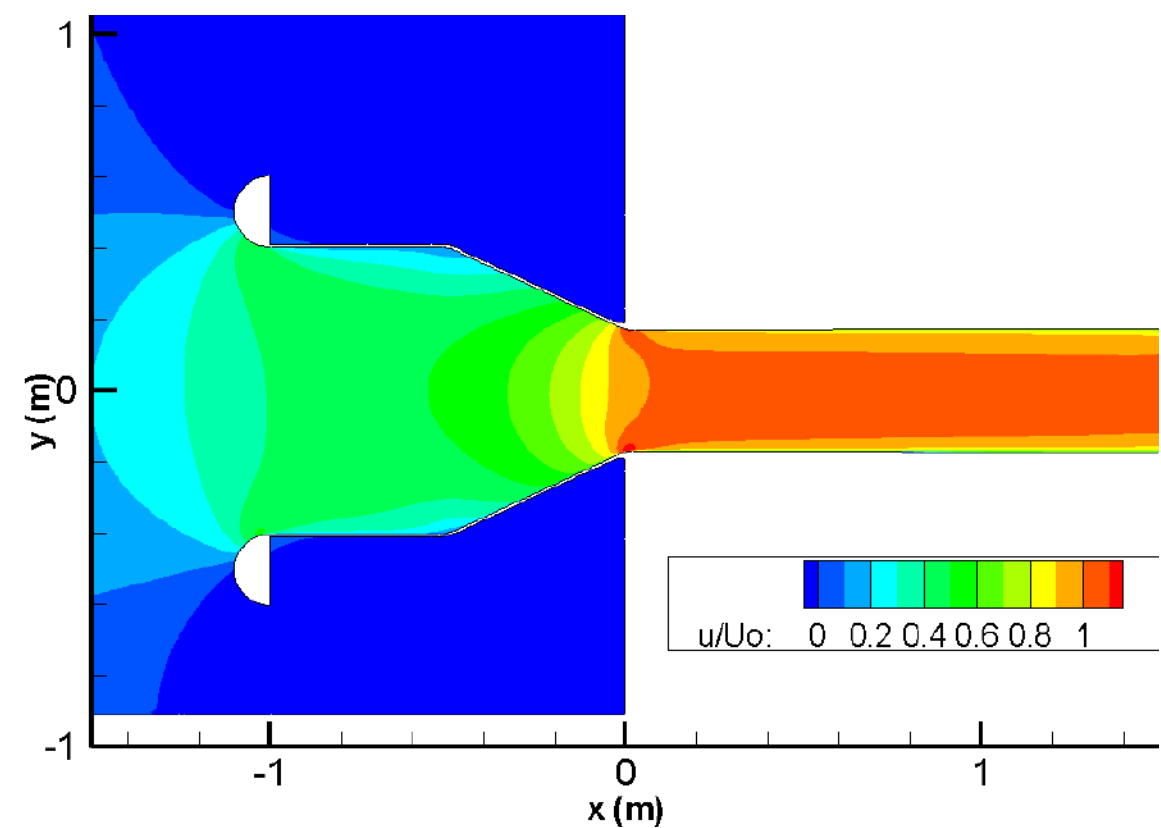
Figure A.4 Short Curved Inlet Geometry
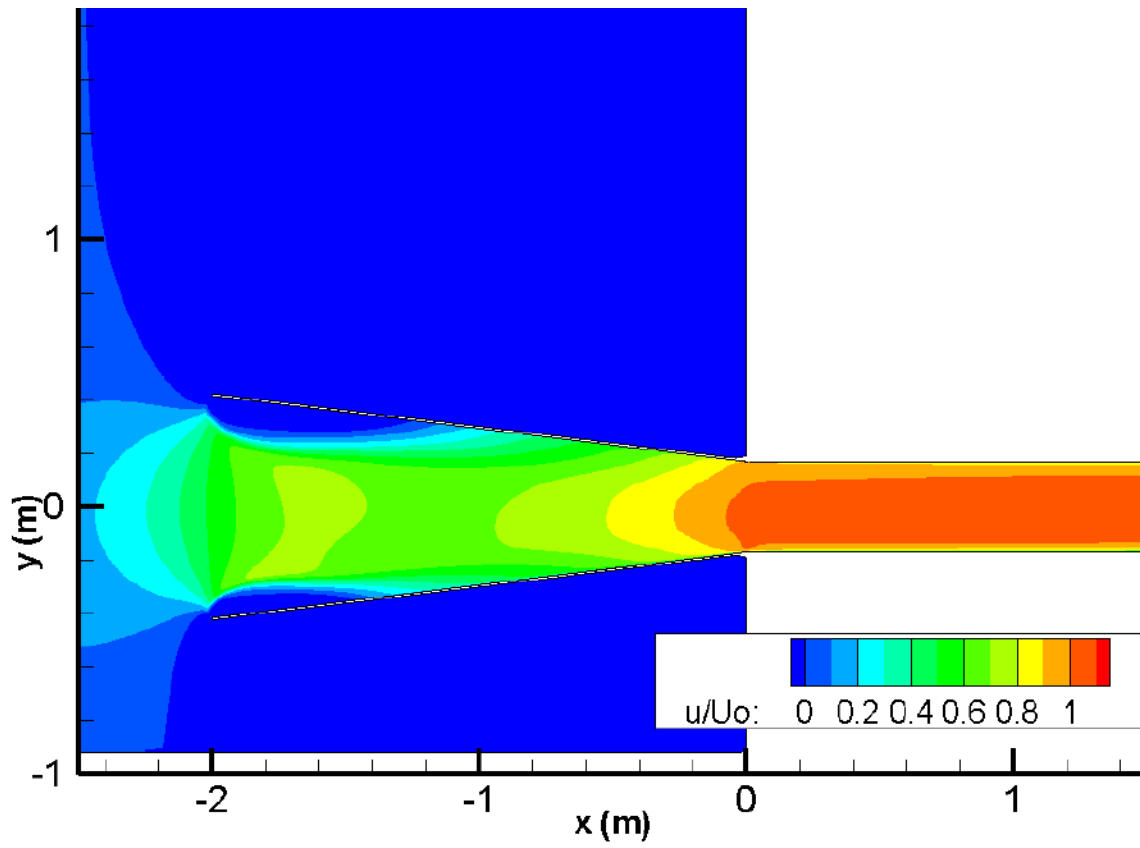
Figure A.5 No Inlet Fairing Geometry
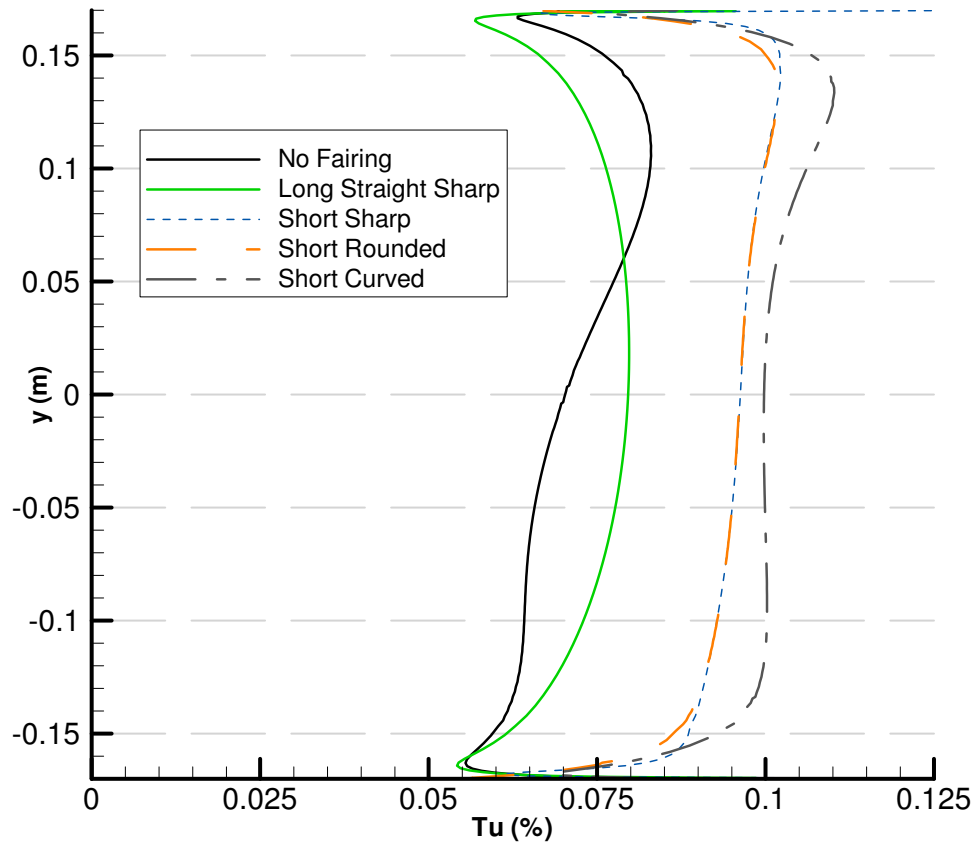
Figure A.6 Turbulence Intensity at Test Section Inlet (CFD: k- RNG)
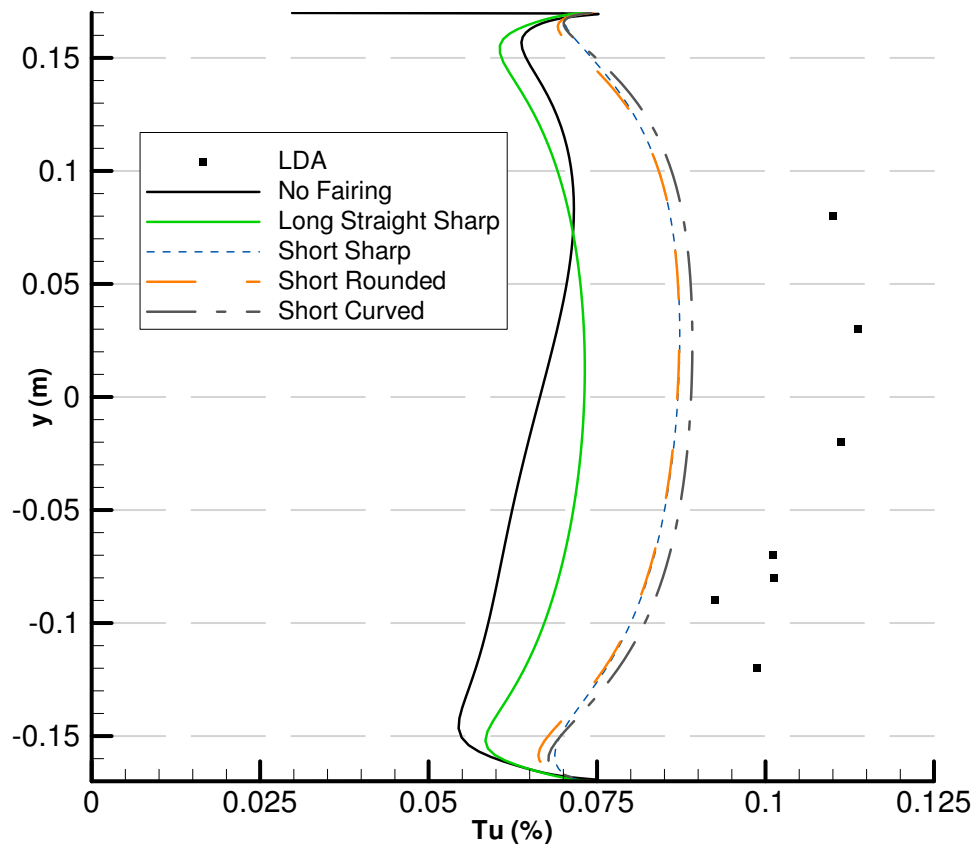
Figure A.7 Turbulence Intensity at x=0.55m in Test Section (CFD: k- RNG)

a)

100mm

140mm

Zero Slip Wall:

Test Section Wall, Contraction Inlet and Outlet

Roof, Side walls, Moving Ground Fairings and Duct

555mm

235mm

350mm

880mm

U_o=10 m/s

1150mm

225mm

200mm

Pressure Outlet

340mm

1500mm

980mm

Moving Wall (vel.=U_o)

620mm

Extended +1000mm
on Numerical Model

Velocity Profiles: u, v, w

Turbulence Profiles: k, ε, ω (where

Pressure Outlet

appropriate) Taken from larger model and

read into Velocity Inlet of the refined model.

Velocity Inlet:

Tu=0.1%

L=0.00686 m

b)

235mm

350mm

1500mm

U_o=10 m/s

70mm

285mm

1020mm

60mm

340mm

Moving Wall (vel.=U_o)

310mm

225mm

Zero Slip Wall:

Test Section Roof, Side walls, Moving

Ground Fairings and Duct

Figure B.1 Moving Ground Test Section a) Full Wind Tunnel, b) Refined Test Section

a)

Zero Slip Wall:

Roof, Walls, Floor and Dimple

235mm

320mm

1500mm

U_o =1.4 m/s

415.5mm

1150mm

Pressure Outlet

1412mm

340mm

200mm

225mm

980mm

620mm

Velocity Profiles: u, v, w

Turbulence Profiles: k, ε, ω (where appropriate) Taken from larger model and read into Velocity Inlet of the refined model.

Velocity Inlet:

Tu=0.1%

L=0.00686 m

b)

230mm

500mm

Pressure Outlet

U_o=1.4 m/s

317.5mm

320mm

115mm

Zero Slip Wall:

Roof, Walls, Floor and Dimple

Figure B.2 Single 90mm Diameter Dimple Model a) Full Wind Tunnel, b) Refined Test Section

a)

235mm

1500mm

U_o=4.5 m/s

660mm

Pressure Outlet

225mm

Periodic Boundary:
Side Walls

1150mm

200mm

620mm

500mm

Velocity Profiles: u, v, w

Turbulence Profiles: k, ε, ω (where appropriate) Taken from larger model and read into Velocity Inlet of the refined model.

Pressure Outlet

b)

235mm

Velocity Inlet:
Tu=0.1%
L=0.00686 m

1500mm

16° Rearward
Facing Ramp

660mm

175mm

175mm

U_o=4.5 m/s

300mm

225mm

365mm

"W"

(200mm)

Zero Slip Wall:
Roof, Ramp and Floor

Periodic Boundary:
Side Walls

Width "W": varied 100mm, 200mm and 300mm until effect of perodic side walls on the flow separation was minimal; little difference existed from 200mm-300mm.

Figure B.3 16° Rearward Facing Ramp Model a) Full Wind Tunnel, b) Refined Test Section

Upwind Differencing Scheme

One-Dimensional Diffusion of a property φ in a flow field, u, is:

$$\frac{d}{dx}(\rho u \Phi) = \frac{d}{dx}\left(\Gamma \frac{d\Phi}{dx}\right)$$

And continuity needs to be satisfied, thus: $\frac{d(\rho u)}{dx} = 0$

Integrating over the one-dimensional control volume "WPE" in figure 4.2:

$$(\rho u A \Phi)_e - (\rho u A \Phi)_w = \left(\Gamma A \frac{\partial \Phi}{\partial x}\right)_e - \left(\Gamma A \frac{\partial \Phi}{\partial x}\right)_w \qquad \text{............................} [B.1]$$

And integrating continuity: $\qquad (\rho u A)_e - (\rho u A)_w = 0 \qquad \text{..}[B.2]$

F and D are defined such that: $F = \rho u$ and $D = \frac{\Gamma}{\delta x}$ and are the convective mass flux and the diffusion conductance respectively.

$$F_w = (\rho u)_w, \; F_e = (\rho u)_e, \; D_W = \frac{\Gamma_w}{\partial x_{WP}}, \; D_e = \frac{\Gamma_e}{\partial x_{PE}}.$$

Assuming $A_w = A_e = A$, we now have:

$$F_e \Phi_P - F_w \Phi_W = D_e(\Phi_E - \Phi_P) - D_w(\Phi_P - \Phi_W) \qquad \text{............................}[B.3]$$

And continuity: $\qquad\qquad F_e - F_w = 0 \qquad \text{...}[B.4]$

When the flow is in the positive direction, $u_w > 0$, $u_e > 0$ ($F_w > 0$, $F_e > 0$), the upwind scheme sets $\varphi_w = \varphi_W$ and $\varphi_e = \varphi_P$ we now rearrange [3]:

$$\Phi_P(D_w + D_e + F_e) = \Phi_W(D_w + F_w) + D_e \Phi_E$$

$$\Phi_P[(D_w + F_w) + D_e + (F_e - F_w)] = \Phi_W(D_w + F_w) + D_e \Phi_E \qquad \text{.....................}[B.5]$$

When the flow is negative, $u_w < 0$, $u_e < 0$ ($F_w < 0$, $F_e < 0$), the scheme takes $\varphi_w = \varphi_P$ and $\varphi_e = \varphi_{E,}$:

$$\Phi_P[D_w + (D_e - F_e) + (F_e - F_w)] = D_w \Phi_W + (D_e - F_e)\Phi_E \qquad \text{.....................}[B.6]$$

Identifying φ_W and φ_E as a_W and a_E, can re write [3] and [4] in the general form:

$$a_P \Phi_P = a_W \Phi_W + a_E \Phi_E$$

With central coefficient: $\qquad a_P = a_W + a_E + (F_e - F_w)$

Where:
$$a_W = \frac{\Gamma_w A_w}{\delta x_{WP}} \text{ \& } a_E = \frac{\Gamma_e A_e}{\delta x_{PE}}$$

And neighbor coefficients which account for the flow direction:

Flow Direction	a_W	a_E
$F_w > 0$, $F_e > 0$	D_w+	D_e
(positive)	F_w	
$F_w < 0$, $F_e < 0$	D_w	$D_e - F_e$
(negative)		

Or more in general terms: $a_W = D_w + \max(F_w, 0)$ and $a_E = D_e + \max(0, -F_e)$

RANS

Reynolds decomposition refers to the separation of a variable (u) into the time averaged ($\bar{u}$) and the fluctuating (u') components shown in figure 4.2. This accounts for the RANS method, thus:

$$u(\mathbf{x}, t) = \bar{u}(\mathbf{x}) + u'(\mathbf{x}, t) \quad \text{.. [B.7]}$$

Given continuity and momentum equations:

$$\frac{\partial \bar{u}_i}{\partial x_i} = 0, \qquad \frac{\partial u_i}{\partial t} + u_i \frac{\partial u_i}{\partial x_j} = f_i - \frac{1}{\rho} \frac{\partial p}{\partial x_i} + \nu \frac{\partial^2 u_i}{\partial x_j \partial x_j}$$

Substituting for u and p etc yields:

$$\frac{\partial \bar{u}_i}{\partial x_i} = 0, \qquad \frac{\partial u_i}{\partial t} + u_i \frac{\partial u_i}{\partial x_j} + \overline{u'_j \frac{\partial u'_i}{\partial x_j}} = \bar{f}_i - \frac{1}{\rho} \frac{\partial \bar{p}}{\partial x_i} + \nu \frac{\partial^2 \bar{u}_i}{\partial x_j \partial x_j}$$

$$\frac{\partial \bar{u}_i}{\partial t} + u_i \frac{\partial \bar{u}_j \bar{u}_i}{\partial x_j} = \bar{f}_i - \frac{1}{\rho} \frac{\partial \bar{p}}{\partial x_i} + \nu \frac{\partial^2 \bar{u}_i}{\partial x_j \partial x_j} - \frac{\partial \overline{u'_i u'_j}}{\partial x_j}$$

Re-arranging:

$$\rho \frac{\partial \bar{u}_i}{\partial t} + \rho \frac{\partial \bar{u}_j \bar{u}_i}{\partial x_j} = \rho \bar{f}_i + \frac{\partial}{\partial x_i} \left(-p \delta_{ij} + 2\mu \bar{S}_{ij} - \rho \overline{u'_i u'_j} \right)$$

Where the strain tensor, $\bar{S}_{ij}$, is:

$$\bar{S}_{ij} = \frac{1}{2} \left(\frac{\partial \bar{u}_i}{\partial x_j} + \frac{\partial \bar{u}_j}{\partial x_i} \right)$$

Turbulence Modeling

The Boussinesq hypothesis relates the Reynolds Stresses to the mean velocity gradients:

$$-\rho \overline{u'_i u'_j} = \mu_t \left(\frac{\partial u_i}{\partial x_j} + \frac{\partial u_j}{\partial x_i} \right) - \frac{2}{3} \left(\rho k + \mu_t \frac{\partial u_k}{\partial x_{jk}} \right) \delta_{ij}$$

The turbulent eddy viscosity, μ_t, is computed by combining k and ε as in:

$$\mu_t = \rho C_\mu \frac{k^2}{\varepsilon}$$

Combining Boussinesq relationship and the eddy viscosity definition, the following expression is obtained for the normal Reynolds Stress in an incompressible, strained mean flow:

$$\overline{u^2} = \frac{2}{3} k - 2 v_t \frac{\partial U}{\partial x}$$

Where: $\qquad\qquad\qquad\qquad v_t \equiv \frac{\mu_t}{\rho}$

Results in that the normal stress, u^2, which is by definition a positive quantity becomes negative (non-realizable), when the strain is large enough such that:

$$\frac{k}{\varepsilon} \frac{\partial U}{\partial x} > \frac{1}{3 C_\mu} \approx 3.7$$

k-ε Realizable transport equations

$$\frac{\partial}{\partial t} (\rho k) + \frac{\partial}{\partial x_j} (\rho k u_j) = \frac{\partial}{\partial x_j} \left[\left(\mu + \frac{\mu_t}{\sigma_k} \right) \frac{\partial k}{\partial x_j} \right] + G_k + G_b - \rho \varepsilon - Y_M + S_k$$

and:

$$\frac{\partial}{\partial t} (\rho \varepsilon) + \frac{\partial}{\partial x_j} (\rho \varepsilon u_j) = \frac{\partial}{\partial x_j} \left[\left(\mu + \frac{\mu_t}{\sigma_\varepsilon} \right) \frac{\partial \varepsilon}{\partial x_j} \right] + \rho C_1 S_\varepsilon - \rho C_2 \frac{\varepsilon^2}{k + \sqrt{v \varepsilon}} + C_{1\varepsilon} \frac{\varepsilon}{k} C_{3\varepsilon} G_b + S_\varepsilon$$

where: $\qquad\qquad C_1 = max \left[0.43, \frac{\eta}{\eta + 5} \right], \quad \eta = S \frac{k}{\varepsilon}, \qquad S = \sqrt{2 S_{ij} S_{ij}}$

G_k represents the generation of turbulence kinetic energy due to the mean velocity gradients.

G_b is the generation of turbulence kinetic energy due to buoyancy. Y_M represents the contribution of the fluctuating dilatation in compressible turbulence to the overall dissipation rate. C_2 and $C_{1\varepsilon}$ are constants. σ_k and σ_ε are turbulent Prandtl numbers for k and ε respectively. S_k and S_ε are user-defined source terms.

The Turbulent Viscosity

Again we have:

$$\mu_t = \rho C_\mu \frac{k^2}{\varepsilon}$$

However C_μ is no longer constant as in standard k-ε and RNG k-ε, thus:

$$C_\mu = \frac{1}{A_0 + A_S \frac{kU^*}{\varepsilon}}$$

Where:

$$U^* \equiv \sqrt{S_{ij}S_{ij} + \tilde{\Omega}_{ij}\tilde{\Omega}_{ij}}$$

And:

$$\tilde{\Omega}_{ij=}\Omega_{ij} - 2\varepsilon_{ijk}\omega_k$$

$$\Omega_{ij=}\overline{\Omega_{ij}} - \varepsilon_{ijk}\omega_k$$

Where $\overline{\Omega_{ij}}$ is the mean rate of rotation tensor viewed in a rotating reference frame with the angular velocity ω_k. A_0 and A_S are constants:

$$A_0 = 4.04, \qquad A_S = \sqrt{6}\cos\o$$

Where:

$$\o = \frac{1}{3}\cos^{-1}(\sqrt{6}W), \qquad W = \frac{S_{ij}S_{jk}S_{ji}}{\tilde{S}^3}, \qquad \tilde{S} = \sqrt{S_{ij}S_{ij}}, \qquad S_{ij} = \frac{1}{2}\left(\frac{\partial u_j}{\partial x_i} + \frac{\partial u_i}{\partial x_j}\right)$$

k-ω Shear Stress Transport Equations

$$\frac{\partial}{\partial t}(\rho k) + \frac{\partial}{\partial x_j}(\rho k u_j) = \frac{\partial}{\partial x_j}\left[\Gamma_k \frac{\partial k}{\partial x_j}\right] + \tilde{G}_k - Y_k + S_k$$

And:

$$\frac{\partial}{\partial t}(\rho \omega) + \frac{\partial}{\partial x_j}(\rho \omega u_j) = \frac{\partial}{\partial x_j}\left[\Gamma_\omega \frac{\partial \omega}{\partial x_j}\right] + G_\omega - Y_\omega + D_\omega + S_\omega$$

Here, $\tilde{G}_k$ represents the generation of turbulence kinetic energy due to mean velocity gradients. G_ω represents generation of ω. Γ_k and Γ_ω represent the effective diffusivity of k and ω respectively. Y_k and Y_ω are the dissipation of k and ω due to turbulence. D_ω represents the cross-diffusion term. S_k and S_ω are user defined source terms.

Modeling the Effective Diffusivity:

$$\Gamma_k = \mu + \frac{\mu_t}{\sigma_k}$$

$$\Gamma_\omega = \mu + \frac{\mu_t}{\sigma_\omega}$$

Where σ_k and σ_ω are the turbulent Prandtl numbers for k and ω respectively. The turbulent viscosity, μ_t, is:

$$\mu_t = \frac{\rho k}{\omega} \frac{1}{max\left[\frac{1}{\alpha^*}, \frac{SF_2}{\alpha_1 \omega}\right]}$$

Where S is the strain magnitude and

$$\sigma_k = \frac{1}{\dfrac{F_1}{\sigma_{k,1}} + \dfrac{(1 - F_1)}{\sigma_{k,2}}}$$

$$\sigma_\omega = \frac{1}{\dfrac{F_1}{\sigma_{\omega,1}} + \dfrac{(1 - F_1)}{\sigma_{\omega,2}}}$$

The blending functions are given by F_1 and F_2 where D is the positive portion of the cross-diffusion term. α^* is a coefficient that damps the turbulent viscosity causing a low Reynolds number correction:

$$F_1 = \tanh\left(\Phi_1^4\right)$$

$$\Phi_1 = \min\left[\max\left(\frac{\sqrt{k}}{0.09\omega y}, \frac{500\mu}{\rho y^2 \omega}\right), \frac{4\rho k}{\sigma_{\omega,2} D_\omega^+ y^2}\right]$$

$$D_\omega^+ = \max\left[2\rho \frac{1}{\sigma_{\omega,2}} \frac{1}{\omega} \frac{\partial k}{\partial x_j} \frac{\partial \omega}{\partial x_j}, 10^{-10}\right]$$

$$F_2 = \tanh\left(\Phi_2^2\right)$$

$$\Phi_2 = \max\left[2\frac{\sqrt{k}}{0.09\omega y}, \frac{500\mu}{\rho y^2 \omega}\right]$$

And for α^*

$$\alpha^* = \alpha_\infty^*\left(\frac{\alpha_0^* + Re_t/R_k}{1 + Re_t/R_k}\right)$$

Where:

$$Re_t = \frac{\rho k}{\mu\omega}, \qquad R_k = 6$$

$$\alpha_0^* = \frac{\beta_i}{3}, \qquad \beta_i = 0.072$$

In high Reynolds number form of the k-ω model, $\alpha^* = \alpha_\infty^* = 1$.

Modeling of the Turbulence Production

The Production of k is defined by:

$$\tilde{G}_k = \min(G_k, 10\rho\beta^* k\omega)$$

The production of ω is given by:

$$G_\omega = \frac{\alpha}{\nu_t} G_k$$

Here α_∞ is evaluated differently to the standard k-ω model, thus:

$$\alpha_\infty = F_1\alpha_{\infty,1} + (1 + F_1)\alpha_{\infty,2}$$

Where:

$$\alpha_{\infty,1} = \frac{\beta_{i,1}}{\beta_\infty^*} - \frac{\kappa^2}{\sigma_{\omega,1}\sqrt{\beta_\infty^*}}$$

$$\alpha_{\infty,2} = \frac{\beta_{i,2}}{\beta_\infty^*} - \frac{\kappa^2}{\sigma_{\omega,2}\sqrt{\beta_\infty^*}}$$

And κ=0.41

Modeling the turbulence Dissipation

The dissipation of k, the term Y_K, differs from the standard k-ω turbulence model in that the term f_{β^*} is equal to 1 for the SST model, and is a piece-wise function for the standard k-ω model. Therefore: $\qquad Y_K = \rho\beta^* k\omega$

The dissipation of ω, the Y_ω term, is defined similarly as the standard k-ω model. However the difference lies in how β_i and f_β are derived, for k-ω SST f_β=1, thus for k-ω SST:

$$Y_\omega = \rho\beta\omega^2$$

$$\beta_i = F_1\beta_{i,1} + (1 - F_1)\beta_{i,2}$$

The Cross-Diffusion Modification

In order to blend the k-ω SST model together with the k-ε model, the k-ε model is transformed into equations based on k and ω, leading to the introduction of a cross diffusion term, D_ω. This is defined as:

$$D_\omega = 2(1 - F_1)\rho\sigma_{\omega,2}\frac{1}{\omega}\frac{\partial k}{\partial x_j}\frac{\partial \omega}{\partial x_j}$$
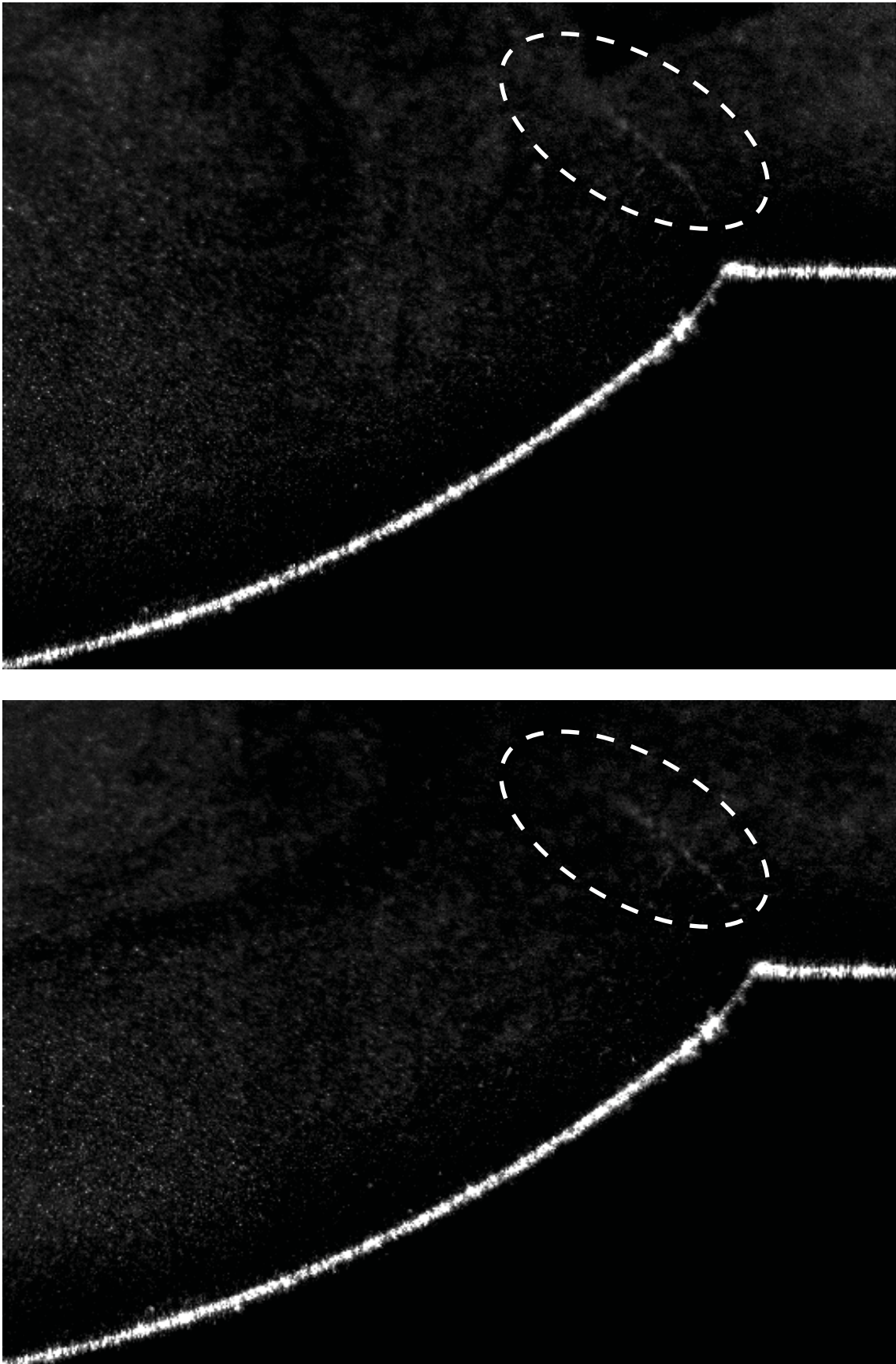
Figure C.1 Non-Consecutive Image Pairs Showing Dimple Rim PIV Laser Sheet Reflection
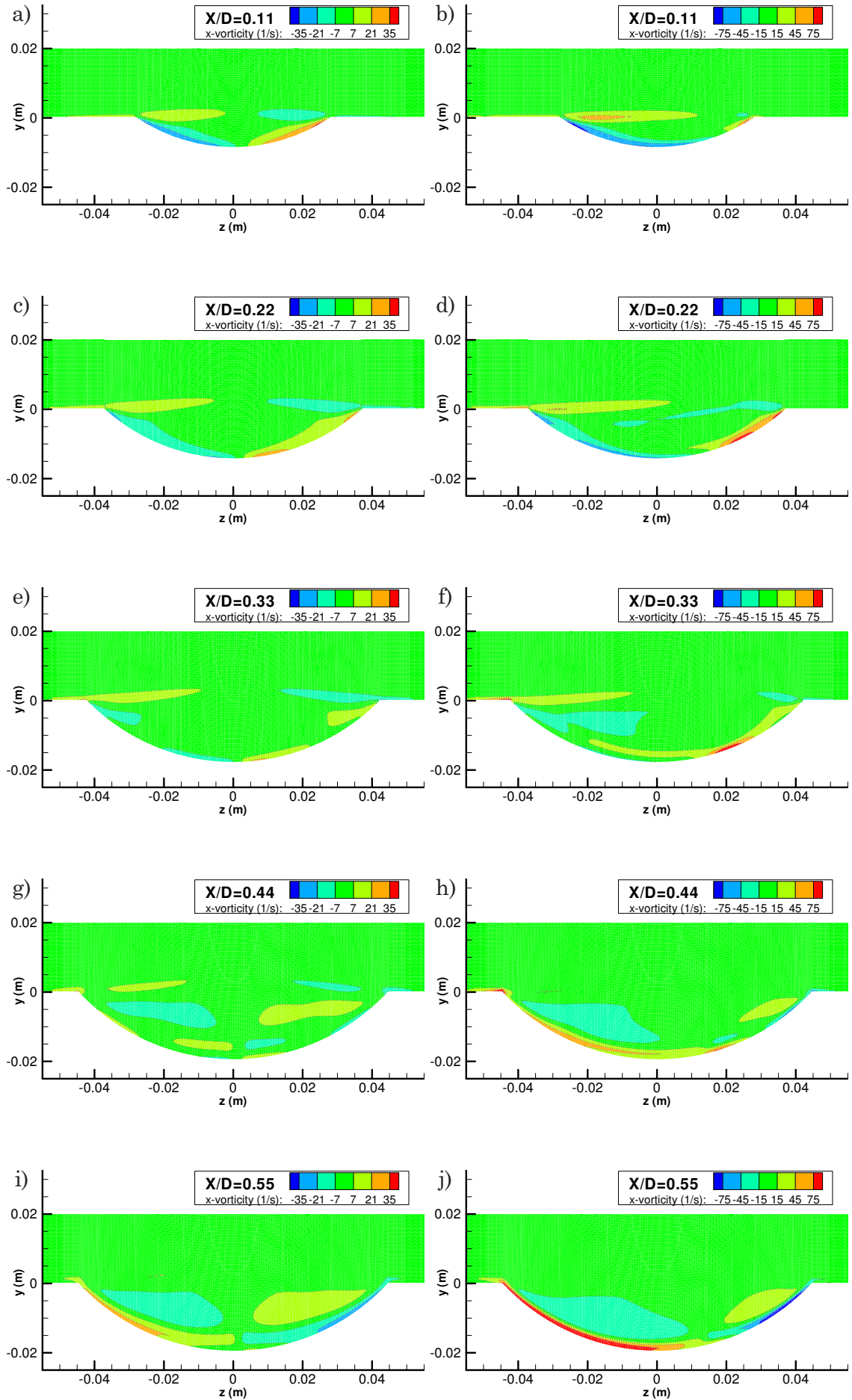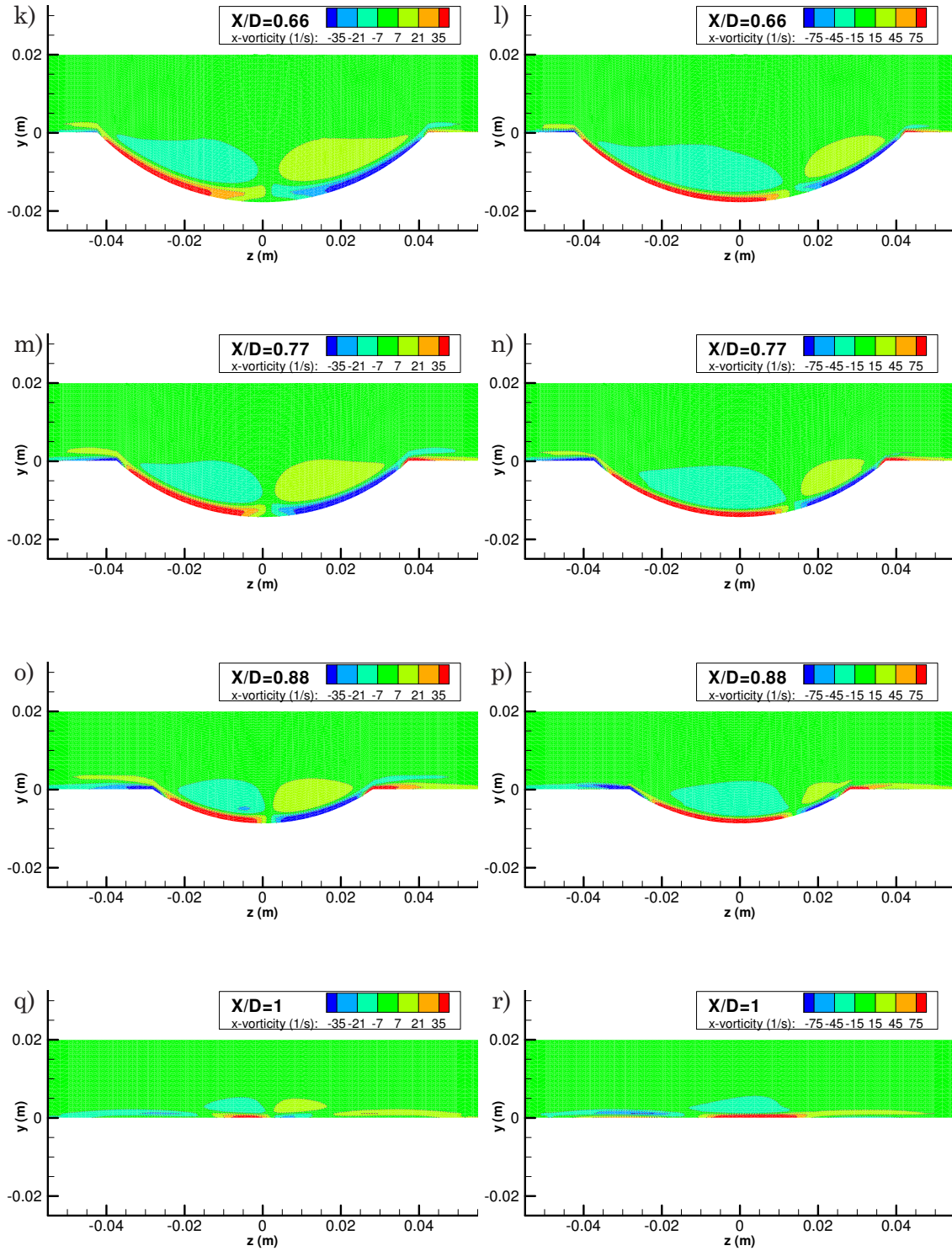
Figure C.2 Streamwise Vorticity (Ω_x) from x/D=0.1-x/D=1, (CFD: k-ω SST)

Re_D=4.3x10³: a,c,e,g,i,k,m,o,q

Re_D=9.0x10³: b,d,f,h,j,l,m,p,r
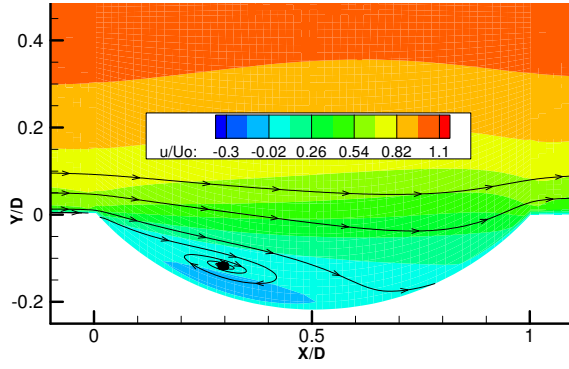
Figure C.3 Grid 1 Single Dimple (*k-ε* Realizable)
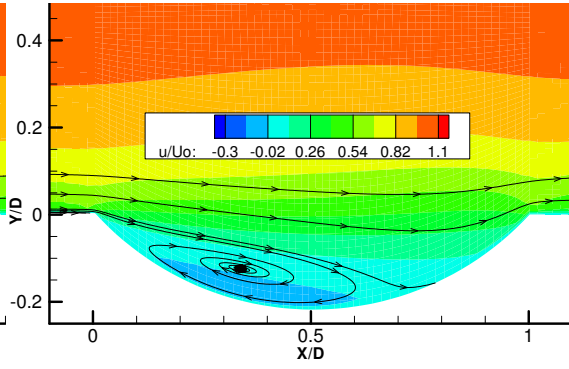
Figure C.4 Grid 1 Single Dimple (*k-ε* RNG)
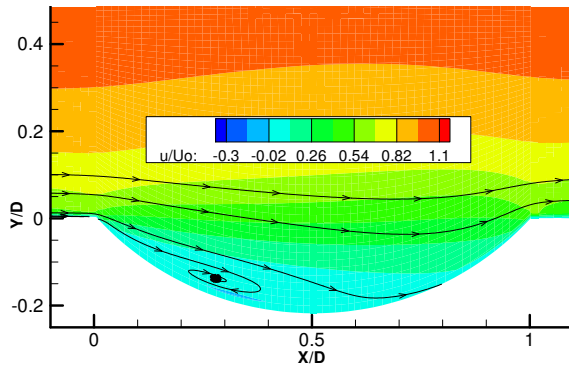
Figure C.5 Grid 1 Single Dimple (*k-ε* Standard)
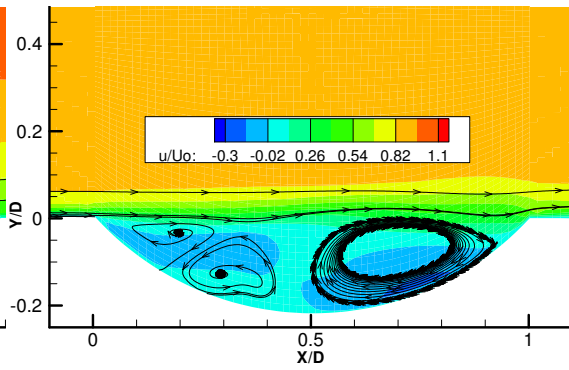
Figure C.6 Grid 1 Single Dimple (*k-ω* Standard)
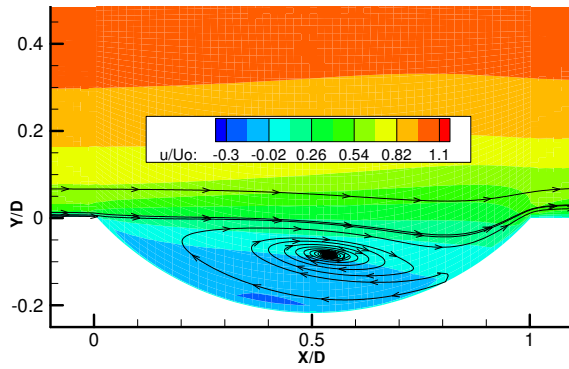
Figure C.7 Grid 1 Single Dimple (RSM)
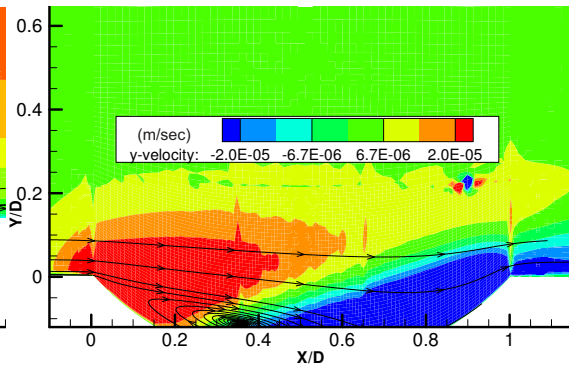
Figure C.8 Grid 2 Single Dimple (*k-ε* Realizable)
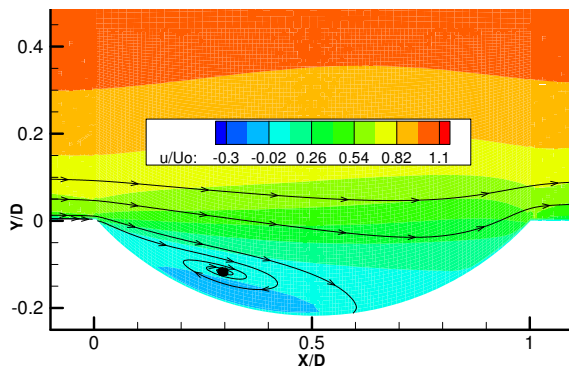
Figure C.9 Grid 3 Single Dimple (*k-ε* Realizable)
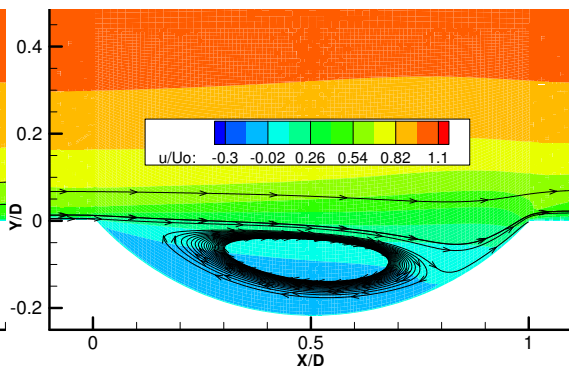
Figure C.10 Grid 3 Single Dimple (RSM)
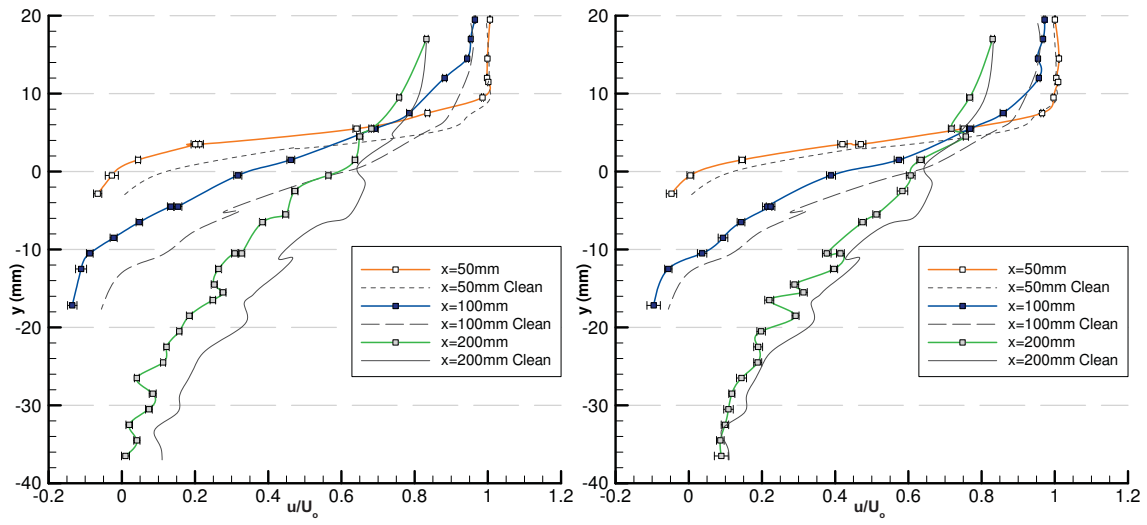
Figure D.1 **A1.5-R1-D0** and Clean u/U$_o$ Profile

Figure D.4 **A1.5-R1-D1** and Clean u/U$_o$ Profile
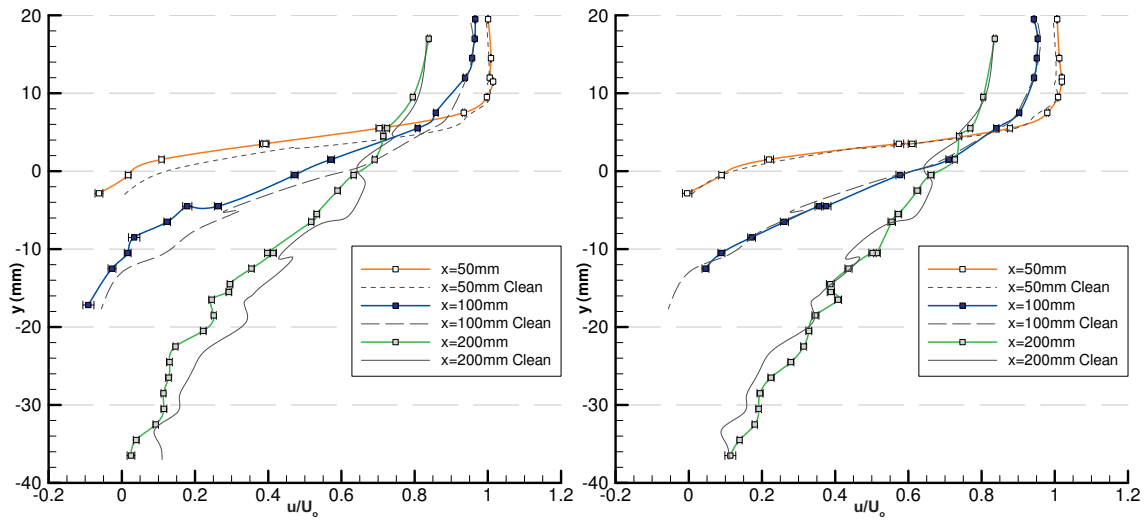
Figure D.2 **A1.5-R3-D0** and Clean u/U$_o$ Profile

Figure D.5 **A1.5-R3-D1** and Clean u/U$_o$ Profile
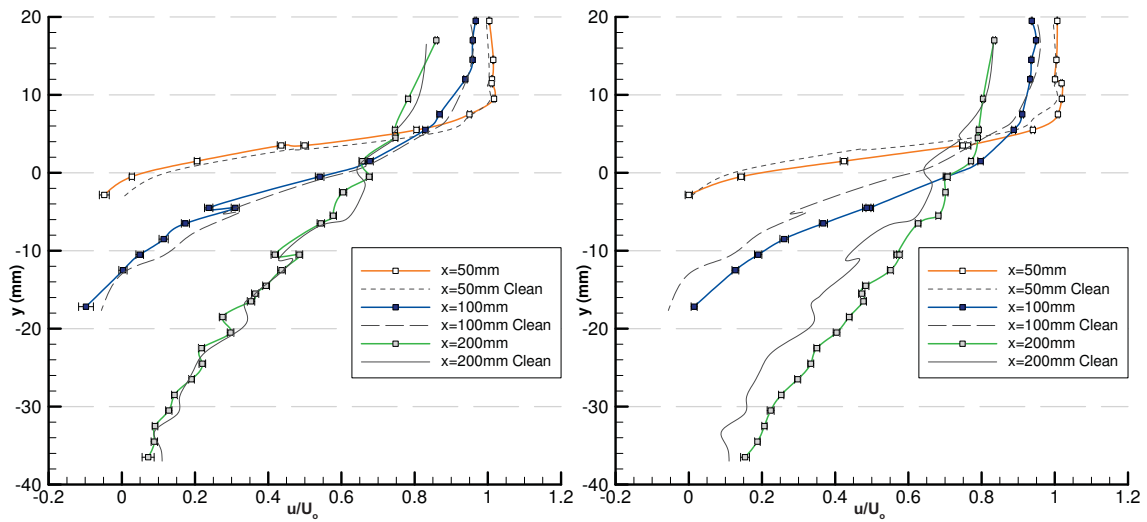
Figure D.3 **A1.5-R5-D0** and Clean u/U$_o$ Profile

Figure D.6 **A1.5-R5-D1** and Clean u/U$_o$ Profile
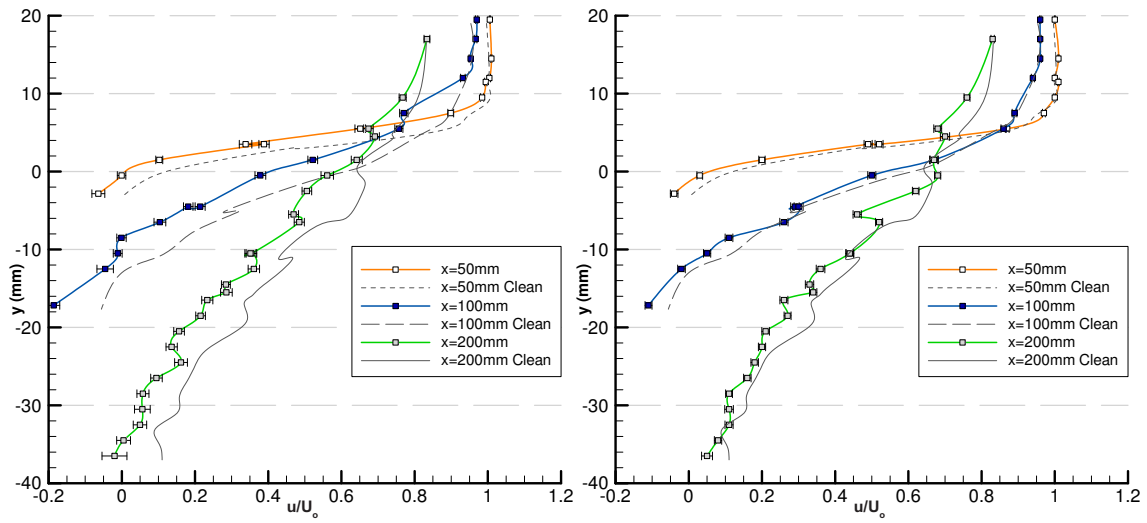
Figure D.7 **A1.5-R1-D3** and Clean u/U_o Profile

Figure D.10 **A1.5-R1-D5** and Clean u/U_o Profile
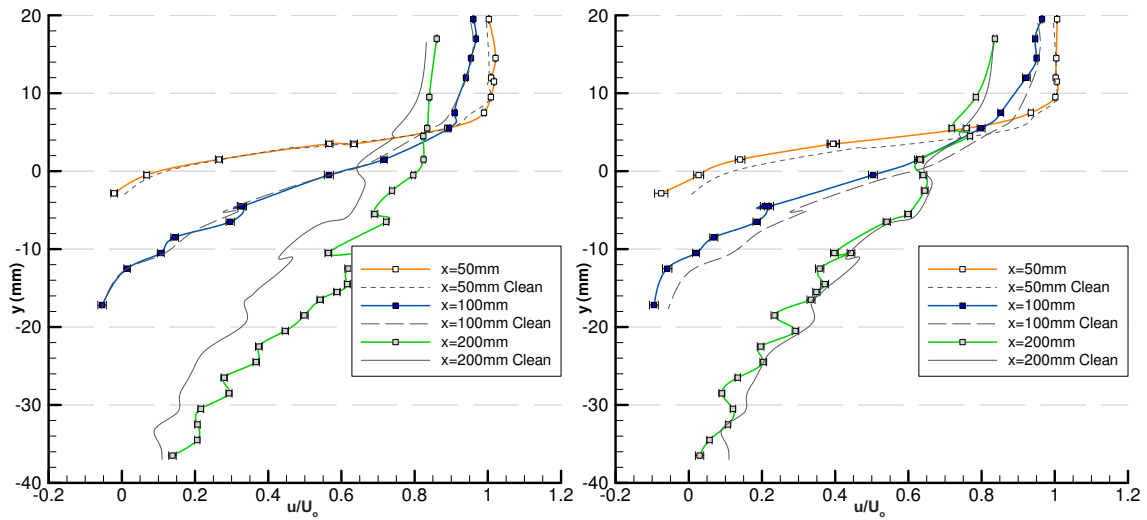
Figure D.8 **A1.5-R3-D3** and Clean u/U_o Profile

Figure D.11 **A1.5-R3-D5** and Clean u/U_o Profile
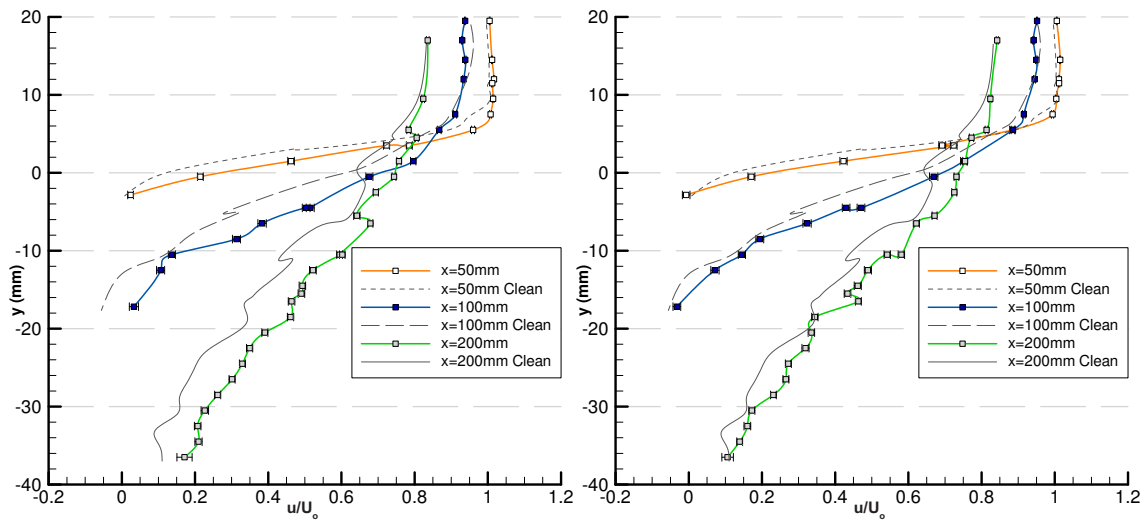
Figure D.9 **A1.5-R5-D3** and Clean u/U_o Profile

Figure D.12 **A1.5-R5-D5** and Clean u/U_o Profile
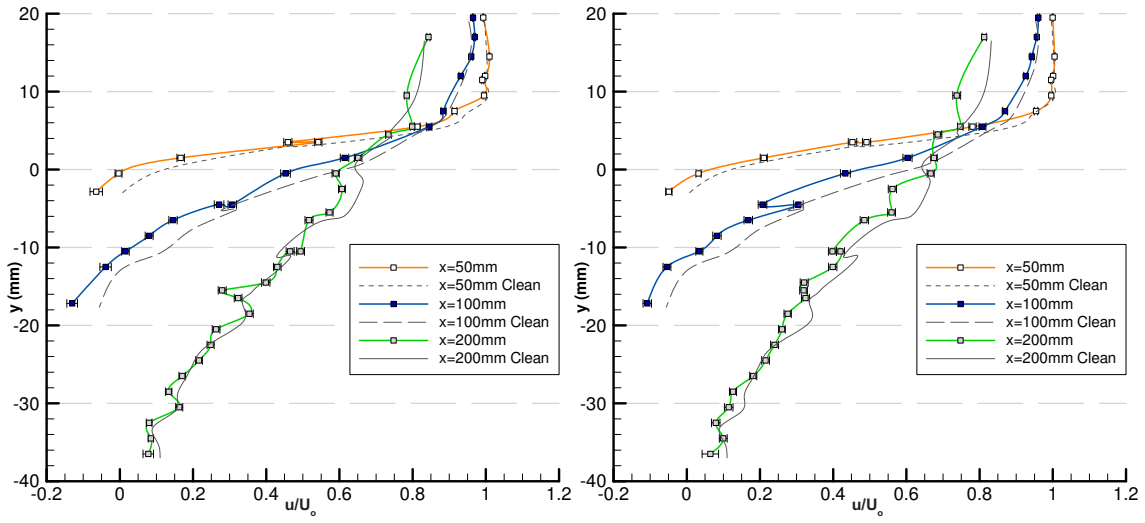
Figure D.13 **A2-R1-D0** and Clean u/U_o Profile

Figure D.16 **A2-R1-D1** and Clean u/U_o Profile
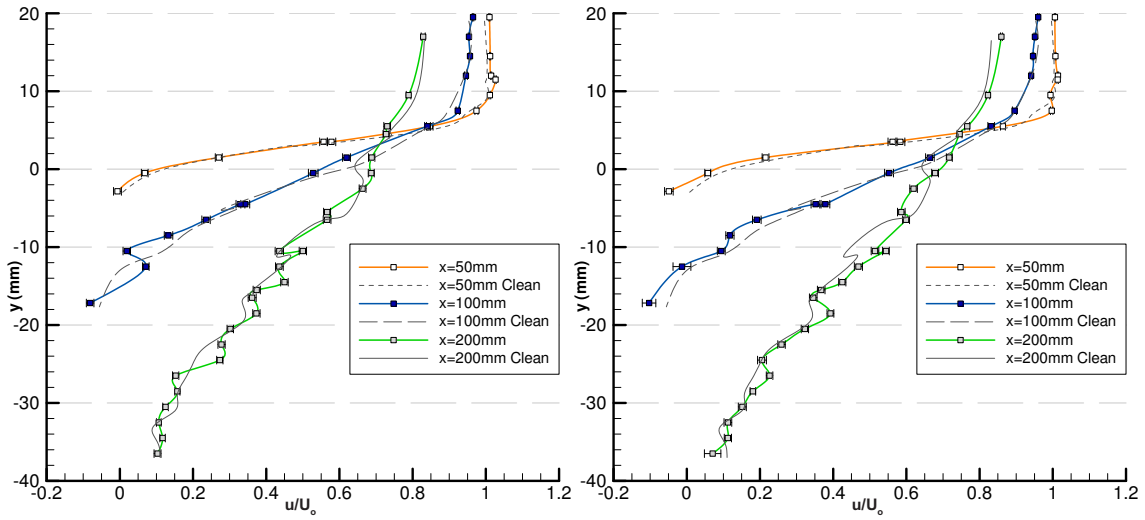
Figure D.14 **A2-R3-D0** and Clean u/U_o Profile

Figure D.17 **A2-R3-D1** and Clean u/U_o Profile
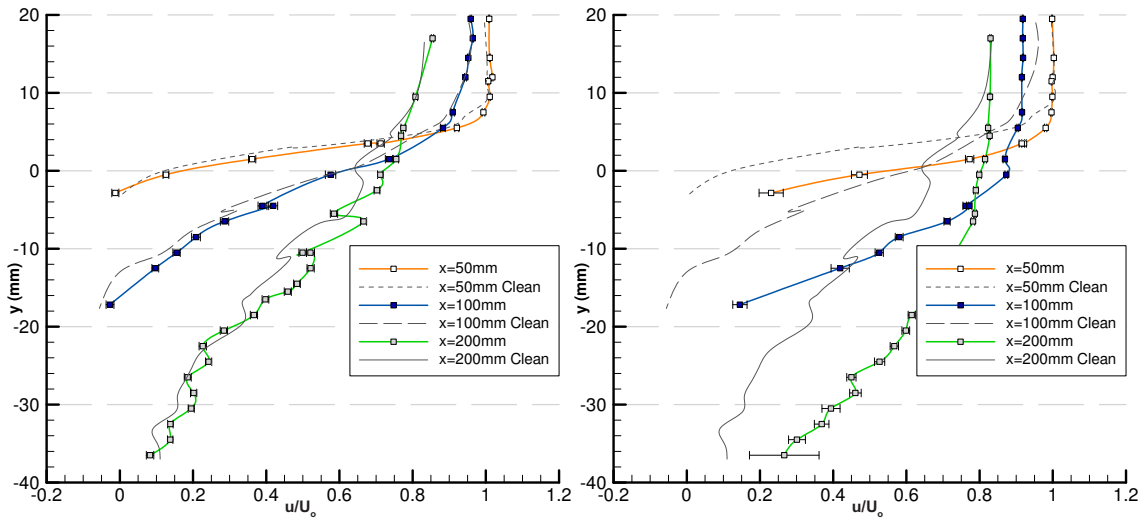
Figure D.15 **A2-R5-D0** and Clean u/U_o Profile

Figure D.18 **A2-R5-D1** and Clean u/U_o Profile
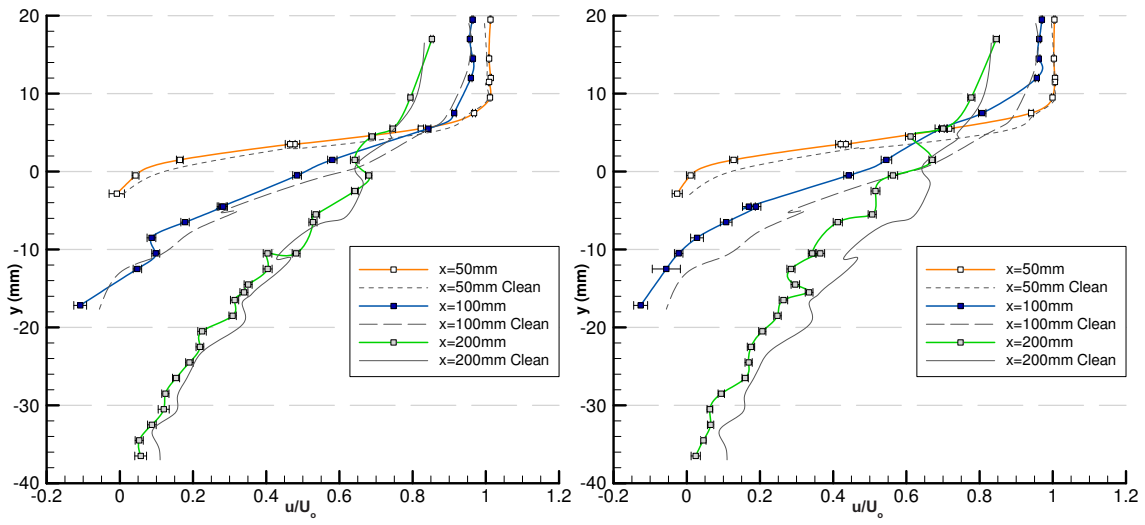
Figure D.19 **A2-R1-D3** and Clean u/U_o Profile

Figure D.22 **A2-R1-D5** and Clean u/U_o Profile
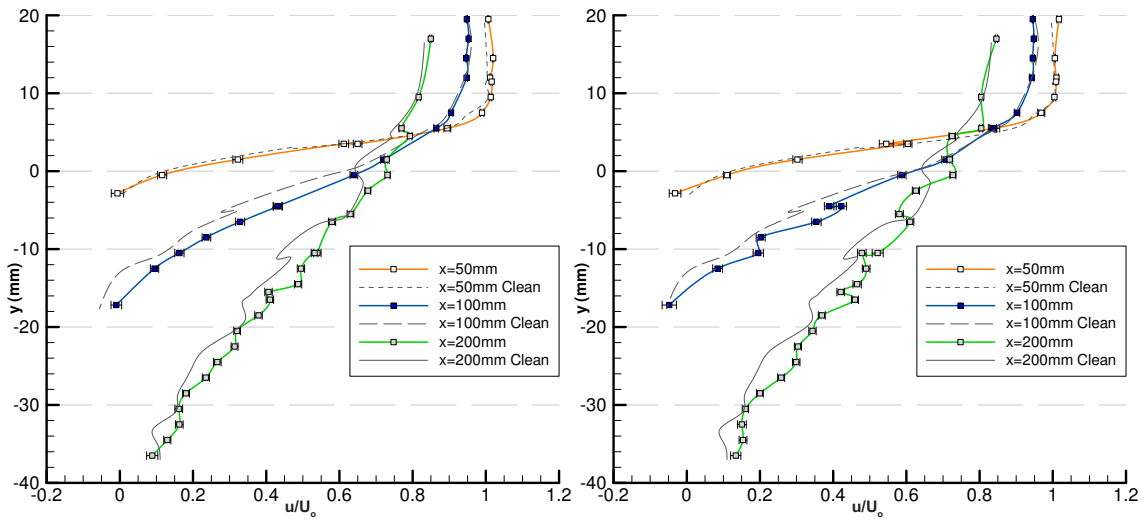
Figure D.20 **A2-R3-D3** and Clean u/U_o Profile

Figure D.23 **A2-R3-D5** and Clean u/U_o Profile
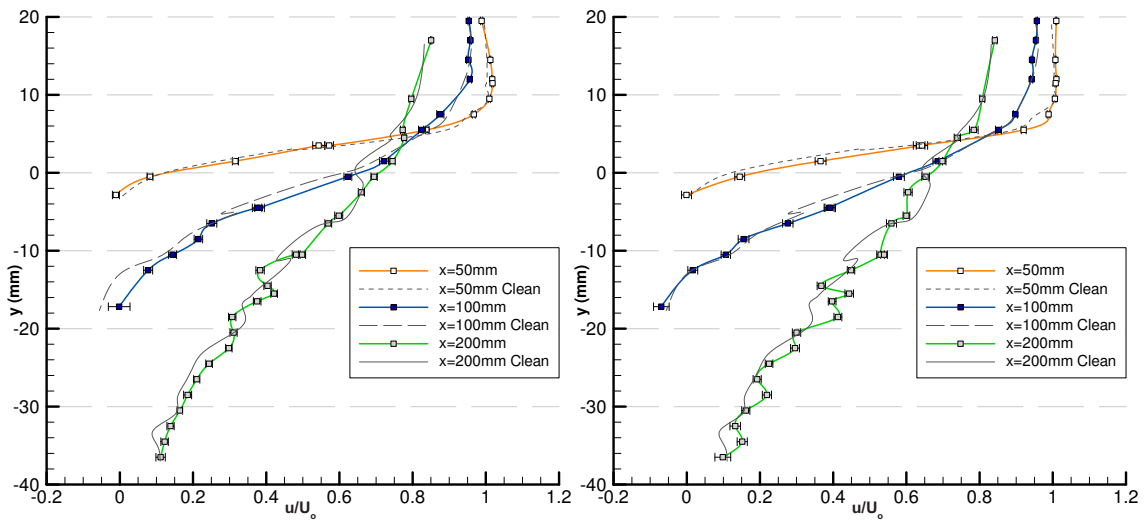
Figure D.21 **A2-R5-D3** and Clean u/U_o Profile

Figure D.24 **A2-R5-D5** and Clean u/U_o Profile
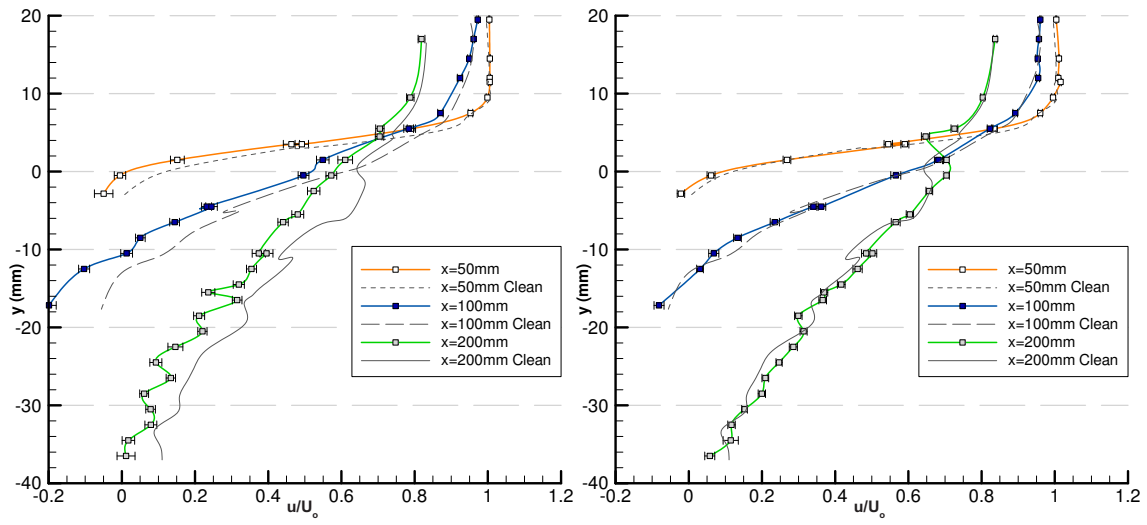
Figure D.25 **A2.5-R1-D0** and Clean u/U$_o$ Profile Figure D.28 **A2.5-R1-D1** and Clean u/U$_o$ Profile
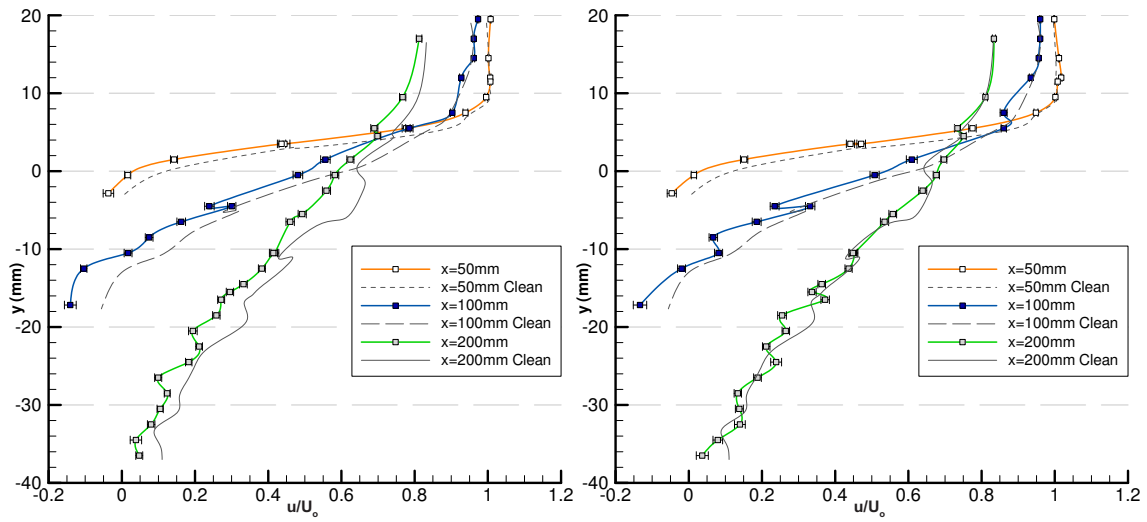
Figure D.26 **A2.5-R3-D0** and Clean u/U$_o$ Profile Figure D.29 **A2.5-R3-D1** and Clean u/U$_o$ Profile
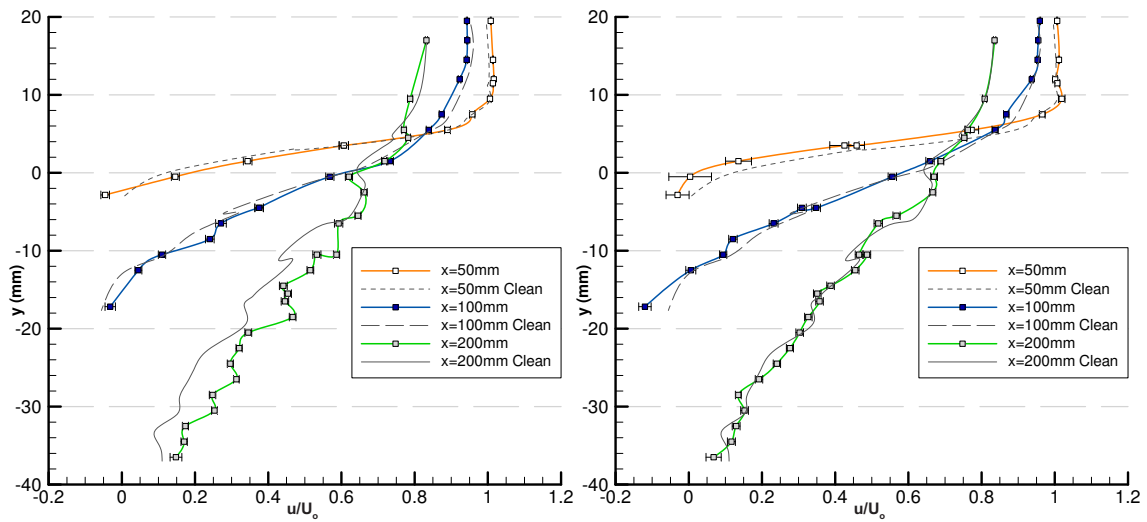
Figure D.27 **A2.5-R5-D0** and Clean u/U$_o$ Profile Figure D.30 **A2.5-R5-D1** and Clean u/U$_o$ Profile
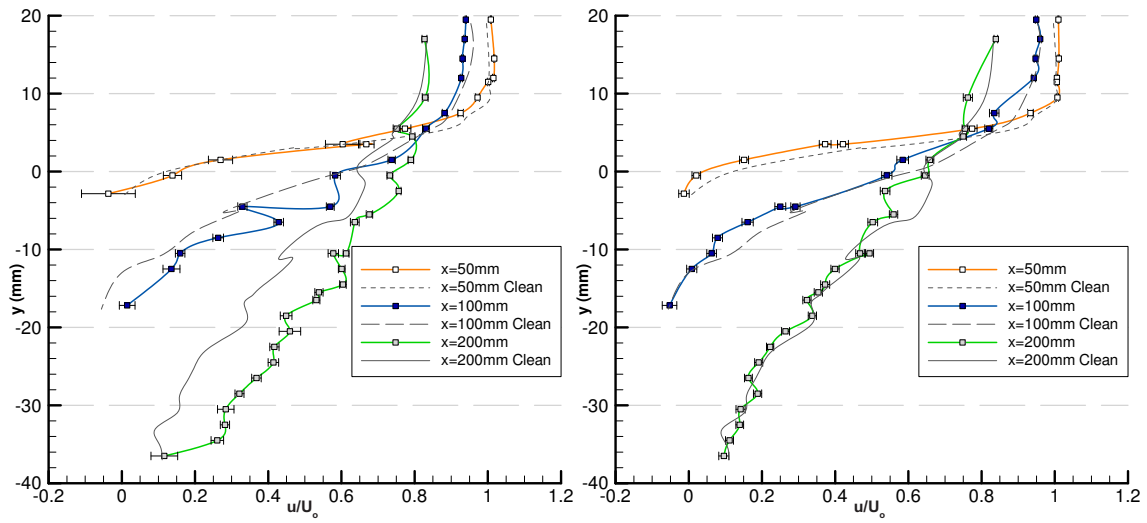
Figure D.31 **A2.5-R1-D3** and Clean u/U$_o$ Profile Figure D.34 **A2.5-R1-D5** and Clean u/U$_o$ Profile
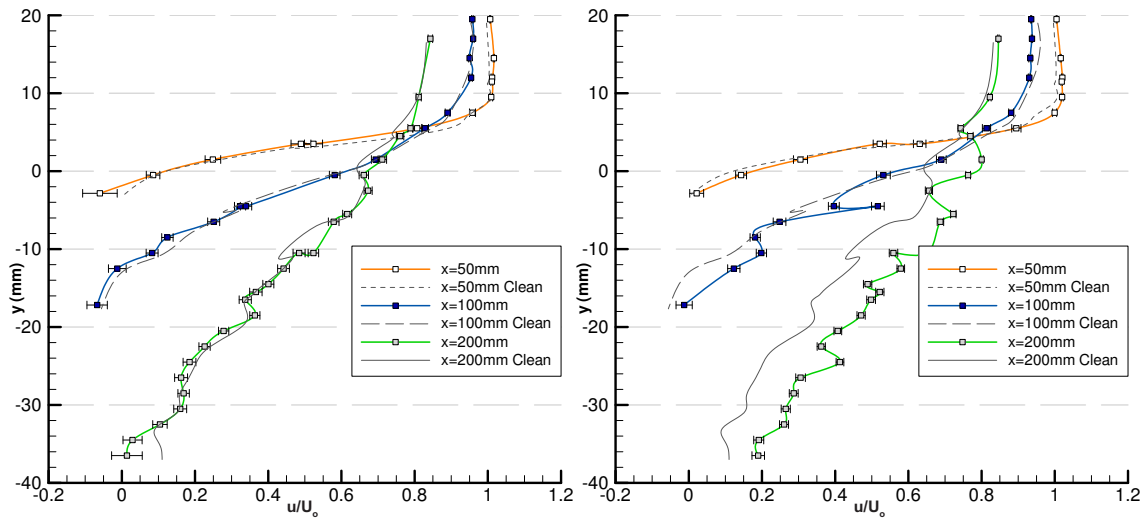
Figure D.32 **A2.5-R3-D3** and Clean u/U$_o$ Profile Figure D.35 **A2.5-R3-D5** and Clean u/U$_o$ Profile
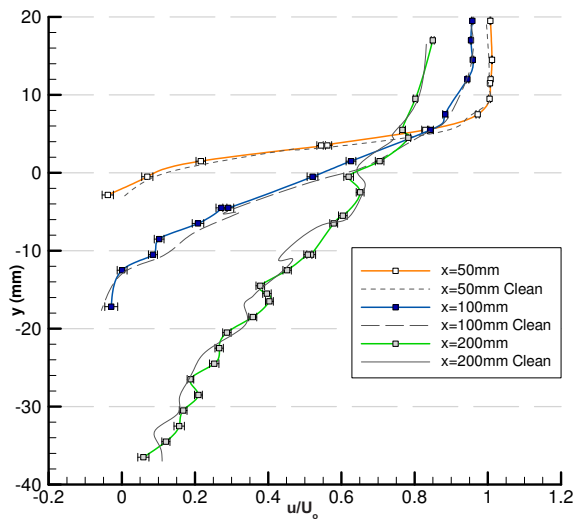
Figure D.33 **A2.5-R5-D3** and Clean u/U$_o$ Profile
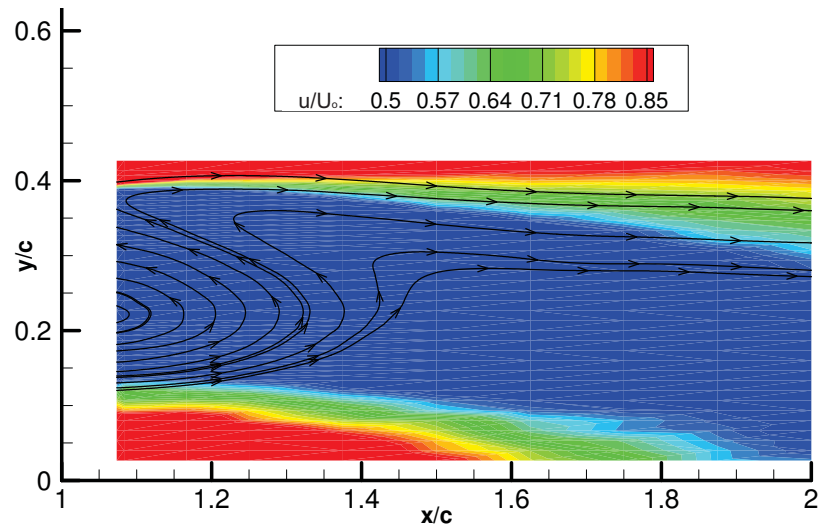
Figure E.1 Clean Tyrrell026 Airfoil Wake: α=15˚, h/c=0.112
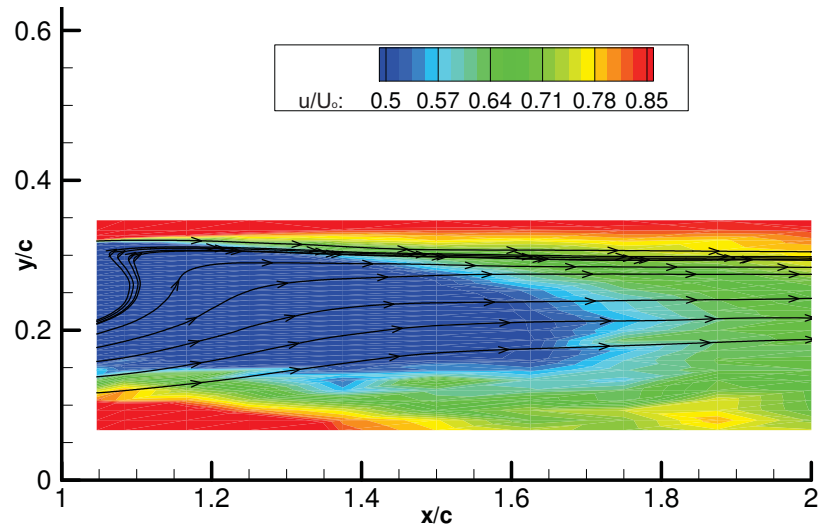
Figure E.2 Clean Tyrrell026 Airfoil Wake: α=10˚, h/c=0.112
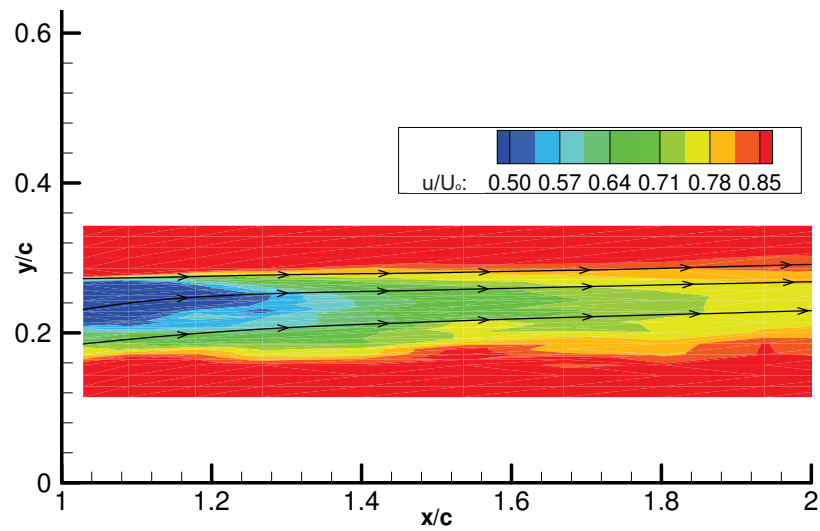
Figure E.3 Clean Tyrrell026 Airfoil Wake: α=5˚, h/c=0.112
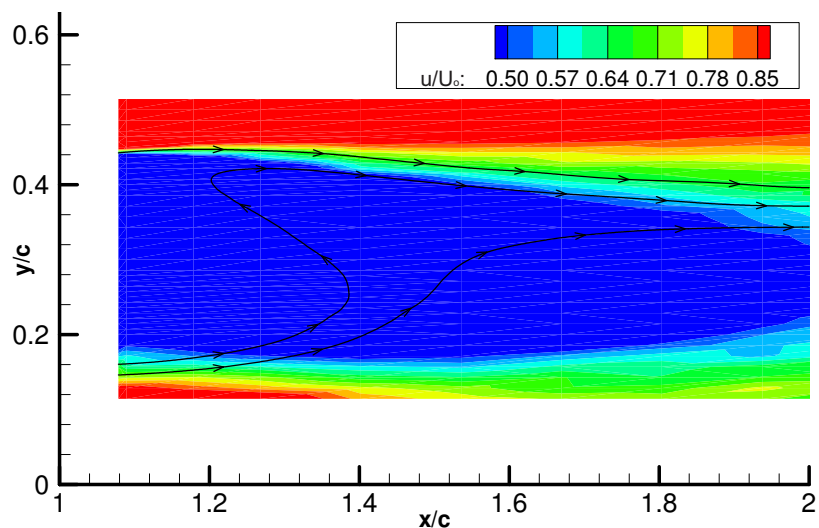
Figure E.4 Clean Tyrrell026 Airfoil Wake: α=15˚, h/c=0.134
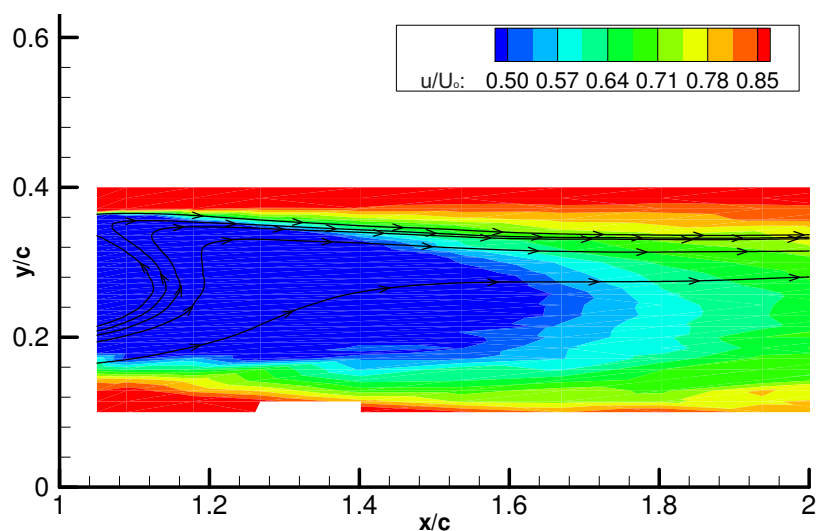
Figure E.5 Clean Tyrrell026 Airfoil Wake: α=10˚, h/c= 0.134
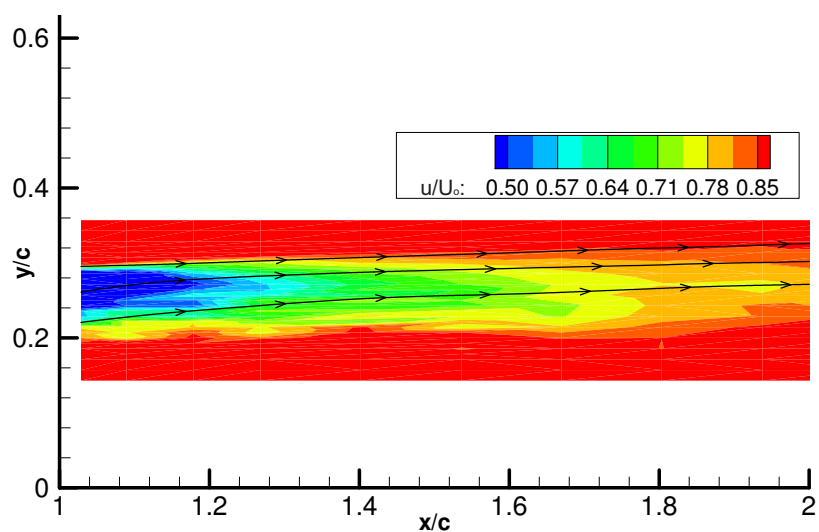
Figure E.6 Clean Tyrrell026 Airfoil Wake: α=5˚, h/c= 0.134
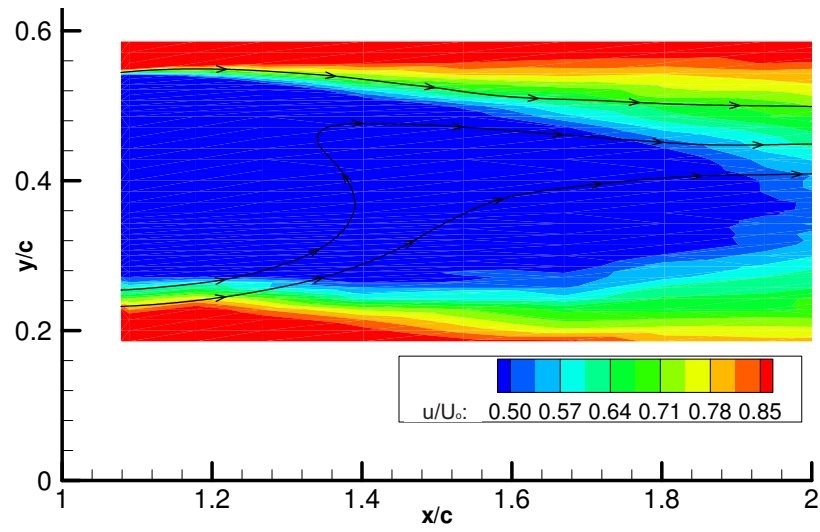
Figure E.7 Clean Tyrrell026 Airfoil Wake: α=15˚, h/c=0.224
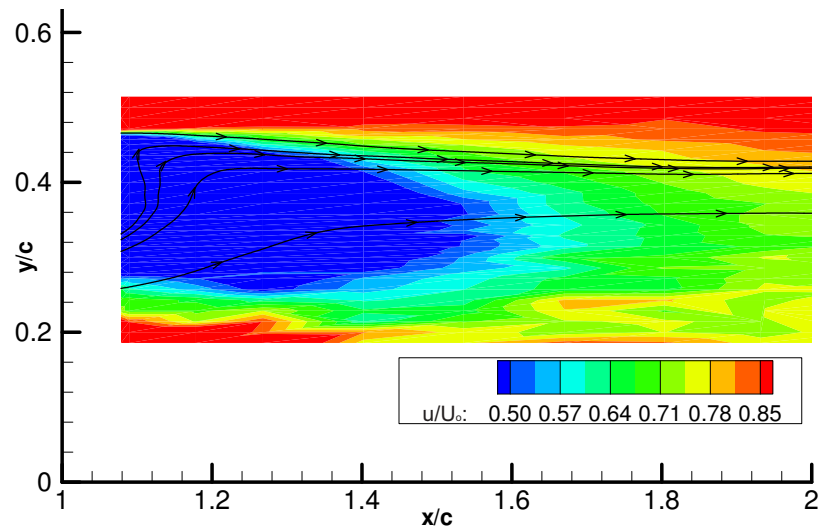
Figure E.8 Clean Tyrrell026 Airfoil Wake: α=10˚, h/c=0.224
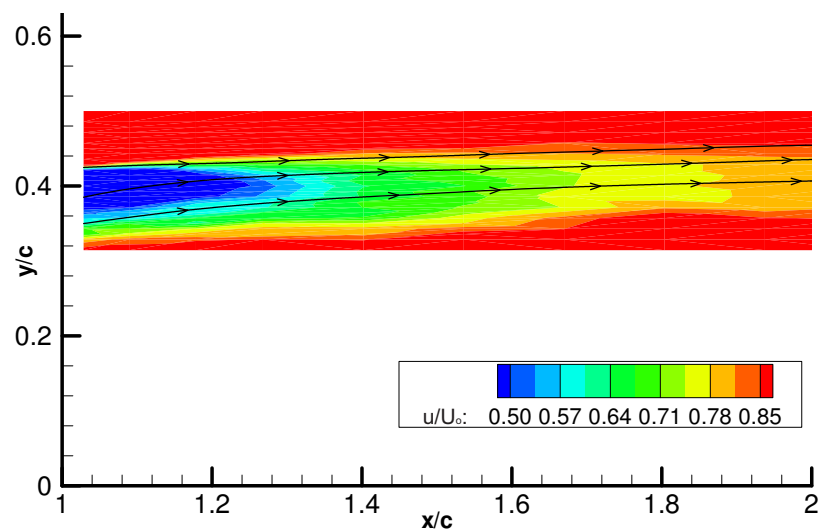
Figure E.9 Clean Tyrrell026 Airfoil Wake: α=7˚, h/c=0.224
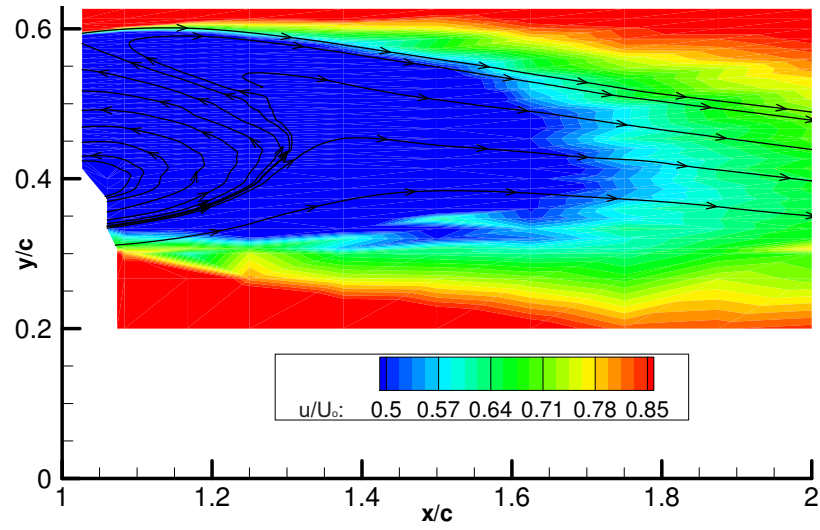
Figure E.10 Clean Tyrrell026 Airfoil Wake: α=15˚, h/c=0.313
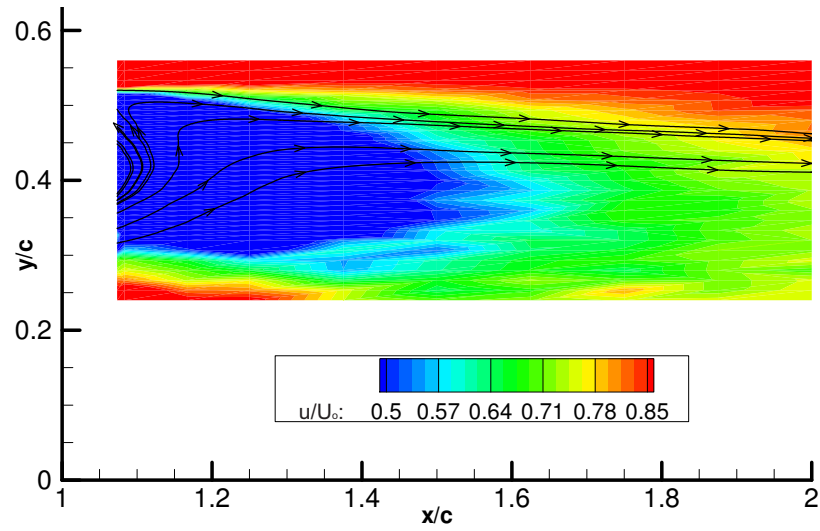
Figure E.11 Clean Tyrrel026 Airfoil Wake: α=10˚, h/c=0.313
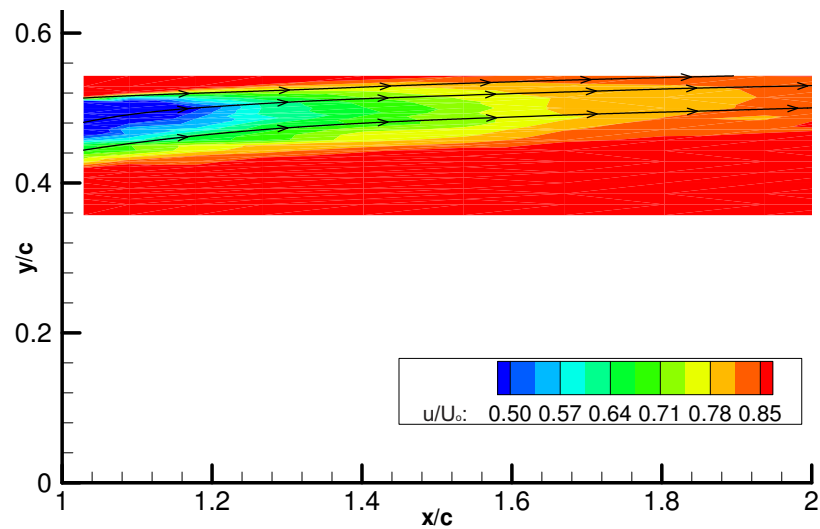
Figure E.12 Clean Tyrrell026 Airfoil Wake: α=7˚, h/c=0.313

Figure E.13 Clean Tyrrell026 Airfoil Wake Turbulence Intensity

Figure E.13 Clean Tyrrell026 Airfoil Wake Turbulence Intensity

Figure E.13 Clean Tyrrell026 Airfoil Wake Turbulence Intensity

Figure E.13 Clean Tyrrell026 Airfoil Wake Turbulence Intensity

Figure E.13 Clean Tyrrell026 Airfoil Wake Turbulence Intensity

Figure E.13 Clean Tyrrell026 Airfoil Wake Turbulence Intensity

Figure E.13 Clean Tyrrell026 Airfoil Wake Turbulence Intensity

a) α=-2˚, h/c=0.112   b) α=-2˚, h/c=0.134   c) α=-2˚, h/c=0.224   d) α=-2˚, h/c=0.313

e) α=0˚, h/c=0.134   f) α=0˚, h/c=0.224   g) α=2˚, h/c=0.134   h) α=2˚, h/c=0.224

i) α=5˚, h/c=0.134   j) α=7˚, h/c=0.224   k) α=10˚, h/c=0.134   l) α=10˚, h/c=0.224

m) α=15˚, h/c=0.134   n) α=15˚, h/c=0.224

Figure E.14 Clean Tyrrell026 Airfoil Wake Turbulent Normal Stress a) α=-2°, h/c=0.134 b) α=-2°, h/c=0.224

Figure E.14 Clean Tyrrell026 Airfoil Wake Turbulent Normal Stress c) α=0°, h/c=0.134 d) α=0°, h/c=0.224

Figure E.14 Clean Tyrrell026 Airfoil Wake Turbulent Normal Stress e) α=2°, h/c=0.134 f) α=2°, h/c=0.224

Figure E.14 Clean Tyrrell026 Airfoil Wake Turbulent Normal Stress g) α=5˚, h/c=0.134 h) α=7˚, h/c=0.224

Figure E.14 Clean Tyrrell026 Airfoil Wake Turbulent Normal Stress i) α=10˚, h/c=0.134 j) α=10˚, h/c=0.224

Figure E.14 Clean Tyrrell026 Airfoil Wake Turbulent Normal Stress k) α=15˚, h/c=0.134 l) α=15˚, h/c=0.224

Figure E.15 Clean Tyrrell026 Airfoil Wake Primary Shear Stress a) α=-2°, h/c=0.134 b) α=-2°, h/c=0.224

Figure E.15 Clean Tyrrell026 Airfoil Primary Shear Stress c) α=0°, h/c=0.134 d) α=0°, h/c=0.224
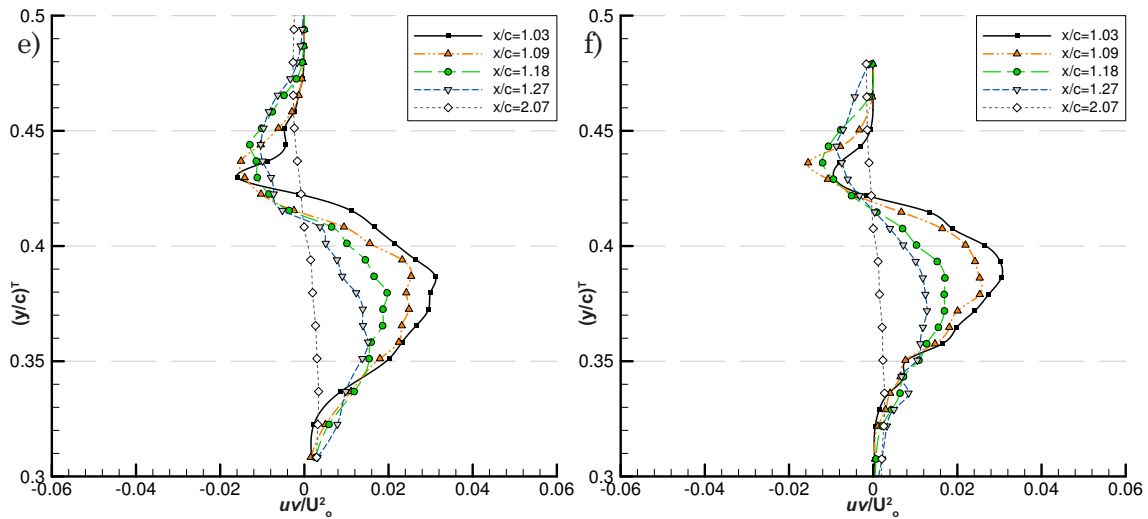
Figure E.15 Clean Tyrrell026 Airfoil Wake Primary Shear Stress e) α=2°, h/c=0.134 f) α=2°, h/c=0.224
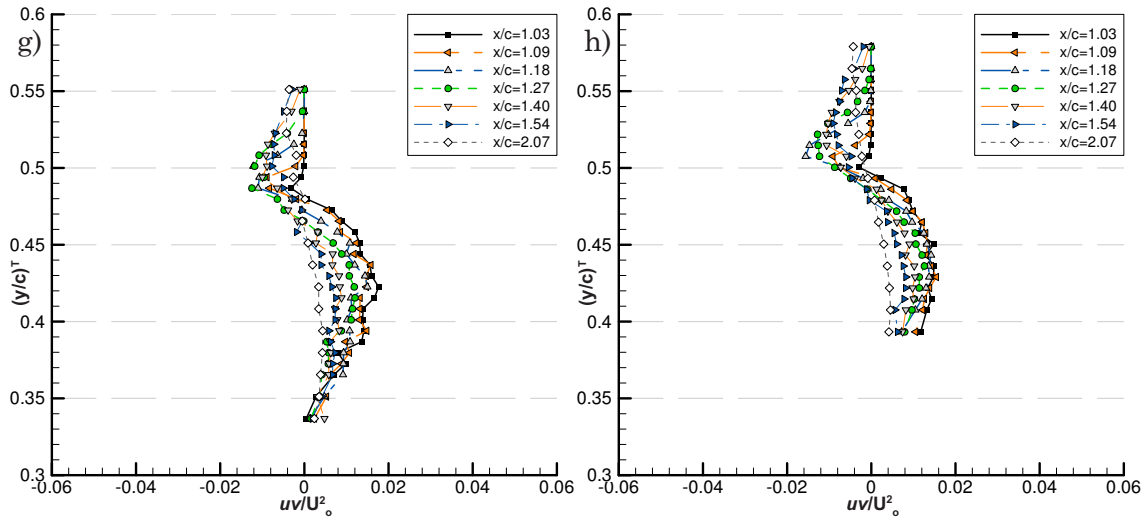
Figure E.15 Clean Tyrrell026 Airfoil Wake Primary Shear Stress g) α=5˚, h/c=0.134 h) α=7˚, h/c=0.224
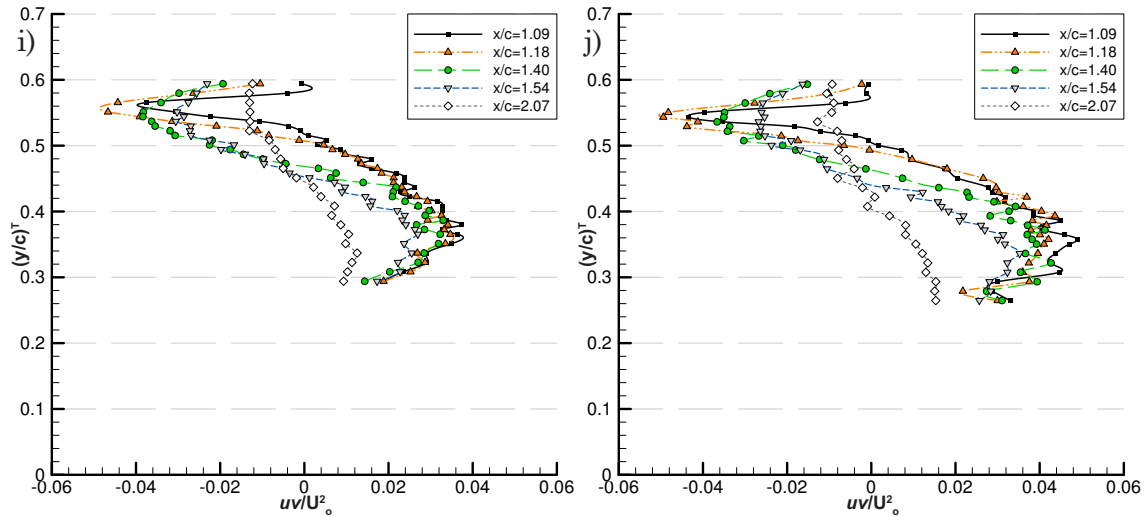
Figure E.15 Clean Tyrrell026 Airfoil Wake Primary Shear Stress i) α=10˚, h/c=0.134 j) α=10˚, h/c=0.224
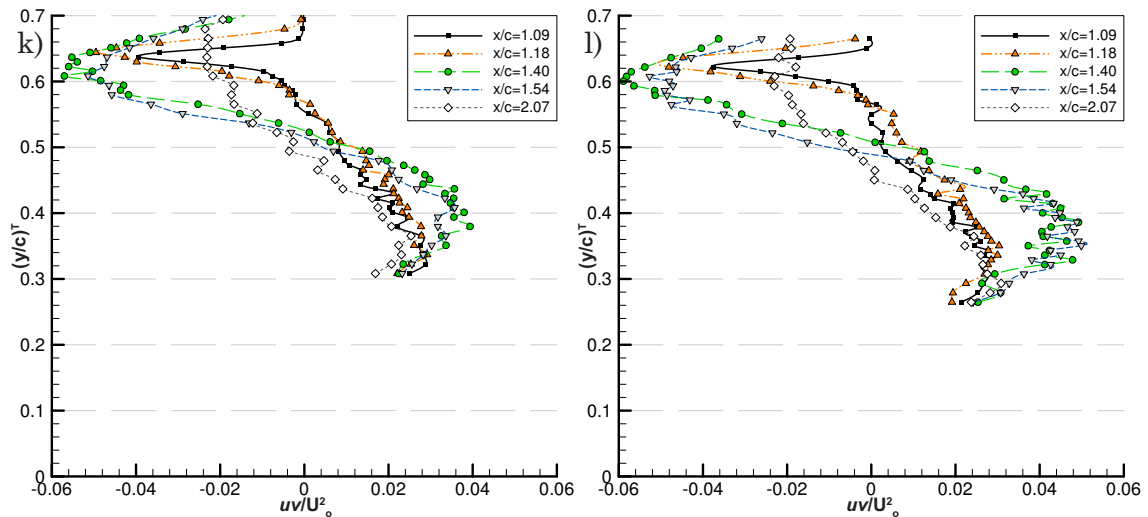
Figure E.15 Clean Tyrrell026 Airfoil Wake Primary Shear Stress k) α=15˚, h/c=0.134 l) α=15˚, h/c=0.224
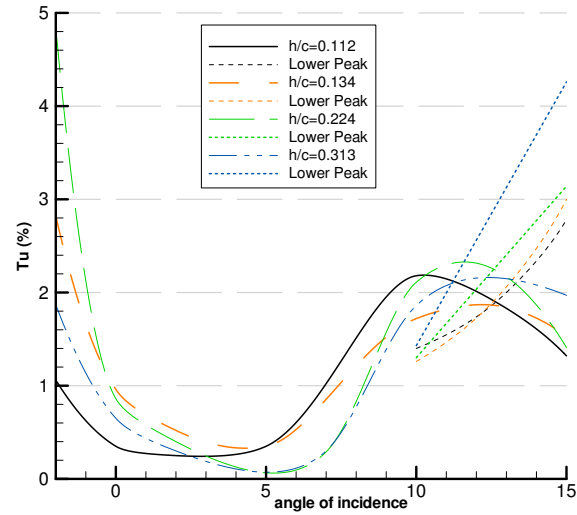
Figure E.16 Peak Turbulence Intensity in the Wake of the Clean Tyrrell026 Airfoil
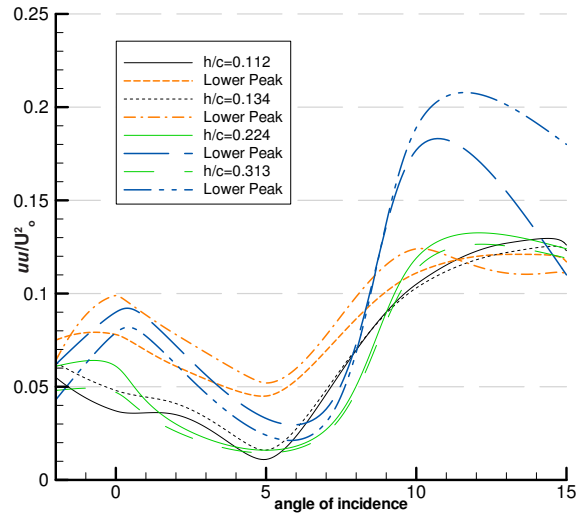
Figure E.17 Peak Turbulent Normal Stress in the Wake of the Clean Tyrrell026 Airfoil
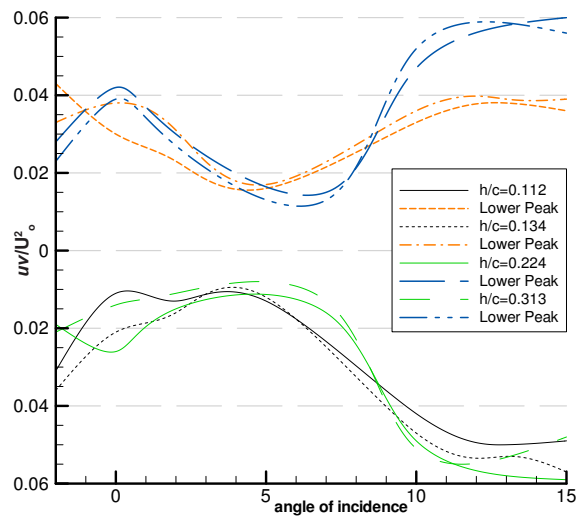
Figure E.18 Peak Primary Shear Stress in the Wake of the Clean Tyrrell026 Airfoil
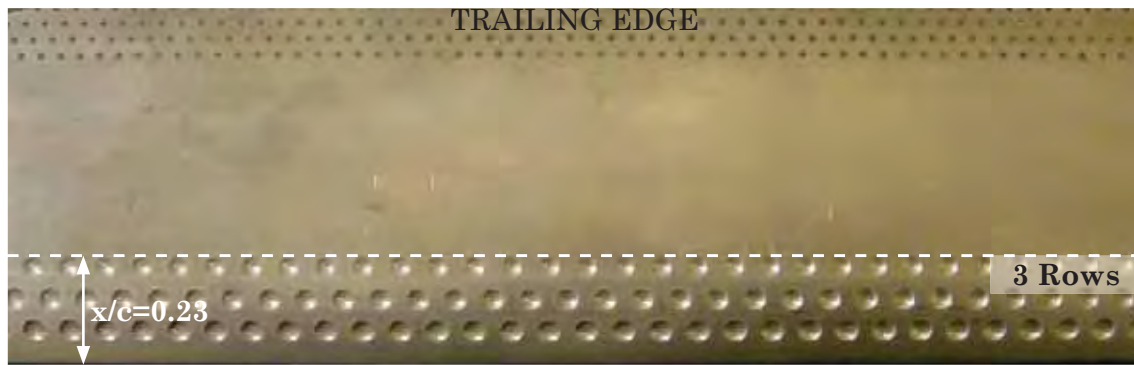
Figure F.1 Tyrrell026 Airfoil with **1.5-3-23** Series Dimple Array Modification

Figure F.2 Tyrrell026 Airfoil with **1.5-5-53** Series Dimple Array Modification

Figure F.3 Tyrrell026 Airfoil with **1.5-5-675** Series Dimple Array Modification

Figure F.4 Tyrrell026 Airfoil with **1.5-5-8** Series Dimple Array Modification
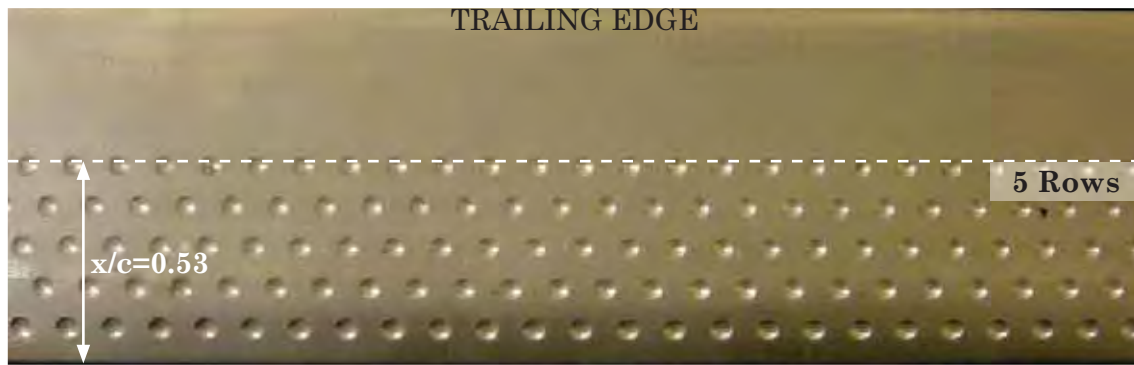
Figure F.5 Tyrrell026 Airfoil with **2-5-53** Series Dimple Array Modification
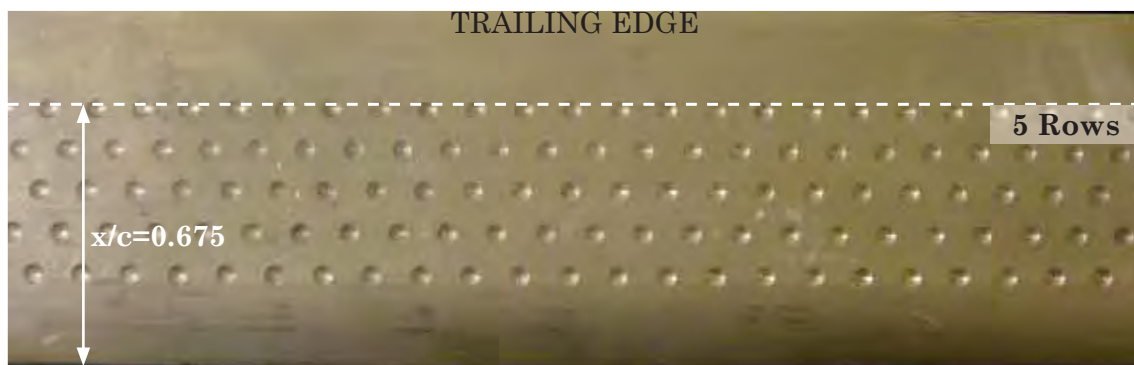
Figure F.6 Tyrrell026 Airfoil with **2-5-675** Series Dimple Array Modification

Figure F.7 Tyrrell026 Airfoil with **2-5-8** Series Dimple Array Modification
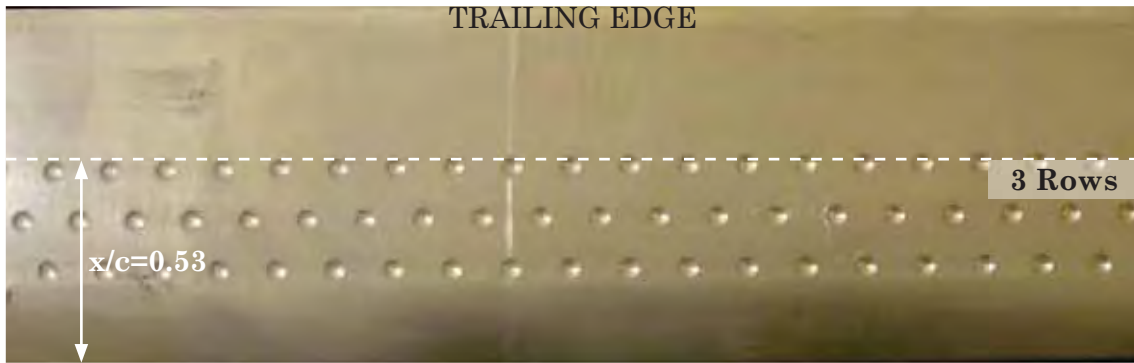
Figure F.8 Tyrrell026 Airfoil with **2.5-3-53** Series Dimple Array Modification

Figure F.9 Tyrrell026 Airfoil with **2.5-5-675** Series Dimple Array Modification
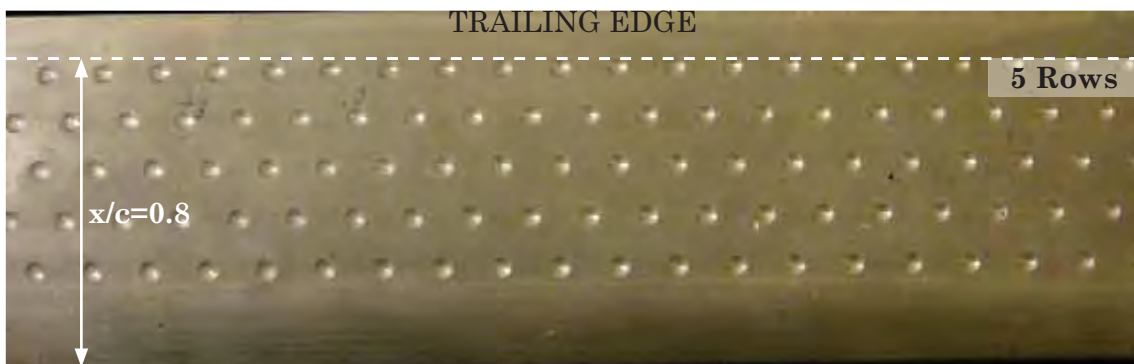
Figure F.10 Tyrrell026 Airfoil with **2.5-5-8** Series Dimple Array Modification
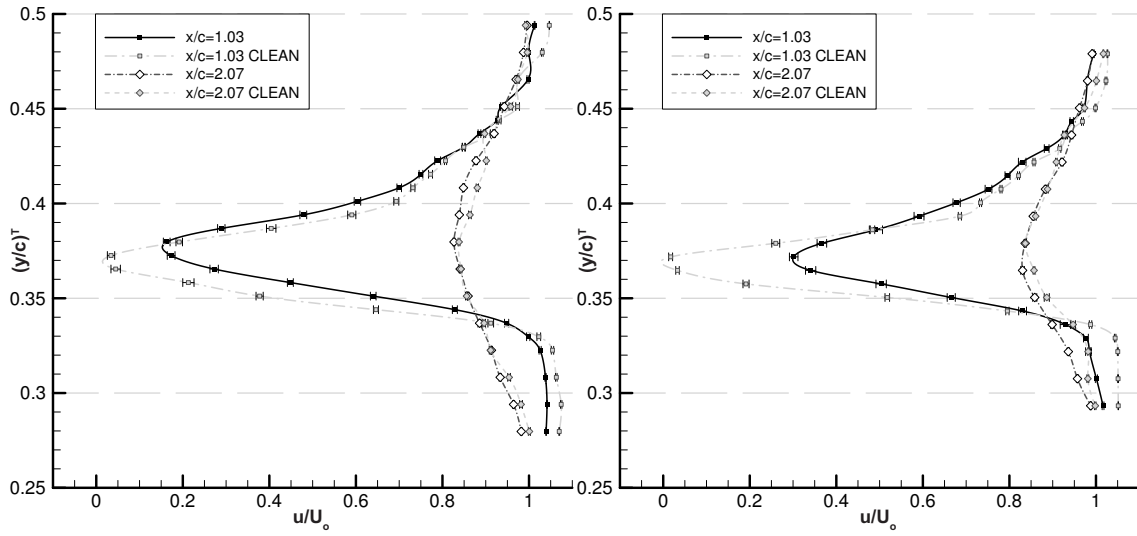
Figure F.11 u/U$_o$ **1.5-3-23:** α=-2˚, h/c=0.134

Figure F.12 u/U$_o$ **1.5-3-23:** α=-2˚, h/c=0.224
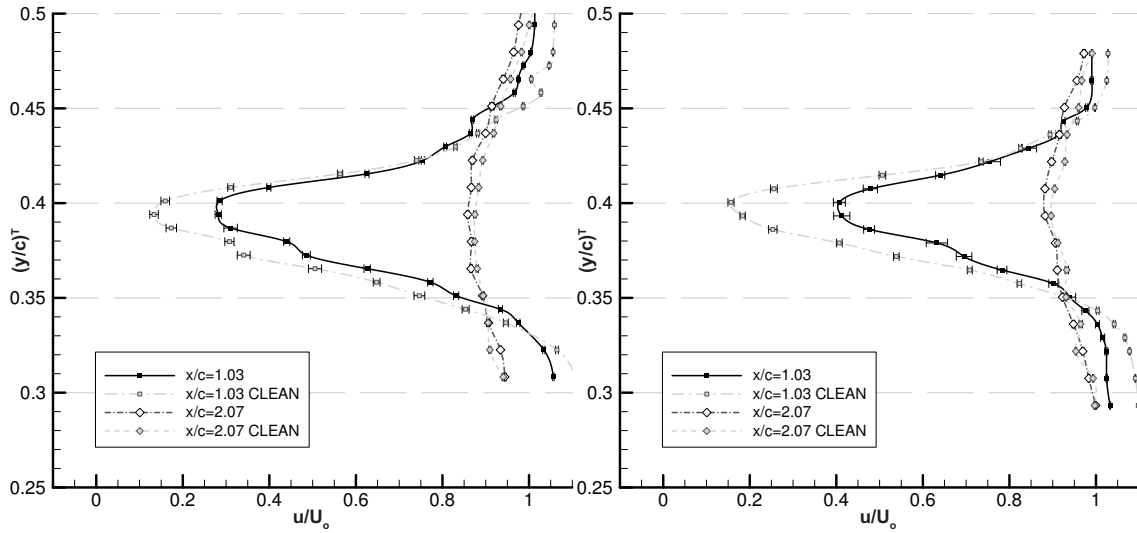
Figure F.13 u/U$_o$ **1.5-3-23:** α=0˚, h/c=0.134

Figure F.14 u/U$_o$ **1.5-3-23:** α=0˚, h/c=0.224
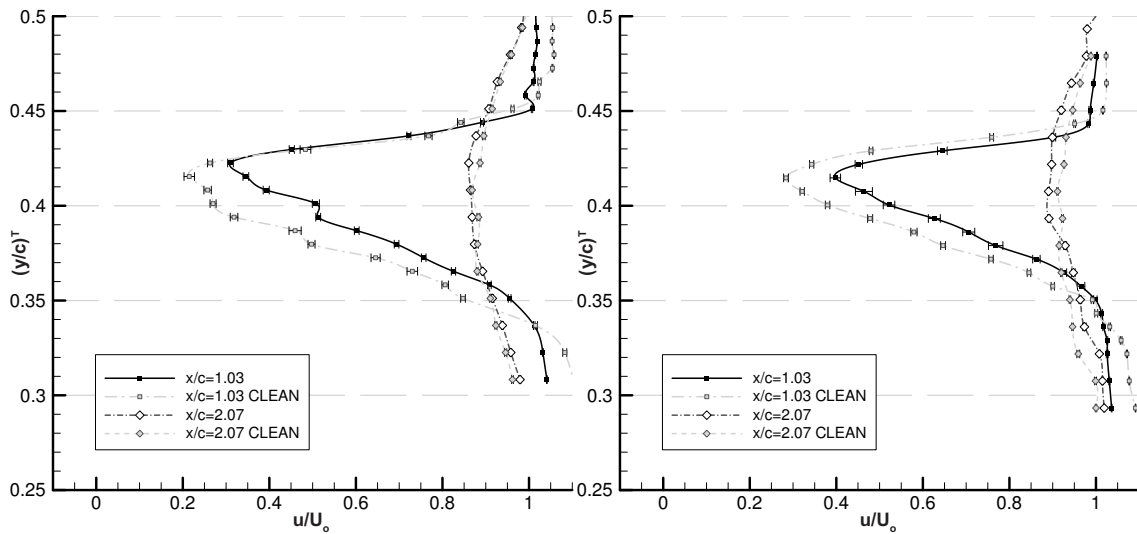
Figure F.15 u/U$_o$ **1.5-3-23:** α=2˚, h/c=0.134

Figure F.16 u/U$_o$ **1.5-3-23:** α=2˚, h/c=0.224
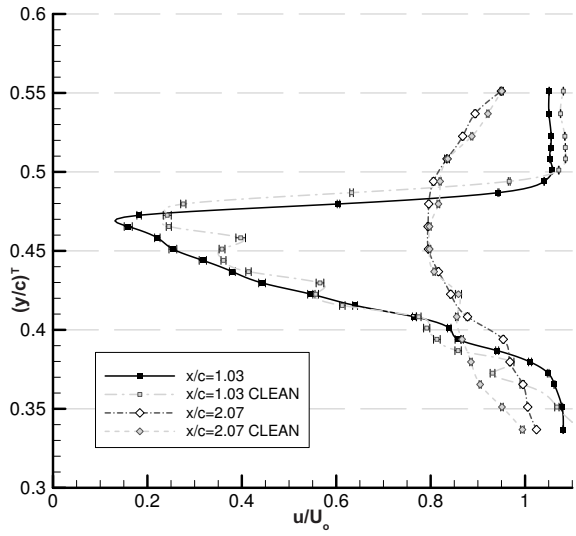
Figure F.17 u/U$_o$ **1.5-3-23:** α=5˚, h/c=0.134
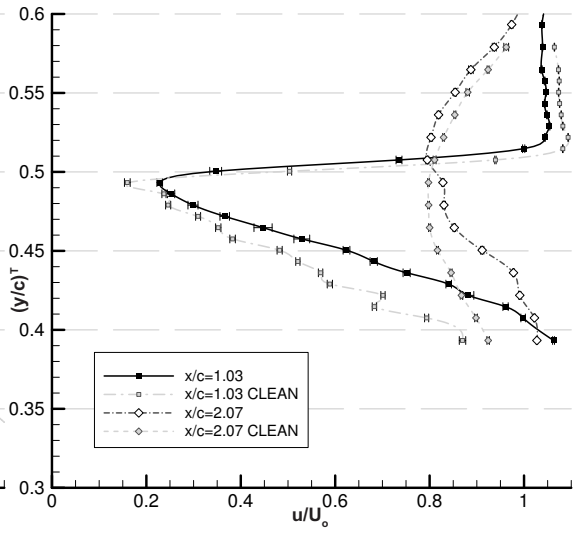
Figure F.18 u/U$_o$ **1.5-3-23:** α=7˚, h/c=0.224
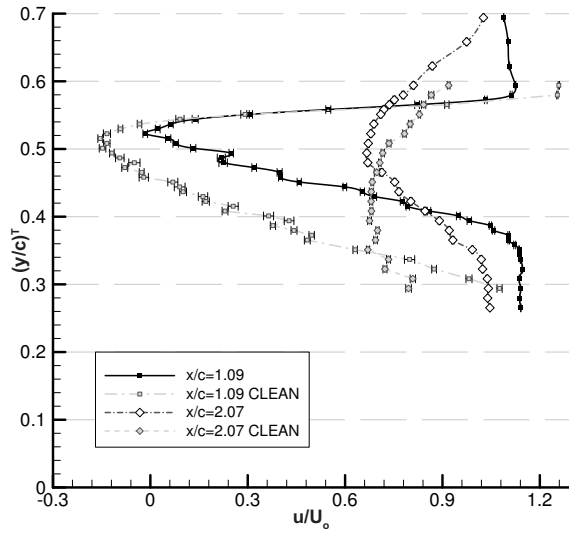
Figure F.19 u/U$_o$ **1.5-3-23:** α=10˚, h/c=0.134
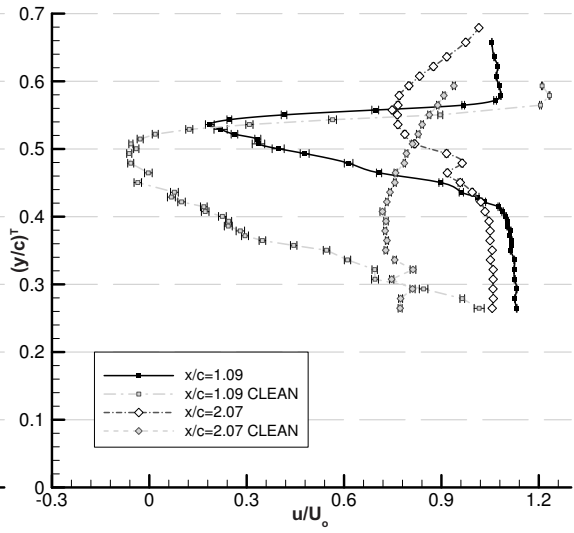
Figure F.20 u/U$_o$ **1.5-3-23:** α=10˚, h/c=0.224
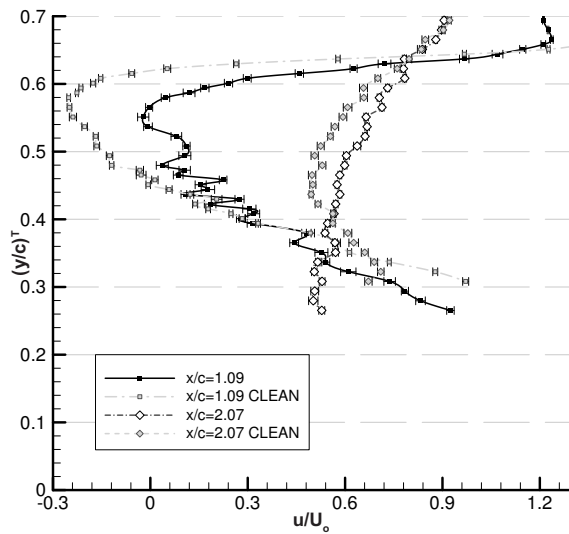
Figure F.21 u/U$_o$ **1.5-3-23:** α=15˚, h/c=0.134
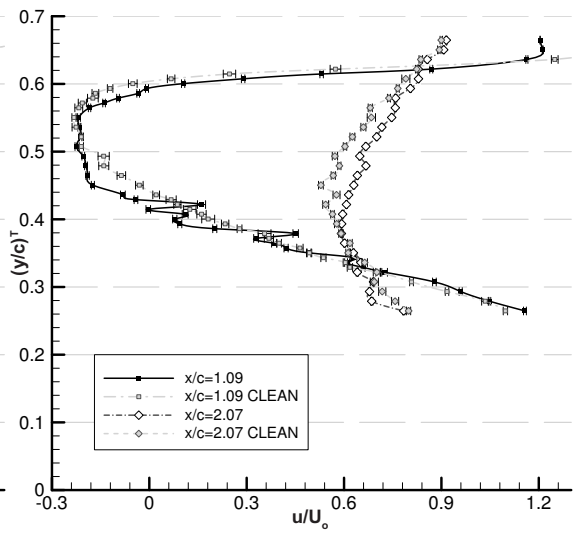
Figure F.22 u/U$_o$ **1.5-3-23:** α=15˚, h/c=0.224
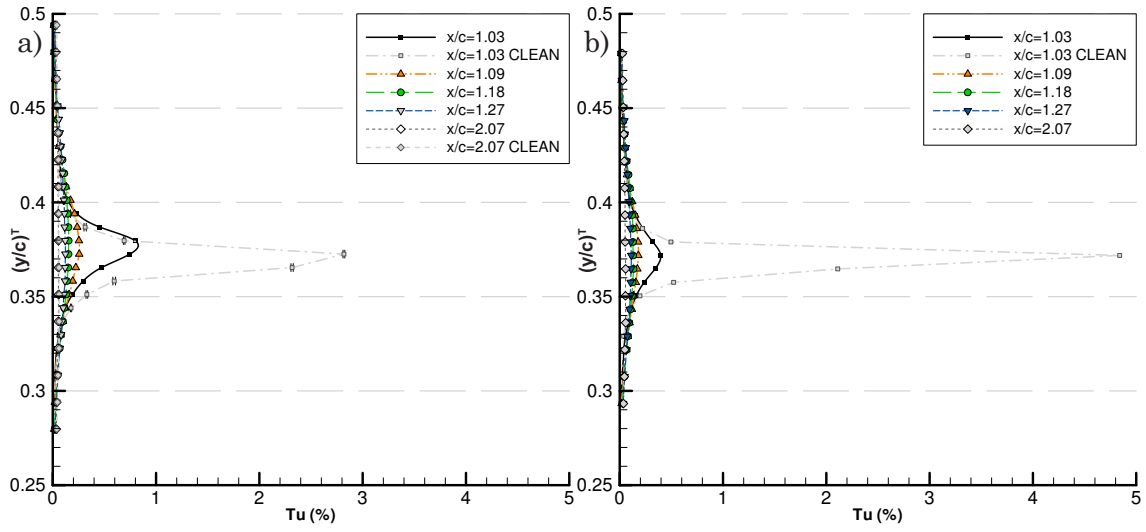
Figure F.23 Turbulence Intensity **1.5-3-23** : a) α=-2° h/c=0.134, b) α=-2° h/c=0.224
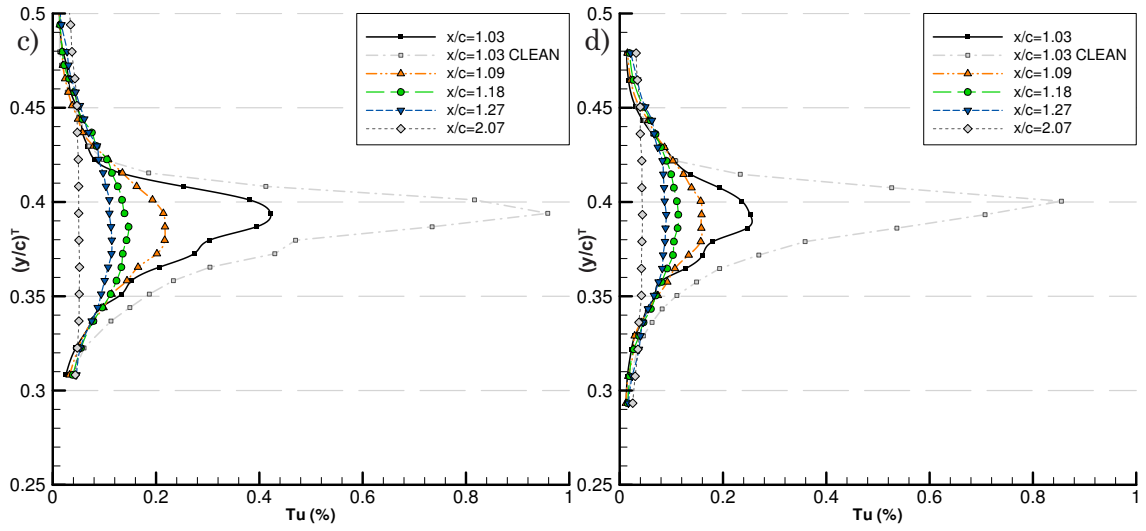
Figure F.23 Turbulence Intensity **1.5-3-23** : c) α=0° h/c=0.134, d) α=0° h/c=0.224
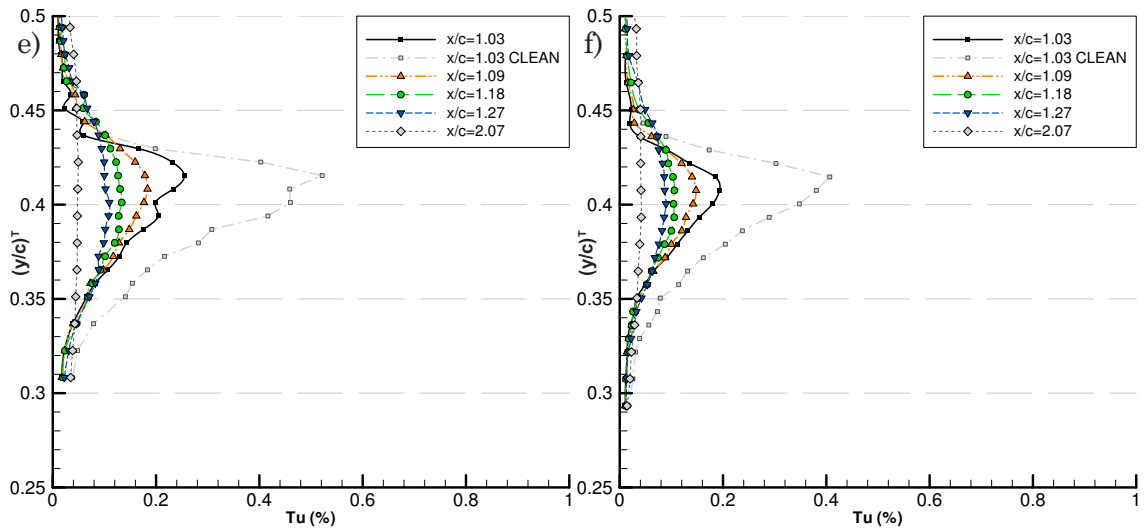
Figure F.23 Turbulence Intensity **1.5-3-23** : e) α=2° h/c=0.134, f) α=2° h/c=0.224
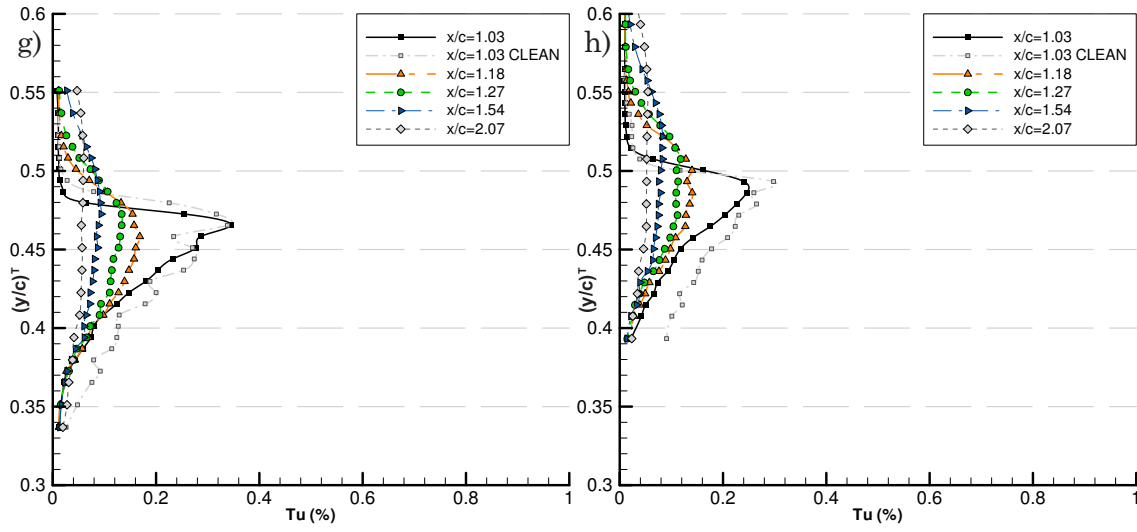
Figure F.23 Turbulence Intensity **1.5-3-23** : g) α=5˚ h/c=0.134, h) α=7˚ h/c=0.224
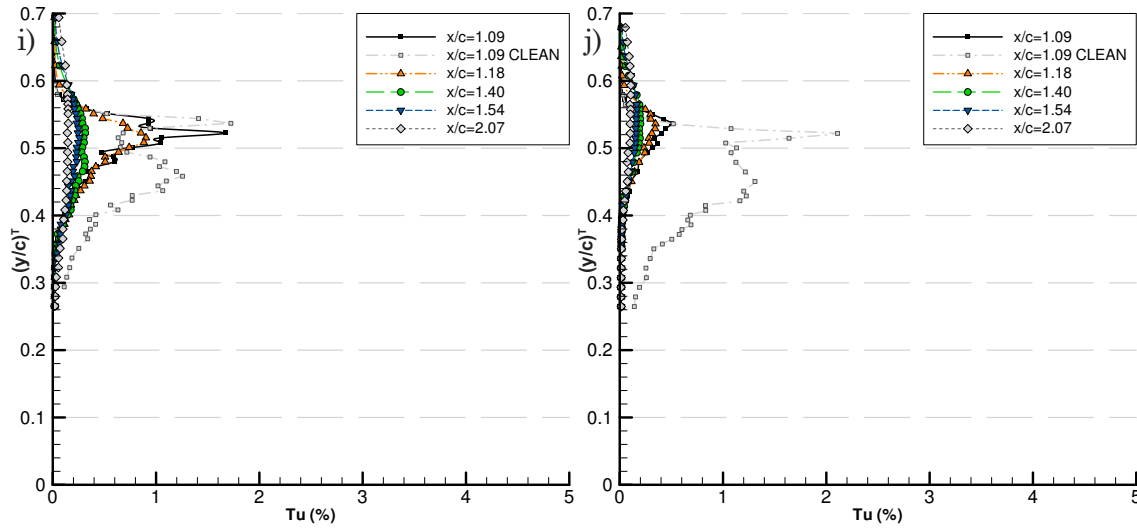
Figure F.23 Turbulence Intensity **1.5-3-23** : i) α=10˚ h/c=0.134, j) α=10˚ h/c=0.224
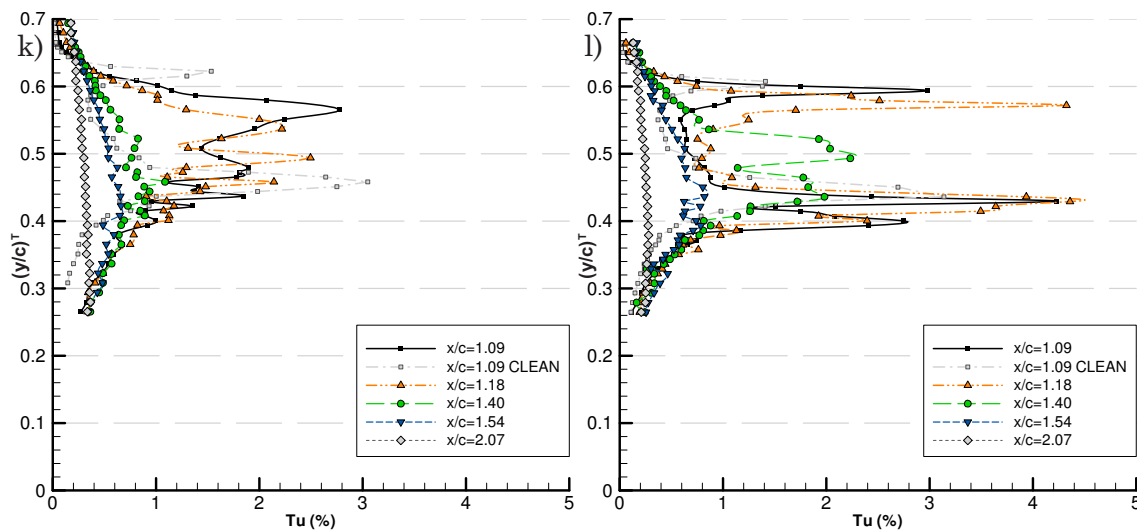
Figure F.23 Turbulence Intensity **1.5-3-23** : k) α=15˚ h/c=0.134, l) α=15˚ h/c=0.224
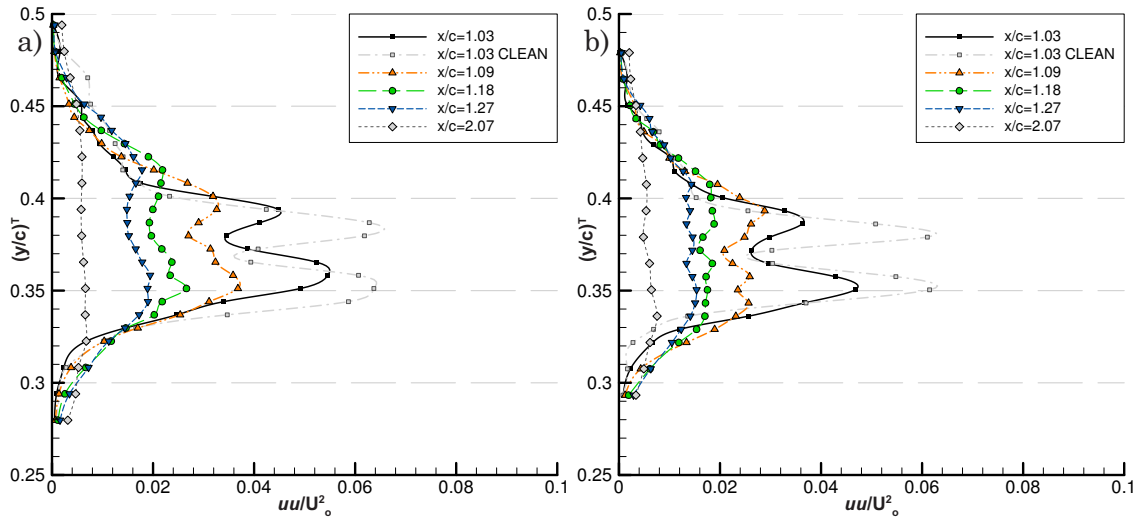
Figure F.24 Turbulent Normal Stress **1.5-3-23** : a) α=-2˚ h/c=0.134, b) α=-2˚ h/c=0.224
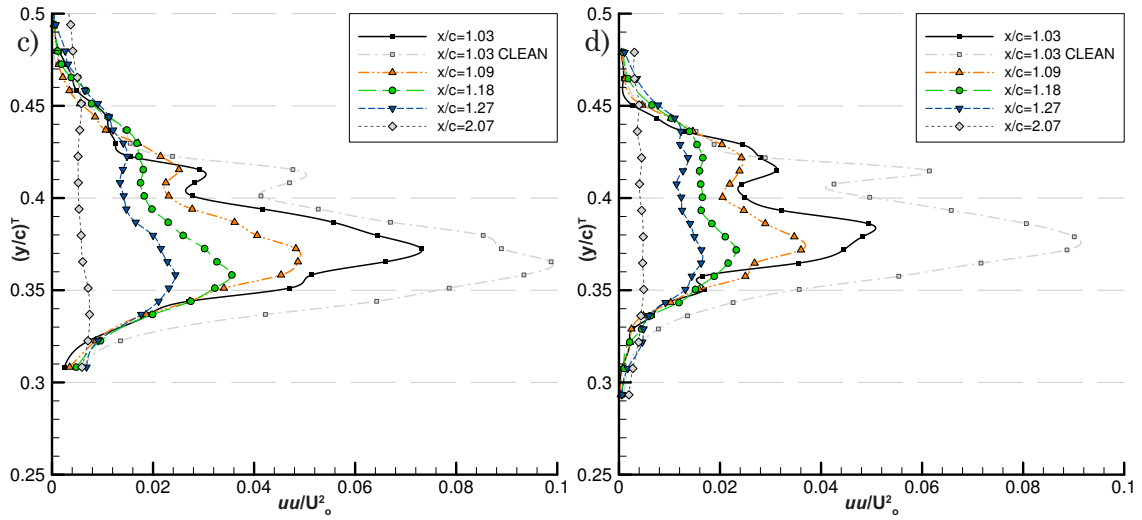
Figure F.24 Turbulent Normal Stress **1.5-3-23** : c) α=0˚ h/c=0.134, d) α=0˚ h/c=0.224
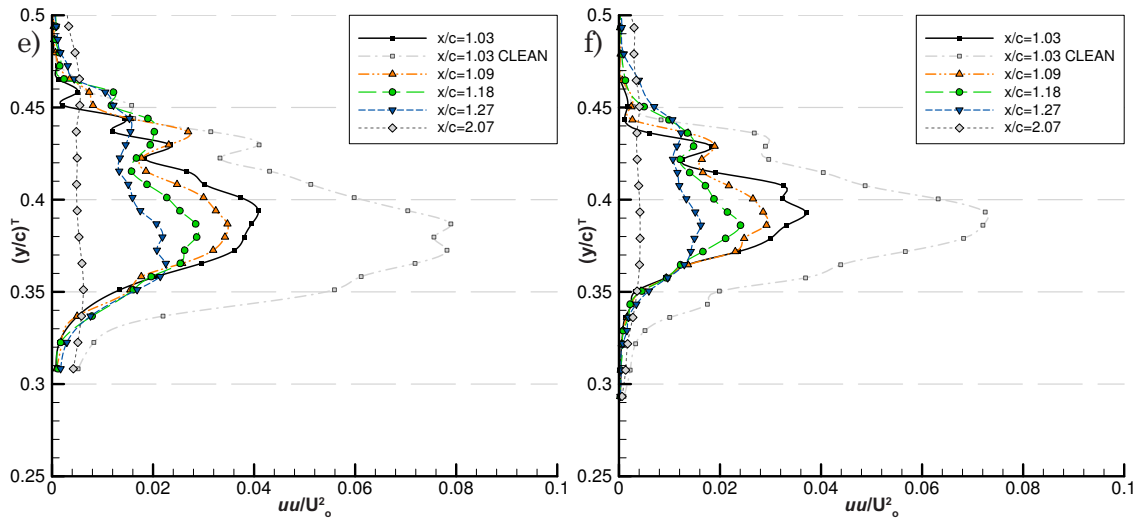
Figure F.24 Turbulent Normal Stress **1.5-3-23** : e) α=2˚ h/c=0.134, f) α=2˚ h/c=0.224
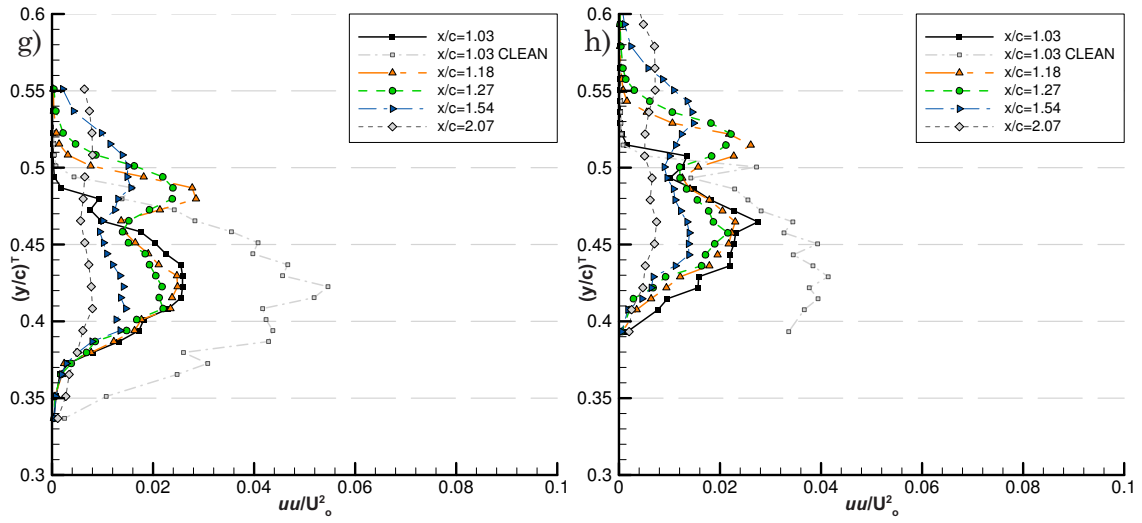
Figure F.24 Turbulent Normal Stress **1.5-3-23** : g) α=5˚ h/c=0.134, h) α=7˚ h/c=0.224
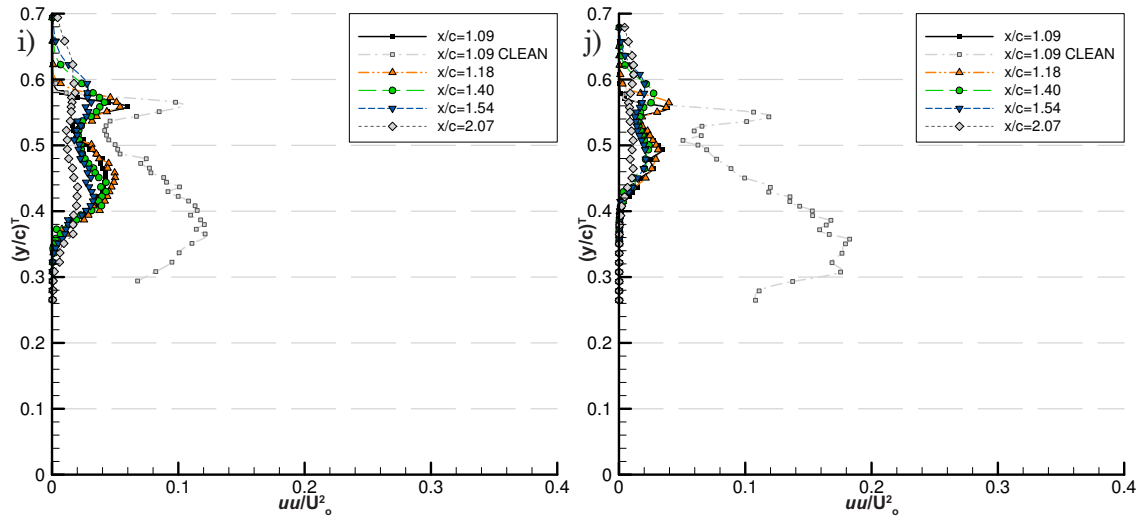
Figure F.24 Turbulent Normal Stress **1.5-3-23** : i) α=10˚ h/c=0.134, j) α=10˚ h/c=0.224
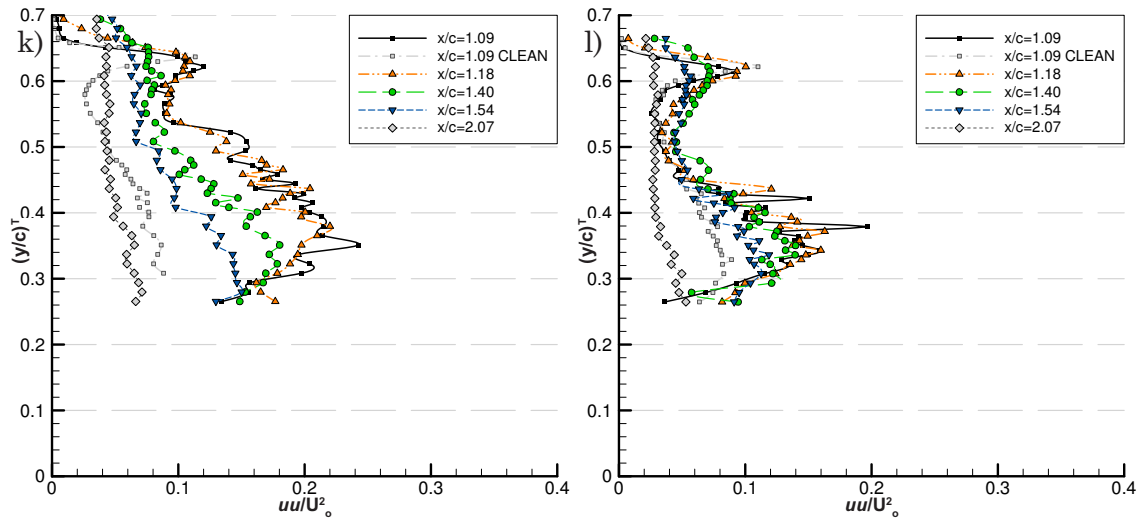
Figure F.24 Turbulent Normal Stress **1.5-3-23** : k) α=15˚ h/c=0.134, l) α=15˚ h/c=0.224
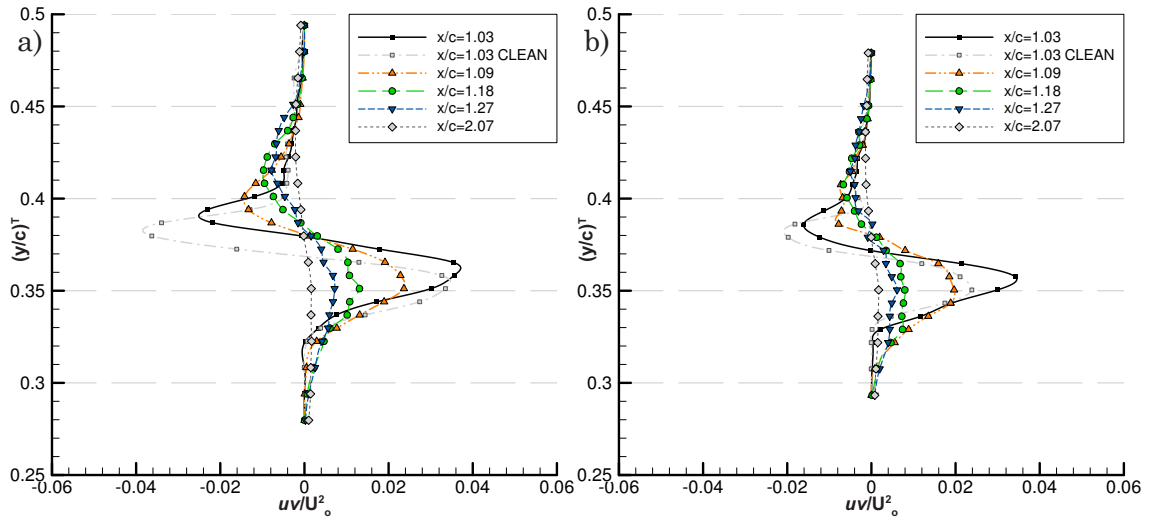
Figure F.25 Primary Shear Stress **1.5-3-23** : a) α=-2˚ h/c=0.134, b) α=-2˚ h/c=0.224
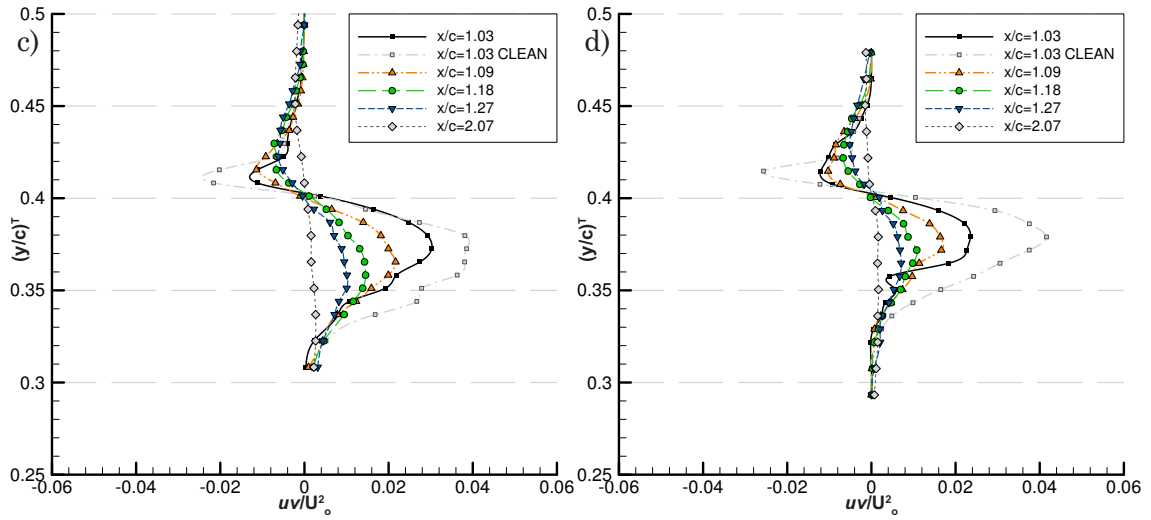
Figure F.25 Primary Shear Stress **1.5-3-23** : c) α=0˚ h/c=0.134, d) α=0˚ h/c=0.224
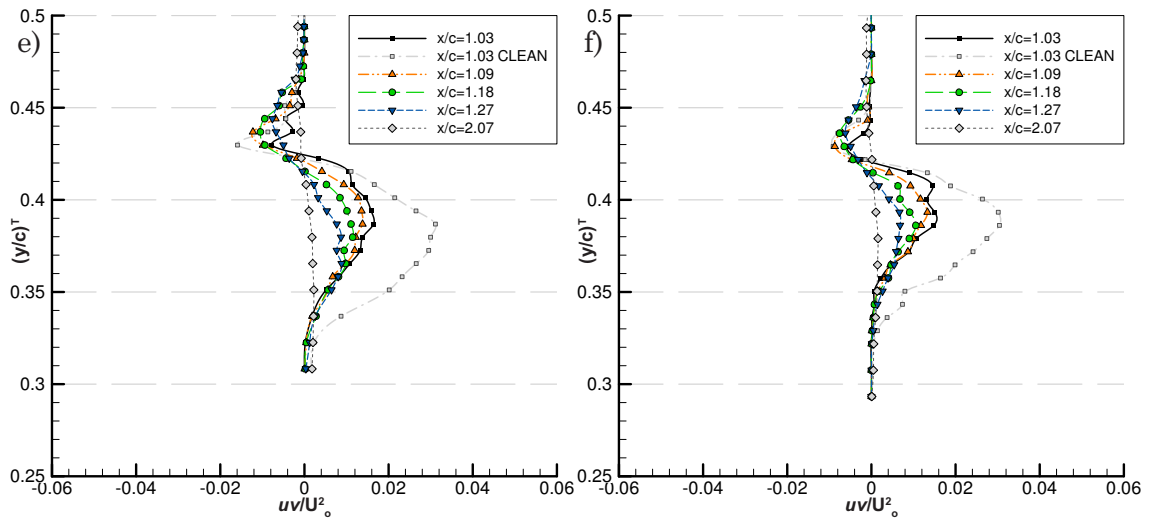
Figure F.25 Primary Shear Stress **1.5-3-23** : e) α=2˚ h/c=0.134, f) α=2˚ h/c=0.224
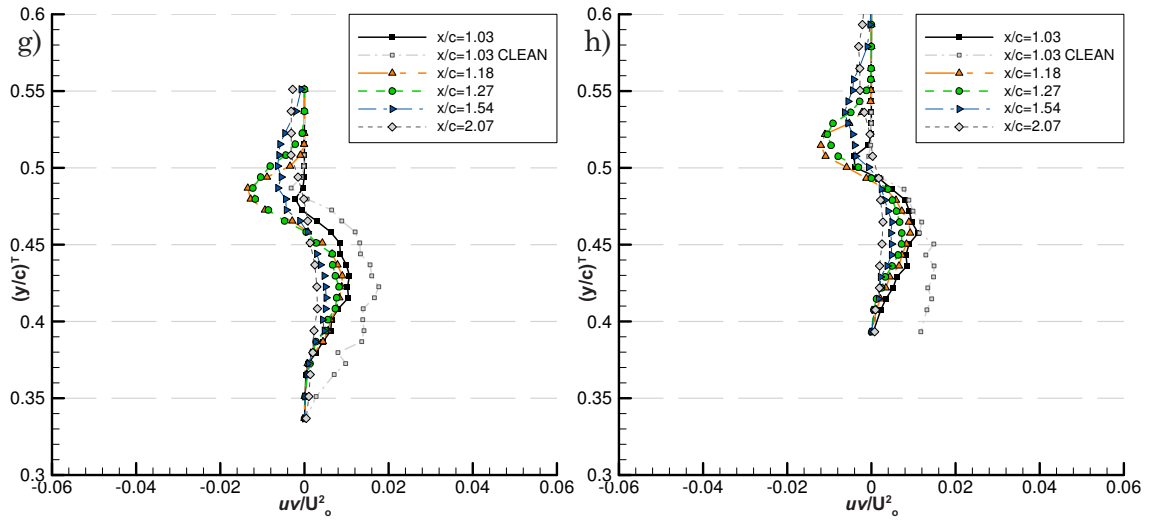
Figure F.25 Primary Shear Stress **1.5-3-23** : g) α=5˚ h/c=0.134, h) α=7˚ h/c=0.224
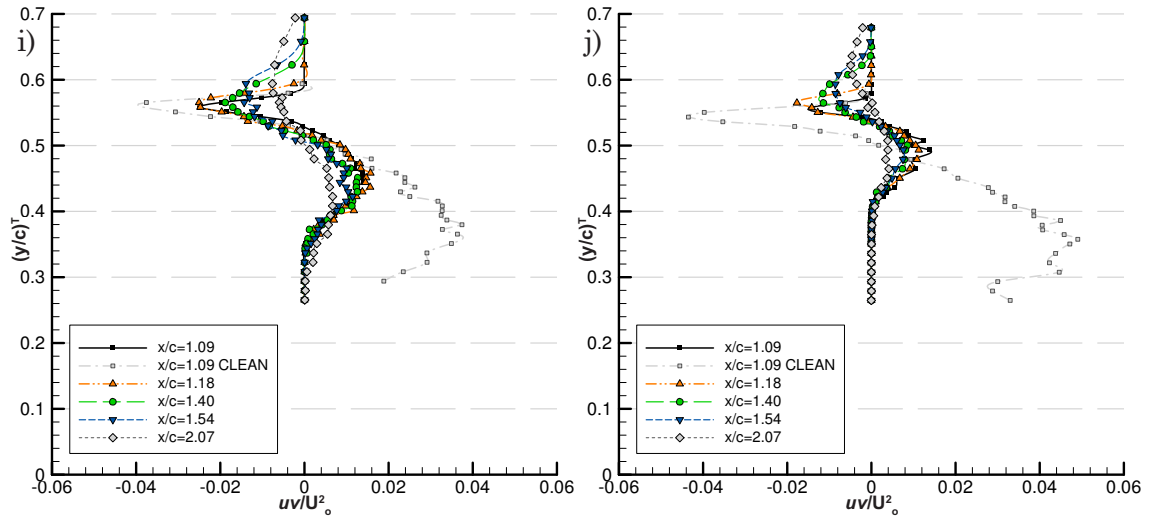
Figure F.25 Primary Shear Stress **1.5-3-23** : i) α=10˚ h/c=0.134, j) α=10˚ h/c=0.224
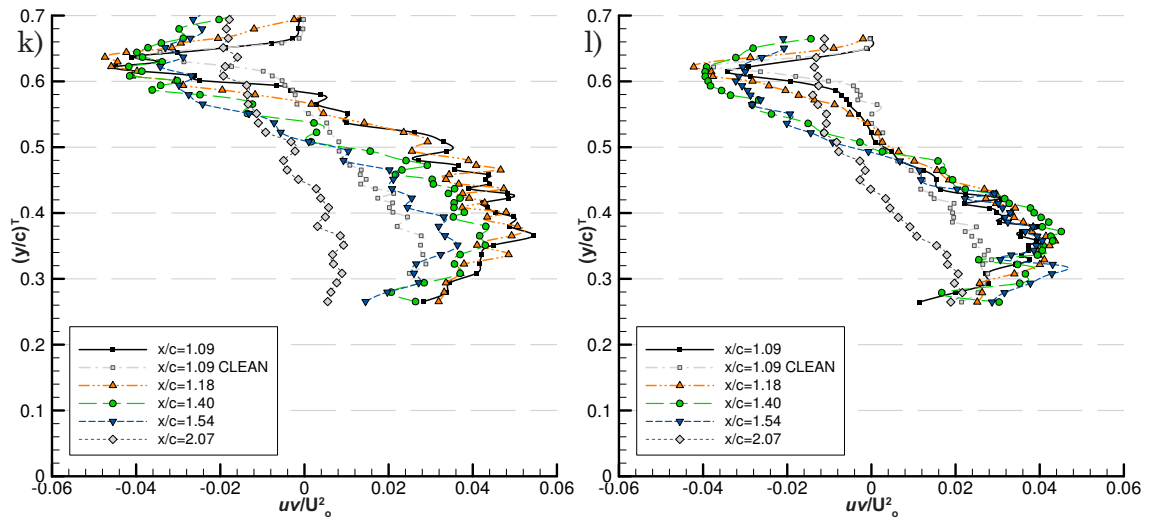
Figure F.25 Primary Shear Stress **1.5-3-23** : k) α=15˚ h/c=0.134, l) α=15˚ h/c=0.224
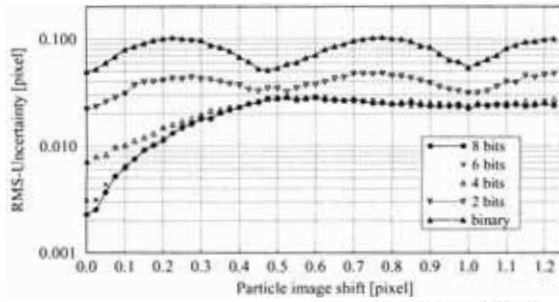
Fig. 5.30. Measurement uncertainty for single exposure/double frame PIV as a function of displacement and image quantization (simulation parameters: d_e = 2.2 pixel, N_I = 10.2, 32 × 32 pixel, no noise, optimum exposure, top-hat light sheet profile)

Figure G.1 Raffel et al. (1998)
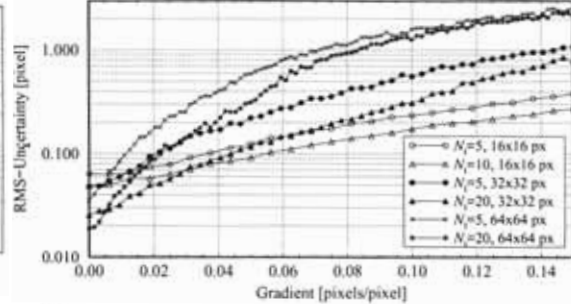
Fig. 5.33. Measurement uncertainty as a function of displacement gradient for various particle image densities and interrogation window sizes (simulation parameters: d_e = 2.0 pixel, QL = 8 bits/pixel, no noise, optimum exposure, top-hat light sheet profile)
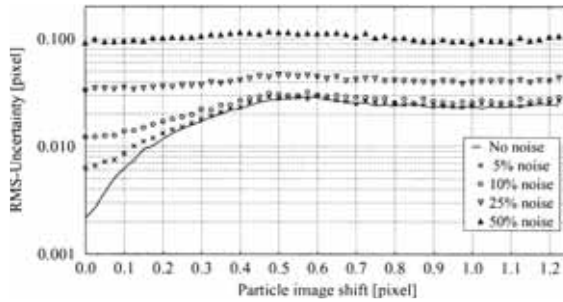
Figure G.2 Raffel et al. (1998)

Fig. 5.32. Measurement uncertainty as a function of displacement and various amounts of white background noise (simulation parameters: d_e = 2.2 pixel, N_I = 10.2, 32 × 32 pixel, optimum exposure, top-hat light sheet profile)
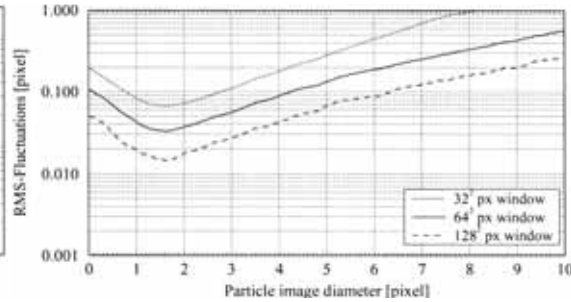
Figure G.3 Raffel et al. (1998)

Fig. 5.23. Measurement uncertainty (RMS random error) in digital cross-correlation PIV evaluation with respect to varying particle image diameter: (a) single exposure/double frame PIV imaging, (b) double exposure/single frame PIV imaging. Simulation parameters: QL = 8 bits/pixel, no noise, optimum exposure, top-hat light sheet profile, N = 1/64 pixel^{-1}.

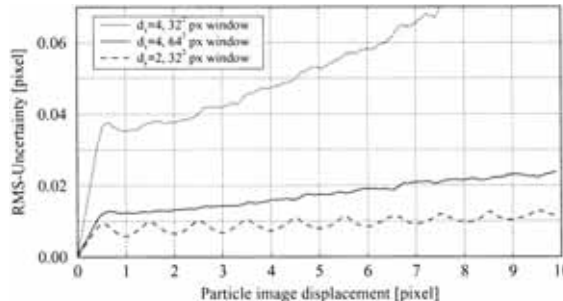Figure G.4 Raffel et al. (1998)

Fig. 5.26. Monte Carlo simulation results for the measurement uncertainty in digital cross-correlation PIV evaluation as a function of particle image displacement
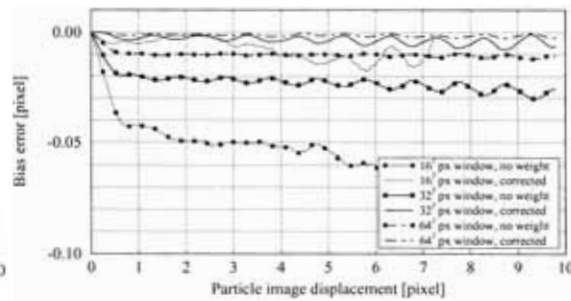
Figure G.5 Raffel et al. (1998)

Fig. 5.27. Simulation results showing the difference between actual and measured displacement as a function of the particle image displacement. Bias correction removes the displacement bias (simulation parameters: d_e = 2.0, no noise, top-hat intensity profile, N = 1/64 pixel^{-1})
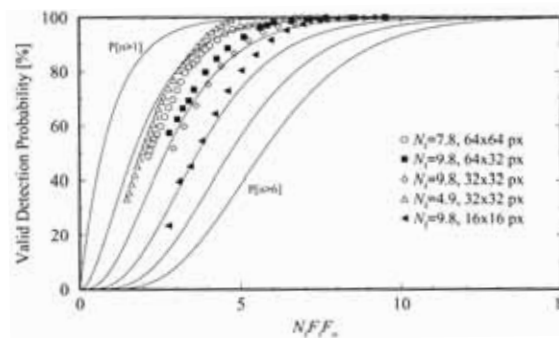
Figure G.6 Raffel et al. (1998)

Fig. 5.28. Vector detection probability as a function of the product of image density N_I, in-plane loss of pairs F_I and out-of-plane loss of pairs F_o. The solid line represents the probability for having at least a given number of particle images in the interrogation spot (see also figure 4 in KEANE & ADRIAN [66])
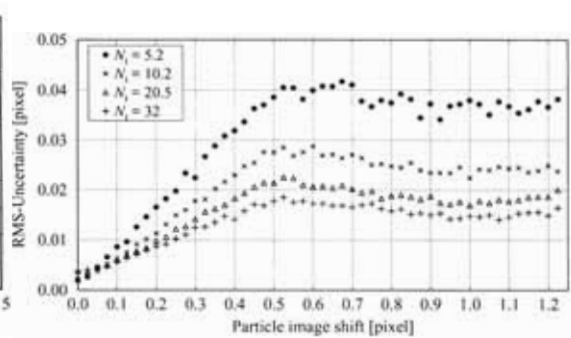
Figure G.7 Raffel et al. (1998)

Fig. 5.29. Measurement uncertainty for single exposure/double frame PIV as a function of particle image shift for various particle image densities N_I. (Simulation parameters: d_e = 2.2 pixel, QL = 8 bits/pixel, 32 × 32 pixel, no noise, optimum exposure, top-hat light sheet profile.)

Figure G.8 Raffel et al. (1998)